UNIVERSIDAD NACIONAL AUTÓNOMA DE MÉXICO
Programa de posgrado en Astrofísica

Instituto de Astronomía de la UNAM (Ensenada)

Estudio estadístico de la cinemática de distintas poblaciones de nebulosas planetarias basado en el SPM Kinematic Catalogue of Planetary Nebulae

Para optar por el grado de
DOCTOR EN ASTROFÍSICA

PRESENTA
Emma Margarita Pereyra Talamantes

TUTORES
Dr. José Alberto López García, Instituto de Astronomía
&
Dr. Michael Richer, Instituto de Astronomía

Ensenada, B.C. Septiembre 2014

A kinematic study of different populations of Planetary Nebulae base on the SPM Kinematic Catalogue

by

Emma Margarita Pereyra Talamantes

Advisors:

Dr. José Alberto López García, Instituto de Astronomía

&

Dr. Michael Richer, Instituto de Astronomía

Thesis submitted in partial fulfillment
of the requirements of the degree
Doctor of Science

Programa de posgrado en Astrofísica
INSTITUTO DE ASTRONOMÍA DE LA UNAM
UNIVERSIDAD NACIONAL AUTÓNOMA DE MÉXICO

Ensenada, B.C. September 2014

Acknowledgments

There were so many people involved in this project that I'm sure I might not be able to remember their names to list them all now. However, I would like to let them know that I greatly appreciate every one of the tips, scolding, hugs, calls, drinks and talks that made my PhD studies easier and fun. Thanks to all the people from the Instituto de Astronomía and from the Observatorio Astronómico Nacional from UNAM in Ensenada, my friends and colleagues (Fer, Isa, Steph, Maru, Jesus, Manuel, Diego, Angel, Lily, Isaura, Luis, Poli, Carlos, Tamayo, mmm ... I told you, I can't list you all) for always making me feel at home.

I want to specially thank my family, the most important thing in my life. Thank you Mom and Dad, once again, for your care, love, advice and support during these 4 years. You are my greatest blessing. To my little sister, my BFF, for all the laughs and tears we shared. Talking to you was the best method to reduce my stress, love you so much "mi gordis". Thanks to my "bro" and my older sister Diana, for always being there when I needed it. To "Tito Friend" for starting this project with me, holding my hand all the way long, ILYMB.

I would like to express my deepest and sincere gratitude to my thesis advisors, Beto and Michael. Thanks a lot for your patience and support at the different stages of this project, and for all the typos corrected at the end (so many!!). From them I learned that a good researcher requires a dedicated interest to do the best research possible. It is not just about publishing articles in leading journals, but is implies motivation, commitment and sacrifice.

From the bottom of my heart, thanks so much to everyone.

Abstract

A Planetary Nebula is, in simple terms, a shell of ionized gas produced by a star in its late stages of evolution. For more than five decades, the study of Planetary Nebulae (PNe) has played a very important role in describing the late stages of evolution of low and intermediate mass stars (1 $M_\odot$ - 8 $M_\odot$) because they represent a link between two important evolutionary stages in the lifetime of this kind of stars: the Asymptotic Giant Branch (AGB) and the White Dwarf (WD) stage. In this thesis, we have performed an study of different groups of PNe in order to understand the existing relation between the global kinematics of the nebular shell and the central star of a PN from an statistical point of view. It is well know now that the kinematical evolution of the ionized shell is directly related to the evolution of the ionizing flux and wind properties of the post AGB star. Although there are studies on the kinematics of PNe, they are usually focused on single objects or relatively small samples. For this reason, we have selected two large samples of planetary nebulae taking into account different ages, compositions and stellar populations. We considered only galactic PNe, with the aim to characterize in detail the global kinematics of the different stellar populations within our Galaxy (Disc, Halo and Bulge) with the largest sample of homogenous data used to date for this purpose.

The kinematical study is based upon spatially-resolved, long-slit, echelle spectroscopy. Every object studied in this work was selected from the San Pedro Martir Kinematic Catalogue of Planetary Nebulae (López et al., 2012). It contains high resolution spectra of 614 galactic and 211 extragalactic PNe, observed over several years from the Observatorio Astronómico Nacional in San Pedro Mártir (OAN-SPM) in Ensenada, B.C., México. The observations were obtained with the Manchester Echelle Spectrograph, a long slit, echelle spectrograph without cross-dispersion. Narrow-band filters isolate orders 87 and 114 containing Hα (including [NII] $\lambda\lambda$6548,6584) and [OIII] λ5007, respectively. The spectral resolution is 5.5 or 11 km s^{-1}, depending on the slit width,

easily resolving the internal kinematics of typical PNe. The spectra are calibrated using exposures of a ThAr lamp, achieving an accuracy of ± 1 km s^{-1} when converted to radial velocity. The use of only one catalogue for data acquisition guarantees homogeneity of the systematic errors, allowing us to get more reliable statistical results.

We present here the statistical study of two different populations of PNe. One sample contains PNe in advanced stages of evolution and the other one consider only PNe with low metal content ($\log(\mathrm{O/H})+12 \lesssim 8.0$), including the known PNe in the galactic Halo. Since most of the Evolved PNe are located within a radius of 2.5 kpc, it is likely that they belong to the disk population. In the case of low-metallicity objects, most of the selected PNe correspond to locations within the Bulge and Halo of the Milky Way Galaxy. Using these samples we were able to caracterize, in a statistical way, the kinematics of two different populations of PNe from our Galaxy.

For the Evolved PNe sample, the results reveal groups that share kinematics, morphology, and photo-ionization characteristics of the nebular shell and central star luminosities at the different late stages under study. The expansion velocities are typically larger than seen in earlier evolutionary stages, with the largest velocities occurring in objects with very weak or absent [N II] $\lambda\lambda$6548,6584 emission line, by all indications the least evolved objects in this sample. The most evolved objects expand more slowly. This apparent deceleration during the final stage of PNe evolution is predicted by hydrodynamical models, but other explanations are also possible. These results provide a template for comparison with the predictions of theoretical models.

On the other hand, we found that the velocities observed in the nebular shells of PNe with low metal content are usually small, with an average velocity value around 18 ± 2 km s^{-1}, from all the emission lines considered. For the objects with available central star data, the locations of the central stars of low metallicity PNe in the H-R diagram, confirm that this kind of objects originates from low mass progenitor stars. Similar to the Evolved PNe sample, we found that the higher velocities correspond to those objects with the highest effective temperature. However, the average velocity obtained for low metallicity objects with the hottest central stars is 24 km s^{-1}, significantly lower that the average value found for their counterparts in the Evolved PNe sample (37 km s^{-1}). Thus, we conclude that the low velocities found in this sample could be a consecuence of the weak stellar wind prevailing in low-mass stars progenitors of these low metallicity objects.

Contents

Resumen

Escribir un trabajo de tesis siempre suele ser una tarea dura y extenuante cuando se trata de explicar de manera clara y concisa, el trabajo de investigacion realizado. Con la intención de obtener un documento suficientemente digerible y sobre todo breve, la presente tesis esta dividida en 4 capítulos únicamente.

En el capítulo 1 se describen brevemente los orígenes y la motivación de este proyecto, así como algunos temas que fueron fundamentales en el estudio de las diferentes muestras de Nebulosas Planetarias (NPs)consideradas a lo largo de esta tesis, como son: el origen y formación de las nebulosas planetarias, el modelo estándar para la evolución cinemática de este tipo de objetos y las características fundamentales del catálogo utilizado para la obtención de los datos cinemáticos analizados en este trabajo.

En el capítulo 2 se muestra el análisis realizado a un grupo de nebulosas planetarias evolucionadas, presentando la publicación obtenida a partir de dicho estudio. Incluímos también una muestra de objetos evolucionados que fueron excluídos del análisis inicial debido a que las propiedades cinemáticas observadas en su cascarón nebular sugieren que podrían estar interactuando con el medio interestelar. Para evitar posibles sesgos en los resultados estadísticos obtenidos de nuestra muestra inicial de objetos evolucionados, las nebulosas que presentaban indicios de interacción con el medio fueron estudiados de manera independiente, con el fin de analizar los efectos que la interacción podría estar causando en la cinemática global de la nebulosa planetaria.

En el capítulo 3 abordaremos el estudio realizado a una muestra de 31 nebulosas planetarias cuya composición química es muy diferente a la de nuestro sol, a los que hemos denominado objetos de Baja Metalicidad.

Finalmente, el Capítulo 4 muestra las principales conclusiones del proyecto. En el documento se incluyen 5 anexos, en ellos se presentan imágenes y espectros de cada una de las nebulosas planetarias analizadas, así como un par de artículos previos a este estudio que fueron parte importante durante el desarrollo de este proyecto de tesis.

Capítulo 1

Origen y descripción de las Nebulosas Planetarias

En el siglo XVIII, los objetos observables que eran fuentes de luz difusa fueron clasificados de manera genérica como nebulosas. En 1785 William Herschel fue el primero en catalogar como nebulosas planetarias, a todos aquellos objetos cuya apariencia era como un disco verdoso, semejante a lo que se veía al observar planetas como Urano y Neptuno. Estudios posteriores mostraron que las nebulosas planetarias representaban una parte importante del proceso evolutivo de una estrella y aunque aparentemente no tenían relación directa con los planetas, el nombre se mantuvo por razones históricas. Las nebulosas planetarias, son una clase importante de objetos debido a que constituyen un vínculo entre dos etapas evolutivas sumamente relevantes en la vida de las estrellas de masa intermedia: la rama asintótica de gigantes (AGB por sus siglas en inglés) y las enanas blancas. Una descripción somera de las Nebulosas Planetarias, dada por Peimbert (1990), las define como objetos compuestos básicamente por un cascarón de gas ionizado de baja densidad, resultado de la eyección de la envolvente de una estrella. Durante la etapa AGB, la estrella se desprende de sus capas más externas dejando el núcleo estelar expuesto, que se convertirá posteriormente en la denominada estrella central de la nebulosa planetaria. Una vez que la envolvente ha sido expulsada, el aumento gradual de la temperatura superficial del remanente estelar, permite que eventualmente el flujo de fotones emergente de éste sea suficientemente energético para ionizar la mayoría del material circundante y formar lo que se conoce como el cascarón nebular. Se estima que la velocidad de expansión típica de dicha envolvente ionizada es de aproximadamente 25 $\mathrm{km\,s^{-1}}$, por lo que se esperaría que las nebulosas planetarias tarden 25,000 años en disiparse dentro del medio interestelar. Sin embargo, en este trabajo mostraremos que la velocidad del cascarón nebular no es constante a lo largo de la vida de una nebulosa planetaria, ya que depende fuertemente del estado evolutivo de su estrella central.

Respecto a las características físicas de las NP, se sabe que la densidad típica de la envolvente varía en un rango de $10^5\,\mathrm{cm^{-3}}$ para nebulosas compactas y $1\,\mathrm{cm^{-3}}$ para objetos muy extendidos. La temperatura electrónica típica en la región ionizada oscila entre $5,000\,K$ y $2,000\,K$, mientras que la temperatura superficial para la estrella central se encuentra en un rango de $30,000\,K$ y $300,000\,K$ (Peimbert, 1990).

Evolución cinemática de una Nebulosa Planetaria

Durante las últimas tres décadas, se han desarrollado diferentes modelos teóricos para describir la evolución cinemática del cascarón nebular a lo largo de la vida de una nebulosa planetaria, a partir del esquema básico del Modelo de Vientos Estelares Interactuantes (ISW model, en inglés), presentado por Kwok (1982). Dicho modelo, propone que una nebulosa planetaria es un sistema de dos componentes dinámicamente activos (Estrella + Envolvente ionizada) que no evolucionan de manera independiente. Bajo ésta hipótesis, el modelo define dos fases cinemáticas fundamentales:

Fase dirigida por momento.

a) El viento durante la AGB. La estrella expulsa el material de la envolvente estelar generando una cavidad de baja densidad entre el material eyectado y el remanente estelar.

b) Se enciende el viento rápido en el remanente del núcleo estelar y rellena la cavidad creada durante la fase de AGB.

c) El frente de onda generado por el viento rápido avanza hacia las partes más externas del cascarón hasta encontrarse con el material denso y lento, previamente eyectado en la fase AGB, ionizándolo y comprimiéndolo. Este proceso es el que dará origen al denominado "rim", la zona más brillante del cascarón nebular.

d) Debido a la alta densidad en el "rim", el frente de onda del viento rápido no es capaz de atravesarlo y choca con él como si fuera una pared rígida. Esto produce un nuevo frente de onda (un "frente chocado") en dirección opuesta al original, que se mueve hacia la estrella central.

Fase dirigida por energía.

e) La interacción del "frente chocado"con el viento rápido de la estrella forma una nueva zona de confinamiento entre la región del "rim"y la estrella central, conocida como la zona de viento chocado o "búrbuja caliente"(10^8 K), que se mueve casi isotrópicamente. Las altas velocidades involucradas en esta zona ($10^3\,\mathrm{km\,s^{-1}}$) provocan un aumento de temperatura, que conduce a una diferencia de presión entre las zonas que componen el cascarón y a la expansión de las zonas externas más frías del mismo(10^4 K).

f) El cascarón nebular se encuentra ahora en expasión por conservación de momento y por presión térmica.

Desde hace mucho tiempo los modelos hidrodinámicos predicen claramente los cambios cinemáticos que experimenta a lo largo de su vida una nebulosa planetaria (Mellema, 1994; Perinotto et al., 2004; Villaver et al., 2002). No obstante, aunque se ha demostrado una concordancia entre los modelos numéricos y los resultados observacionales en muchos objetos individuales, han sido pocos los estudios que enfrentan las predicciones de la secuencia evolutiva de los modelos hidrodinámicos con las observaciones. En gran parte, esto se debe a la falta de observaciones de muestras suficientemente grandes de NPs proviniendo de poblaciones estelares bien definidas. Usualmente, las muestras observacionales incluyen objetos de varias poblaciones estelares, haciendo difícil la meta de aislar los efectos evolutivos de aquellos efectos resultantes de las propiedades de las estrellas progenitorias. Por primera vez, el San Pedro Mártir Kinematic Catalogue of Planetary Nebulae reúne suficientes observaciones cinemáticas homogéneas que hacen factible estudiar, de manera estadística, muestras grandes segregadas según su población estelar progenitora. Estas muestras permiten definir secuencias evolutivas desde el punto de vista observacional, los cuales a su vez, permiten poner a prueba las predicciones de los modelos de una manera distinta a como lo hacen las observaciones individuales.

Descripción del proyecto

Nuestro grupo ha avanzado sustancialmente en el estudio estadístico de las nebulosas planetarias del Bulbo de nuestra Vía Láctea (ver anexo E). Sin embargo, estudios comparativos con otras poblaciones de nebulosas planetarias no han sido realizados. Con este proyecto se pretende ampliar este tipo de estudio a otras poblaciones estelares y otras fases evolutivas de una manera sistemática. Los grupos considerados para este propósito fueron los siguientes:

a) 100 Nebulosas planetarias evolucionadas: una fase evolutiva, posiblemente múltiples poblaciones progenitoras. Esta muestra fue seleccionada utilizando un criterio puramente morfológico, buscando nebulosas planetarias con rasgos característicos de objetos altamente evolucionados:

i) Esencialmente redondos, sin estructuras complejas como jets, FLIERS, lóbulos bipolares, nudos, halos extendidos o múltiples cascarones.

ii) De bajo brillo superficial.

iii) Sin "rim"ni bordes brillantes.

b) 31 Nebulosas planetarias de Baja Metalicidad: múltiples fases evolutivas, una población progenitora (probablemente baja masa). Los criterios de selección en este caso fueron los siguientes:

i) Nebulosas Planetarias con $log\,(\mathrm{O/H}) + 12 \lesssim 8.0$, obtenidos de las compilaciones de determinaciones de abundancias disponibles hasta ahora (Costa et al., 1996, 2004; Escudero et al., 2001; Górny et al. , 2004; Henry et al., 2004, 2010; Howard et al., 1997; Pereira et al., 2007; Ratag et al., 1997; Stanghellini & Haywood, 2010; Stasińska et al., 2010).

ii) Nebulosas Planetarias del Halo de la Vía Láctea. Los objetos del Halo de la Vía Láctea, al ser objetos de población II han sido clasificados como objetos con bajo contenido en metales. Sus características poblacionales se encuentran en principio bien definidas, por lo que resultan una muy buena muestra de control para los demás objetos de baja metalicidad.

Estudios presentados por Richer et al. en 2007, y posteriormente en 2008, sugieren que las nebulosas planetarias brillantes provienen de estrellas progenitoras similares en todas las galaxias, una hipótesis fundada en la similitud observada en los cocientes de las abundancias químicas y en las propiedades cinemáticas de nebulosas planetarias en muchas galaxias. No obstante, las características espectrales de nebulosas planetarias provenientes de galaxias con y sin formación estelar difieren de manera importante, lo que indica diferencias sistemáticas en las propiedades de las estrellas progenitoras, diferencias que podrían sugerir la existencia de distintas vías para producir nebulosas planetarias. Se espera que este esfuerzo aporte elementos que ayuden a esclarecer dichas discrepancias, probablemente resultantes de las características particulares que poseen las estrellas progenitoras(metalicidad, masa) en los distintos grupos propuestos para el análisis. Existen actualmente trabajos que sugieren que las nebulosas planetarias más evolucionadas poseen velocidades de expansión del orden de $10 - 20\mathrm{km\,s^{-1}}$, menores a la velocidad típica de nebulosas planetarias más jóvenes. No obstante, estos estudios parecen limitarse a grupos de objetos que carecen de homogeneidad y que aparentemente no pertenecen a una misma etapa evolutiva, pues la temperatura de sus estrellas centrales presenta discrepancias considerables entre sí (Hippelein & Weinberger, 1990). Por otro lado, generalmente estos resultados se basan en muestras con una cantidad limitada de objetos ($\leq$14 NPs), que no representa un número de objetos confiable para la obtención de resultados estadísticos concluyentes (Bohuski & Smith, 1974).

Por su parte, Medina et al. (2006) han obtenido resultados estadísticos interesantes comparando la cinemática de nebulosas planetarias típicas con aquellas que poseen estrellas centrales tipo Wolf-Rayet. Sin embargo, aunque analizan una muestra de objetos relativamente grande ($\approx$ 50 PNe), este estudio considera objetos en diferentes estados evolutivos sin ninguna distinción entre ellos. En el caso de los estudios estadísticos realizados para las nebulosas planetarias del Bulbo y extragalácticas, los resultados obtenidos demuestran cualitativamente la existencia de una conexión entre el cascarón nebular y el estado evolutivo de la estrella central. La relación encontrada corresponde a lo sugerido en estudios teóricos que proponen que el cascarón nebular es acelerado durante las etapas evolutivas más tempranas de la nebulosa planetaria. Empero, queda por investigar en detalle los efectos en la cinemática de las nebulosas planetarias debido a la masa y la metalicidad de las estrellas progenitoras, así como el comportamiento de la misma en fases tardías de evolución.

El proyecto aquí presentado nos otorga la posibilidad de investigar si esta relación es aplicable de manera general a los distintos tipos de poblaciones progenitoras y si, en el caso particular de nebulosas planetarias evolucionadas, es posible observar los efectos de dicha aceleración reflejados en la cinemática de nebulosas planetarias que se encuentran en etapas tardías.

The San Pedro Mártir Kinematic Catalogue of PN

Este catálogo posee información de alrededor de 650 Nebulosas Planetarias galácticas (López et al., 2012) y 211 extragalácticas (Richer et al., 2010a), observadas durante el transcurso de varios años desde el Observatorio Astronómico Nacional ubicado en la Sierra de San Pedro Mártir (OAN-SPM) en Ensenada, B.C.. Las ventajas que ofrece la utilización del SPM Kinematic Catalogue of Planetary Nebulae son las siguientes:

1.- Las imágenes del catálogo ya han sido reducidas y están disponibles para ser analizadas de forma inmediata, por lo que nos ofrece una ventaja sobre el tiempo destinado al análisis.

2.- Las imágenes utilizadas pertenecen a observaciones de rendija larga (6.5 minutos de arco) realizadas con el MISMO TELESCOPIO ($2{,}1m$ $f/7{,}9$) y el MISMO INSTRUMENTO (Manchester Echelle Spectrometer-SPM) con una resolución espectral instrumental (FWHM) de 5.5 u 11 km/s, lo que permite resolver fácilmente la cinemática interna de las nebulosas.

Por todo lo anterior, *The SPM Kinematic Catalogue of Planetary Nebulae* resulta una excelente herramienta para construir una muestra suficientemente amplia, observacionalmente homogénea y precisa, que permita realizar un estudio de peso estadístico.

Mediciones

Con los datos obtenidos del catálogo fue posible medir la velocidad de expansión del cascarón nebular para cada uno de los objetos a partir de las imágenes espectroscópicas. La alta resolución que nos otorga la espectroscopía Echelle de rendija larga nos da la oportunidad de obtener espectros que nos permitan observar una distribución de velocidades producida por corrimientos Doppler, tal que algunas partes del gas estarán corridas al rojo y otras hacia el azul respecto a un punto de expansión central que estará caracterizado por la longitud de onda de la línea en cuestión (ver Figura 1).

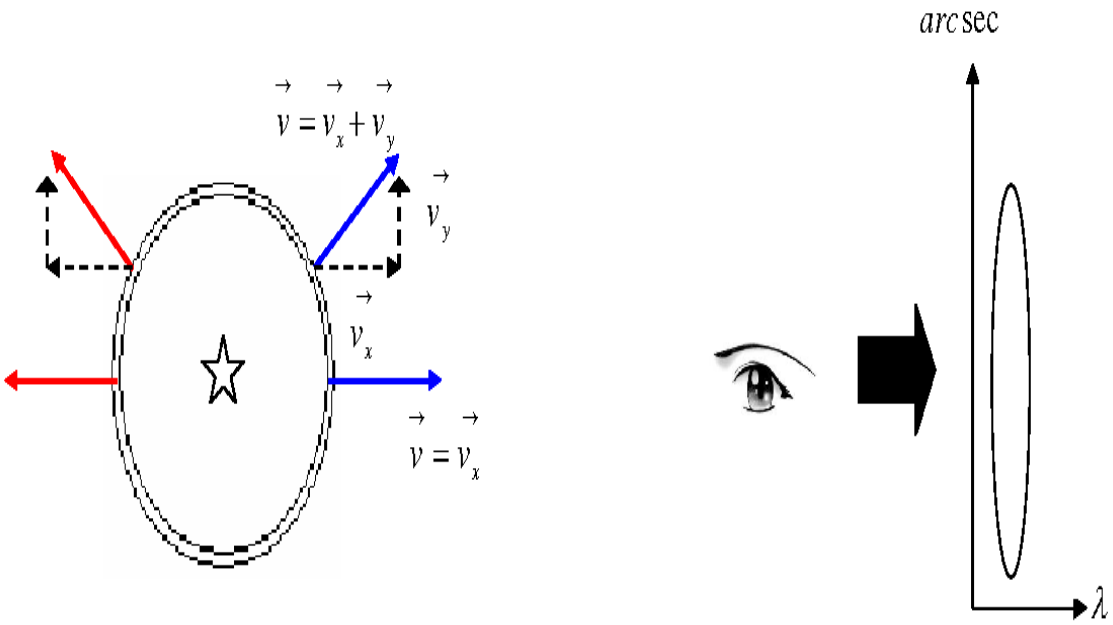

Figura 1 .- Diagrama básico de la estructura de una nebulosa planetaria esférica, formada por la estrella central y un cascarón delgado de material ionizado. A la izquierda se indican las componentes de velocidad V_x (corridas al rojo y/o al azul) que un observador es capaz de detectar, a lo largo de la rendija, bajo una línea de vista perpendicular al plano del cielo. En la derecha se muestra el elipsoide de velocidad típico que se observaría en el espectro bidimensional de una nebulosa planetaria de este tipo.

El rango espectral manejado en la mayoría de las observaciones del catálogo va desde 6500 $\breve{A}$-6600 $\breve{A}$ y permite detectar las líneas de Hα λ6563, HeII λ6560, así como el doblete de [NII]λ6548, λ6584. Para algunos objetos, fue posible obtener también espectros en el rango correspondiente a la línea de emisión de [OIII]λ5007. En el caso de las nebulosas planetarias con extremadamente bajo brillo superficial, el único espectro disponible fue obtenido en [OIII]λ5007 debido a la poca señal a ruido obtenida en el rango de Hα.

Velocidad de expansión

El método utilizado para medir la velocidad de expansión (V_{flow}), que corresponde a la velocidad de flujo del grueso del material del cascarón nebular, consiste básicamente en medir el desdoblamiento de la línea de $[NII]$, en su defecto $[OIII]$ o bien $H\alpha$. Para la mayoría de los objetos se tiene emisión de $[NII]$, pero para aquellos en los que solo se cuenta con la línea de $H\alpha$ u $[OIII]$ las mediciones se hicieron bajo el mismo método, usando el desdoblamiento de la línea, o utilizando el Full Width Half Maximum en el caso de perfiles de velocidad no desdoblados, haciendo un ajuste gaussiano a la línea de emisión y tomando su anchura media como dato. Ejemplos de los dos métodos utilizados se muestran en las Figuras 2 y 3.

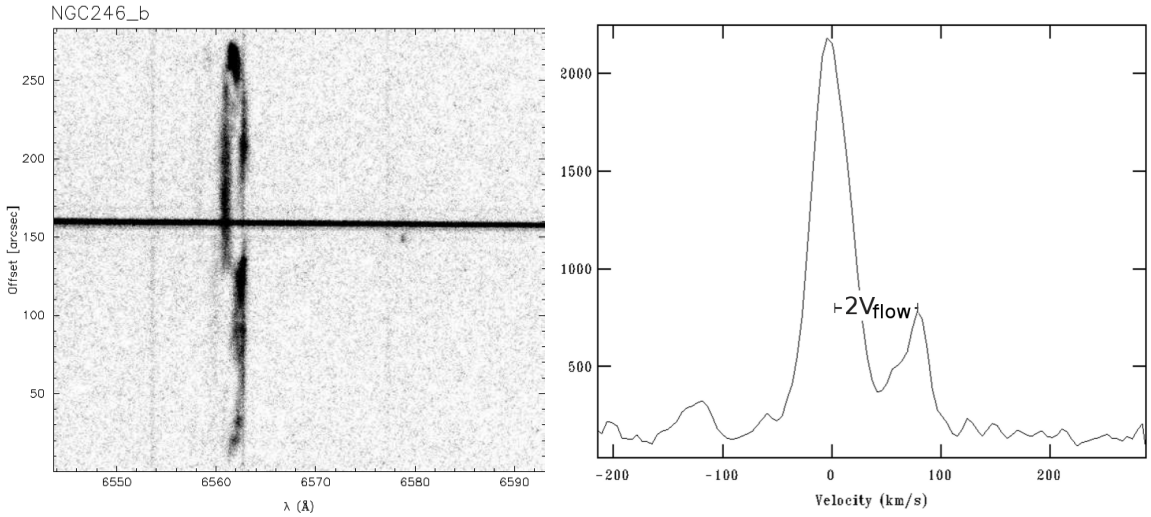

Figura 2 .- Espectro bidimensional (*izq.*) y ajustes gaussianos (*der.*) para la nebulosa planetaria NGC 246. Utilizando el paquete IRAF se realizaron cortes paralelos al eje de longitud de onda en las imagen del espectro nebular, considerando la zona correspondiente a la región central del objeto, donde se observa el mayor desdoblamiento de la línea de emisión. Esto nos permitió obtener la máxima velocidad de expansión observada en el cascarón nebular.

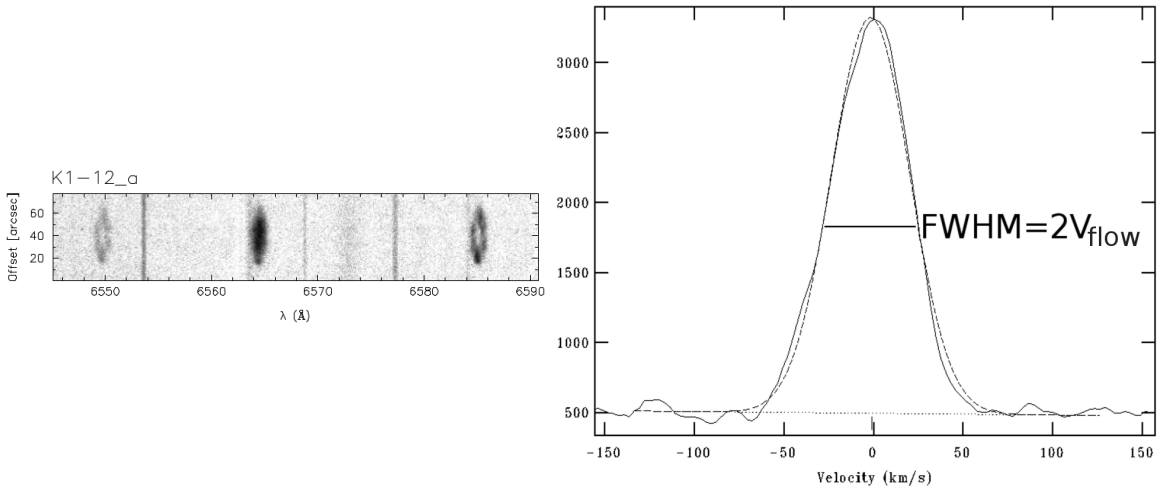

Figura 3 .- Espectro bidimensional (*izq.*) y ajuste gaussiano (*der.*) para la nebulosa planetaria K1-12. Este caso se utilizó la medida del FWHM, obtenida a partir de un corte paralelo al eje de longitud de onda en la imagen del espectro nebular en la región donde se observa el mayor ensanchamiento de la línea de emisión (la máxima velocidad de expansión).

Capítulo 2

Nebulosas Planetarias Evolucionadas

Basádos en las imágenes y espectros bidimensionales del SPM Kinematic Catalogue of Planetary Nebulae hemos seleccionado una muestra de 100 nebulosas planetarias evolucionadas. Se realizó un análisis estadístico de este grupo, con la intención de caracterizar de manera detallada la cinemática interna de las NP en esta etapa evolutiva. Los modelos hidrodinámicos actuales predicen claramente la evolución de la cinemática de las nebulosas planetarias pero son pocos, hasta la fecha, los estudios observacionales de suficiente peso estadístico que permitan sustentar dichas predicciones. Dado el tamaño de nuestra muestra y la homogeneidad de los datos utilizados, este trabajo proporciona la oportunidad ideal para empatar la teoria con las observaciones de una manera distinta a como lo hacen los estudios de objetos individuales. Los criterios de seleccion de la muestra en este caso, nos permitieron obtener solo objetos esencialmente redondos y espacialmente resueltos para nuestro estudio, por lo que mostraban el perfil tipo elipsoide, es decir, un perfil de velocidades que se muestra completamente desdoblado. Por

ello, en la mayoría de los casos, fue posible obtener mediciones utilizando el primero de los métodos mostrados en Figure 2 y 3. Sólo para 6 de las mediciones realizadas (en $H\alpha$) se utilizó el método de FWHM, lo que nos proporciona homogeneidad en la obtención de los parámetros considerados en el análisis estadístico. Dicho análisis indica que la velocidad de expansión promedio de las NP evolucionadas ($30 km\, s^{-1}$) es mayor que el valor promedio típico de expansión en nebulosas planetarias.

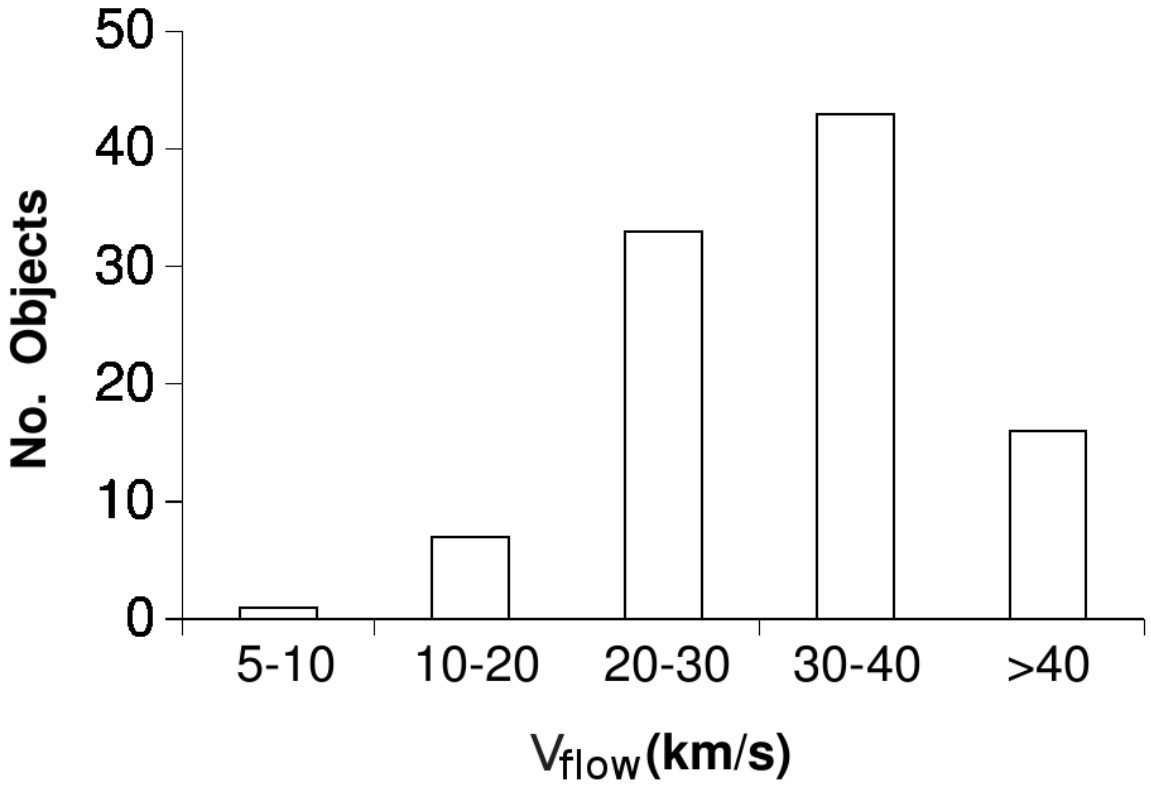

Figura 4 .- Distribución de velocidades (V_{flow}) para la muestra total de nebulosas planetarias evolucionadas.

Se observa además, la existencia de dos distintos grupos evolutivos dentro de nuestra muestra de objetos evolucionados. Los objetos que componen estos grupos comparten entre sí, características cinemáticas, morfológicas y espectrales. Los objetos moderadamente evolucionados, denominados Maduros (Mature), poseen generalmente las V_{flow} mas altas ($> 40 km\, s^{-1}$), muestran una estructura remanente de lo que pudiera haber sido el *rim* y se encuentran en la zona de alta luminosidad del diagrama H-R. Además, la mayoría de estos objetos no presentan emisión en $[NII]\lambda 6584$, probablemente debido al alto grado de ionización que posee el cascarón nebular en esta etapa evolutiva.

Los objetos más evolucionados de la muestra, clasificados como Altamente Evolucionados (Highly Evolved), tienen V_{flow} menores($< 40 km\, s^{-1}$), son poco estructurados y están localizados en la zona donde la luminosidad de la estrella central ya ha disminuído de manera considerable. Contrario a lo observado en los objetos Maduros, la emisión de $[NII]\lambda 6584$ esta presente en estos objetos (ver Figura 5).

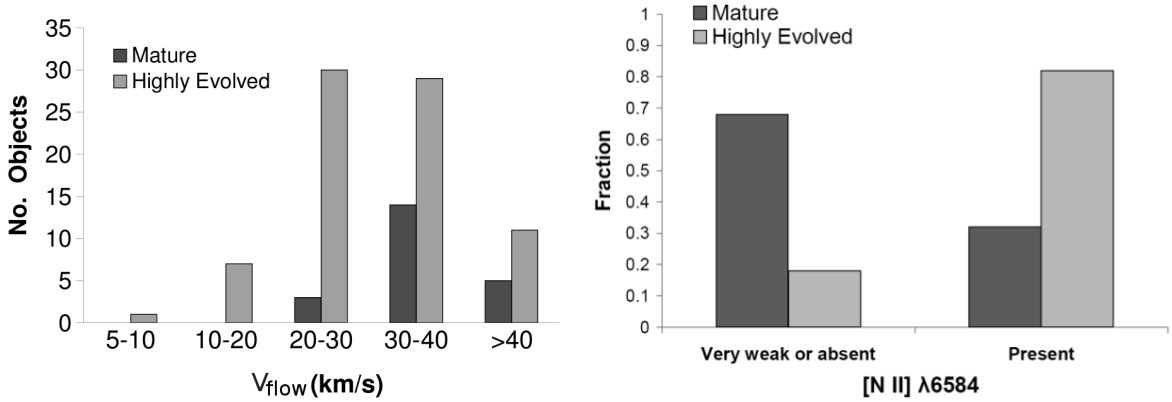

Figura 5 .- *Izquierda:* Distribución de velocidades (V_{flow}) para los grupos de objetos Maduros (Mature) y Altamente Evolucionados (Highly Evolved). *Derecha:* Fracción de objetos que muestra emisión de $[NII]\lambda 6584$ en cada uno de los grupos analizados. Las gráficas muestran claramente que las nebulosas planetarias clasificadas como Maduras tienen valores de velocidad más altos que las nebulosas Altamente Evolucionadas, y menor número de objetos con emisión de $[NII]$ presente.

Capítulo 3

Nebulosas Planetarias de Baja Metalicidad

Bajo el esquema utilizado para la muestra de nebulosas planetarias evolucionadas, se realizó el análisis cinemático de 31 nebulosas planetarias (NPs) con abundancias químicas inferiores al valor de la abundancia solar ($log\,(\mathrm{O/H}) + 12 = 8.7$), incluyendo la población del Halo (Howard et al., 1997; Peña et al., 1992). Con la intención de caracterizar la cinemática global del cascarón nebular de una población de estrellas de baja metalicidad, se consideraron objetos con un valor de abundancia en oxígeno tal que $log\,(\mathrm{O/H}) + 12 \lesssim 8.0$. Los objetos fueron seleccionados de distintas fuentes existentes en la literatura, considerando aquellos cuyos métodos de determinación de abundacias

fueran más confiables, entre los que destacan aquellos de Costa et al. (1996, 2004); Escudero et al. (2001); Górny et al. (2004); Henry et al. (2004) y Henry et al. (2010). Una vez seleccionados los objetos de baja metalicidad, los datos cinemáticos fueron extraídos del San Pedro Mártir Kinematic Catalogue of PNe (López et al., 2012). Las nebulosas de la muestra final obtenida, fueron sometidas a un último filtro de selección considerando ahora las características espectrales de las mismas. En este análisis algunos objetos fueron excluídos de la muestra inicial y presentados de manera independiente en el Anexo D, pues presentaban continuos estelares muy brillantes, característico de estrellas binarias con compañeras gigantes rojas, además de alas muy extendidas en los perfiles de H$\alpha\lambda$6562.83, las cuales son un fuerte indicador de la existencia de Dispersión Ramman, un fenómeno característico de estrellas simbióticas o nebulosas planetarias muy jóvenes que poseen una envolvente de gas frío y denso a su alrededor. Utilizando imágenes de alta resolución obtenidas del acervo en línea *Hubble Legacy Archive* fue posible identificar algunos objetos con morfología bipolar que se encontraban dentro de nuestra muestra. Sin embargo, estos objetos no fueron excluídos del análisis debido a que no parecen afectar el comportamiento general de la ditribución de velocidades encontrada.

Los resultados revelan una gran consistencia entre los valores de velocidad promedio obtenidos para el grupo de objetos del Halo con aquellos obtenidos para el grupo de Baja Metalicidad, en todas las líneas de emisión consideradas (ver Figure 6).

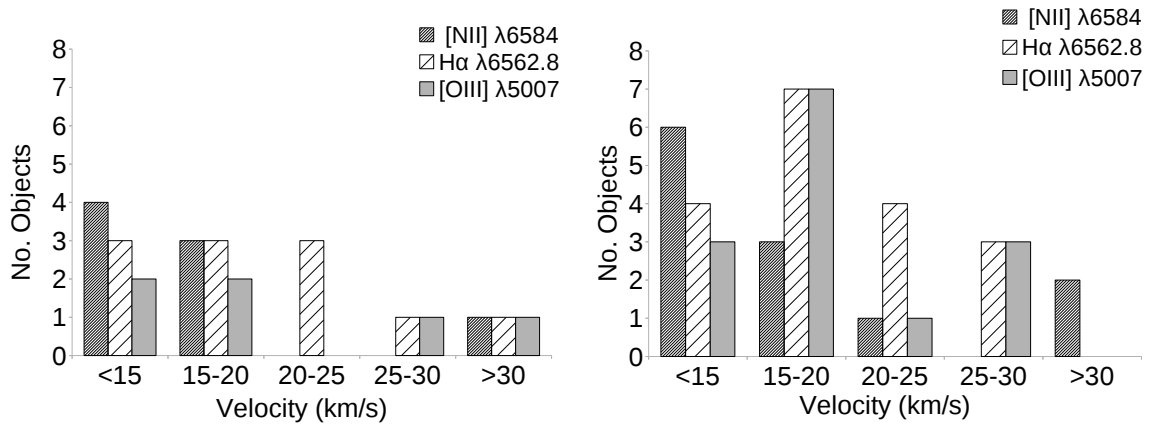

Figura 6 .- Distribución de velocidades para los 12 objetos del Halo (*izq.*) y las 19 NPs de Baja Metalicidad (*der.*), en las tres diferentes líneas de emisión disponibles para mediciones.

Dicho comportamiento sugiere que es existe una gran probabilidad que ambos provengan de poblaciones estelares semejantes (baja metalicidad y posiblemente baja masa). En consecuencia, para la muestra total (Halo + Baja Metalicidad), las velocidades típicas obtenidas resultaron generalmente más pequeñas a las observadas en las nebulosas planetarias del disco de la Vía Láctea, donde se esperan valores de abundancia cercanos a la abundancia solar.

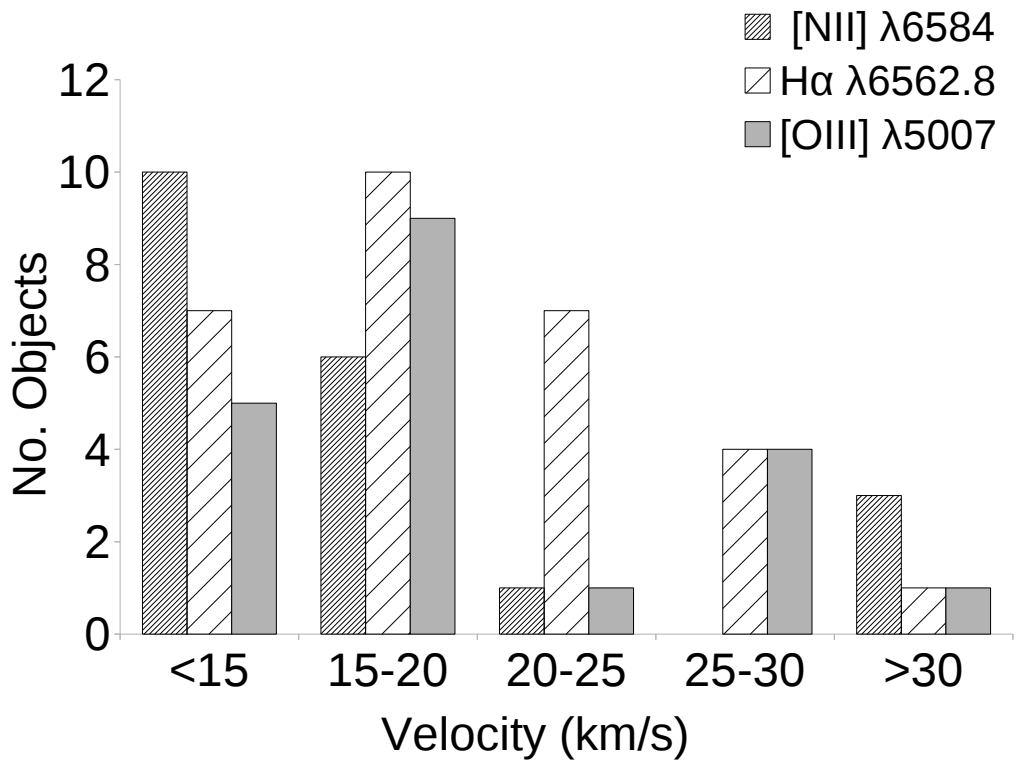

Figura 7 .- Distribución de velocidades para la muestra total de NPs de baja metalicidad.

Nuestros resultados parecen estar en contra de las predicciones de los modelos hidrodinámicos propuestos hasta la fecha (Schönberner et al., 2010), donde se propone que las velocidades de expansión de los cascarones en nebulosas planetarias con bajo contenido metálico deberán expanderse mucho más rápido. No obstante, las predicciones de los modelos estan referidas a consideraciones unidimensionales, que generalmente utilizan un mismo tipo de caracterización para la estrella central (α=3 y M_*=0.595$M_\odot$), dejando de lado las implicaciones que trae consigo considerar objetos con progenitores de muy baja masa.

Capítulo 4

Conclusiones Finales

Los resultados obtenidos en esta tesis en conjunto con los estudios previos realizados por Richer et al. (2008, 2010) permiten, por primera vez, construir un esquema general que describe la evolución temporal de la cinemática del cascarón nebular a lo largo de toda la vida de una nebulosa planetaria, tomando en cuenta tres distintas poblaciones de nebulosas planetarias galácticas.

La muestra de nebulosas planetarias del Bulbo galáctico muestra que el cascarón nebular se acelera durante las primeras etapas de la evolución de la nebulosa, conforme la estrella central se vuelve más caliente. Por otro lado, la muestra de objetos Evolucionados muestra claramente una desaceleración del cascarón en las etapas más avanzadas de evolución. Estos resultados se ilustran claramente en la Figura 8.

De esta figura, es fácil ver que la velocidad promedio encontrada para la muestra de nebulosas planetarias de Bulbo es siempre menor a los valores obtenidos para la muestra Evolucionada. Por lo tanto, podemos concluir que las velocidades del cascarón nebular de los objetos evolucionados son generalmente más altos que los del Bulbo, los cuales se encuentran en las primeras etapas de evolución, confirmando que el cascarón nebular de una nebulosa planetaria se acelera conforme la estrella central alcanza su máxima temperatura efectiva y cesa la combustión nuclear. Una vez que la luminosidad de la estrella central disminuye de manera considerable el cascarón sufre una desaceleración, en las etapas más tardías de evolución, en su camino hacia la zona de enanas blancas.

Por su parte, la muestra de Baja Metalicidad parece indicar que la mayor parte del las nebulosas planetarias con bajo contenido de metales poseen estrellas progenitoras de baja masa y que además, sus envolventes nebulares se mueven más lento que las envolventes de nebulosas planetarias típicas.

La realización de estudios estadísticos como el que se presenta en este trabajo de tesis resultan de gran relevancia en el entendimiento del comportamiento de la cinemática global de las nebulosas planetarias, pues constituyen una útil herramienta observacional que nos permite comparar los resultados obtenidos de los modelos hidrodinámicos. Este tipo de esfuerzos, requerirá indudablemente de observaciones de alta calidad, que nos proporcionen datos cinemáticos confiables y que además, nos permitan determinar con precisión los parámetros físicos de la estrella central.

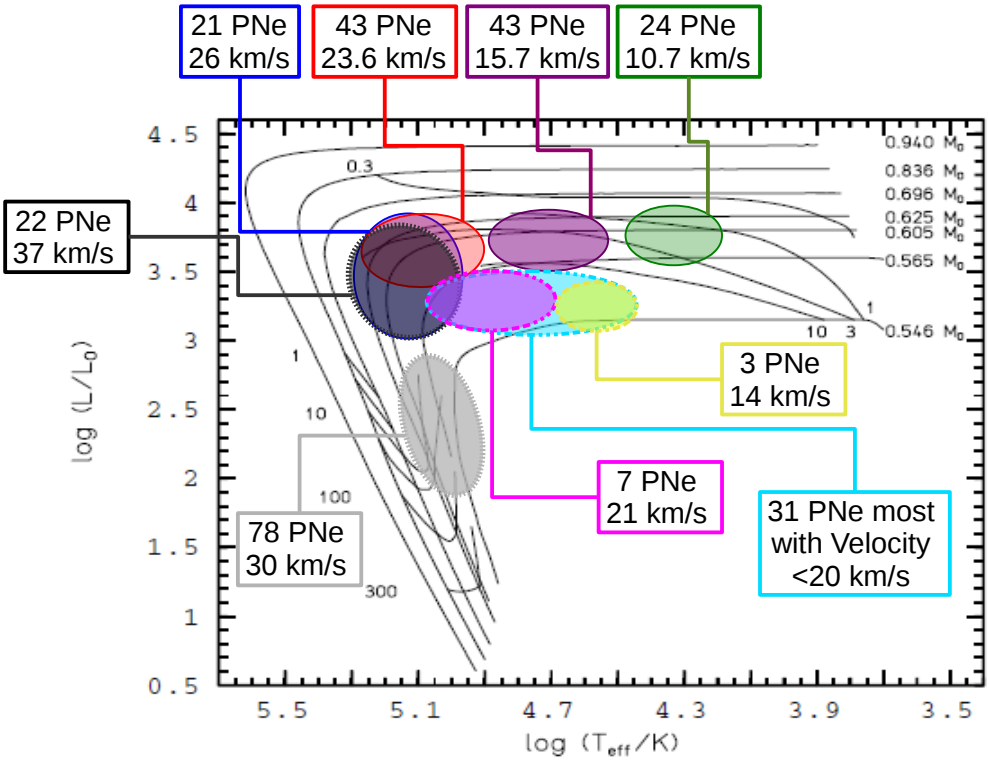

Figura 8 .- Velocidades de expansión promedio para el cascarón nebular de una nebulosa planetaria en diferentes estados de evolución de su estrella central, considerando diferentes poblaciones de nebulosas planetarias. El número de objetos cosiderados en cada grupo y su velocidad de expansión promedio estan indicadas en los rectángulos de colores, los cuales estan ligados a una ellipse del color correspondiente que indica la ubicacin aproximada de cada grupo dentro del diagrama evolutivo. Los grupos que componen la muestra del Bulbo estan representados por los colores verde, morado, rojo y azul. Los grupos de la muestra de nebulosas Evolucionadas corresponden a las elipses grises. Dado que no fue posible separar en etapas evolutivas la muestra de baja metalicidad, no se reporta en este caso una velocidad de expansion promedio pero se indica cual es el valor de velocidad tpico en estos objetos (color verde-azul). Los colores rosa y amarillo, representan dos grupos que estan compuestos por nebulosas de baja metalicidad para las cuales fue posible encontrar datos de luminosidad y temperatura efectiva de la estrella central. El diagrama evolutivo Hertzsprung-Russell, con las trayectorias evolutiva para diferentes masas de la estrella central (0.8, 1, 3 to 7 $M_{\odot}$ resp.) fue tomado de Perinotto et al. (2004). Las lneas que aparecen sobre las diferentes trayectorias evolutivas son isocronas con marcas de tiempo en unidades de 10^3 años.

Chapter 1

Introduction

Although understanding Planetary Nebulae (PNe) involves knowing the evolutionary history of a star, most current studies are focused on the nebular component of the PNe (the nebular shell) and rarely on the star itself (also called the Central Star). When we look at the central star we learn about its properties at the present time whilst when we study the properties and physical parameters of the nebular shell, we are able to infer both: the past and future of the PNe. Since the nebular shell is material ejected by the star in previous stages, it keeps information about the mass loss on the AGB and the nucleosynthesis processes that the progenitor star has experienced in the past. Futhermore, the ionization properties of the nebular shell are directly related to the physical parameters of the star at the present time, allowing us to understand its current evolutionary stage. Since the development of the *Interacting Stellar Winds Model* (ISW model) introduced by Kahn (1983) and Kwok (1982) to explain the basic structure of the nebular shell, it is clear that the kinematic evolution of the nebular shell is significantly influenced by the evolution of the central star. So, if we understand the relationship between the star and the kinematics of the nebular shell we could infer their past and make predictions about their future. In this chapter we will briefly review the theory of the origin and evolution of planetary nebulae in order to provide the necessary knowledge to understand the results obtained from the analysis made for each sample considered in this thesis work, presented in Chapters 2 and 3. We also describe here the main features of the San Pedro Mártir Kinematic Catalogue of Planetary Nebula (herafter SPM Kinematic Catalogue) and its usefulness in the performance of statistical studies such as those conducted in this thesis work.

1.1 Planetary Nebulae: Origin and Description

Historical Overview

In the eighteenth century, the observable objects that are diffuse light sources were given the generic name of Nebulae. William Herschel in 1785, was the first to analyze the nebular objects cataloged to that date and dubbed them Planetary Nebulae (PNe) to those nebulae whose observable appearance was similar to that of a greenish disc similar to what was observed for planets like Uranus and Neptune. Although it was soon established that there is no connection between planets and PNe, the name is still used today for historical reasons. At the begining of the 20th century, Planetary Nebulae were classified as young stars because, contrary to what we know today, it was believed that stellar evolution started from high temperatures and proceeded to low temperatures. However, the studies of Curtis (1918) about the velocity distributions of PNe contradicted this hypothesis, because the physical characteristics he observed in planetary nebulae seemed to be more consistent with the properties of late-type stellar objects. Theoretical understanding of the origin of PNe began with Shklovsky (1956), who suggested that PNe are progenitors of White Dwarfs (WDs) and descendants of red giants. On the other hand, Abell & Goldreich (1966) used the expansion velocity of PNe and the escape velocities of red giants to argue that PNe were the ejected atmospheres of red giants. Using the total number of galactic PNe estimated by Shklovsky (1956) and a life time of 2×10^4 yr, Abell and Goldreich showed that PNe must be forming at a rate of 3 per year, the same number of stars leaving the main sequence. Therefore, they suggested that all low-mass stars should become a PN at some point in their life, establishing the importance of PNe in the scheme of stellar evolution.

Structure of the Planetary Nebula System

In the 1990's, a planetary nebula was defined as a shell of low-density ionized gas that has been expelled by a star at a late stage of evolution (Peimbert, 1990). At this stage, the star (hereafter the Central Star or CS) has shed its outer layers leaving an exposed stellar core. Eventually, the surface temperature of the stellar remanent becomes hot enough (up to $30,000$ K) to produce photons capable of ionizing the surrounding gas to form a PN. Once the envelope of the star has been ejected and ionized by the star, the resulting structure is called *the nebular shell*.

What originally began as a star has now turned into a two component system (the central star and the nebular shell) known as a PN. Among the observational properties of PNe are the typical densities in the nebular shell that range from 10^5 cm^{-3}, for young and compact PN, to about 1 cm^{-3}, for very extended objects. The electron temperatures, T_e, for the ionized region of the shell, range from 5,000 K to 20,000 K, while the surface temperature of the CS range from 30,000 K to 300,000 K. Theoretical models of the kinematics of the nebular shell have been developed over the last three decades, since Kwok (1982) and Kahn (1983) introduced the ISW model to explain the evolution of the shell kinematics during the lifetime of a PN. Figure 1.1 is a schematic diagram of a PN, with the main components: the central star, the halo (from the remanent AGB wind) and a fast wind from the CS. It also indicates the corresponding emission from the different regions of a PN. If the PNe indeed descend from AGB

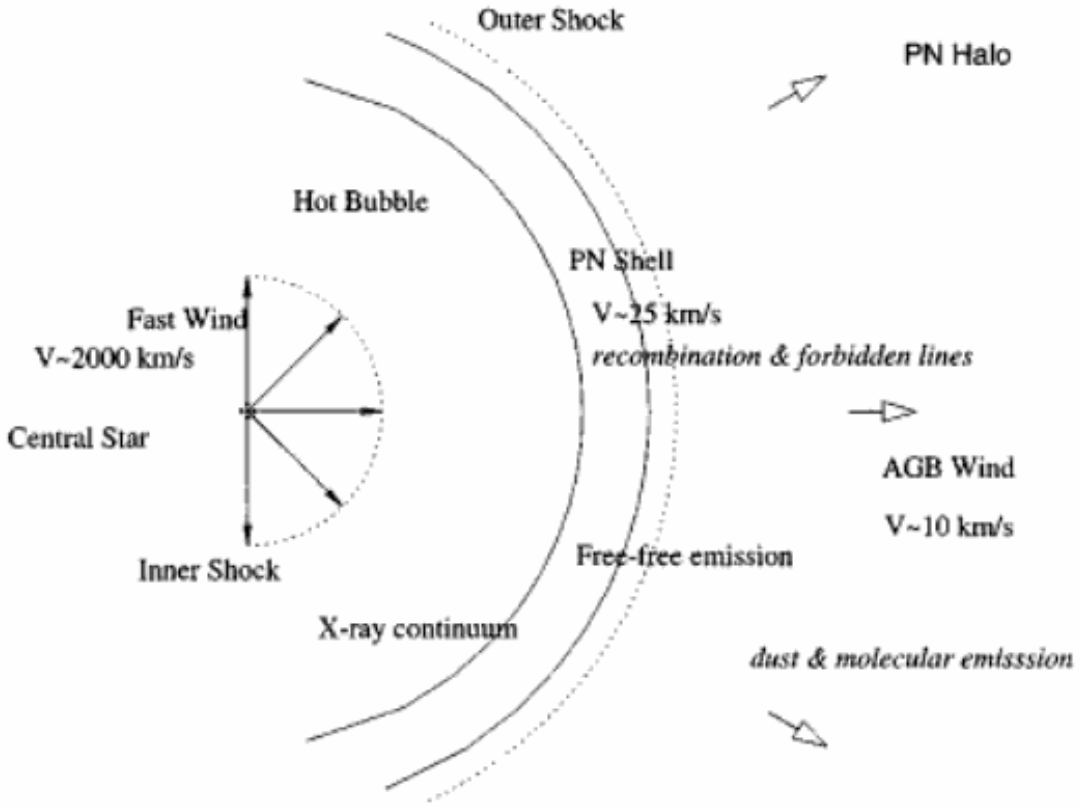

Figure 1.1 A schematic diagram of the structure of a PN from Kwok (2000).

stars which have undergone large-scale mass loss, then a dynamical interaction between the CS wind and the remanent AGB envelope is inevitable. Since the CS wind is 100 times faster than the AGB wind, it can act as a "snow plow" and sweep up the matter in the AGB wind into a high density shell (PN shell). In the simple one-dimensional adiabatic case, the interactions between the CS wind and the shell, and between the shell and the AGB wind will create two shocks. The inner shock is situated near the CS and most of the volume interior of the shell is made up of shocked CS wind with temperatures in the millions of degrees (also called the *hot bubble*). The outer shock is likely to be isothermal as the high density in the shell is efficient in cooling the gas. From this model the expected expansion velocity of the PN shell are typical values of about 25 $\mathrm{km\,s^{-1}}$, with an AGB wind velocity of 10 $\mathrm{km\,s^{-1}}$. It is now well known that a planetary nebula is a dynamic system strongly associated with the evolution of the central star. Trying to summarize the theory behind PNe, in the following section we present an overview of the theoretical and observational work existing to date about stellar and kinematic evolution of this kind of objects.

1.2 Evolution of Planetary Nebulae

1.2.1 *The Central Star Evolution*

In order to plot a star on the Hertzsprung-Russell evolutionary diagram (H-R diagram), one needs to know its luminosity and effective temperature. For most PNe it is not easy to observe the central star directly and its temperature has to be inferred from the nebular properties. To obtain the luminosity one needs to know the distance and the total emitted flux, but the difficulty of finding reliable distance determination methods and the fact that the CS of a PN emit a significant fraction of their total flux in the UV, outside the visible-optical range, may lead to an uncertain luminosity determination. In spite of the uncertainties in the observational data, our modern understanding of the correct evolutionary tracks for central star evolution began with studies made by Paczyński (1971), who based his models on theoretical considerations alone. He obtained post-AGB evolutionary tracks by beginning with AGB stars with H envelopes added on cores of various masses. Since the luminosity of a red supergiant is only dependent on its core mass but not its envelope mass, he argued that the progenitors of PN must have similar luminosities as the observed central stars of PN. Therefore,

the only candidates for the progenitors of PNe, having luminosities of $\sim 10^4\,L_\odot$, are double-shell-burning AGB stars. The properties of these stars are presented in the following, as described by Kwok (2000). *For an AGB star of core mass of* $0.6\,M_\odot$ *to evolve to an effective temperature of* $30,000\,K$ *(just hot enough for photoionization of the nebula), the envelope mass* (M_e) *estimated by Paczyński must be less than* $4 \times 10^{-4}\,M_\odot$. *For a core mass of* $1.2\,M_\odot$, *the corresponding value for the* M_e *was* $10^{-6}\,M_\odot$. *These findings had profound implications on our understanding of PN evolution because they mean that the life of a PN must be very short. Over such short times scales, the core masses are essentially unchanged and the central stars of PN will evolve with constant luminosity until the H in the H-burning shell is exhausted.* Thanks to this, we know that PN descend from double-shell-burning AGB stars and then, we can draw now the complete evolution of the central star of a PN. The annual review presented by Herwig (2005) stablished that *Asymptotic giant branch (AGB) stars are the penultimate evolutionary stage of low-mass and intermediate-mass stars driven by nuclear burning. This phase of evolution is characterized by nuclear burning of hydrogen and helium in thin shells surrounding an electron-degenerate core of carbon and oxygen, or for the most massive super-AGB stars a core of oxygen, neon, and magnesium. Prior to the AGB phase low- and intermediate-mass stars follow a characteristic evolutionary track in the H-R diagram. Such a complete evolution track is shown in Figure 1.2 for an initial stellar mass of* $2\,M_\odot$, *for solar metallicity, from the main sequence to the white dwarf evolution phase. The number labels for each evolutionary phase indicates the log of the approximate duration for a* $2\,M_\odot$ *star. The evolution starts after the star formation and pre-main-sequence evolution with the core H-burning phase (observationally the main sequence). When all H is transformed into He in the core, nuclear energy release ceases and the core contracts under the influence of gravity. H burning now starts in a shell around the He core, and in the H-R diagram the star evolves quickly to the base of the Red Giant Branch (RGB). As the core continues to contract, the envelope of the star expands and the H-shell luminosity grows. The star climbs up the RGB, or first giant branch. The star is cool and the entire envelope is convectively unstable. Eventually, the combustion is ignited in the core. The ignition of core He burning depends on the intial mass, if the initial mass is less than approximately* $1.8\,M_\odot$ *the He core will be electron-degenerate by the time the star evolves to the tip of the RGB. These stars experience a degenerate core He flash and settle afterwards in quiescent He-core burning on the zero-age horizontal branch (ZAHB).*

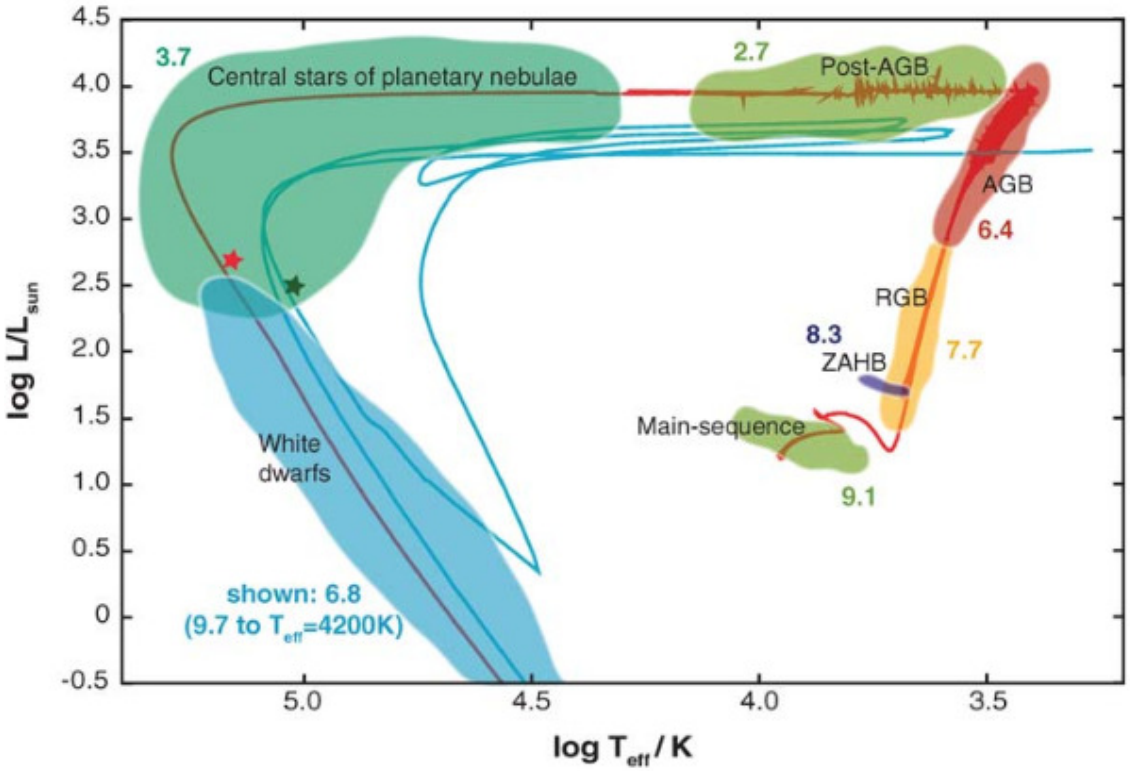

Figure 1.2 Hertzsprung-Russell diagram of a complete $2\,M_\odot$ evolution track, from Herwig (2005). Larger or smaller mass cases would have smaller or larger evolutionary timescales, respectively. The blue track shows a born-again evolution, when the central star experienced a late H or He flash, of the same mass (shifted for clarity).

Initially, more-massive stars ignite He burning in the core in a nonviolent mode and like less-massive stars continue their evolution on the horizontal branch. The He-core burning phase is about a factor of 10 shorter than the H-core burning phase. He-core burning leaves a C/O core behind that is surrounded by both a He and a H-burning shell. For stars with initially less than $8\,M_\odot$ carbon does not ignite, and the C/O core contracts and becomes increasingly electron-degenerate. During the early AGB phase, the He shell dominates nuclear production. It burns outward in mass and reaches the H shell. At that point, nuclear energy release is dominated by the H shell and interrupted periodically by thermonuclear runaway He-shell flash events. Then follows the evolution up the AGB with the characteristic thermal pulses during the advanced AGB phase. Increasing mass loss leads to the ejection of the envelope. This promotes the post-AGB evolution and finally the central star of planetary nebulae and white dwarf evolution phases.

According to Paczyński (1971), the evolution of central stars of PN can be separated into two phases:

i) First, the envelope of the remnant star has just a few percent of the total mass, but it is still able to release enough gravitational energy to maintain the temperature needed for nuclear burning at the base of the envelope. The luminosity of the star stays constant and the star evolves horizontally across the H-R diagram.

ii) When H burning shell stars to die out and the luminosity drops; the star moves to the cooling track toward the white dwarf phase.

Since 1979, these models have been improved by several authors as Schönberner (1979, 1981), Iben (1984), Wood & Faulkner (1986), Vassiliadis & Wood (1994), Blöcker (1995) and Schönberner & Blöcker (1996), by including the effects of thermal pulses. The Schönberner models show that H-burning central stars evolve three times faster than He-burning stars in the parts of the H-R diagram where PN are found and then the observed PN can be very well explained by H-burning models with core masses between 0.55 and 0.64 $M_{\odot}$. If this is the case, one may conclude that PN ejection occurrs during the quiescent H-burning phase on the AGB. However, for lower mass models (core masses $< 0.6\,M_{\odot}$) the times needed to reach $30,000$ K are much larger than the dynamical ages of PN. This problem was avoided by Schönberner & Blöcker (1996) introducing post-AGB mass loss. The choice of the termination point of AGB mass loss has significant implications on the subsequent evolution. Vassiliadis & Wood (1994) assume an early termination of mass loss, which results in longer transition times to PN and more frequent occurrence of He ignition during post-AGB evolution. Examples of evolutionary tracks obtained from the most recent theoretical models are shown in Figure 1.3. The upper panel shows evolutionary tracks for H-burning central stars from Vassiliadis & Wood (1994) with $Z = 0.0016$. Each track is labeled with its initial and final mass values. Tick marks on the upper (or left) side of the tracks are steps of 100 yrs and tick marks on the under (or right) in steps of 1000 yrs. Filled circles represent times steps of $100,000$ yrs. At the bottom panel are the tracks from Schönberner & Blöcker (1996), the isochrones and some observational data points are also showing. Time marks in this case are in units of 10^3 yrs. Although the models differ in terms of the initial conditions and parameters considered in the numerical calculations, the most noticeable difference between them is the inclusion of a very low-mass evolutionary track in Schönberner & Blöcker (1996) models.

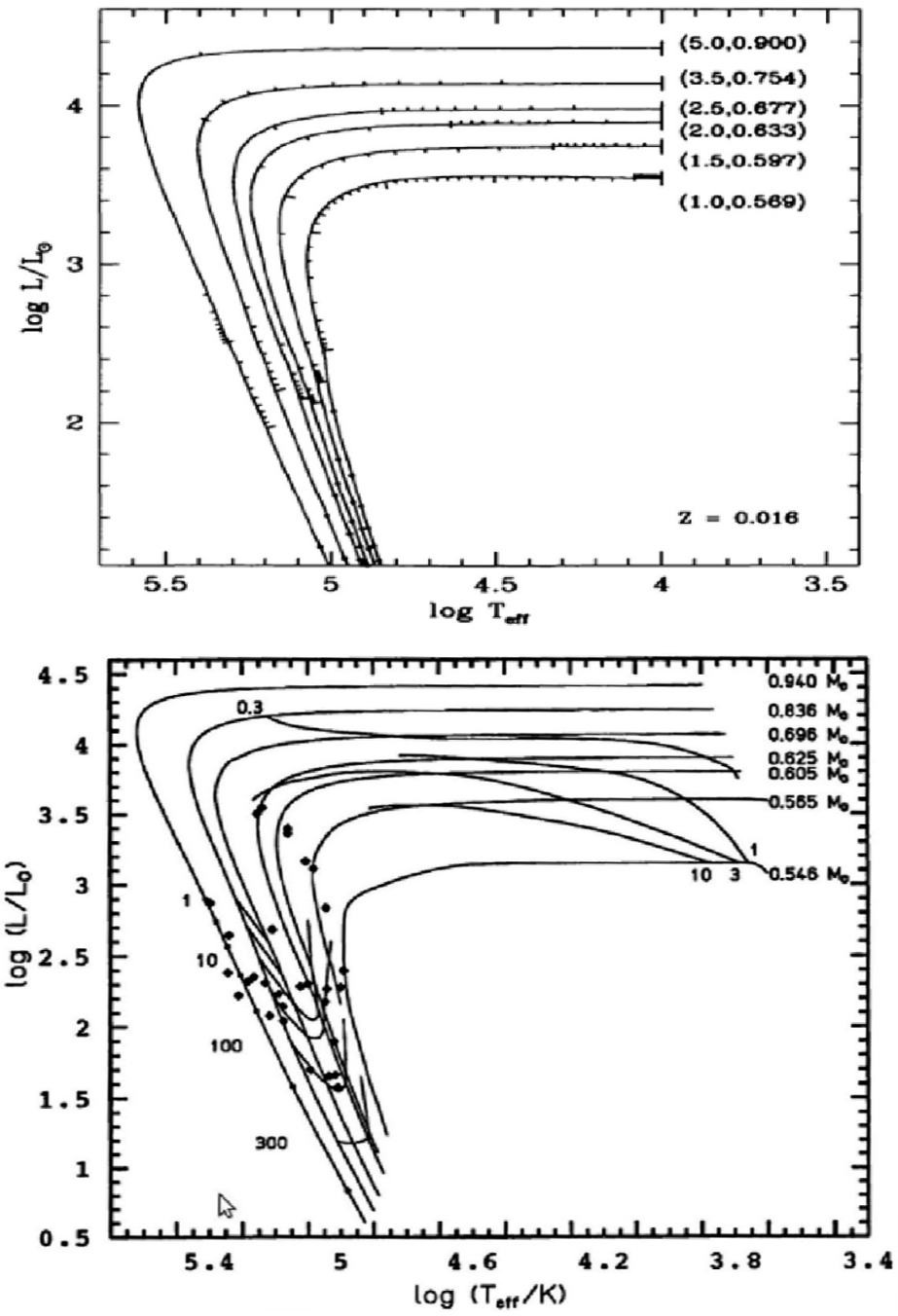

Figure 1.3 Theoretical evolutionary tracks for central stars of PN from Vassiliadis & Wood (1994) (upper) and from Schönberner & Blöcker (1996) (bottom) to ilustrate the similarity between these two models. In both models, the first part of the central star evolution is at constant luminosity, with $log\ L/L_{\odot}$ values between $3.5-4.5$, and then drops at similar values of $log\ T_{eff}$ when the stars goes towards the cooling track.

Because the theoretical evolutionary tracks cover a wide area of the H-R diagram it becomes very difficult to relate an individual star of the observed central stars of PN to an specific track. Nonetheless, it is clear that the general evolution of central stars of planetary nebulae with similar masses in the two models is almost the same. As a result, we shall use the Vassiliadis & Wood (1994) models to compare our statistical studies because they are the most used for several authors to date.

1.2.2 *The Kinematics of the Nebular Shell*

Since a PN is a two component system (star and nebular shell) that does not evolve independently, the dynamical evolution of the nebular shell should be determined by the amount of energy injected by the star through the stellar wind and the radiation field, which in turn depends on the position of the star in the H-R diagram. PNe are a consequence of the mass loss from AGB stars and therefore, the effects of a pre-existing circumstellar envelope on the dynamics of PN expansion have to be considered. Because these objects are not simply envelopes diffusing into the interstellar medium, a separate mechanism is needed to accelerate, compress, and shape the AGB envelope into PNe. Many efforts have been made on the last four decades trying to explain the kinematic evolution of the PNe. Here we present a summary of the dynamic models existing to date; introducing the mathematical description made by Kwok (2000) of the Interacting Stellar Winds model or ISW , the standard model of the kinematics evolution in planetary nebulae, and a brief review on the latest hydrodynamic models.

The Interacting Stellar Winds Model

The model was developed by Kwok (1982) and Kahn (1983) to explain the dynamical evolution of the nebular shell in planetary nebula. The two main components in the Interacting Stellar Winds (ISW) model are the previously ejected envelope of the AGB or *slow wind*, and the stellar wind of the remnant core or *fast wind*. Since the stellar wind is faster than the AGB wind, it will eventually run into the AGB wind and sweep it up like a snow plough creating a high-density shell. In this process the swept-up shell is compressed on both sides by dynamical pressure and develop a definite shell structure that is observed in PNe. The standard model consider two different phases in the kinematic evolution of the nebular shell. The mathematical basics of these phases, as described by Kwok (2000), are presented in the following.

Momentum Conserving Case

Assuming that t= 0 corresponds to the time that the slow wind ends and the fast wind begins, and the nebular shell is formed by an inelastic collision between the two winds, the mass of the shell (M_s) at time t is

$$M_s = \int_{Vt}^{R_s} \frac{\dot{M}}{V} dr + \int_{R_s}^{vt} \frac{\dot{m}}{v} dr = (\frac{\dot{M}}{V} - \frac{\dot{m}}{v}) R_s - (\dot{M} - \dot{m})t, \tag{1.1}$$

where R_s is the shell radius at time t. $\dot{M}$, V, $\dot{m}$ and v are the mass-loss rate and wind expansion velocity for the AGB and the central star respectively. The stellar radius is assumed to be much smaller than Vt and vt. From the conservation of momentum, the equation of motion can be written as

$$M_s \ddot{R}_s = \frac{\dot{m}}{v}(v - \dot{R}_s)^2 - \frac{\dot{M}}{V}(V - \dot{R}_s)^2. \tag{1.2}$$

Integrating this equation, the shell radius at time t is

$$R_s = \frac{(\dot{M} - \dot{m}) + (v - V)\sqrt{\frac{\dot{M}\dot{m}}{Vv}}}{\frac{\dot{M}}{V} - \frac{\dot{m}}{v}}. \tag{1.3}$$

If $\dot{M} = 10^{-5}\, M_\odot\, yr^{-1}$, $V = 10\ km\, s^{-1}$, $\dot{m} = 10^{-8}\, M_\odot\, yr^{-1}$, and $v = 2,000\ km\, s^{-1}$, the Eqs. 1.1 and 1.3 give $V_s = \dot{R}_s = 14\ km\, s^{-1}$ and $M_s = 0.05\, M_\odot$ after $10^4\, yrs$. Although the obtained values were comparable to the observed expansion velocities and masses of many PNe, not all PNe can be explained by the ISW model under the momentum conserving case.

Energy Conserving Case

The momentum conserving case assumes that all the excess energy of the fast wind is radiated away. However, as the wind velocity increases, eventually the cooling is not sufficiently efficient and the temperature of the gas in the post-shock region begins to rise. The thermal pressure of this very hot gas will provide additional acceleration to the nebular shell. Therefore, the ISW model had to be extended to the energy-conserving case by Kwok (1982) and Kahn (1983). In this case the formation of an adiabatic "hot bubble"is considered. Futhermore, since the temperature in the post-shock region is low

enough to allow for the existence of metal ions for forbidden-line cooling, the outer shock can be treated as isothermal and hence the resulting shell should have a thin thickness and a very high density. In order to simplify the problem, it is assumed that a contact discontinuity exists. It separates the hot bubble and the shell across which no gas or heat pass. Thus the shell is made up of swept-up slow wind only, and gas in the hot bubble is all from the central-star wind. Assuming mass conservation, the shell mass at time t is given by

$$M_s = \frac{\dot{M}}{V}(R_s - Vt). \tag{1.4}$$

Considering the adiabatic aproximation, it is found that the total energy input into the bubble from the fast wind ($\frac{1}{2}\,\dot{m}v^2$) must be balanced by change in the internal energy in the bubble. Thus, the work done because of expansion is:

$$\frac{d}{dt}[\frac{4\,\pi}{3}\,R_s^3 \cdot \frac{3}{2}\,P] = \frac{1}{2}\,\dot{m}v^2 - 4\,\pi R_s^2\,P\frac{dR_s}{dt}. \tag{1.5}$$

From these equations, the mass and pressure for the shell can be written as

$$M_s = \dot{M} \cdot (\frac{V_s}{V} - 1)t, \tag{1.6}$$

$$P = \frac{\frac{1}{2}\,\dot{m}v^2}{6\,\pi V_s^3}t^{-2}, \tag{1.7}$$

Using typical observed values for the two winds ($\dot{M} \sim 10^{-5}\,M_\odot\,yr^{-1}$, $V \sim 10\,km\,s^{-1}$, $\dot{m} \sim 10^{-8}\,M_\odot\,yr^{-1}$ and $v \sim 2,000\,km\,s^{-1}$), the obtained values are higher than the corresponding values found in the momentum conserving case ($V_s \sim 30\,km\,s^{-1}$ and $M_s \sim 0.15\,M_\odot$ after $10^4\,yr$), demostrating that the ISW model has no difficulty explaining the obseved properties of PN.

The current Hydrodynamical Models

Although the interacting stellar winds model of Kwok (1982) provides a general framework for understanding planetary nebulae, a variety of theoretical and numerical studies of the hydrodynamics have been undertaken to understand and predict the kinematic properties of planetary nebulae in the last three decades. A proper modeling of planetary nebulae starts already on the upper AGB, since the enviroment out of which they form is set up by the preceding mass loss history.

Our modern view of the kinematics of PNe was established in the early 1990's (e.g., Kahn, 1983; Mellema, 1994). These studies showed that the AGB envelope is accelerated in two phases. The first phase is a result of the shock wave initiated by the ionization front that sweeps through the AGB envelope as the central star's temperature increases. Then, as the central star's wind energy increases, it drives a pressure-driven central bubble that accelerates the AGB envelope through ram pressure. More recent numerical work that attempts to include more realistic AGB evolution confirms these basic results (e.g., Perinotto et al., 2004; Villaver et al., 2002). In these studies, the complex AGB evolution is not restricted to a simple r^{-2} density law and the consequences of long-term thermal pulse AGB at small and large scale are considered. Once again, although the analitical and numerical treatment in the models is different, the general results are quite similar. Acording to these models, the dynamical evolution of planetary nebulae can be summarized as follows:

⋆At early stages of PNe evolution, the expansion velocity of the nebular shell is similar to the AGB wind velocity ($\sim 5 - 15\,\mathrm{km\,s^{-1}}$) (Mellema, 1994).

⋆When the star becomes hot enough to ionize the nebular gas ($\sim 35,000$ K) and then drives an ionization front through the nebula, the change in thermal gas pressure increases the expansion velocity of the shell by $\sim 5 - 6\,\mathrm{km\,s^{-1}}$, in the case of solar metallicity (Perinotto et al., 2004).

⋆As the stellar wind velocity increases, the cooling processes in the shell interior becomes inefficient and the hot bubble is formed behind the leading ionized shell, inducing an extra acceleration to the nebula by $\sim 5-10\,\mathrm{km\,s^{-1}}$ (Perinotto et al., 2004).

⋆In later stages of evolution, it is expected that the central star's wind ceases, the luminosity drops and the inner parts of the envelope may backfill the region towards the central star while the outer part maintains its momentum-driven evolution (e.g., García-Segura et al. , 2006).

In recent times, the dynamical models have been used extensively to interpret observational studies of the kinematics of many individual planetary nebulae. Unfortunately, systematic, homogeneous studies of planetary nebula populations to compare with these theoretical efforts to date are scarce. For this reason it is useful to study large samples of planetary nebulae, like the ones presented in this thesis, that allow us to test the results of theoretical models in a more comprehensive way than in the studies of individual objects.

1.3 The SPM Kinematic Catalogue

To get enough observational data to analyze large samples of planetary nebulae from well-defined stellar populations is not an easy task because it requires large amounts of observing time. For the first time the SPM Kinematic Catalogue of Planetary Nebulae (*SPM-Catalogue*) draw together homogeneous kinematic observations, presented by López et al. (2012) for galactic PNe and by Richer et al. (2010a) for extragalactic PNe, that make feasible the study of large samples segregated by groups that share common characteristics, such as morphological classes, galactic population, binary cores, presence of fast outflows, etc. The SPM-Catalogue is the most extensive and homogeneous single source of data concerning the internal kinematics of the ionized nebular material in planetary nebulae. It provides spatially resolved, long-slit, echelle spectra for about of 614 galactic and 211 extragalactic PNe obtained over several years at the Observatorio Astronómico Nacional in the Sierra de San Pedro Mártir (OAN-SPM) in Ensenada, B.C., México. The data are wavelength calibrated and corrected for heliocentric motion. The spectral resolution is 5.5 or 11 $\mathrm{km\,s^{-1}}$, depending on the slit width, easily resolving the internal kinematics of typical PNe. The spectra are calibrated using exposures of a ThAr lamp, achieving an internal accuracy of ± 1 $\mathrm{km\,s^{-1}}$ when converted to radial velocity. For many objects multiple spectra have been acquired and images with accurate slit positions on the nebula are also available for each object. All of the spectra are contained in a database accessible via the world wide web at http://kincat.astrosen.unam.mx/. Every object in the PNe samples presented in this thesis was selected from this catalogue. The observations were obtained with the Manchester Echelle Spectrograph, a long slit, echelle spectrograph without cross-dispersion (Meaburn et al. , 1984, 2003) using narrow-band filters to isolate orders 87 and 114 containing Hα (including [NII] $\lambda\lambda$6548,6584) and [OIII] λ5007, respectively.

For the reasons mentioned above, The SPM-Catalogue is an excellent tool to study the kinematics of large samples of PNe; it is observationally accurate and homogeneous, allowing us to build evolutionary sequences and test the predictions of theoretical models in a statistical way, from an observational point of view. Our group has made substantial progress with the Bulge PNe sample of our Milky Way (Richer et al., 2008, 2010), but comparative studies with other populations of planetary nebulae (from different stellar populations) have not been made yet. This thesis project aims to extend the study to other stellar populations and evolutionary phases in a systematic way.

1.4 The Expansion Velocity of PNe

Finally, something that has to be considered very carefully in kinematical studies like the one performed here, is the concept of the *expansion velocity* of the nebular shell of a planetary nebula. This is a very important concept that is defined in different ways according to theoretical or observational work.

From spherically symmetric radiation-hydrodynamics simulations of PNe (Perinotto et al., 2004; Schönberner et al., 2005a), in an expanding nebular shell it is possible to define four different expansion velocities:

i).- the propagation of the outer shock (ionization front) whose distance from the star defines the actual PN radius, R_{out}, and $\dot{R}_{out}$ is the *true* expansion velocity of a PN,

ii).- the post-shock velocity,

iii).- a representative, emissivity or mass average expansion velocity, derived from the peak to peak separation of Doppler split emission line profiles, provided the spatial resolution is sufficiently high, and

iv).- a representative, emissivity or mass average velocity, from the half width at half maximum of emission line profiles of spatially unresolved objects.

However, to obtain the observational counterpart for each of these velocities presents different challenges. In the lifetime of the planetary nebula, the dynamical evolution of the nebular shell is determined by several observational properties, such as the amount of energy injected by the star via ionizing photons, the stellar wind, size, electronic density and temperature. At the early stages of PN evolution the expanding ionization front redistributes the density and velocity structures into the neutral and cool ambient of the AGB wind.

According to the hydrodinamical models presented by Perinotto et al. (2004) and Schönberner et al. (2005a) once most of the AGB wind becomes fully ionized, a double shell structure develops, consisting of the *shell* which is the remnant of the shock set up earlier by the ionization front (the outer shock), and the *rim*, created from compressed shell matter by the dynamical interaction with the central-star wind, which develops rapidly into the brightest part of a typical round/elliptical planetary nebula. To ilustrate the potential problems that must be addressed in observational estudies when

trying to measure the *true* expansion velocity defined from numerical simulations, an snapshot of a theoretical model taken from Perinotto et al. (2004) and Schönberner et al. (2005a) is presented in Figure 1.4. From this figure we can see that, once the double shell configuration is established, the outer region of the nebula (where the actual PN radius R_{out} is defined) has the lowest Hα surface brightness and thus, it is not possible to measure spectroscopically the *true* expansion velocity of a PN, $\dot{R}_{out}$, from any emission line profile.

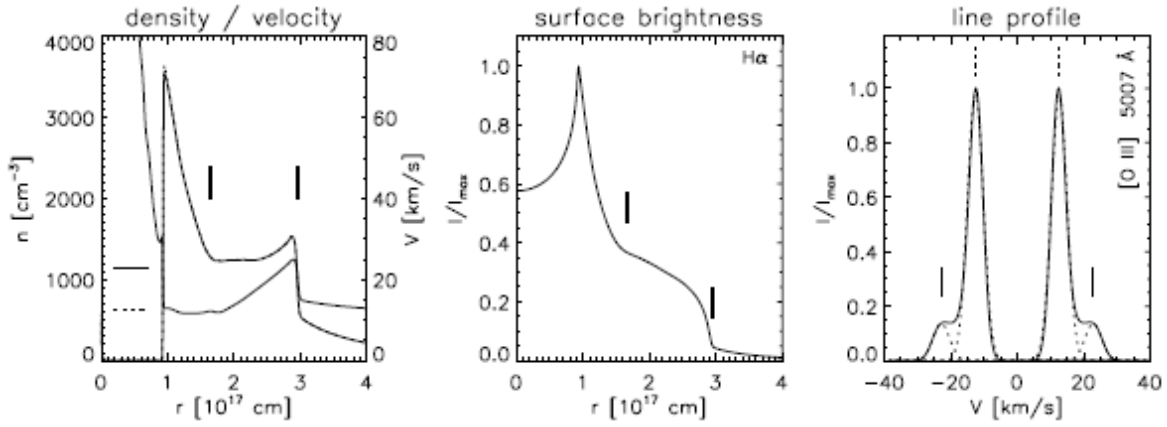

Figure 1.4 Radial dependence of heavy-particle number density (thick) and velocity (thin) (left), H surface brightness (middle), and central emission-line profile of [OIII] λ5007 (right), both normalized to their maximum emission, for a hydrodynamical model from Perinotto et al. (2004), as presented by Schönberner et al. (2005a). In the structure and surface-brightness plots, the positions of the leading shock fronts of the rim (inner) and the shell (outer) are indicated by thick vertical marks, while the thin horizontal marks in the structure panel correspond to the vertical marks in the profile panel indicating the velocities within the respective shells as they result from our decomposition of the emission-line profile (right, dotted profiles).

A similar behavior is found for the post-shock regions where, compared with the surface brightness of the brightest part of the nebular shell, a very low surface brightness is observed. Some attempts have been recently done trying to determine accurately the post-shock expansion velocity of a PN, using the derivative of the line profile, but unfortunately they require observations, on large and brigth nebulae, with high resolution (spatial and spectral) and high signal-to-noise ratio that are not always available (Corradi et al., 2007).

On the other hand, by definition, the representative velocity derived from the peak to peak separation of Doppler split or the half width of emission lines always correspond to

the regions where the bulk of matter is located and hence, the higher surface brightness is observed. From this, we can conclude that just the two last velocities from the list above will be accessible to observations and for this reason, in most observational studies, these are the velocities often referred as the expansion velocity of the PN. Taking this into account, in this thesis work we will consider the flow velocity of the bulk of matter (V_{flow}) measured from the the peak to peak separation of Doppler split or the half width at half maximum of emission line profiles (depending on the case), to describe the general kinematical behavior of the nebular shell of PNe.

Chapter 2

Evolved PNe Sample

2.1 Introduction

Large and evolved PNe were first studied in the 80's when the spatial resolution of the instruments was still unable to resolve the complex inner structures we now know exist in planetary nebulae. Later on, with the advent of the Hubble Space Telescope, the detection of structures such as bipolar, point symetric, and jets in many PNe, led astronomers to focus their attention on young objects that exhibited the most exciting structures, and evolved, essentially roundish PNe were left with little attention. Because of this, the studies about evolved PNe were scarce and generally related to the central star properties, the kinematics or other properties of the nebular shell, usually for individual objects or small groups. Examples of these previous studies are those made by Bohuski & Smith (1974), Hippelein & Weinberger (1990) and Kaler et al. (1990), from which just the two first are related to the kinematics of the nebular shell. Furthermore, these studies are based on small samples (14 PNe in the largest sample considered) complicating the task of obtaining statistically significant results from them. To address the need for reliable statistical studies about old PNe, we have analized a sample of 100 Evolved PNe selected from the SPM-Catalogue with the aim to characterize the global kinematics of the nebular shells at advanced stages of evolution. We present here our recently published results about the deceleration of nebular shells in PNe at advanced stages of evolution. Recent observational studies of the PNe at the Milky Way Bulge have already shown that, at early evolutionary stages, the nebular shell in PNe is accelerated with time (Richer et al., 2008, 2010) as predicted by the current theoretical models (Kwok, 1982; Mellema, 1994; Perinotto et al., 2004; Schönberner et al., 2005a,b; Villaver et al., 2002). With our results, it is possible for

the first time, to have a global observational overview of the evolutionary behavior of the kinematics of the nebular shell over the lifetime of the PN.

Finally, we analized the kinematics of some Evolved planetary nebulae that are classified as PNe with Interstellar Medium interaction. with the aim to understand the peculiar kinematical behavior observed in this kind of objects. The results are presented in the last section of this chapter.

2.2 Published Results

2.2.1 The deceleration of nebular shells in evolved PNe

RESUMEN

Basádos en imágenes de espectroscopía echelle de rendija larga, se estudiaron las propiedades cinemáticas de un grupo de 100 nebulosas planetarias evolucionadas que fueron seleccionadas del Catálogo Cinemático de Nebulosas Planetarias de San Pedro Mártir (López et al., 2012; Richer et al., 2010a). El objetivo del estudio era caracterizar en detalle la cinemática global del cascarón nebular en nebulosas planetarias viejas, con la muestra de datos homogéneos más grande disponible hasta la fecha para este propósito.

Los resultados revelan la existencia de dos grupos que están, dentro de los objetos evolucionados, en diferentes fases evolutivas. Los objetos de la muestra han sido catalogados como Maduros o Altamente Evolucionados dependiendo de las características cinemáticas, morfológicas y de fotoionización observadas en el cascarón nebular, así como de la luminosidad de la estrella central. Las velocidades típicas obtenidas son generalmente más grandes para el grupo Maduro, donde la mayoría de los objetos muestran emisión nebular en [N II] λ6584 muy débil o ausente. Por el contrario, el cascarón nebular de los objetos que corresponden al grupo Altamente Evolucionado, parece expandirse más lentamente. Esta aparente desaceleración en las etapas tardías de la evolución de una nebulosa planetaria ha sido anteriormente predicha por los modelos hidrodinámicos.

Mi contribución en este artículo consistió en la obtención de las velocidades para cada uno de los objetos considerados, así como la reducción de las imágenes espectrales de algunas nebulosas planetarias que fueron observadas e incorporadas durante

el desarollo del proyecto, utilizando el paquete de reducción de datos IRAF[1]. Estuve involucrada también en la elaboración y análisis de los histogramas de velocidades, de las características espectrales y morfológicas, además de realizar la revisión bibliográfica para la obtención de los parámetros físicos de las estrellas centrales y del subsecuente análisis.

Pruebas estadísticas fueron aplicadas a las distintas distribuciones de velocidad para determinar la probabilidad de que los subgrupos puedan resultar de una sola población progenitora. Dichas pruebas fueron realizadas por mis asesores, sin embargo, a lo largo del análisis logré interpretar los resultados obtenidos a partir de ellas y pude correlacionarlos con los resultados observados de las distribuciones de velocidad que había obtenido anteriormente. Utilizando este análisis estadístico, mediante las pruebas Kolmogorov-Smirnov (K-S) y Wilcoxon-Mann-Whitney (U-test) se obtuvo una probabilidad menor al 1 % de que las muestras consideradas provengan de una misma población progenitora. Esto implica que los resultados aquí obtenidos no son necesariamente una consecuencia impuesta por los criterios de selección considerados al construir la muestra de objetos evolucionados, sino resultado de las características propias y particulares de cada grupo evolutivo analizado.

Otra de las actividades en las que participé activamente, fue la redacción del texto del artículo. El primer borrador del texto fue escrito por mí, para que posteriormente fuera revisado y corregido por mis asesores. Estuve directamente involucrada también, en el proceso de revisión y respuesta al arbitraje de este artículo, que es sin duda parte fundamental en mi formación académica y profesional.

El trabajo presentado en este artículo contribuye de manera directa al conocimiento actual acerca de las nebulosas planetarias debido a que en él se presentan, por primera vez, estudios observacionales estadísticos que muestran que el cascarón nebular sufre una desaceleración en etapas tardías de evolución de la estrella central, lo cual permite poner a prueba las predicciones de los modelos teóricos desde una perspectiva distinta a la obtenida previamente en trabajos donde se considera el estudio de la cinemática de las nebulosas planetarias analizando objetos de manera individual.

[1]IRAF es distribuído por The National Optical Astronomy Observatories, el cual es operado por The Association of Universities for Research in Astronomy, Inc., en colaboración con The National Science Foundation.

The Astrophysical Journal, 771:114 (10pp), 2013 July 10 doi:10.1088/0004-637X/771/2/114

THE DECELERATION OF NEBULAR SHELLS IN EVOLVED PLANETARY NEBULAE*

Margarita Pereyra, Michael G. Richer, and José Alberto López
OAN, Instituto de Astronomía, Universidad Nacional Autónoma de México, Apartado Postal 106, 22800 Ensenada, BC, Mexico;
mally@astrosen.unam.mx, richer@astrosen.unam.mx, jal@astrosen.unam.mx
Received 2012 December 21; accepted 2013 May 17; published 2013 June 24

ABSTRACT

We have selected a group of 100 evolved planetary nebulae (PNe) and study their kinematics based upon spatially-resolved, long-slit, echelle spectroscopy. The data have been drawn from the San Pedro Mártir Kinematic Catalogue of PNe. The aim is to characterize in detail the global kinematics of PNe at advanced stages of evolution with the largest sample of homogenous data used to date for this purpose. The results reveal two groups that share kinematics, morphology, and photo-ionization characteristics of the nebular shell and central star luminosities at the different late stages under study. The typical flow velocities we measure are usually larger than seen in earlier evolutionary stages, with the largest velocities occurring in objects with very weak or absent [N II] λ6584 line emission, by all indications the least evolved objects in our sample. The most evolved objects expand more slowly. This apparent deceleration during the final stage of PNe evolution is predicted by hydrodynamical models, but other explanations are also possible. These results provide a template for comparison with the predictions of theoretical models.

Key words: evolution – ISM: kinematics and dynamics – planetary nebulae: general – stars: evolution

1. INTRODUCTION

Over the last three decades, many efforts have focused on describing the kinematic behavior of the nebular shell throughout the life of a planetary nebula (PN), from the interacting stellar wind model proposed by Kwok (1982) to the recent hydrodynamical models (Villaver et al. 2002b; Perinotto et al. 2004; Schönberner et al. 2005a, 2005b). According to these models, the kinematic evolution of nebular shells in PNe depends basically on two factors: the mass loss on the asymptotic giant branch (AGB) and the energy provided by the central star (CS) through its wind and radiation field. Initially, the nebular shell expands with the velocity of the wind ejected during the AGB phase (∼10 km s^{-1}). As the CS evolves and contracts, increasing its temperature and surface gravity, its wind velocity also increases. The now fast wind of the CS expands against the previously ejected slow wind from the AGB stage in a momentum-conserving phase, forming a high density region between them. As the CS evolves to higher temperatures, its UV radiation becomes sufficient to ionize the surrounding material and we see the nebular shell in optical line emission. The CS's radiation field drives an ionization front through the nebular shell, increasing the observed outflow velocity of the bulk of the mass (by ∼5 km s^{-1}; Chevalier 1997; Perinotto et al. 2004). Eventually, the energy accumulated behind the shock between the two winds is so high that radiation cooling becomes inefficient and an energy-driven hot bubble forms inside the shell. The pressure from the hot bubble imposes an additional acceleration upon the bulk of the nebular shell, of the order of 15 km s^{-1} (Kwok 2000), depending upon the metallicity and probably AGB wind properties (Figure 13, Schönberner et al. 2010). What happens at the latest stages of evolution is less clear, but theoretical work suggests that, after a quick drop in both CS luminosity and stellar wind energy, the hot bubble cools, allowing a deceleration of the nebular shell and a possible backflow of the inner parts of the shell toward the CS (García-Segura et al. 2006).

Our current theoretical understanding of the kinematics of the nebular shells in PNe clearly predicts an evolution of the kinematics with time (Kwok 1982; Mellema 1994; Villaver et al. 2002b; Perinotto et al. 2004; Schönberner et al. 2005a, 2005b). Richer et al. (2008, 2010) clearly recover the early evolution. Some studies provide observational support for the predictions of theoretical models during the latest stages of PN evolution (Bohuski & Smith 1974; Chu et al. 1984; Hippelein & Weinberger 1990; Kaler et al. 1990; Phillips 2002; Peña et al. 2003). However, their results are often based on small samples where the relation between the evolution of the CS and the kinematic evolution of the nebular shell is difficult to assess.

In order to gain a better understanding of the evolution of the nebular shell for PNe in advanced stages of evolution, we analyze the kinematics of a large sample (100 PNe) of evolved PN drawn from the San Pedro Mártir Kinematic Catalogue of Planetary Nebulae (SPM Catalogue; López et al. 2012), the largest homogeneous database of its kind existing today. The sample's size and homogeneity provide a greater opportunity to tie the theory to observations from a solid statistical basis. The selection criteria and the resulting data are described in Section 2. In Section 3, we present the statistical results for the kinematic behavior of the entire sample and the analysis of two distinct evolutionary stages we find. In this section, we also present the analysis for a subsample of objects for which we have adopted stellar parameters ($L/L_{\odot}$, $T_{\rm eff}$, and distance) from Frew (2008). Finally, in Sections 4 and 5 we discuss the results and summarize our conclusions.

2. THE EVOLVED PN SAMPLE

2.1. Observations and Selection Criteria

Every object in this sample was selected from the SPM Catalogue (López et al. 2012). This catalogue contains high resolution spectra of 614 galactic and 211 extragalactic PNe, observed over several years from the Observatorio Astronómico Nacional in the Sierra de San Pedro Mártir (OAN-SPM) in Ensenada, B.C., México. The observations were obtained with the Manchester Echelle Spectrograph, a long slit, echelle spectrograph without cross-dispersion (Meaburn et al. 1984, 2003).

* The observations reported herein were acquired at the Observatorio Astronómico Nacional in the Sierra San Pedro Mártir (OAN-SPM), BC, Mexico.

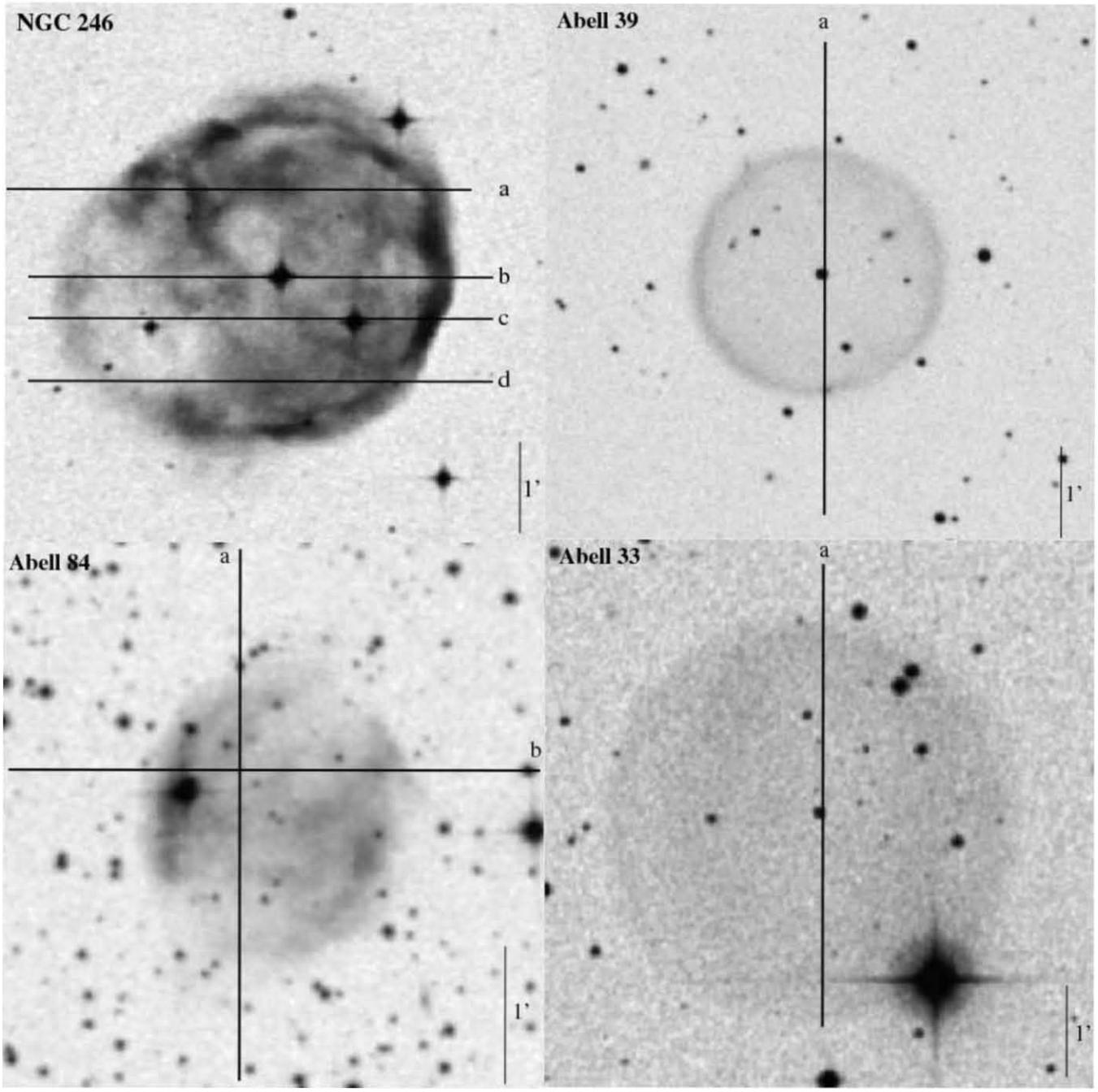

Figure 1. We present images, for NGC 246, A39, A84, and A33 to illustrate our morphological groups. NGC 246 and A39 are classified as mature PNe, because they show some remnant structure, possibly reflecting an ionization front. On the other hand, A84 and A33 are classified as HE PNe due to their completely diffuse and structureless morphology. The solid lines in each image indicate the slit position used for each object.

Narrow-band filters isolate orders 87 and 114 containing Hα (including [N II] $\lambda\lambda$6548,6584) and [O III] λ5007, respectively. The spectral resolution is 11 km s^{-1}, easily resolving the internal kinematics of typical PNe. The spectra are calibrated using exposures of a ThAr lamp, with an accuracy of $\pm$1 km s^{-1} when converted to radial velocity.

We selected a sample of evolved PNe that are extended and spatially resolved from the SPM Catalogue classifying as an evolved PN those objects with (1) essentially roundish morphology, without complex inner structures like FLIERS, jets, point symmetry, bipolarity, knots, extended halos or multiple shells, (2) low surface brightness, and (3) mostly no bright rims or edges. These objects should be those that may be compared most easily with existing one-dimensional hydrodynamical models. Within the selected group we further subdivided them into moderately evolved or mature (M) and highly evolved (HE) nebulae. The highly evolved nebulae display very low surface brightness, no inner structure, and no bright rim, whereas the mature nebulae may show some structure and/or some bright edges, but, apart from that, have the characteristics mentioned above of well developed PNe. This somewhat arbitrary classification is complemented with data for the CSs, when available, as explained below. Representative examples of both classes of evolved PNe from our sample are showed in Figure 1.

The complete sample of 100 objects is presented in Table 1. The first two columns show the common and PNG name for

Table 1
Evolved Planetary Nebula Sample

Object	PN G	$V_{[\mathrm{N\,II}]}$ ± 2(km s^{-1})	$V_{\mathrm{H}\alpha}$ ± 2(km s^{-1})	$V_{[\mathrm{O\,III}]}$ ± 2(km s^{-1})	[N II] Present	Group[a]	log L/Lo [b]	log T [b] (K)	I(He II)[c] H$\beta = 100$
A 01[1]	119.4+06.5	41	34		Yes	HE			
A 03	131.5+02.6	33	24		Yes	HE			65
A 06[1]	136.1+04.9	26	30		Yes	HE			7
A 08	167.0−00.9	37	36		Yes	HE			30
A 13[1]	204.0−08.5	24	20		Yes	HE	1.99	5.05	
A 15	233.5−16.3		25		No	HE			130
A 16	153.7+22.8			37	[O III]	HE			33
A 18	216.0−00.2	15	12		Yes	HE			
A 19	200.7+08.4	21	19		Yes	HE			
A 20	214.9+07.8		33		No	M			150
A 21	205.1+14.2	29	26		Yes	HE	2.04	5.3	
A 24	217.1+14.7	20	19		Yes	HE	1.9	5.14	33
A 26	250.3+00.1	27	17		Yes	HE			
A 29	244.5+12.5	23			Yes	HE	1.69	5.01	
A 31	219.1+31.2	18	17		Yes	HE	1.69	4.97	30
A 33	238.0+34.8			37	[O III]	HE	2.27	5	58
A 34	248.7+29.5			34	[O III]	HE	2.05	4.99	40
A 36	318.4+41.4		38		No	M	3.43	5.05	118
A 39	047.0+42.4		32		No	M	2.82	5.07	69
A 40	359.1+15.1		35		No	M			
A 42	016.0+13.5		38		No	M			
A 43	036.0+17.6		40		No	M	3.61	5.04	93
A 45	020.2−00.6	20	21		Yes	HE	2.02	5.26	
A 50	078.5+18.7	33	30		Yes	HE			34
A 57[2]	058.6+06.1		24*		Yes	M			
A 65[2]	017.3−21.9	28	26*		Yes	HE			38
A 68	060.0−04.3	37	30		Yes	HE			
A 71	084.9+04.4	22	18		Yes	HE	2.37	5.09	29
A 72	059.7−18.7		54		No	M			110
A 73	095.2+07.8	33	26		Yes	HE			
A 75	101.8+08.7		39		No	M	3.28	4.9	81
A 80[1]	102.8−05.0	23	18		Yes	HE	1.79	5.09	25
A 82	114.0−04.6	30	25		Yes	HE			15
A 83	113.6−06.9	32	25		Yes	HE			
A 84[1]	112.9−10.2	28	24		Yes	HE	1.94	5	17
DeHt 2	027.6+16.9		48		No	HE			
DS1	283.9+9.7		19	18	Yes	HE	3.48	4.95	
EGB 1	124.01+10.7	9	14		Yes	HE	2.37	5.17	
HDW 2	138.1+04.1	17	15		Yes	HE			
HDW 3	149.4−09.2	18:			Yes	HE			
HDW 6[1]	192.5+07.2	21	18		Yes	HE			
HDW 7	211.4+18.4		21:		No	HE			
HFG 1[2]	136.3+05.5			18:	[O III]	HE	3.33	5	
IC 1295	025.4−04.7	34	31		Yes	HE	2.4	4.99	50
IC 972	326.6+42.2	25	20		Yes	HE			20
Jn 1	104.2−29.6		40:		Yes	HE	2.59	5.18	50
JnEr1	164.8+31.1	35	31		Yes	HE	2.02	5.06	
K 1–1	252.6+04.4	20	19		Yes	HE			33
K 1–11	215.6+11.1	40	31		Yes	HE			
K 1–12[2]	236.7+03.5	23	22*		Yes	M			
K 1–13	224.3+15.3	47	42		Yes	HE			
K 1–14	045.6+24.3			58	No	M			155
K 1–20	110.6−12.9	37	33		Yes	M			10
K 1–22	283.6+25.3	40	33		Yes	HE	2.3	5.06	10
K 1–28	270.1+24.8		30		No	M			
K 1–3	346.9+12.4	22	20:		Yes	HE			25
K 2–1	173.7−05.8		34		No	HE	2.63	5.05	115
K 2–16	352.9+11.4	30	29		Yes	HE			
K 2–5	014.9+06.4	37	27		Yes	M			
Kn 34	149.1+08.8	38	35		Yes	HE			
Kn 36[2]	PASA2010-1	30	26		Yes	HE			
Kn 37	165.5−05.2		26		No	HE			
Kn 39[2]	PASA2010-2		31:,*		Yes	HE			
Kn 40	198.9−06.1		32		No	HE			
Lo 11	340.8+12.3	48	47		Yes	HE			

Table 1
(Continued)

Object	PN G	$V_{[\mathrm{N\,II}]}$ ±2(km s^{-1})	$V_{\mathrm{H}\alpha}$ ±2(km s^{-1})	$V_{[\mathrm{O\,III}]}$ ±2(km s^{-1})	[N II] Present	Group[a]	log L/Lo [b]	log T [b] (K)	I(He II)[c] Hβ = 100
Lo 12	340.8+10.8	34	33		Yes	HE			
Lo 13	345.5+15.1		20		No	HE			
Lo 8	310.3+24.7		50:		No	HE	3.89	4.95	
LoTr 1	228.2−22.1			22	Yes	HE			
LoTr 5	339.9+88.4			31	[O III]	HE	2.01	5	
NGC 1360[2]	220.3−53.9		28		No	M	3.3	5.04	120
NGC 1501	144.1+06.1	41	39		Yes	M	3.66	5.13	70
NGC 246	118.7−74.7		40	37	No	M	3.63	5.15	100
NGC 3587	148.4+57.0	40	34		Yes	HE	1.95	5.02	14
NGC 7094	066.7−28.2		38		No	M	3.61	5.04	120
NGC 7139	104.1+07.9	38	33		Yes	M			14
NGC 7293	036.1−57.1	21			Yes	HE	1.95	5.04	10
Pa 5	076.3+14.1		42	46	No	HE			
Pa 9	189.1−07.7	38:	37		No	HE			
PHR J0843−2514	248.5+10.5		31	32	No	HE			
PHR J1710−3732	348.7+01.3	31	29		Yes	HE			
PHR J1715−2905	356.2+05.3			51	[O III]	HE			
PHR J1734−2000	006.2+06.9		40		No	HE			
PHR J1754−3533[2]	355.2−05.0		30*		No	HE			
Pu 1	181.5+00.9	21	22*		Yes	HE			20
Pu 2	173.5+03.2		23	22	No	HE			
PuWe 1[2]	158.9+17.8	30	34		Yes	HE	1.7	5.04	37
Ri 1	204.8+02.7	26	26		Yes	HE			
Sa 2–21	238.9+07.3	38	29		Yes	M			
SaWe 1	233.0−10.1		32		No	HE			
Sb 32	349.7−09.1	38	33		Yes	HE			
We 1–1	121.6+03.5	31	22		Yes	HE			15
We 1–10	086.1+05.4	27:			Yes	HE		4.76	
We 1–2	160.5−00.5	26	18		Yes	HE			
We 1–3[2]	163.1−00.8	28			Yes	HE			
We 1–4	201.9−04.6	18	21		Yes	HE			
We 1–5	216.3−04.4		34		No	M			95
WeSb 1	124.3−07.7	27	25		Yes	HE			
Wray16–22	255.7+03.3	39	34		Yes	HE			
YM16	038.7+01.9	25	26		Yes	HE			

Notes.
[a] The HE and M classifications correspond to highly evolved and mature objects, respectively.
[b] Data taken from Frew (2008).
[c] The I(He IIλ4686) data were taken from Tylenda et al. (1994).
[1] Slit position is not at center of the PN. Lower limit for V_{flow}.
[2] Upper limit for V_{flow}.
* V_{flow} measurement obtained from the FWHM of a Gaussian fit.
: Very faint PN. Velocity measurements must be treated carefully.

each object. Columns 3–5 present our measurements of the bulk flow velocity (V_{flow}), from [N II] λ6584, Hα, and [O III] λ5007. Columns 6 and 7 indicate when the [N II] λ6584 emission is present and the evolutionary group, respectively. Columns 8, 9, and 10 list the temperature and luminosity for the CS (Frew 2008) and the He II λ4686 intensity (Tylenda et al. 1994), respectively.

2.2. Measurements

The calibrated spectra were analyzed using the IRAF[1] package to obtain the bulk flow velocity, V_{flow}. Given the high spectral resolution and our selection of essentially round and spatially resolved objects, we expect that a spherical expansion will be represented by the shape of a typical velocity ellipse in the bi-dimensional line profile or position–velocity (P–V) diagram (e.g., Figure 2).

We measured the bulk flow velocities, V_{flow}, as half the peak to peak difference in velocity between the blue- and red-shifted components at the point of maximum splitting, usually the center of the line profile. Thus, these flow velocities correspond to the typical outflow velocities for the matter with the highest emission measure within the spectrograph slit. Although this is often what is usually understood as the expansion velocity, in strict terms the expansion velocity should be understood as the velocity of the outer shock (e.g., Schönberner et al. 2005a).

For six objects (K1–12, A65, Kn39, A57, Pu1, PHRJ 1754−3533), the Hα line profile shows no splitting. For these few cases, we fit a single Gaussian profile to the line profile and assign half of the resulting FWHM as the bulk flow velocity (Gesicki & Zijlstra 2000). We correct the measured FWHM

[1] IRAF is distributed by the National Optical Astronomy Observatory, which is operated by the Association of Universities for Research in Astronomy, Inc., under cooperative agreement with the National Science Foundation.

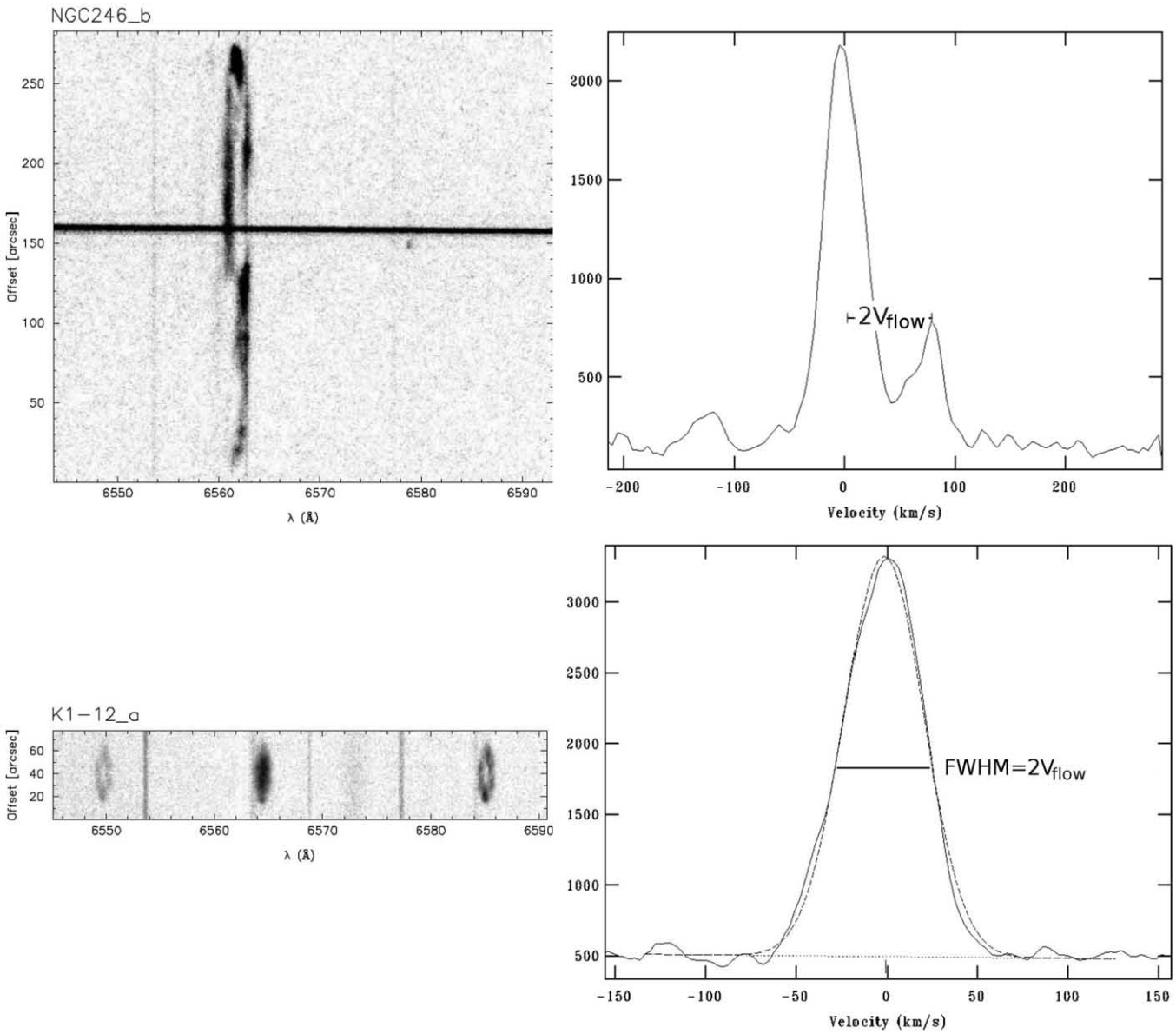

Figure 2. We present our data for NGC 246 and K1–12 to illustrate our method for determining the bulk flow velocities in the objects of our sample. In the top panel, the Hα line profile for NGC 246 is clearly split and the bulk flow velocity is taken as half the peak to peak difference in velocity between the blue- and red-shifted components at the point of maximum splitting, at the center of the line profile in this case. In the bottom panel, the Hα line profile for K1–12 is filled, so we fit a single Gaussian profile to the line profile and assign half of the resulting FWHM as the bulk flow velocity. We used the first method in the great majority of cases, including all measurements of the [N II] λ6584 and [O III] λ5007 lines, but the second was required for six Hα measurements (see Table 1).

for instrumental broadening (11.5 km s^{-1} FWHM), thermal Doppler broadening (assuming a temperature of 10^4 K), and fine structure broadening (assuming a value of 7.5 km s^{-1} FWHM; García-Díaz et al. 2008) as in Richer et al. (2008). Examples of both kinds of measurement are shown in Figure 2. We measured $V_{\rm flow}$ from all available spectra (Hα, [N II] λ6584, and [O III] λ5007 emission lines, as may be the case).

3. RESULTS

3.1. Velocity Distributions

The histogram in Figure 3 shows the distribution of bulk flow velocities for our entire sample. Most of the PNe in this sample have bulk flow velocities exceeding 25 km s^{-1}, in good agreement with the predictions from theoretical models (Villaver et al. 2002b; Perinotto et al. 2004), though there is a group of nebulae also found at lower velocities. The bulk flow velocities in Figure 3 are those measured from, in order of preference, [N II], [O III] and Hα, depending upon the velocities available.

Figure 4 presents the distributions of the mature and HE PNe. The mature PNe preferentially populate the bins at higher bulk flow velocities. The bulk flow velocities of HE PNe span a wide range, but tend to lower values than typically found for mature PNe (see also Hippelein & Weinberger 1990). The median bulk flow velocities are 37 km s^{-1} for mature PNe and 30 km s^{-1} for HE PNe. Based upon their CS properties and nebular spectra, HE PNe are more evolved than mature PNe.

The mature PNe also distinguish themselves spectrally. The [N II] λ6584 emission line is often absent in mature PNe. From Figure 5, it is clear that weak or absent [N II] λ6584 emission is a common feature in the mature PNe, but not for HE PNe, since most of the latter have [N II] λ6584 emission even though they present no evidence of an ionization front. In Figure 6, objects

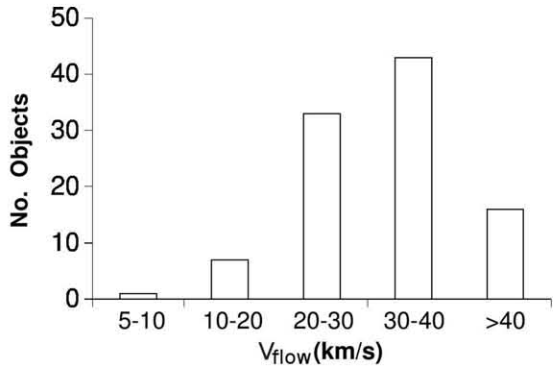

Figure 3. We present a histogram of the bulk flow velocities of the nebular shell for the evolved PNe in our sample. Here, we use velocity measurement from the [N II] λ6584 line when available. Otherwise, we use the bulk flow velocity from [O III] λ5007 or, as a last resort, Hα. The average $V_{\rm flow}$ for our sample PNe (31 km s^{-1} or 29 km s^{-1} using $V_{\rm H\alpha}$ only) is higher than the average $V_{\rm flow}$ for younger PNe ($\sim$25 km s^{-1}; Richer et al. 2008).

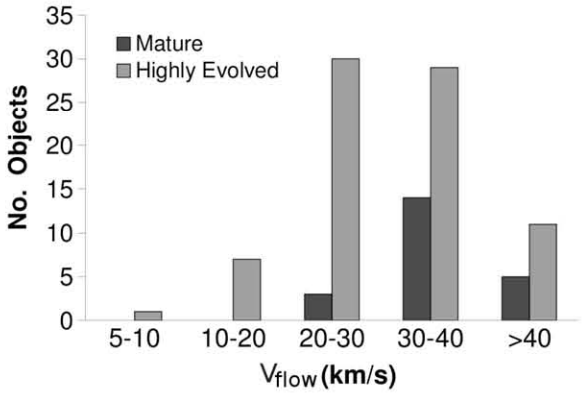

Figure 4. These histograms present the distribution of bulk flow velocities for mature and HE PNe. The bulk flow velocities for the 22 mature (M) PNe are biased to larger values than those for the 78 highly evolved (HE) PNe. The mean bulk flow velocity and standard deviation about the mean are 37 km s^{-1} and 8 km s^{-1} for mature PNe and 30 km s^{-1} and 9 km s^{-1} for HE PNe. These histograms use the same bulk flow velocities as in Figure 3.

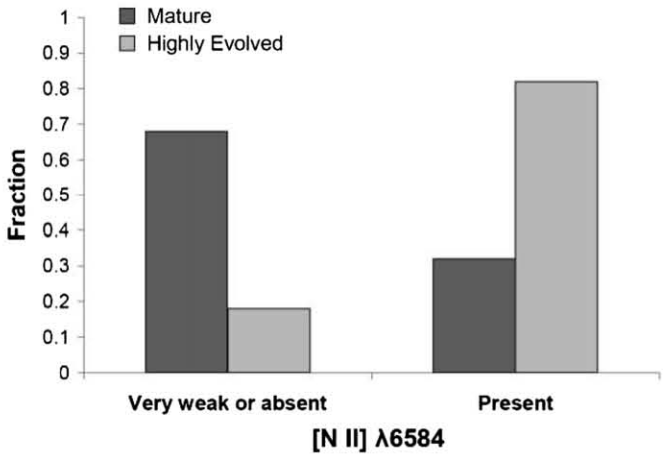

Figure 5. The presence or absence of [N II] λ6584 emission correlates with the morphological classes of mature and HE PNe. The mature objects from our sample tend to have very weak or absent [N II] λ6584 emission whereas the HE PNe present emission in this line.

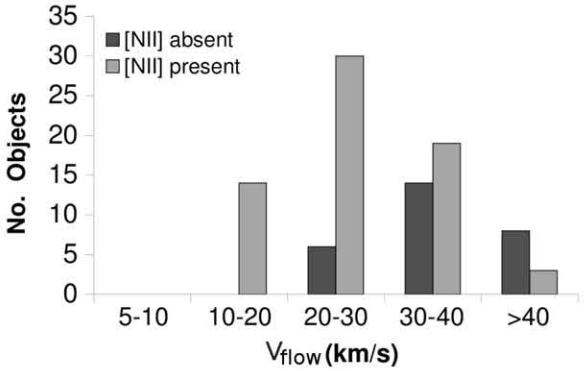

Figure 6. The incidence of the [N II] λ6584 emission line is not random as a function of the bulk flow velocity of the nebular shell, $V_{\rm flow}$. The absence of [N II] λ6584 emission is a common characteristic of objects with high $V_{\rm flow}$ whilst the opposite behavior is observed for objects with low $V_{\rm flow}$. The similarity of this result with that of Figure 4 implies that our classification selects distinct evolutionary phases. For consistency, in this plot we use velocities measured from Hα only.

with weak or absent [N II] λ6584 emission have higher bulk flow velocities than do PNe who present this emission. The similarity of Figures 4 and 6 indicates that our rough classification indeed distinguishes two different evolutionary stages.

The spectral difference between HE and mature PNe found in Figure 5 introduces a systematic bias into Figure 4. Typically, the [N II] velocities are usually slightly larger than the [O III], and Hα velocities (the latter two are similar; cf. Table 1). On average, then, the bulk flow velocities used for HE PNe in Figure 4 will be slightly overestimated compared to those used for mature PNe. This bias acts to *minimize* the difference between the two samples, so, in spite of this bias, the difference between the two samples persists and does not affect the basic result (see Section 3.3, Figure 10, panel (c)).

3.2. Location in the H-R Diagram

From the discussion in Section 1, we expect the CSs in our sample of PNe to be found on or near the white dwarf cooling track in the H-R diagram. We searched for luminosities and temperatures for the CSs in our sample to locate them in an H-R diagram (e.g., Kaler et al. 1990; Stanghellini et al. 2002; Frew 2008, among many others). To avoid the uncertainties due to different distance scales (different systematic errors), we adopted the data based upon the Frew (2008) distance scale. Our primary reasons for doing so are that this distance scale was designed for evolved objects, there exist data for a large number of our objects, and the concordance with theoretical evolutionary tracks is reasonably good (Vassiliadis & Wood 1994; Schönberner & Blöcker 1996; Stanghellini & Renzini 2000).

In Figure 7 we present the H-R diagram of our objects with available data, with different symbols for our two classes (mature or HE PNe). Again, there is a clear separation, indicating that the two classes represent distinct evolutionary stages. Mature PNe are located near the point of maximum temperature of the evolutionary tracks. These objects are therefore at a moderately evolved stage and have high luminosity CSs. On the other hand, the vast majority of HE PNe are well down the white dwarf cooling track and have low luminosity CSs.

In Figure 8, we present the same data, but now using different symbols for different ranges of bulk flow velocities. Again, there is a clear general trend for the evolution of the kinematics of the nebular shell, with the highest bulk flow velocities found at the highest luminosities and the lowest velocities at the lowest luminosities. In general, as the CS luminosity declines, we observe a deceleration of the nebular shell, as predicted by some hydrodynamical models (Villaver et al. 2002b; Perinotto

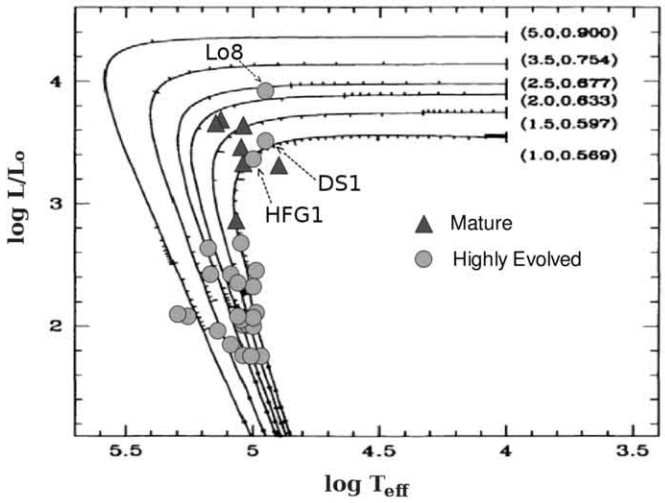

Figure 7. The locations of mature and HE PNe in the H-R diagram, with evolutionary tracks from Vassiliadis & Wood (1994), reveal a systematic difference, again reflecting different evolutionary stages. Mature PNe (8 PNe) have systematically higher luminosities than HE PNe (24 PNe), which are already evolving toward to white dwarf phase. DS 1 and HFG 1 contain binary central stars whose luminosities are uncertain.

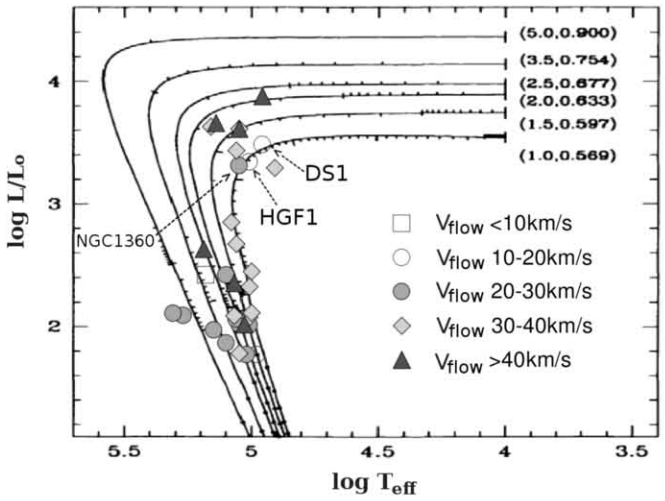

Figure 8. We find a clear evolution of the kinematics for the most evolved phases of evolution of the nebular shell. The nebular shell decelerates systematically as the central star luminosity decreases. The mean bulk flow velocity and standard deviation about the mean are 37 km s^{-1} and 4 km s^{-1} for mature PNe (8 PNe) and 28 km s^{-1} and 10 km s^{-1} for HE PNe (24 PNe), similar to what are found for the entire sample (Figure 4). Here, we use the same bulk flow velocities as in Figure 3. Although there is some mixture of velocities at high and low luminosities, we find a clear decrease in the V_{flow} as the CS luminosity drops. Again, the evolutionary tracks are from Vassiliadis & Wood (1994). DS 1 and HFG 1 contain binary central stars whose luminosities are uncertain.

et al. 2004). Since we use the same bulk flow velocities as in Figures 3 and 4, Figure 8 incorporates the same bias as Figure 4 in the same sense. Clearly, it does not affect our conclusion (see Section 3.3).

In Figure 9, we present the line intensity data for our sample of PNe. The top panel concerns the presence or absence of the [N II] λ6584 emission line. Most of the objects where this line is weak or absent are near the point of maximum temperature on the evolutionary tracks. The bottom panel in Figure 9 considers the intensity of He II λ4686 ($I_{He\,II}$; Tylenda et al. 1994), where we divide our objects into groups of higher and lower degrees of excitation. For the higher degree of excitation, we adopt $I_{He\,II} > 80$ (scale: $I_{H\beta} = 100$), with the remaining objects being

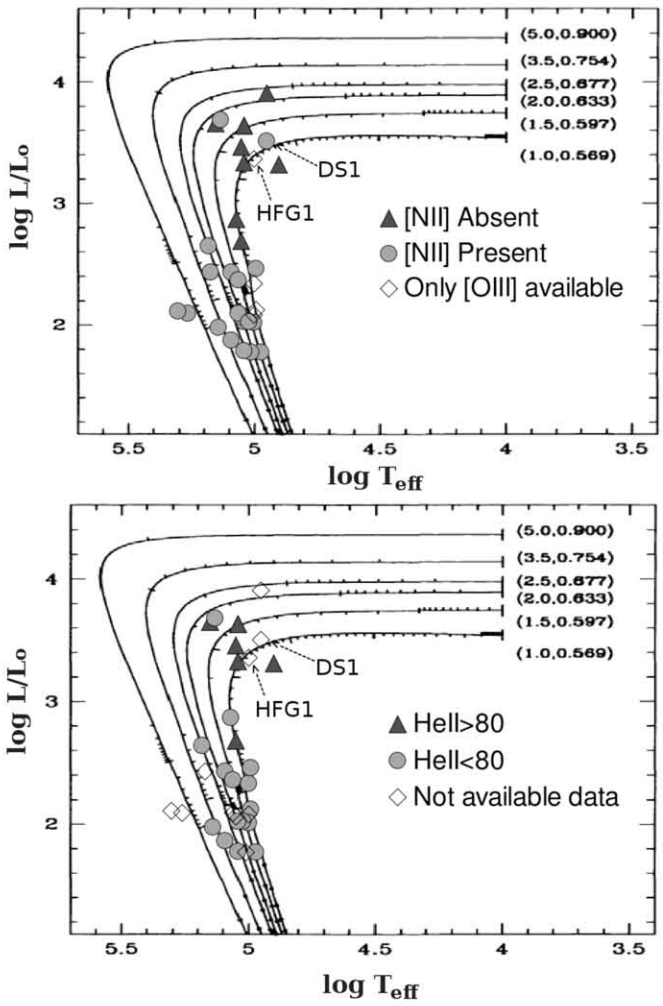

Figure 9. The degree of excitation of the nebular spectrum supports the luminosities deduced for the CSs in our sample. Since the CS temperature varies little, the degree of ionization is controlled by the CS luminosity. Here, we see that nebulae surrounding high luminosity CSs typically have weak or absent [N II] λ6584 emission, but strong He II λ4686 emission, reflecting their high degree of excitation. The opposite occurs for the nebulae surrounding low luminosity CSs. Considered with Figures 7 and 8, it is evident that the CS luminosity, nebular morphology, nebular bulk flow velocity, and the degree of nebular excitation vary coherently and consistently. Once more, the evolutionary tracks are from Vassiliadis & Wood (1994). DS 1 and HFG 1 contain binary central stars whose luminosities are uncertain.

of lower degree of excitation. (By normal standards, all of these objects are of a high degree of excitation.) In this plot, the objects with the higher degree of excitation tend to have higher luminosities. There is little variation in temperature for the CSs of these evolved PNe, so the degree of excitation is controlled principally by the luminosity of the CS. Where He II λ4686 is strongest, [N II] λ6584 emission is generally weak or absent due to the high degree of ionization.

From Figures 7–9, the PNe with high luminosity CSs typically tend to (1) fall into our mature PN category, (2) lack the presence of [N II] λ6584 emission, (3) have the strongest He II λ4686 lines, and (4) have higher bulk flow velocities. While we shall see that the above hold true generally in a statistical sense (Section 3.3), they are not strict general rules and exceptions to each are observed. An obvious complication in these diagrams is the effect of binary CSs, and, indeed, DS1 and HFG1, two of the anomalous data points in all of these diagrams, appear to have binary CSs (Montez et al. 2010). Fortunately, our large

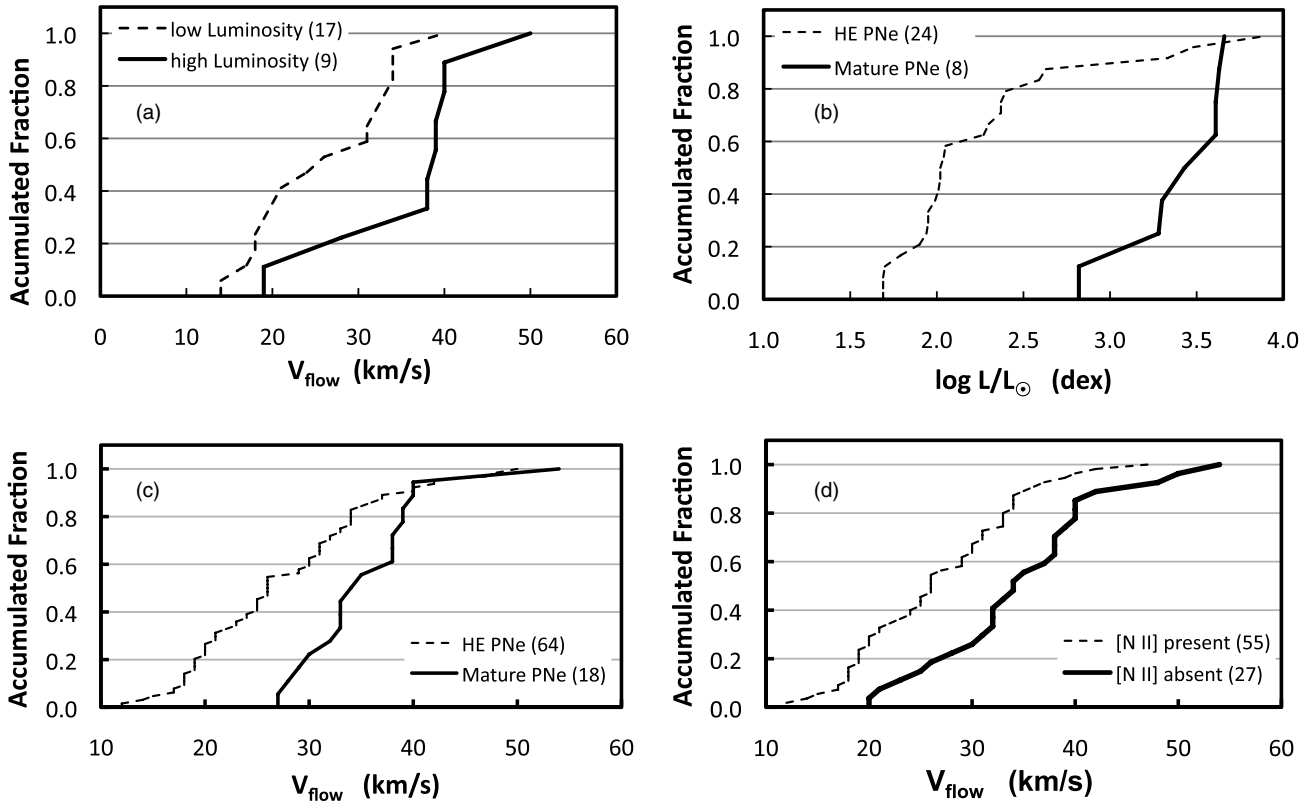

Figure 10. We present the cumulative distribution of $V_{\rm flow}$ or CS luminosity for different subsamples of our objects that we used to test (a) whether PNe surrounding high and low luminosity CS have the same bulk flow velocities, whether mature and HE PNe have (b) similar CS luminosities or (c) bulk flow velocities, and (d) whether PNe with and without [N II] λ6584 emission have similar bulk flow velocities. In all cases, the distributions differ at high statistical significance, based upon the K-S and *U* tests (see text for details). For these tests, we use $V_{\rm flow}$ measured from the splitting of the Hα line (method 1, Figure 2). The numbers in parentheses indicate the number of objects in each sample.

data set allows us to distinguish these general trends in spite of these complications.

3.3. Statistical Tests

In Figure 10, we present cumulative distributions to quantify the foregoing statistically. For the distributions in panels (b), (c), and (d), we use $V_{\rm flow}$ measured from the splitting of the Hα line. The results do not depend significantly upon this choice of data and we obtain similar results using the data adopted for Figures 3 and 4. However, the comparison among objects is clearer if we adopt a single emission line and measurement method for all objects. The data set used in panels (a) and (b) is entirely drawn from the Frew (2008) sample, which is volume-limited.

In panel (a), we plot the cumulative distributions of the bulk flow velocities for PNe with CSs of high and low luminosity. We divide the CS luminosities at a luminosity of $L/L_{\odot} = 3.0$ dex because (1) it approximately divides between mature and HE PNe (Figure 7), (2) it roughly divides the PNe between those of higher and lower nebular excitation (Figure 9), and (3) theoretically, we expect a gap in luminosity at about this value because of the rapid decrease in luminosity following the termination of nuclear reactions. The accumulated fraction is the fraction of objects in a given sample with bulk flow velocities below the value plotted, e.g.,

$$\text{Accumulated Fraction}(V_{\rm flow}) = \frac{N(V < V_{\rm flow})}{N_{\rm total}},$$

where $V_{\rm flow}$ is the abscissa value, $N(V < V_{\rm flow})$ is the number of objects with bulk flow velocities less than $V_{\rm flow}$, and $N_{\rm total}$ is the total number of objects in the sample. Thus, from the first panel in Figure 10 we see that none of the high luminosity objects have bulk flow velocities below 18 km s^{-1} and the majority have bulk flow velocities exceeding 37 km s^{-1} whereas 80% of the low luminosity objects have bulk flow velocities below 37 km s^{-1}.

Two common tests for comparing such cumulative distributions are the Kolmogorov–Smirnov (K-S) test and the Wilcoxon–Mann–Whitney non-parametric *U*-test (Wall & Jenkins 2003). The K-S test uses the sample sizes and the maximum difference between the ordinate values of the two distributions to determine the probability that the two distributions may be drawn randomly from a single parent distribution. The *U*-test is conceptually similar to the Student's *t*-test (Wall & Jenkins 2003) in that it uses the rank values of the data from the two samples to derive statistics analogous to the mean and variance and uses these to determine the probability that the two samples may be drawn randomly from the same parent distribution. Using the K-S and *U* tests to compare the distributions for PNe with high- and low-luminosity CSs in the first panel in Figure 10, we find a 99% probability that they do not arise from the same parent distribution. Note that we do not consider whether a given PN falls in the mature or HE category for this comparison, but we can only use the data for PNe with known CS parameters.

In panel (b) of Figure 10, we present the cumulative distributions of the CS luminosity for mature and HE PNe, finding extremely small probabilities ($\ll$1%) from both the K-S and *U* tests that the two distributions arise from the same parent distribution. Clearly, HE PNe have lower luminosity CSs. Again, this

analysis includes only the objects in our sample with known CS parameters.

In panels (c) and (d) of Figure 10, we analyze our entire PN sample. Panel (c) presents the cumulative distributions of bulk flow velocities for mature and HE PNe. Panel (d) presents the cumulative distributions of bulk flow velocities for objects in which the [N II] λ6584 emission line is present and absent. In both cases, both the K-S and *U* tests return very small probabilities (<1%) that the distributions arise as a result of a random draw from the same parent distribution. We can conclude that HE PNe have lower bulk flow velocities than mature PNe and that PNe in which the [N II] λ6584 is present likewise have lower bulk flow velocities than those in which this line is absent. If we restrict these tests to the subset of objects from Frew (2008) as in panels (a) and (b), we obtain similar results, though the significance for the K-S test is 96% and 98% for panels (c) and (d), respectively, while the significance from the *U*-test remains $\ll$1%.

Therefore, our statistical analysis reveals that, with high significance, (1) nebulae surrounding CSs of high luminosity expand faster than do those surrounding low luminosity CSs, (2) mature PNe have higher luminosity CSs than do HE PNe, (3) mature PNe have larger bulk flow velocities than HE PNe, and (4) PNe in which the [N II] λ6584 line is absent have larger bulk flow velocities than do their counterparts for which this line is present. Since CS luminosity, nebular morphology, and nebular excitation are all related to the evolutionary stage of the PN system, our results indicate clear trends with evolutionary stage. High luminosity CSs are found in PNe with higher nebular excitation, better-defined morphological structure, and higher bulk flow velocity. PNe with low luminosity CSs have lower excitation, more diffuse structure, and lower bulk flow velocity.

4. DISCUSSION

We have characterized the global kinematics of the nebular shell in PNe at advanced stages of evolution with the largest sample used to date for this purpose. Generally, we find a good correlation between the evolutionary stage of the CS and the kinematics, morphology, and spectral properties of the nebular shell, as predicted by modern hydrodynamical models (e.g., Villaver et al. 2002b; Perinotto et al. 2004; Schönberner et al. 2005a, 2010). Nebular shells with the highest degrees of excitation, largest bulk flow velocities, and best-defined structure usually have moderately evolved, high luminosity CSs that inhibit [N II] λ6584 emission. On the contrary, nebular shells with lower degree of excitation, lower bulk flow velocity, and the least structure contain the most evolved CSs. In agreement with Richer et al. (2010), we find that the highest bulk flow velocities occur for CSs with temperatures and luminosities for which we expect the stellar wind still has a strong influence on the kinematics of the nebular shell. At the latest stages of PN evolution, we find clear observational and statistical evidence for the deceleration of the nebular shell.

While it is clear that the nebular shell decelerates with time, its interpretation is not necessarily so simple. As the CS ceases nuclear reactions at the point of maximum temperature, its luminosity drops, initially precipitously, then more slowly. At the same time, the (luminosity-driven) wind energy imparted to the hot bubble likewise drops. However, the over-pressure of the hot bubble is likely to continue to affect the kinematics of the nebular shell until the expansion of the hot bubble causes its pressure to drop significantly. At some point, the pressure must drop, decelerating the expansion of the nebular shell, but it might be so severe to allow some backflow of the nebular shell toward the CS (e.g., García-Segura et al. 2006). In addition, the loss of CS luminosity may allow recombination of the nebular shell.

The CS luminosities of the mature and HE PNe differ by an order of magnitude for the objects in our sample (Figures 7–9). Thus, it is unclear whether the HE PNe are entirely ionized and that their lower luminosity CSs can maintain the same mass ionized as do the higher luminosity CSs in mature PNe. If not, recombination will occur in the outermost part of the nebular shell and, in HE PNe, we may observe only the innermost material observed in mature PNe. If that is the case, the lower bulk flow velocities in HE PNe could reflect the slower motions of matter closer to the CS at earlier evolutionary stages.

It is also conceivable that the CS is not the only or the most important influence at the latest evolutionary stages. In some instances, interaction with the ambient interstellar medium (ISM) may affect the nebular kinematics. Oey & García-Segura (2004) find that this effect is important for the evolution of ISM superbubbles and Villaver et al. (2002a) find that it is responsible for slowing down the AGB wind in their models. In our sample, we find that all PNe, whether classified as mature or HE, more than ∼350 pc from the galactic plane expand more rapidly than 30 km s^{-1} (see also Hippelein & Weinberger 1990). However, this may not constitute evidence that the ambient ISM decelerates HE PNe, since we cannot guarantee that our sample is statistically representative within or beyond this scale height.

Any study of nebular sizes immediately confronts the uncertainties in the distances, which are considerable. Plotting the nebular size as a function of the CS luminosity or the bulk flow velocity of the nebular shell, we do not find that HE PNe (or any substantial sub-group of these) have smaller radii than mature PNe (Table 1). Neither plot shows an especially tight correlation, though that between nebular radius and CS luminosity shows more, perhaps because both depend upon the distance. On average, then, if the loss of CS luminosity allows recombination, it is either not sufficient to cause a decrease in the nebular size or is sufficiently short that our HE PNe have all been re-ionized (see Perinotto et al. 2004, Figure 21).

Further observational progress is possible, but requires efforts on several fronts. First, more reliable distance scales are necessary. Second, in order to apply these distance scales, larger databases of homogeneous data are necessary, for both nebular shells and CSs. Third, more detailed knowledge of CSs is necessary, particularly concerning binarity. For example, DS1 and HFG1 are among the "anomalous" data points in Figures 7–9 whose CS luminosity disagrees with the nebular morphology, bulk flow velocity, and degree of excitation. For these two cases, Montez et al. (2010) found X-ray evidence for binarity that could contribute to a mistaken estimate of the luminosity data from Frew (2008). In fact, if we consider the luminosity values presented by Montez et al. (2010) for the whole binary system, the obtained luminosity is less than the value estimated by Frew for both PNe. On the other hand, we cannot avoid the presence of some objects in the sample that behave in a peculiar way and for which it is not easy to find an explanation. Lo 8, for example, has spectral features of a mature PN, high luminosity, and even evidence for the continued presence of a stellar wind (Patriarchi & Perinotto 1991), but clearly exhibits an HE PNe morphology. Its discrepant location in the H-R diagram is indicated in Figure 7. Another case is the well studied PN NGC 1360, an

object with an accurate luminosity estimate, but whose bulk flow velocity (26 km s^{-1}) does not agree with the expectations for its evolutionary stage (see Figure 8; for contrasting discussions: García-Díaz et al. 2008; Schönberner et al. 2010). Nonetheless, the use of large samples such as ours allows us to distinguish the general trends in the data and recognize individual discrepancies for particular objects that deserve further study.

5. CONCLUSIONS

We have analyzed the kinematics of evolved PNe using the largest homogeneous data set to date, drawn from the SPM Catalogue. We characterize the kinematics using the bulk flow velocities for these PNe, i.e., the typical outflow velocity for the matter with the highest emission measure within the spectrograph slit. Typically, the bulk flow velocities are larger than those for younger PNe, i.e., PNe whose CSs are on the horizontal part of the evolutionary track in the H-R diagram (e.g., Richer et al. 2008, 2010). We find a clear kinematic evolution of the nebular shell at these most advanced evolutionary stages, correlating with the CS evolutionary stage as well as the nebular morphology and the degree of excitation of the nebular spectrum. As expected from hydrodynamical models (Villaver et al. 2002b; Perinotto et al. 2004), mature PNe, whose CSs are still at high luminosity and whose hot bubbles are still adequately powered, have more structured nebular morphologies, larger bulk flow velocities, and nebular spectra with a higher degree of excitation. Highly evolved PNe have low luminosity CSs, now on the white dwarf cooling tracks, and nebular shells whose morphology have the least structure, lower bulk flow velocities, and spectra with a lower degree of excitation.

These results complement prior work, illustrating the coupling between the CS's evolution and that of the nebular shell predicted by theory (e.g., Villaver et al. 2002b; Perinotto et al. 2004). The bulk of the mass of the nebular shell is continuously accelerated until the CS reaches its maximum temperature and ceases nuclear burning (e.g., Richer et al. 2010). Thereafter, the bulk of the mass of the shell decelerates as the CS approaches the white dwarf stage of evolution, presumably due to the loss of energy from the CS or possibly its interaction with the surrounding ISM or even due to recombination of the outermost nebular matter. Distinguishing among these options is not simple and will be done best on a case-by-case basis.

The authors gratefully acknowledge financial support from CONACyT (82066) and UNAM-PAPIIT (IN116908, IN110011) grants. M.P. is also grateful to the Dirección General de Estudios de Posgrado de la UNAM for additional financial assistance. We thank the anonymous referee for helpful comments.

REFERENCES

Bohuski, T. J., & Smith, M. G. 1974, ApJ, 193, 197
Chevalier, R. A. 1997, ApJ, 488, 263
Chu, Y.-H., Kwitter, K. B., Kaler, J. B., & Jacoby, G. H. 1984, PASP, 96, 598
Frew, D. J. 2008, PhD Thesis, Macquarie Univ.
García-Díaz, M. T., López, J. A., Richer, M. G., & Steffen, W. 2008, ApJ, 676, 402
García-Segura, G., López, J. A., Steffen, W., Meaburn, J., & Manchado, A. 2006, ApJL, 646, L61
Gesicki, K., & Zijlstra, A. A. 2000, A&A, 358, 1058
Hippelein, H., & Weinberger, R. 1990, A&A, 232, 129
Kaler, J. B., Shaw, R. A., & Kwitter, K. B. 1990, ApJ, 359, 392
Kwok, S. 1982, ApJ, 258, 280
Kwok, S. 2000, The Origin and Evolution of Planetary Nebulae (Cambridge Astrophysics, Series 31; Cambridge: Cambridge Univ. Press)
López, J. A., Richer, M. G., García-Díaz, Ma. T., et al. 2012, RMxAA, 48, 3
Meaburn, J., Blundell, B., Carling, R., et al. 1984, MNRAS, 210, 463
Meaburn, J., López, J. A., Gutiérrez, L., et al. 2003, RMxAA, 39, 185
Mellema, G. 1994, A&A, 209, 915
Montez, R., Jr., De Marco, O., Kastner, J. H., & Chu, Y.-H. 2010, ApJ, 721, 1820
Oey, M. S., & García-Segura, G. 2004, ApJ, 613, 302
Patriarchi, P., & Perinotto, M. 1991, A&AS, 91, 325
Peña, M., Medina, S., & Stasińska, G. 2003, RMxAC, 15, 38
Perinotto, M., Schönberner, D., Steffen, M., & Calonaci, C. 2004, A&A, 414, 993
Phillips, J. P. 2002, A&A, 393, 1027
Richer, M. G., López, J. A., García-Díaz, Ma. T., et al. 2010, ApJ, 716, 857
Richer, M. G., López, J. A., Pereyra, M., Riesgo, H., & García-Díaz, Ma. T. 2008, ApJ, 689, 203
Schönberner, D., & Blöcker, T. 1996, Ap&SS, 245, 201
Schönberner, D., Jacob, R., Sandin, C., & Steffen, M. 2010, A&A, 523, A86
Schönberner, D., Jacob, R., & Steffen, M. 2005a, A&A, 441, 573
Schönberner, D., Jacob, R., Steffen, M., et al. 2005b, A&A, 431, 963
Stanghellini, L., & Renzini, L. 2000, ApJ, 542, 308
Stanghellini, L., Villaver, E., Manchado, A., & Guerrero, M. A. 2002, ApJ, 576, 285
Tylenda, R., Stasińka, G., Acker, A., & Stenholm, B. 1994, A&AS, 106, 559
Vassiliadis, E., & Wood, P. R. 1994, ApJS, 92, 125
Villaver, E., García-Segura, G., & Manchado, A. 2002a, ApJ, 571, 880
Villaver, E., Manchado, A., & Garía-Segura, G. 2002b, ApJ, 581, 1204
Wall, J. V., & Jenkins, C. R. 2003, Practical Statistics for Astronomers (Cambridge: Cambridge Univ. Press)

2.2.2 Comparison with Jacob et al. 2013

In a recently published paper, Jacob et al. (2013) expressed some disagreement with the results presented Pereyra et al. (2013). In order to confirm the validity of our conclusions, here we will briefly discuss the source of this disagreement and demostrate that after a detailed analysis of their sample objects and measurements, our results stand correct.

The statistical analysis

They started the analysis with a *volumen limited sample* from Frew (2008) having slightly more than 200 objects within a distance of 2 kpc. For statistical purposes only 78 objects were selected in the final sample, from which H-deficient (13) and binary nuclei (6) PNe were discarded, ended up with a sample of 59 objects. From this sample, just 41 nebulae belong to the evolutionary stages of interest: 13 with $3 \leq M_V$[1] ≤ 5 (Mature objects) and 28 with $M_V > 5$ (Highly Evolved objects). In Table 2.1 the 41 objects considered by Jacob et al. (2013) in their statistical analysis are listed, separated by evolutionary groups. In column 1, the Common Name of the PN is presented. Column 2 presents the central star absolute magnitud M_V, taken from Frew (2008). For the objects in common with Pereyra et al. (2013), column 3 presents the evolutionary stages that we adopt. The expansion velocities used by them (obtained from different compilations) and those obtained from our measurements are presented in Column 4-7 for each object and from different ions. Velocity data of PNe which are in common in both studies agree for the most part except for A31. Since this nebula has an extremly low surface brightness (see Fig. A.16) it is likely that the difference observed may arise from the quality of the spectra used for the velocity measurements in each case. A comparison of the gaussian fits used by Hippelein & Weinberger (1990) to velocity measurements, from which the expansion velocity of A31 reported by Jacob et al. (2013) was taken, with those used by Pereyra et al. (2013) is show in Fig. 2.1. Taking this into account, we concluded that the peak-separation velocities ($V_{[NII]}$) reported by Jacob et al. (2013) are not all obtained from reliable data and should be treated carefully.

[1] M_V is the absolute magnitude in the visual (V) band. For all central star masses the maximum stellar effective temperature corresponds to an absolute magnitude M_V between 4.0. . . 4.5. Brighter central stars are at the high-luminosity horizontal part of their evolution, while fainter stars are beyond maximum stellar temperature and are descending to the white-dwarf domain (Jacob et al., 2013).

Table 2.1 Planetary Nebulae considered by Jacob et al. (2013).

PNe with 3≤Mv≤5							
			Expansion Velocities ($km\,s^{-1}$)				
Common Name	M_V [a]	Group[b]	Jacob et al.		Pereyra et al.		
			$V_{[NII]}$	$V_{[OIII]}$	$V_{[NII]}$	$V_{H\alpha}$	$V_{[OIII]}$
NGC6905	3.14			44			
NGC7662	3.15		28	26			
A36	3.17	M		35		38	
NGC4361	3.24			26			
NGC3918	3.35		27	24			
NGC7027	3.37		27	24			
NGC1360	3.41	M		28		28	
NGC7008	3.5			39			
A51	3.53			42			
NGC 2792	4.12			20			
Sh2-200/HDW2	4.3	HE		13	17	15	
NGC2899	4.49			32			
NGC2610	4.79			34			
A39	4.81	M	37	32		32	
PNe with Mv> 5							
			Expansion Velocities ($km\,s^{-1}$)				
Common Name	M_V [a]	Group[b]	Jacob et al.		Pereyra et al.		
			$V_{[NII]}$	$V_{[OIII]}$	$V_{[NII]}$	$V_{H\alpha}$	$V_{[OIII]}$
NGC6818	5.16		32	27			
IC1295	5.34	HE	34		34	31	
NGC6445	5.54			38			
A33	5.71	HE		32			37
NGC6894	5.81			43			
NGC6537	5.87			18			
NGC3132	5.91		33	14			
NGC3211	5.91		31	27			
NGC3195	6		30	25			
NGC6853	6.05		30	15			
K1-22	6.06	HE		28	40	33	
NGC6720	6.11		39	25			
NGC6563	6.16			11			
A34	6.2	HE	37	32			34
NGC6772	6.25		25	11			
NGC2438	6.25		20	23			
A62	6.37		24	13			
Wray17-31	6.46		28				
IC5148/50	6.49			53			
A84	6.55	HE	25	16	28	24	
NGC3587	6.66	HE	40	37	40	34	
A61	6.68			32			
NGC4071	6.73			17			
A13	6.77	HE	23	20	24	20	
NGC7293	6.8	HE	24	14	21	21	
NGC7048	6.84			17			
A31	6.99	HE	35		18	17	
EGB6	7.03		41	35			
PuWe1	7.4	HE	27	27	30	34	

[a] Central star absolute magnitud, M_V, taken from Frew (2008).
[b] The HE and M classifications correspond to highly evolved and mature objects.

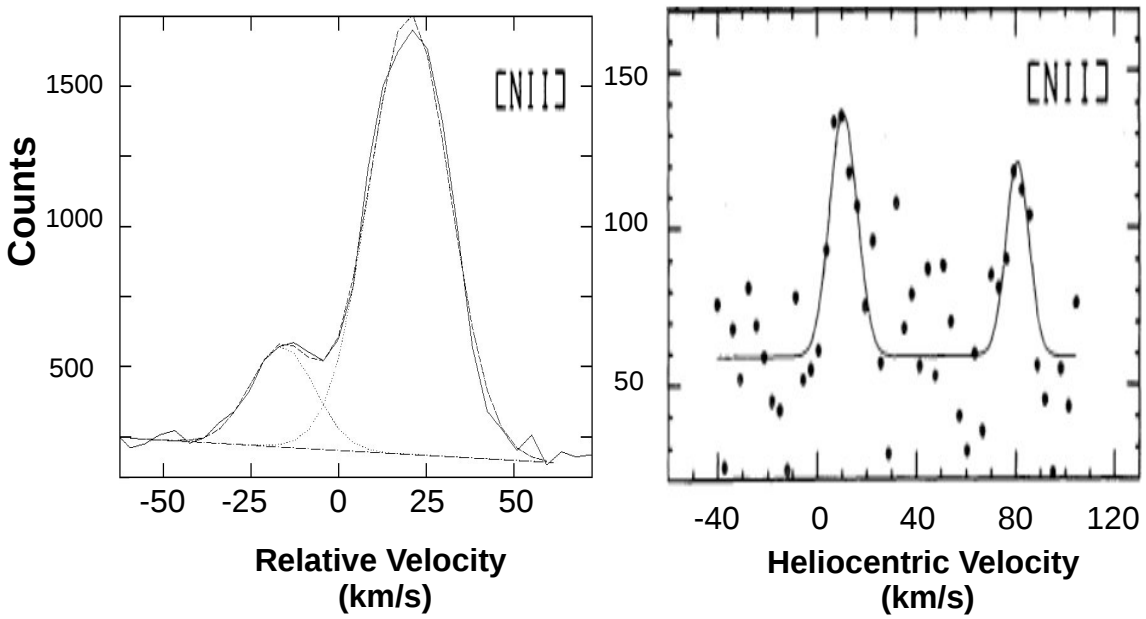

Figure 2.1 Gaussian fits used to velocity measurements for A31 from Pereyra et al. (2013) (left panel) and Hippelein & Weinberger (1990) (right panel), for nitrogen emission line. Since the quality of the spectra depends on the signal-to-noise ratio, it is easy to see that the expansion velocities obtained from gaussian fits of the left panel will yield more reliable data.

For the entire sample of Table 2.1, a statistical analysis was performed by Jacob et al. (2013) concluding that no deceleration of peak-separation velocities is found. According to their results, V_{exp}[OIII] decreases only slightly from 28.8 ± 9.4 km s^{-1} for the PNe with $3 \leq M_V < 5$ to 25.1 ± 10.2 km s^{-1} for those with $M_V \geq 5$. For nitrogen emission lines no deceleration is observed: V_{exp}[NII] $= 27.2 \pm 7.1$ km s^{-1} ($3 \leq M_V < 5$) vs. V_{exp}[NII] $= 28.7 \pm 7.9$ km s^{-1} ($M_V \geq 5$).

Under a detailed analysis we found that these results are based on relatively small samples and then, they may not be statistically relevant. To illustrate the implications of using small samples, in Fig. 2.2 we present the comparison made by Jacob et al. (2013) of models vs. observations, complemented with data from Pereyra et al. (2013). In the first row a small decrease of V_{exp}[OIII] velocities at advanced stages of evolution is clearly observed. In the second row, no deceleration is found for V_{exp}[NII] and V_{exp}Hα velocities. However, in this plot just a few objects are found within the region where moderately evolved PNe are located ($3 \leq M_V < 5$) and no conclusive results can be obtain for this particular evolutionary stage. In the third row, all of the objects from Pereyra et al. (2013) for which there exist M_V magnitudes are included in the plot.

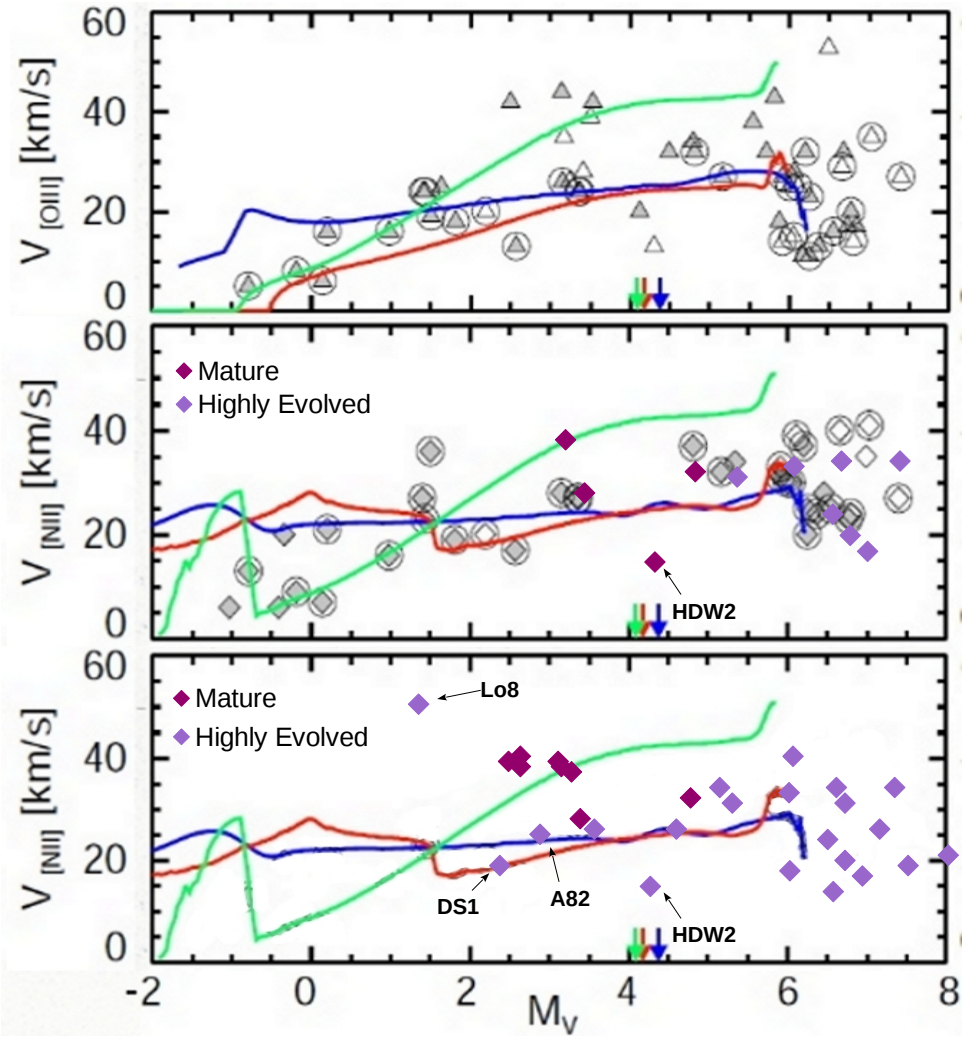

Figure 2.2 Peak-separation velocities V_{exp}[OIII] and V_{exp}[NII] as they follow from central line-of-sight line profiles computed from the models (solid lines) and measured (symbols), as a function of central star absolute magnitud M_V. Velocities for three models sequences from Jacob et al. (2013) are plotted, 0.595 $M_\odot$ α=3 (green), 0.605 $M_\odot$ "hydro "(red) and 0.625 $M_\odot$ α=2 (blue). The vertical arrows on the abscissae mark the stellar brightness where the central star models reach their maximum effective temperatures, separating between younger models (and objects) and older ones. *Top row:* V_{exp}[OIII] velocities models/measured from Jacob et al. (2013). Open and filled symbols correspond to objects with distances $\leq$ 1 kpc and $>$ 1 kpc, respectively. Circles around symbols indicate objects for which velocities from both nitrogen and oxygen ions were available in Jacob et al. (2013). *Second row:* V_{exp}[NII] velocities measured from Jacob et al. (2013) are presented in gray symbols. Colored symbols represents Hα velocities measured from Pereyra et al. (2013) for the PNe which are in common in both studies, separated by evolutionary groups. Hα velocities were considered for consistency in this case because of the lack of V_{exp}[NII] velocities. "Anomalous" PNe are indicated with labels. *Third:* Again, colored symbols are Hα velocities, but in this case we plotted all the PNe from the whole sample of Pereyra et al. (2013) with M_V available data.

Comparing the results for the data from Pereyra et al. (2013) in the second and third rows, the virtue of undertaking studies of this nature with large samples is obvious. With the small samples in the second panel, there is no clear difference between Mature and HE PNe, but the larger samples in the third row make clear that HE PNe have lower $V_{exp}H\alpha$ velocities.

2.3 Evolved PNe with ISM interaction

2.3.1 Introduction

Since the majority of PNe have non-zero space velocity relative to the interstellar medium (ISM), the interaccion between the nebular gas and the ISM is not an unusual case. Morphological studies of evolved PNe show strong evidence of asymmetries which can be attributed to this interaction. The influence of ISM interaction on the nebular shell properties was extensively studied by Borkowski et al. (1990) and Tweedy & Kwitter (1994), who explain that at later stages of evolution the nebulae become significantly affected by the interstellar material with which they will eventually merge. Borkowski et al. (1990) discuss PN/ISM interaction in terms of the expansion velocity of the PN and the velocity of the progenitor star with respect to its surroundings. They suggested that a PN with high space velocities in a homogeneous, isotropic ISM, will start to interact on its leading edge. Assuming a thin shell model, they found that as the PN expansion causes the nebular density to fall below a critical value, the gas in the shell is compressed, resulting in a brightness enhancement in the direction of the stellar motion. In these models the interaction process is studied when the nebular shell is already formed and therefore, the interactions with the ISM are expected to occur during late stages of the nebular evolution. Meanwhile Tweedy & Kwitter (1994) proposed that such interactions are characterised by three observable criteria:

- An asymmetry in the periphery of the nebula.
- An increase in surface brightness at the interacting edge.
- The rim exhibits a drop in the ionization level, i.e., an increased $[NII]/H\alpha$ ratio with respect to the rest of the nebula. The higher $[NII]/H\alpha$ ratio results from material being compressed at the PN/ISM boundary, increasing the density which, in turn, elevates the recombination rate and lowers the ionization state of the gas.

Acoording to this, relatively high ISM densities, large relative velocities, or both were needed to explain PN asymmetries due to interaction with the ISM. However, recent numerical simulations made by Villaver et al. (2003) found that the formation of the planetary nebula is highly influenced, even at a low relative velocity of the star: with typical systemic velocity of $20\,\mathrm{km\,s^{-1}}$, a PNe will interact with the ISM and will have observable bow shock structures. They demostrate that when the PN formation is followed from the time when the shell is still being formed (by considering the evolution of the stellar wind from the asymptotic branch), high velocities, high ISM densities, or the presence of a magnetic field is not necessary to explain the observed asymmetries in the external shells of PNe. In contrast to what is commonly believed, they argued that the interaction is observable even during the very early stages of the PN phase. Moreover, as the interaction develops, the leading edge of the nebula is slowed by the ISM and the PN shell becomes distorted.

2.3.2 ISM interactions in the Evolved PNe sample

If the deceleration of the nebular shell due to its interaction with the ISM is important, it will be more likely to observed this effect during the latest stages of the nebula's evolution. Therefore, it might be expected that in our evolved PNe sample we could find some nebulae showing signs of this kind of interaction. Based on the latest compilation published by Ali et al. (2012), the classification scheme introduced by Wareing et al. (2007) (presented in Table 2.2) and the observational criteria of Tweedy & Kwitter (1994), we listed in Table 2.3 the evolved PNe from our sample that seem to be interacting with the ISM. Columns 1, 2, 3-6, 7, 8 and 9 of Table 2.3 present the common name, PNG name, the expansion velocities for different ions ([NII], Hα and [OIII]), the interaction stage of the nebula, references and the evolutionary group according to Pereyra et al. (2013) respectively.

Table 2.2 The four stages of PN-ISM interaction from Wareing et al. (2007).

Stage	Observable effects
WZO 1	PN as yet unaffected; faint bow shock may be observable
WZO 2	Brightening of PN shell in the direction of motion
WZO 3	Geometric centre shifts away from the central star
WZO 4	PN completely disrupted, central star is outside the PN

From an observational point of view, the classification of Wareing et al. (2007) suggest that the WZO1 stage of the interaction is unlikely to be observed, while in the case of the WZO2 stage, the interaction would be observable in some objects probably as a local effect in their morphology. At the WZO3 stage of interaction the observable effect will be evident in the whole nebula, but it is unclear whether or how much the kinematics of the nebular shell would be affected by the influence of the ISM or not. When the PNe is completely disrupted and the central star is outside the nebula, at the WZO4 stage, the nebula could be in the process of merging to the interstellar medium and hence its observed physical properties could be similar to an HII region.

Table 2.3 Evolved planetary nebula with ISM interaction.

Common Name	PNG Name	$V_{[NII]}$ ($km\,s^{-1}$)	$V_{H\alpha}$ ($km\,s^{-1}$)	$V_{[OIII]}$ ($km\,s^{-1}$)	Interaction stage[a]	Ref.	Group[b]
A 13[1]	204.0-08.5	24	20		WZO2	*A*	HE
A 15	233.5-16.3		25		WZO2	*A*	HE
A 16	153.7+22.8			37	WZO2	*A*	HE
A 19	200.7+08.4	21	19		WZO2	*A*	HE
A 21	205.1+14.2	29	26		WZO3	*A*	HE
A 31	219.1+31.2	18	17		WZO2	*A*	HE
A 34	248.7+29.5			34	WZO2	*A*	HE
A 36	318.4+41.4		38		WZO2	*A*	M
A 45	020.2-00.6	20	21		WZO2	*A*	HE
A 59	053.3+03.0	18*	15		WZO3	*A*	HE
A 71	084.9+04.4	22	18		WZO2	*A*	HE
A 75	101.8+08.7		39		WZO1	*A*	M
BV 5-2	121.6+00.0	8*	14*		WZO3	*B*	HE
DeHt 2	027.6+16.9		48		WZO1	*A*	HE
DeHt 4	048.7-01.5	11*	13*		WZO2	*A*	HE
HaWe 5	156.9-13.3	9*	15*		WZO3	*B*	HE
HDW 5	218.9-10.7	7*	12*		WZO3	*A*	HE
HDW 6[1]	192.5+07.2	21	18		WZO4	*A*	HE
HFG 1[2]	136.3+05.5			18:	WZO1	*A*	HE
Jn 1	104.2-29.6		40:		WZO3	*A*	HE
K 1-28	270.1+24.8		30		WZO2	*A*	M
K 1-3[†]	346.9+12.4	22	20:			*A*	HE
LoTr 1	228.2-22.1			22	WZO3	*A*	HE
NGC 1360[2]	220.3-53.9		28		WZO2	*A*	M
NGC 246	118.7-74.7		40	37	WZO3	*A*	M
NGC 3587	148.4+57.0	40	34		WZO1	*A*	HE
NGC 7094	066.7-28.2		38		WZO2	*A*	M
NGC 7293	036.1-57.1	21			WZO1	*A*	HE
PuWe 1[2]	158.9+17.8	30	34		WZO2	*A*	HE
We 1-5	216.3-04.4		34		WZO2	*A*	M
YM 16	038.7+01.9	25	26		WZO3	*A*	HE

[a] According to the clasification scheme of Wareing et al. (2007).
[b] The HE and M classifications correspond to highly evolved and mature objects, respectively.
[1] Slit position is not at center of the PN. Lower limit for the expansion velocity.
[2] Upper limit for the expansion velocity.
References: *A*).- Ali et al. (2012). *B*).- This thesis.
: Velocity measurements must be treated carefully. Very faint PN.
* Velocity measurement obtained from the FWHM of a Gaussian fit.
† The object is included in the compilation of Ali et al. (2012) but its interaction stage is not indicated.

In order to investigate whether the kinematics of the nebular shell is affected by the ISM, we obtained the average velocities for the Evolved PNe with and without ISM interaction. We used the velocity measurements available from [NII], [OIII] or Hα, in order of preference. The results are presented in Table 2.4. It is found that the nebulae with ISM interaction have an average velocity slightly lower than the average velocity obtained for nebulae without ISM interaction. It seems that the kinematics of the nebular shell is actually being affected by the ISM at these advanced stages, in good agreement with the predictions from Villaver et al. (2003). Segregating the samples into Highly Evolved and Mature objects, according to the evolutionary groups considered in section 2.2, we found that the difference in the average velocities obtained for the Highly Evolved objects with and without ISM interaction indicates that it is likely that the nebular shell of Highly Evolved PNe with ISM interaction is being slowed by the ISM. For Mature PNe the average values obtained are very similar and therefore, we conclude that the ISM interaction is not affecting the kinematics of the nebular shell in this case.

Table 2.4 Average velocities for the Evolved PNe with and without ISM interaction.

Evolved PNe	Average Velocities ($\mathrm{km\,s^{-1}}$)			Standard error ($\mathrm{km\,s^{-1}}$)		
	HE [a]	M [a]	All	HE [a]	M [a]	All
with interaction	24(24)	35(7)	26(31)	2.1	1.8	1.9
without interaction	31(60)	34(14)	32(74)	1.1	2.5	1.1

[a] As in Table 2.3 HE and M correspond to highly evolved and mature (less evolved) objects, respectively. The number of PNe considered is indicated in parentheses beside the average velocity value.

This effect is more evident from Table 2.5, where Mature and Highly Evolved nebulae with ISM interaction are analized as a function of the interaction stage.

Table 2.5 Interaction stage vs expansion velocity.

Stage [a]	Average Velocities ($\mathrm{km\,s^{-1}}$)		Standard error ($\mathrm{km\,s^{-1}}$)	
	HE [c]	M [c]	HE [c]	M [c]
WZO 1	32(4)	39(1)	7.3	–
WZO 2	24(10)	34(5)	2.5	2.0
WZO 3/4[b]	20(9)	37(1)	3.6	–

[a] According to the clasification scheme of Wareing et al. (2007).
[b] For statistical purposes WZO3 and WZO4 have been consider as a single stage.
[c] As in Table 2.3 HE and M correspond to highly evolved and mature (less evolved) objects, respectively. The number of PNe considered is indicated in parentheses beside the average velocity value.

It is clear that the expansion of the nebular shell in Highly Evolved PNe tends to

slow down as the ISM interaction increases. In the case of Mature PNe no clear trend is observed, but it might be due to the small number of PNe within this group.

2.3.3 Discussion

We have seen that one of the main features of the nebular shell that is used to classify a PN as an ISM interacting object is the asymmetric surface brightness. But it is well-known that the brightness along the entire nebula will depend on the density distribution of the whole nebular shell, since in most of the cases the density distribution is not isotropic, it is expected that the brightness will likewise not uniform. Moreover, since the mass loss history of the progenitor star is very important on the formation and shaping of a PN, it will also contribute to the final density distribution of the PN. If this is true, at advanced stages of evolution (when the effects of ISM interaction are commonly observed) it is possible, though unlikely, that some PNe show an increase in surface brightness in the direction of motion that is not necessarily a result of an interaction with the ISM but rather a consequence of non-uniform density distribution arising from the processes of mass loss on the AGB. As explained in section 2.2, it is important to consider also the changes in the physical properties of the central star at advanced stages of evolution that make the nebular shell to decelerate regardless of whether the nebula is experiencing an interaction with the ISM or not. Therefore, it is likely that the apparent deceleration observed for the HE group of PNe with ISM interaction from Table 2.5 is enhanced by its highly evolved condition.

2.3.4 A case study: A 59

Among the evolved PNe classified as ISM-interacting PN that show remarkable morphological indicators of an interestellar medium interaction, presented in Table 2.3, A59 is the only one which has probably a clear kinematical evidence of a deceleration of the nebular shell due to its interaction with the ISM. We present in Fig. 2.3 the data obtained for A59, to show the ISM interaction it is experiencing and how strong this may be affecting the kinematics of the nebular shell. From Fig. 2.3 the effects of this nebula with the ISM are clearly observed. An asymmetry in the periphery of the nebula, an increase in surface brightness at the interacting edge and a very distorted nebular shell are the main features in the morphology of A59.

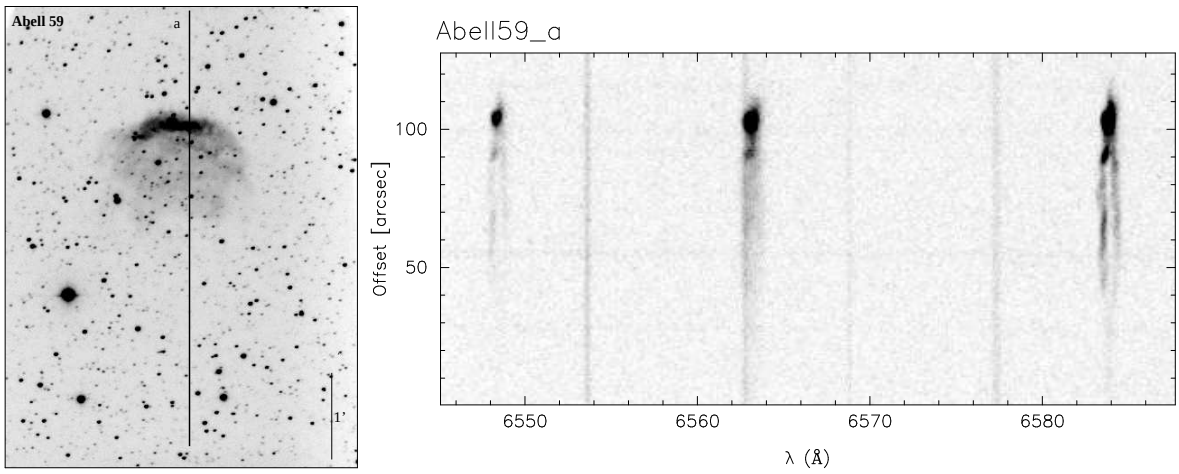

Figure 2.3 Image and spectra of A 59. The right panel shows the image of A 59 taken from DSS2R with the slit position indicated as a solid line. The spectral image is presented at the left panel where the emission lines detected are [NII] $\lambda\lambda$6548,6584, HeII λ6560, and Hα λ6562.8.

Trying to find some clues about the conditions of the ISM surrounding A 59 we calculated the height above the galactic plane (z) of its central star. Using a distance value of 1540 pc obtained from Frew (2008) and the galactic coordinates of the nebula, we found that the nebulae is located 80 pc above the galactic plane, within the galactic thin disk. Acoording to Dickey & Lockman (1990) for the thin disk ($z \leq 325$ pc) the expected densities are $10 - 10^2$ times greater than those of the thick disk (325 pc$\leq$ z $\leq$1 kpc), suggesting that the ISM density surrounding A 59 is relatively high and hence, the interaction could be stronger there. Since the PN space velocity relative to the interstellar medium is also an important parameter involved in an ISM interaction, using the spectra from the SPM Catalogue we obtained a systemic, radial, heliocentric velocity of $-20.20\,\mathrm{km\,s^{-1}}$ for the central star of A 59. Unfortunately, there is not enough information available to derive the space velocity and no comparison could be done in this case. Nonetheless, the best indication of deceleration of the nebular shell in the north direction of the image at the left panel of Fig.2.3, at the brightest edge of A 59, is that the line profile tend to close up before reaching this bright edge, which means that the shell actually stops expanding due to accumulation of material further out.

2.3.5 Use kinematics to search for ISM interactions

Usually, to search for ISM interaction astronomers analize the morphology of the PN and the kinematical properties are not considered. In this section we present a brief description of a few objects that were excluded from the Evolved PNe sample presented in section 2.2 because of their peculiar morphology and emission line profiles, from which kinematic indicators of ISM interaction are found. Even though objects with very disrupted morphology like BV 5-2, HaWe 5, HDW 5, and DeHt 4 could be considered as HII regions and not as true PNe, e.g. HDW 5 and HaWe 5 by Frew (2008), we can see from Figures A.38, A.40, A.43, and A.46 that they actually exhibit the expected velocity profile for objects experiencing an ISM interaction: most of the nebular material is moving at low velocities ($V_{flow} \approx 9\,\mathrm{km\,s^{-1}}$) and accumulated in the position where an enhancement in the surface brightness is observed.

One of the main features that is commonly used to classify an object as a PN with ISM interaction is undoubtedly the non-uniform surface brightness along the nebular shell, which requires a preferential line of sight that allows to see the motion of the nebula on the plane of the sky, and thus easily appreciate the increase in surface brightness at the interacting edge. However, it is likely that some PNe with ISM interaction are moving in the direction of the line of sight and then, the cometary shapes commonly found in ISM interacting objects will be imposible to observe in these cases. As an example, imagine a spherical planetary nebula that is moving in the direction of our line of sight, and is experiencing an ISM interaction. According to the theory, one should observe an asymmetry in the surface brightness of the nebula. But since we are observing the nebula in a pole-on direction, the face of the nebula that we would be able to see is that of the interacting edge, where most of the nebular gas is acumulated due to the ISM interaction and hence, it is possible that the surface brightness on this face will be uniform. In this particular case, we can not classify the PNe as an ISM-interaction object although it is actually interacting. Furthermore, even if we are able to detect an asymetry in surface brightness of the nebula, in most cases it does not allow us to determine whether the effect of the interaction on the nebular shell is local or global. In these particular cases, the inclusion of the kinematical properties of a PNe in the selection criteria use to date to determine if a PNe is interacting with the ISM, could serve as an additional tool in the clasification of this kind of objects.

Chapter 3

Low Metallicity PNe Sample

3.1 Introduction

From theory of stellar evolution and galactic structure it is well known now the existence of many different types of stars within galaxies, each one with its particular and individual properties. The first astronomer that classified these stars into groups was Walter Baade, who in 1944 introduced the concept of *stellar populations* based on observations of resolved stars in the center of the Andromeda galaxy. By analyzing the colors and brightnesses of the stellar images he defined two distinct *populations* for stars: *Population I and Population II*. His observations suggested that *Population I* contained luminous blue stars, accompanied by dust and gas, whilst *Population II* was dominated by luminous red stars in an essentially gas and dust free environment.

Later, studies from detailed spectral analysis of stars from the two populations came to confirm this distinction. The studies allowed the astronomers to determine the chemical compositions of stars from the strengths of characteristic spectral absorption features. *Population II* stars are found to be very deficient in all elements heavier than helium (or metals), whereas *Population I* stars have higher metal abundances, comparable to the solar fraction of heavy elements. Some of the heavy elements found in stars are only produced in the supernova explosions which end massive stars's lives. Hence, the presence of these elements in a star indicates that the star must contain material synthesized by supernovae from a previous stellar generation. The difference between the metal content in the two stellar populations thus points to a difference in ages. A star that formed late in the history of a galaxy will be made from material that has had time to be processed through several earlier generations of stars and will thus generally have high metal abundances; the star will therefore be classified as a

Population I object. On the contrary, a star that formed much earlier will have been produced from material whose chemical abundances lie much closer to the primordial composition of the Universe with only very small amounts of metals, and so the star will be a *Population II* object.

Taking into account this classification, it is easy to recognize the existence of these stellar populations within our Milky Way (MW) Galaxy distributed in three of its main components: the disk, the bulge and the halo. *Population I* stars make up the vast majority of visible stars bright enough to see with the unaided eye, most of them belonging to the MW disk, where dust and gas is still available for star formation processes and the presence of young stars, with high metal content. In the case of *Population II* objects, although they are rare in our Galaxy, there are prominent representatives of them in globular clusters in the Milky Way halo, where the absence of dust and gas inhibits the formation of new stars leaving old and low-metal stars in this galaxy's component.

Even though *Population I* objects are expected to be found mainly in regions where star formation has been recently active, there are regions with no recent star formation events, like the MW bulge, where stars are usually older than those from the disk population but younger than the halo objects. In fact, nowadays it is found that within the MW Galaxy there actually are a continuum of stellar populations where the classical *Population I* and *Population II* are just extreme examples. Nevertheless, using the concept of stellar Populations, we can divide stars into groups according to its location in the galaxy or metal content, making possible to study the different stars in the Galaxy from statistical points of view, trying to understand the general behavior of them as a group and not only as individual cases.

In the case of PNe it is often assumed that their chemical abundances are dependent on the mass of the central star. Peimbert (1990) classifies PNe into four classes: Type I have high He and N abundances, usually show bipolar morphology, and are assumed to originate from a high-mass population (e.g. $3 - 5 M\odot$), Type II and III are galactic disk nebulae with respectively low- and high-velocity dispersions perpendicular to the galactic plane, and Type IV are halo objects. On the other hand, we know that abundances in PNe trace both the abundances of the interstellar medium from which the progenitor stars were born and the products of nucleosynthesis during the progenitor's evolution. Therefore, with data of the chemical abundances obtained from the nebular shell it is possible to segregate samples of PNe that consider the chemical properties for the progenitors of their central stars that in turn, according to the Peimbert's clas-

sification, will be related to the mass of their progenitor star and galactic population (disk, bulge and halo) to which they belong. Since heavier elements like oxygen (O), neon (Ne), argon (Ar), an so on, are not synthesized in most intermediate-mass star, the abundances of these elements will trace the metallicity of the region where the star was formed. For these reasons, the use of abundances data of these elements represents a powerful tool to study the relationship existing between the chemical properties of the progenitor star and the kinematic evolution of the nebular shell of a PN. (Peña et al., 2007) found that the oxygen and neon abundances may have been enhanced by dredge-up processes in the metal-poor progenitors of the PNe they studied in NGC 3109. On the other hand, no studies find that oxygen abundances are depleted. Thus, in the worst case, the observed oxygen abundance appears to be an upper limit to that contained by its progenitor star at the time of its formation.

With the aim to characterize the kinematics of the nebular shell of planetary nebulae and its relationship with the chemical properties of their central stars, in this chapter we present the analysis of 31 PNe that, according to the literature data available (Costa et al., 1996, 2004; Escudero et al., 2001; Górny et al. , 2004; Henry et al., 2004, 2010; Howard et al., 1997; Pereira et al., 2007; Ratag et al., 1997; Stanghellini & Haywood, 2010; Stasińska et al., 2010), have chemical O abundances well below the solar abundance value ($\log(O/H) + 12 \leq 8.7$, Meléndez & Asplund (2008)). We have also included in this low metallicity sample the Halo's PNe population, which is expected to have lower abundance values because they were form at early stages of the chemical enrichment in the Milky Way Galaxy evolution.

3.2 Overview

As we have seen in Chapter 1, a Planetary Nebula is a dynamically active system composed of two components. Our current theoretical understanding of the kinematics of the nebular shells in PNe clearly predicts an evolution of the kinematics with time (Kwok, 1982; Mellema, 1994; Perinotto et al., 2004; Schönberner et al., 2005a,b; Villaver et al., 2002). Rencently, Richer et al. (2008, 2010) and Pereyra et al. (2013) have provided observational support for the predictions of these theoretical models. Using large samples of PNe, segregated by evolutionary stages, they clearly demostrated for the first time the kinematic evolution of the nebular shell along the whole life of a PN from observational data.

Recent hydrodynamical models presented by Schönberner et al. (2010) suggest that

the metal content of the PN signifcantly influences also its dynamical evolution. Some studies have been done in past trying to understand the relationship that the central star has with the kinematic evolution of the nebular shell of a PN. Statistical analyzes were performed using samples that consider the central star properties (Medina et al. , 2006), stellar population (Richer et al., 2008, 2010) and evolutionary stages (Bohuski & Smith, 1974; Hippelein & Weinberger, 1990; Pereyra et al., 2013), but to date there is no study of this kind related to the metal content of the planetary nebula. In order to address this problem, using the San Pedro Mártir Kinematic Catalogue of PNe (López et al., 2012), we have performed a kinematical analysis of a low metallicity PNe sample to provide observational constraints for theoretical models. Based upon spatially-resolved, long-slit, echelle spectroscopy we characterize the global kinematics of the nebular shell of 31 low metallicity PNe. The selection criteria, measurements, results and conclusions obtained from the study are presented in the following sections.

3.3 Planetary Nebula with Low Metal Content

3.3.1 Selection criteria

To select the low metallicity sample we used the compilations of abundance determinations from papers published within the last two decades (1990-2010). Taking into account the chemical abundance of the sun ($\log(\mathrm{O/H})+12 = 8.7$, Meléndez & Asplund (2008)) and the mean O/H abundance ratio in PNe for the bulge ($\log(\mathrm{O/H})+12 \approx 8.6$, Richer et al. (1998)) and disk ($\log(\mathrm{O/H})+12 = 8.6$, Kwok (2000)), we considered as low metallicity objects those PNe with a value of $\log(\mathrm{O/H})+12 \lesssim 8.0$. Because we are dealing with low metallicity objects, it is important to consider that in these cases dredge-up processes may possibly increase the chemical composition of the shell during the evolution of the central star at the AGB stage. However, the consequence of dredge-up processes in these cases will be always an enrichment of oxygen abundance of the shell and thus, even if we select PNe with these characteristics, the sample will still be composed of low metallicity objects.

Due to the uncertainties and differences in the methods used to determine chemical abundances, compiling a large sample of low metallicity PNe with reliable data is not a trivial task. But, the choice of an oxygen abundance value below 8.0 allows us to consider uncertainties of up to 0.3dex in abundace determinations and still have a PNe sample with low metallicity relative to galactic disk and bulge. Since the Halo or Type

IV PNe (Peimbert, 1990) are characterized by their low metallicity relative to disc PNe, as a well defined group of metal-deficient objects within the Galaxy, this PNe population is also included in the sample. The low metallicity objects obtained from compilations of abundance determinations are listed in Table 3.1. The first two columns correspond to the common and PNG name of the PNe, respectively. Columns 3 and 4 show their abundance values and their references. In the last column, we indicated if high resolution data were available from the San Pedro Martir Kinematic Catalogue of Planetary Nebulae (SPM Catalogue; López et al., 2012) for each listed object.

Once we get the images and spectral data available from the SPM Catalogue for the initial sample, we finally were able to obtain the Low Metallicity sample needed to performance our statistical study. To discuss the uncertainties inherent in the abundance determinations (due to ionization correction factors or fluctuations in electron temperature and densities) is beyond the scope of this thesis, however, we present in Appendix D a brief discussion about the potential problems in the abundance determinations of some particular objects, that have been excluded from the statistical analysis presented in this chapter in order to avoid contaminants in the sample and misunderstandings of the general results.

The final sample and the data obtained for these PNe are presented in Table 3.2. In the first two columns the common and PNG name for each object is show. Columns 3 through 5 present our measurements of the expansion velocity (V_{ion}), from [NII] λ6584, Hα, and [OIII] λ5007. Columns 6 and 7 indicate the [O/H] abundance values and classification group, Low Metallicity ($\log(O/H)+12 \lesssim 8.0$) or Halo object, respectively. In column 8 and column 9 we list the HeII λ4686 intensities for each PN and their references, while columns $10-12$ show the luminosity and effective temperature of the central star with their references.

3.3.2 Observations

The observations drawn from the SPM catalogue were obtained with the Manchester Echelle Spectrograph, a long slit, echelle spectrograph without cross-dispersion (Meaburn et al. , 1984, 2003). Narrow-band filters isolate orders 87 and 114 containing Hα (including [NII] $\lambda\lambda$6548,6584) and [OIII] λ5007, respectively. The slit used (150 μm wide and $\sim$6.5 arcmin long) produces a spectral resolution of 11 km s^{-1}. The spectra are calibrated using exposures of a ThAr lamp, with an accuracy of $\pm$1 km s^{-1} when converted to radial velocity. See López et al. (2012) for futher details.

Table 3.1 .- PNe with $\log(\mathrm{O/H})+12 \lesssim 8.0$ compiled from the literature.

Object	PN G	$\log(\mathrm{O/H})+12$	Ref.†	SPM Catalogue
A 18	216.0-00.2	7.99	e	Yes
BoBn 1	108.4-76.1	7.892	f	Yes
H 1-9	355.9+03.6	7.73	m	No
H 1-24	004.6+06.0	7.52	b	Yes
H 1-45	002.0-02.0	7.52	h	Yes
H 2-1	350.9+04.4	7.92	m	No
H 2-17	003.1+03.4	7.55	b	No
H 2-32	000.6-02.3	7.01	b	No
H 2-43	003.4-04.8	6.9	b	Yes
H 2-48	011.3-09.4	7.89	g	Yes
H 4-1	049.3+88.1	7.85	a	Yes
Hen 2-171	346.0+08.5	7.79	b	Yes
K 3-27	061.0+08.0	7.955	k	Yes
K 4-47	149.0+04.4	7.69	j	Yes
K 5-1	000.4+04.4	7.88	d	Yes
K 5-17	004.3+02.0	7.99	g	Yes
K 5-5	001.5+03.6	7.72	d	Yes
KFL 4	003.0-02.6	8	g	No
M 1-6	211.2-03.5	7.732	k	Yes
M 1-37	002.6-03.4	7.98	b	Yes
M 2-24	356.9-05.8	7.9	b	Yes
M 2-29	004.0-03.0	7.47	b	Yes
M 2-39	008.1-04.7	7.17	g	Yes
M 3-2	240.3-07.6	7.83	j	Yes
M 3-21	355.1-06.9	8	g	Yes
M 4-8	018.9+03.6	8	g	No
NGC 6644	008.3-07.3	7.39	g	Yes
PS 1 (K 648)	065.0-27.3	7.851	f	Yes
SB 2	000.5-05.3	7.97	d	No
SB 3	000.7-06.1	7.69	d	No
SB 4	001.1-06.4	7.73	d	No
SB 6	001.6-05.9	7.78	d	No
SB 12	005.4-06.1	7.98	d	No
SB 17	011.1-07.9	7.97	d	No
SB 18	011.4-07.3	7.996	g	No
SB 20	014.8-08.4	7.88	d	Yes
SB 24	017.5-09.2	7.94	g	No
SB 32	349.7-09.1	7.799	g	Yes
SB 33	351.2-06.3	7.62	d	Yes
SB 38	352.7-08.4	7.91	g	Yes
SB 42	355.3-07.5	7.82	d	Yes
SB 50	357.3-06.5	7.99	g	No
SB 55	359.4-08.5	7.58	g	Yes
Th 3-13	356.1+02.7	7.398	g	No
Th 3-25	359.8+03.7	7.86	m	No
Th 4-11	011.3+02.8	6.89	m	No
TS 1	135.9+55.9	6.82	l	Yes

† References for abundance values: a.-Costa et al. (1996), b.-Ratag et al. (1997), c.-Howard et al. (1997), d.-Escudero et al. (2001), e.-Costa et al. (2004), f.-Henry et al. (2004), g.-Górny et al. (2004), h.-Escudero et al. (2004), i.- Pereira et al. (2007), j.-Henry et al. (2010), k.-Stanghellini & Haywood (2010), l.-Stasińska et al. (2010), m.- Cavichia et al. (2010).

Table 3.2 .- The Low Metallicity Sample: PNe with $\log(\mathrm{O/H})+12 \lesssim 8.0$ and Halo objects.

Object	PN G	$V_{H\alpha}$ $\pm2\,(\mathrm{km\,s^{-1}})$	$V_{[NII]}$ $\pm2\,(\mathrm{km\,s^{-1}})$	$V_{[OIII]}$ $\pm2\,(\mathrm{km\,s^{-1}})$	$\log(\mathrm{O/H})+12$	Group★	I(HeII λ4686) Hβ=100	Ref.†	log T (K)	log L/Lo	Ref. ‡
A 18	216.0-00.2	10	16		7.99	LowMet	11.9	c	5.03	1.86	*i*
BD +332642	052.7+50.7	11 *	11 *			Halo					
BoBn 1	108.4-76.1	23 *	19		7.89	Halo	20	a			
DdDm 1	061.9+41.3	18 *	18 *	11	8.13	Halo	$\leq$2	a	4.6	3.5	*ii*
GJJC 1	009.8-07.5			13 *		Halo			4.69	3.34	*ii*
H 1-24	004.6+06.0	16 *	12	18 *	7.52	LowMet	$\leq$4	a			
H 2-48	011.3-09.4	12 *	15 *	7 *	7.89	LowMet	$\leq$1	a			
H 4-1	049.3+88.1	13 *	13 *		7.85	Halo	10	a			
JAFU 1	002.1+01.7	15	18	16		Halo					
JAFU 2	353.5-05.0	28		25		Halo					
K 3-27	061.0+08.0	23			7.955	LowMet	97	a	4.98	3.2	*i*
K 4-47	149.0+04.4	26 *	9 *		7.69	LowMet					
K 5-1	000.4+04.4	16 *	12	18 *	7.88	LowMet					
K 5-17	004.3+02.0	18	35	19	7.99	LowMet					
K 5-5	001.5+03.6	17 *	20	16 *	7.72	LowMet					
M 1-6	211.2-03.5	9 *	9 *	9 *	7.732	LowMet	$\leq$1	a	4.78	3.27	*iii*
M 3-2	240.3-07.6	23 *	16		7.83	LowMet	82	a	4.9	3.67	*i*
M 3-21	355.1-06.9	14 *	13	13 *	8	LowMet	7.5	a			
NGC 4361	294.1+43.6	23			8.15	Halo	115	a	5.1	3.53	*iv*
NGC 6644	008.3-07.3	16 *	13	16 *	7.39	LowMet	17	a			
PRMG 1	006.0-41.9	26 *		26 *	8.06	LowMet			4.84	3.02	*ii*
PRTM 1	243.8-37.1			29	8.1	LowMet	$\leq$15	a	4.9	3.37	*ii*
PS 1 (K 648)	065.0-27.3	17 *	12 *	17 *	7.85	Halo	$\leq$1	a	4.54	3.48	*ii*
SaSt 2-3	232.0+05.7	10 *	10 *		8.29	Halo	$\leq$1	a			
Sb 20	014.8-08.4	19		17	7.88	LowMet	30.2	b			
Sb 32	349.7-09.1	31	36	38	7.799	Halo	25.7	b			
Sb 33	351.2-06.3	27	32		7.62	LowMet	17.5	b			
SB 38	352.7-08.4	21		25	7.91	LowMet	65.6	b			
Sb 42	355.3-07.5	17 *		16 *	7.82	LowMet	4.9	b			
SB 55	359.4-08.5	20		20	7.58	LowMet	126.7	b			
TS 01	135.9+55.9	22			6.82	Halo			4.76	3.14	*v*

* V_{flow} measurement obtained from the FWHM of a Gaussian fit.

★ The Halo and LowMet classifications correspond to Halo and Low Metallicity objects respectively.

† References for I(HeII λ4686) data: a.-Tylenda et al. (1994), b.-Escudero et al. (2001), c.-Costa et al. (2004) .

‡ References for Central Star data: *i*.-Kaler et al. (1990), *ii*.-Peña et al. (1992), *iii*.-Stanghellini et al. (2002), *iv*.-Frew (2008), *v*.-Tovmassian et al. (2010).

3.3.3 Measurements

The calibrated spectra were analyzed using the IRAF[1] package to obtain the expansion velocity (the bulk flow velocity, V_{flow}) of the nebular shell. With observations at high spectral resolution one expects that a spherical expansion will be represented by the shape of a typical velocity ellipse in the bi-dimensional line profile or position - velocity (P–V) diagram. However, this is only possible to observe on spatially resolved objects. Given the selection criteria used for our Low Metallicity sample it is likely that most of the selected objects are not located in the solar neighborhood and then, their spectra will often not be spatially resolved. For this reason, the expansion velocity measurements in this cases must be done very carefully.

As for the Evolved PNe sample, we considered the expansion velocity of the nebular shell as the typical outflow velocities for the matter with the highest emission measure (the bulk flow velocities, V_{flow}) within the spectrograph slit. In the case of spatial, or spectrally, resolved objects we measured V_{flow}, as half the peak to peak difference in velocity between the blue- and red-shifted components at the point of maximum splitting, usually the centre of the line profile. For the objects where the line profile (Hα, [NII] λ6584 and/or [OIII] λ5007) shows no splitting, we fit a single Gaussian profile to the line profile and assign half of the resulting Full Width Half Maximum (FWHM) as the bulk flow velocity (Gesicki & Zijlstra, 2000). In these cases we correct the measured FWHM for instrumental broadening (11.5 km s^{-1} FWHM), thermal Doppler broadening (assuming a temperature of 10^4 K), and fine structure broadening in the case of Hα emission line (assuming a value of 7.5 km s^{-1} FWHM; García-Díaz et al. , 2008) as in Richer et al. (2008). The measurements made for each planetary nebula in the Low Metallicity sample are shown in Appendices B (Halo objects) and C (Low Metal objects). For all the PNe, we measured V_{flow} from all available spectra: Hα, [NII] λ6584, and [OIII] λ5007 emission lines, as may be the case.

3.3.4 Velocity Distributions

We have found that the typical flow velocities measured for the Low Metallicity objects in our sample are usually small.

[1]IRAF is distributed by the National Optical Astronomy Observatories, which are operated by the Association of Universities for Research in Astronomy, Inc., under cooperative agreement with the National Science Foundation.

The results of the statistical analysis performed, using velocity measurements obtained from spectral data, are presented in this section. First, we present the velocity distributions for Halo (12 PNe) and Low Metal (19 PNe) objects, separately. Later, we analyze the kinematical behavior of a sample composed by these two groups with the aim to compare the obtained results with theoretical predictions from hydrodynamical models (Schönberner et al., 2010). These results are discussed taking into account previous statistical studies of different stellar populations like the Bulge PNe from Richer et al. (2008, 2010) and the Evolved PNe from Pereyra et al. (2013), most located at the galactic disc, which are expected to have a typical metallicity, near to the solar value.

Halo and Low Metal PNe

Depending on the emission lines detected for each PNe in our sample, we obtained velocity measurements from [NII] $\lambda\lambda$6548,6584, [OIII] λ5007, and Hα λ6562.8. We plot the velocity distributions for the two groups considered, Halo and Low Metal PNe, using the available measurements from each emission line. The results are presented in Figure 3.1. It is found that most of the PNe, in both groups, tend to have low V_{flow} values (lower than 20 km s^{-1}) independently of the emission line considered.

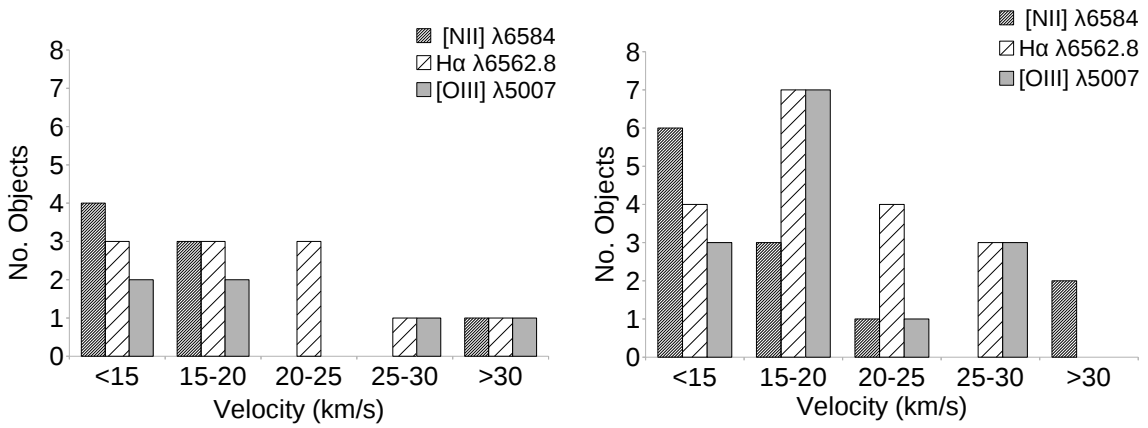

Figure 3.1 Velocity distributions for Halo (left panel) and Low Metal (right panel) objects. For both groups, we plot the measurements obtained from each emission line: [NII] $\lambda\lambda$6548,6584, Hα λ6562.8, and [OIII] λ5007. The plots suggest that, no matter which emission line is considered, most of the objects considered tend to have low expansion velocities.

We obtained the average expansion velocities for the two groups, considering each emission line separately for consistency. The average values and the number of objects

used to calculate them, are shown in Table 3.3. It is easy to see that the number of objects considered to obtain the average expansion velocities, in both groups, is not the same for the different emission lines ([NII], Hα and [OIII]) because it depend on the spectral information available for each PNe. Nevertheless, from all emission lines considered, the average values obtained for Halo and Low Metal PNe are in excellent agreement with each other, which allows to conclude that the kinematical behavior of these two groups of low metallicity objects is very similar.

Table 3.3 Average expansion velocities for Halo and Low Metal PNe.

Group	$\overline{V}_{[NII]}$ ± 2 (km s^{-1})	No. Objects considered	$\overline{V}_{H\alpha}$ ± 2 (km s^{-1})	No. Objects considered	$\overline{V}_{[OIII]}$ ± 2 (km s^{-1})	No. Objects considered
Halo PNe	17	8	19	11	20	6
Low Metal PNe	17	12	18	18	17	14

To better ilustrate this conclusion, in Figure 3.2 a normalization of the velocity distributions shown in Figure 3.1 is presented. For clarity, we show the velocity values obtained from [NII]and Hα emission lines using two different plots.

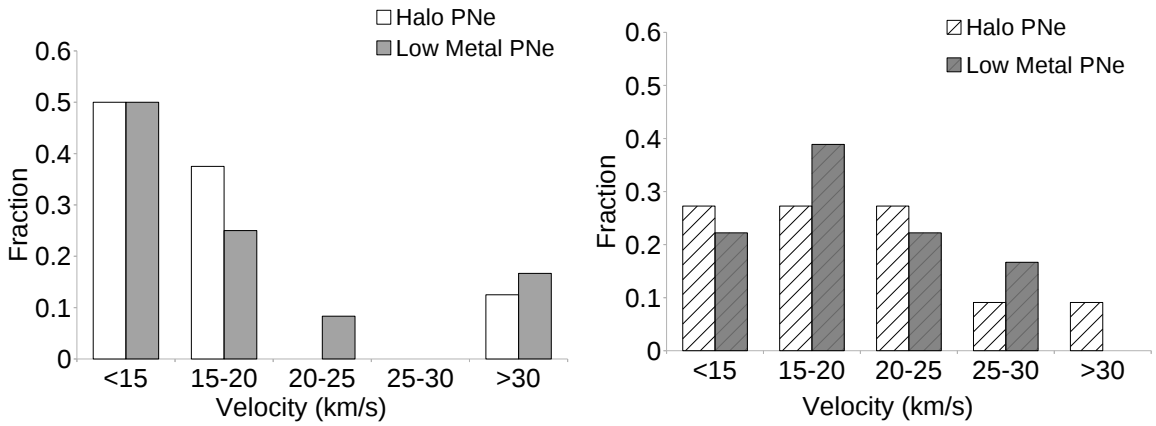

Figure 3.2 Normalized velocity distributions for the Halo PNe and Low Metal PNe using [NII] $\lambda\lambda$6548,6584 (left panel) and Hα λ6562.8 (right panel) measurements. It is clear that the kinematical behavior between the groups is very similar in both emission lines.

According to these plots, it seems that the normalized velocity distributions observed depend on the emission line considered. However, for the two groups the kinematical behavior in each emission line indicates a general trend towards low velocity values. For both, Halo and Low Metal PNe, the velocity distribution from Hα λ6562.8 emission extends over a wide range (right panel), whilst most [NII] $\lambda\lambda$6548,6584 velocities are

found at the lowest values in the plot (left panel). Since the kinematics for the two groups is actually very consistent, we can consider the Halo and Low Metal PNe as a single group of low metallicity objects. Hereafter, we will refer to this group as The Low Metallicity Sample. The velocity distribution and extended kinematical analysis for this sample is presented in the following section.

The Low Metallicity Sample

Using the whole sample, in Fig. 3.3 we show the velocity distribution obtained for the 31 low metallicity PNe considered. Because the number of velocity measurements depend on the number of emission lines available for each PNe, in this plot are presented 20 measurements from [NII]$\lambda\lambda$6548,6584, 29 from Hα λ6562.8, and 20 from [OIII] λ5007. Since the sample is composed by the two groups presented in Section 3.3.4, it is not surprising that the observed velocity distribution for the whole sample is very similar. More than 50% of the velocity measurements in every emission line are found at low velocity values (lower than 20 km s^{-1}), which indicates that the bulk of matter of the nebular shells of most planetary nebulae with low metal content is indeed moving slowly.

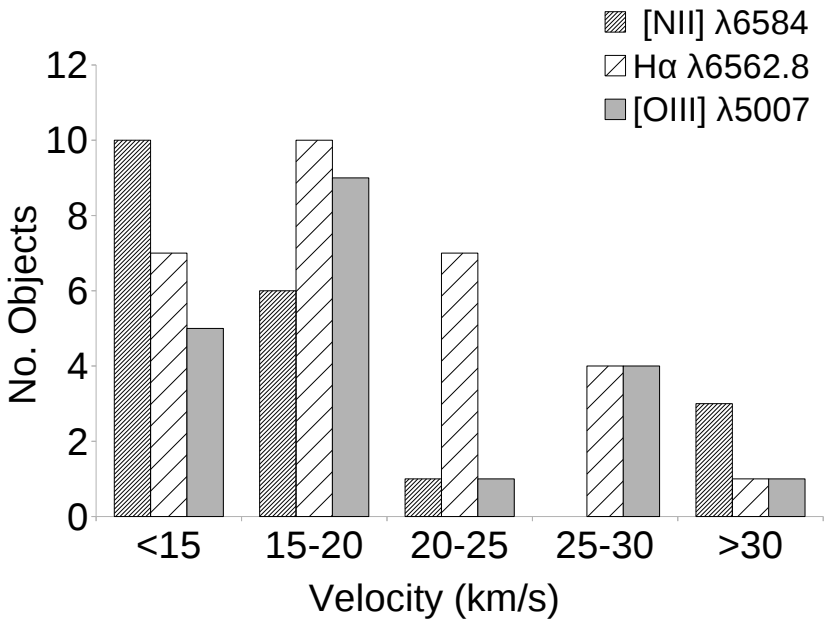

Figure 3.3 Velocity distributions for the Low Metallicity PNe using measurements obtained from all available emission lines in the optical spectra. It is found that the expansion velocities of low metallicity objects tend to have low velocity values.

Upon detailed inspection, we noticed some peculiar kinematical properties in some of the PNe from the Low Metallicity sample that caught our attention. The features observed in the spectral images of K 4-47 and M 3-2 (shown in Figs. C.10 and C.13) seemed to be very similar to those found in PNe having bipolar outflows. Since it is known that the kinematical behavior seen in bipolar planetary nebulae usually differs from that observed in spherical/elliptical PNe, depending on the kinematic structure considered for measurements (the bipolar outflows or the main shell of the nebula), it was very important for us to check that the morphology of the objects in our sample did not bias our results. To confirm the presence of bipolar PNe within the sample, we searched for high resolution images available at the Hubble Planetary Nebula Image Catalogue and the Hubble Legacy Archive. We found images for only 17 objects of the sample, but it was enough to observe clearly the bipolar lobes present in K 4-47 and M 3-2, as well as in three more objects (K 5-17, M 1-6 and NGC 6664) that we also classified as bipolar nebulae. To understand how the presence of these bipolar nebula in the Low Metallicity sample could be affecting the results presented in Fig. 3.3, we excluded the bipolar nebulae and plot the normalized velocity distribution for the new sample. The comparison of the histogram obtained for the whole sample (31 low metallicity PNe) and that of the sample without bipolar PNe (with 26 objects) is presented in Fig. 3.4.

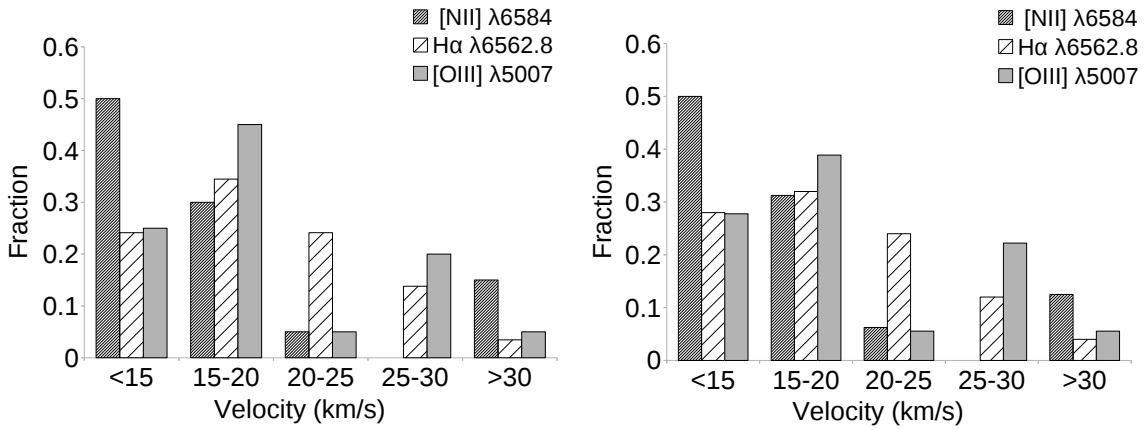

Figure 3.4 Normalized velocity distributions for the 31 low metallicity PNe (left), compared with the normalized velocity distributions found for the same sample excluding PNe with evident bipolar structures (rigth). It seems that the general kinematical behavior of the whole sample is not being affected by the presence of bipolar PNe in our case.

From these plots, it is easy to see that the histograms obtained for the two samples

are very similar. Thus, we conclude that the presence of these bipolar nebula do not influence the general kinematical behavior observed for the low metallicity sample. The likely reason is that for these bipolars we are considering the expansion of the main shell and not the lobes. Therefore, it is possible to perform the statistical analysis for the low metallicity PNe considering the whole sample composed by the 31 low metallicity objects without loss of generality.

Predictions from theoretical models

Before presenting the results obtained from our observations, it is important to give the reader a brief description of what is expected for the kinematics of low metallicity objects, according to the theoretical models existing to date. We mentioned in Section 3.2, that theoretical studies suggest that the metal content influences the kinematic evolution of a PN (Schönberner et al., 2010). Since the cooling efficiency of the gas in ionized nebulae decreases with metallicity, leading to a higher electron temperature, it is expected that the expansion velocity of the hot-ionized gas, which should be roughly proportional to the square root of the electron temperature, becomes higher in stellar populations with low metal content. On the other hand, the strength of the central-star wind decreases with metallicity given the reduced line opacity which drives the wind, limiting its ability to compress and accelerate the inner nebular parts. Taking into account the different effects produced by the central star wind and the electron temperature of the ionized gas in the inner and outer parts of the PN, respectively, we can sumarize the main conclusion from these models as follows: in a planetary nebula with low metal content, the outer parts of the PN (shell), influenced by the high electron temperature of its hot-ionised gas, will expand faster than the inner-bright parts of the PN (rim), which are accelerated mostly by a weak central star wind.

Unfortunately, as has been pointed out in Section 1.4, the *true* expansion velocities considered in theoretical simulations are not always accessible to measurements from observations. Theoretical models predict the formation of a double shell structure (rim and shell) for the nebular envelope of a typical PN, but in the particular case of low metallicity objects the rim formed at the inner parts of the nebula is less pronounced, due to the weak stellar wind of the central star, and hence it is more difficult to distinguish observationally the rim and shell of the nebular envelope in objects with low metal content than in typical nebulae. The case is ilustrated in Figure 3.5 where the radial surface brightness profiles for the different models from Schönberner et al. (2010)

are displayed. Models with the highest metal content ($Z = 3\,Z_{DG}$, Z_{DG}) form a sharp and well-defined rim. In this case, it is relatively easier to distinguish between the rim and shell structure. However, in the lowest metallicity cases ($Z=Z_{DG}/100$, $Z_{DG}/10$), the models develop a wider rim that masks the shell within a single nebular structure. Therefore, it is clear that measuring the velocities of these two structures independently in low metallicity objects is even more difficult than in typical PNe.

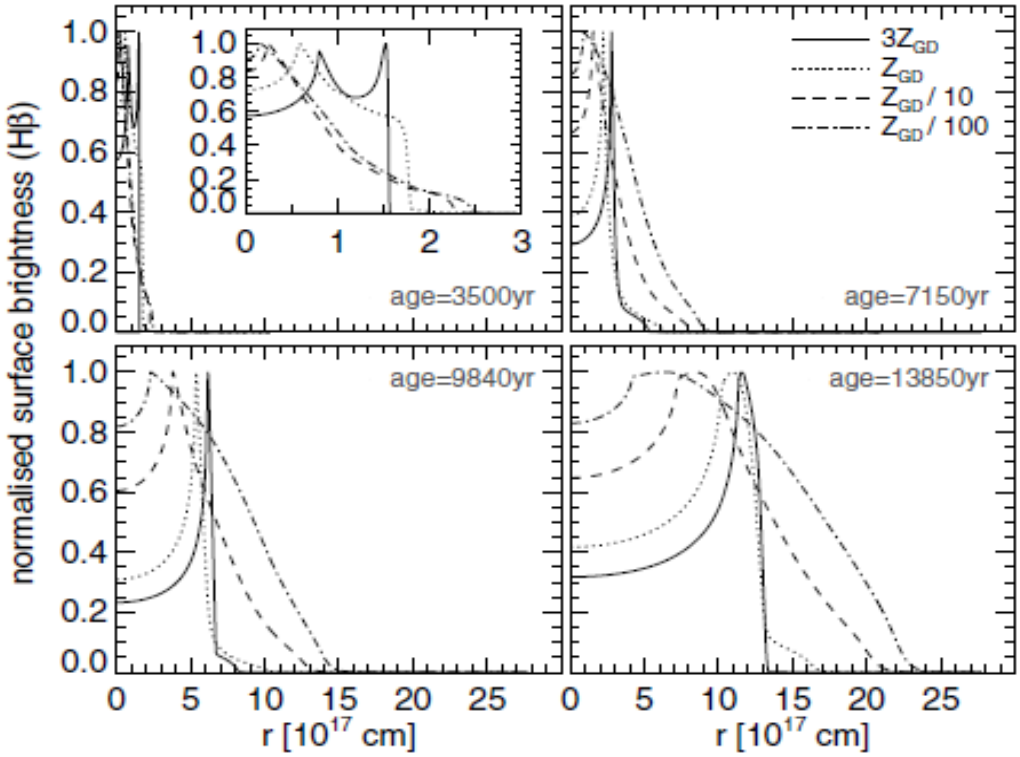

Figure 3.5 Normalised radial surface brightness (intensity) profiles in Hβ of models from Schönberner et al. (2010) for a central star with $0.595\,M_{\odot}$ considering different metal content, relative to the galactic disc metallicity (Z_{DG}). The evolutionary stage is indicated on each plot with the different ages (in years). For clarity, the inset in the top left panel shows the surface brightnesses at an enlarged scale.

Then we can conclude that, in the case of low metallicity objects, the only observable velocities available to compare with those derived from simulations are the outflow velocities for the matter with the highest emission measure (V_{flow}), which is neither the *true* expansion velocity of the fast shell nor that of the slow rim predicted by theoretical models. On the other hand, with the spatially integrated line profiles computed from the models it is possible to measure the nebular expansion using the half width at

half maximum (HWHM) of these line profiles and compare them with the velocity measurements obtained from spectroscopy. Then, although the *true* expansion velocities defined from simulations are not directly comparable to observations, there is actually a way to compare observational results with theoretical predictions. In Fig. 3.6 the expansion properties as derived from the HWHM obtained from models by Schönberner et al. (2010) are presented.

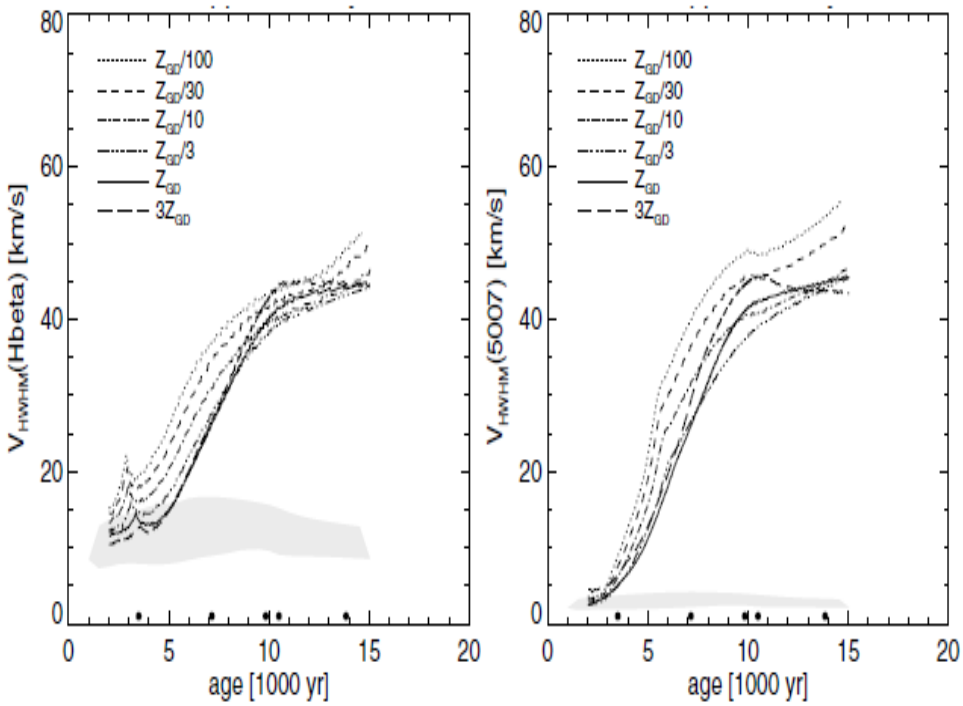

Figure 3.6 Observable expansion properties derived by Schönberner et al. (2010) from theoretical simulations. The time evolution of the half width at half maximum (HWHM) of the spatially integrated line profiles computed for a central star with $0.595\,M_{\odot}$ with different metallicities, relative to the galactic disc metallicity (Z_{DG}), is presented for Hβ (left) and [OIII] λ5007 (right).

In this case, it is clear that the V_{HWHM} of low metallicity PNe ($Z_{DG}/100$) are slightly different from those nebulae with metal content similar to PNe from the galactic disk (Z_{DG}). It is observed that the difference between the highest and lowest metallicity values considered in these models is just around $10\,km\,s^{-1}$. Taking into account the metallicity value used for the selection of our low metallicity sample ($log\,(O/H)+12 \leq 8.0$), we expect that the behavior of the velocity values obtained from our measurements will correspond to models with metal content similar to $Z_{DG}/3$ and $Z_{DG}/10$, for which the predicted velocities will be smaller than $\approx 2\,km\,s^{-1}$ from that of the PNe with

Z=Z_{DG}. A similar behavior is observed in Fig. 3.7 for the peak-to-peak separation of the spatially resolved profiles. In this case, the models show that the time evolution of observed velocities is almost the same for the different metallicity values considered. Considering PNe with different metal content, at early stages of evolution, there is no difference in the velocity measurement obtained from the peak-to-peak separation of the line profile. For advanced stages a small difference is observed, similar to that found in the case of the V_{HWHM}.

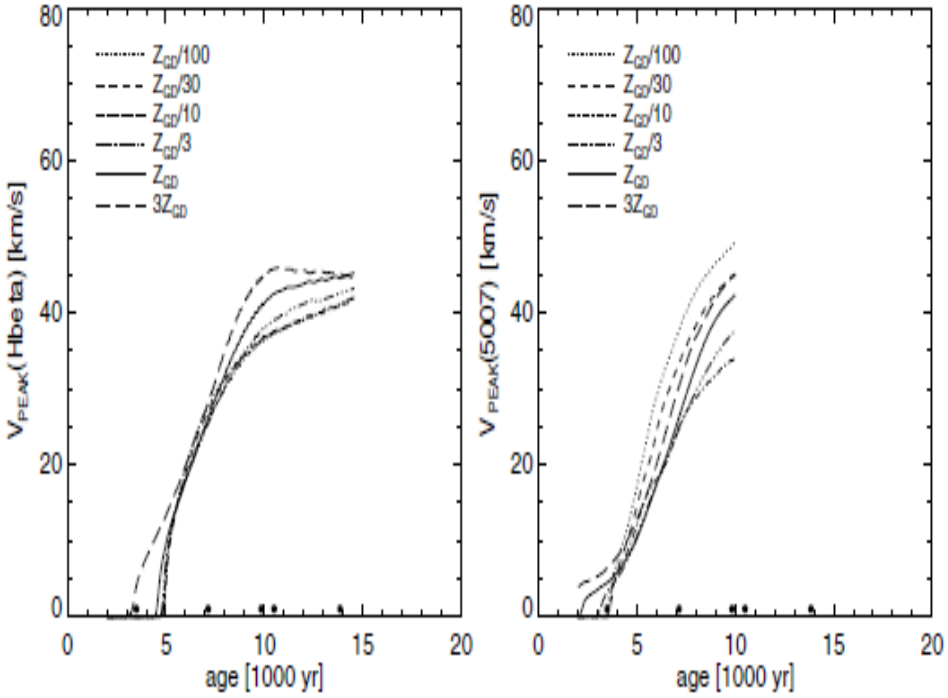

Figure 3.7 The same as Fig. 3.6, considering the peak-to-peak distance of the spatially resolved line profiles for Hβ (left) and [OIII] λ5007 (right).

With the aim to compare these theoretical results with those obtained from our observations, in the following sections we will analyze the kinematical behavior of low metallicity PNe focused on the statistical study of the observable velocities obtained from spectroscopy (using the FWHM or the peak-to-peak distance measurements), taking into account the central star properties (age and metal content) as well as the nebular morphology and the degree of excitation of the PNe.

3.3.5 Location in the H-R Diagram

In this section we present an evolutionary diagram with the objects in the low metallicity sample for which we obtained central star data from the literature. Since there is not a single compilation containing stellar parameters for all the objects in the sample, we have to adopt luminosities ($L/L\odot$) and effective temperatures (T_{eff}) values taken from different sources (e.g., Frew , 2008; Kaler et al., 1990; Peña et al., 1992; Stanghellini et al., 2002). The central star data and the respective references are indicated in Table 3.1 for each object when available.

Once we get the central star data, we locate the PNe of the sample in a H-R Diagram to compare them with theoretical evolutionary tracks from Vassiliadis & Wood (1994). The results are presented in Fig. 3.8. Although we are aware of the inherent uncertainties on the central star's parameters, it is clear that the location of the central stars of these low metallicity PNe suggest that they are most likely originated from low mass progenitors.

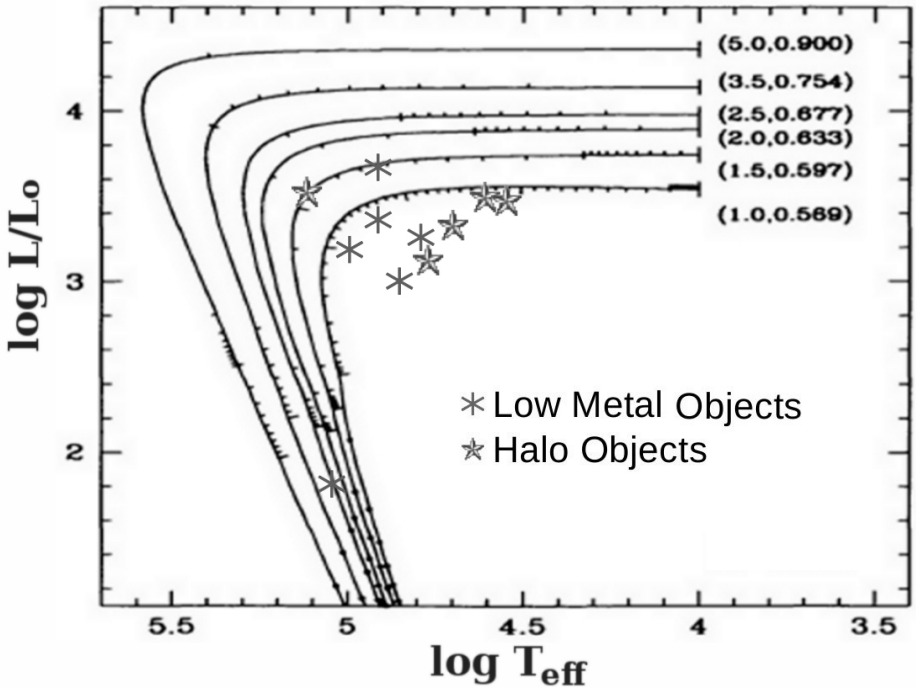

Figure 3.8 Locations of the PNe in the Low Metallicity sample (Halo + Low Metal objects) with available data. It seems that the central stars of the planetary nebulae with low metal content are originated from low mass progenitors. The evolutionary tracks were taken from Vassiliadis & Wood (1994).

In Figure 3.9 we indicate the expansion velocities for the objects in the H-R diagram and compare them with the results obtained from the sample of Evolved PNe (Fig. 8, Section 2.2). According to this, it seems that the central stars of the low metallicity objects originate from progenitors less massive than those of the Evolved PNe.

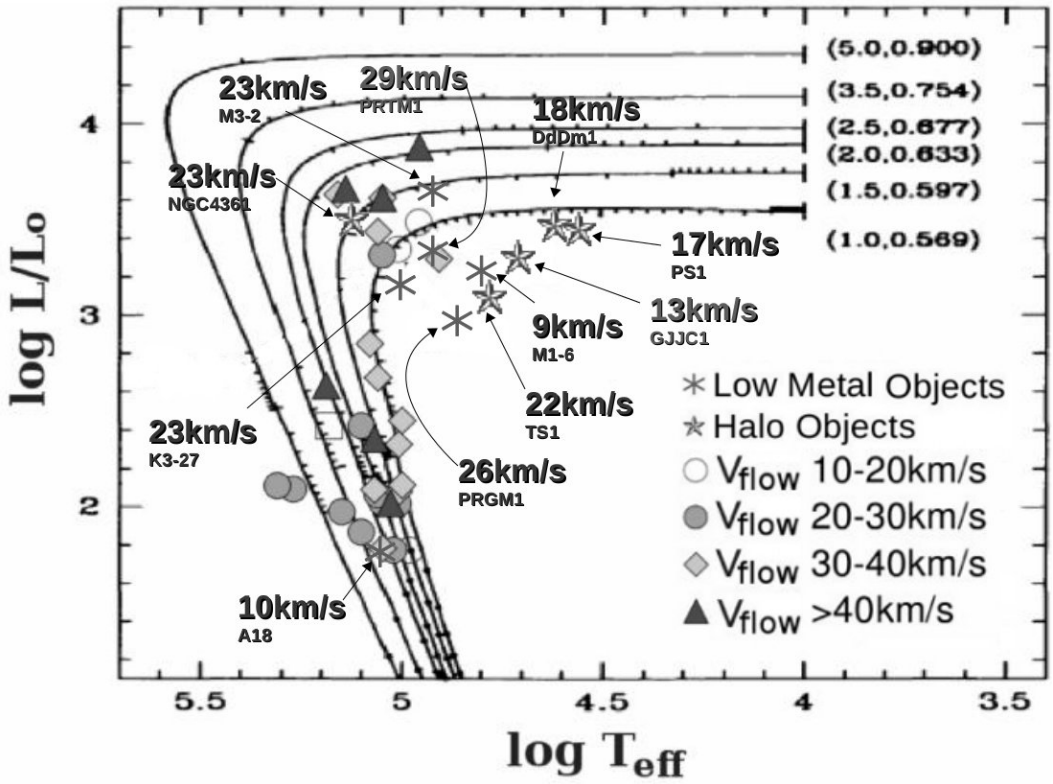

Figure 3.9 Expansion velocities for the low metallicity PNe with available central star data. Inspite of the few low metallicity PNe located in the evolutionary diagram, compared with the objects from the Evolved PNe sample, they are very consistent in their kinematical behavior. We found the high velocity objects at the highest effective temperatures. We consider here the Hα measurements for all objects, excepting GJJC 1 and PRTM 1 for which only [OIII] spectra was available.

Considering that Halo stars have ages similar to those of stars in globular clusters where there is no doubt that we are dealing with a very old stellar population, the most probable progenitor for the Halo PNe in our sample are low mass stars which have evolutionary times slow enough to allow the observation of these planetary nebula (with low metal content) at the actual age of the Milky Way Galaxy. Thus, it is not surprising that the low metal group appear to descend also from low mass stars.

It is clear from Fig. 3.9 that the high velocity objects in the low metallicity sample are located at higher effective temperature, a kinematical behavior that was observed

previously for Mature PNe from the Evolved PNe sample. However, the average expansion velocities for the high velocity objects from each sample is very different. We found an average velocity of $37\,\mathrm{km\,s^{-1}}$ for Mature PNe, while in the case of low metallicity objects the average velocity correspond to $21\,\mathrm{km\,s^{-1}}$ (excluding bipolar objects we obtained a higher average value of $24\,\mathrm{km\,s^{-1}}$). Although this difference is not predicted by theoretical simulations (see Figs. 3.6 and 3.6), it is important to consider that the models from Schönberner et al. (2010) are performed for planetary nebulae with central star masses of $0.595\,\mathrm{M_\odot}$ or higher, which is a typical value for most PNe from the disk and bulge in the MW Galaxy but not for the Halo population.

On the other hand, since theoretical models predict a weak central star wind for low metallicity objects in general, we can expect that for the low mass central stars of the objects in our sample the central star wind will be even weaker. Hence, the expansion of the nebular shells observed in our sample should be lower than those found in models. Therefore, we conclude that the kinematics of the low metallicity PNe behave very consistently with our previous findings and that the low velocities found for these nebulae are most likely a consequence of a weak central star wind driving the kinematics of the nebular shell in the case of low mass stars progenitors of planetary nebulae having low metal content.

3.3.6 Excitation degree of the nebular shells

Because of the lack of stellar parameters for the central stars of all the objects in the low metallicity sample, it is not easy to distinguish between the different evolutionary stages of every PNe involved in our study. Assuming that a higher ionization degree of the PN corresponds to a hotter and luminous central star, according to the results presented by Richer et al. (2008, 2010) and Pereyra et al. (2013), we have performed an analysis about the ionization degree of the PNe in the sample, looking for an indicator of age. Using the spectral images drawn from the SPM catalogue, we classified the sample into groups considering the presence and absence of [NII] λ6584 and HeII λ6560 emission lines, looking for a correlation between the excitation degree and the expansion velocity of the nebular shell. The results are presented in Fig. 3.10

Based on the velocity and cumulative distributions, we conclude that no difference is found between the groups defined by the presence or absence of the HeII λ6560 emission line. This ambiguity may be related to the dilution of the nebular shell after a long

expanding time of PNe with low mass central stars, where optical depth effects in the case of HeII λ6560 may be playing role.

On the other hand, in the case of the [NII] λ6584 emission line, the velocity distribution suggest that the objects with [NII] absent tend to have higher velocities than those with [NII] present. The above conclusion is confirm by the cumulative distribution obtained in this case, where the two groups are clearly distinguishable.

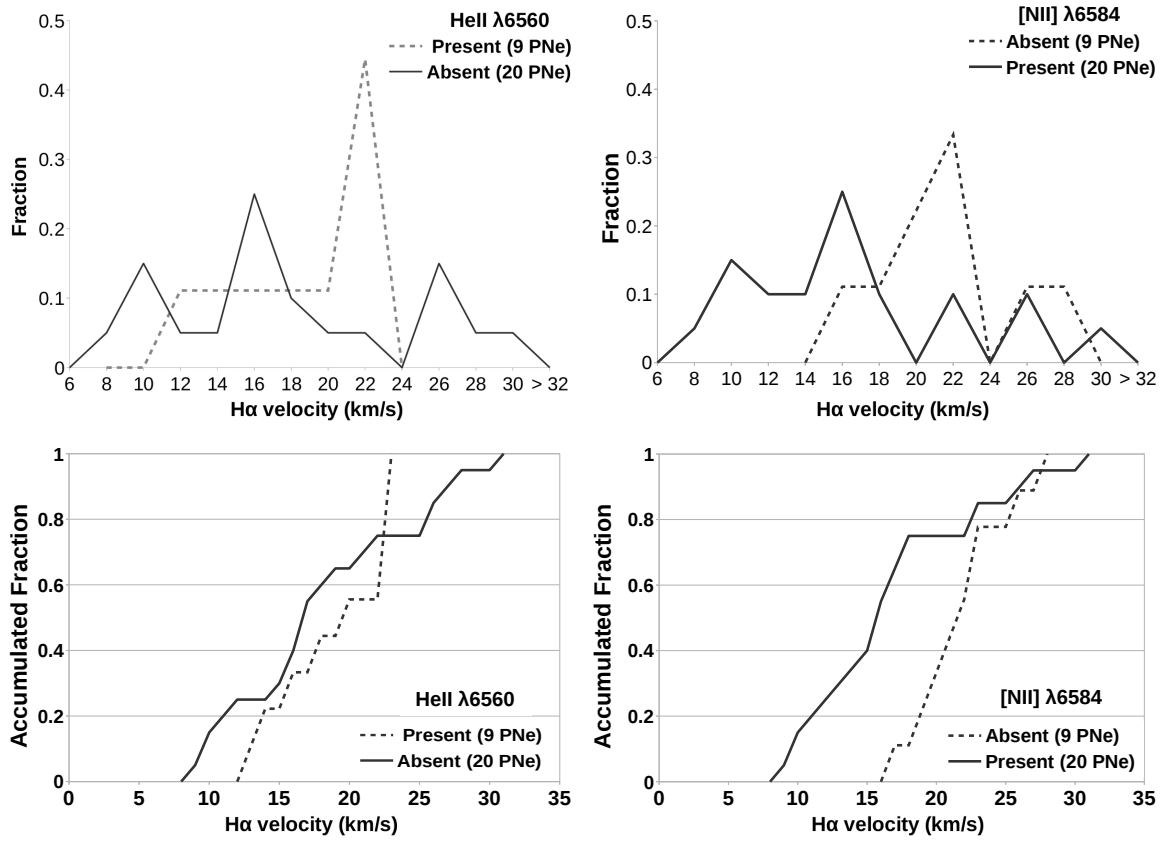

Figure 3.10 Kinematical behavior of the sample considering the excitation degree of the nebular shells. We present here, the normalized velocity distribution (*upper*) and cumulative distributions (*bottom*) for 29 low metallicity PNe according to the presence or absence of HeII λ6560 (*left*) and [NII] λ6584 (*right*). For consistency, we used only Hα λ6562.8 measurements. The number of objects considered for each group is indicated in parenthesis.

Chapter 4

Concluding remarks

In this work, we have performed an statistical analysis of the kinematical behavior of two different population of Planetary Nebulae, using the largest homogeneous data set used for this purpose based upon spatially-resolved, long-slit, echelle spectroscopy.

4.1 Evolved Planetary Nebulae

An Evolved population of PNe was analyzed in order to characterize the global kinematics of PNe at advanced stages of evolution. The main conclusions obtained for this sample can be summarized as follows:

•We found an average bulk flow velocity of $31\,\mathrm{km\,s^{-1}}$ for our sample (100 PNe), higher than the average found by Richer et al. (2008) ($\sim 25\,\mathrm{km\,s^{-1}}$) for younger PNe.

•The selected sample was subdivided in two different samples of Evolved PNe. Nebulae with very low surface brightness, no inner structure, and no bright rim, are classified as Highly Evolved nebula, whereas those PNe showing some structure and/or some bright edges are considered as moderately evolved PNe and cassified as Mature nebula.

•It is found that the kinematical behavior for the subsamples is indeed different. The bulk velocities for the Mature PNe (22 objects) are biased towards larger values, with mean bulk flow velocity of $37\,\mathrm{km\,s^{-1}}$, while for the Highly Evolved PNe (78 objects) we found lower velocity values and a mean bulk flow velocity of $30\,\mathrm{km\,s^{-1}}$.

•Considering the ionization properties of the nebular shell, it is found that the absence of [NII]6584 emission is a common characteristic of objects with high flow velocities in Mature PNe, which implies that our classification actually selects distinct evolutionary phases. The lack of [NII] is a consequence of the high excitation degree of

the nebula present at these advances stage of evolution where the effective temperature of the central star reaches its maximum value.

•Using the central star data available from Frew (2008) for the PNe in the Evolved sample, it is found that the CS luminosity, nebular morphology, nebular bulk flow velocity, and the degree of nebular excitation vary coherently and consistently. Moderately evolved objects tend to have high luminosity CSs, structured nebular morphologies, larger bulk flow velocities, and nebular spectra with a higher degree of excitation, while most of the Highly Evolved PNe show low luminosity CSs, nebular shells less structured, lower bulk flow velocities, and spectra with a lower degree of excitation.

Generally, we find a good correlation between the evolutionary stage of the central star and the kinematics, morphology, and spectral properties of the nebular shell, as predicted by modern hydrodynamical models (e.g., Perinotto et al. (2004); Schönberner et al. (2005a, 2010); Villaver et al. (2002)). At the latest stages of PN evolution, we find clear observational and statistical evidence for the deceleration of the nebular shell.

These results complement prior work, illustrating the coupling between the CS's evolution and that of the nebular shell predicted by theory (e.g., Perinotto et al. (2004); Villaver et al. (2002)). We concluded that the nebular shell of a PN is continuously accelerated until the central star reaches its maximum temperature and ceases nuclear burning (e.g., Richer et al. (2010)). Then, the luminosity and wind power of the star drop fast. Thereafter, the shell decelerates as the CS approaches the white dwarf stage of evolution, presumably due to the loss of energy from the central star and the combined effects of its interaction with the surrounding ISM and recombination of the outermost nebular matter. Distinguishing among these options is not simple and will be done best on a case-by-case basis.

4.2 Low Metallicity Planetary Nebulae

A sample of low metallicity objects was selected to test the influence of the metal content on the kinematical behavior of planetary nebulae predicted by hydrodynamical models. The main conclusions are presented in this section.

•We analyzed the velocity distributions for a sample composed of 19 PNe with low metal content and 12 Halo PNe, a well defined group of metal-deficient objects within the Galaxy. Depending on the emission lines detected for each PNe, we obtained velocity measurements from [NII] $\lambda\lambda$6548,6584, [OIII] λ5007, and Hα λ6562.8. It is found that

most of the PNe, in both groups, tend to have low V_{flow} values (lower than $20\,\mathrm{km\,s^{-1}}$) independently of the emission line considered.

•From all emission lines considered, the average values obtained for Halo and Low Metal PNe are in excellent agreement with each other. We conclude that the kinematical behavior of these two groups of low metallicity objects is very similar.

•Considering the velocity distribution for the whole sample of low metallicity objects (Halo + Low Metal PNe), it is observed that the bulk of matter of the nebular shells of most planetary nebulae with low metal content is indeed moving slowly.

•Using high resolution images we confirmed the existence of some bipolar PNe within our sample. However, it seems that the general kinematical behavior is not being affected by the presence of these particular objects in our case. The likely reason is that for these bipolars we are considering the expansion of the main shell and not the bipolar outflows.

•We located the PNe of the sample in a H-R Diagram adopting luminosities ($L/L\odot$) and effective temperatures (T_{eff}) values taken from different sources (e.g., Frew , 2008; Kaler et al., 1990; Peña et al., 1992; Stanghellini et al., 2002). From this diagram we concluded that the central stars of the planetary nebulae with low metal content seem to originate from low mass progenitors.

•According to the results presented by Richer et al. (2008, 2010) and Pereyra et al. (2013) we classified the sample into groups considering the presence and absence of [NII] λ6584 and HeII λ6560 emission lines, looking for an indicator of age. No clear tendency is observed for the HeII λ6560 emission. This ambiguity may be related to the dilution of the nebular shell after a long expanding time of PNe with low mass central stars, where optical depth effects may be playing role. In the case of the [NII] λ6584 emission line, the velocity distribution suggest that the objects with absent [NII] tend to have higher velocities than those with [NII] present, in good agreement with the results obtained from the Evolved PNe sample.

Finally, we concluded that the kinematics of the low metallicity PNe behave very consistently with our previous findings for the Evolved PNe sample. The high velocity objects in each sample are located at higher luminosities and higher effective temperature, but their average expansion velocities are very different. We found an average velocity of $37\,\mathrm{km\,s^{-1}}$ for Mature PNe, while in the case of high velocity objects in the low metallicity sample the average correspond to $21\,\mathrm{km\,s^{-1}}$. This difference is not ex-

pected from theoretical models because these models have been applied to objects with typical masses for the central stars, of the order of $0.595\,M_{\odot}$ or higher, which are not a representative population for the low metallicity objects included in our sample. We suggest that the low velocities found for these nebulae are most likely a consequence of a weak central star wind driving the kinematics of the nebular shell in the case of planetary nebulae with low mass progenitors.

4.3 Overall conclusions

With the results obtained from this thesis it is possible, for the first time, to complete the evolutionary sequence for the global kinematics of the nebular shell over the lifetime of the PN. Futhermore, we are able to show the different kinematical properties observed in planetary nebulae from different populations. In Fig. 4.1, the presented conclusions are summarized.

It is important to emphasize that although the three population considered are not directly comparable, the analyses performed for each sample are self-consistent. As has been pointed out before, the Bulge sample (green, magenta, red and blue ellipses) shows that the nebular shell is accelerated at the early stages of evolution, as the central star of the PN becomes hotter. On the other hand, the Evolved sample (gray ellipses) clearly demostrates that the nebular shell of a PN actually decelerates at advanced stages of evolution. Meanwhile, the Low Metallicity sample (yellow, pink and cyan ellipses) indicates that most of the PNe with low metal content originate from low-mass stars progenitors and their nebular shells are moving slowly.

One of the main challenges to obtain the expansion velocity of a PN is definitely the choice of a method for measuring. In the particular cases presented here, it is important to consider that not all the samples presented were measured using the same method. In the case of the Evolved sample we obtained the V_{split} (the peak to peak distance), for the Bulge it was used V_{HWHM} (the Half With at Half Maximum), while in the case of the Low Metallicity sample the two methods were used considering the best fit depending on each object. According to Gesicki & Zijlstra (2000), with the use of the V_{HWHM} method the expansion velocity of the nebular shell is usually overestimated. On the contrary, with V_{split} measurements we tend to underestimate the expansion velocity of the nebula. For these reasons, it is very important to be careful in interpreting the diagram shown in Fig. 4.1.

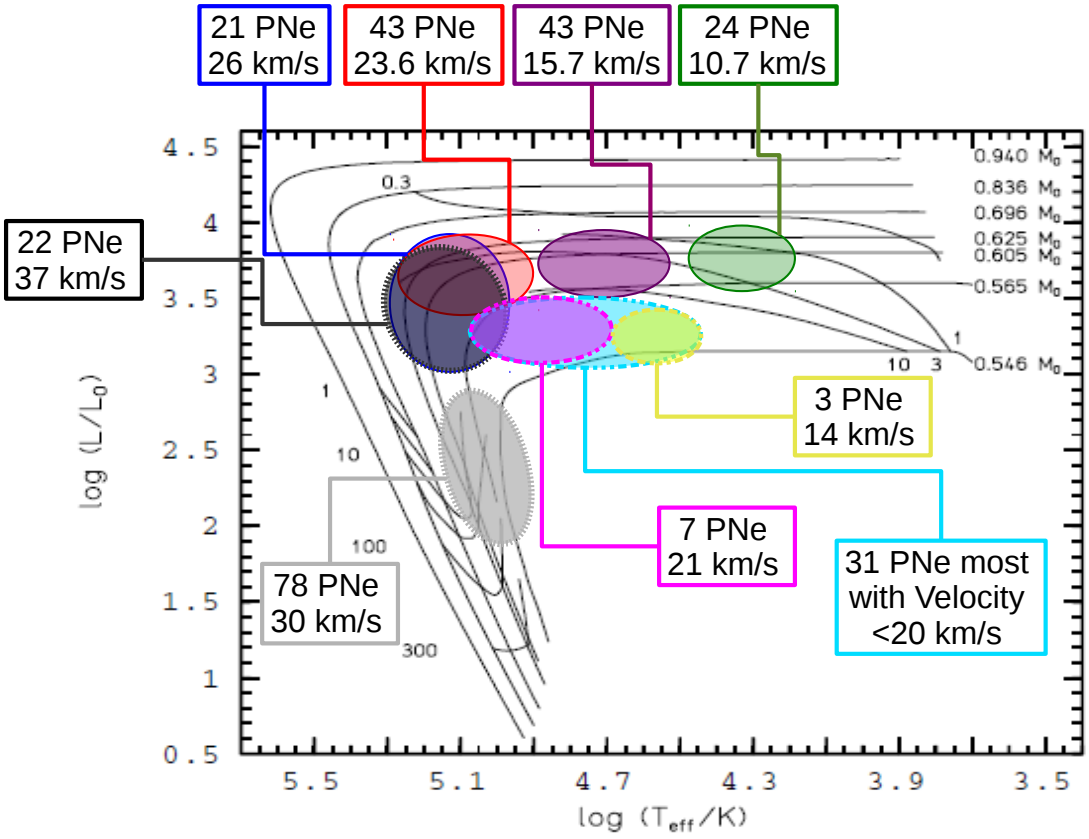

Figure 4.1 Mean bulk flow velocities for the nebular shell of a PN at different stages of the central star evolution, considering different populations of PNe. The number of planetary nebulae considered for each group and their average bulk flow velocity are indicated on the colored squares, which are linked to an ellipse in the same color indicating their approximate location on the evolutionary diagram. The groups from the Bulge sample are represented by the green, purple, red and blue colors. The Evolved PNe correspond to gray ellipses: lighter for Highly Evolved and darker for Mature. Since it was not possible to segregate the whole sample of low metallicity objects (31 PNe) by evolutionary stages, we present the average velocity for two groups of low metallicity PNe (pink and yellow) with central star data available. No average velocity is reported for the whole sample, but we indicate the velocities values commonly found in this case (cyan). The Hertzsprung-Russell diagram with the evolutionary tracks for different central star masses (0.8, 1, 3 to 7 $M_{\odot}$ resp.) was taken from Perinotto et al. (2004). Isochrones for the different evolutionary tracks are indicated with solid lines, with time marks in units of 10^3 years.

Between the three population of PNe presented in the diagram, the groups of objects that seem to be comparable are those located at the higher effective temperature (the black, red, blue and pink circles). Since the velocity measurements for the groups of PNe from the Evolved (black) and the Low Metallicity (pink) samples were made using V_{split}, it is possible to compare them directly and conclude that their kinematical behavior is actually different (see Sec. 3.3.5). However, to compare these samples with the results from the Bulge PNe is not that easy because the method used to measure the velocity in this case was V_{HWHM}.

Acording to Fig. 4.1 it is easy to see that in spite of the overestimation expected from theory in the velocities of the PNe from the galactic Bulge, the average velocity found for these PNe is always lower than the values obtained from the Evolved sample. Thus, it is clear the nebular shells of Evolved PNe tend to have higher velocities than those from the Bulge, which are at early stages of evolution, confirming that the nebular shell of a PN is accelerated until the central star reaches its maximum temperature and ceases nuclear burning. Furthermore, taking into account that most of the PNe from the Evolved sample are located within the galactic disk, it is likely that the observed difference is enhanced by the differences in the galactic environments where the progenitor stars of the planetary nebulae in these two samples were born. Given the physical properties of the galactic Bulge, it is expected that the population of planetary nebulae in this region originates from older population and less massive stars than those that form the nebulae within the galactic disk, where most of the gas within the Galaxy is concentrated. Therefore, we conclude that the remarkable difference observed in the average velocity of the planetary nebulae at higher effective temperatures from the Bulge (blue and red ellipses) and from the Evolved (black ellipse) samples is not because the different methods used for the velocity measurements, but a consequence of the acceleration of the nebular shell and the different masses of the progenitor stars that originate these nebulae. Because of the different methods used to measure the expansion of the nebular shell and the similarity observed in the average velocity values found for the Bulge and Low Metallicity samples, the comparison between these two populations is even harder. Further studies will required accurate central star data for all the objects of the Low Metallicity sample to strengthen our statistics, as well as the use of a single method to measure the expansion velocity of the nebular shell in both cases, with the aim to compare directly the two samples under study. We are planning to address these problems in future research.

Appendix A

Evolved PNe Sample

The objects considered for the analysis performed in Chapter 2 are presented in this appendix. The image of each nebula is shown, indicating the slit position used and the calibrated spectra obtained from it. The two-dimensional array position-velocity (P-V), calibrated in heliocentric velocity and angular scale, is also presented for some emission lines. If there are peculiar properties observed for a PN of the sample, we point them out case by case at the bottom of the images.

Since most of the selected objects for the Evolved PNe sample are essentially round and spatially resolved objects, given the high spectral resolution of our observations it is not surprising that the expansion of these spherical PNe is represented by the shape of a typical velocity ellipse in the bi-dimensional line profile. The expansion for the PNe in the Evolved sample was obtained at the point of maximum splitting of the line profile, usually at the centre of the line profile, averaging 10 of the central lines of the spectral image in most cases. We measure the bulk flow velocities as half the peak to peak difference in velocity between the blue- and red-shifted or, when the line profile shows no splitting (six cases in Hα emission line) , we fit a single Gaussian profile to the line profile and assign half of the resulting FWHM as the velocity of the nebular shell.

For the faintest objects in the sample we have to average more than 10 lines of the spectra in order to get a signal to noise good enough to obtain reliable measurements. In the spectra where the central star of the PN is observed, the measurements were made using 10 lines over or below the emission of the stellar continuum.

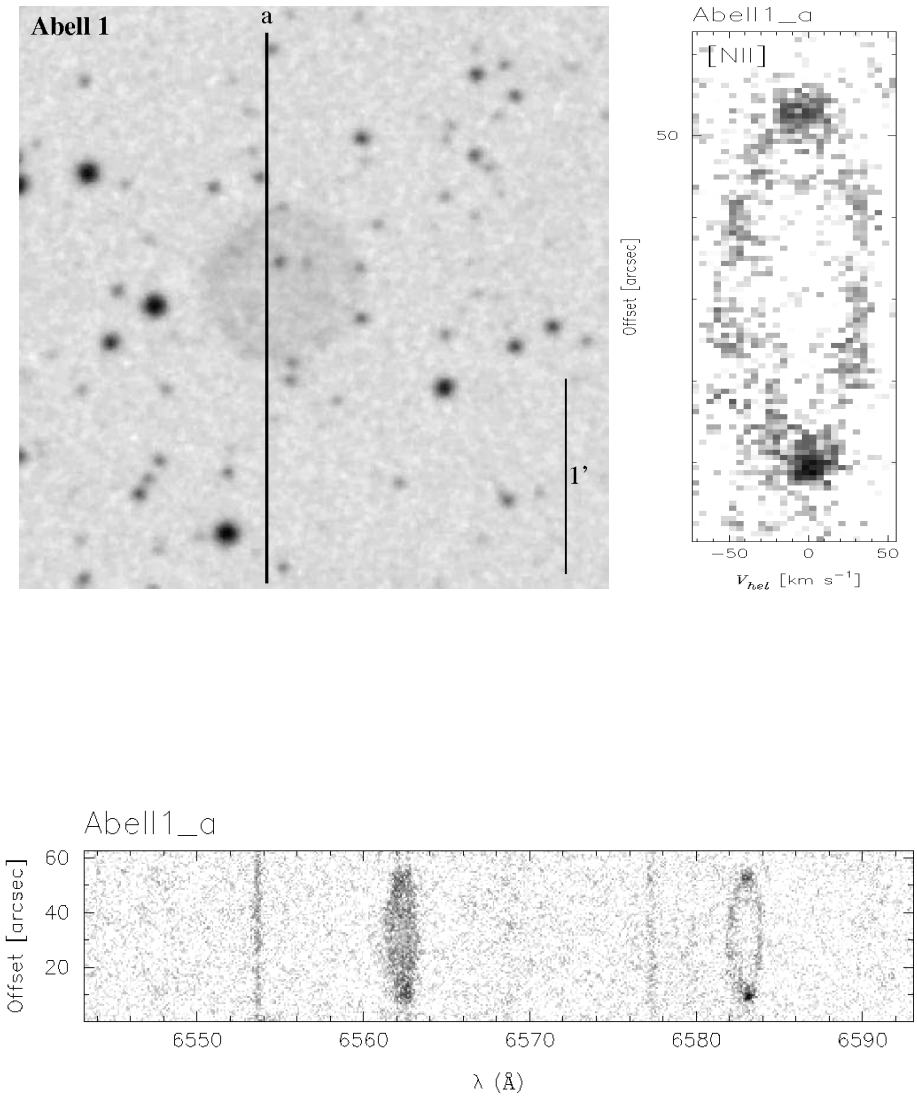

Figure A.1 **Image and spectra of the PN A1 for slit a. The left panel shows the image of the object taken from DSS2R. The right panel present, the two-dimensional array position-velocity (P-V) for the emission line labeled in the upper-left corner. This panel is calibrated in heliocentric velocity (abscissa), and the offset indicates the angular scale along the slit containing the nebular emission from the PNe (ordinate). At the bottom panel is the full spectral range observed for this PN calibrated in wavelength, and angular scale, where the emission lines detected are [NII] $\lambda\lambda$6548,6584, HeII λ6560, and H λ6562.8. The slit position is indicated as a solid line in the DSS2R image. Beside the PN name at the top of the P-V array and in the full spectral range the slit used for measurements is shown.**

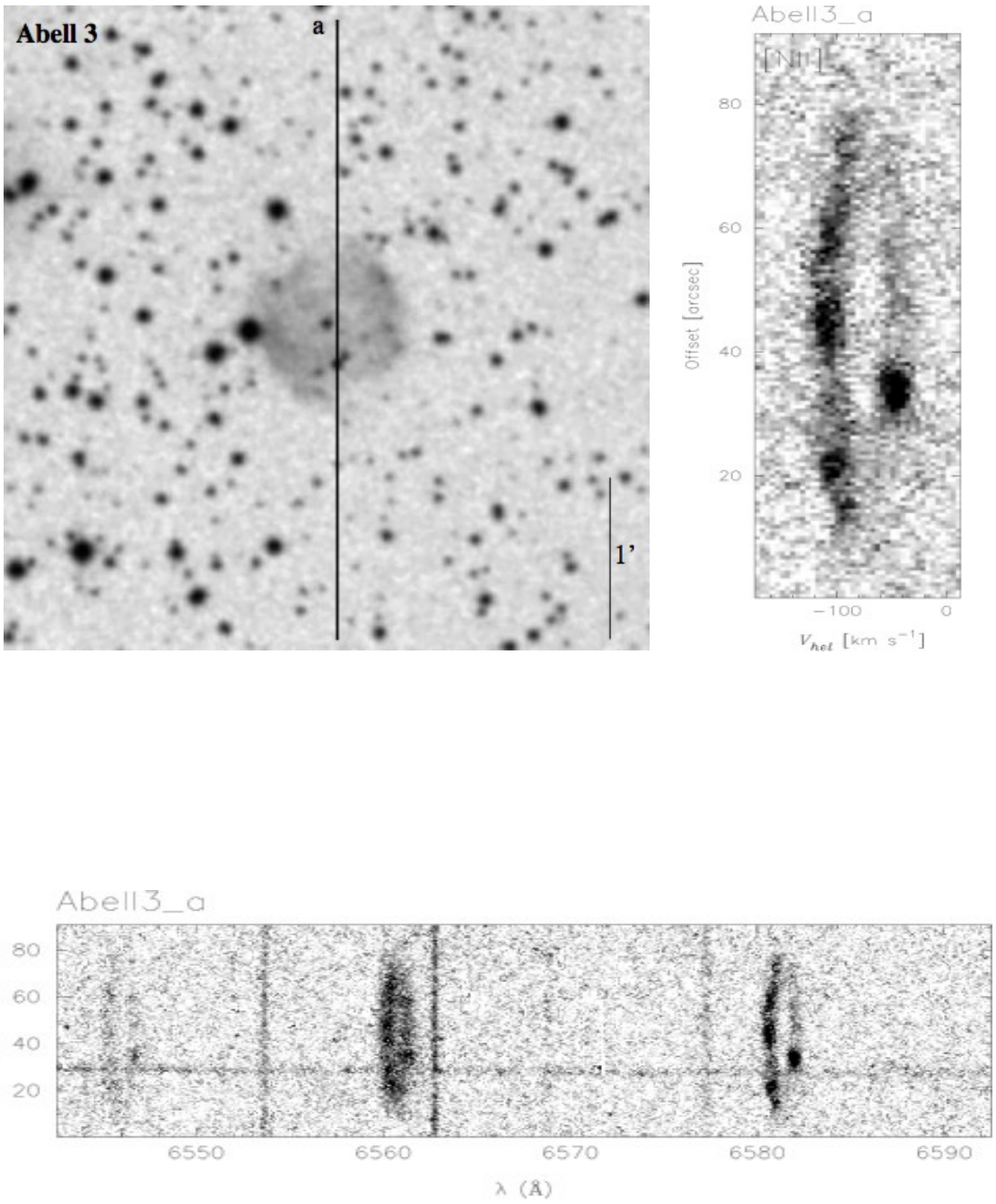

Figure A.2 **Same as Figure A.1.**

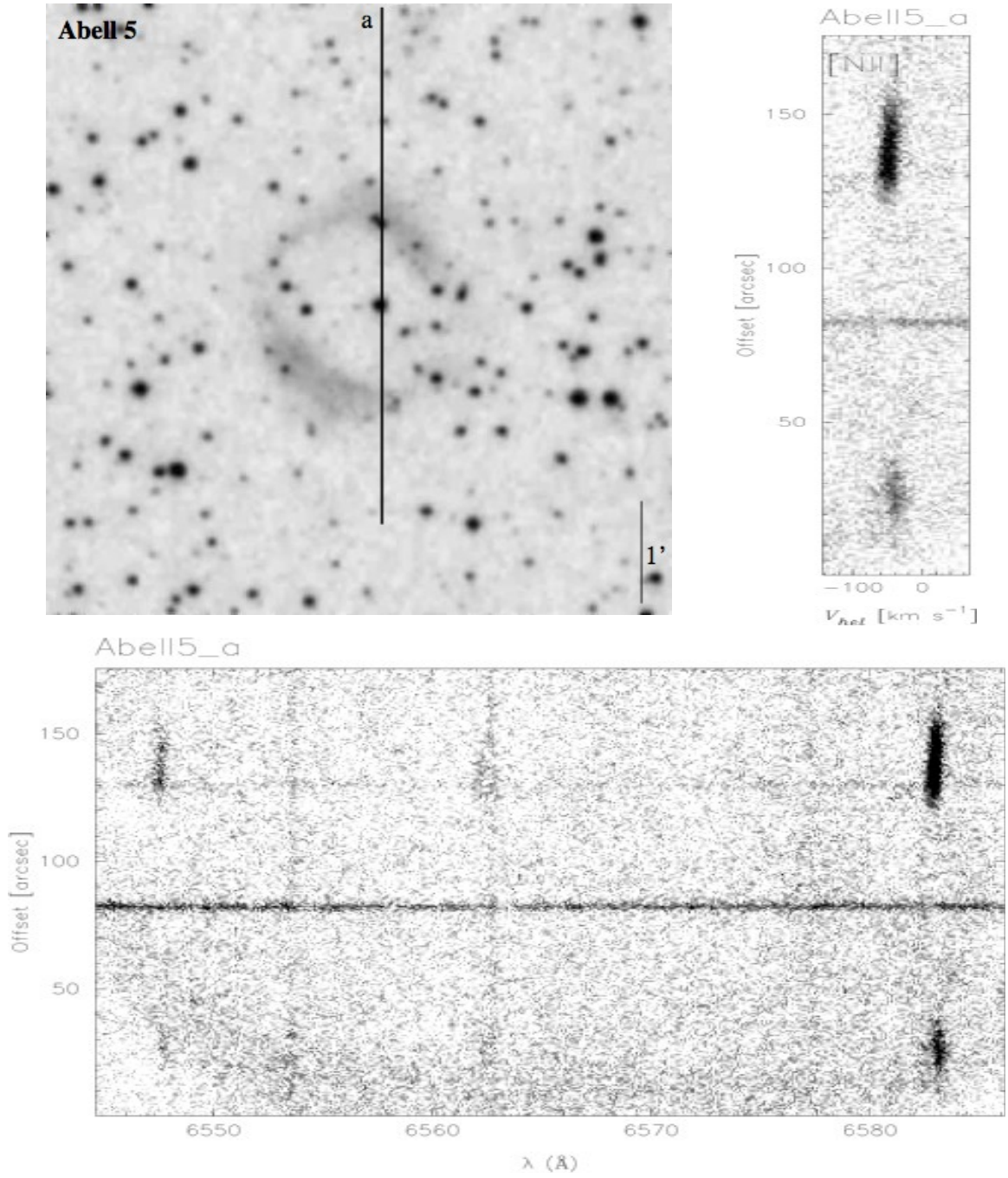

Figure A.3 **Same as Figure A.1. Due to the faint emission seen in the spectra, this object was excluded from the analysis made in Chapter 2**

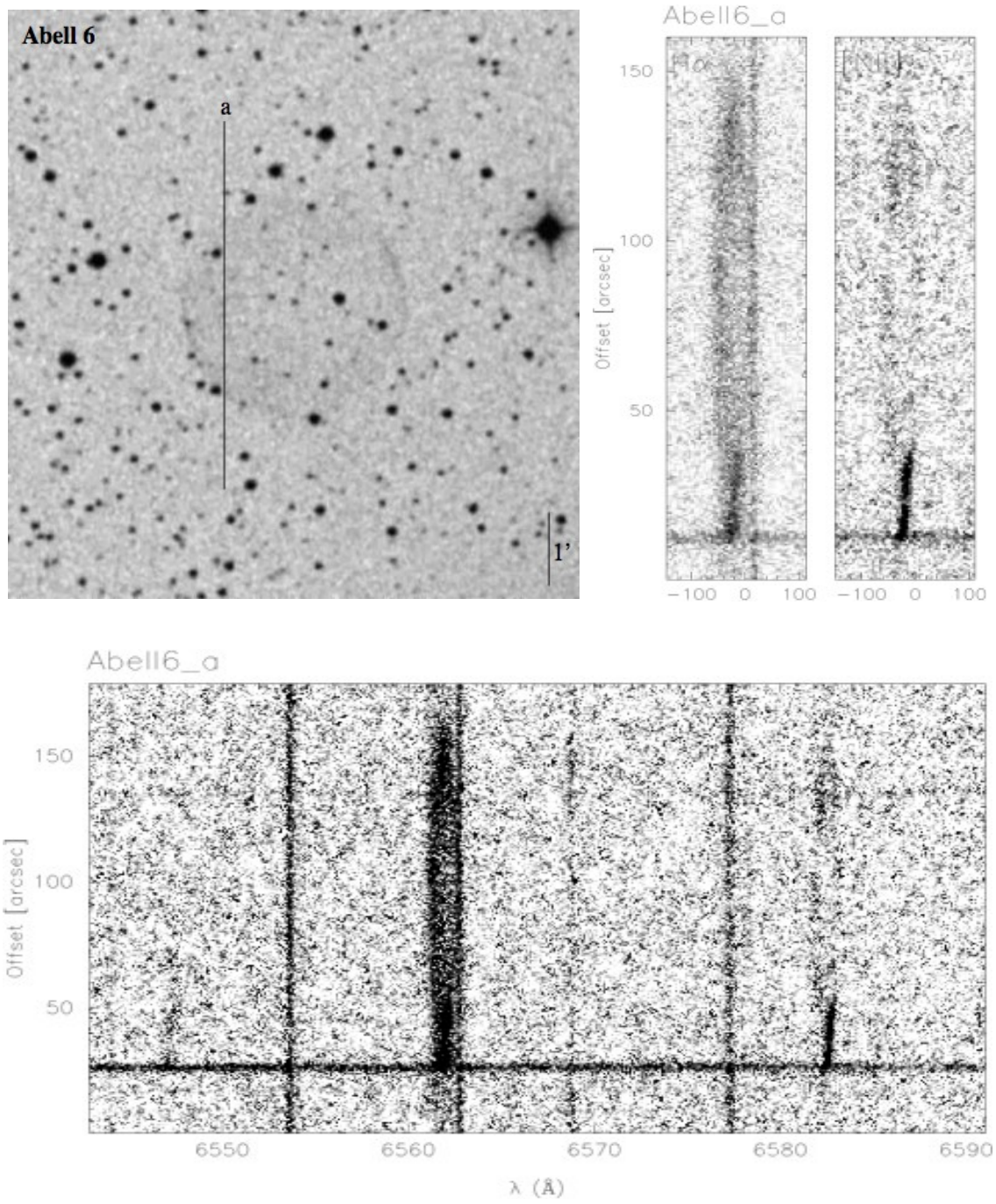

Figure A.4 **Same as Figure A.1.**

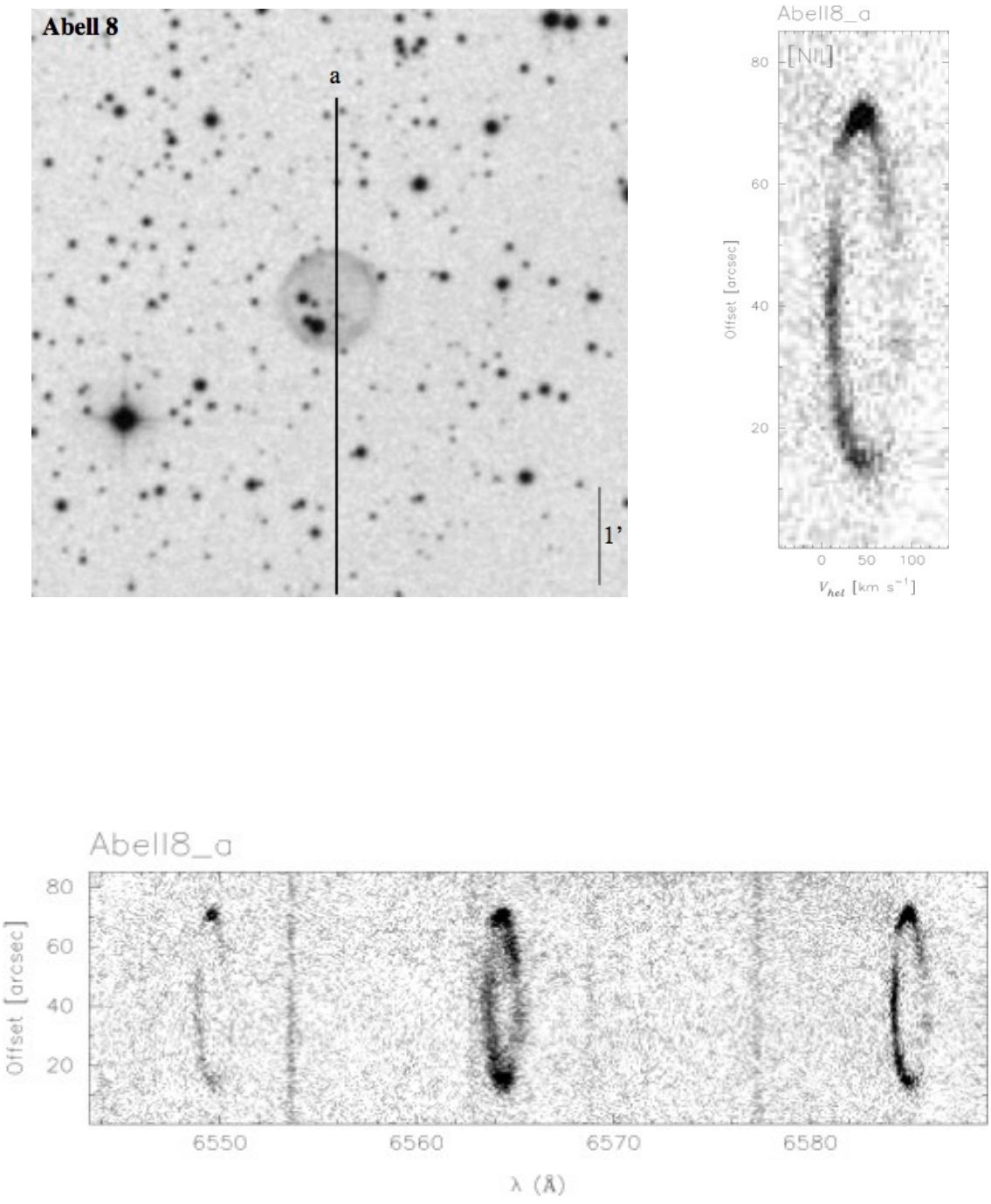

Figure A.5 **Same as Figure A.1.**

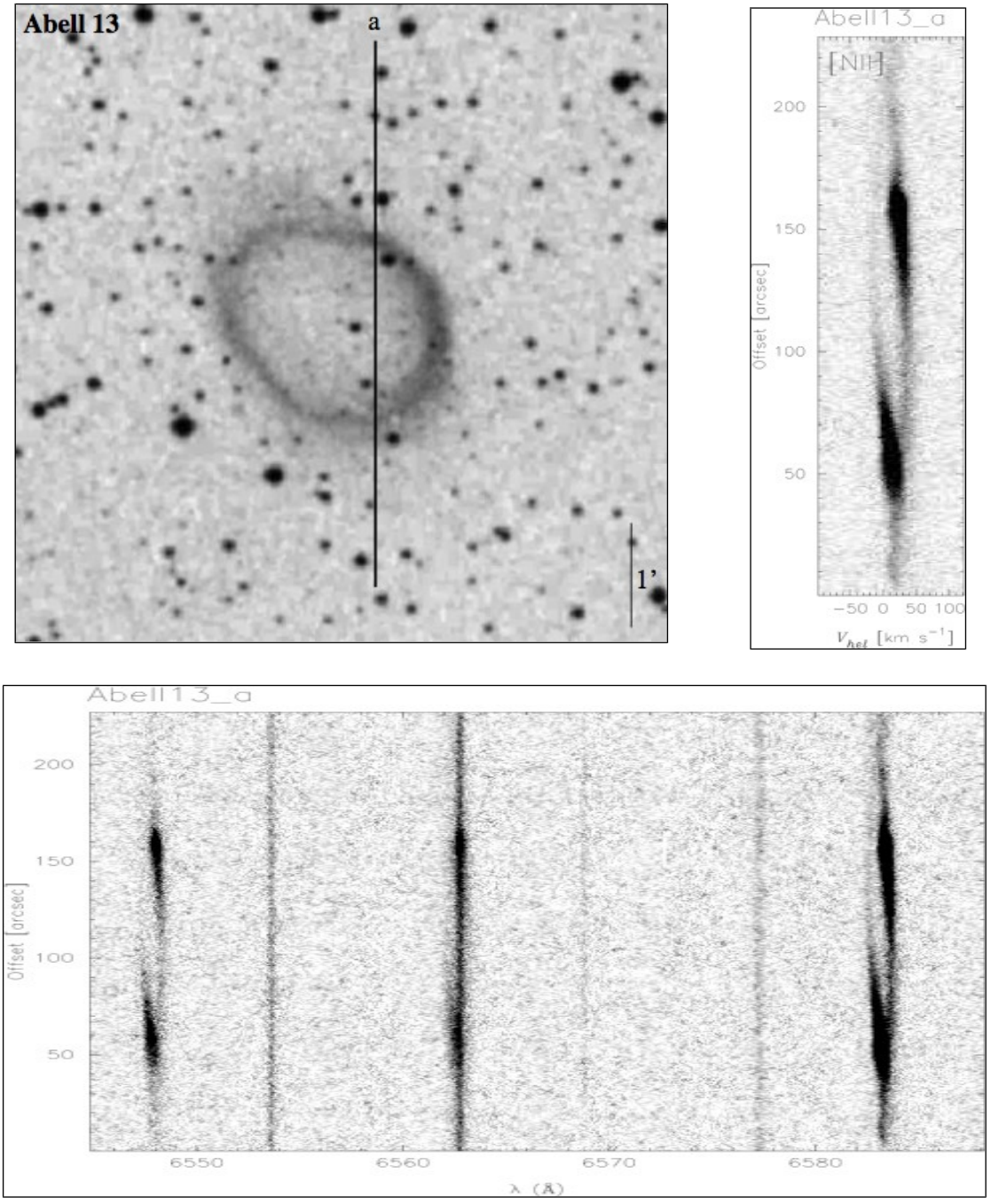

Figure A.6 **Same as Figure A.1.**

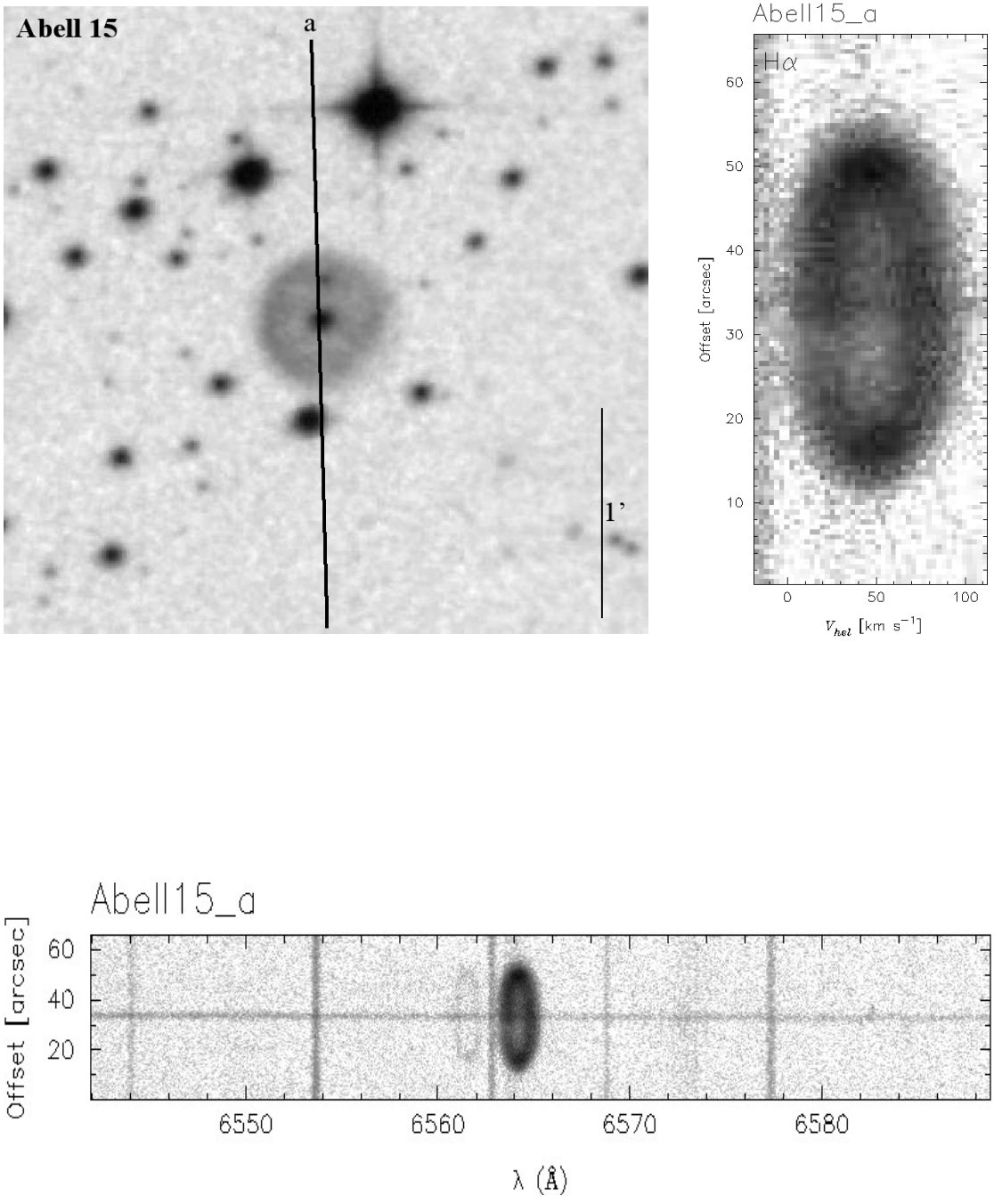

Figure A.7 **Same as Figure A.1.**

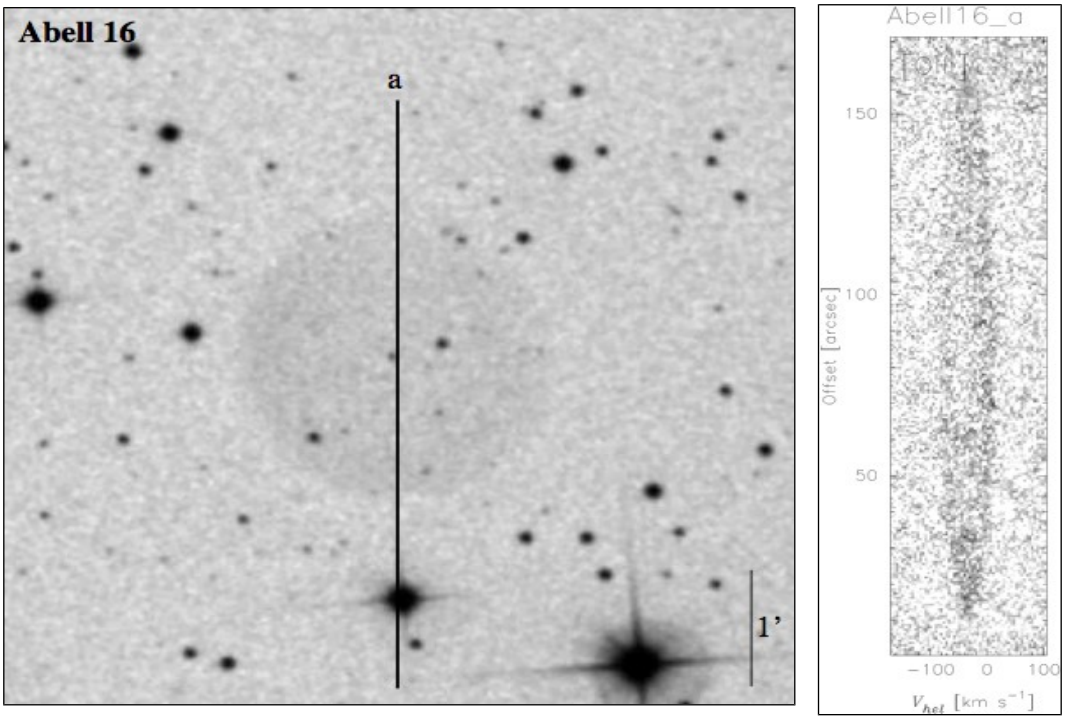

Figure A.8 **Same as Figure A.1. Full spectral range is not available in this case.**

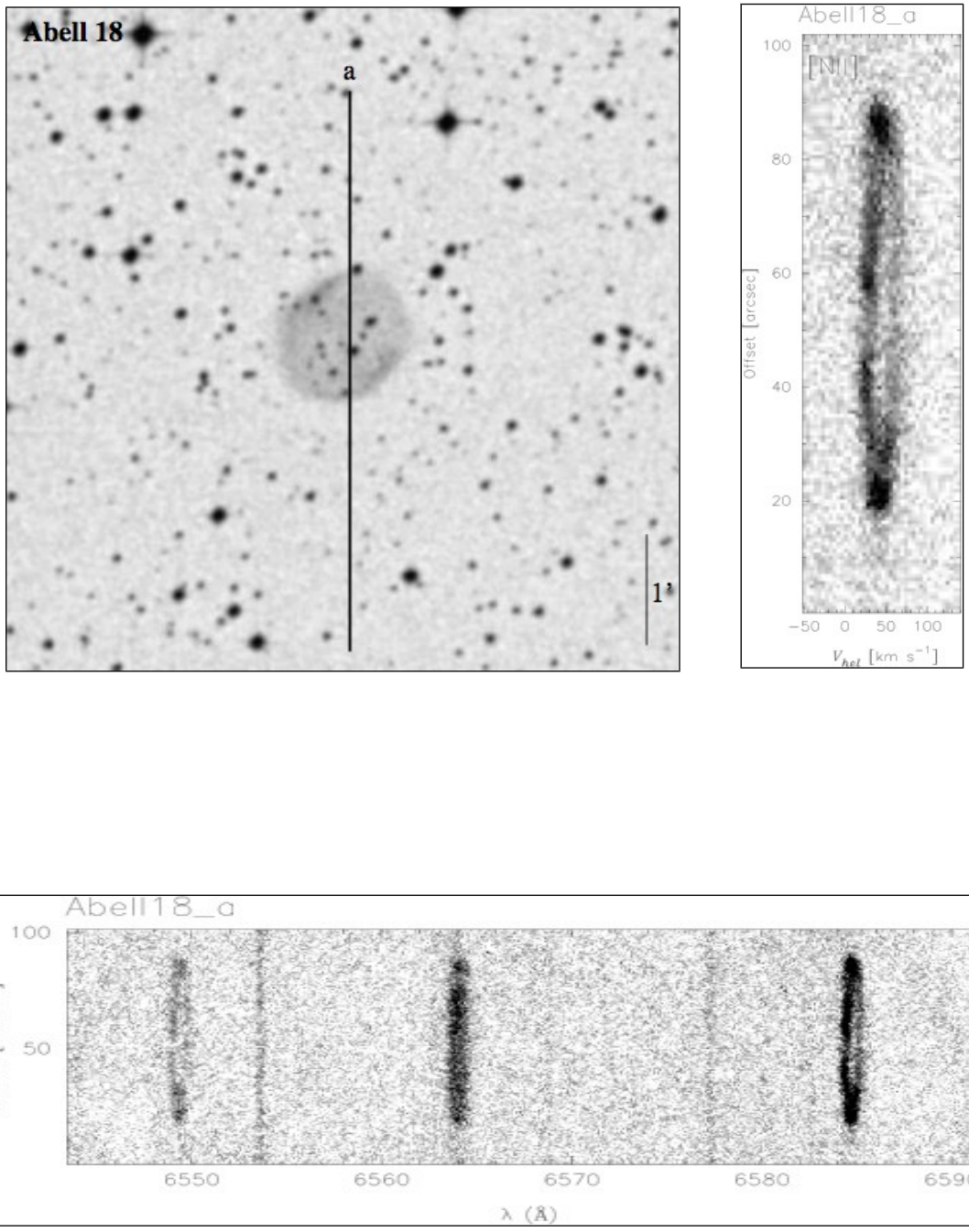

Figure A.9 **Same as Figure A.1.**

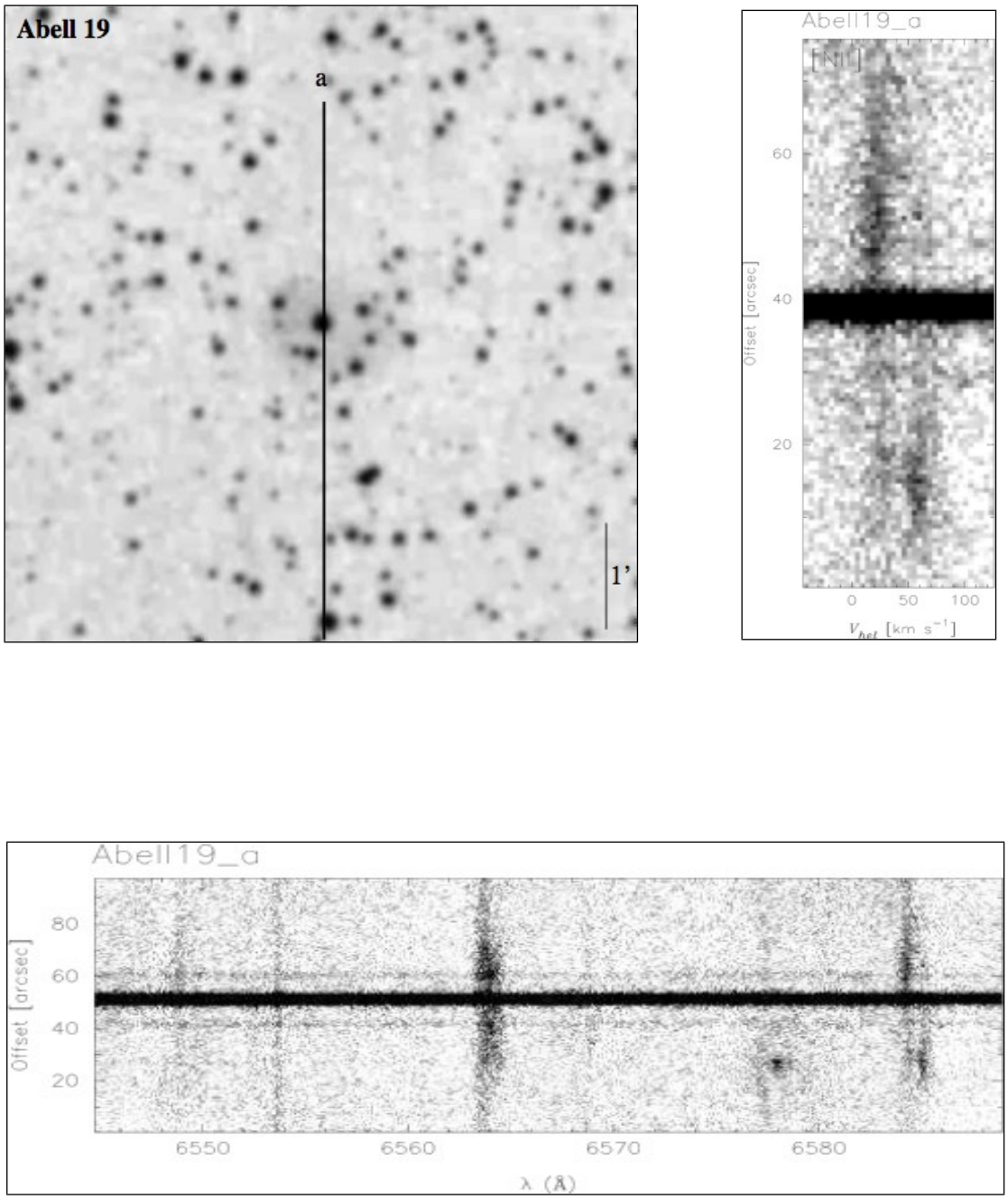

Figure A.10 **Same as Figure A.1.**

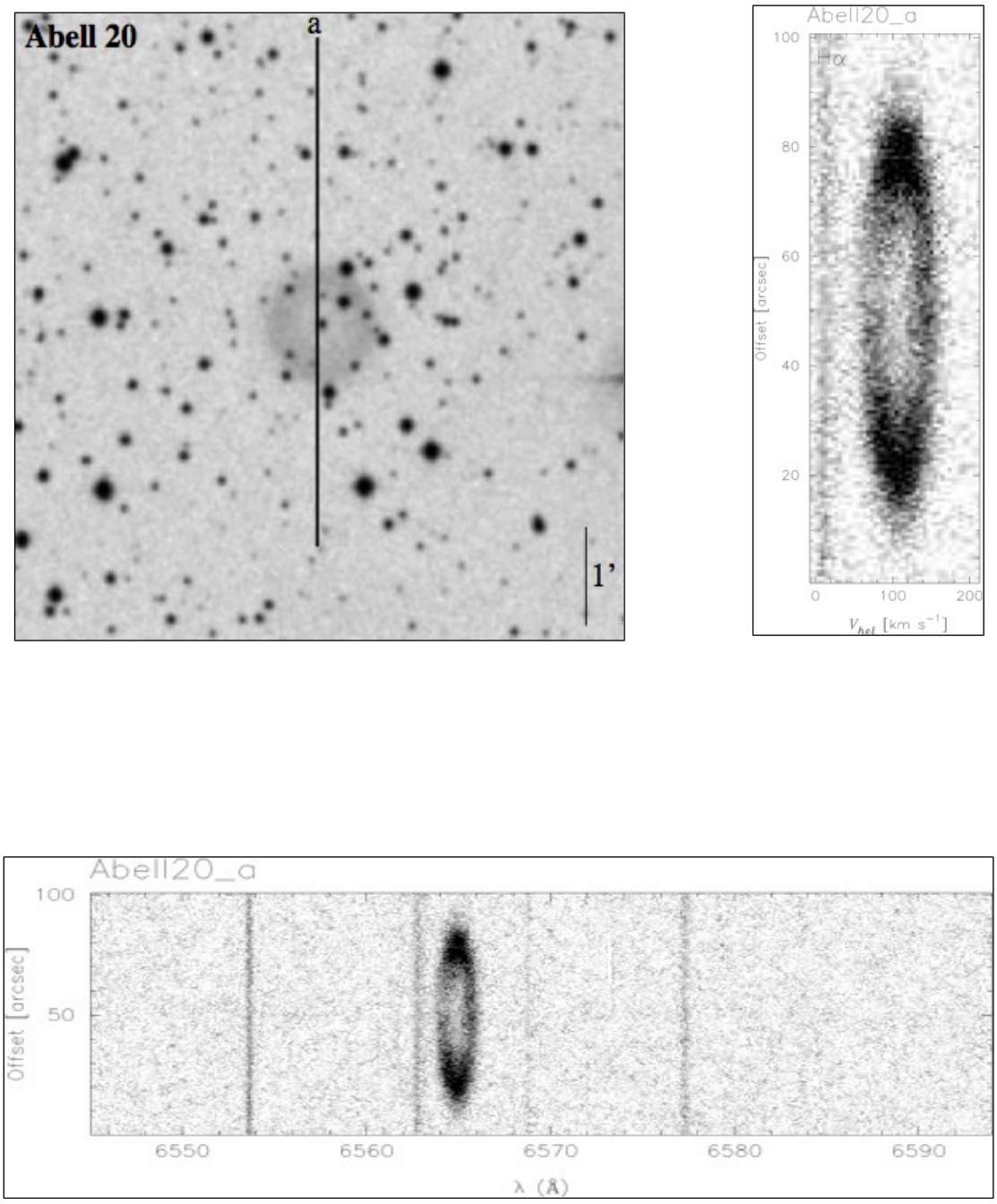

Figure A.11 **Same as Figure A.1.**

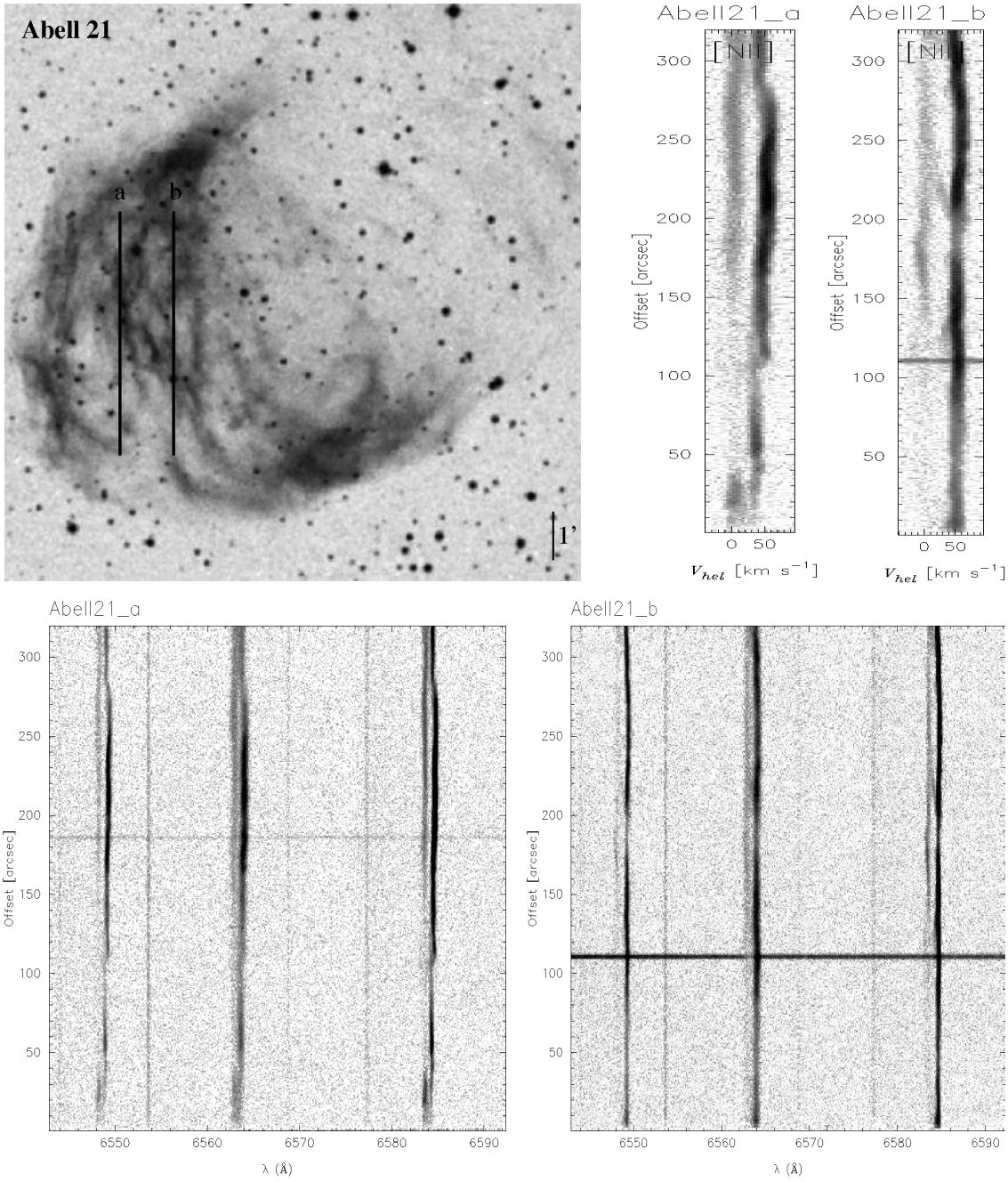

Figure A.12 **Same as Figure A.1.**

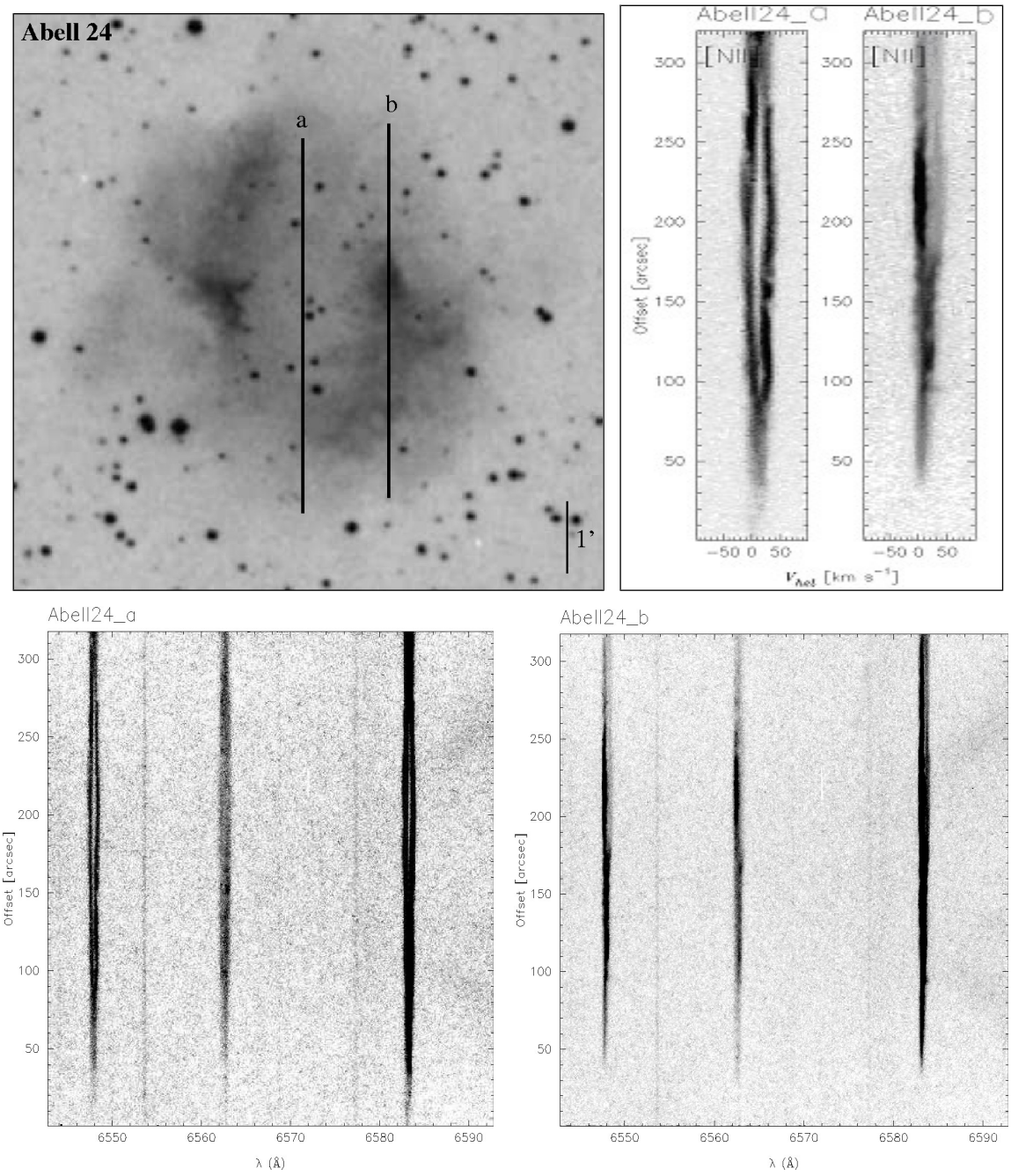

Figure A.13 **Same as Figure A.1.**

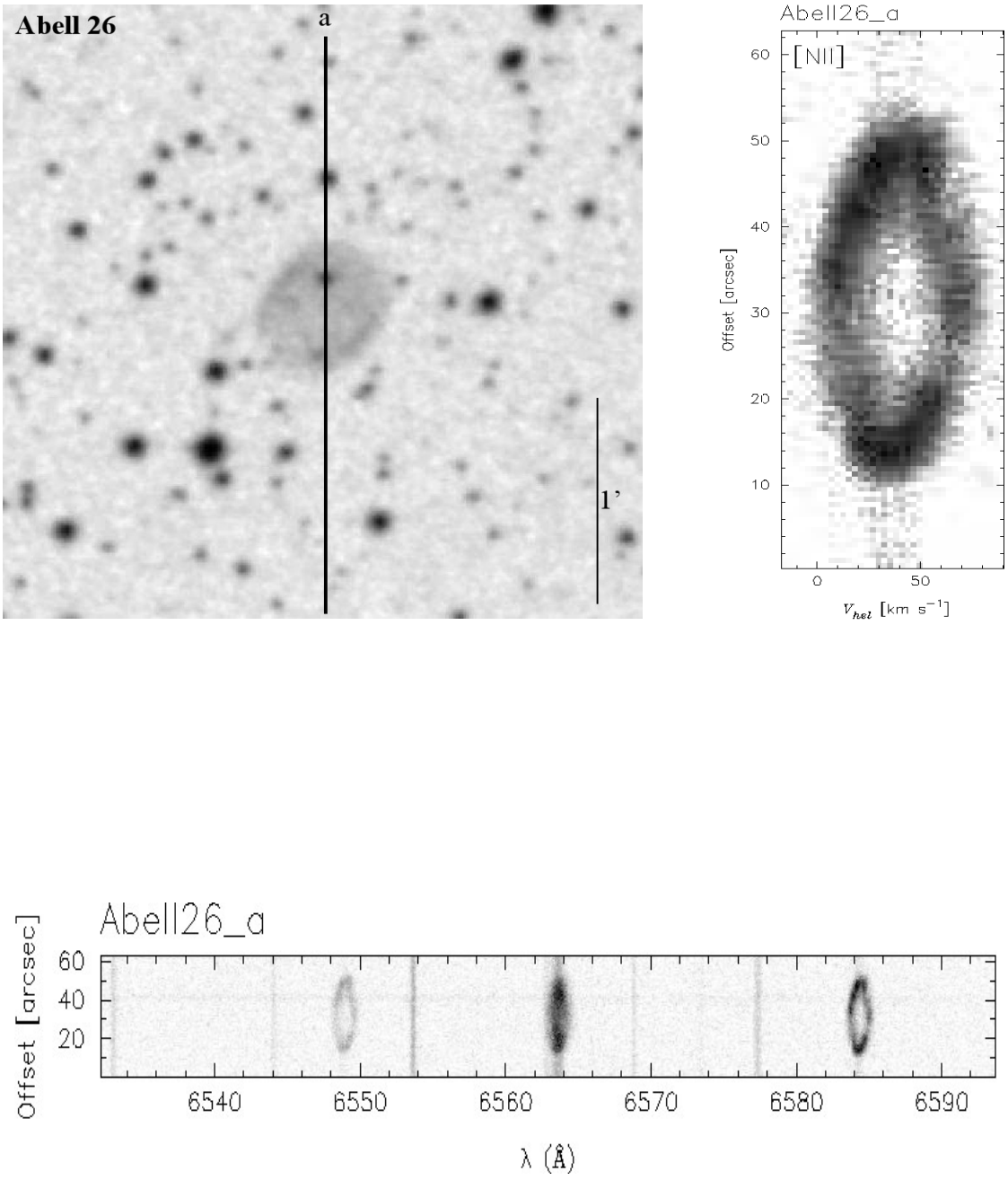

Figure A.14 **Same as Figure A.1.**

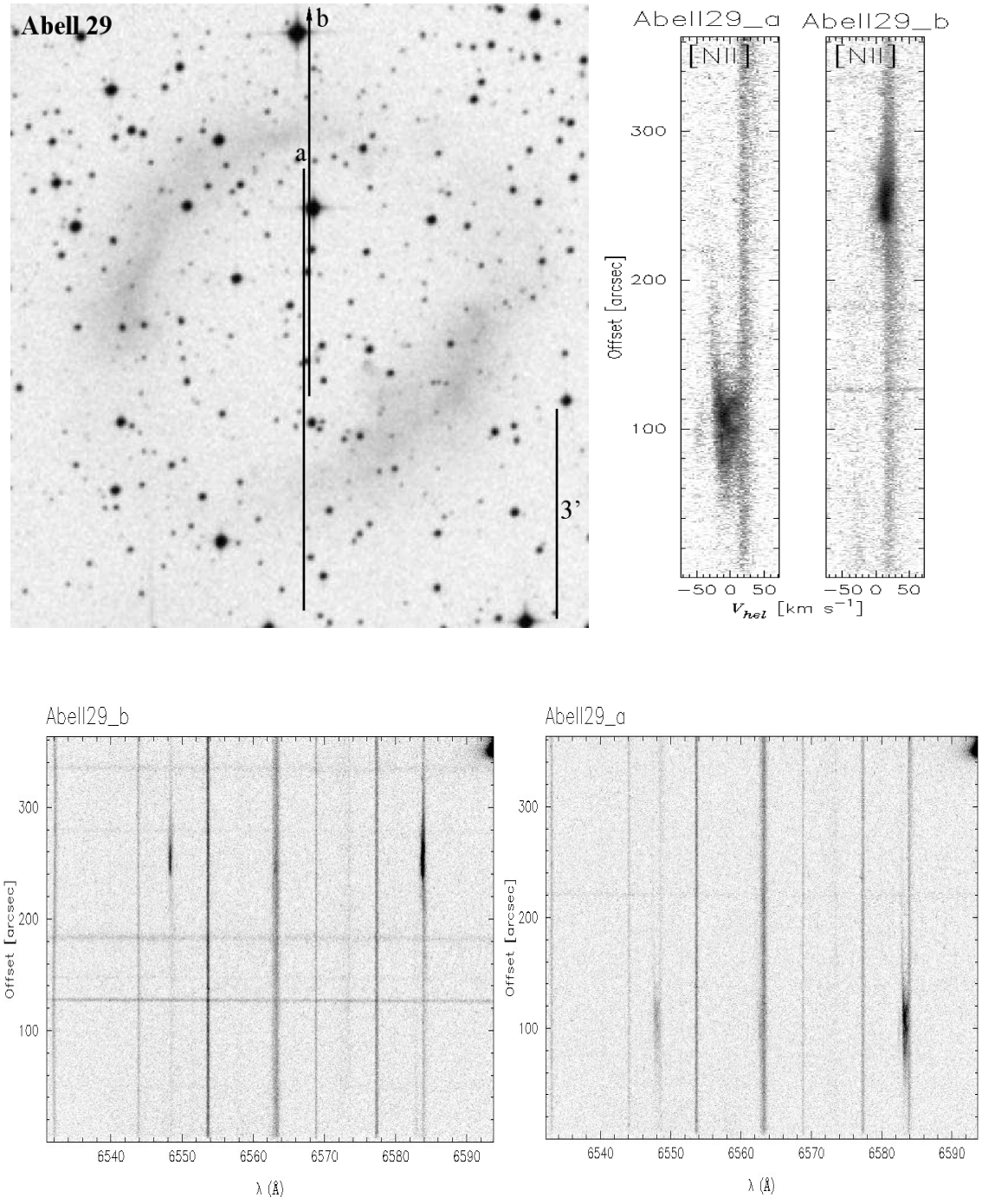

Figure A.15 **Same as Figure A.1.**

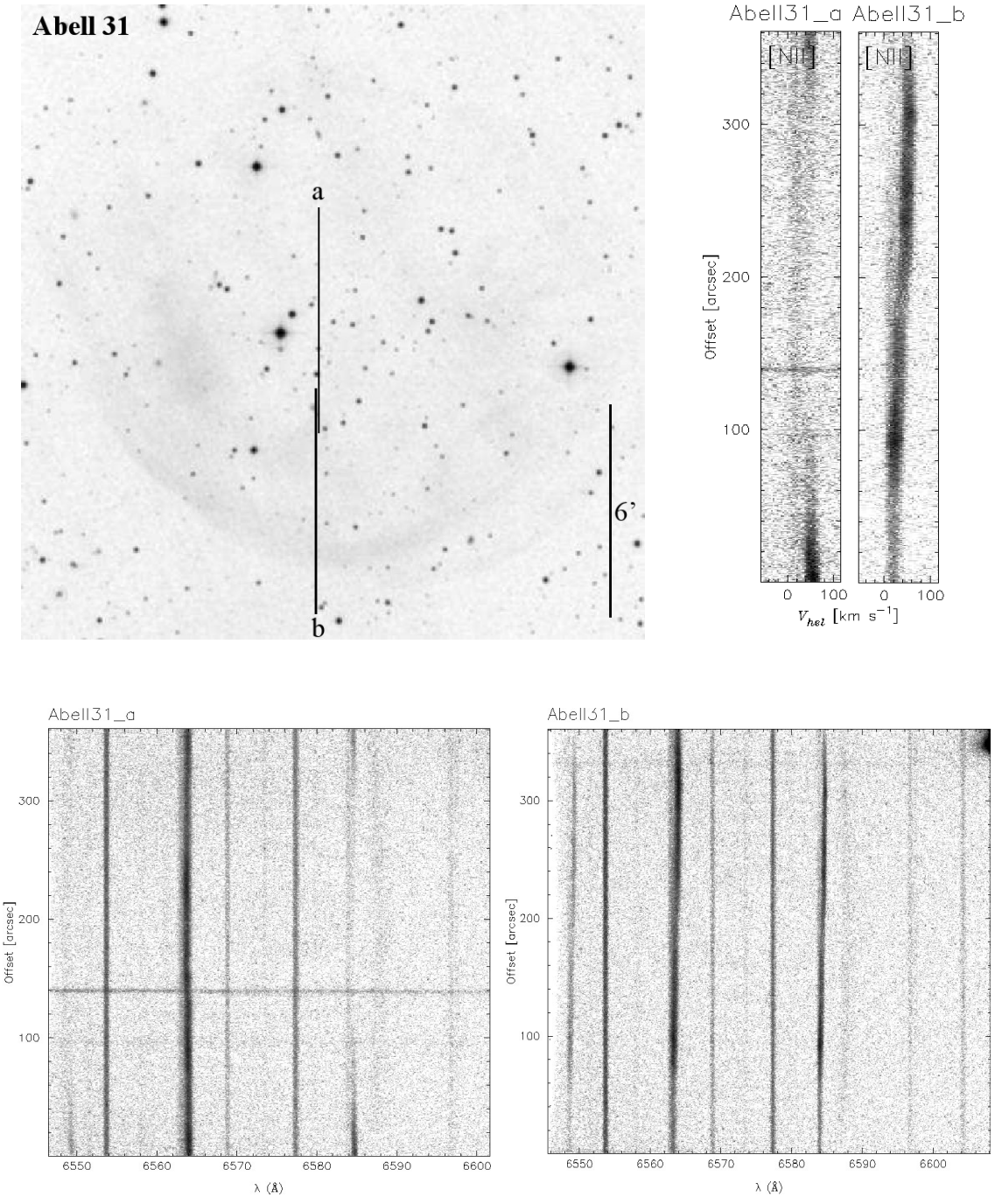

Figure A.16 **Same as Figure A.1.**

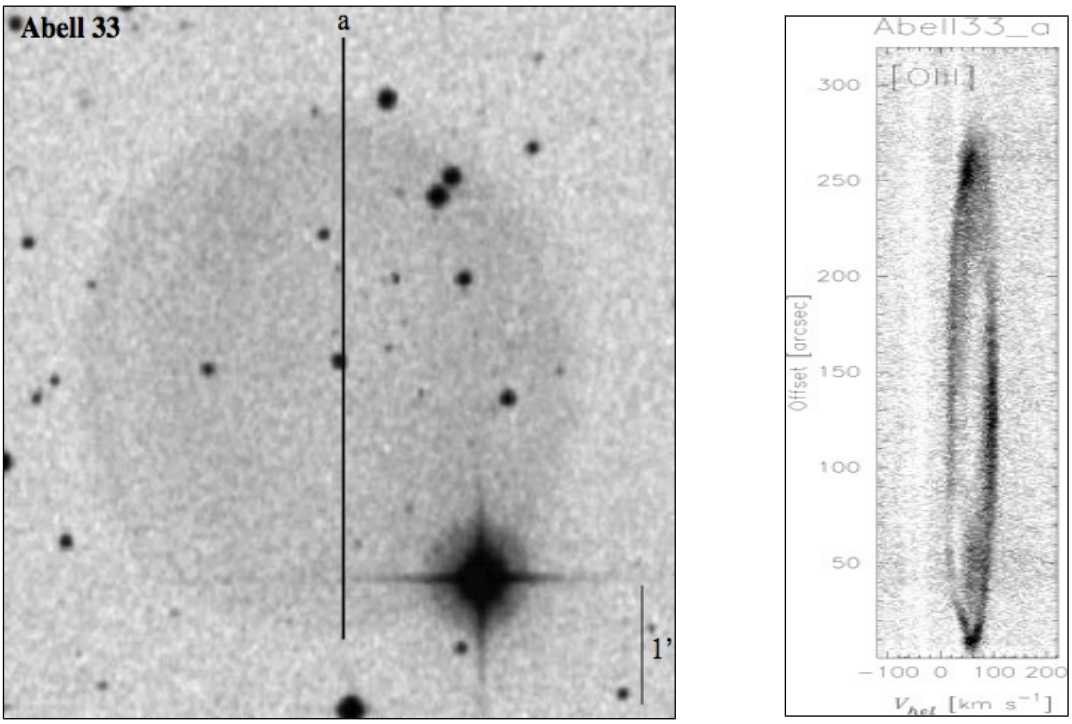

Figure A.17 **Same as Figure A.1. Full spectral range is not available in this case.**

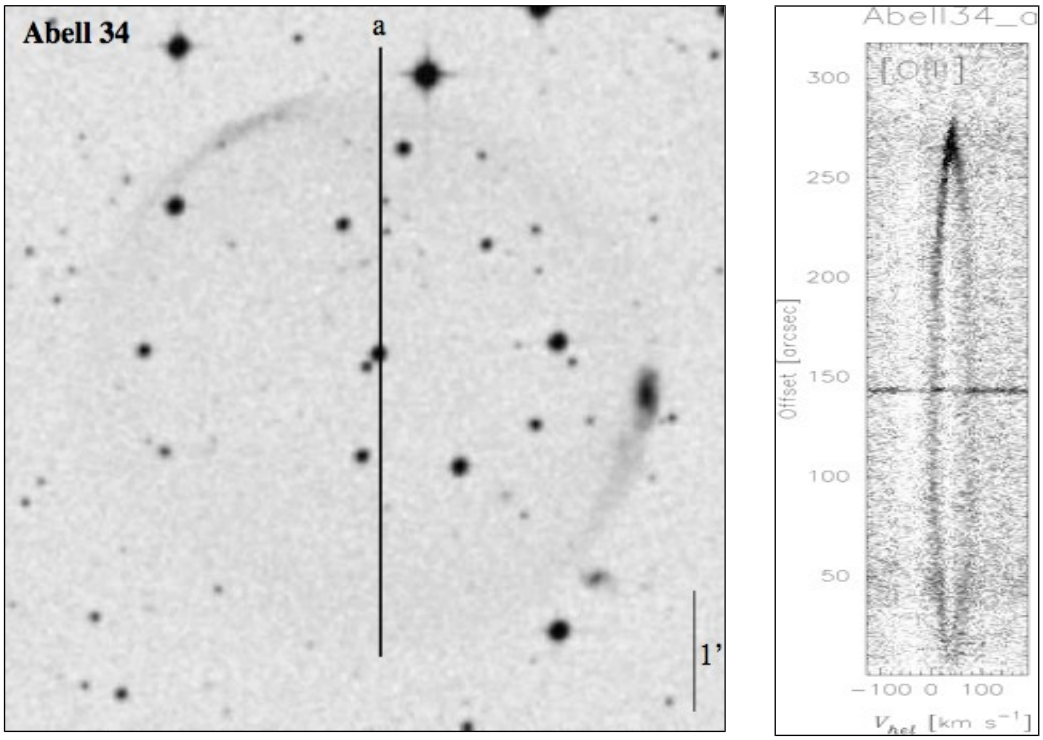

Figure A.18 **Same as Figure A.1. Full spectral range is not available in this case.**

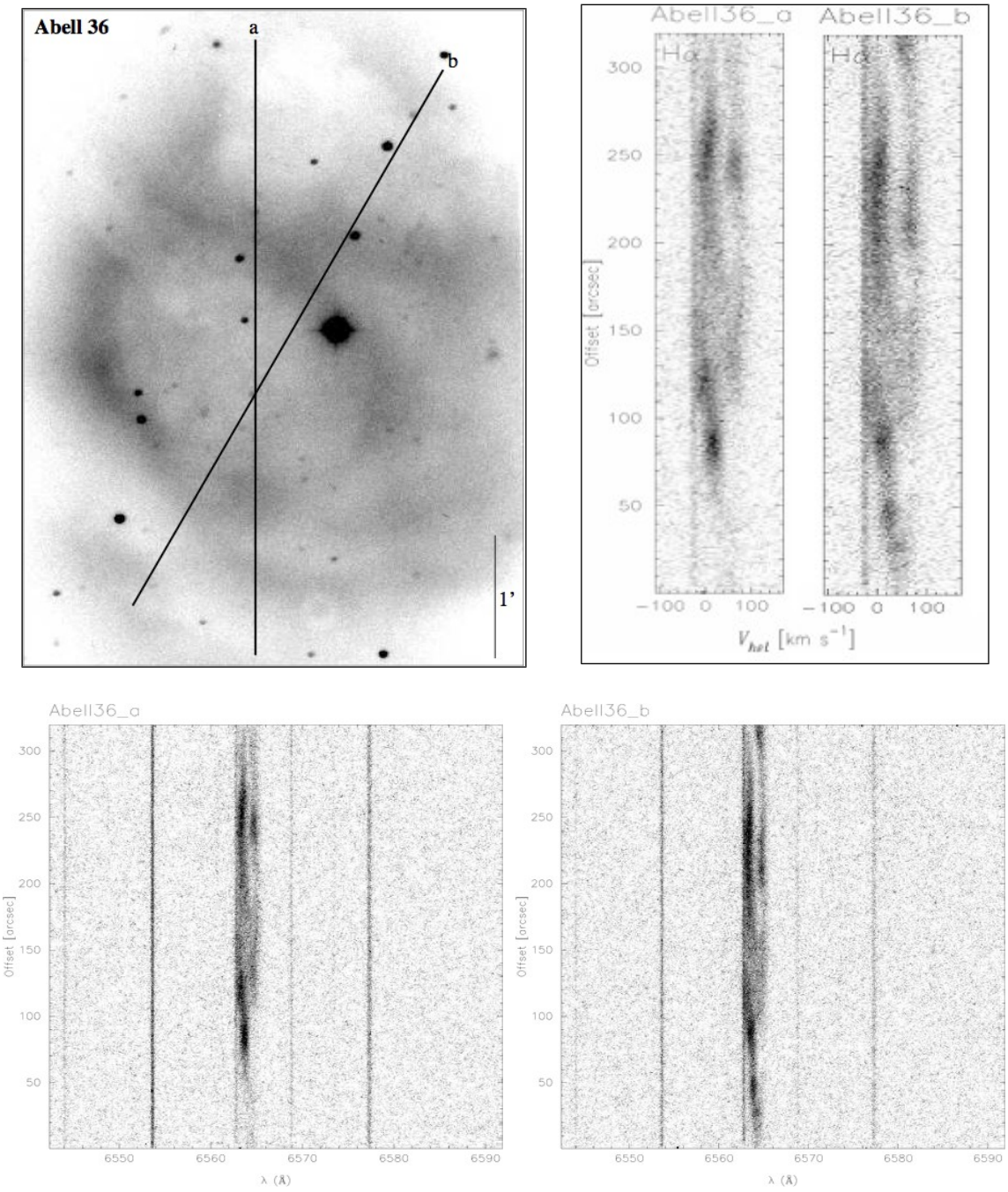

Figure A.19 **Same as Figure A.1.**

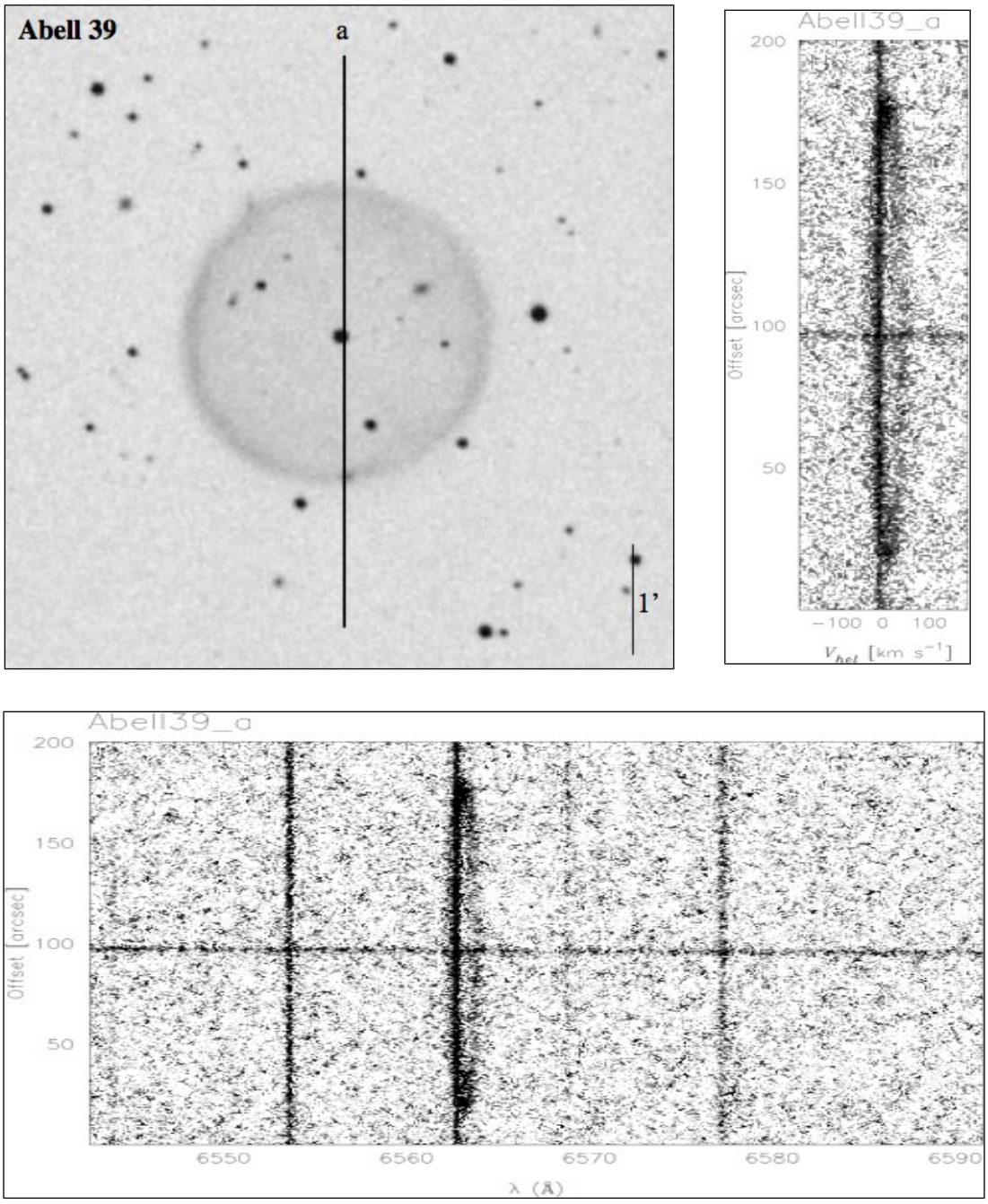

Figure A.20 **Same as Figure A.20.**

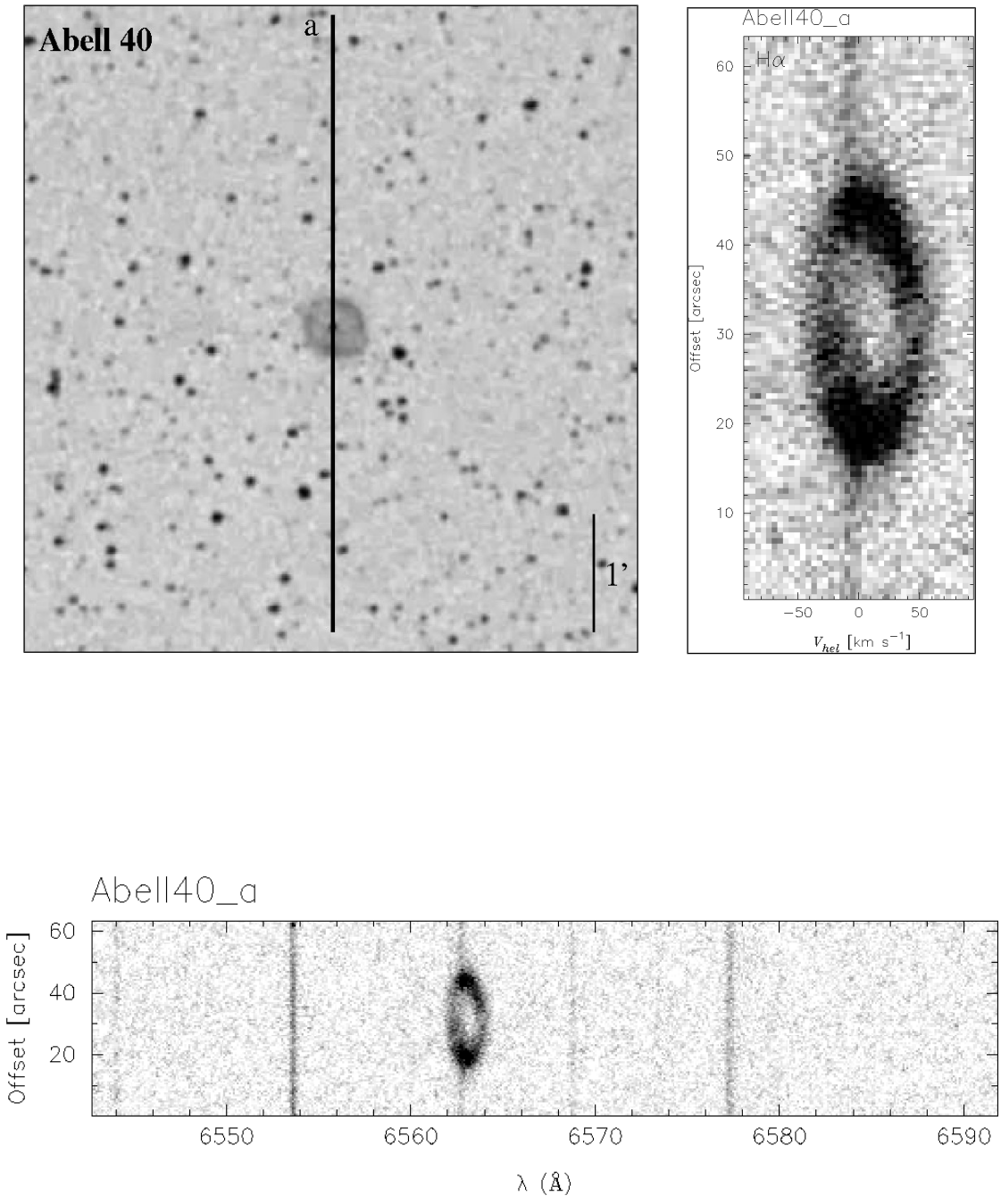

Figure A.21 **Same as Figure A.1.**

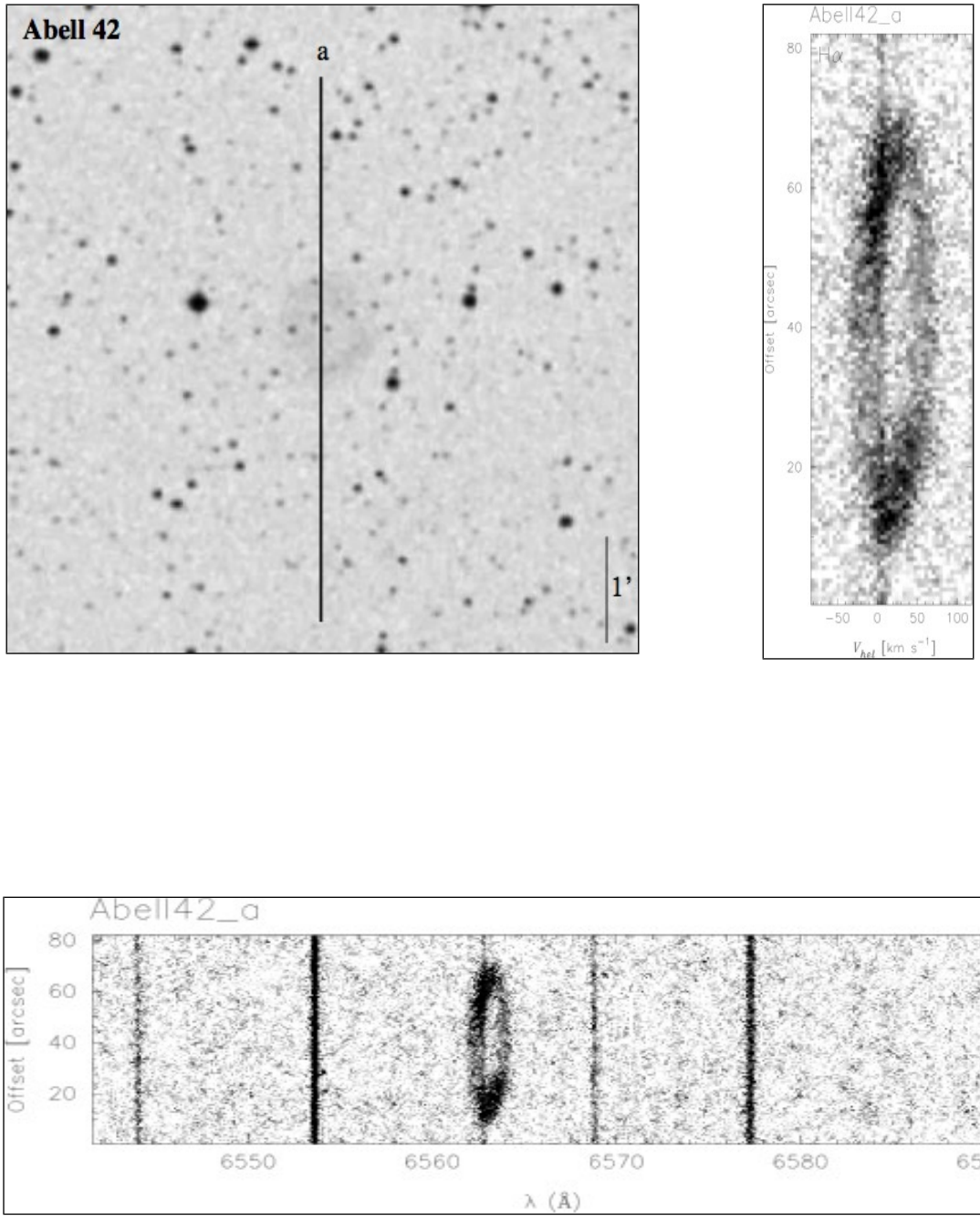

Figure A.22 **Same as Figure A.1.**

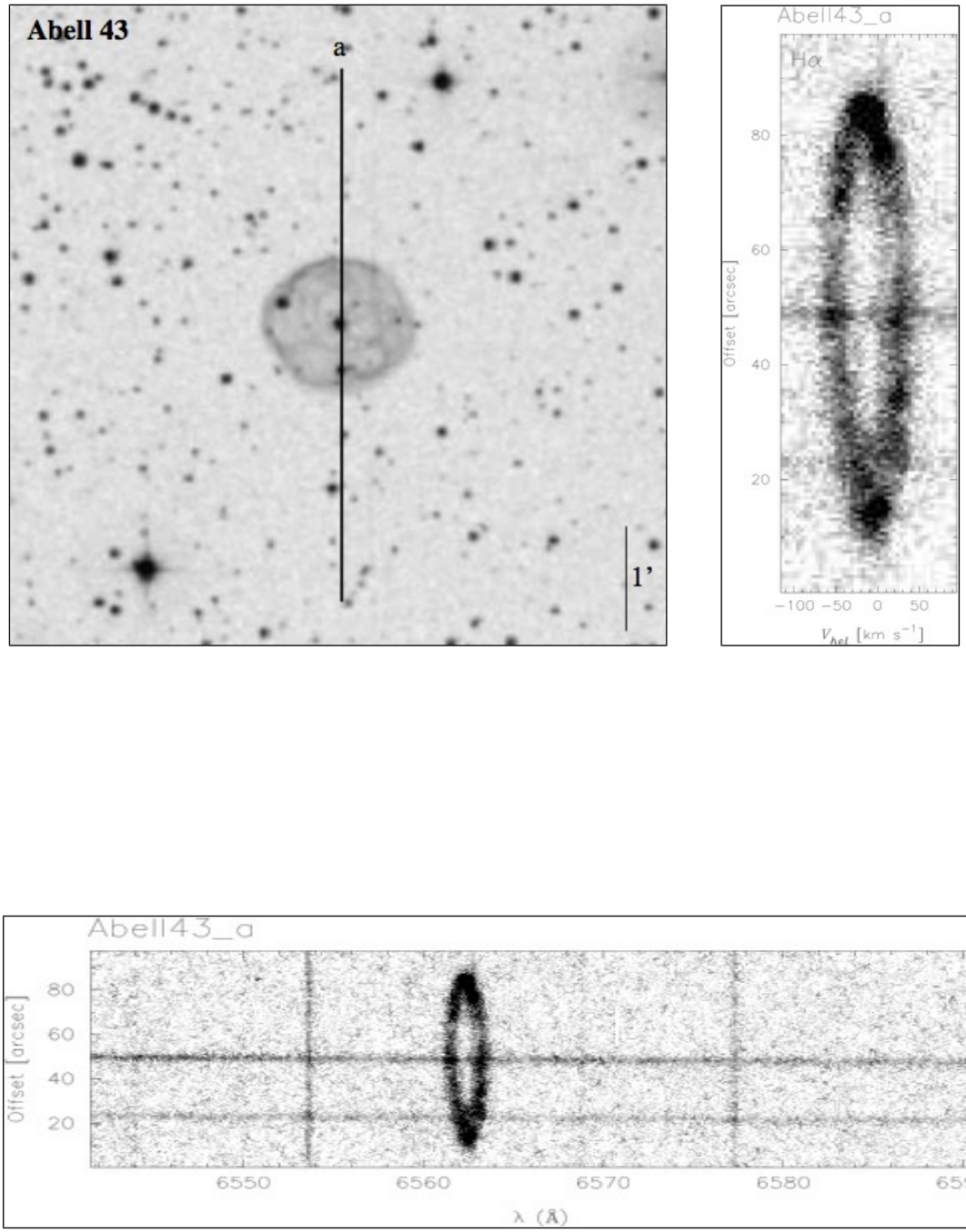

Figure A.23 **Same as Figure A.1.**

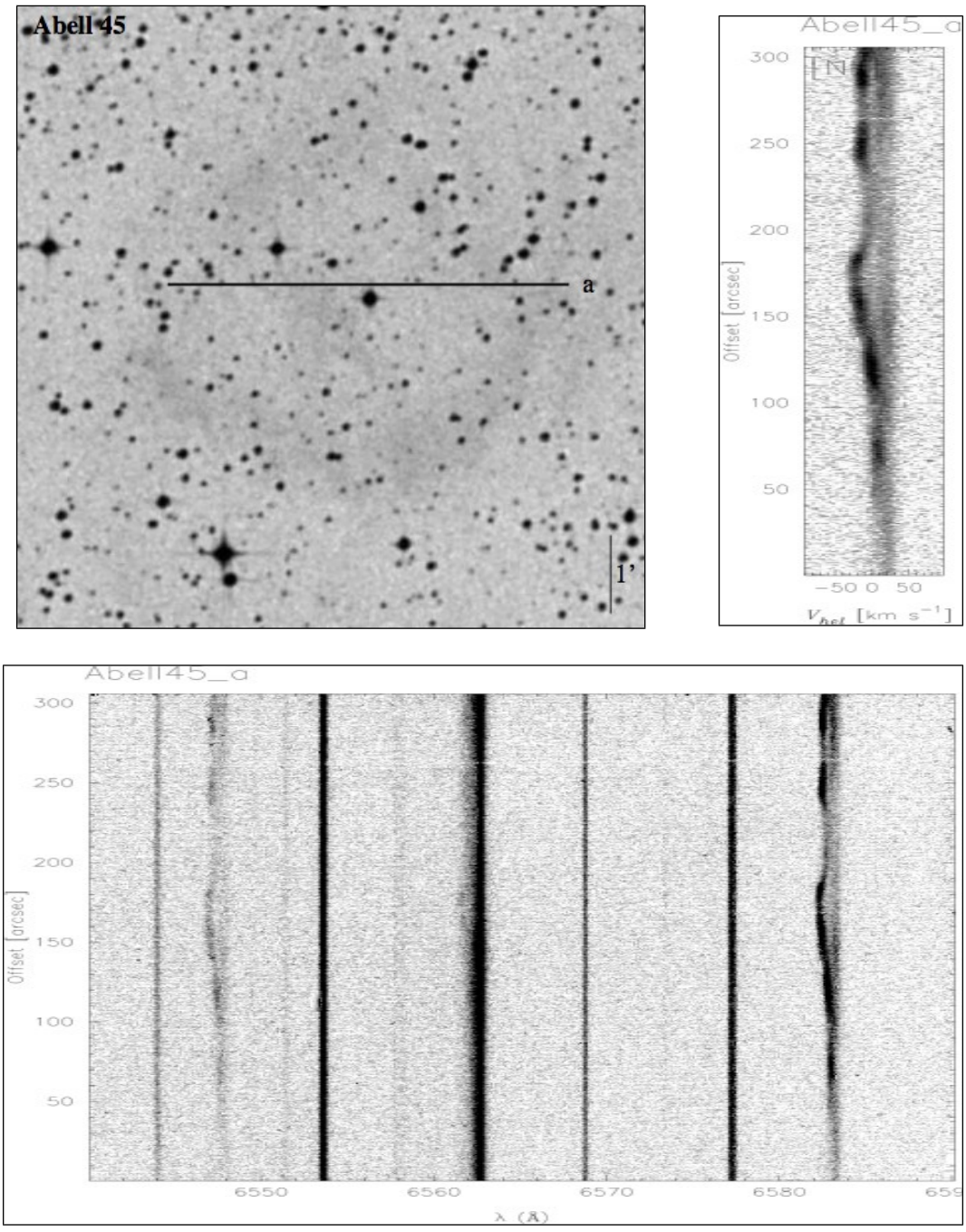

Figure A.24 **Same as Figure A.1.**

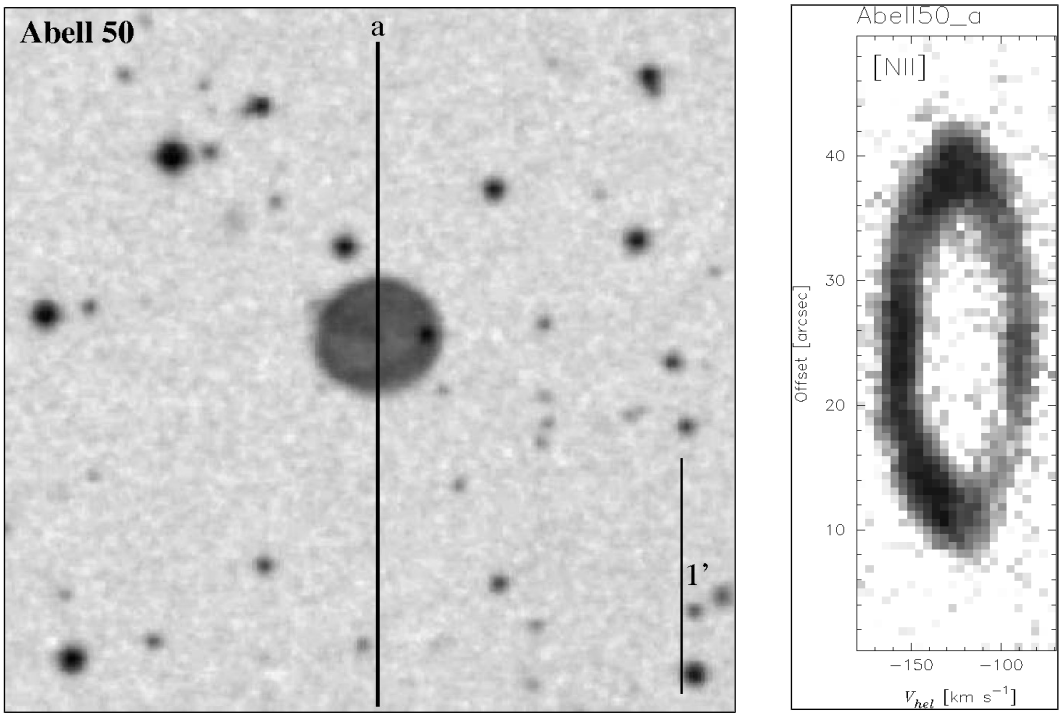

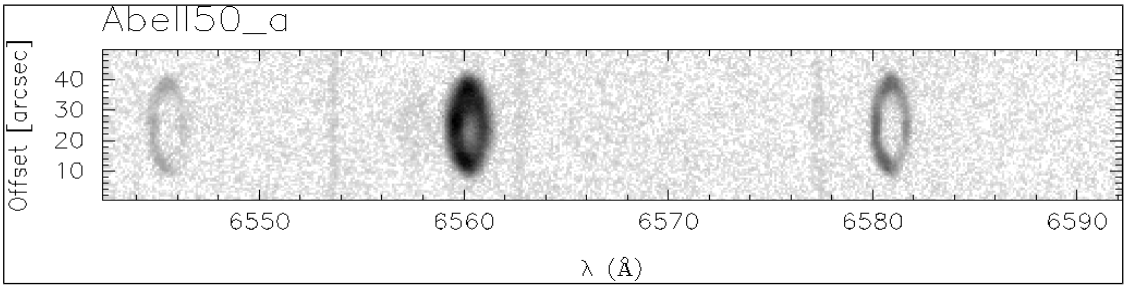

Figure A.25 **Same as Figure A.1.**

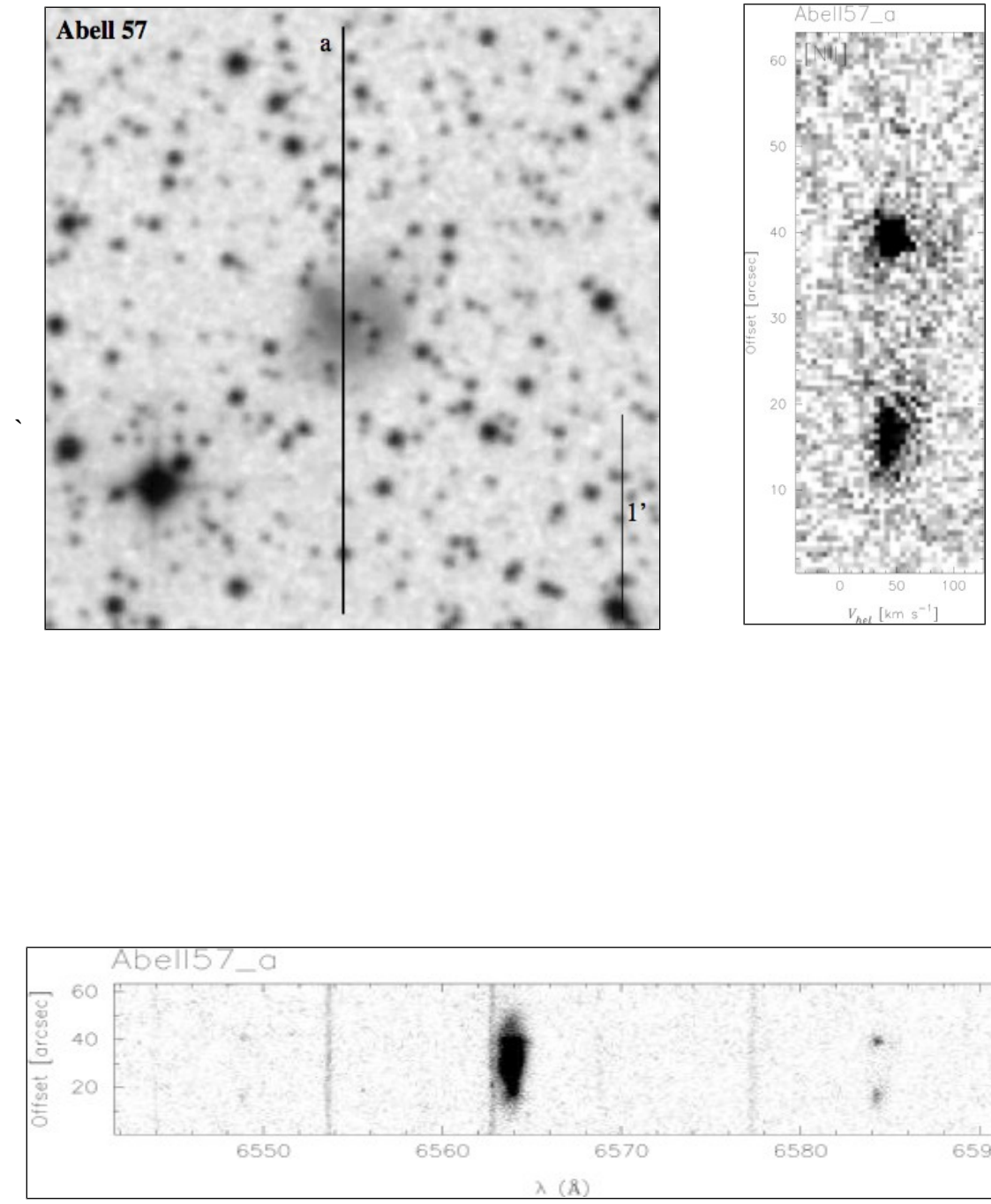

Figure A.26 **Same as Figure A.1.**

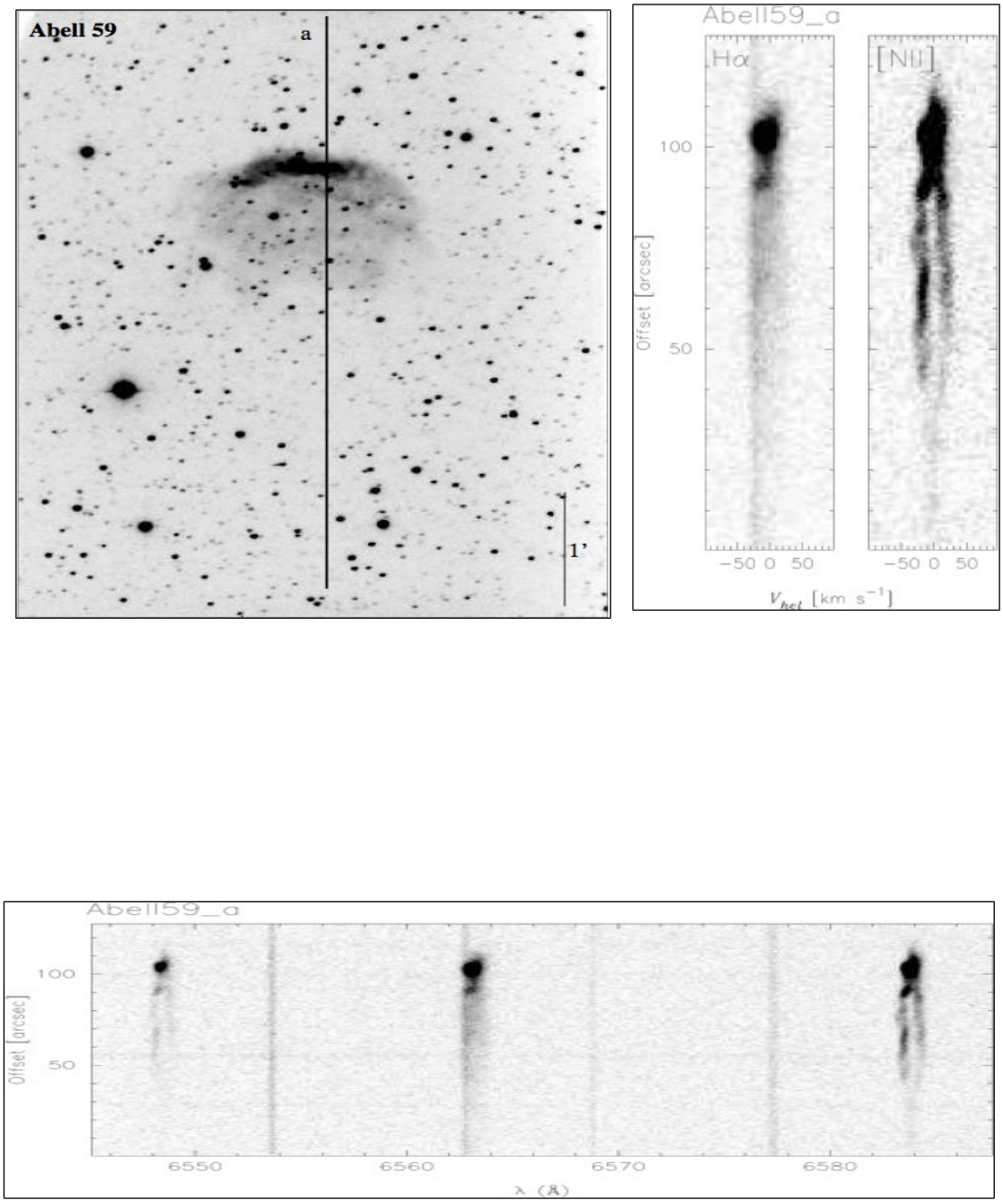

Figure A.27 **Same as Figure A.1.**

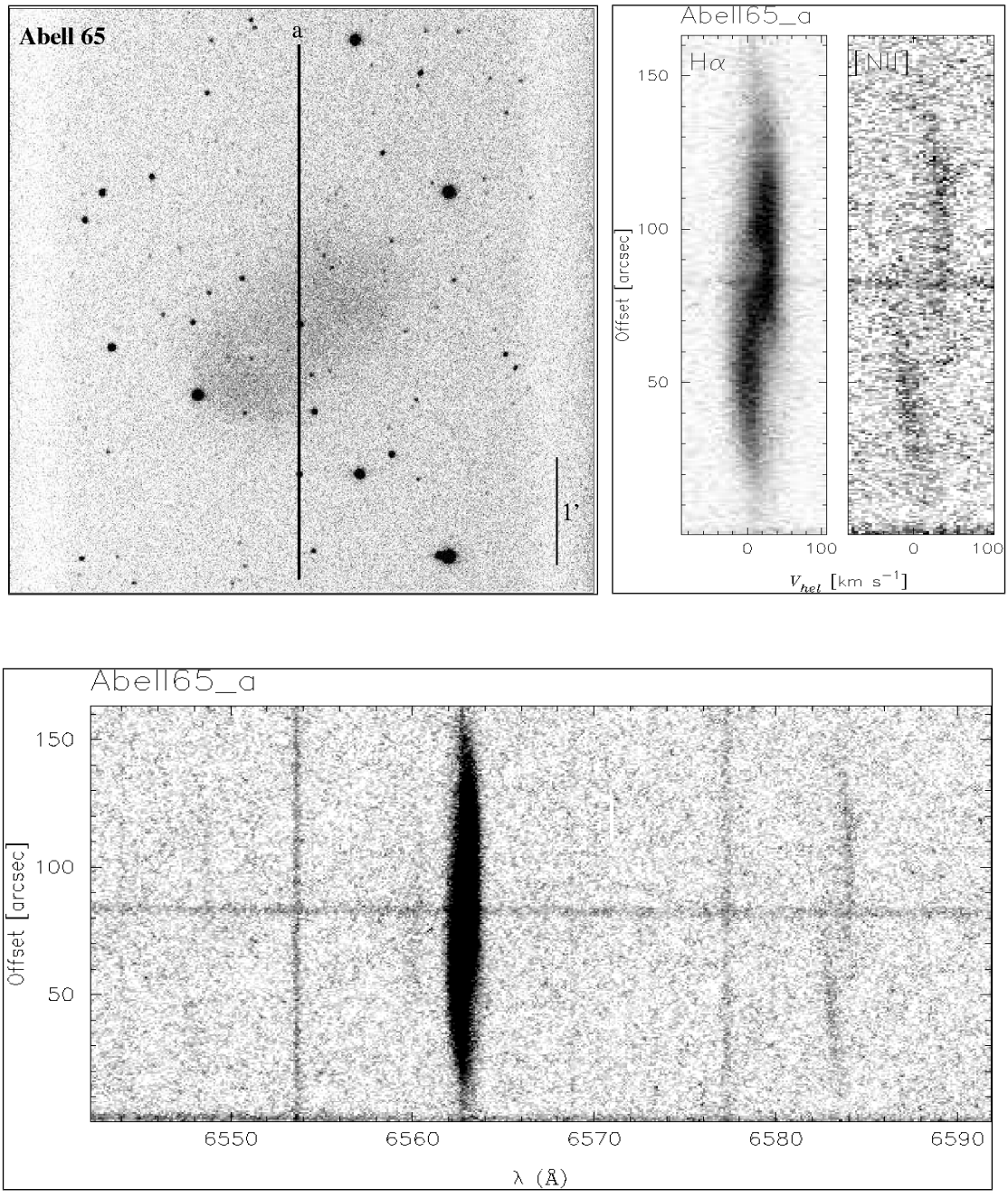

Figure A.28 **Same as Figure A.1.**

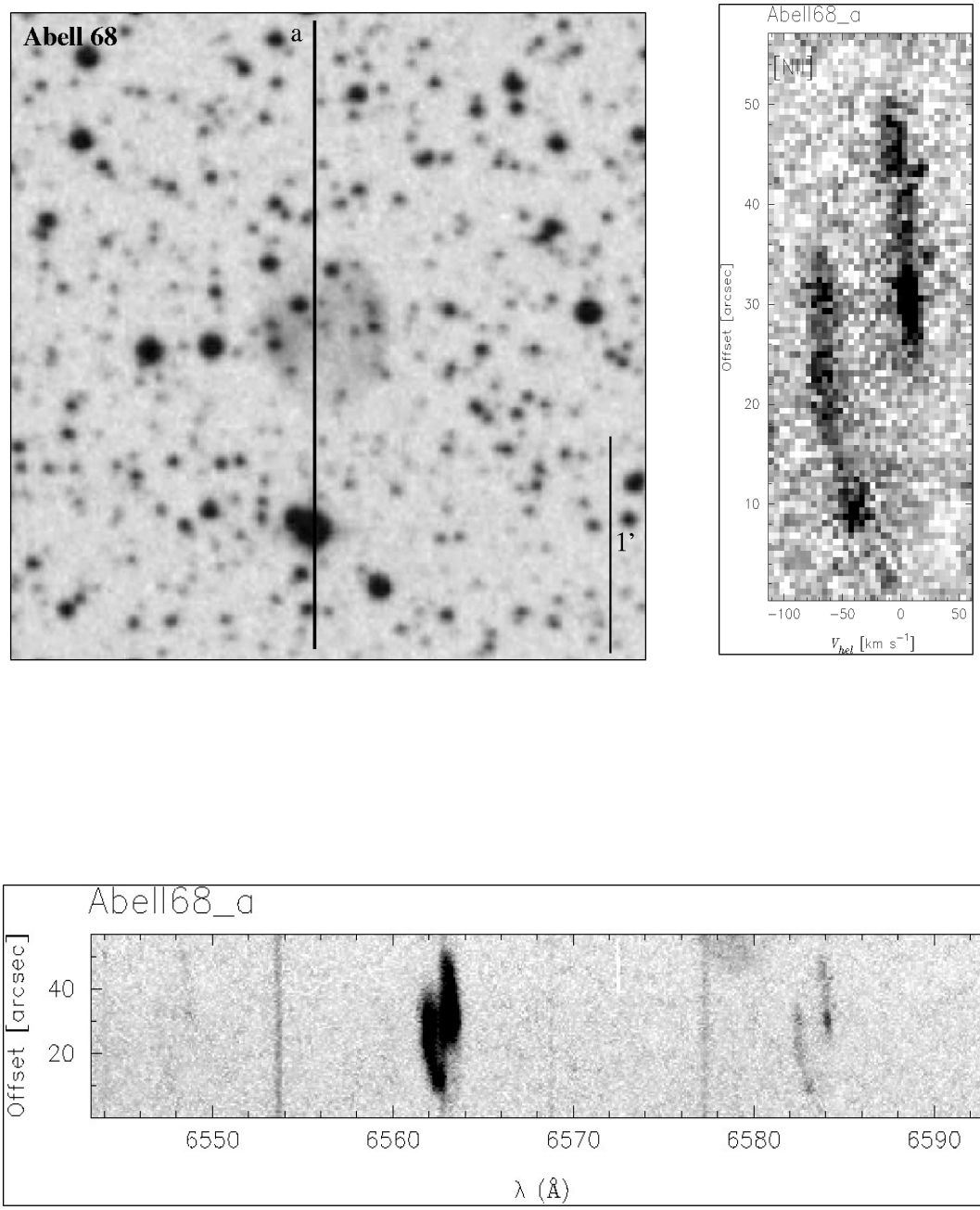

Figure A.29 **Same as Figure A.1.**

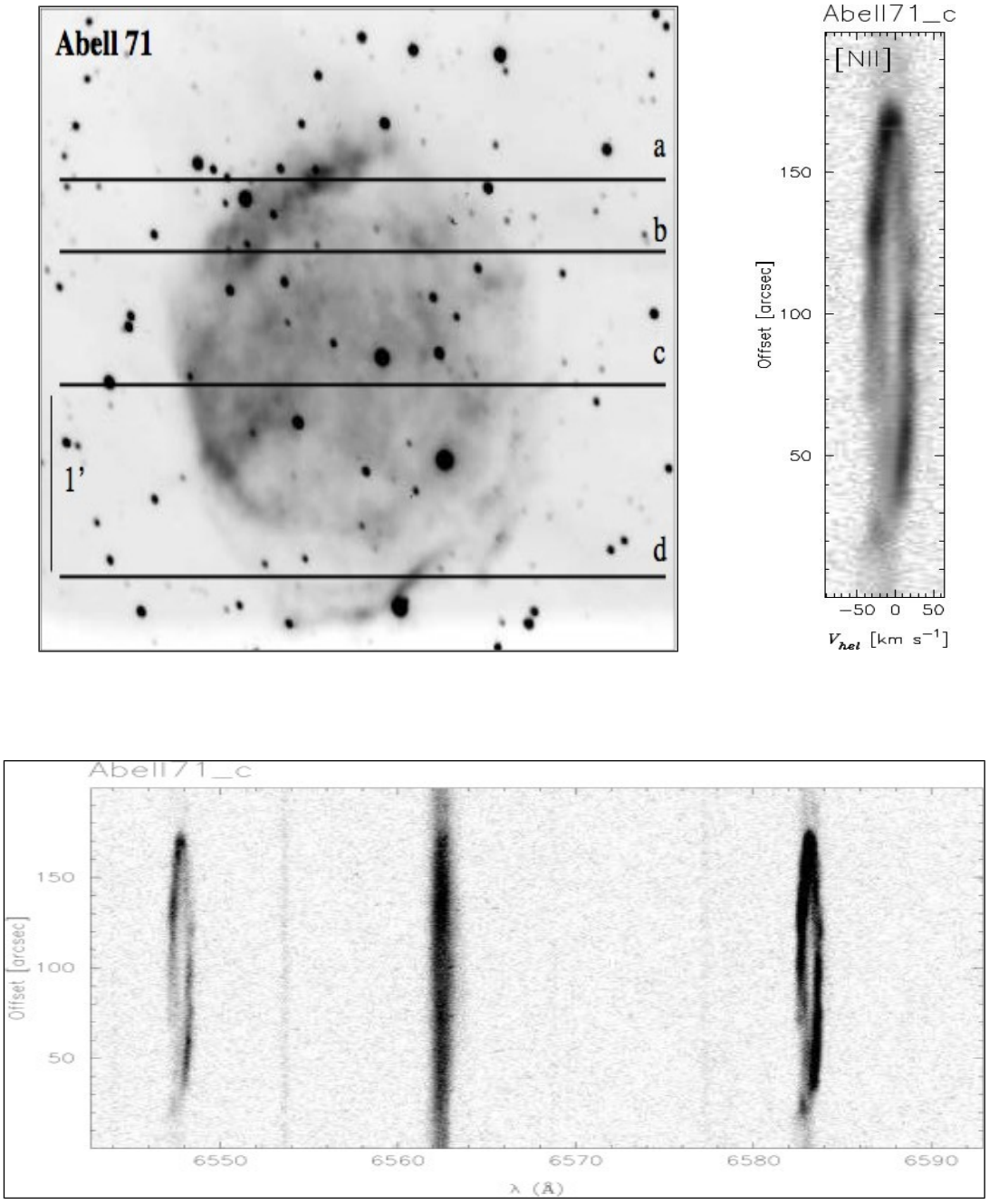

Figure A.30 **Same as Figure A.1.**

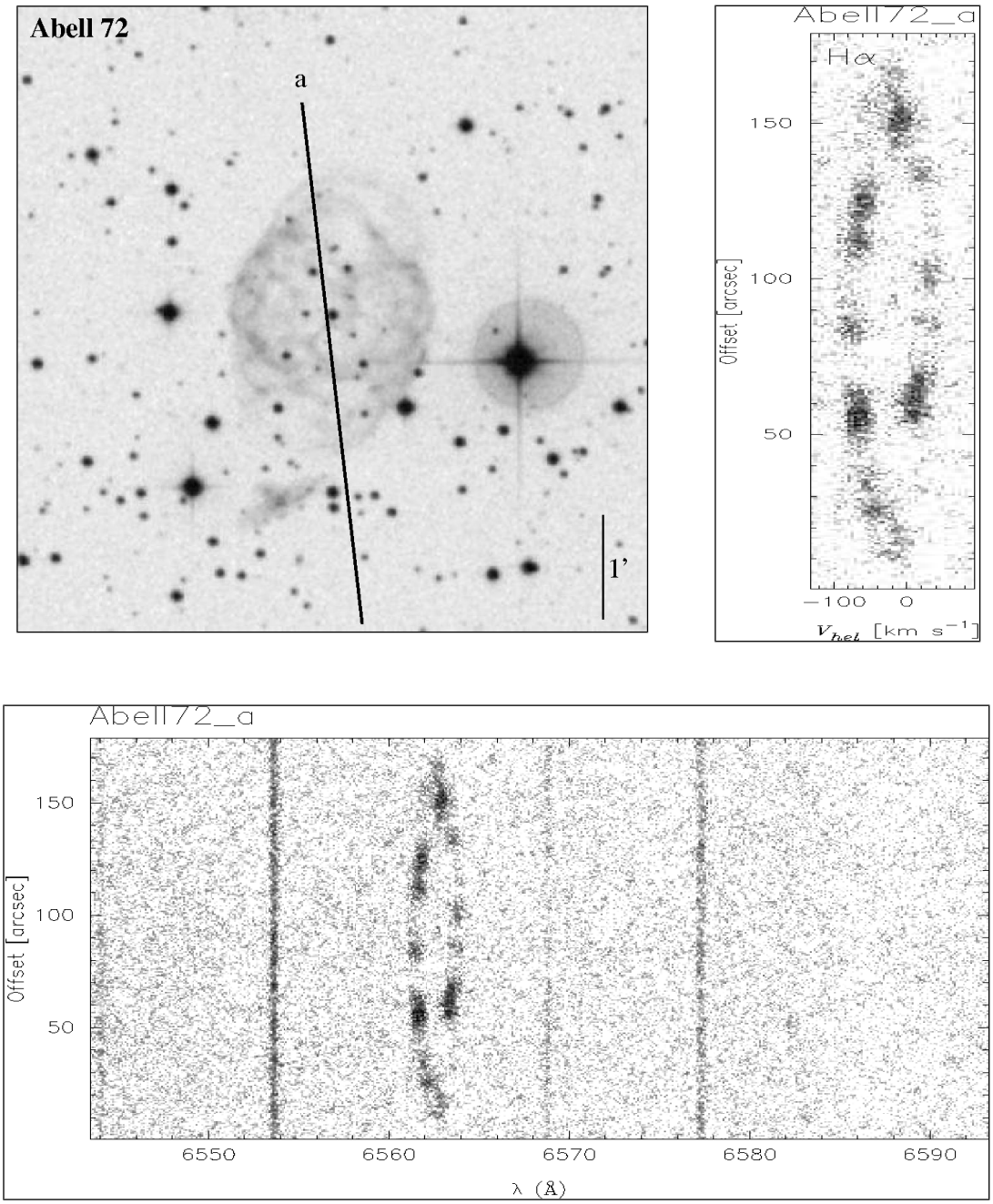

Figure A.31 **Same as Figure A.1.**

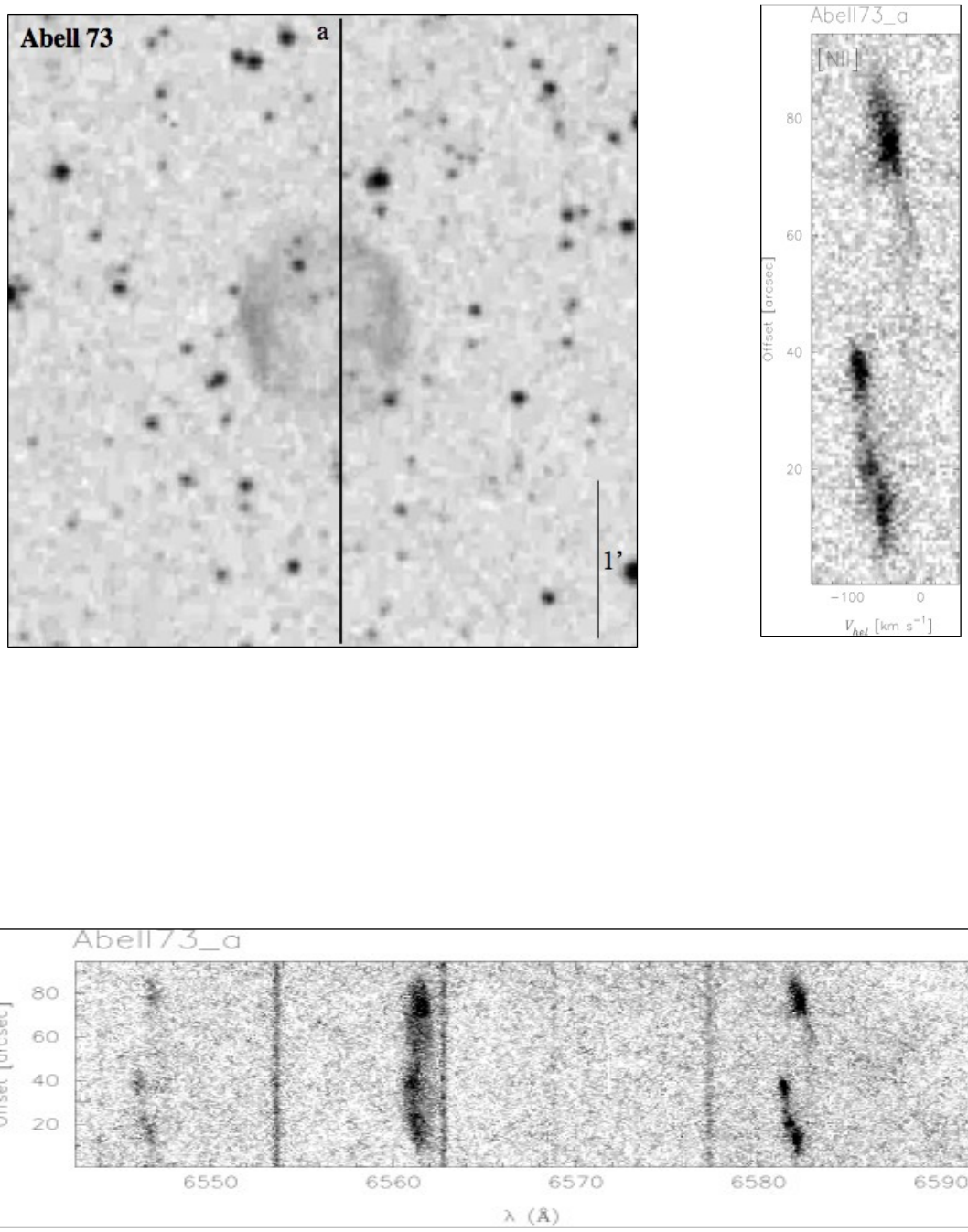

Figure A.32 **Same as Figure A.1.**

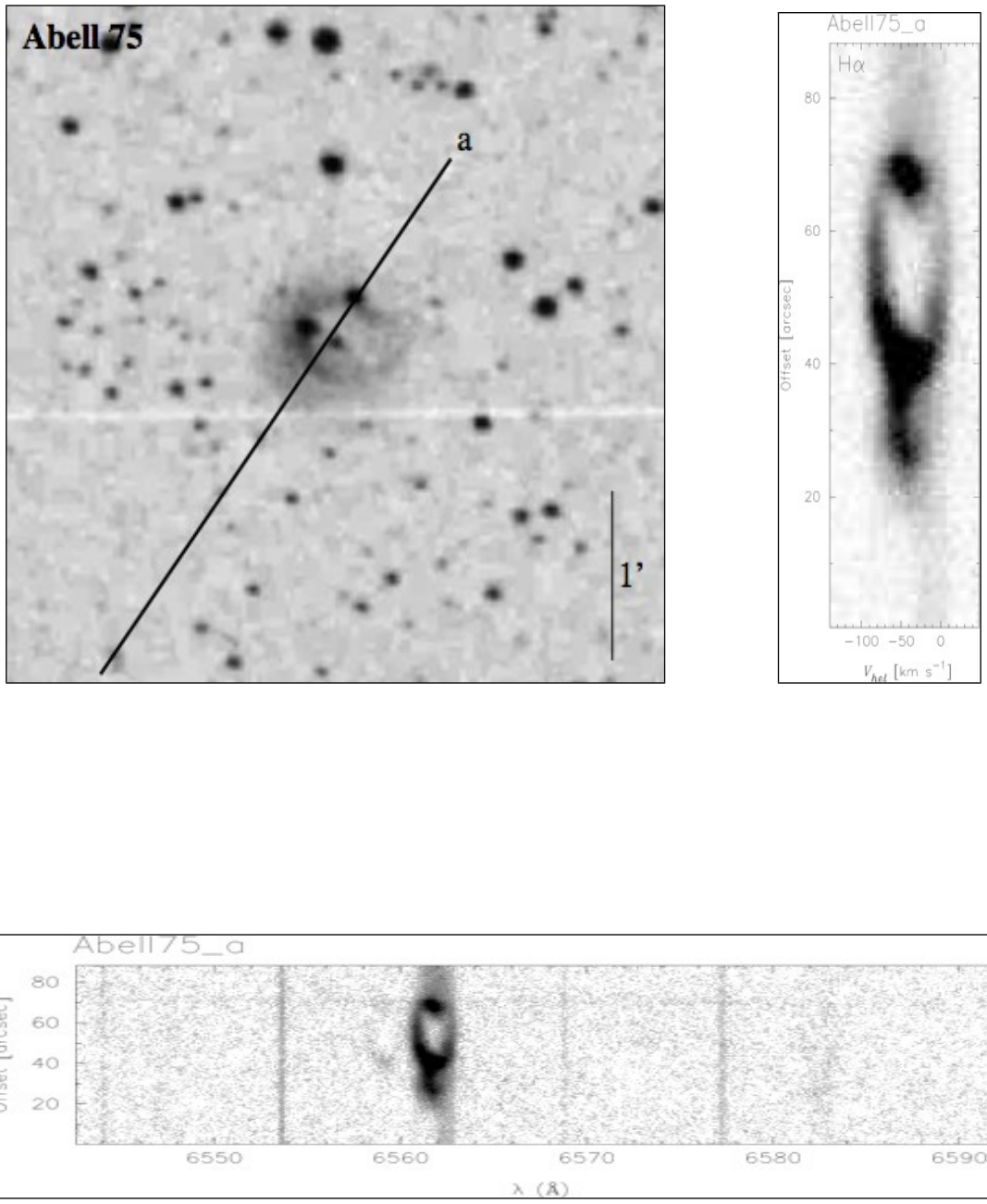

Figure A.33 **Same as Figure A.1.**

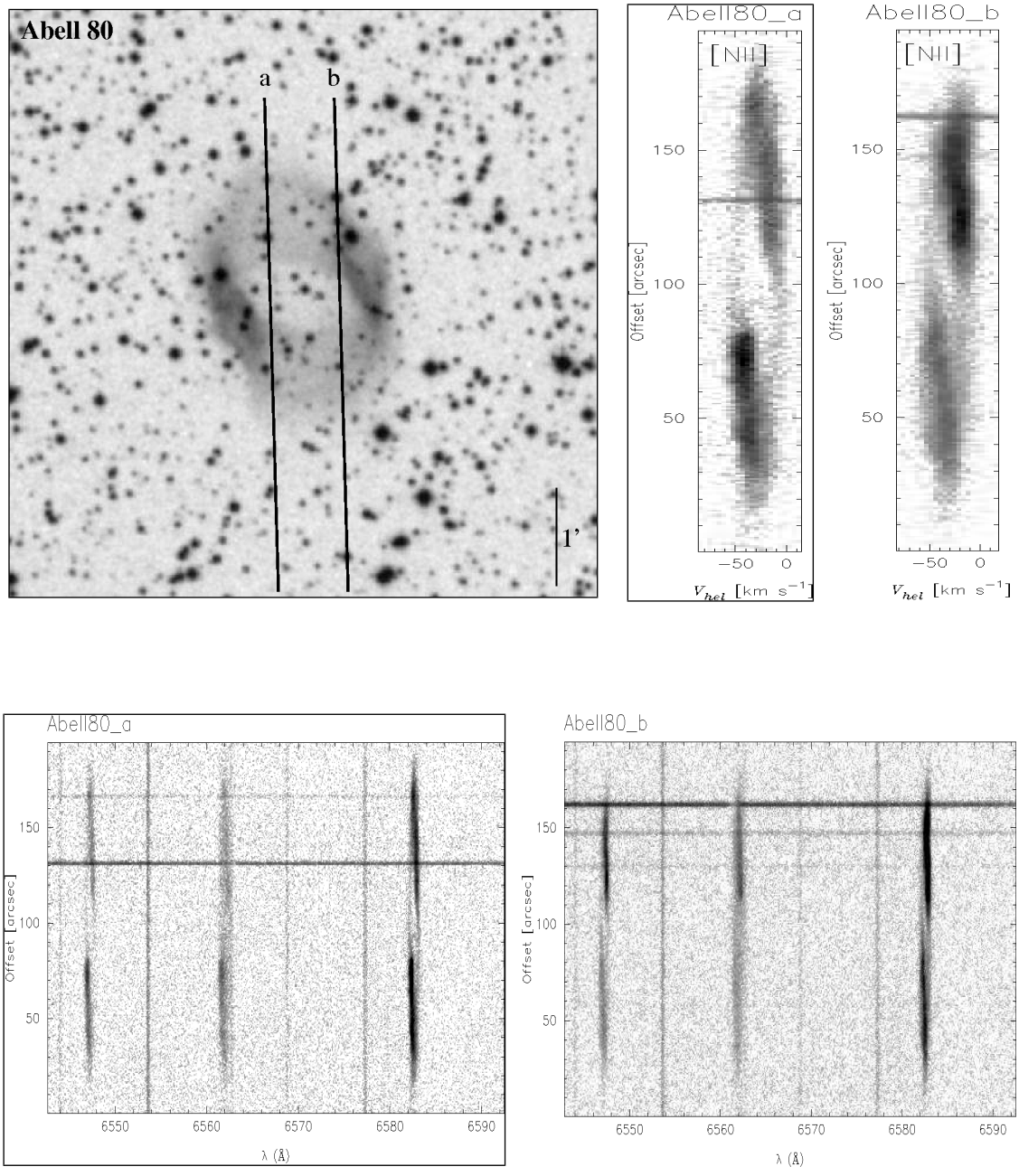

Figure A.34 **Same as Figure A.1.**

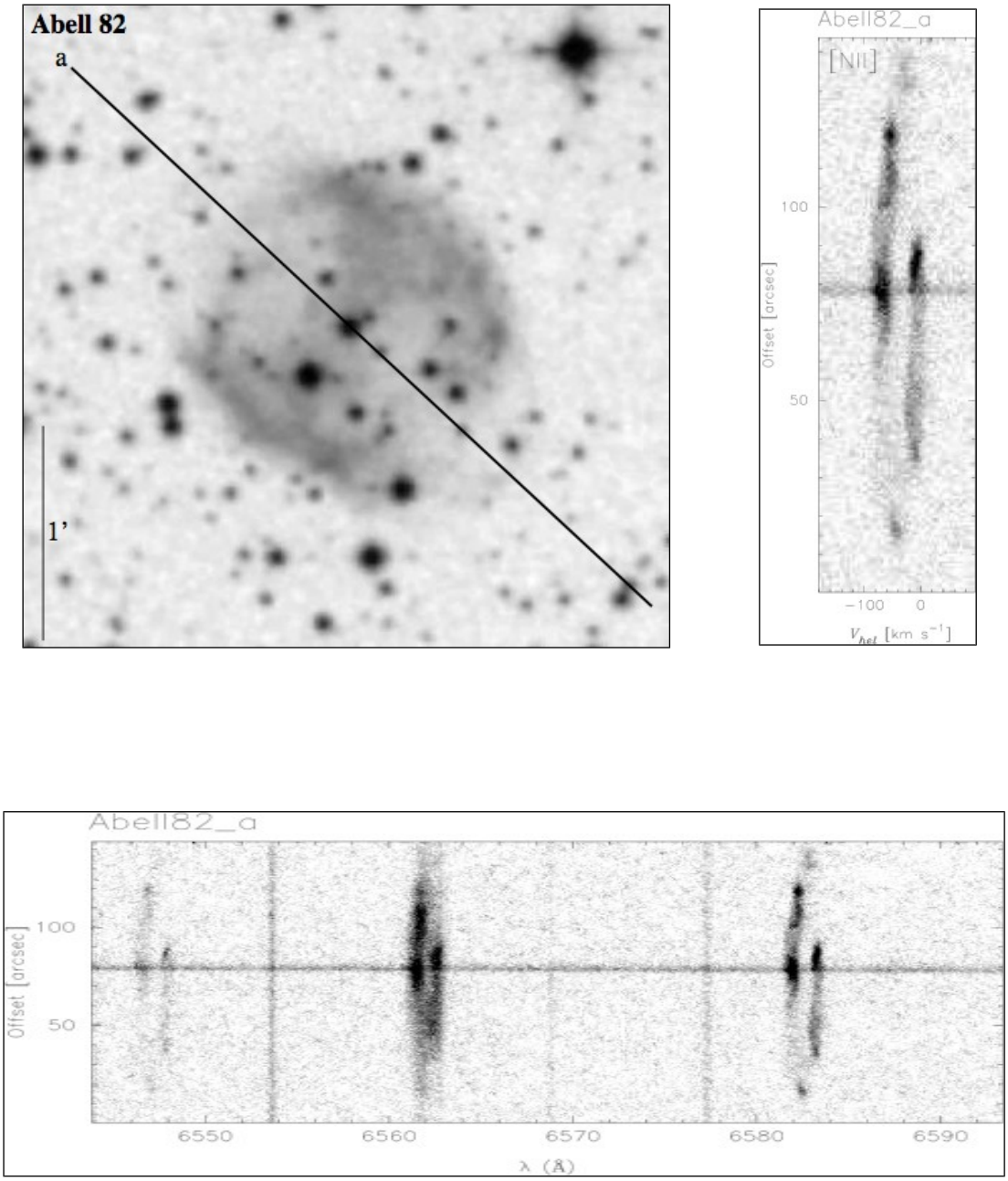

Figure A.35 **Same as Figure A.1.**

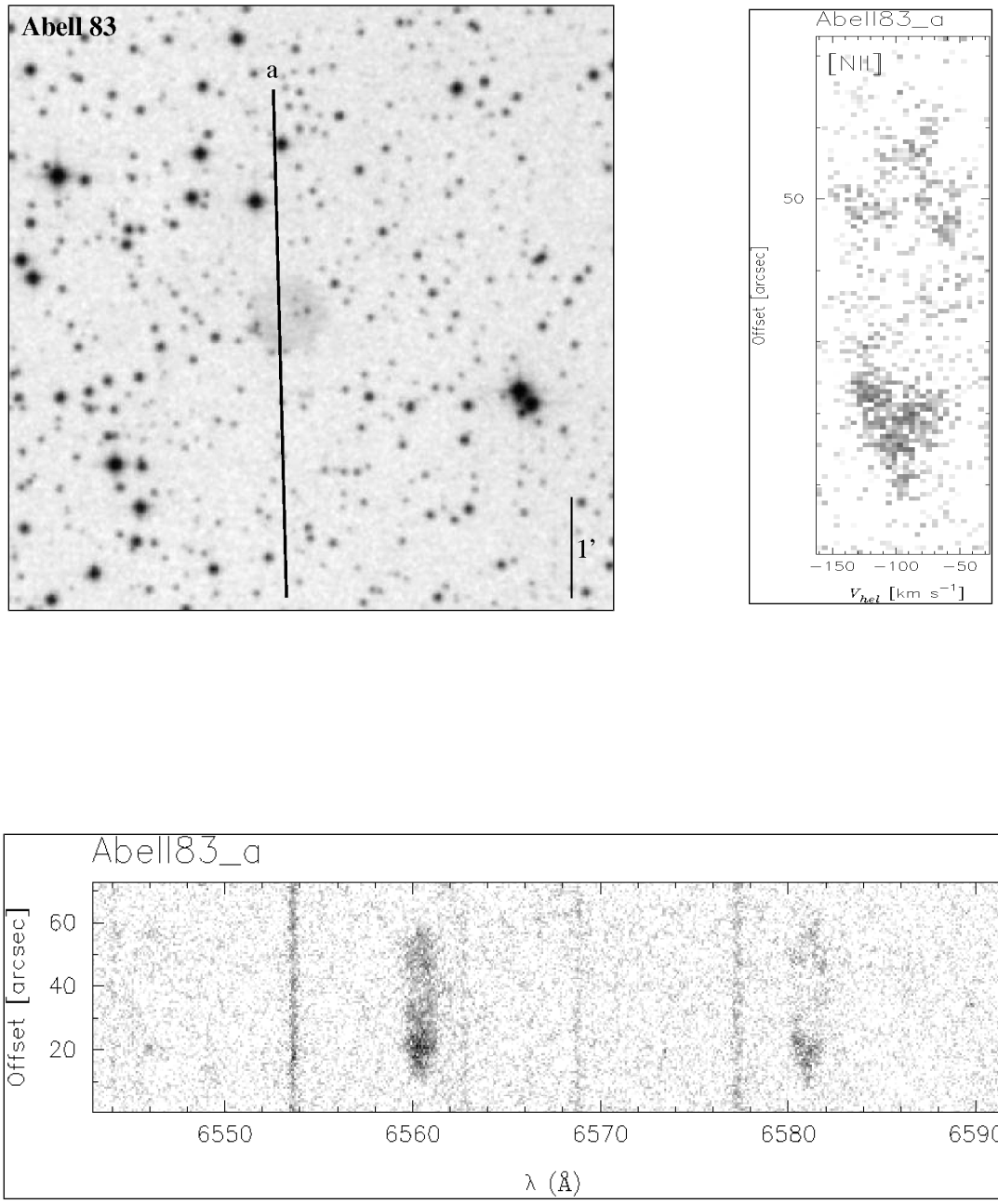

Figure A.36 **Same as Figure A.1.**

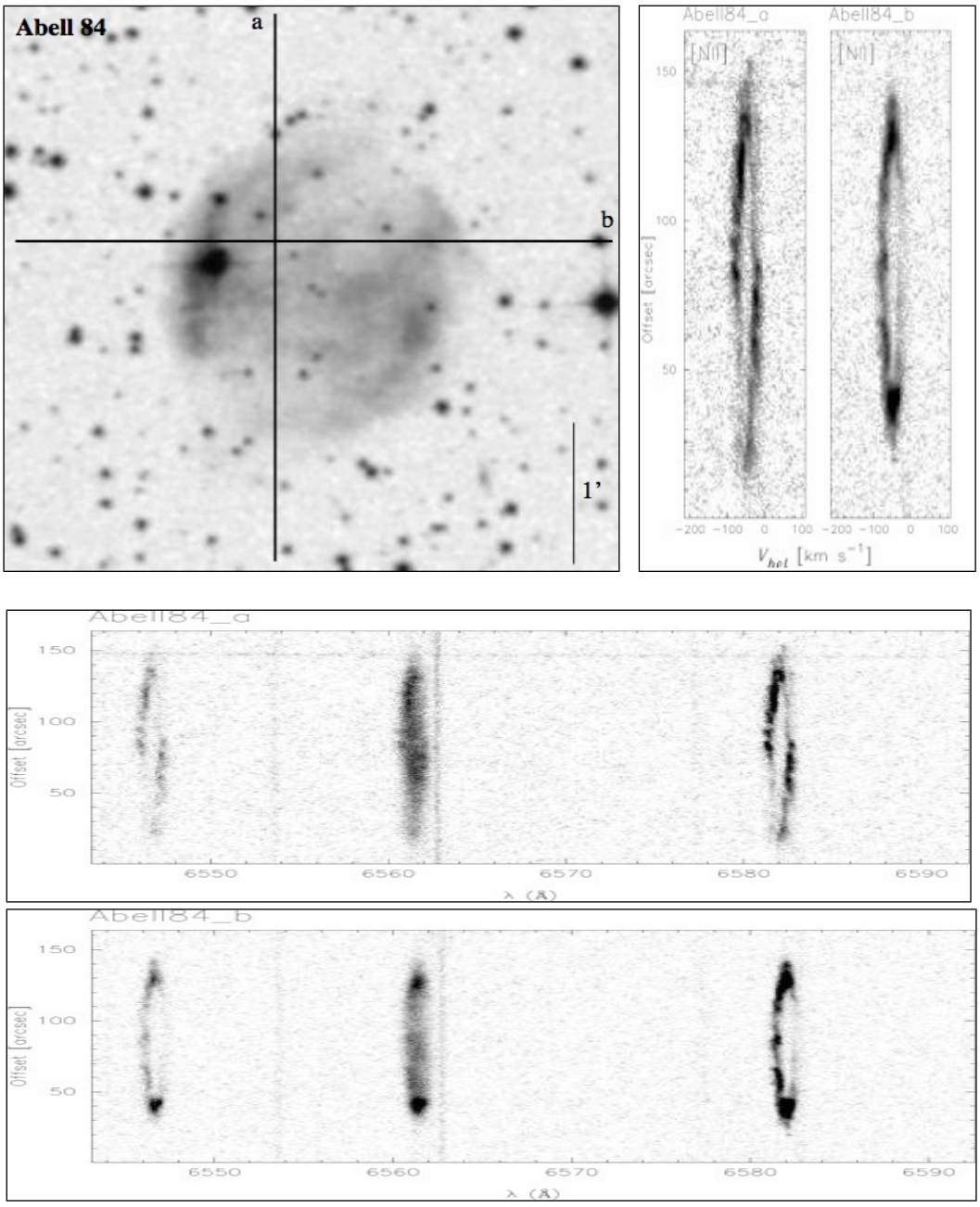

Figure A.37 **Same as Figure A.1.**

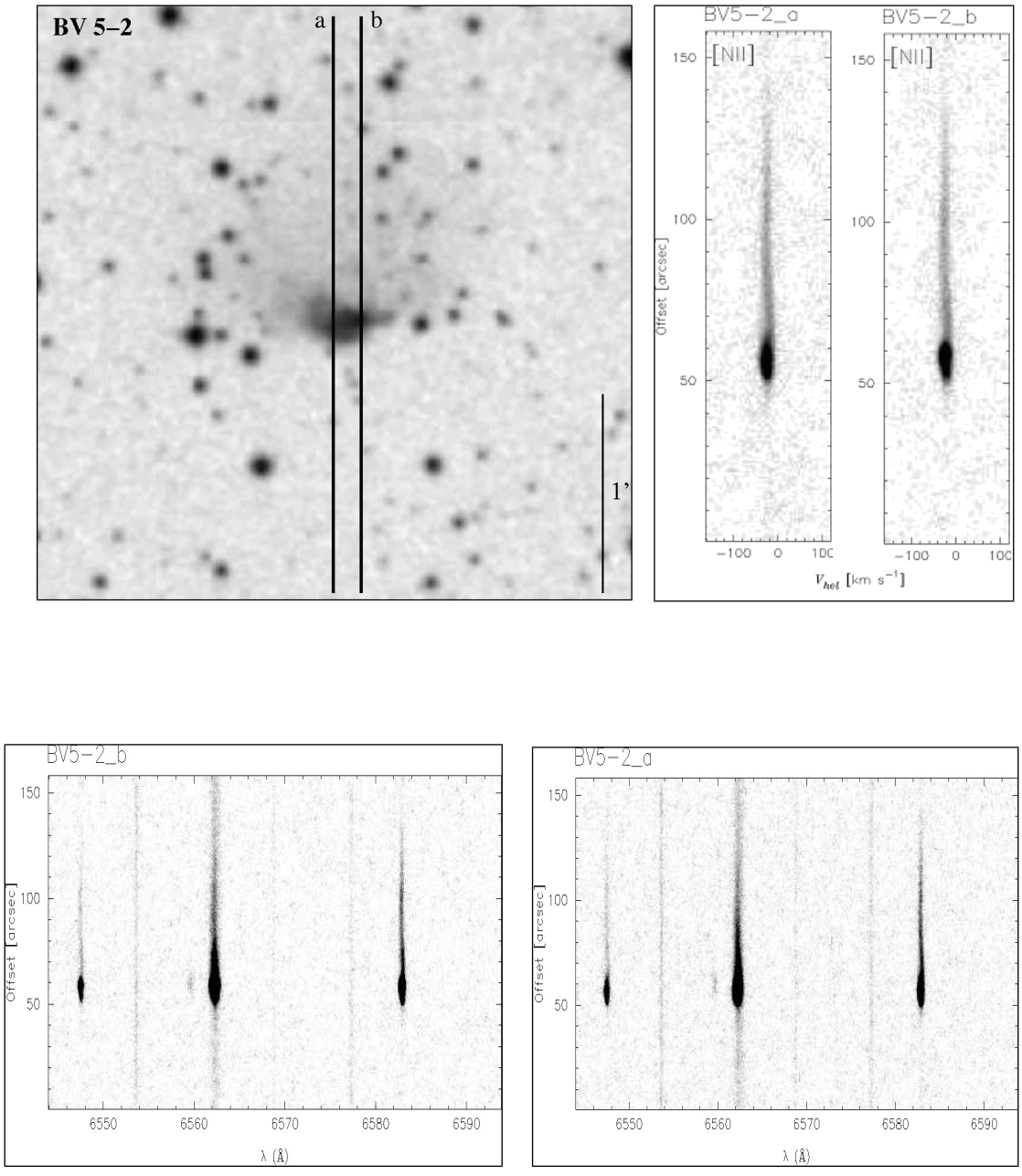

Figure A.38 **Same as Figure A.1.**

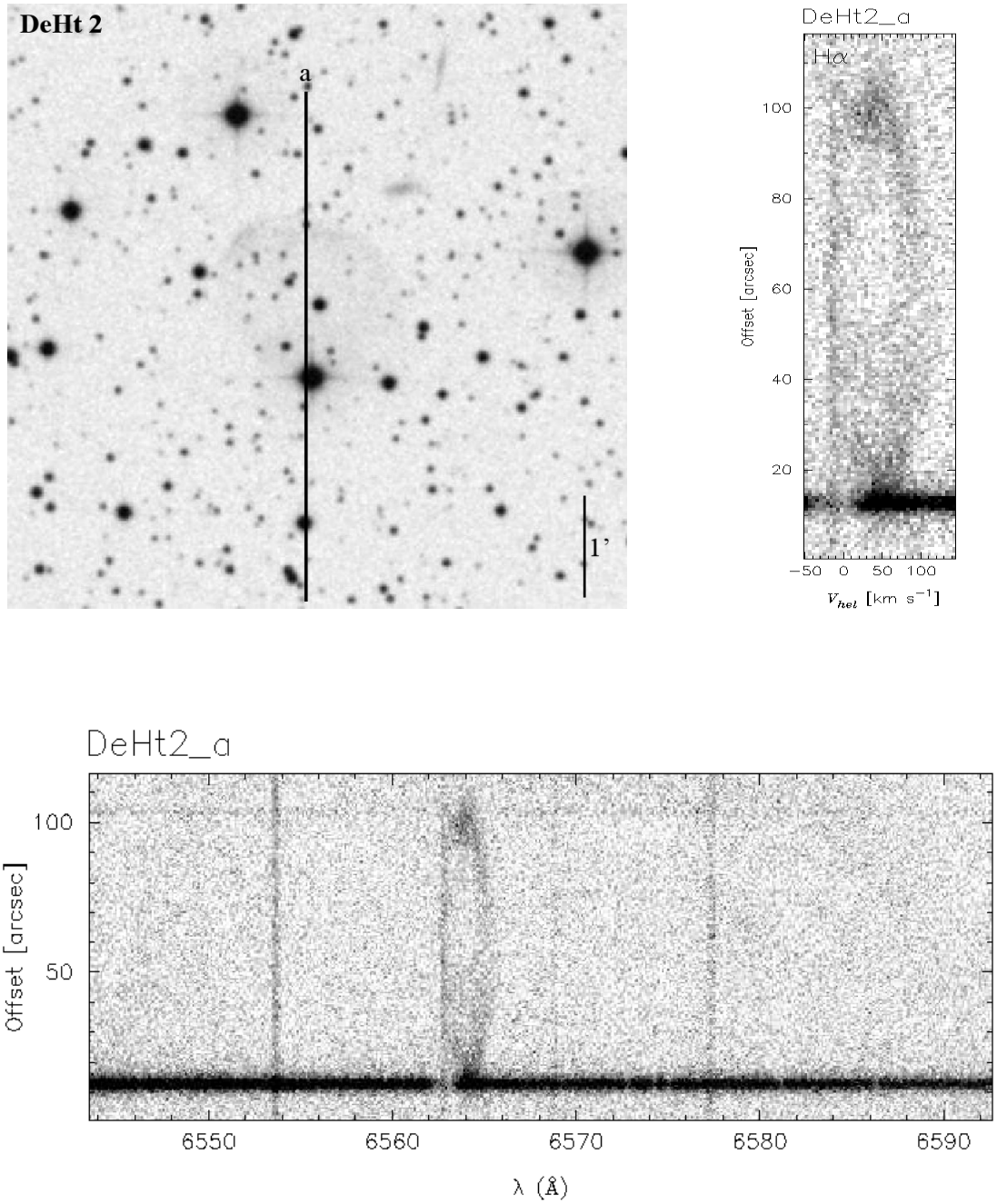

Figure A.39 **Same as Figure A.1.**

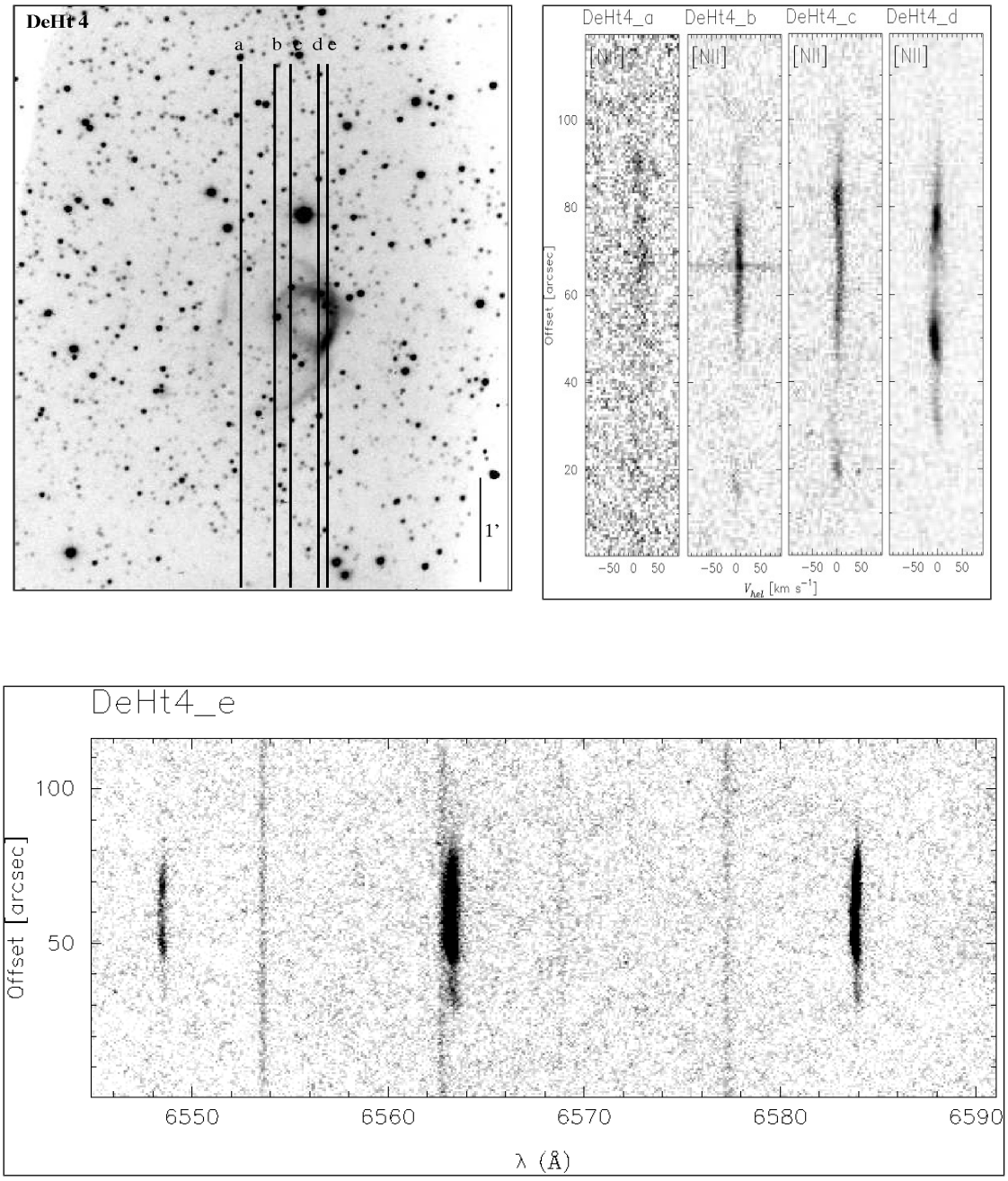

Figure A.40 **Same as Figure A.1.**

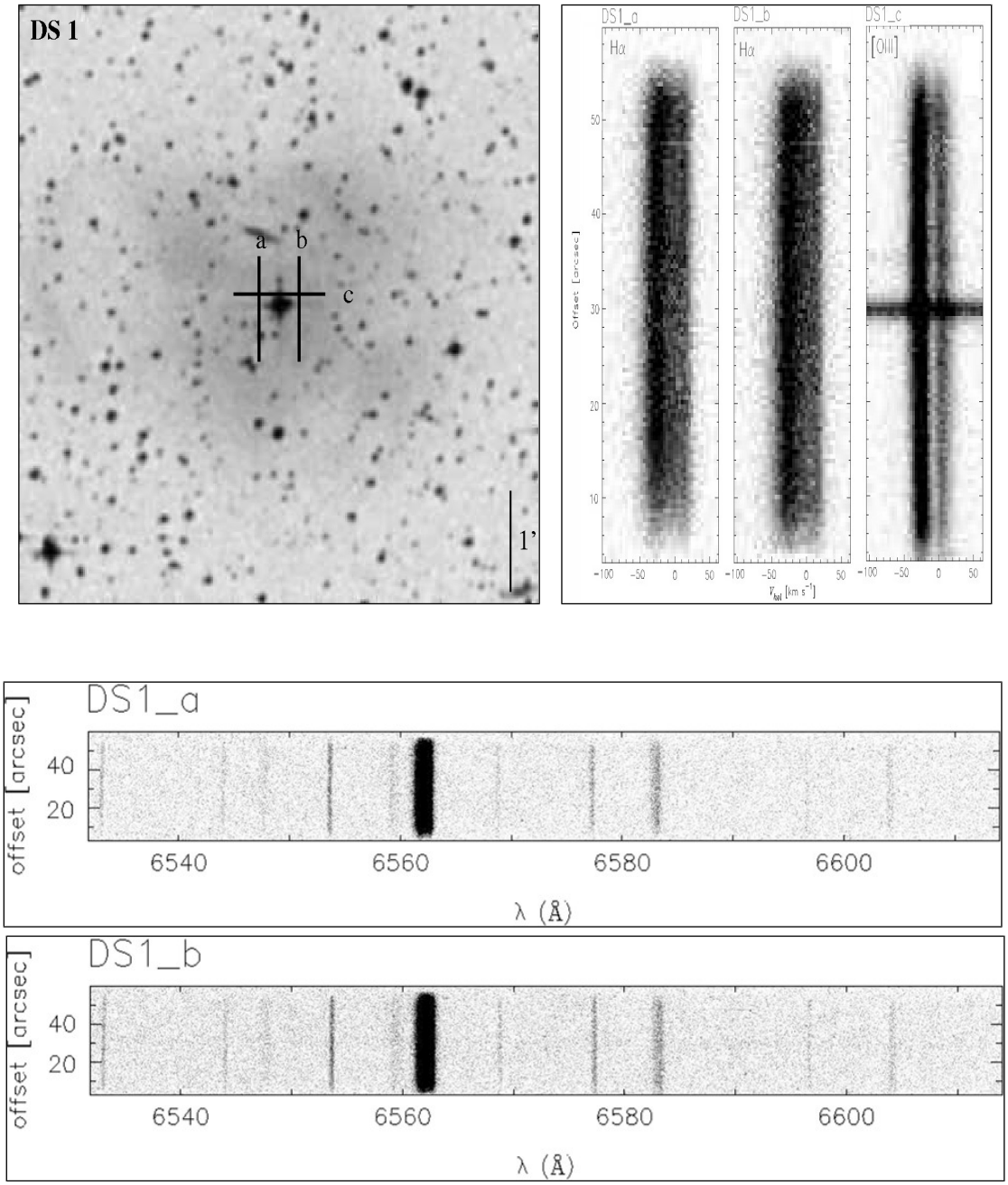

Figure A.41 **Same as Figure A.1.**

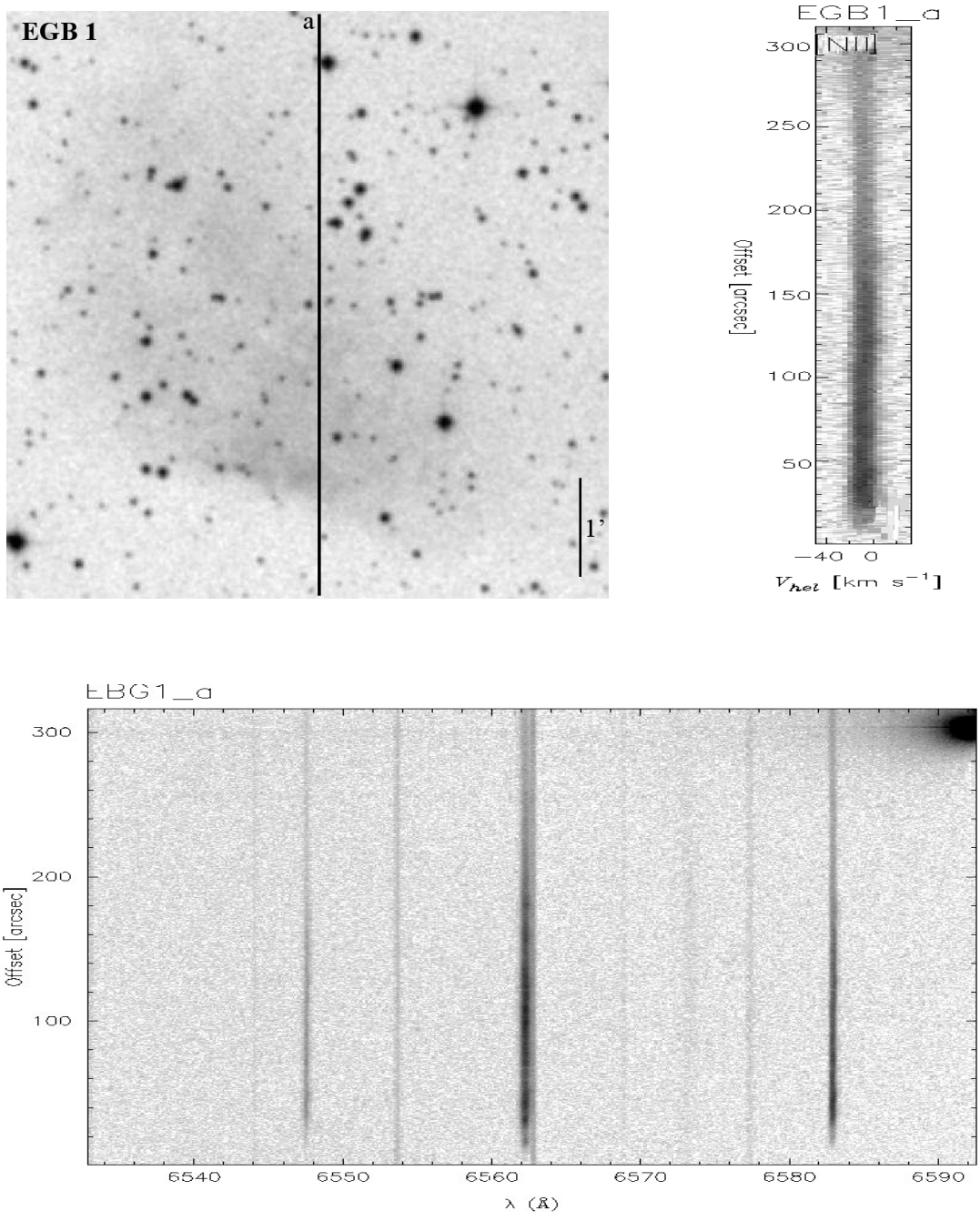

Figure A.42 **Same as Figure A.1.**

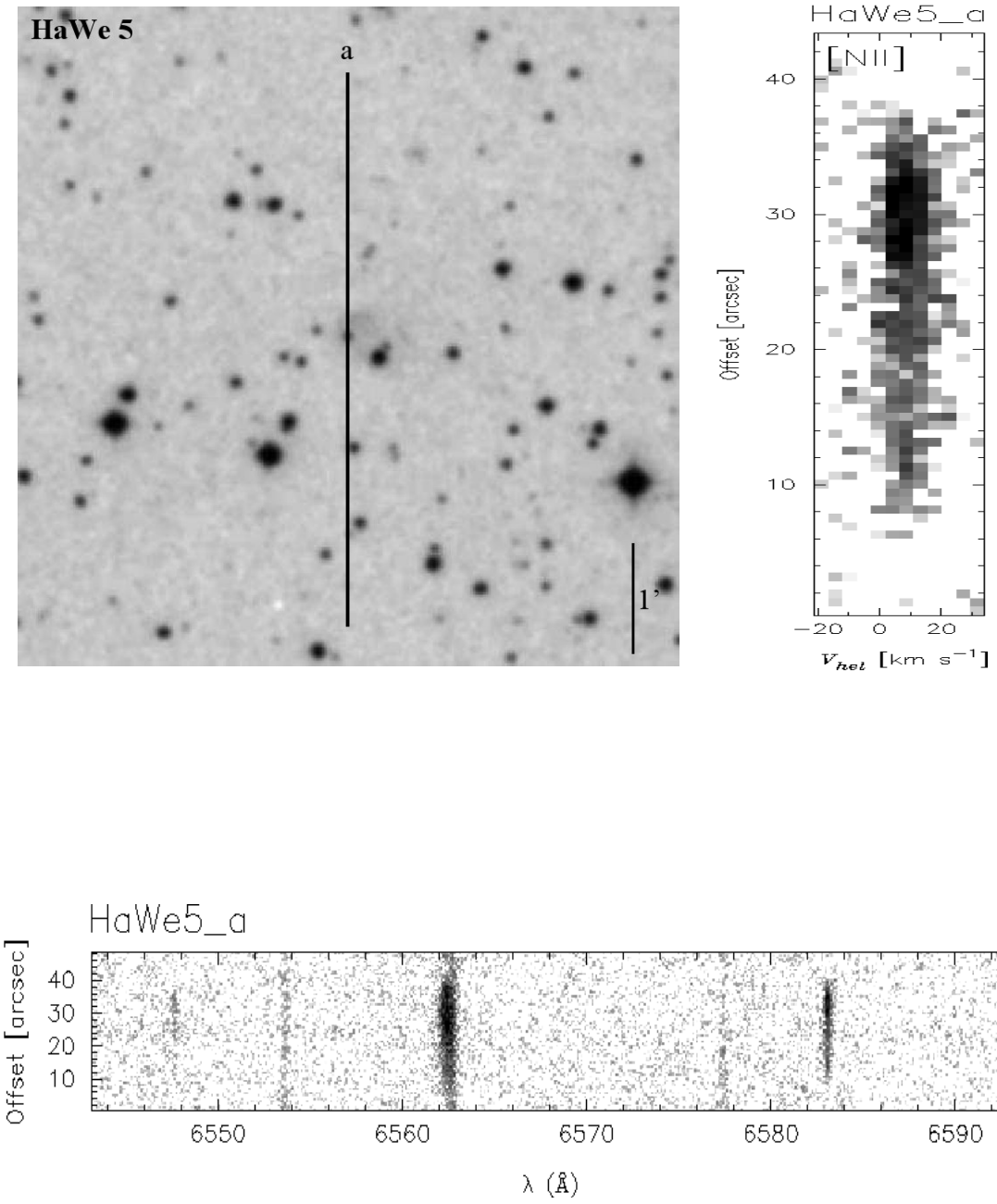

Figure A.43 **Same as Figure A.1.**

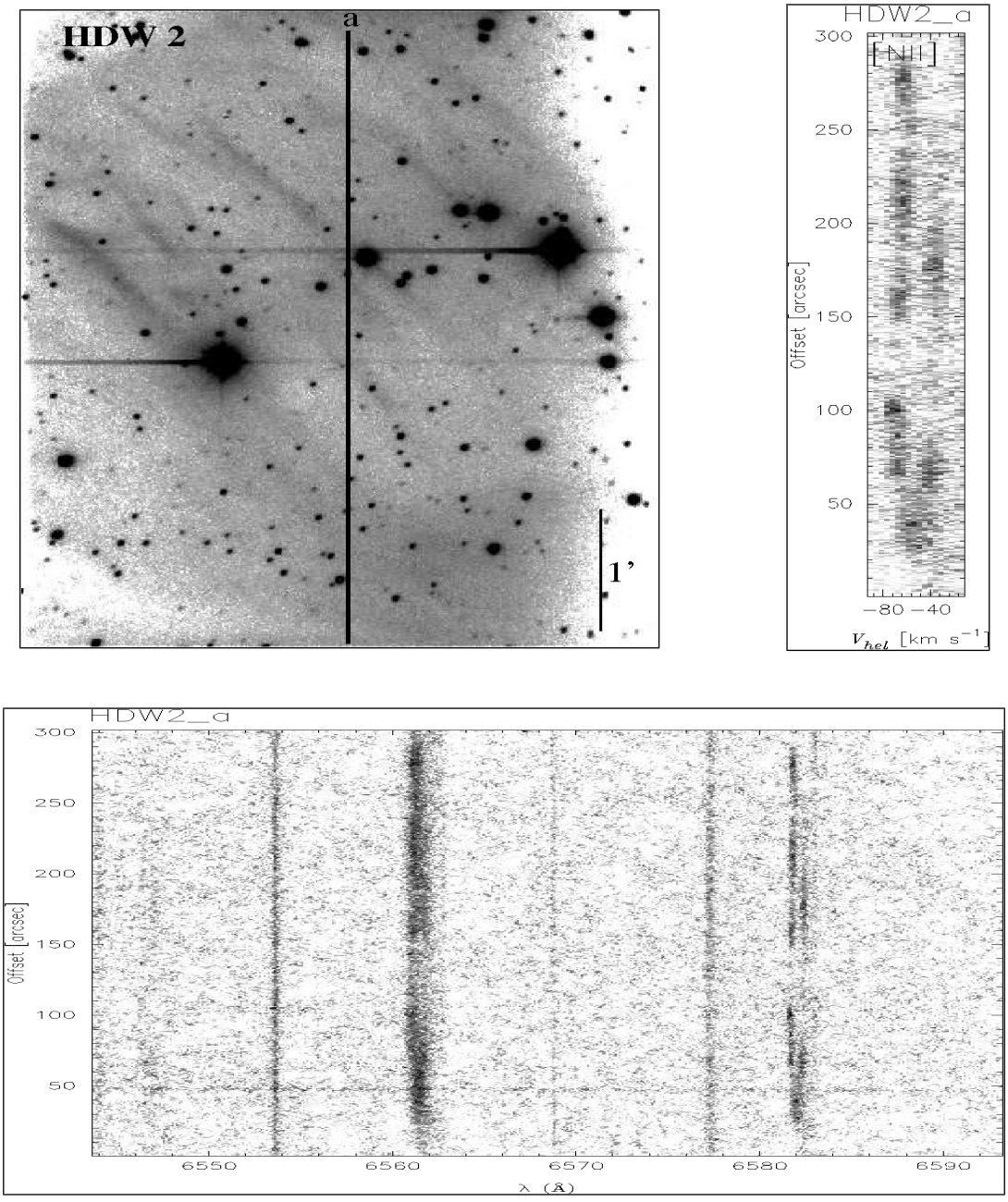

Figure A.44 **Same as Figure A.1.**

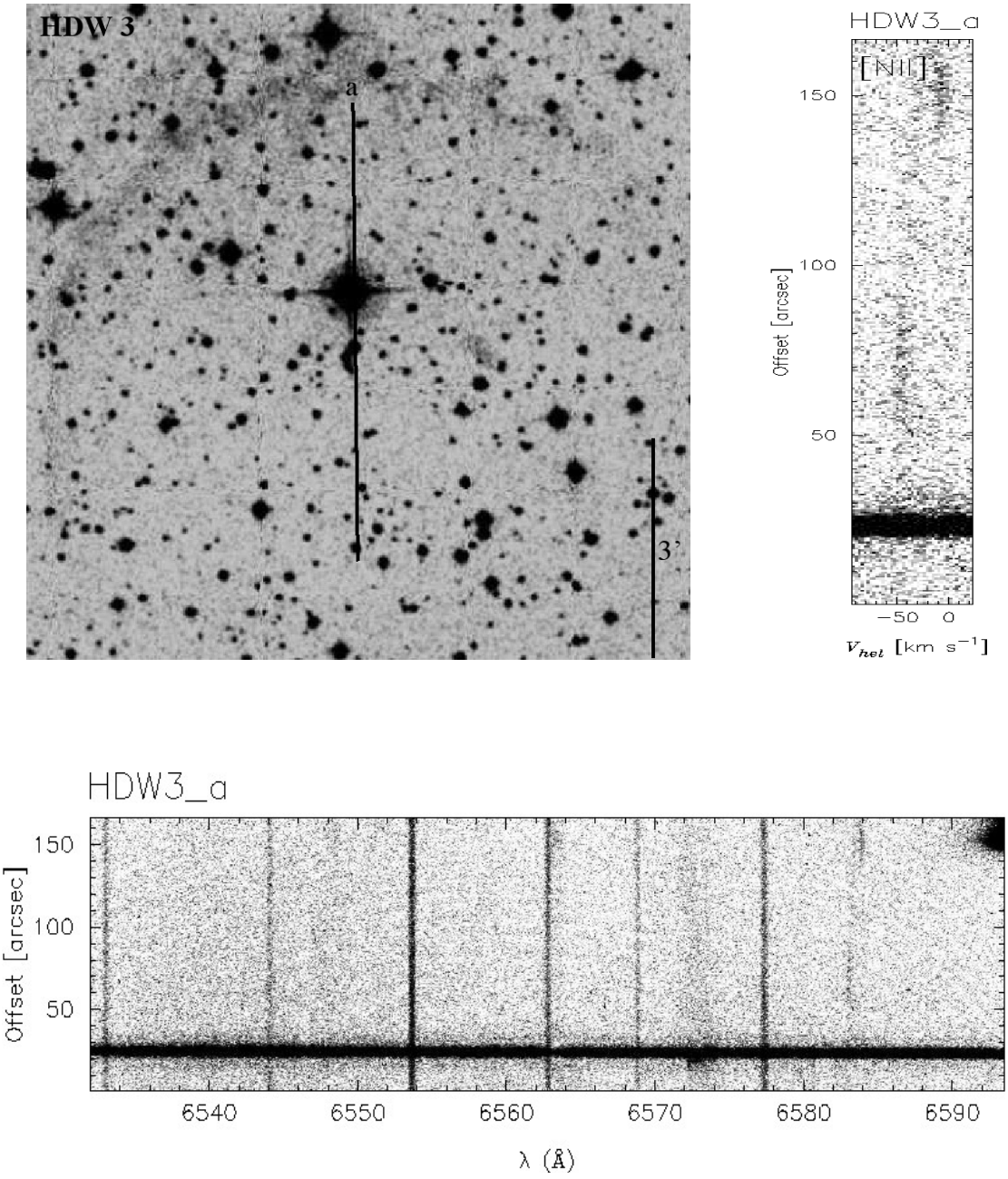

Figure A.45 **Same as Figure A.1.**

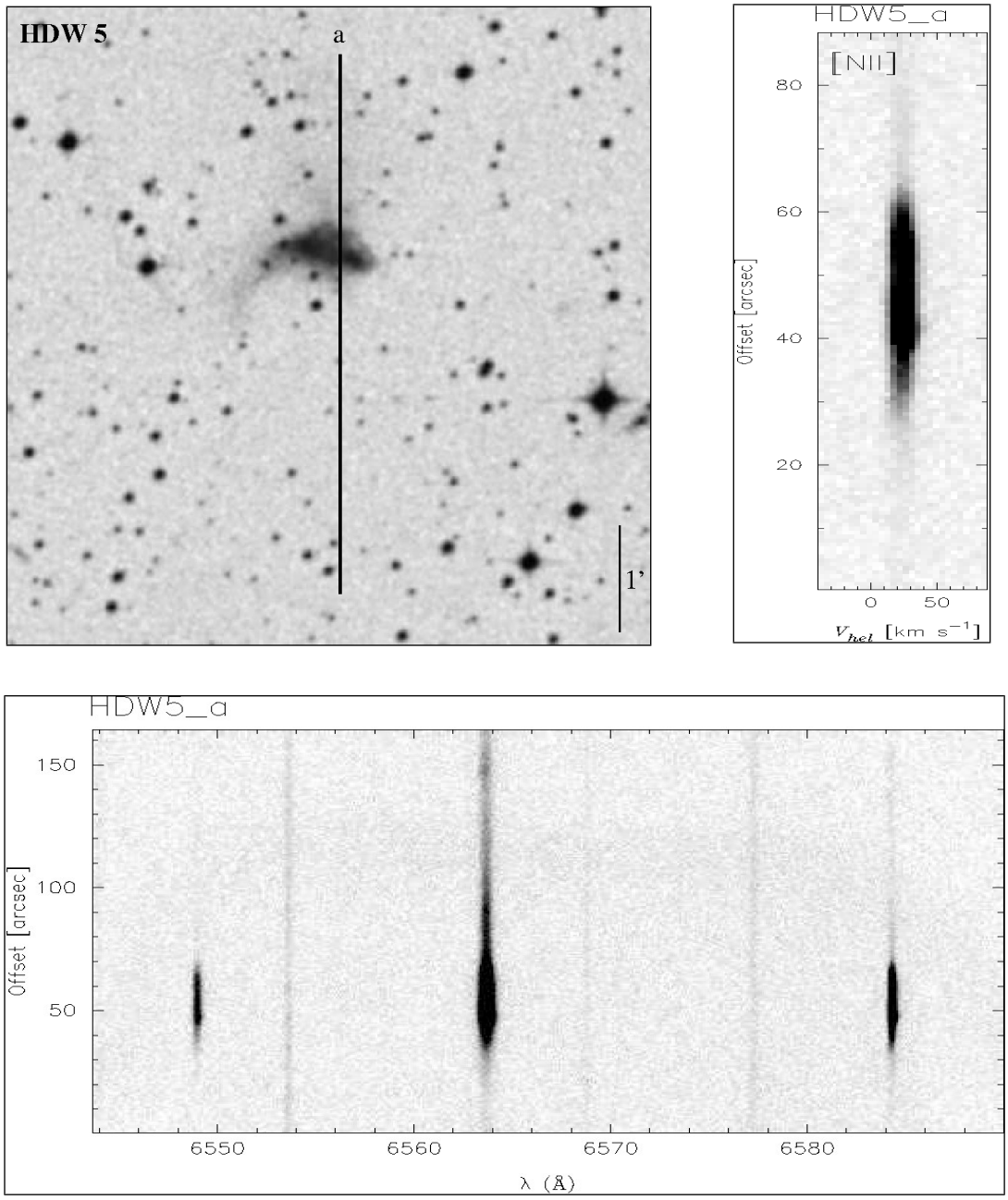

Figure A.46 **Same as Figure A.1.**

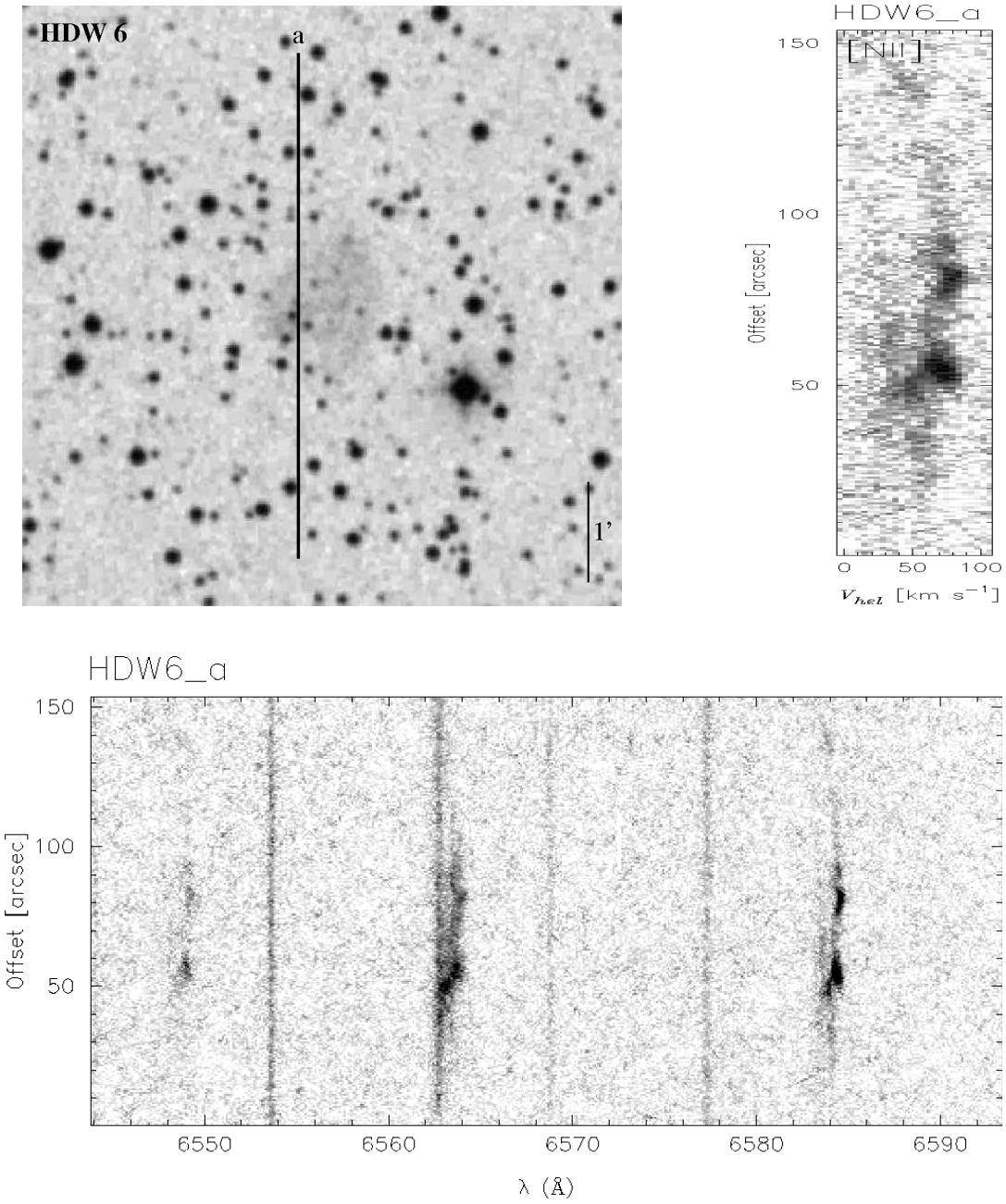

Figure A.47 **Same as Figure A.1.**

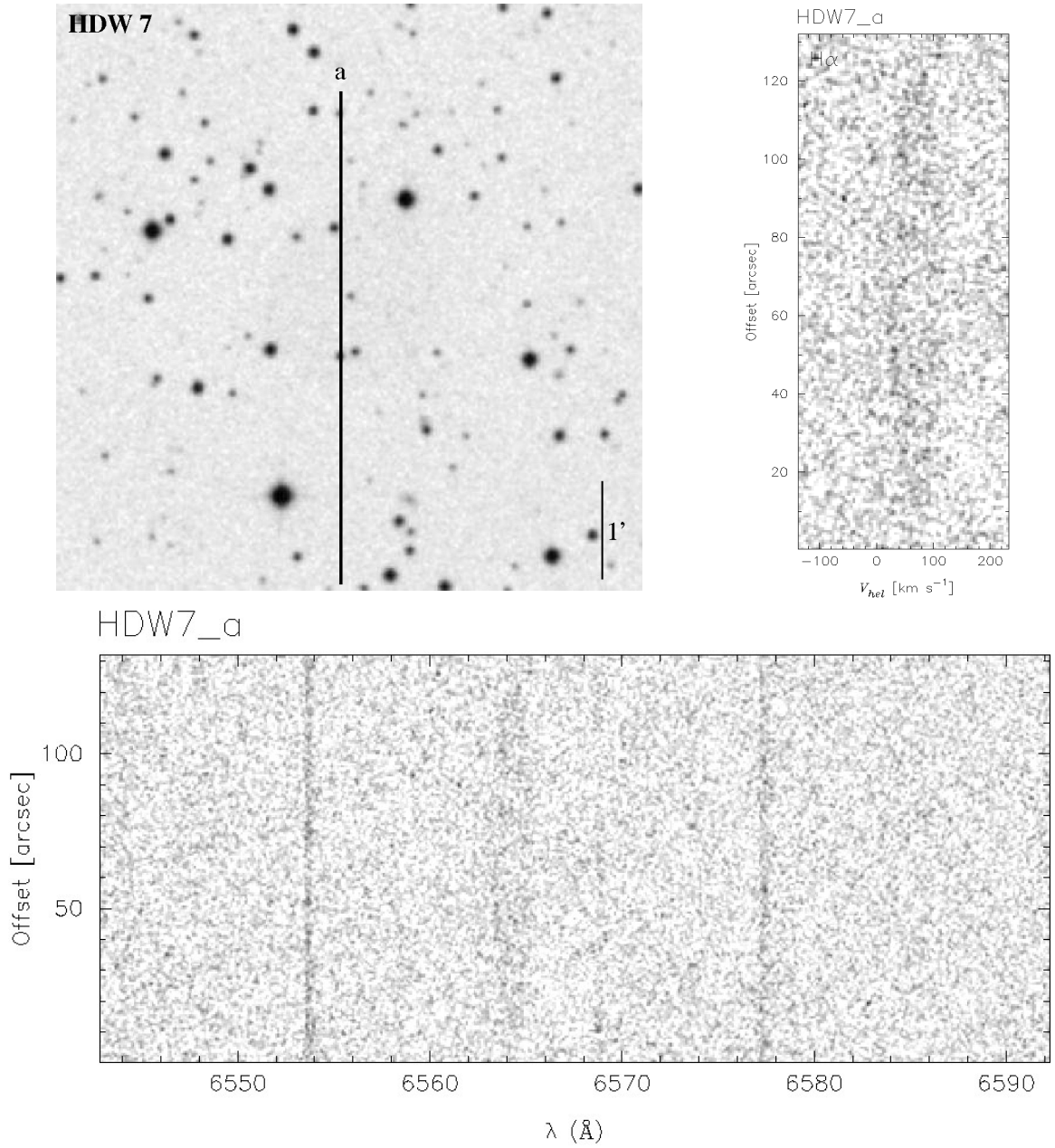

Figure A.48 **Same as Figure A.1.**

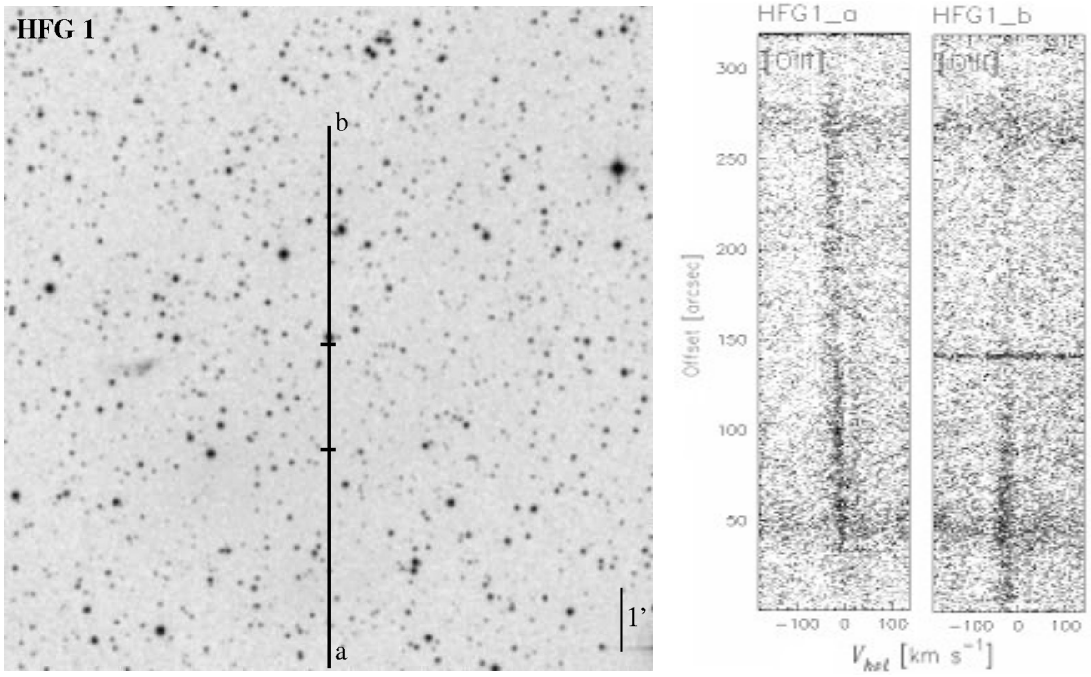

Figure A.49 **Same as Figure A.1.**

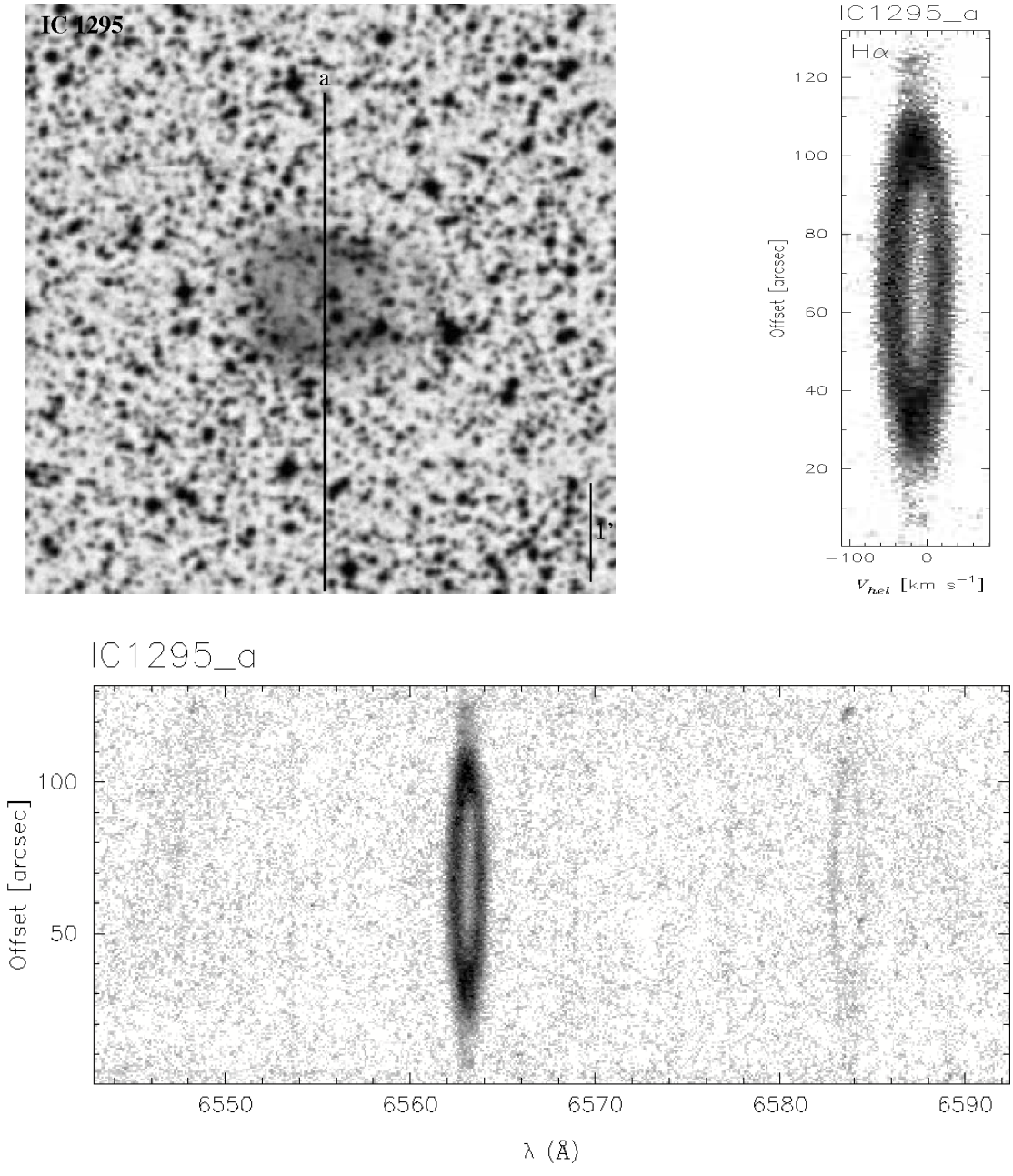

Figure A.50 **Same as Figure A.1.**

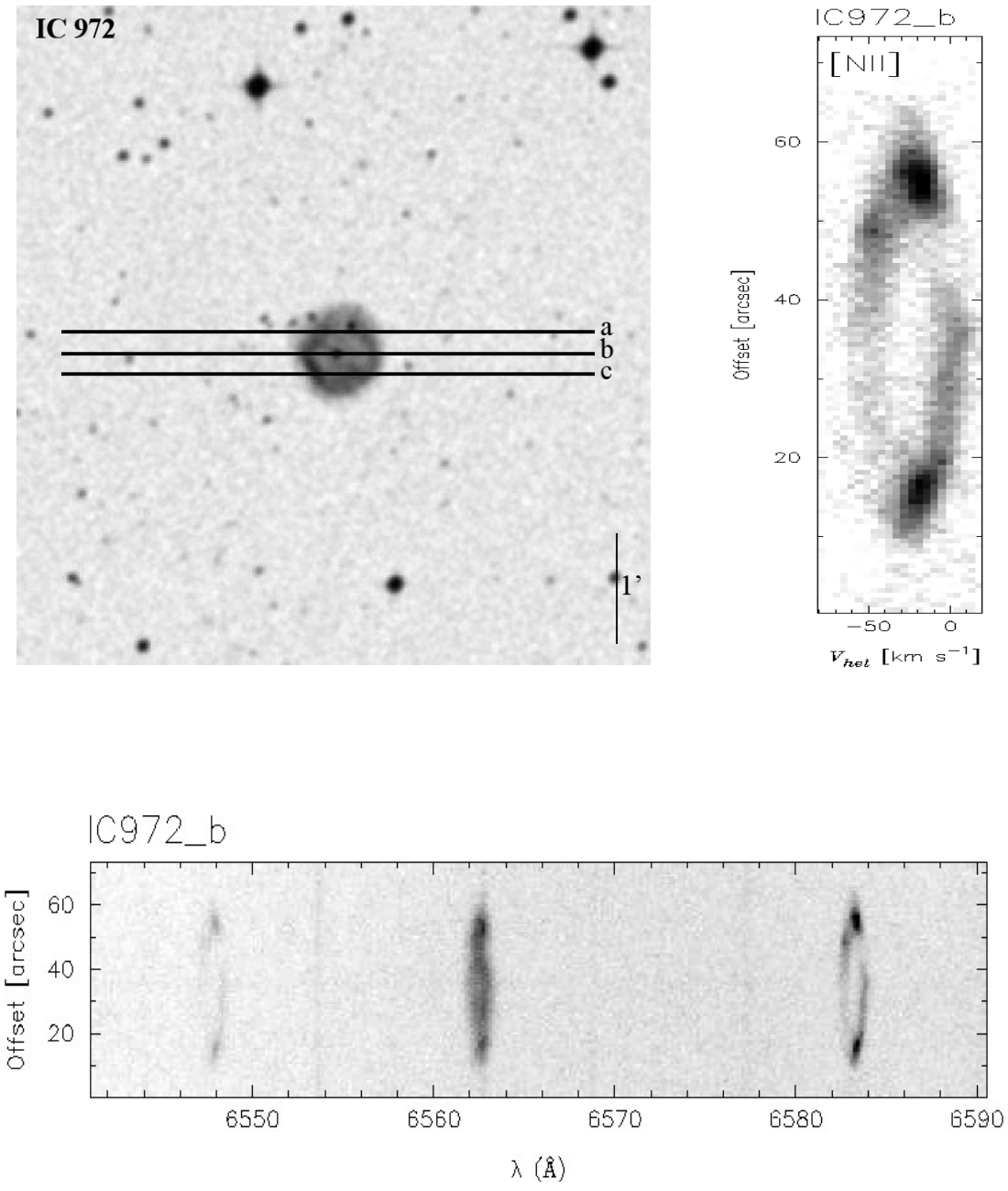

Figure A.51 **Same as Figure A.1.**

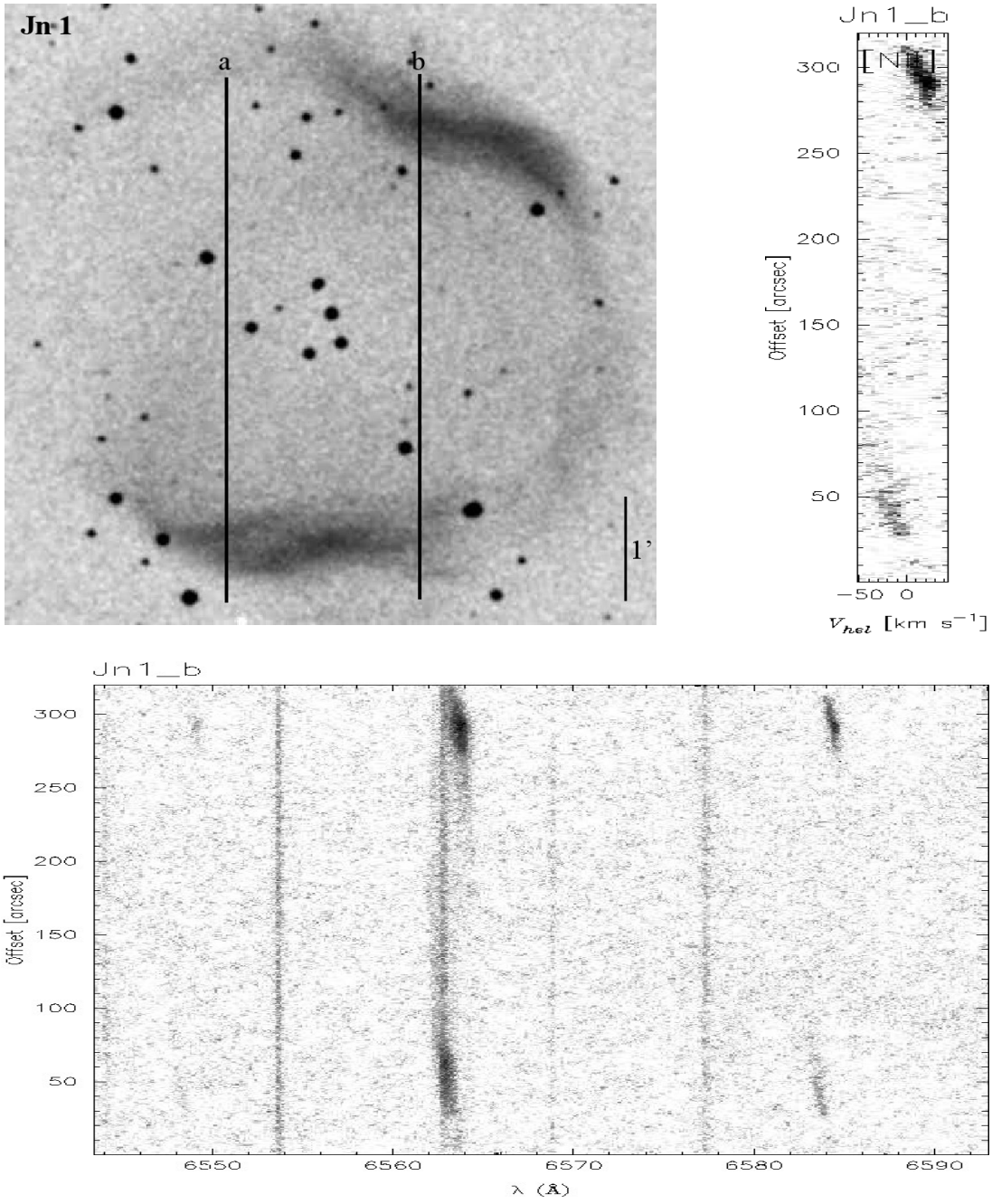

Figure A.52 **Same as Figure A.1.**

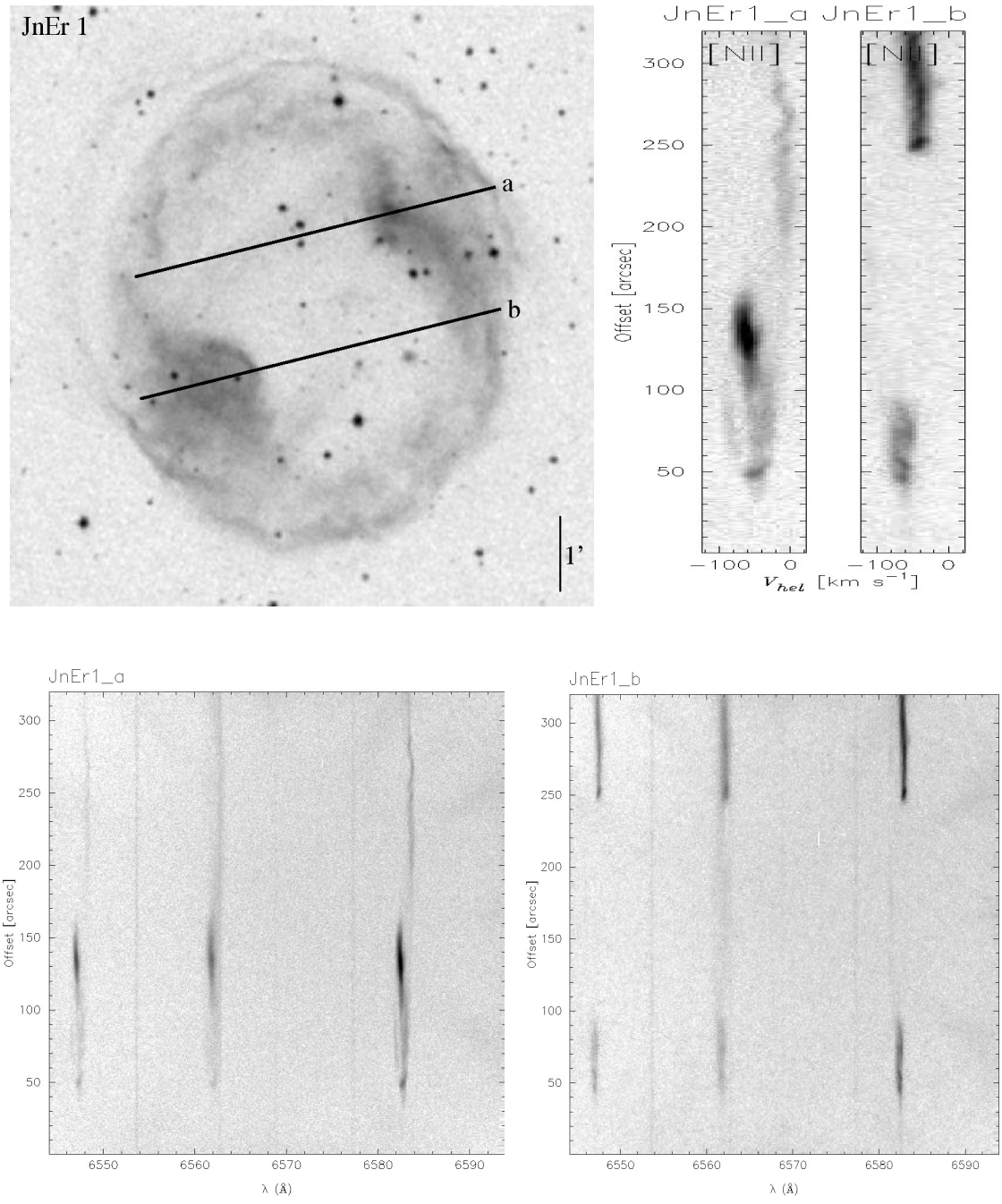

Figure A.53 **Same as Figure A.1.**

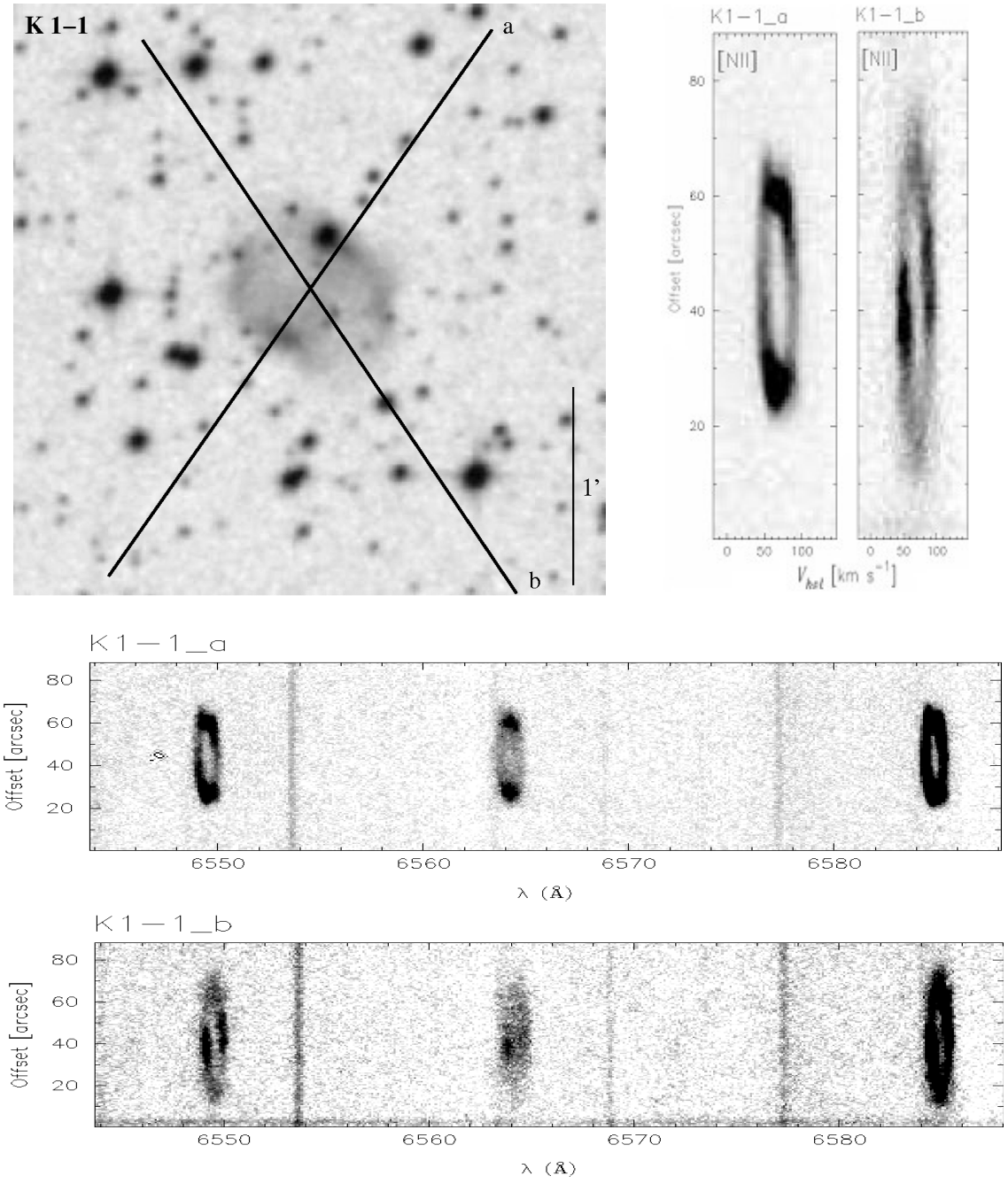

Figure A.54 **Same as Figure A.1.**

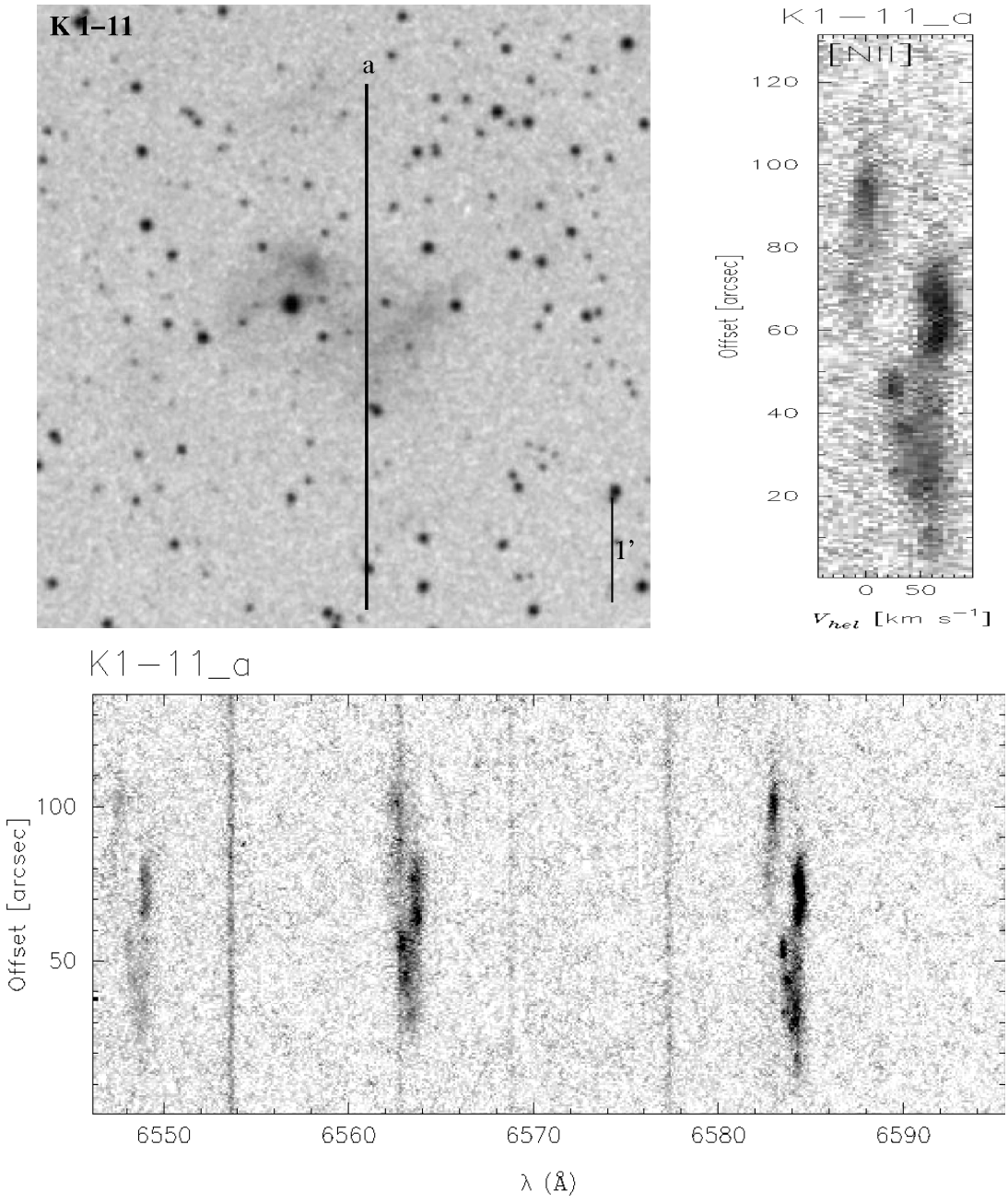

Figure A.55 **Same as Figure A.1.**

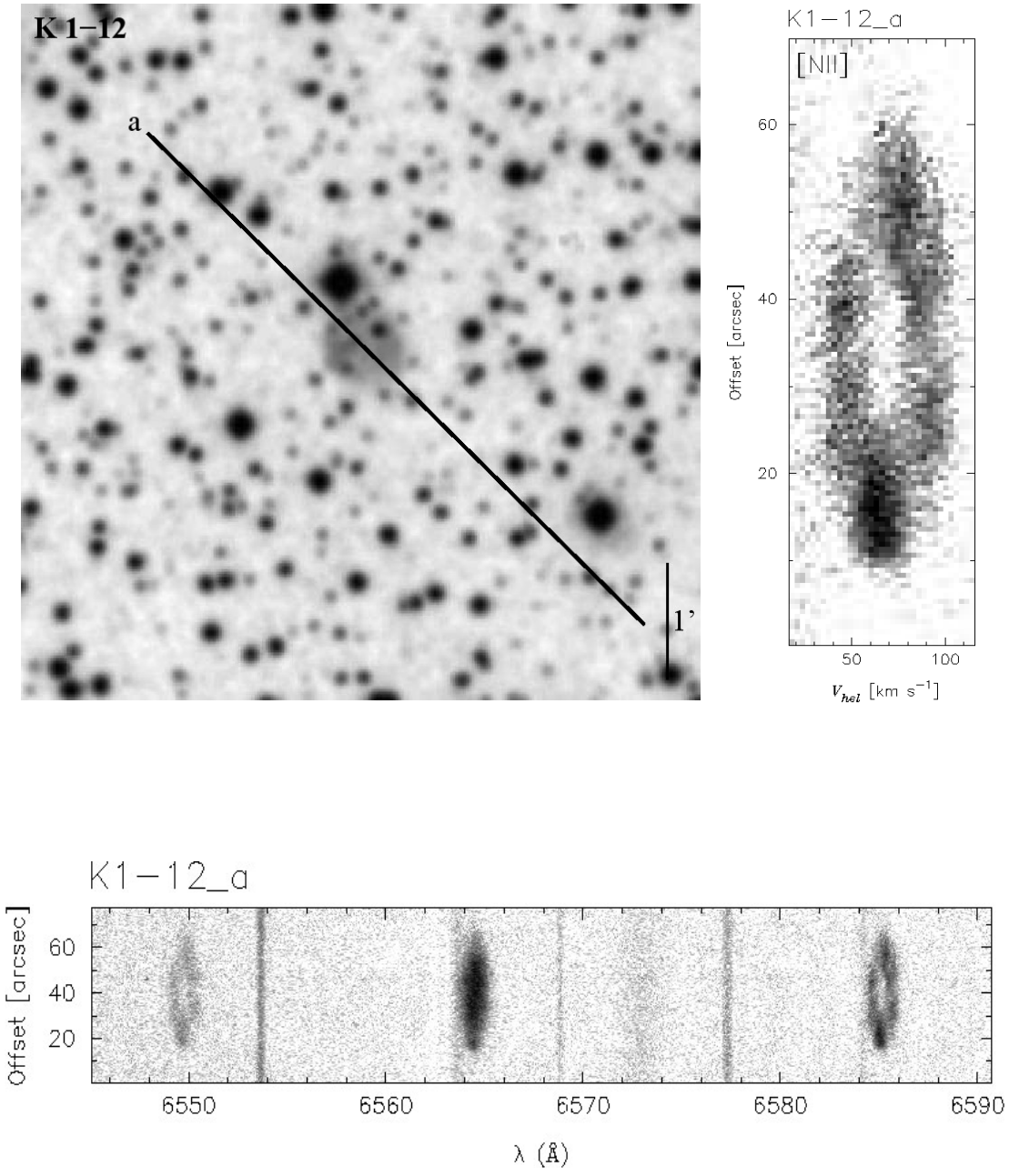

Figure A.56 **Same as Figure A.1.**

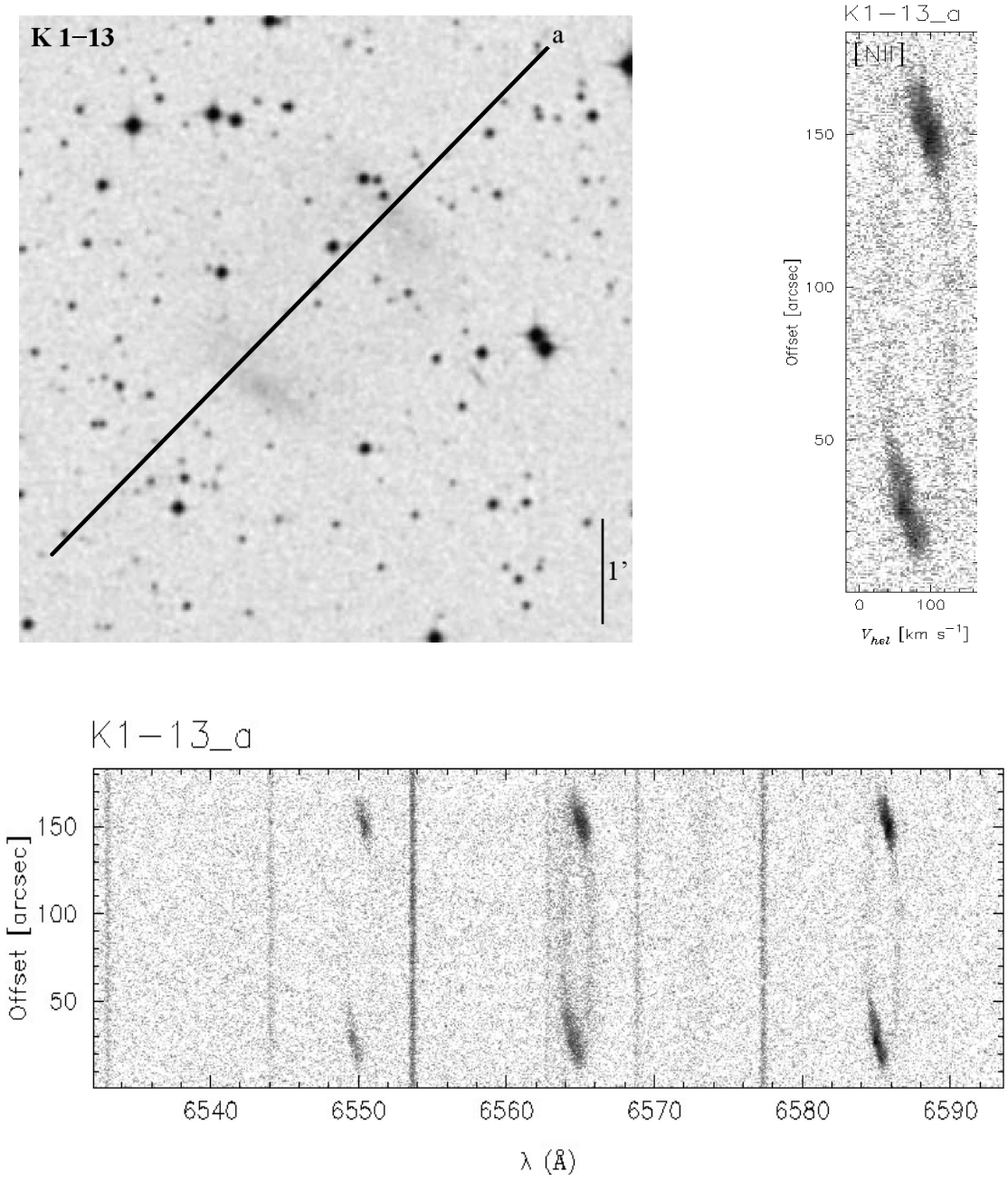

Figure A.57 **Same as Figure A.1.**

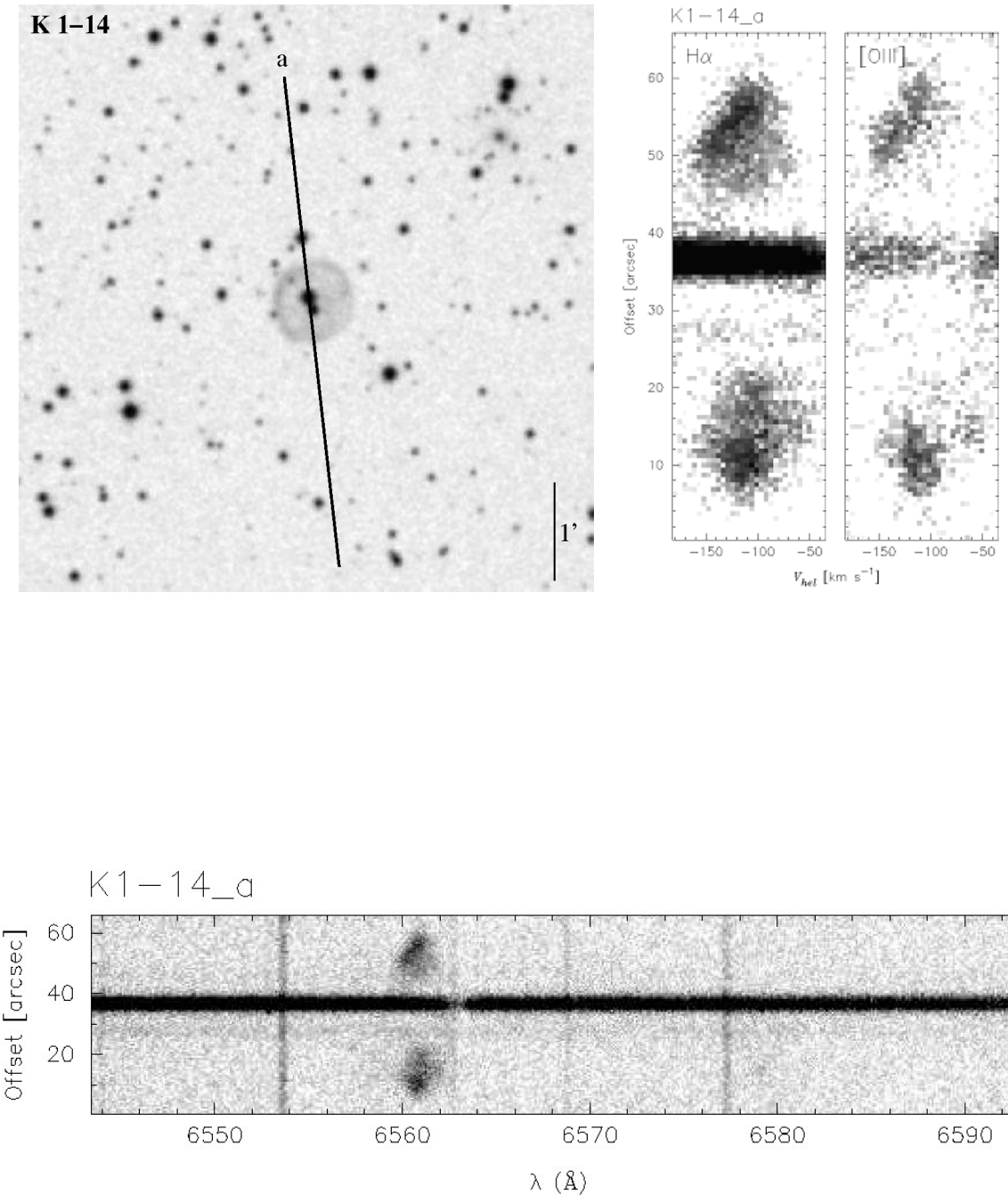

Figure A.58 **Same as Figure A.1.**

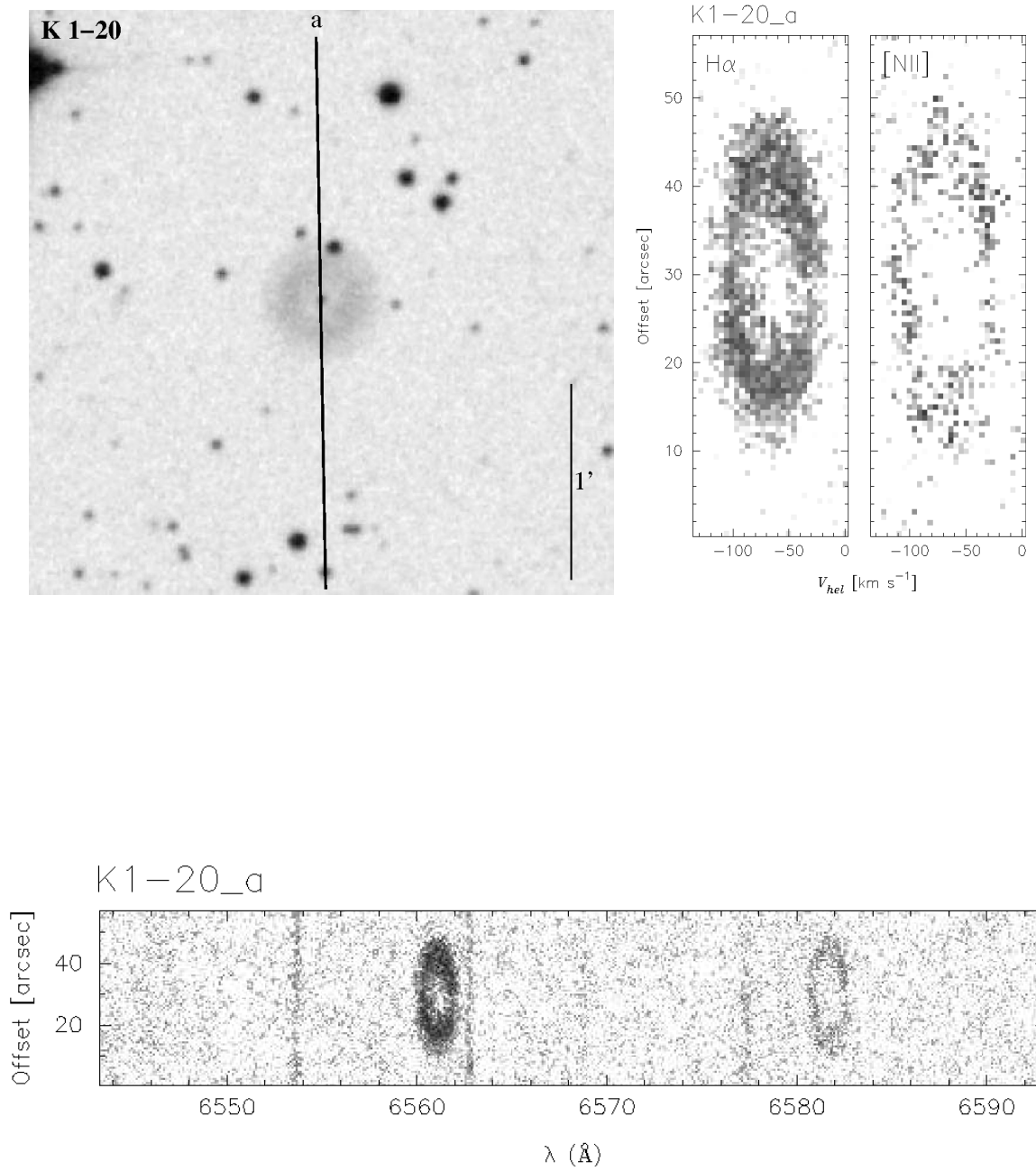

Figure A.59 **Same as Figure A.1.**

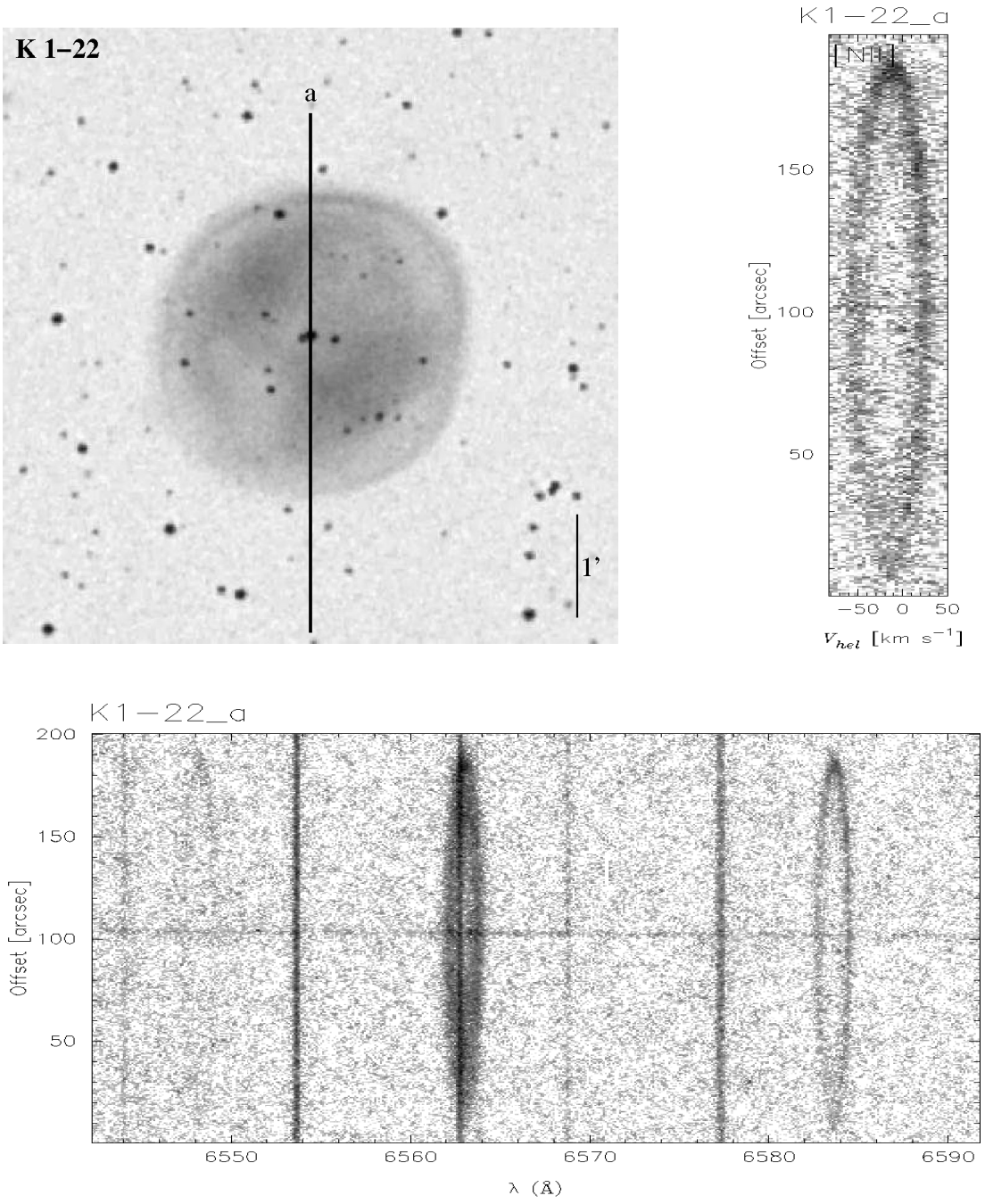

Figure A.60 **Same as Figure A.1.**

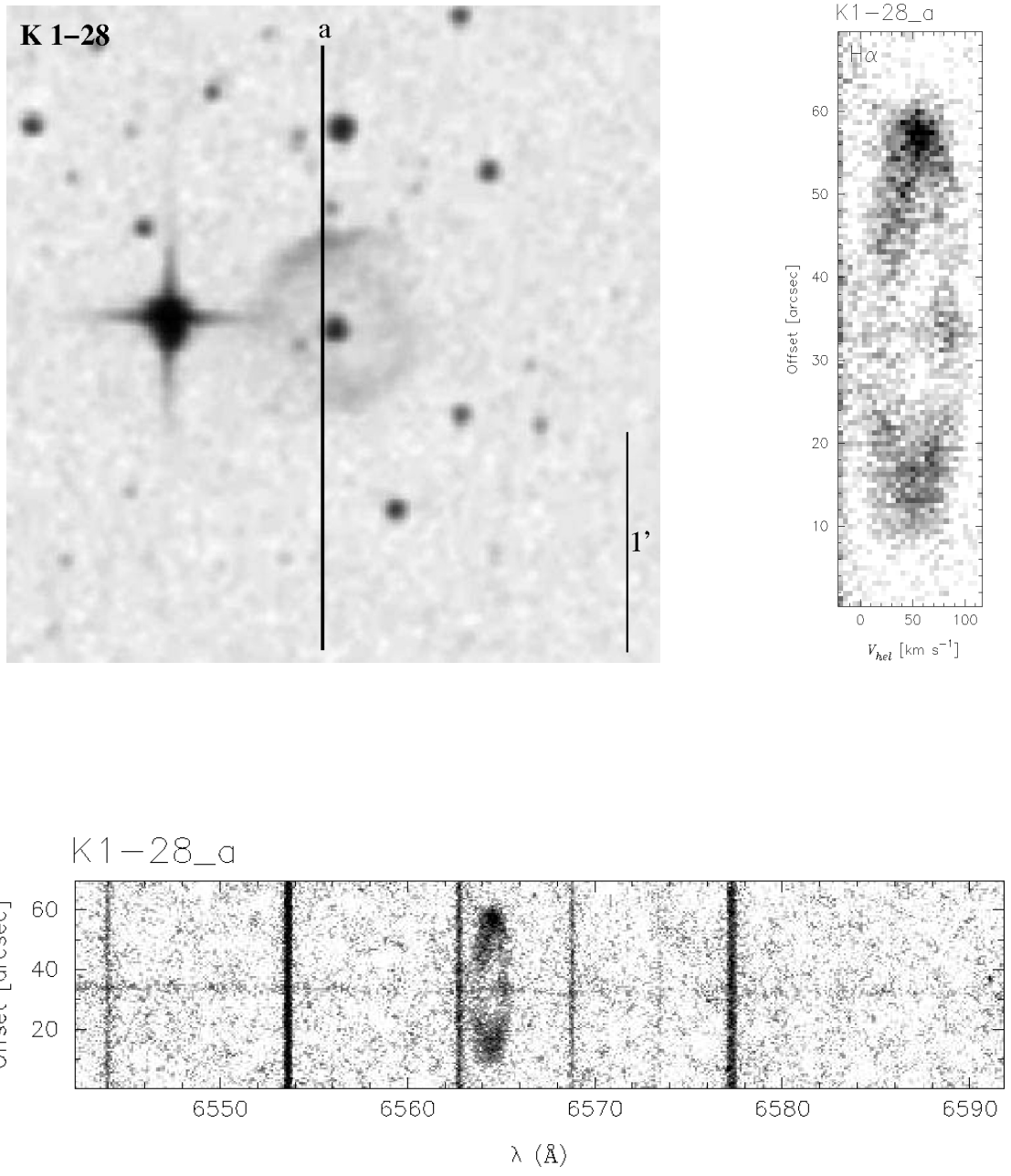

Figure A.61 **Same as Figure A.1.**

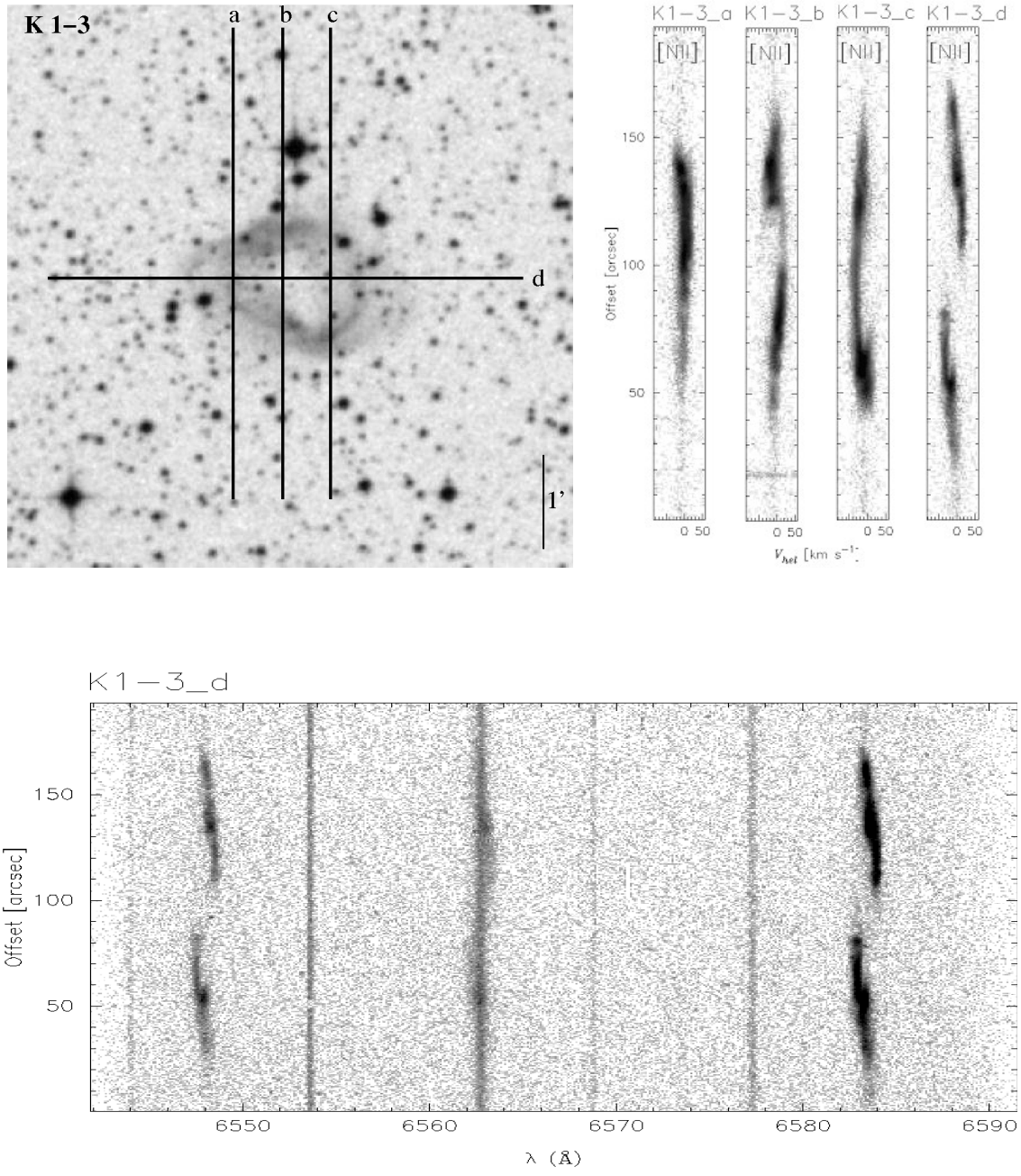

Figure A.62 **Same as Figure A.1.**

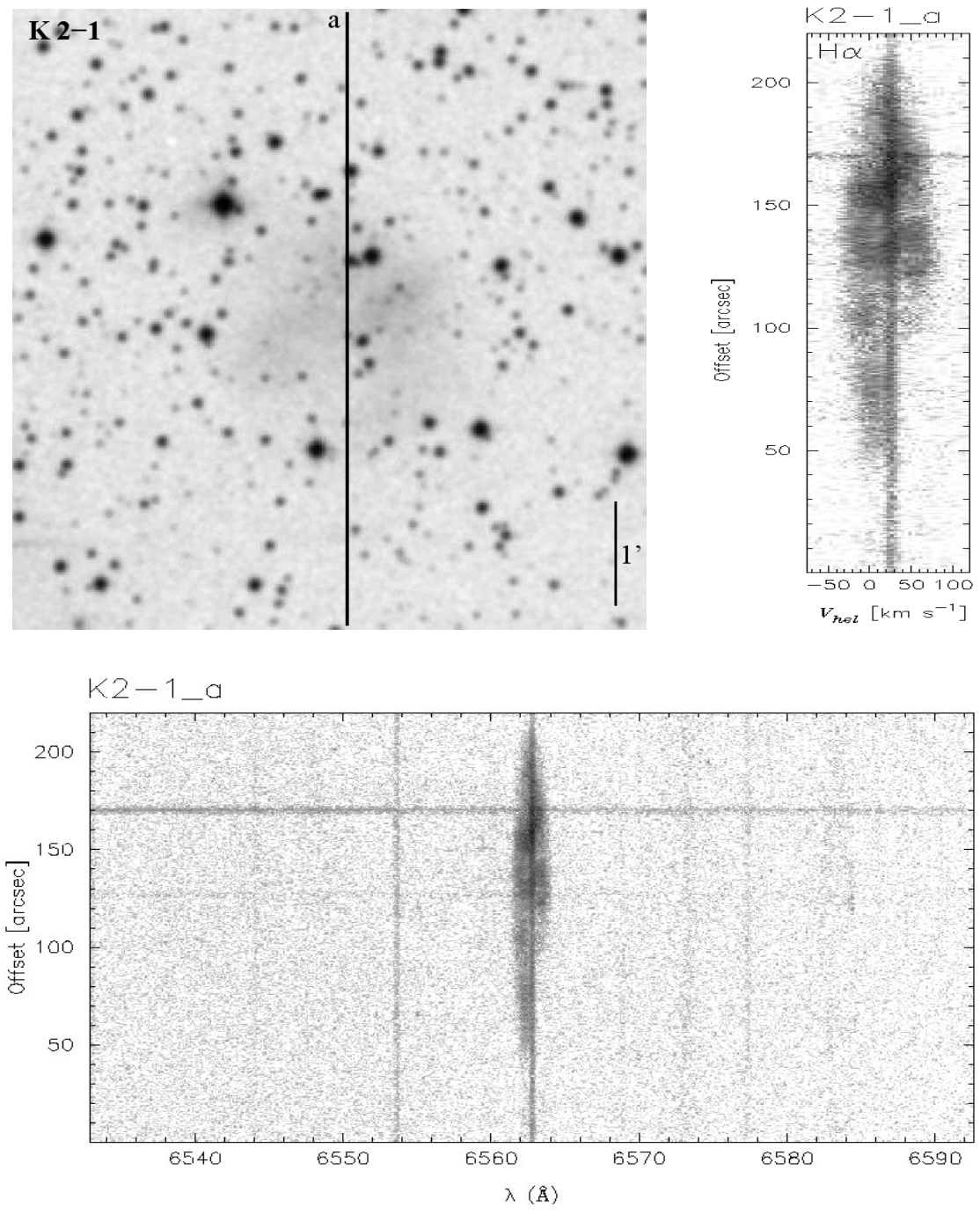

Figure A.63 **Same as Figure A.1.**

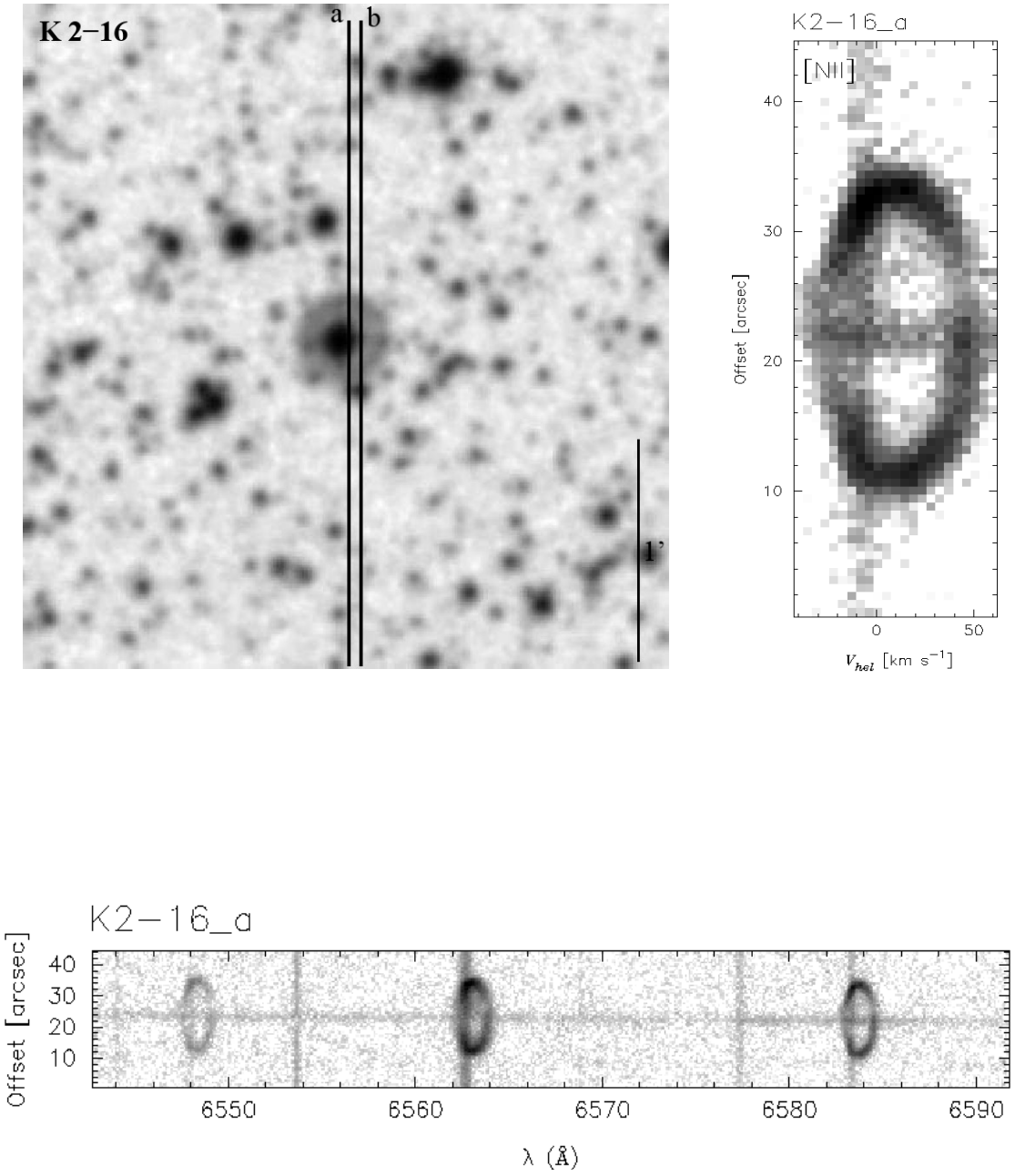

Figure A.64 **Same as Figure A.1.**

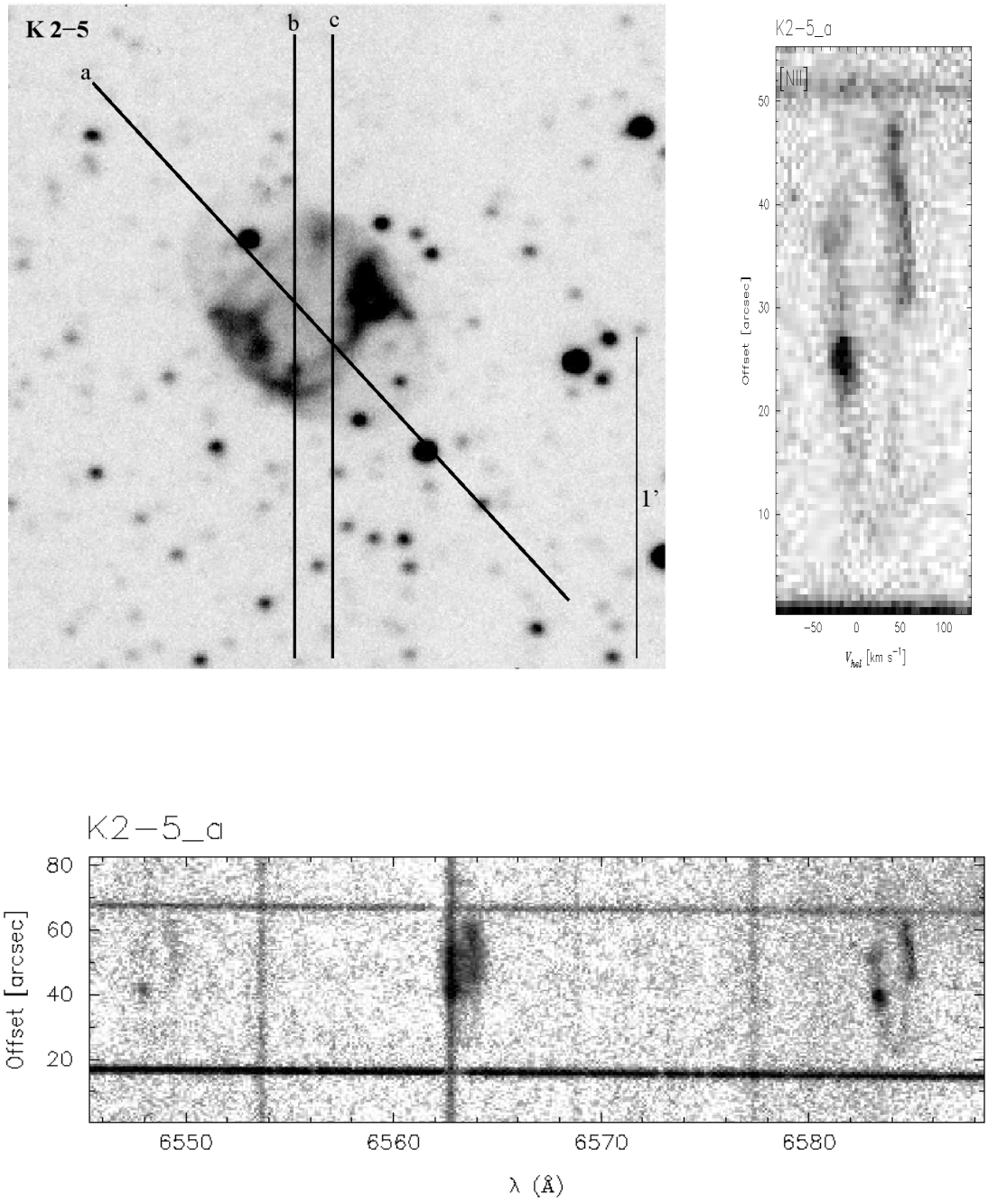

Figure A.65 **Same as Figure A.1.**

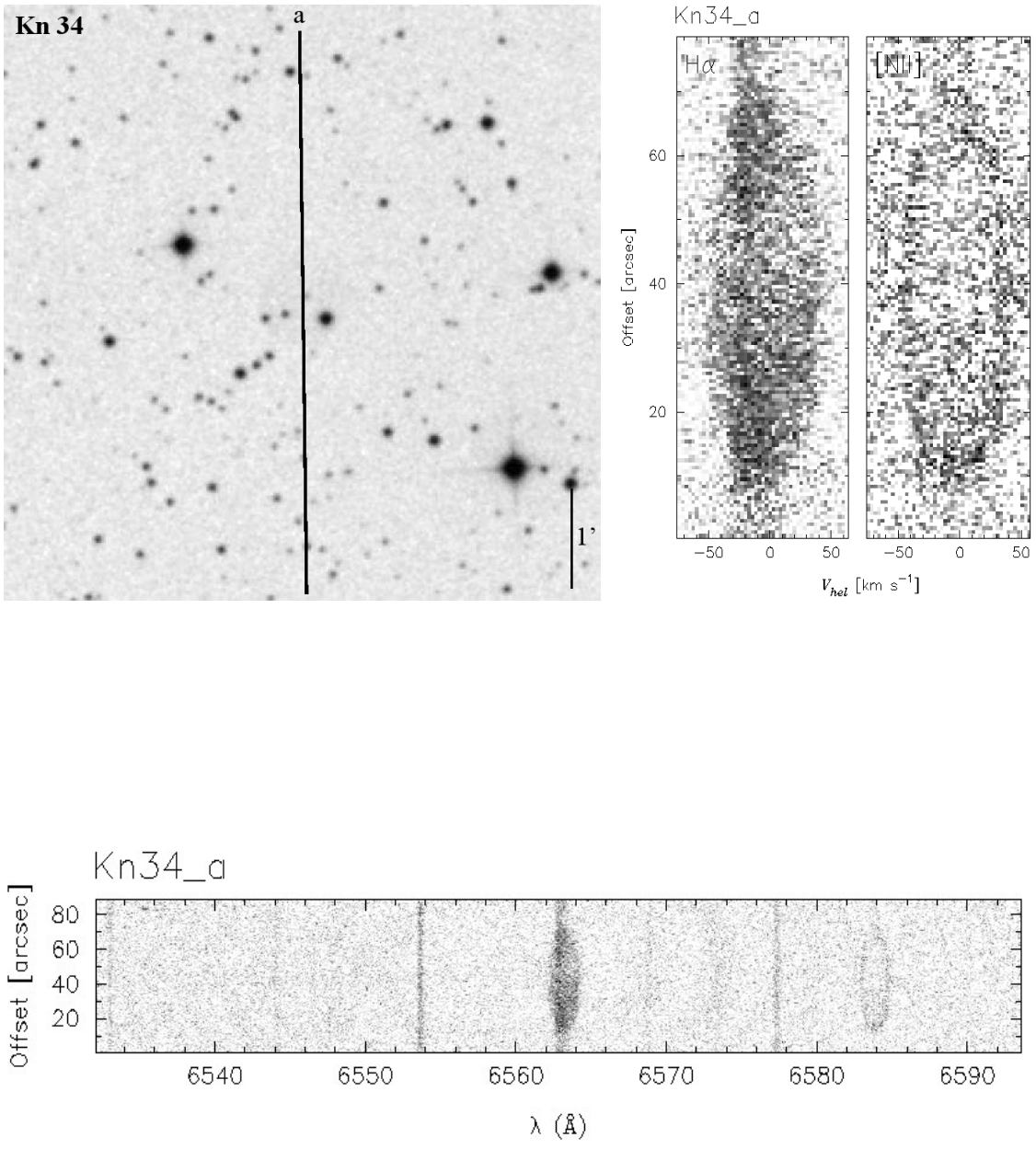

Figure A.66 **Same as Figure A.1.**

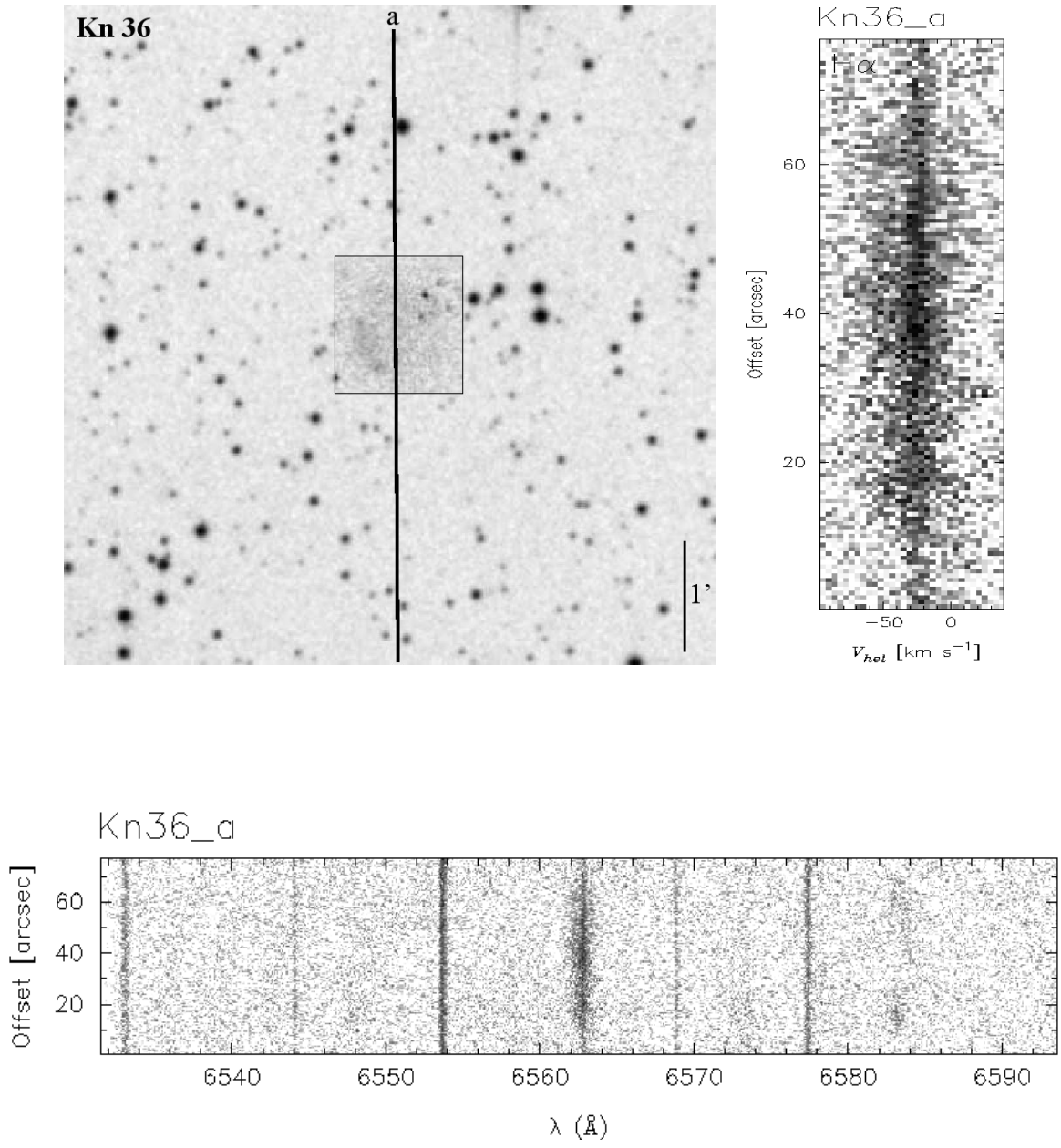

Figure A.67 **Same as Figure A.1.**

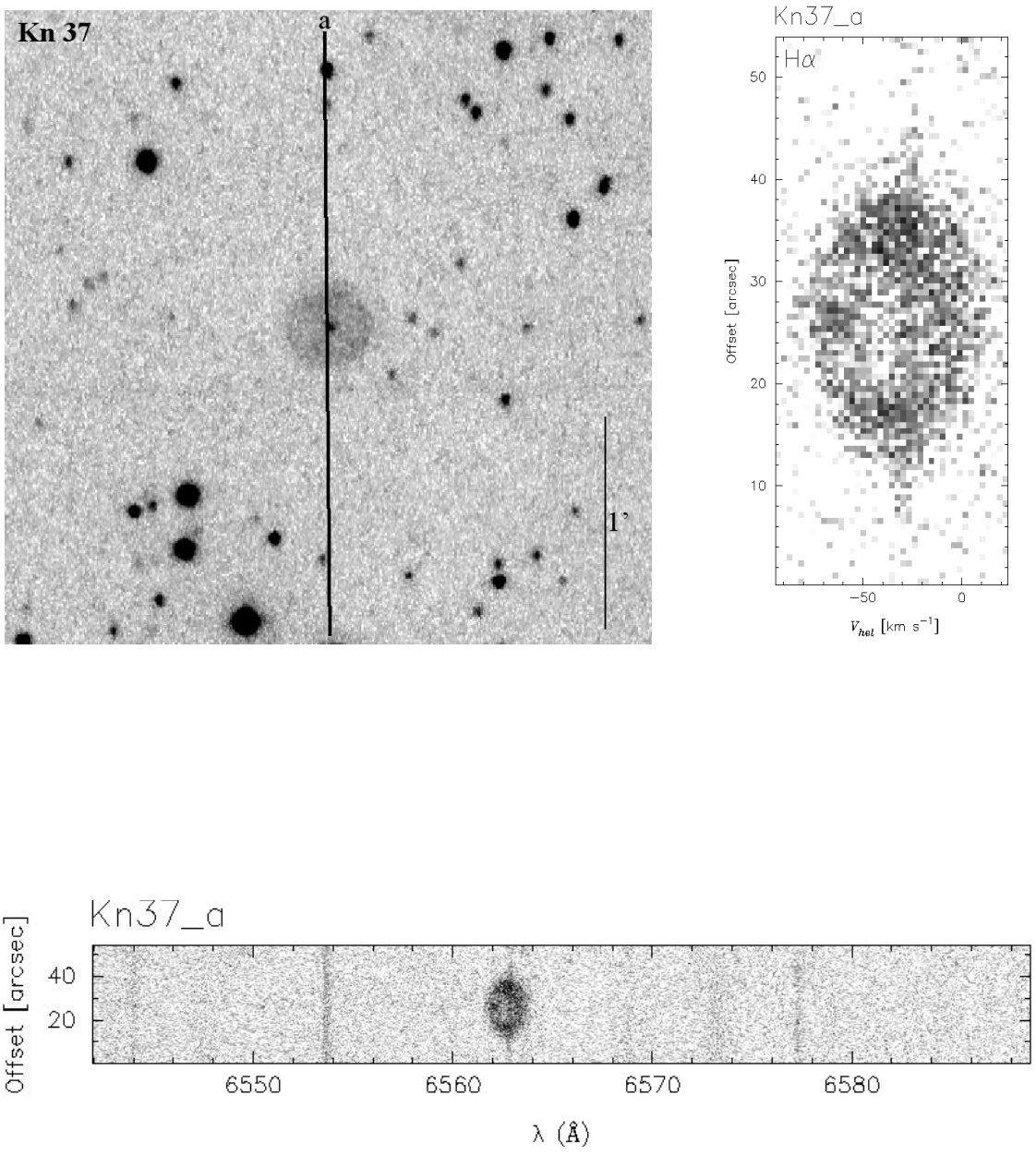

Figure A.68 **Same as Figure A.1.**

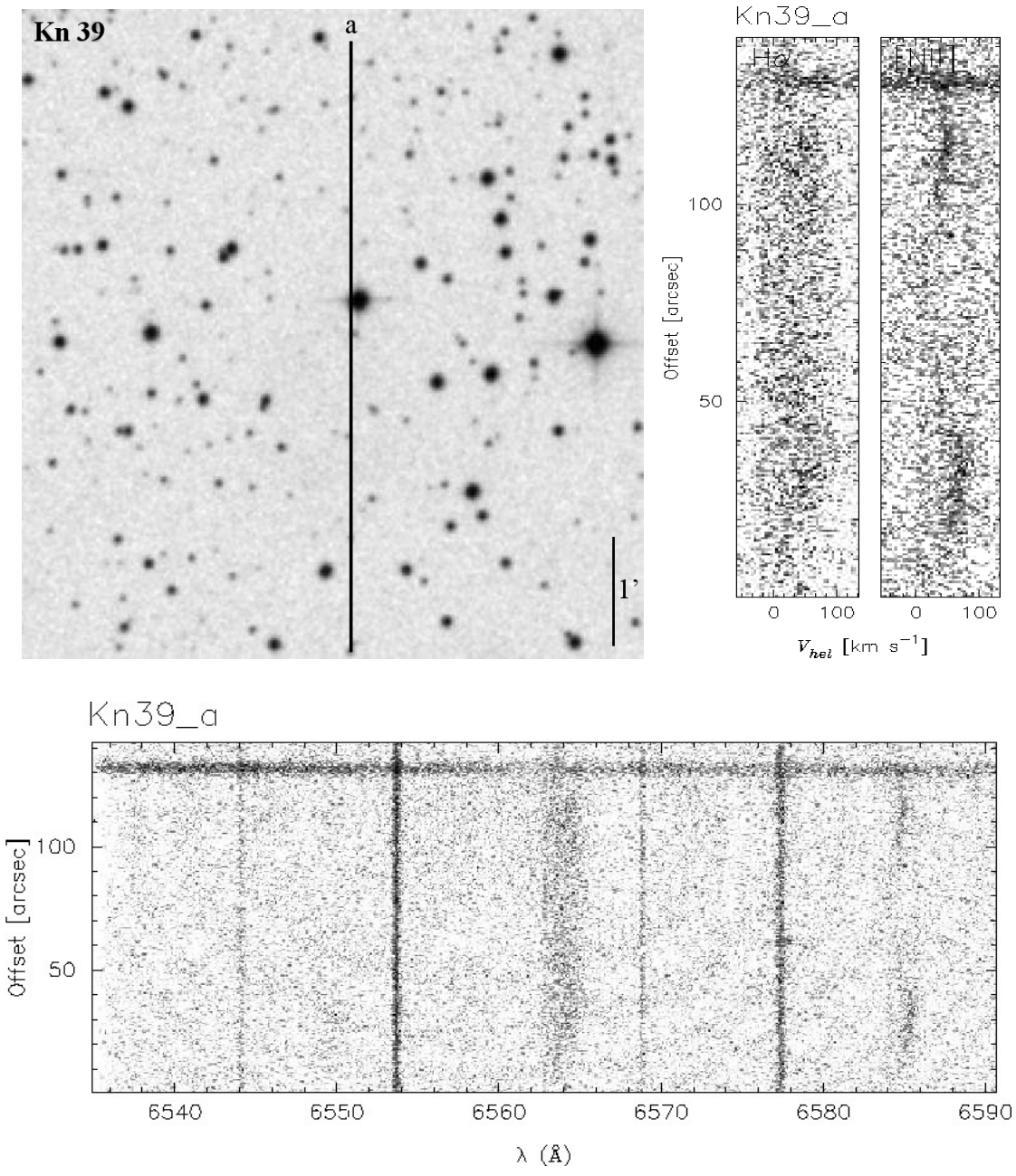

Figure A.69 **Same as Figure A.1.**

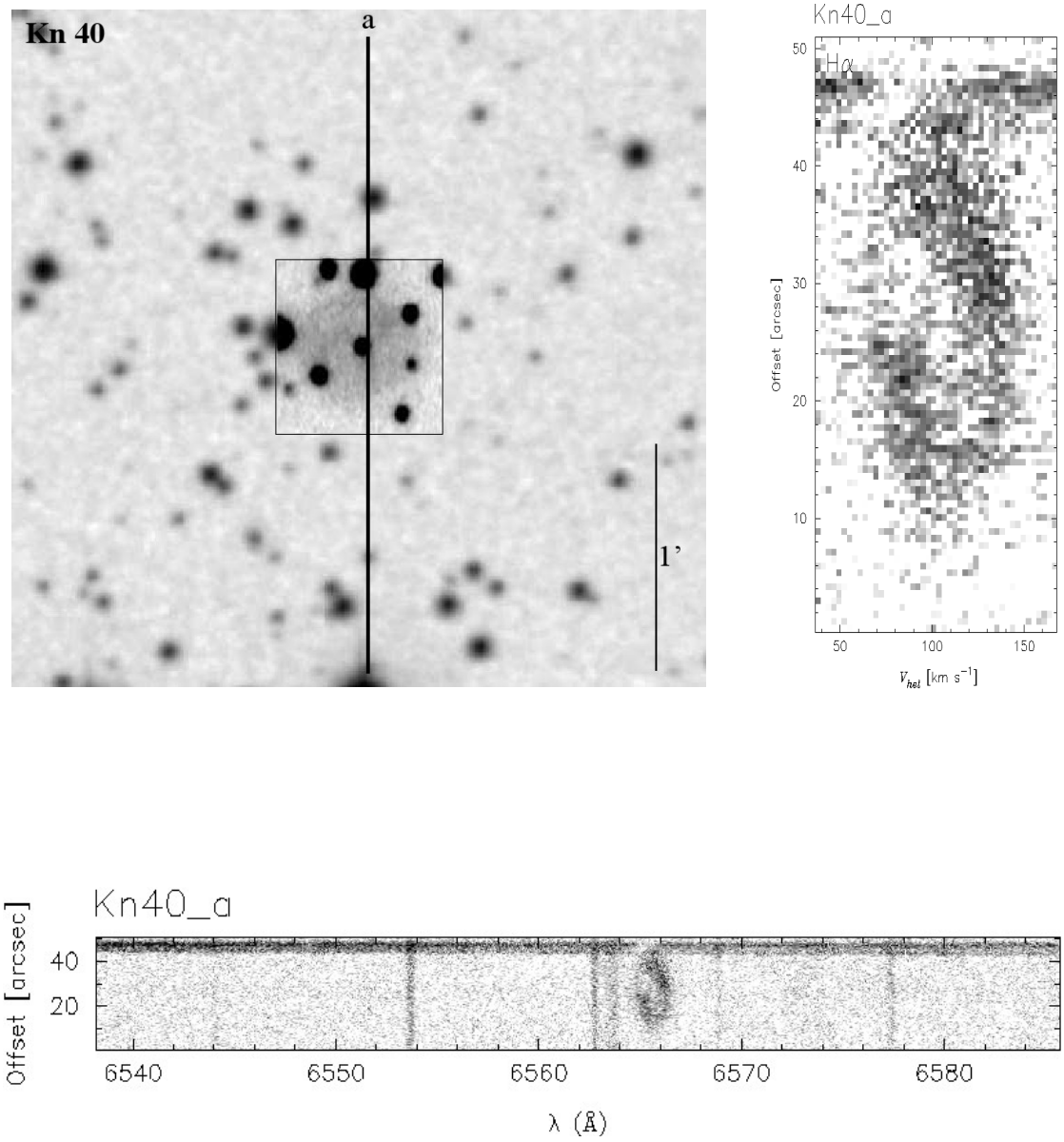

Figure A.70 **Same as Figure A.1.**

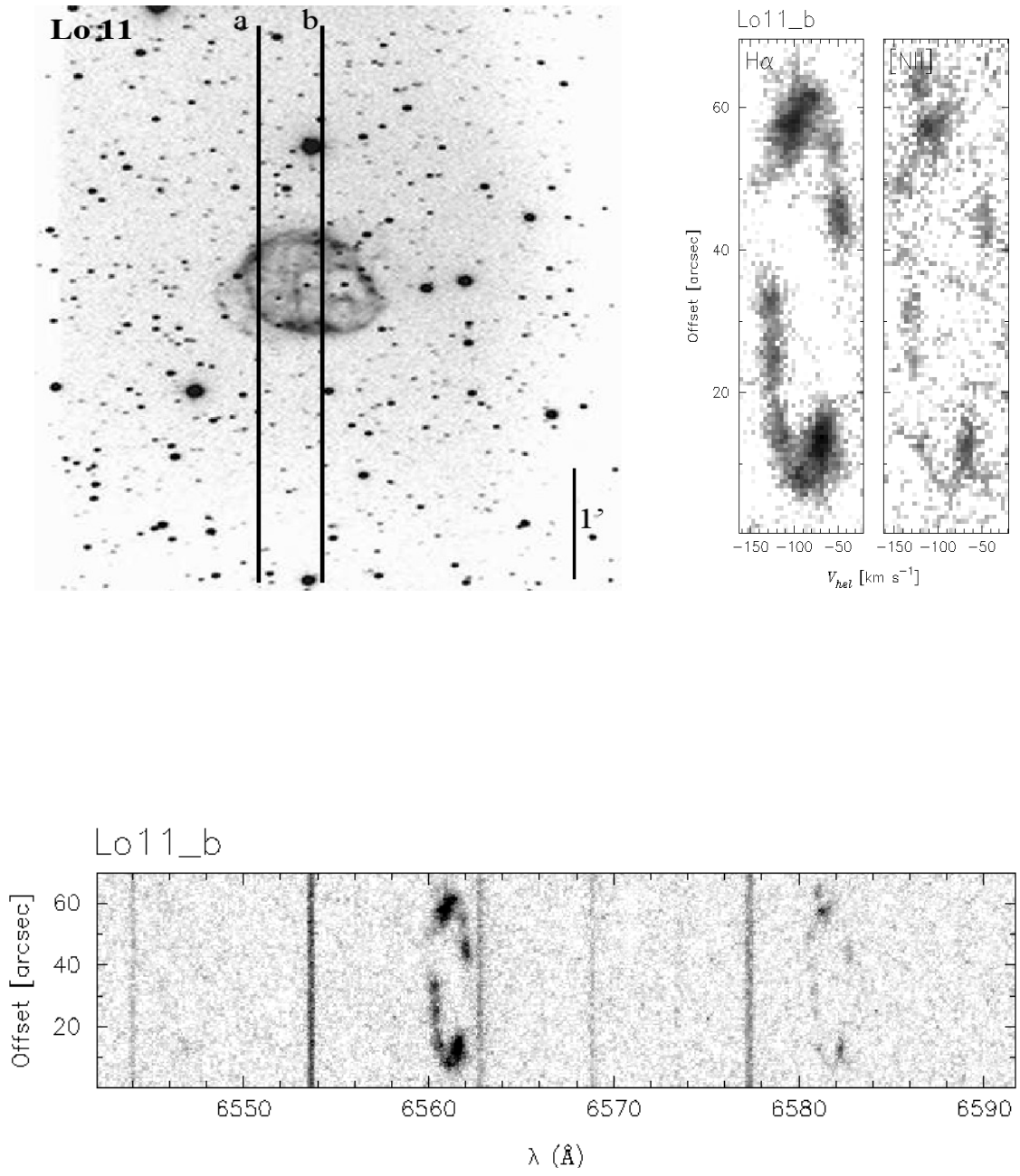

Figure A.71 **Same as Figure A.1.**

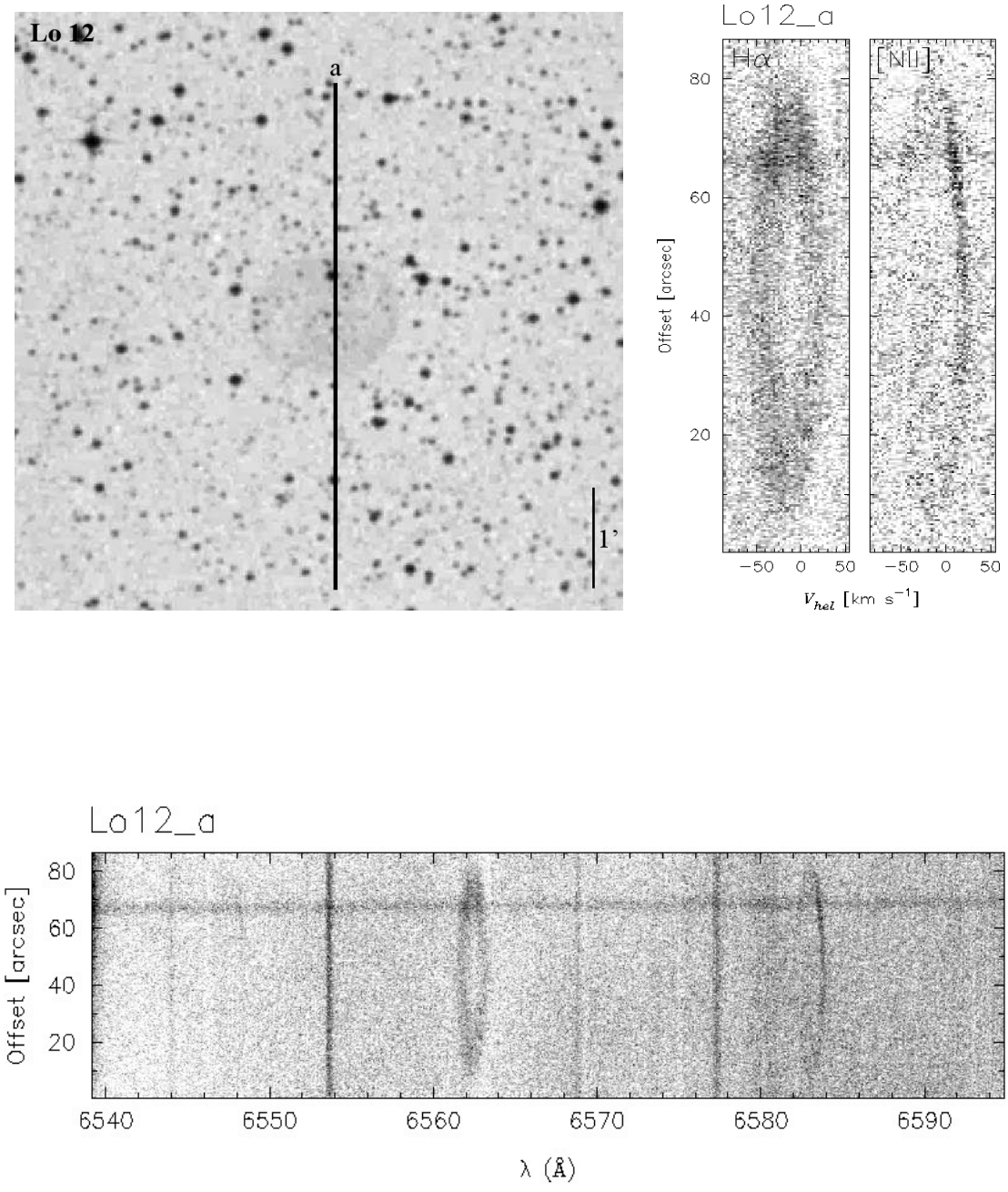

Figure A.72 **Same as Figure A.1.**

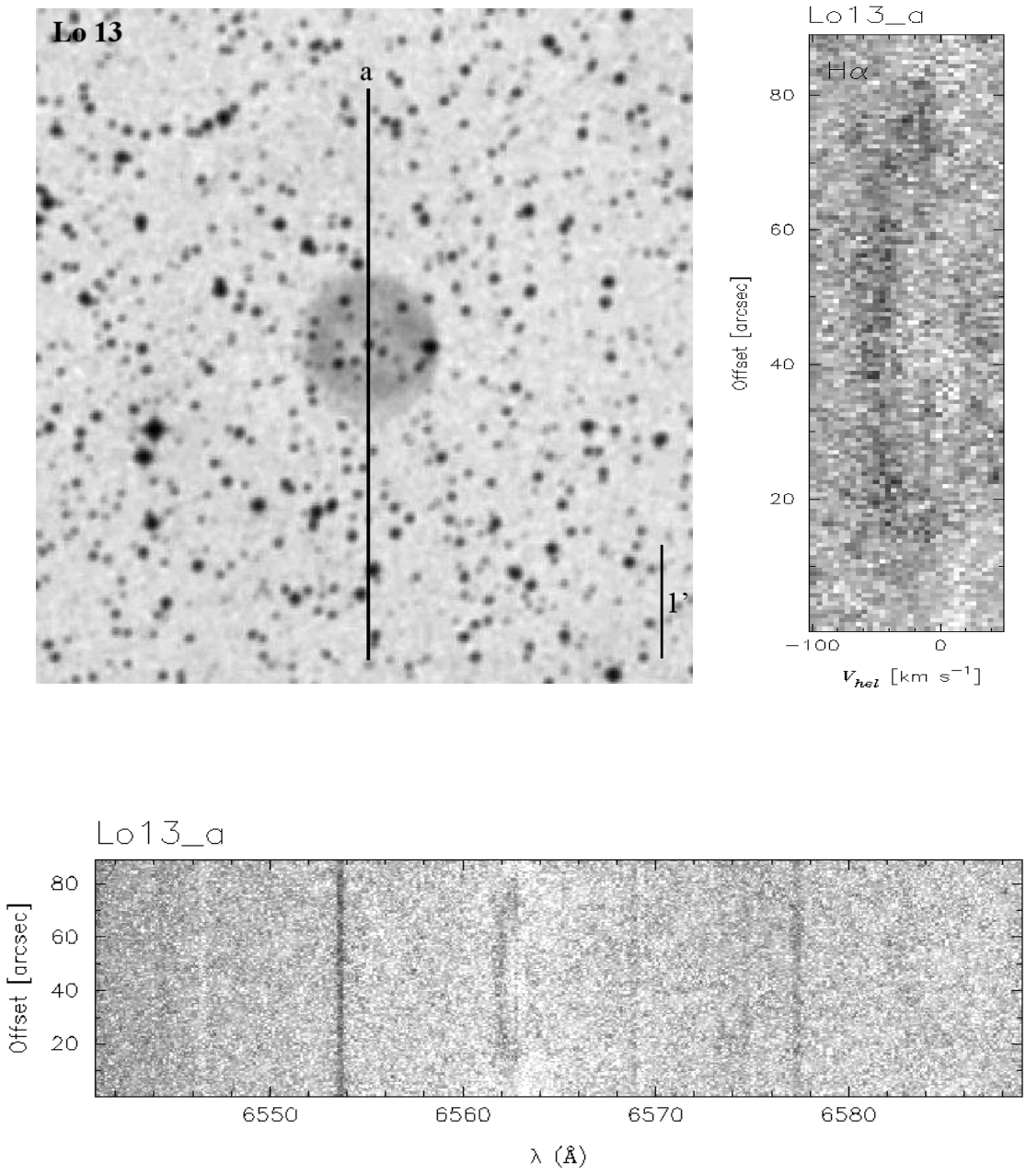

Figure A.73 **Same as Figure A.1.**

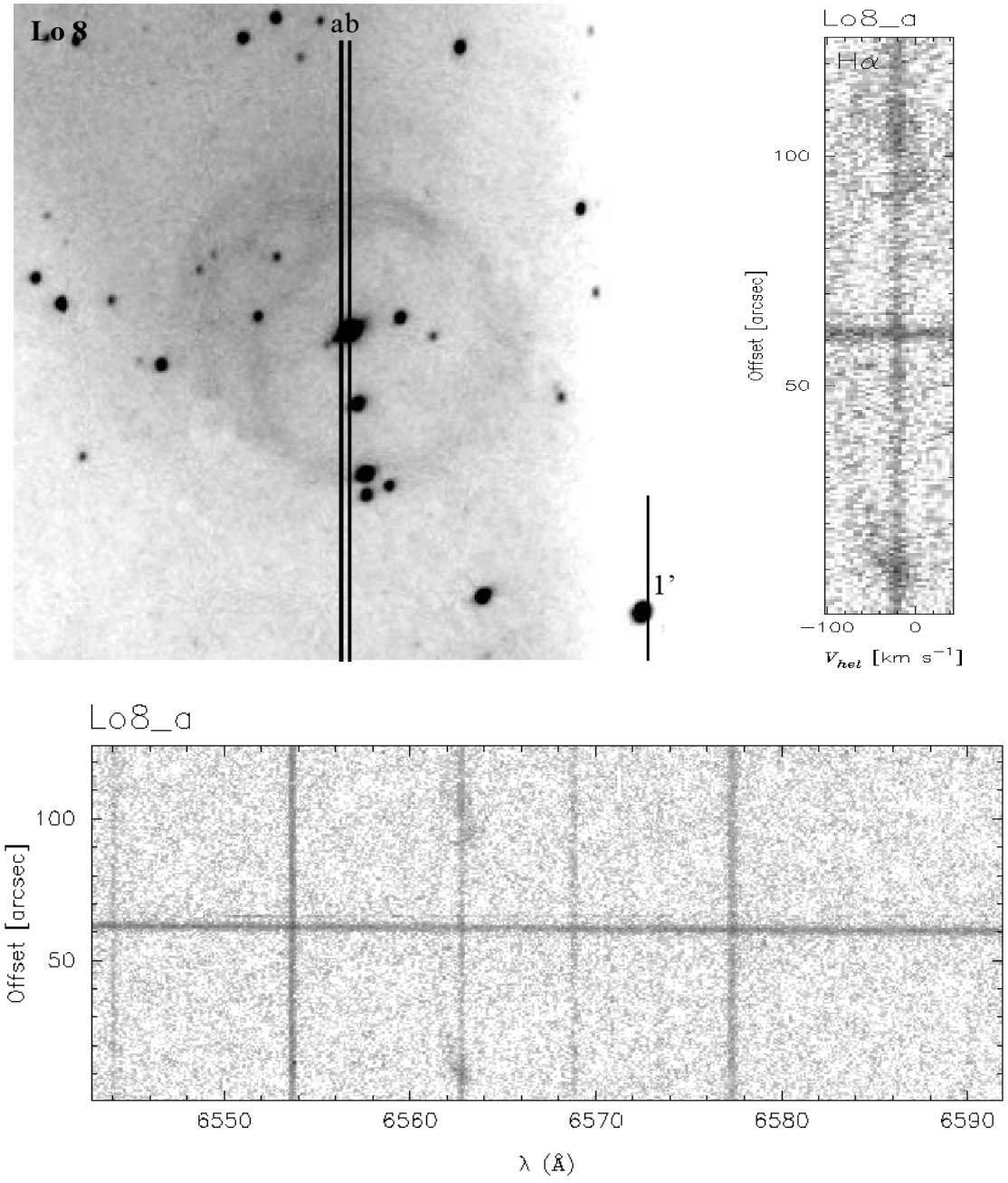

Figure A.74 **Same as Figure A.1.**

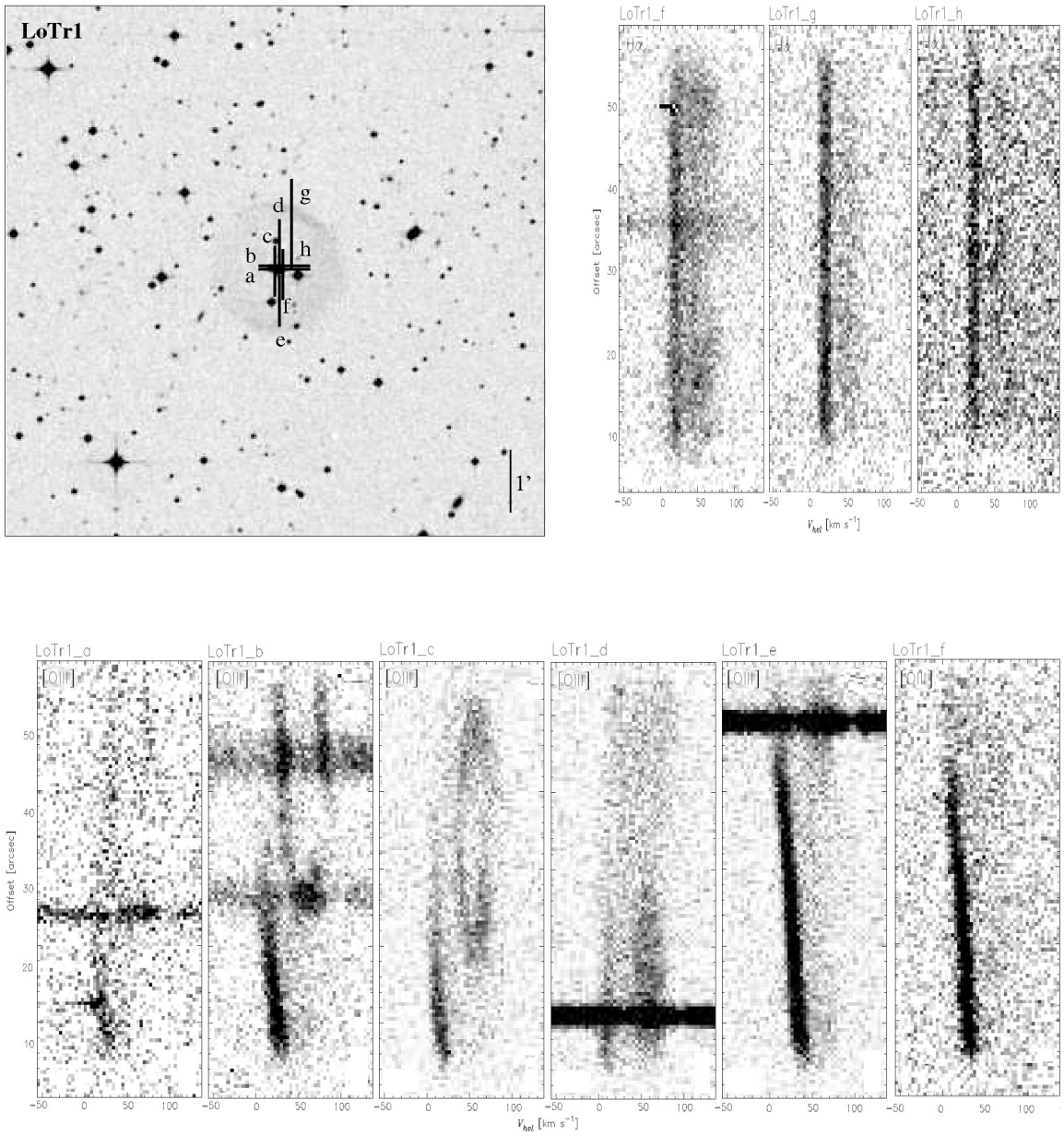

Figure A.75 **Same as Figure A.1.**

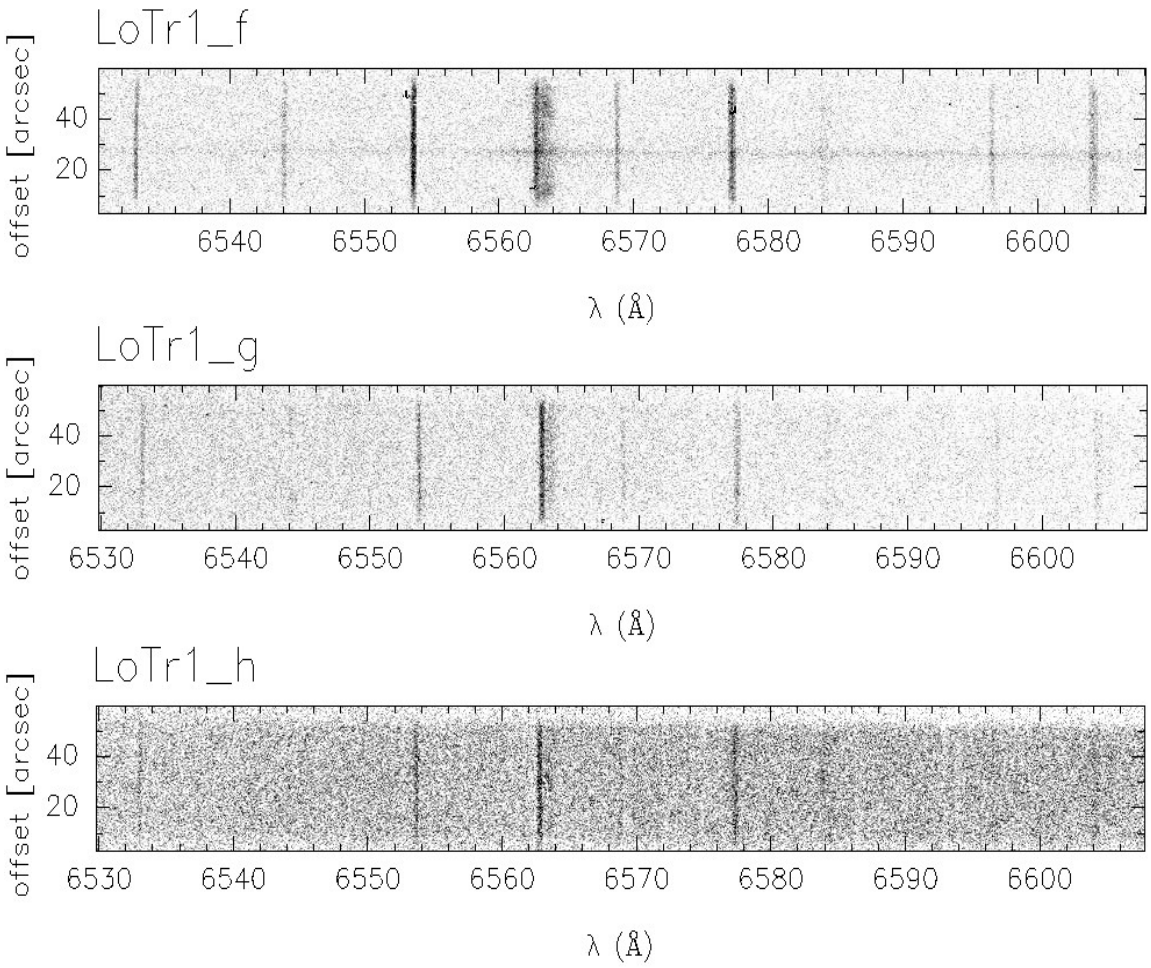

Figure A.76 **Same as Figure A.1.**

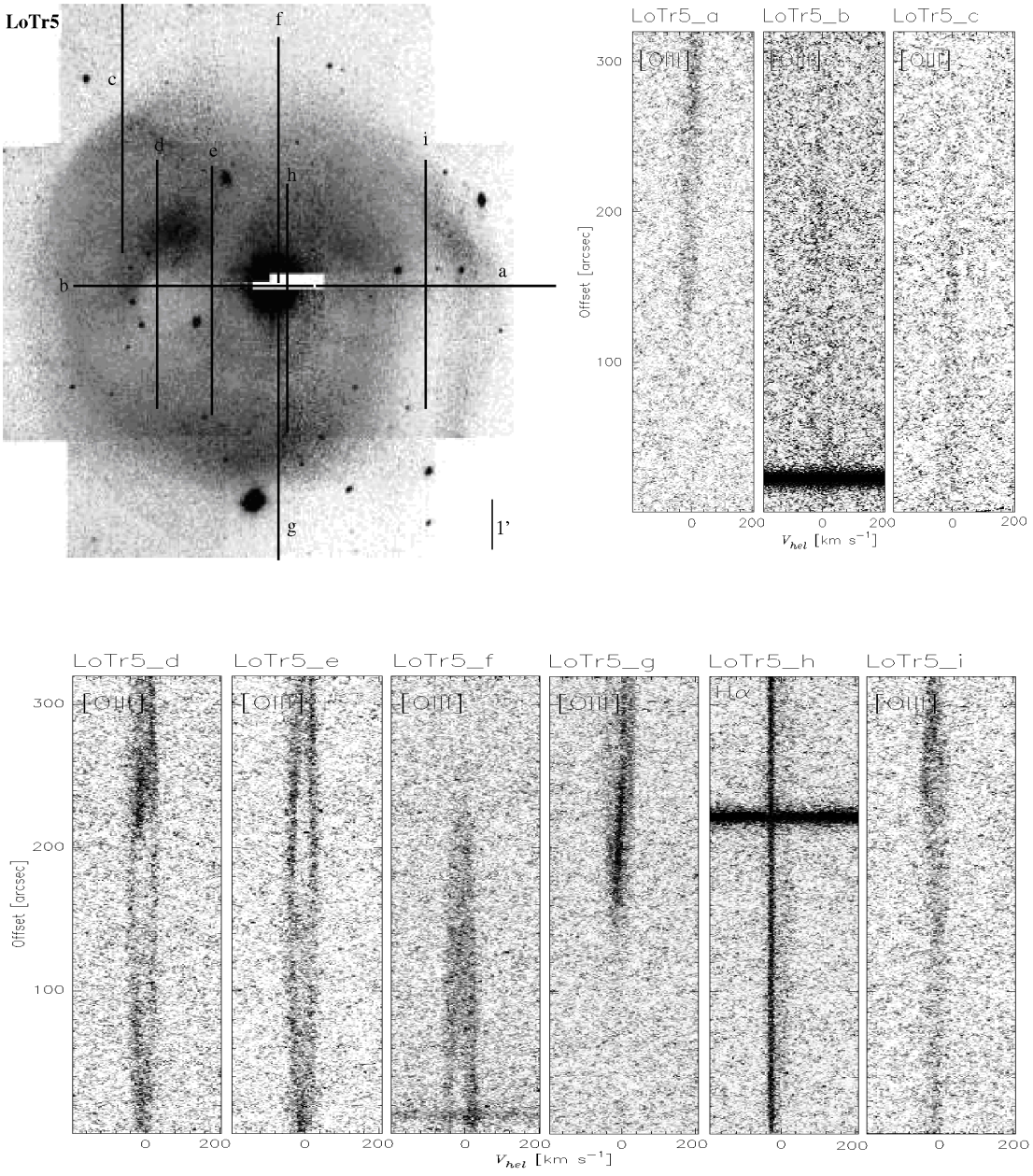

Figure A.77 **Same as Figure A.1.**

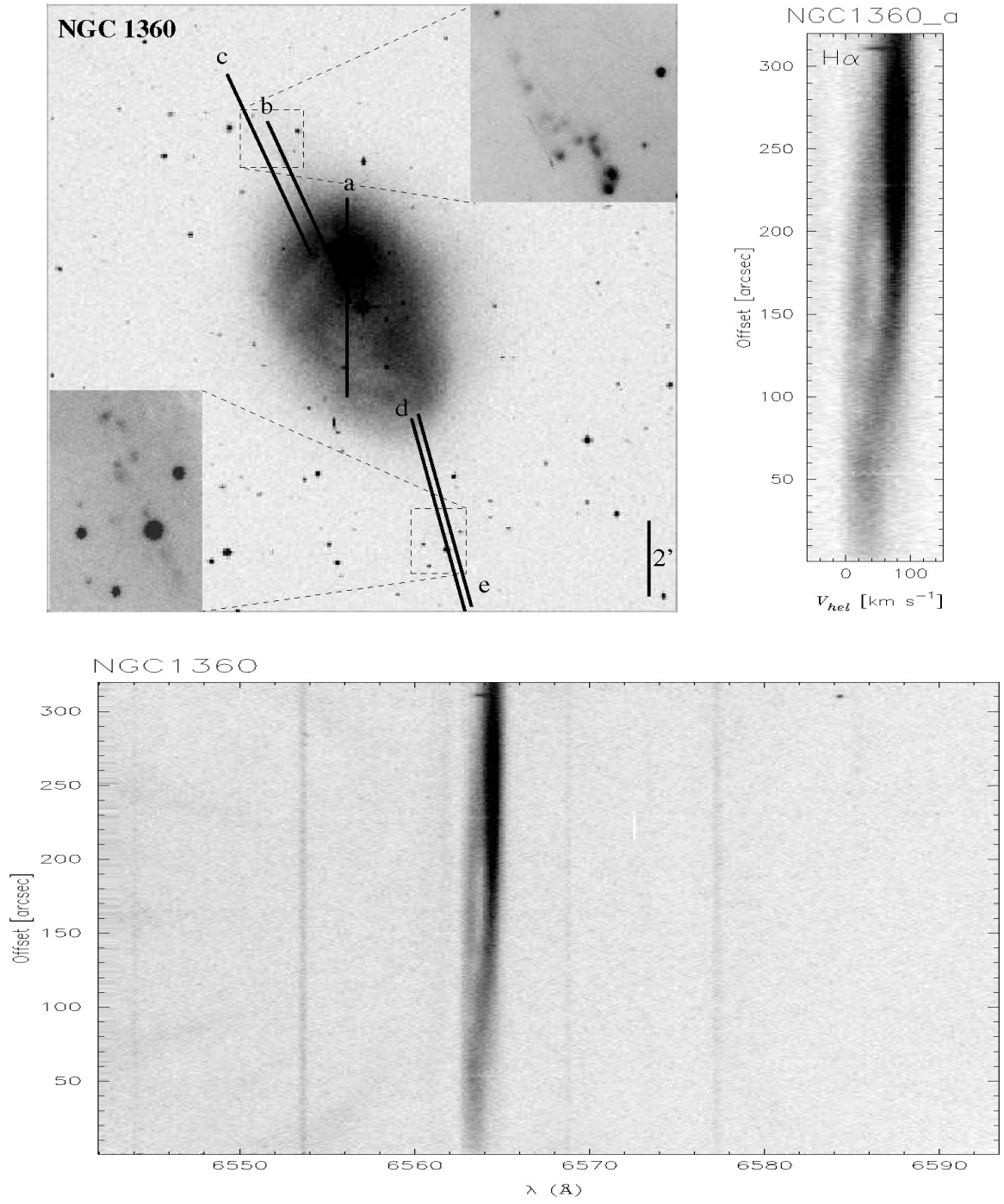

Figure A.78 **Same as Figure A.1.**

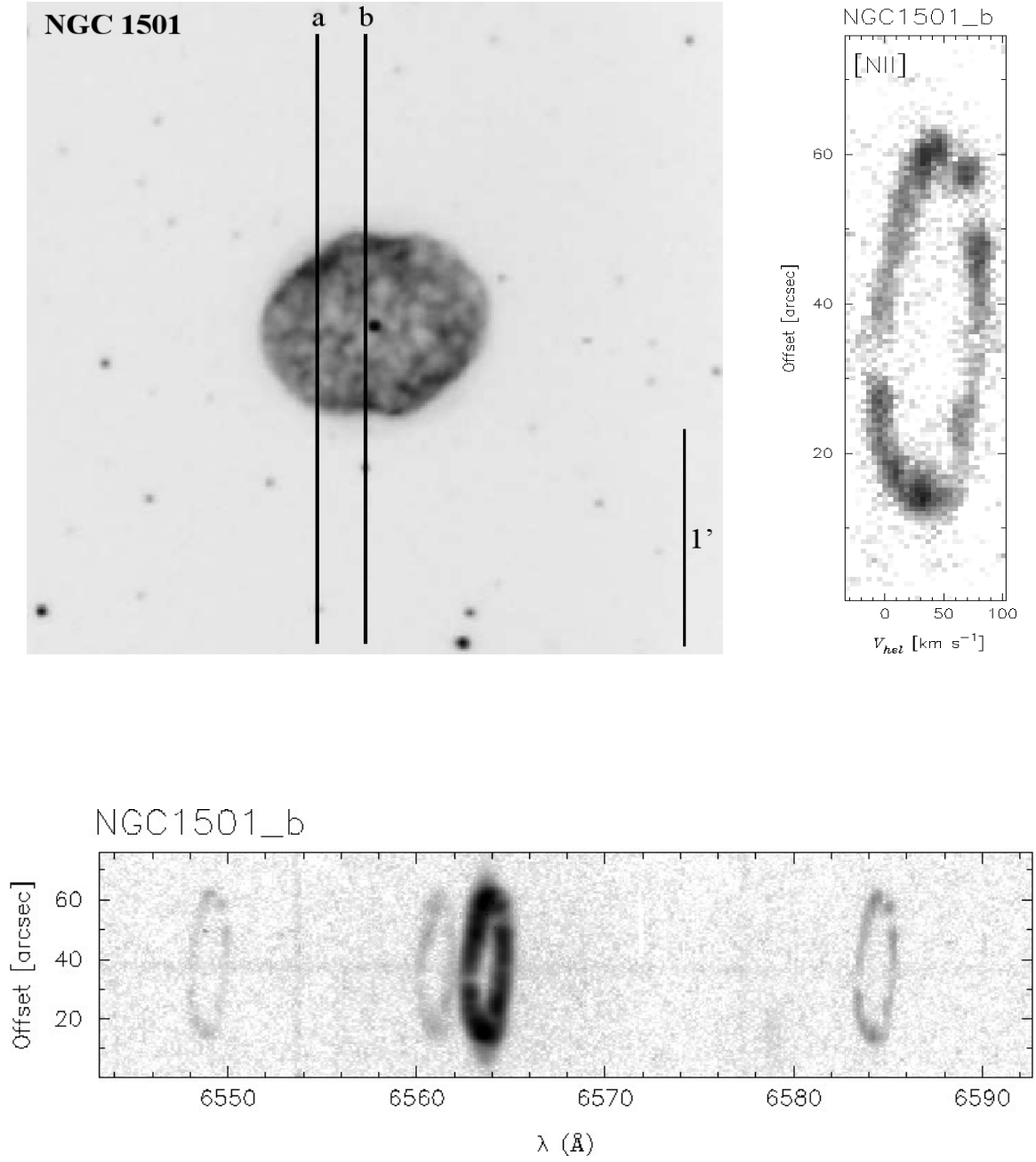

Figure A.79 **Same as Figure A.1.**

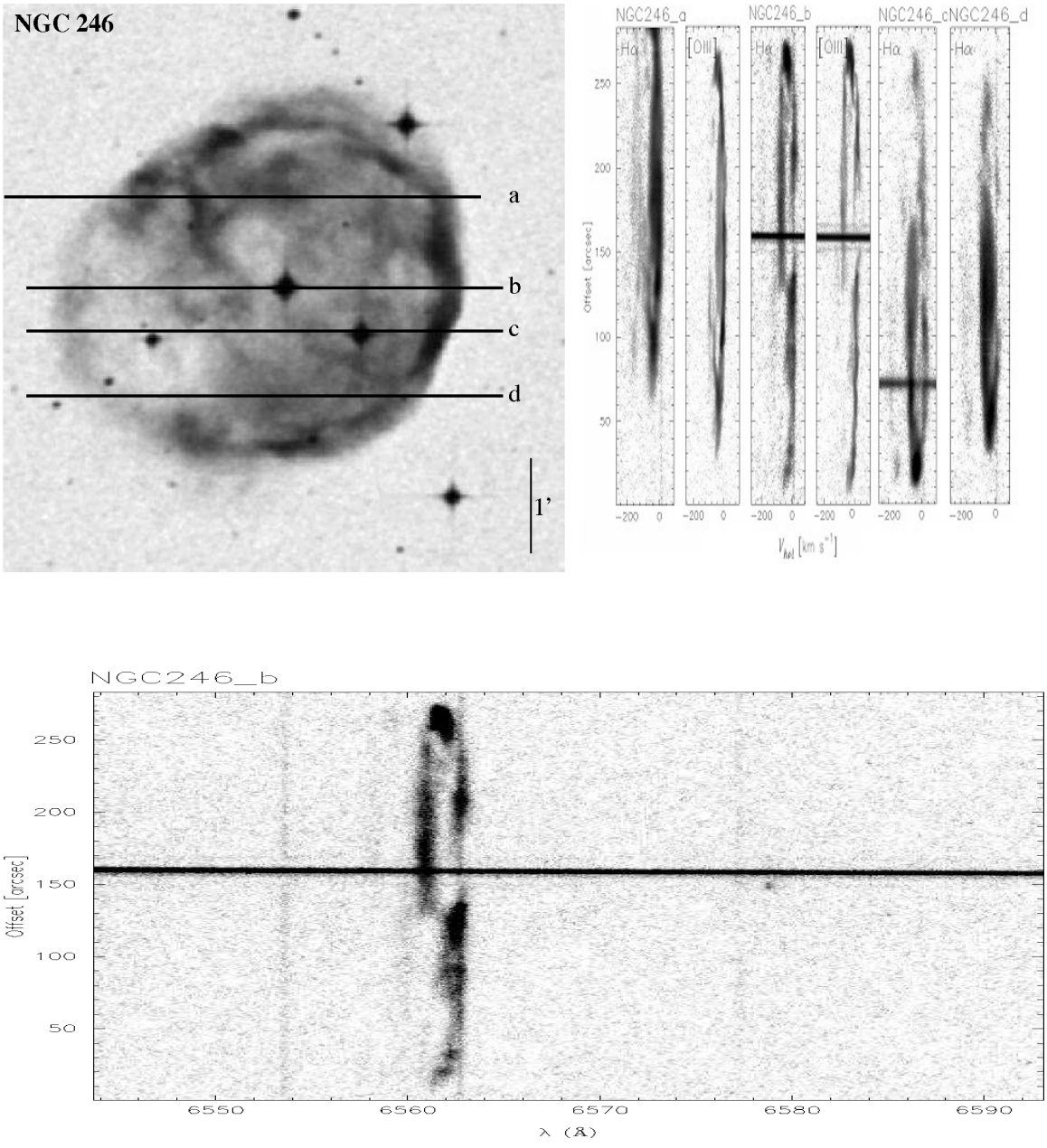

Figure A.80 **Same as Figure A.1.**

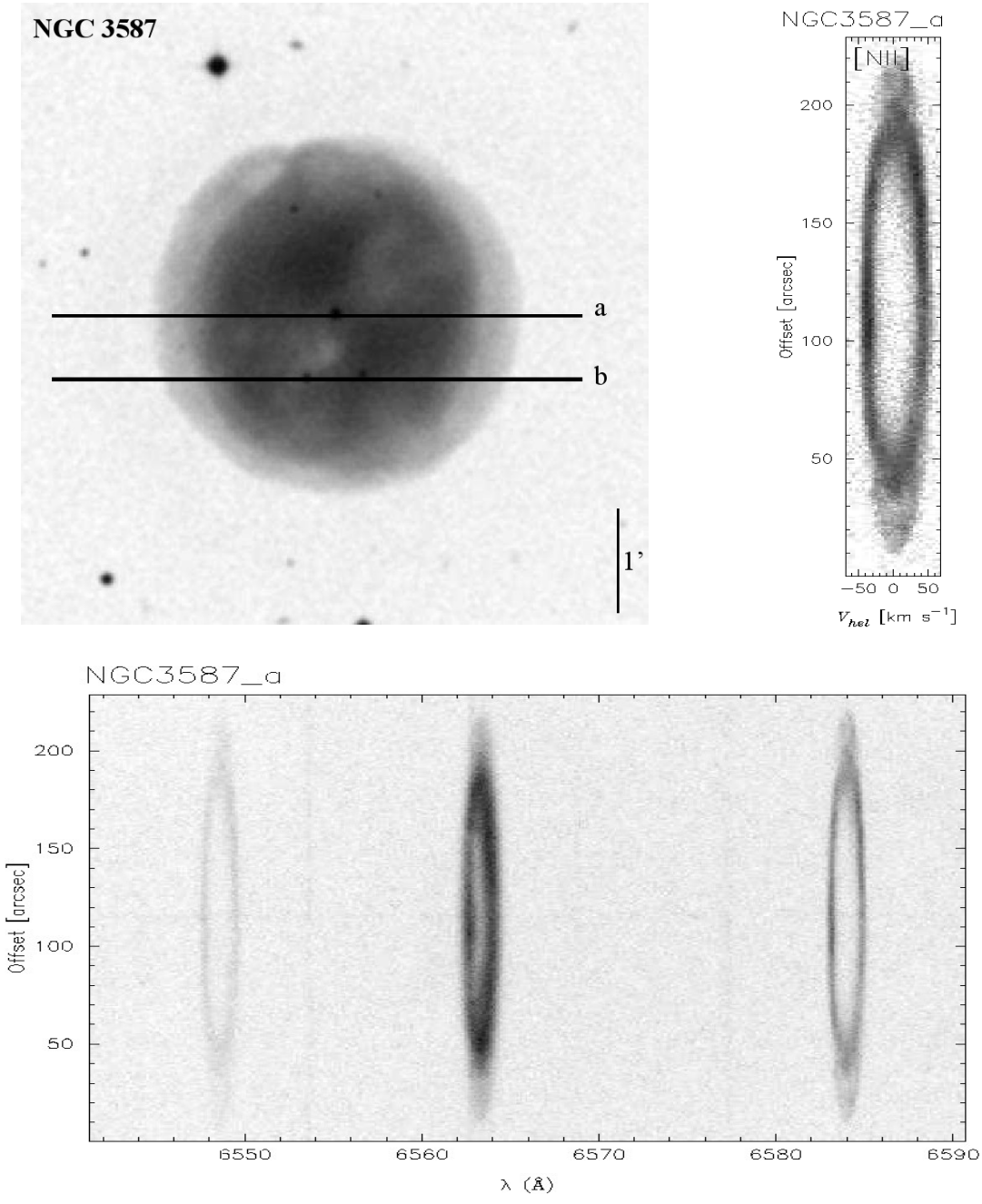

Figure A.81 **Same as Figure A.1.**

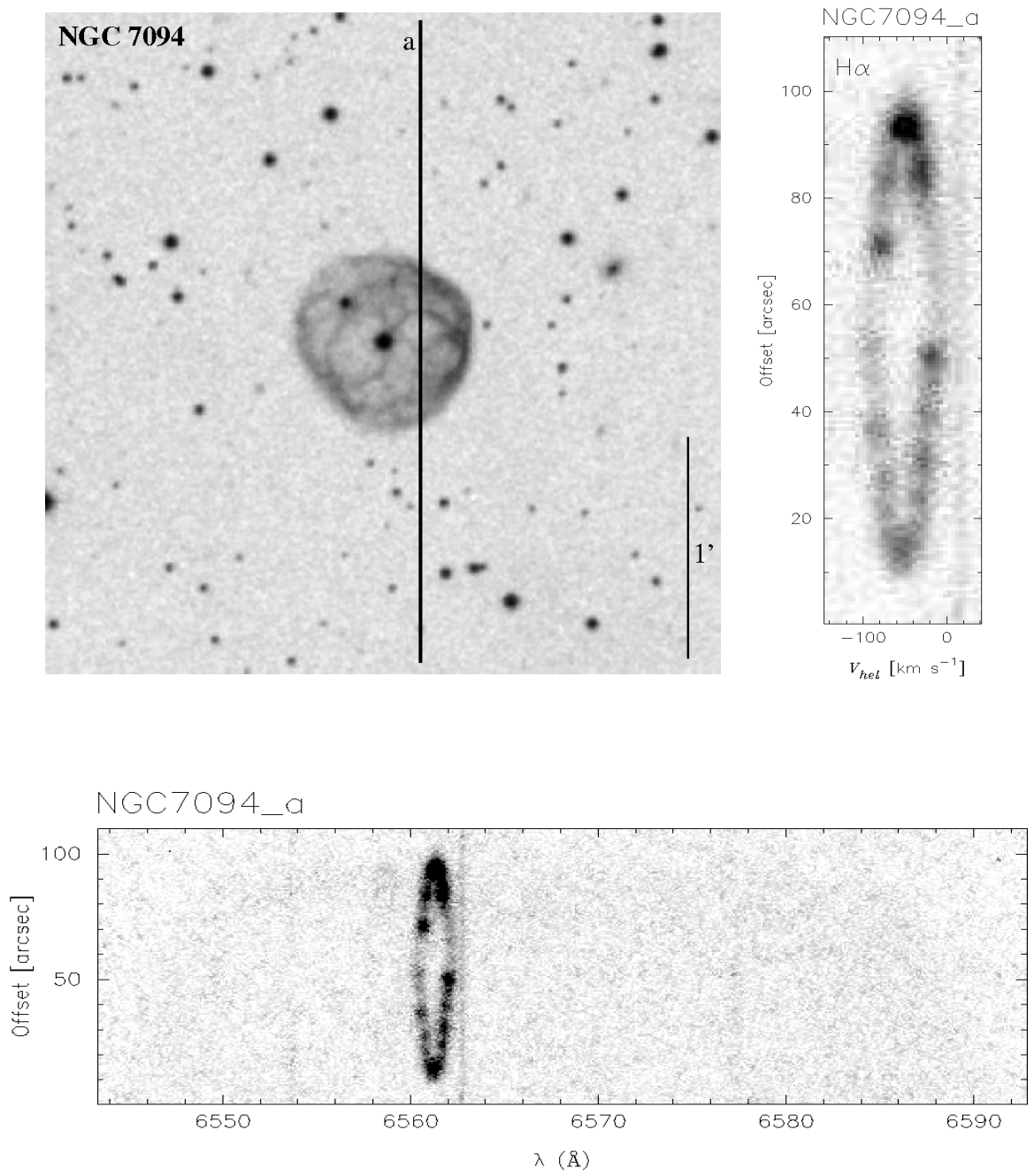

Figure A.82 **Same as Figure A.1.**

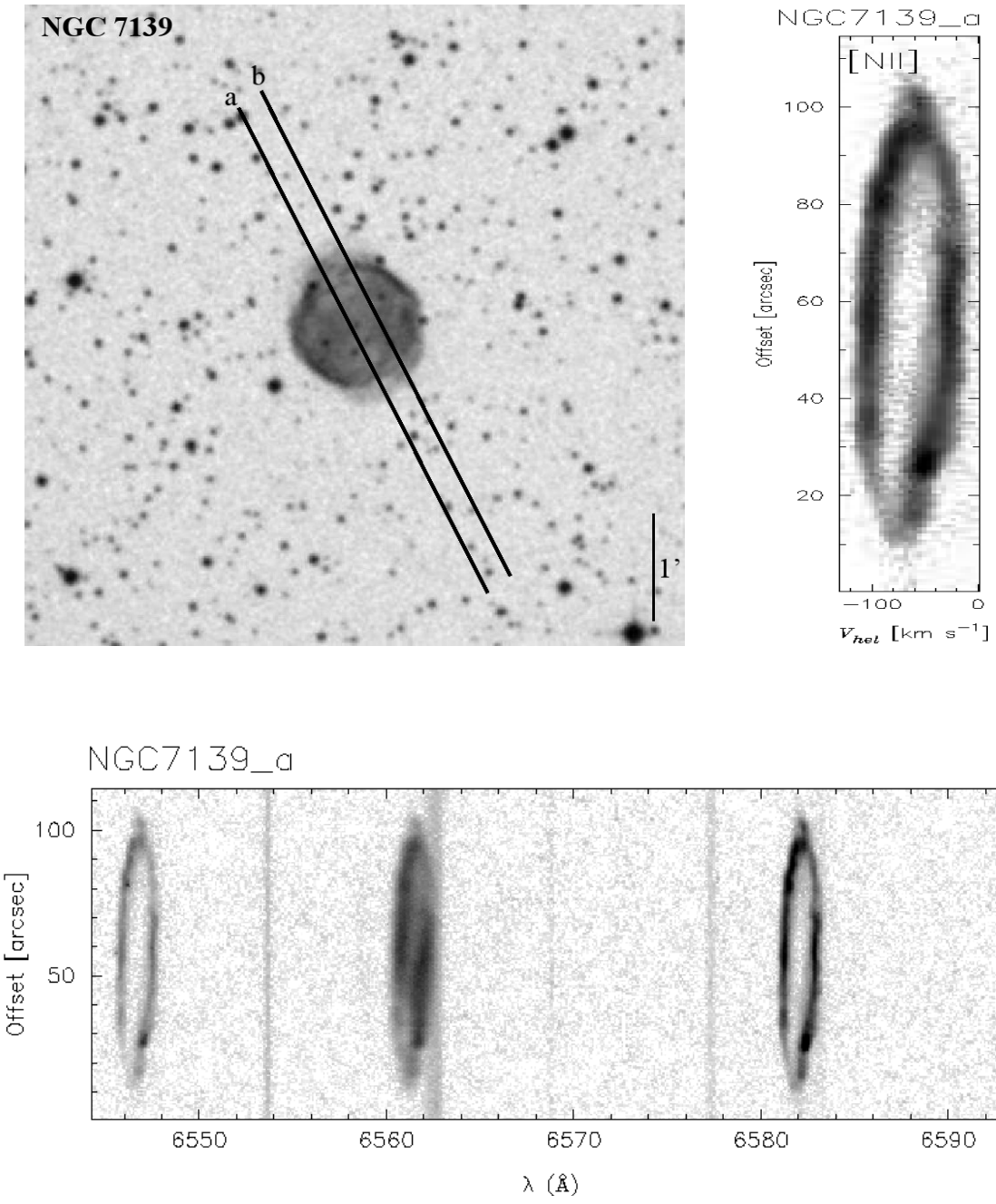

Figure A.83 **Same as Figure A.1.**

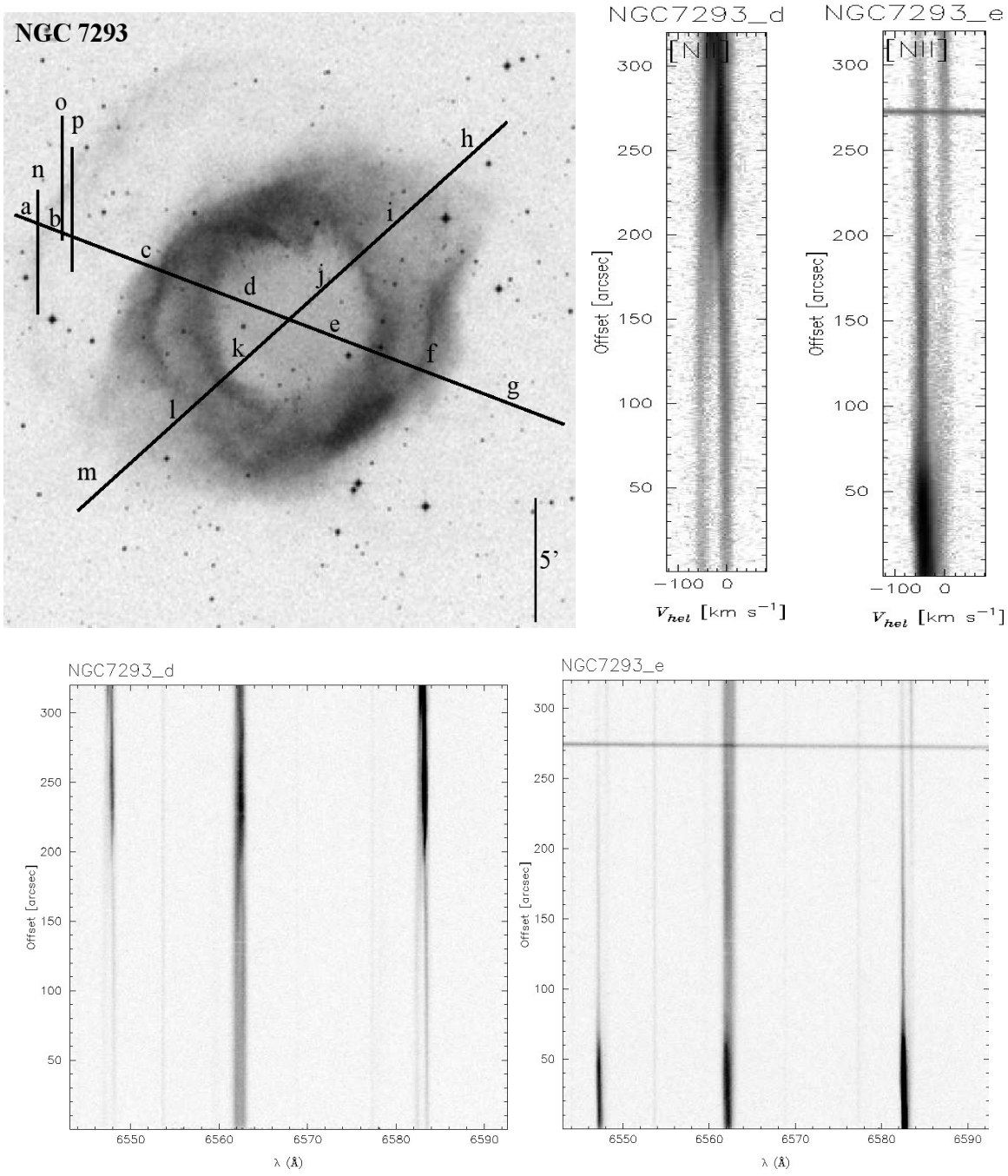

Figure A.84 **Same as Figure A.1.**

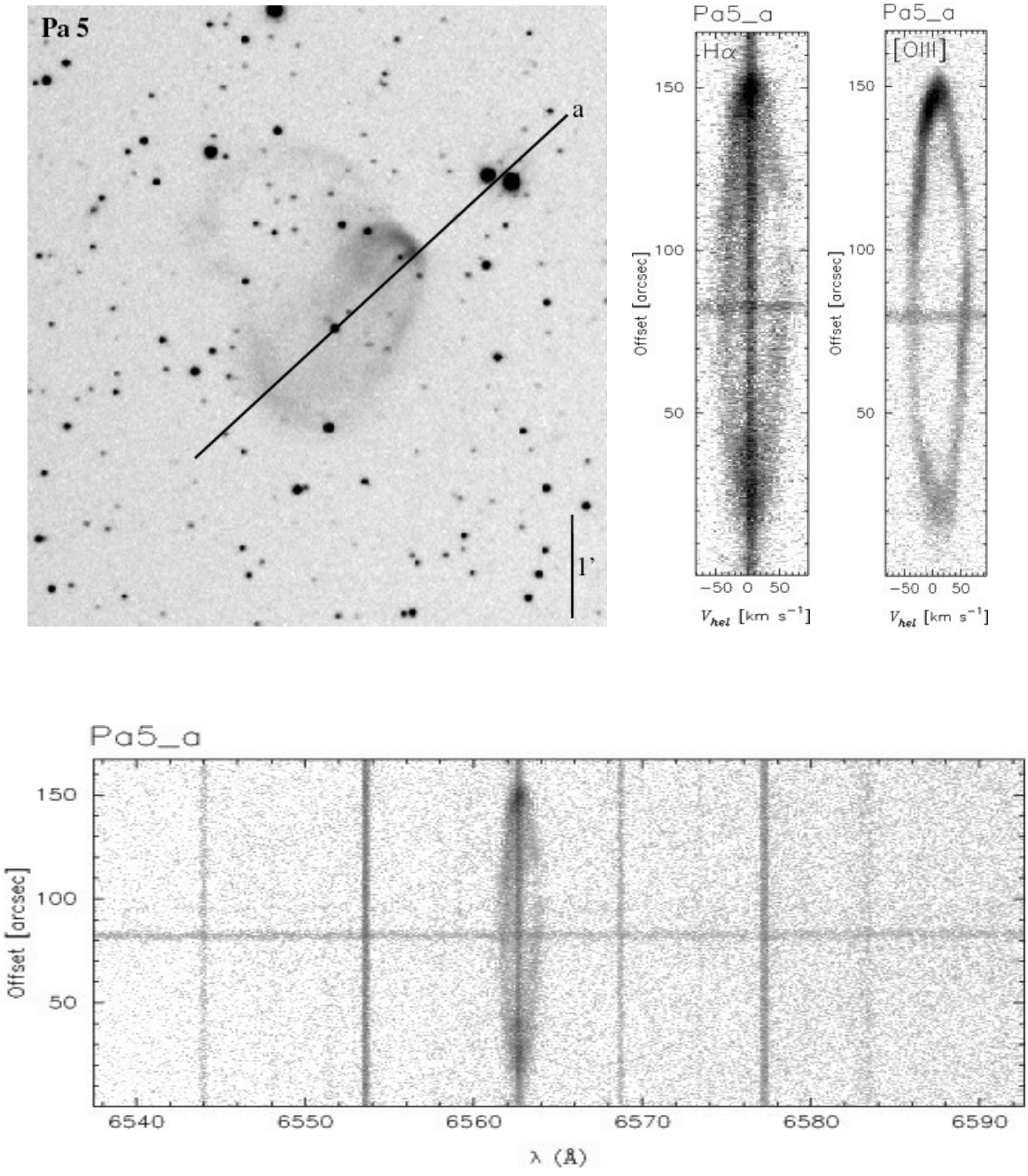

Figure A.85 **Same as Figure A.1.**

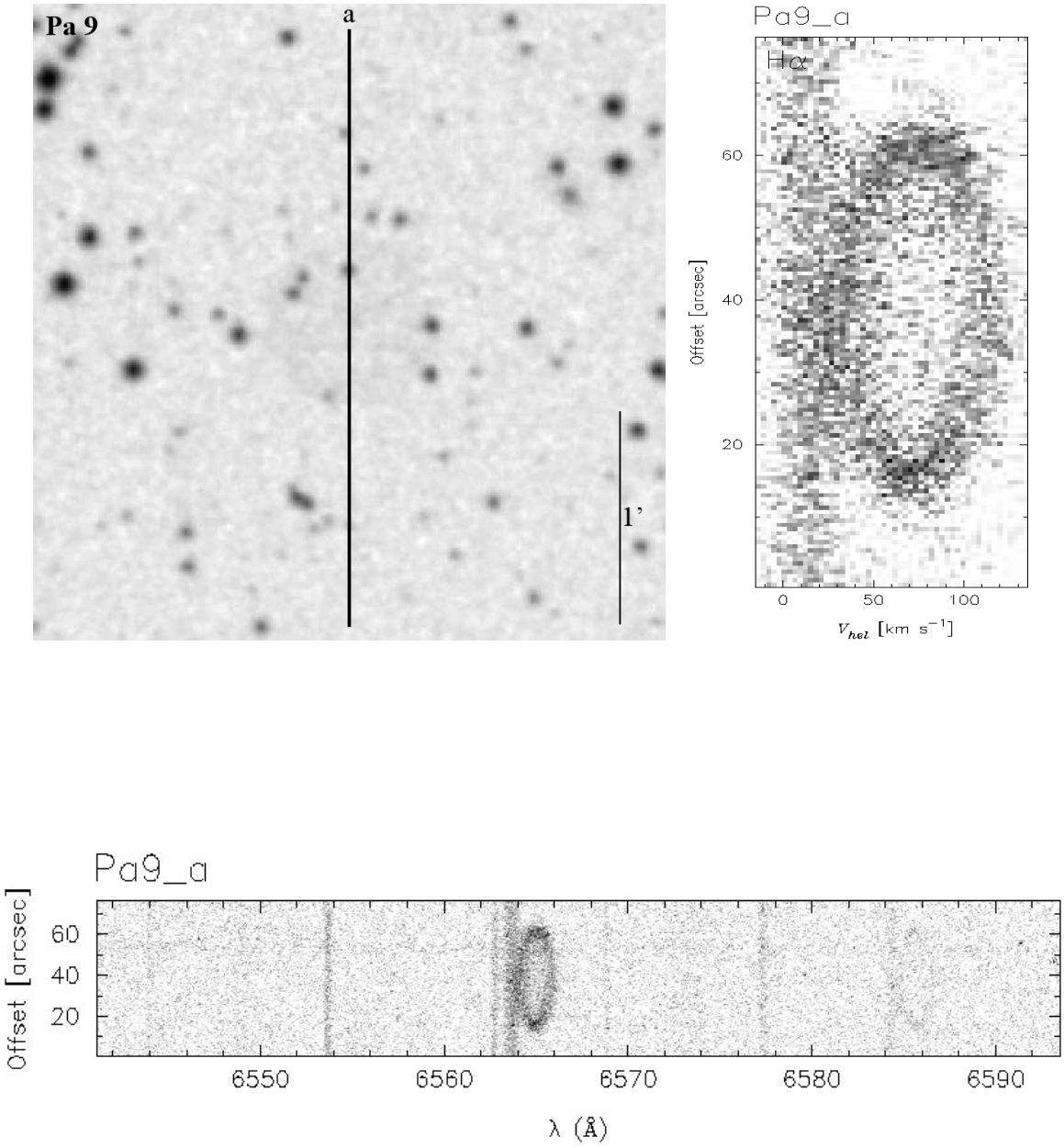

Figure A.86 **Same as Figure A.1.**

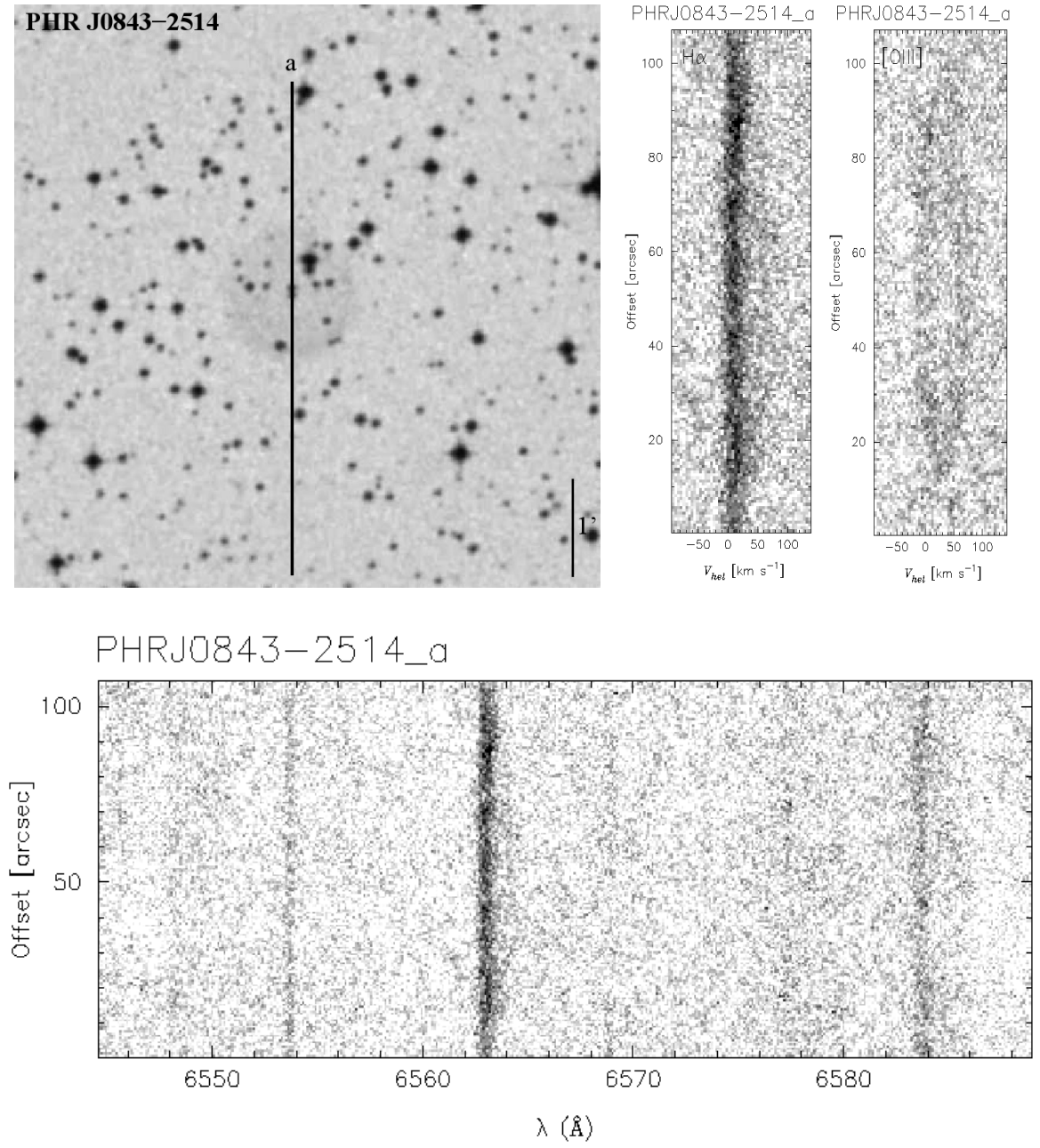

Figure A.87 **Same as Figure A.1.**

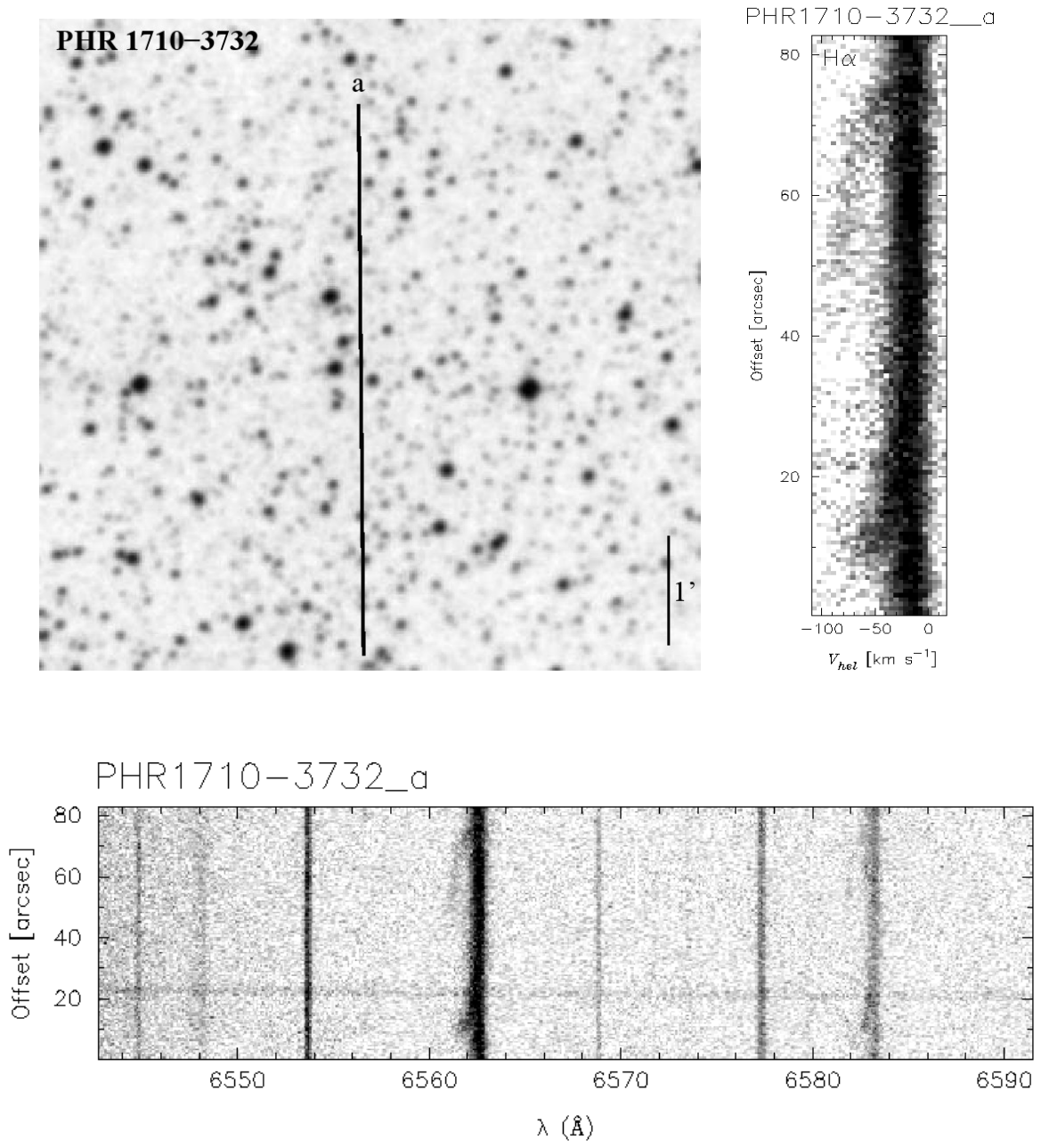

Figure A.88 **Same as Figure A.1.**

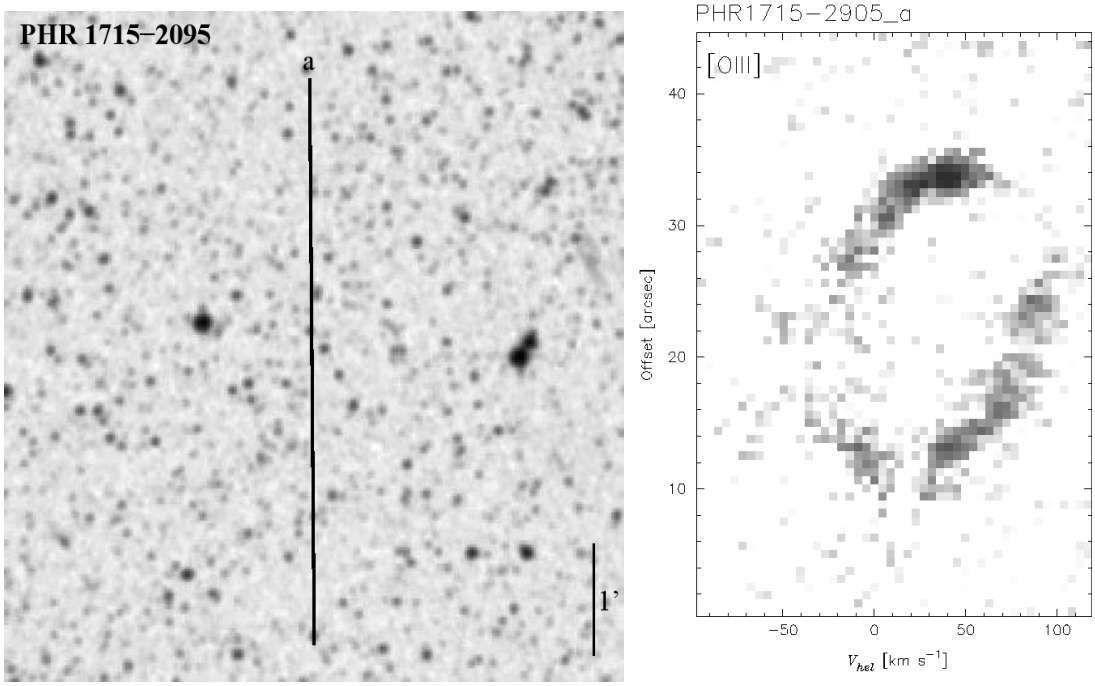

Figure A.89 **Same as Figure A.1.**

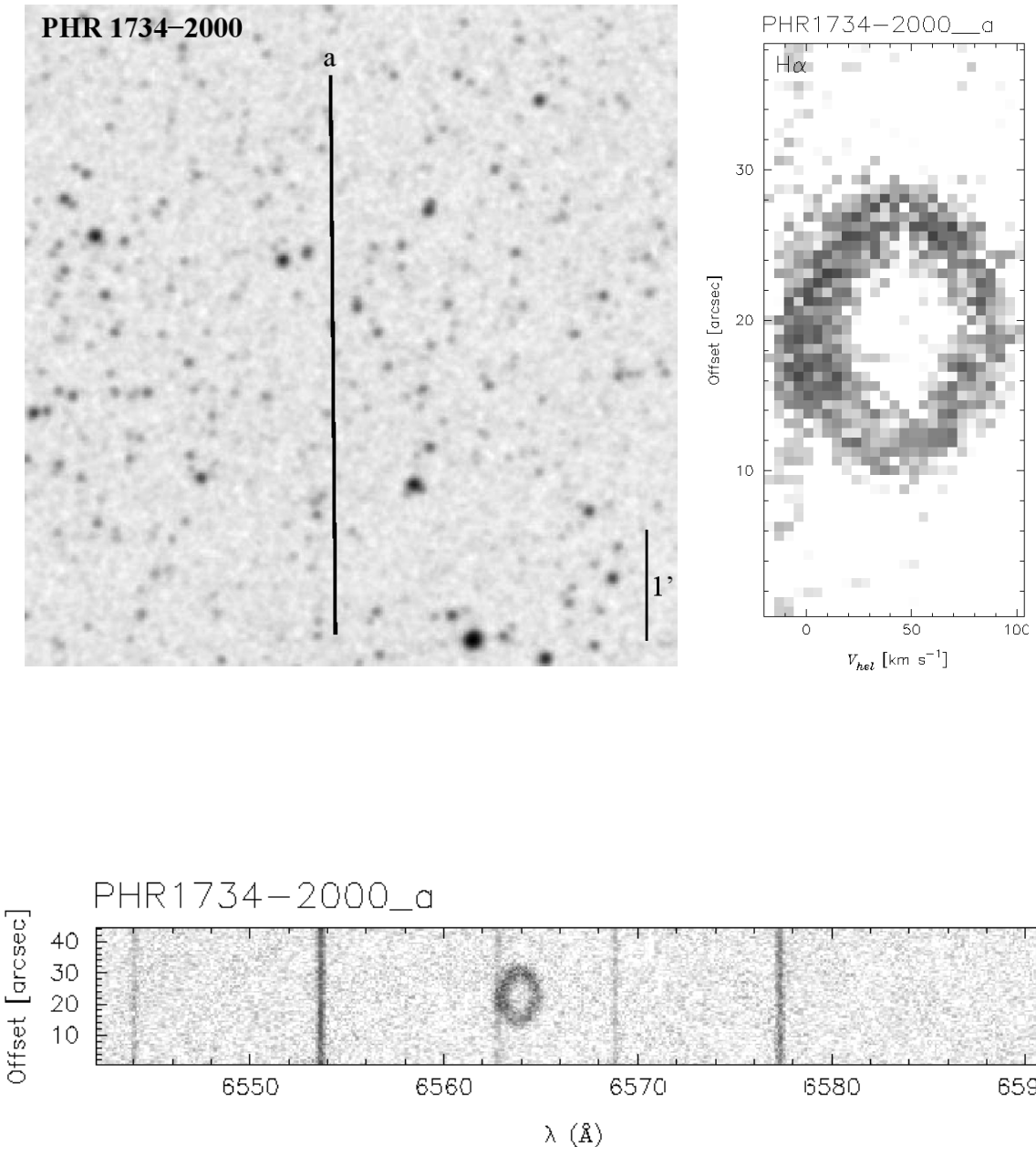

Figure A.90 **Same as Figure A.1.**

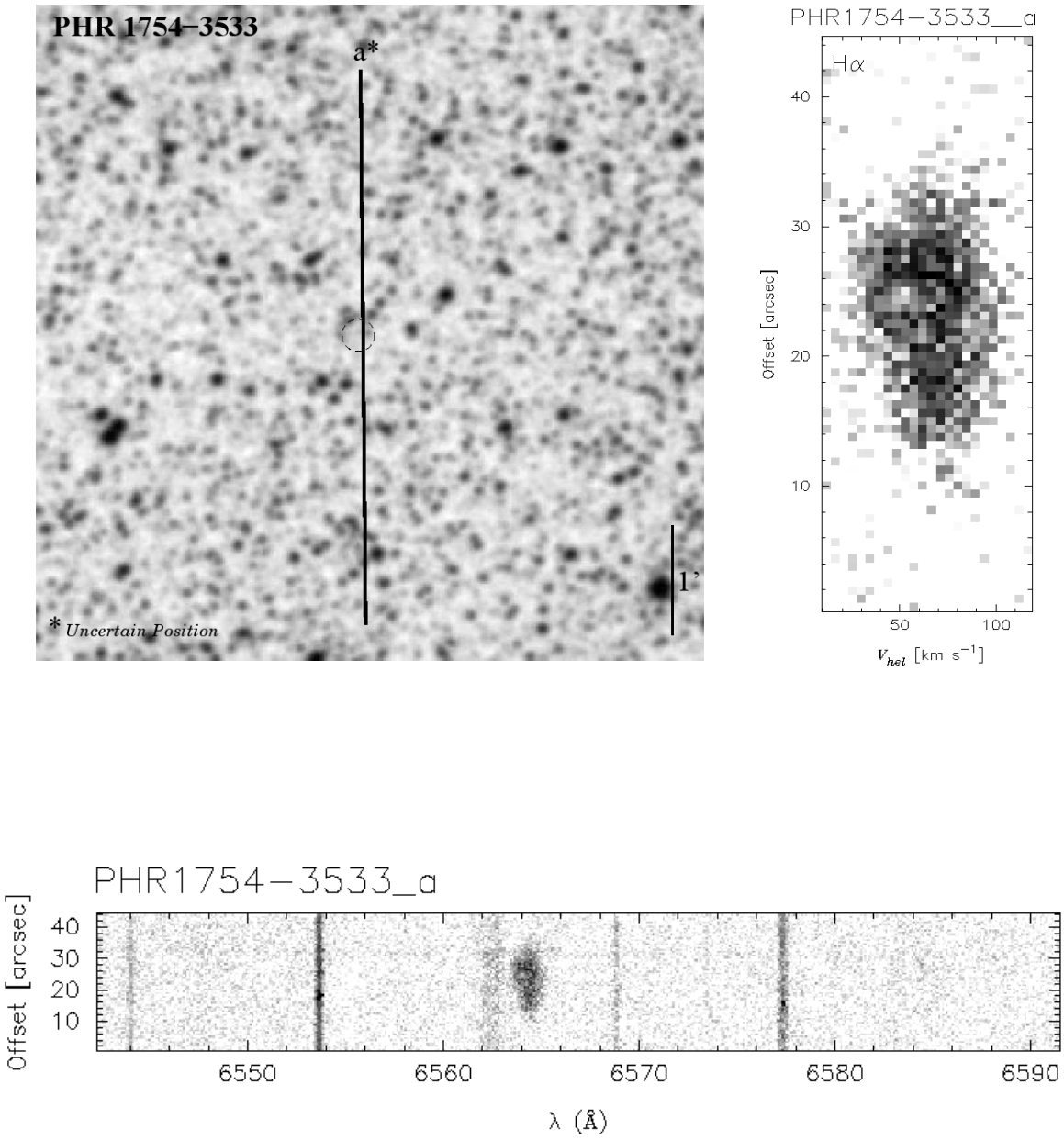

Figure A.91 **Same as Figure A.1.**

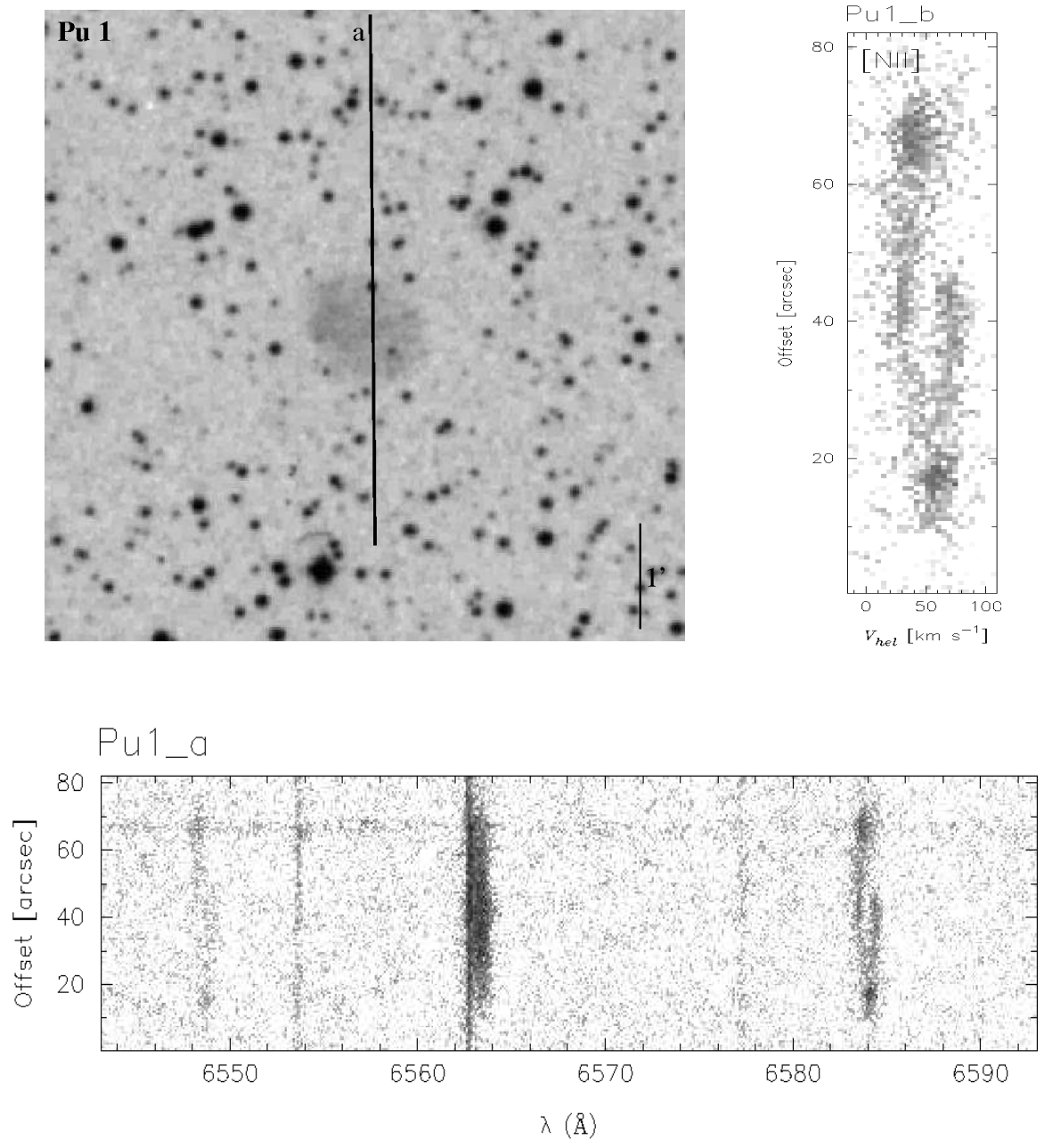

Figure A.92 **Same as Figure A.1.**

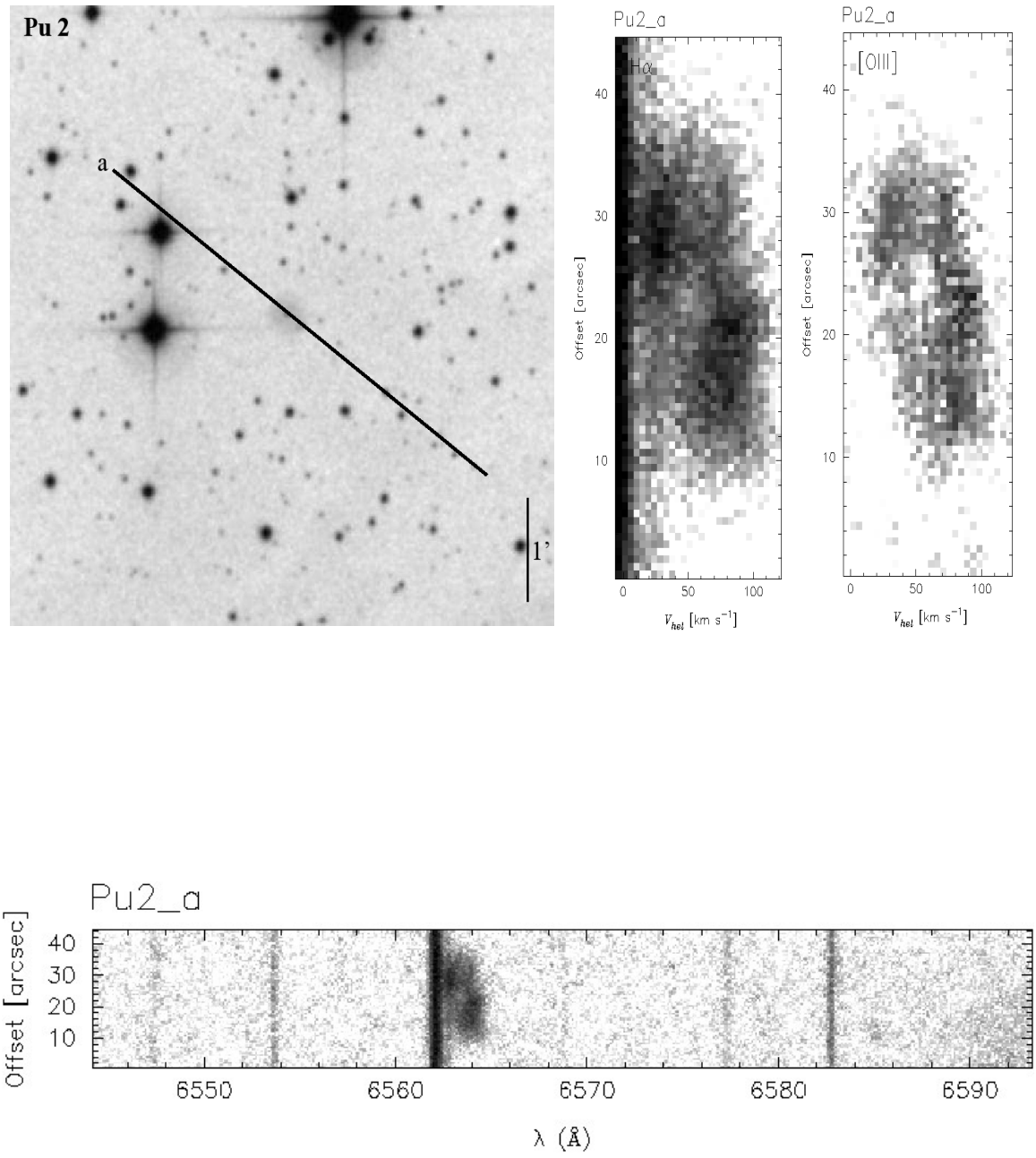

Figure A.93 **Same as Figure A.1.**

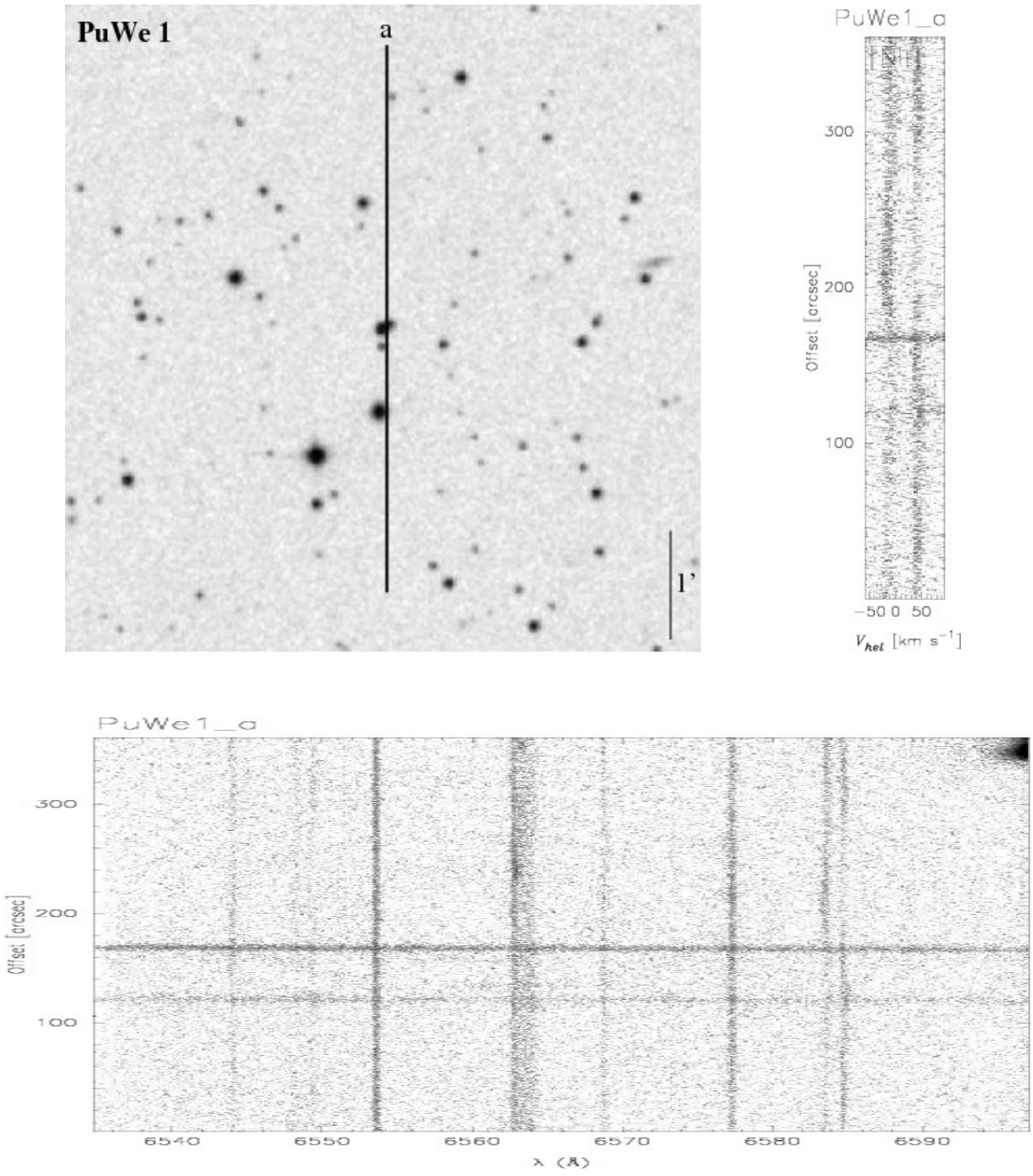

Figure A.94 **Same as Figure A.1.**

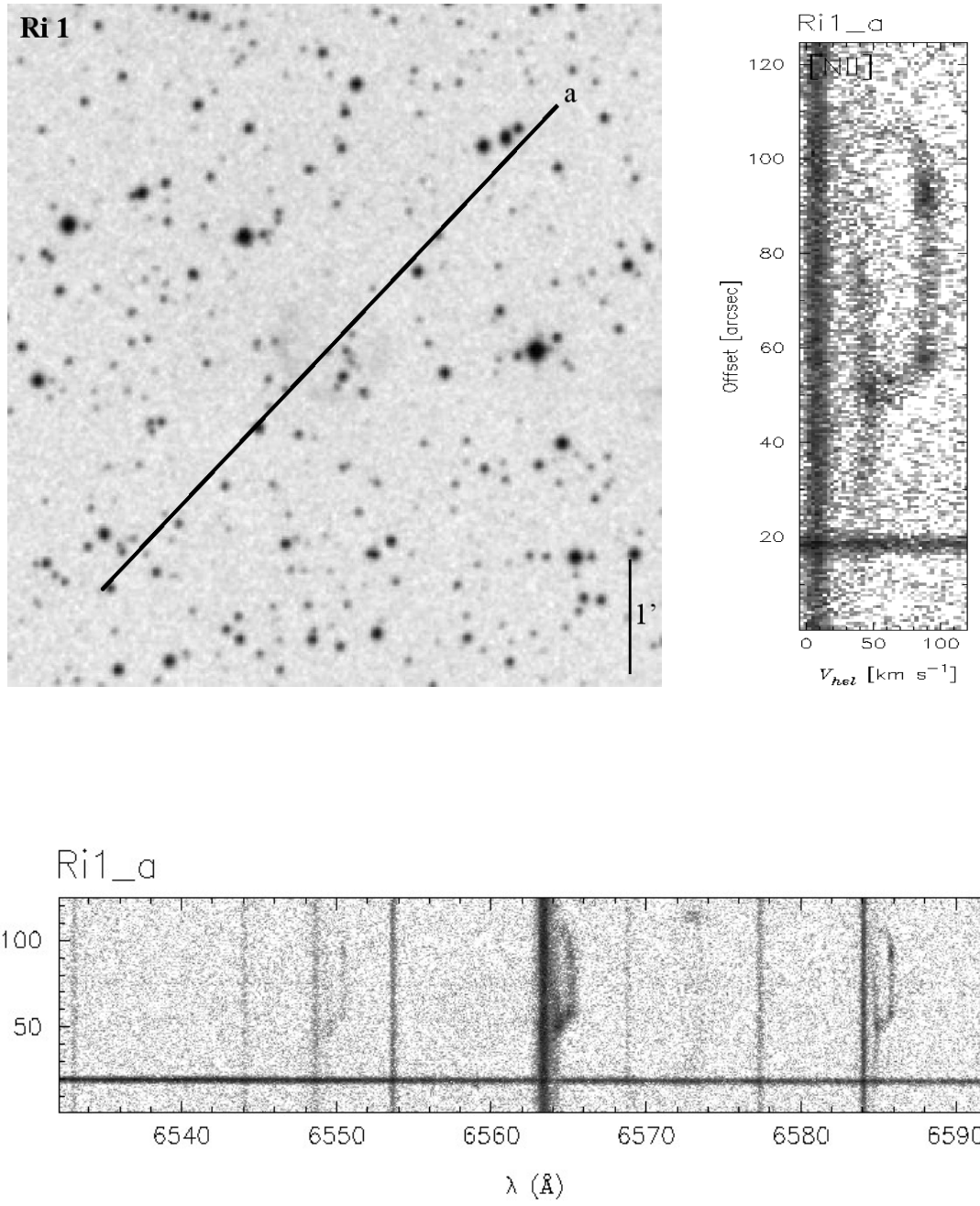

Figure A.95 **Same as Figure A.1.**

*Since we are measure the expansion velocity from the center of the velocity ellipse, the extended emission at the bottom of the line profile (from 25 to 50 arcsec) has no influence on our results. We are not sure about the nature of this emission component but it seems to be moving with a different systemic velocity of that found for the nebula (at the center of the velocity ellipse) and therefore, it is likely that this structure is not part of the nebula. It might be interstellar medium ionized by the bright star located near to it.

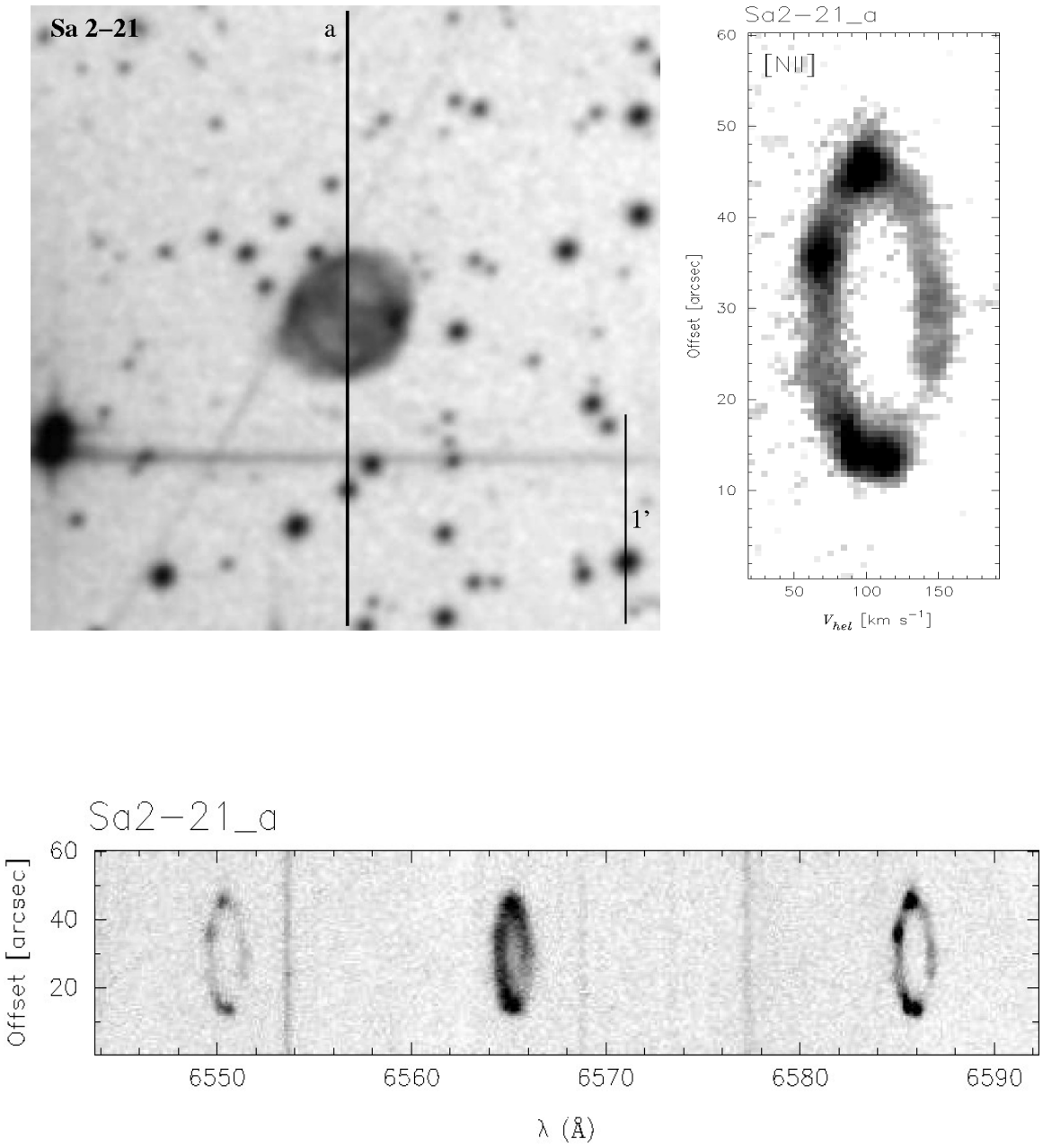

Figure A.96 **Same as Figure A.1.**

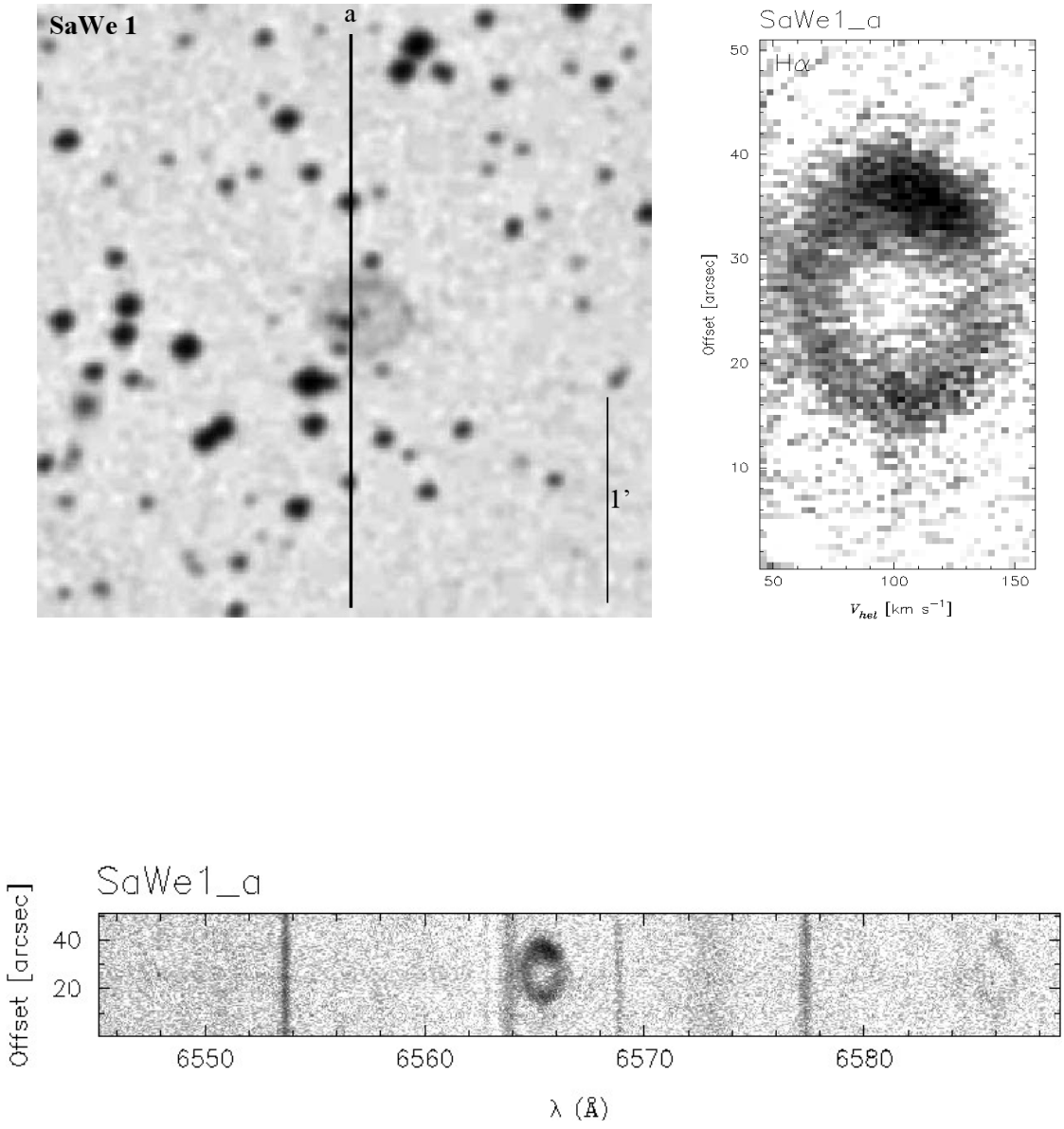

Figure A.97 **Same as Figure A.1.**

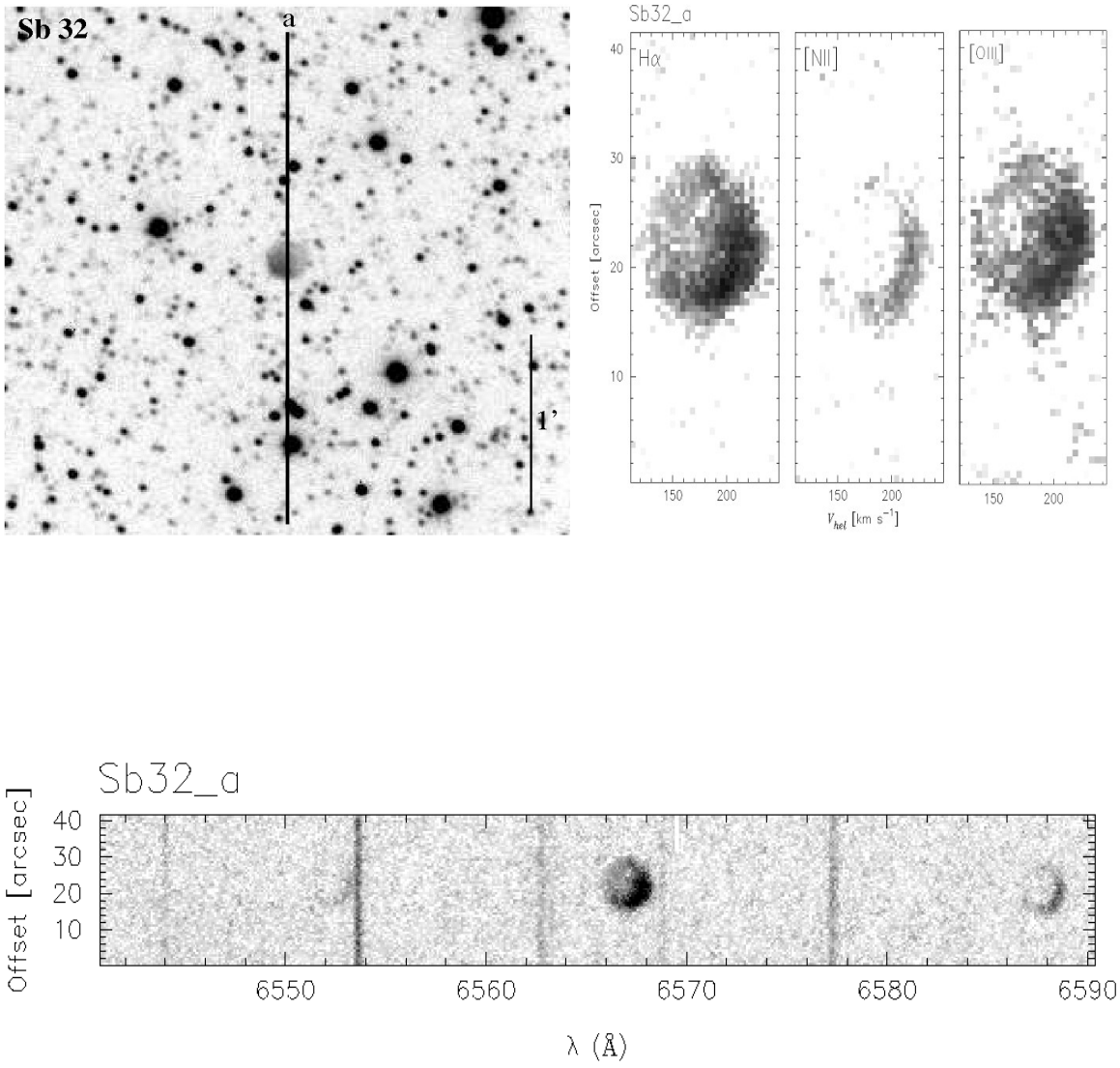

Figure A.98 **Same as Figure A.1.**

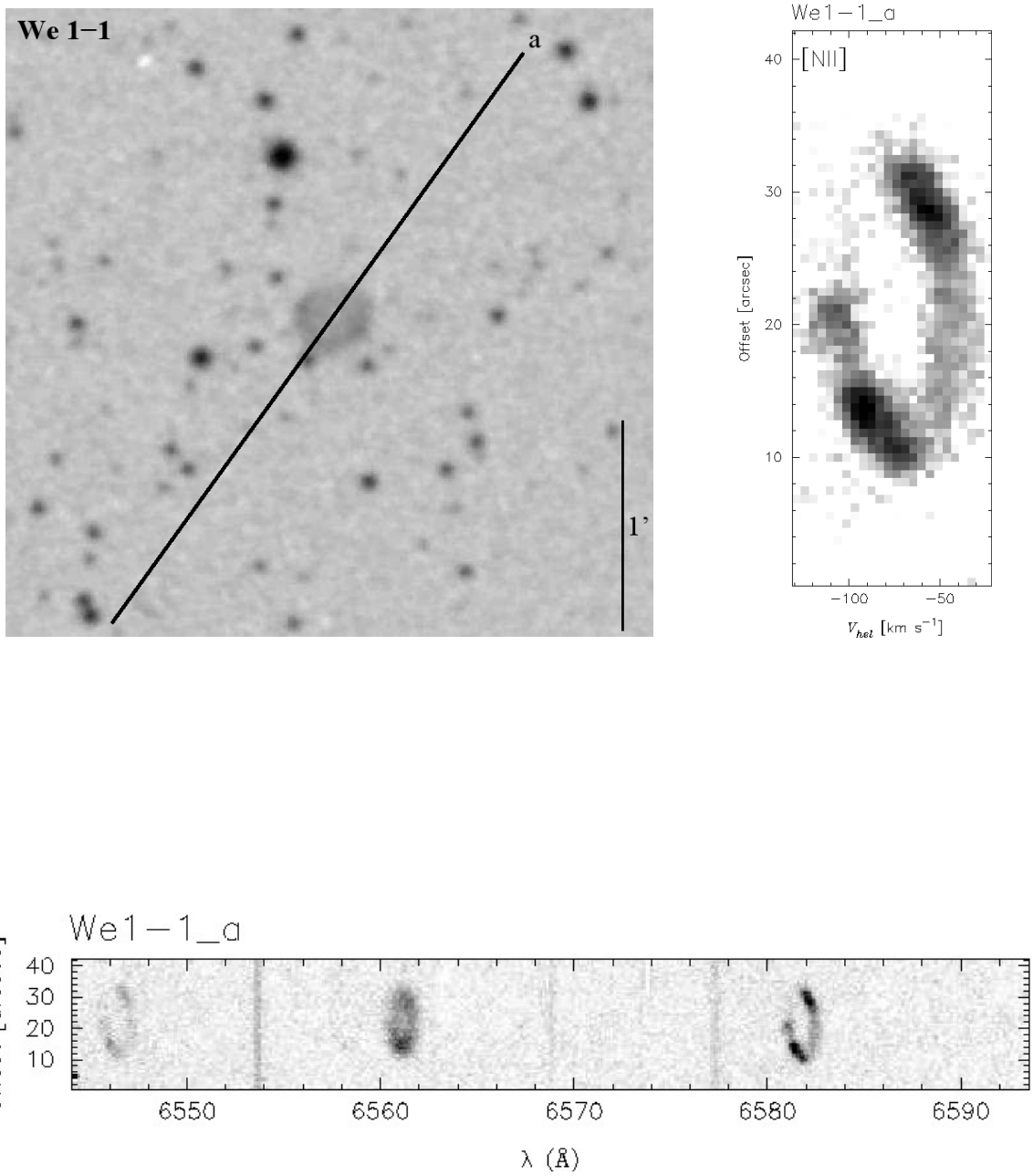

Figure A.99 **Same as Figure A.1.**

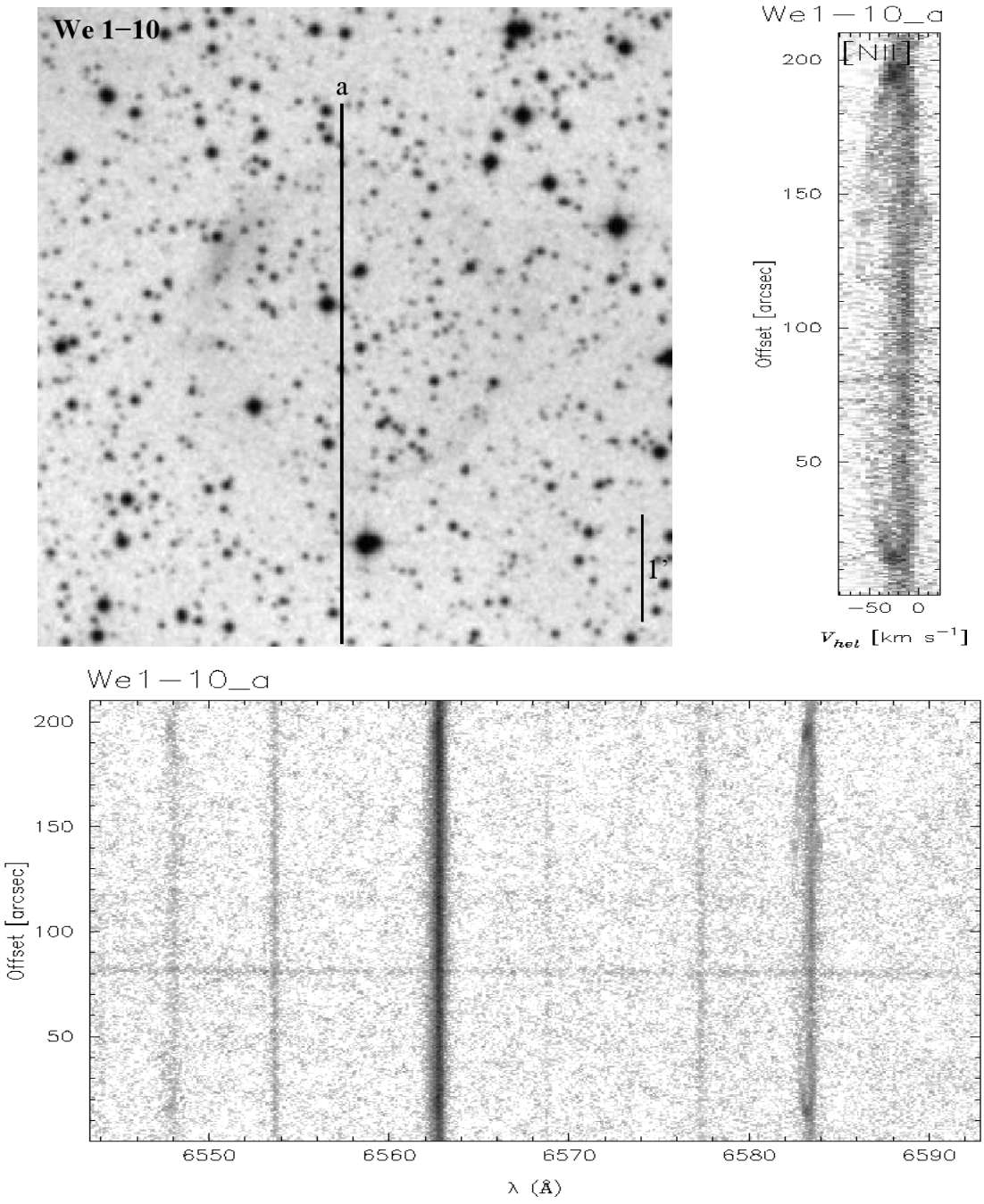

Figure A.100 **Same as Figure A.1.**

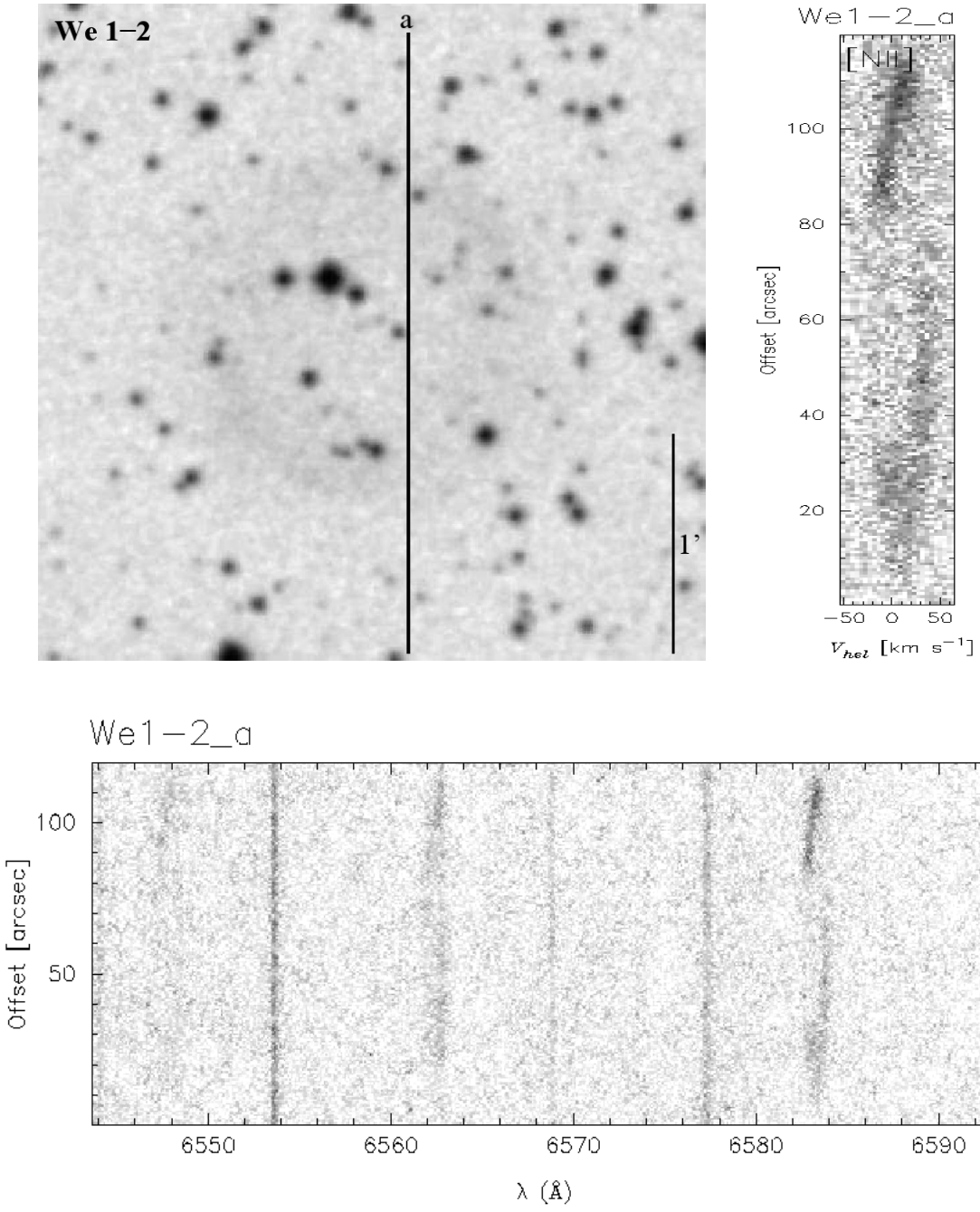

Figure A.101 **Same as Figure A.1.**

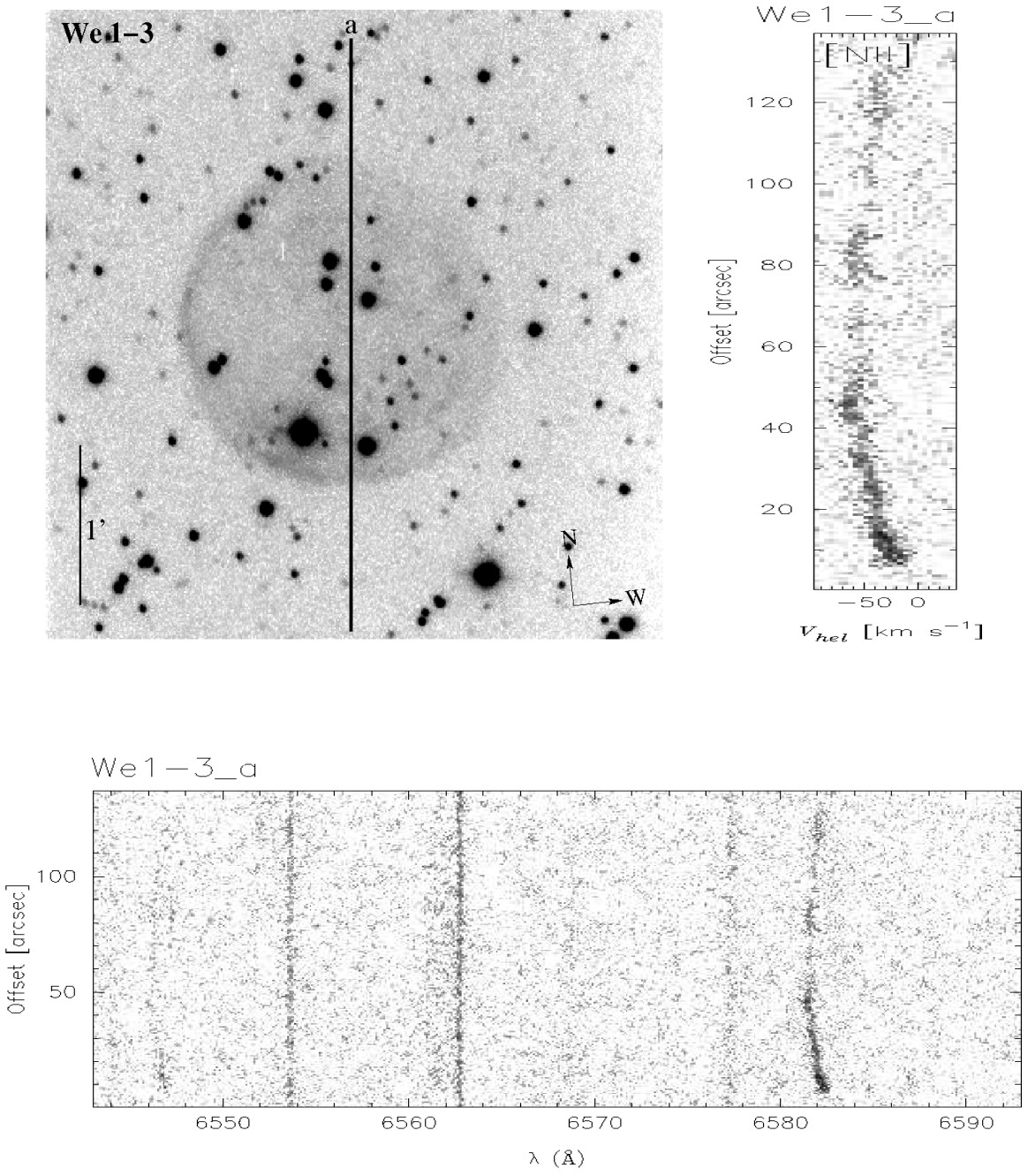

Figure A.102 **Same as Figure A.1.**

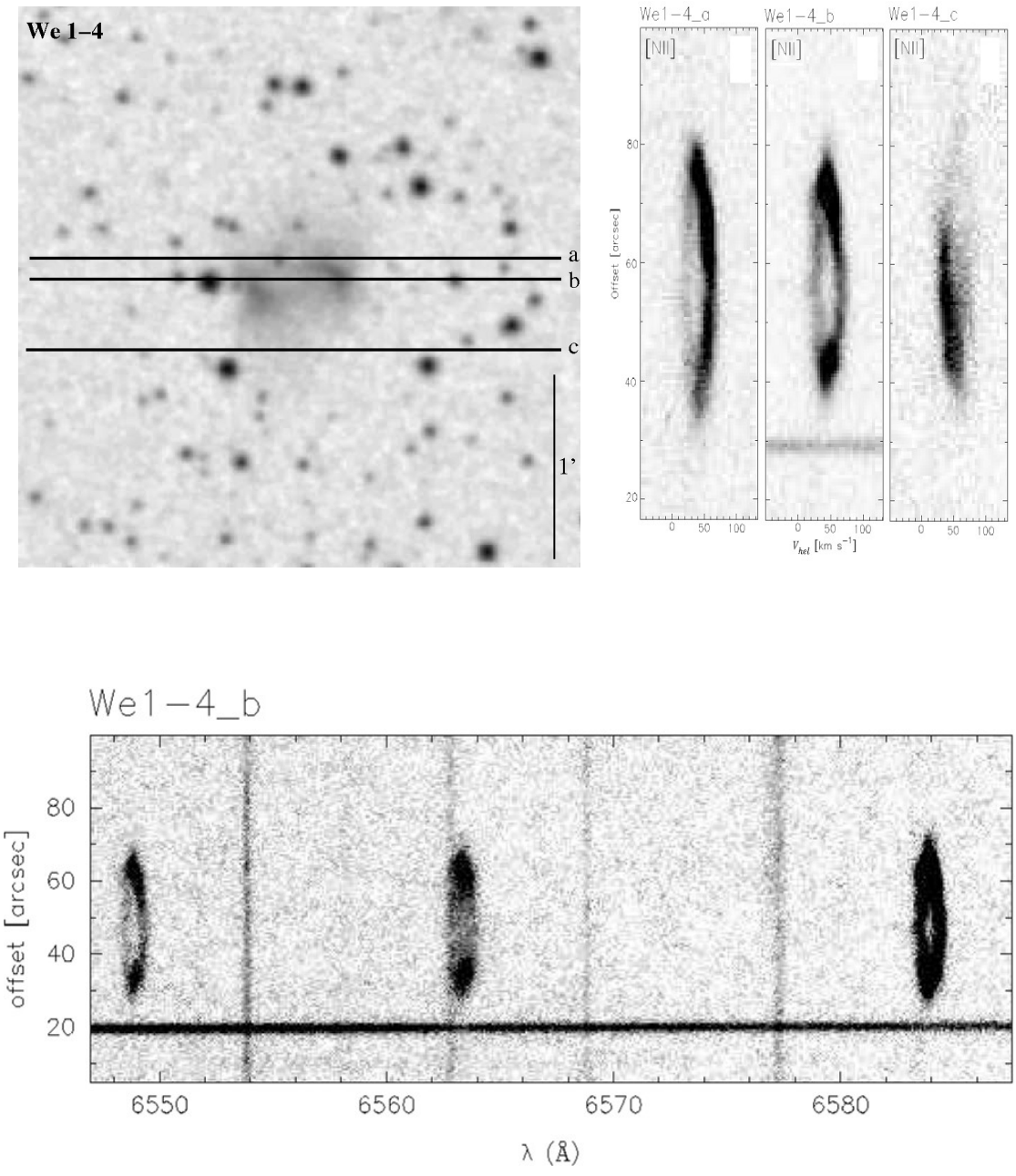

Figure A.103 **Same as Figure A.1.**

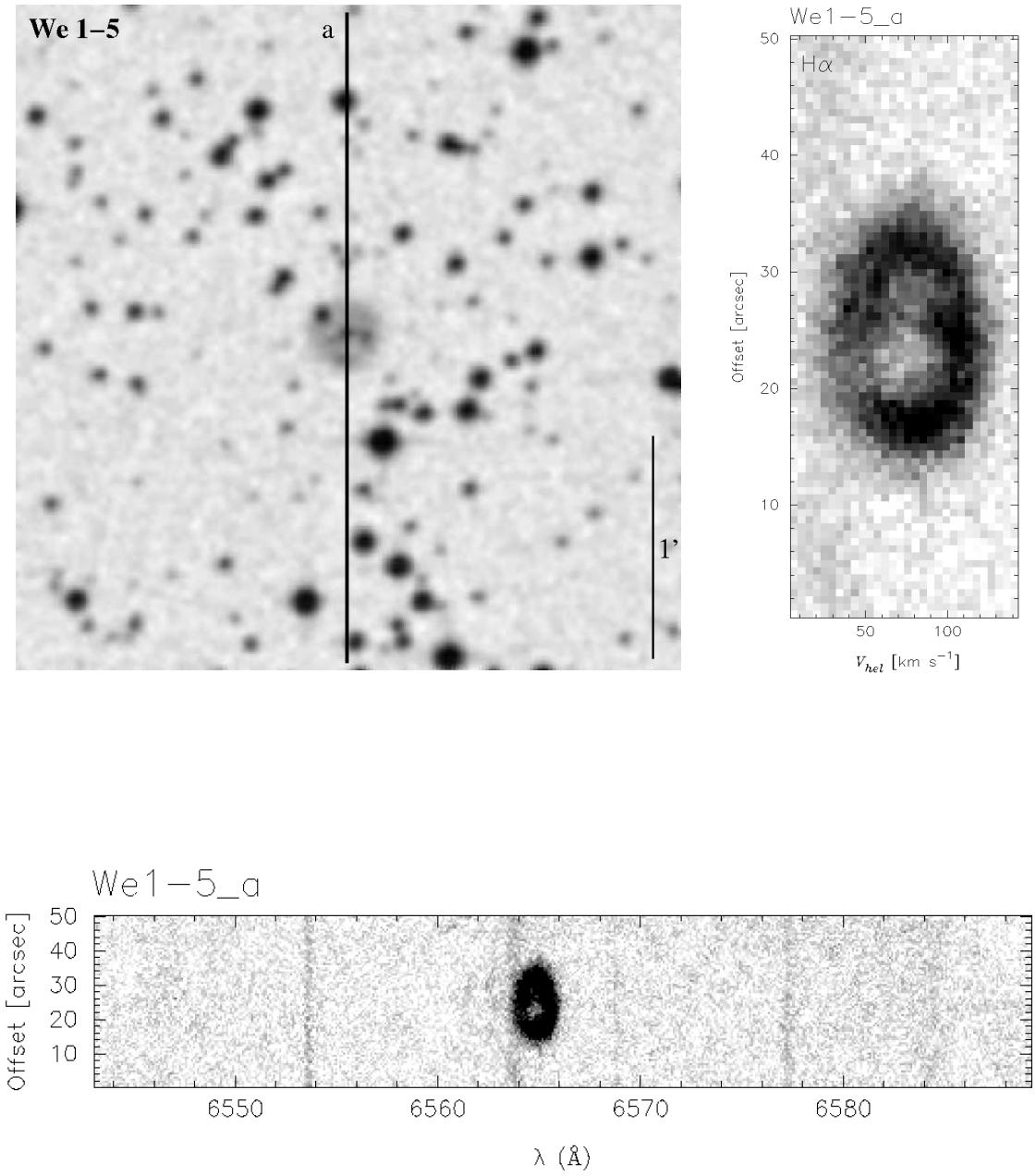

Figure A.104 **Same as Figure A.1.**

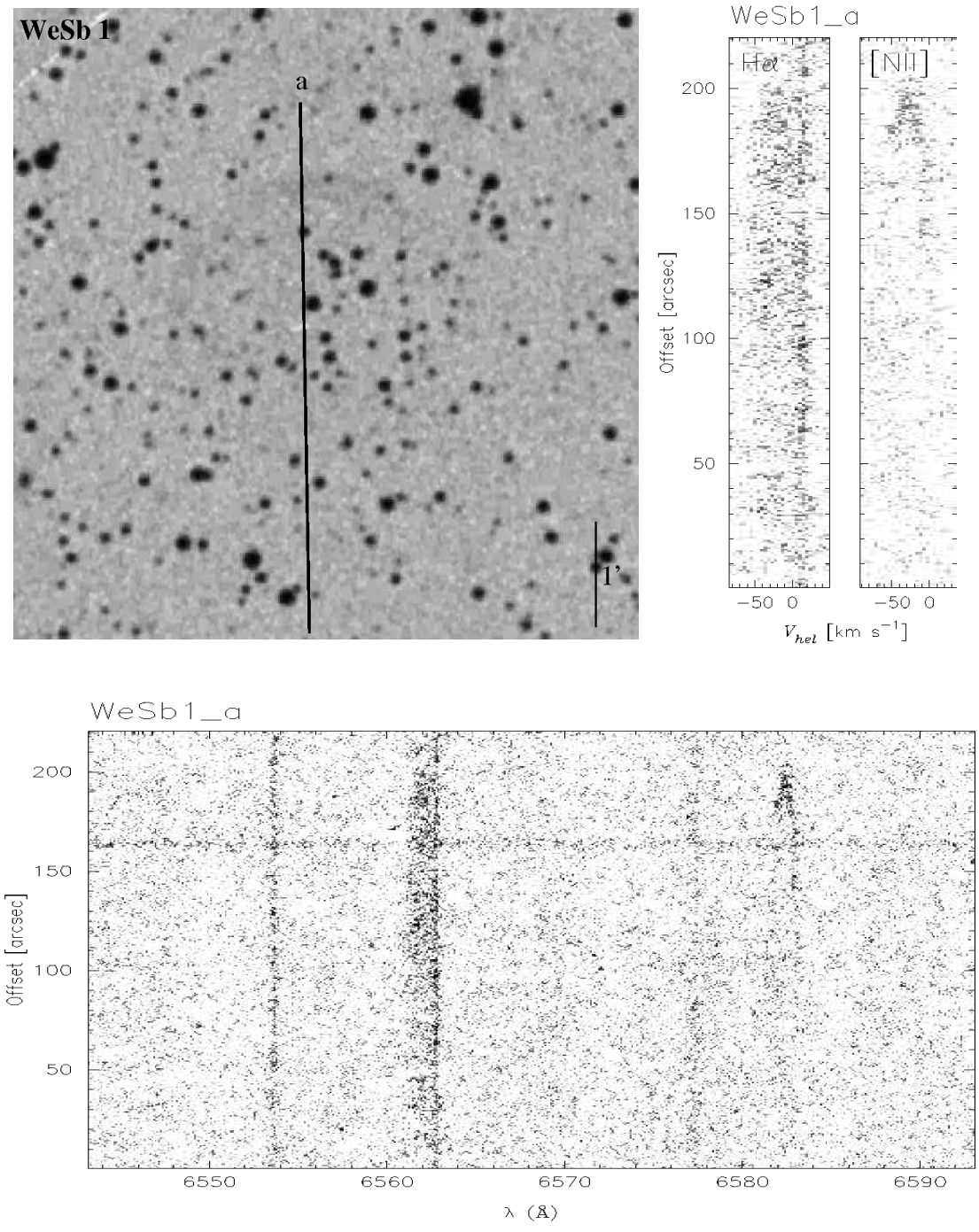

Figure A.105 **Same as Figure A.1.**

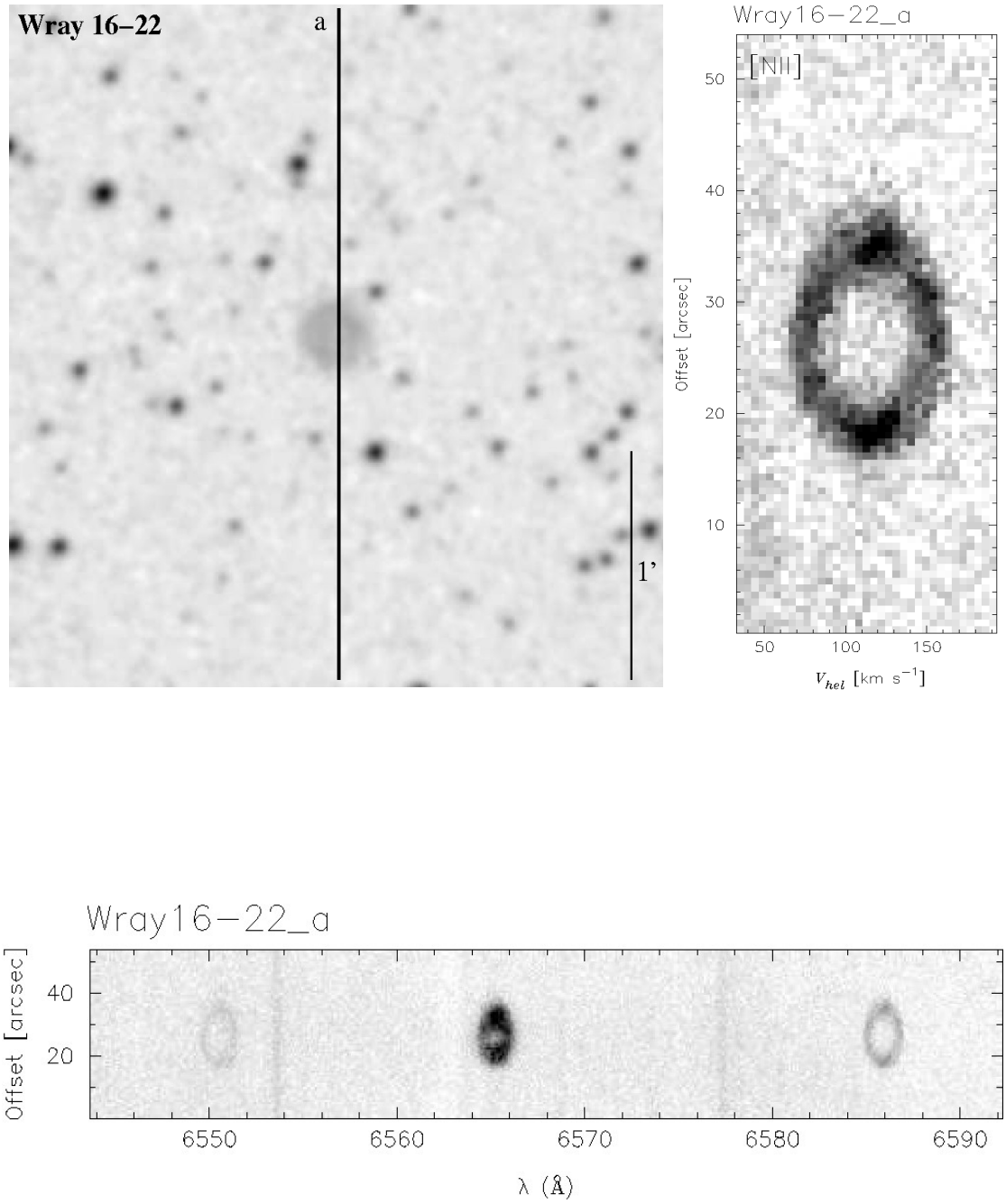

Figure A.106 **Same as Figure A.1.**

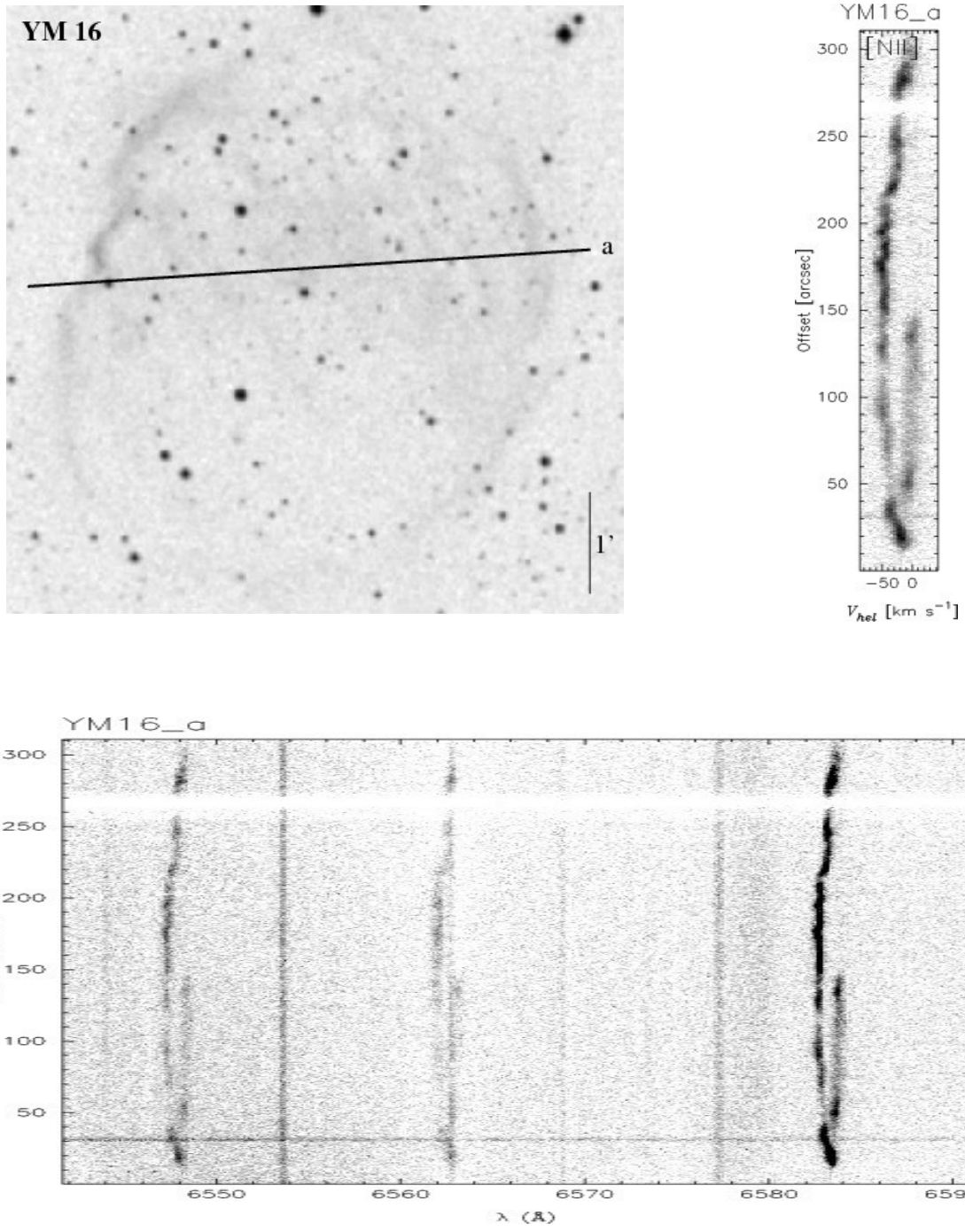

Figure A.107 **Same as Figure A.1.**

Appendix B

Halo PNe

Images and spectra of the Halo PNe are presented in this Appendix. In the first three pages the image from the DSS2R for each PNe is presented, with the slit position indicated as a solid line. Their respective spectra can be found in the following pages, every PN in a single page.

The two-dimensional array position-velocity (P-V), calibrated in heliocentric velocity and angular scale, is shown for the emission lines available in each case, as well as the plot of the horizontal cut made on the spectra (using IRAF[1]) considered for velocity measurements. As in the case of the Evolved sample the expansion of the nebular shell of the PN was obtained at the point of maximum splitting of the line profile, averaging 10 lines of the spectral image in most cases. For the faintest objects the average was calculated using the lines enough to obtain a signal to noise to obtained reliable measurements. We take half of the peak to peak distance between the blue- and red-shifted components or half of the resulting FWHM as the velocity of the nebular shell depending on each case.

At the bottom panel is the full spectral range used, where the emission lines detected are [NII] $\lambda\lambda$6548,6584, HeII λ6560, and H λ6562.8, for each PN. The spectra in this case is calibrated in wavelength and angular scale.

[1]IRAF is distributed by the National Optical Astronomy Observatories, which are operated by the Association of Universities for Research in Astronomy, Inc., under cooperative agreement with the National Science Foundation.

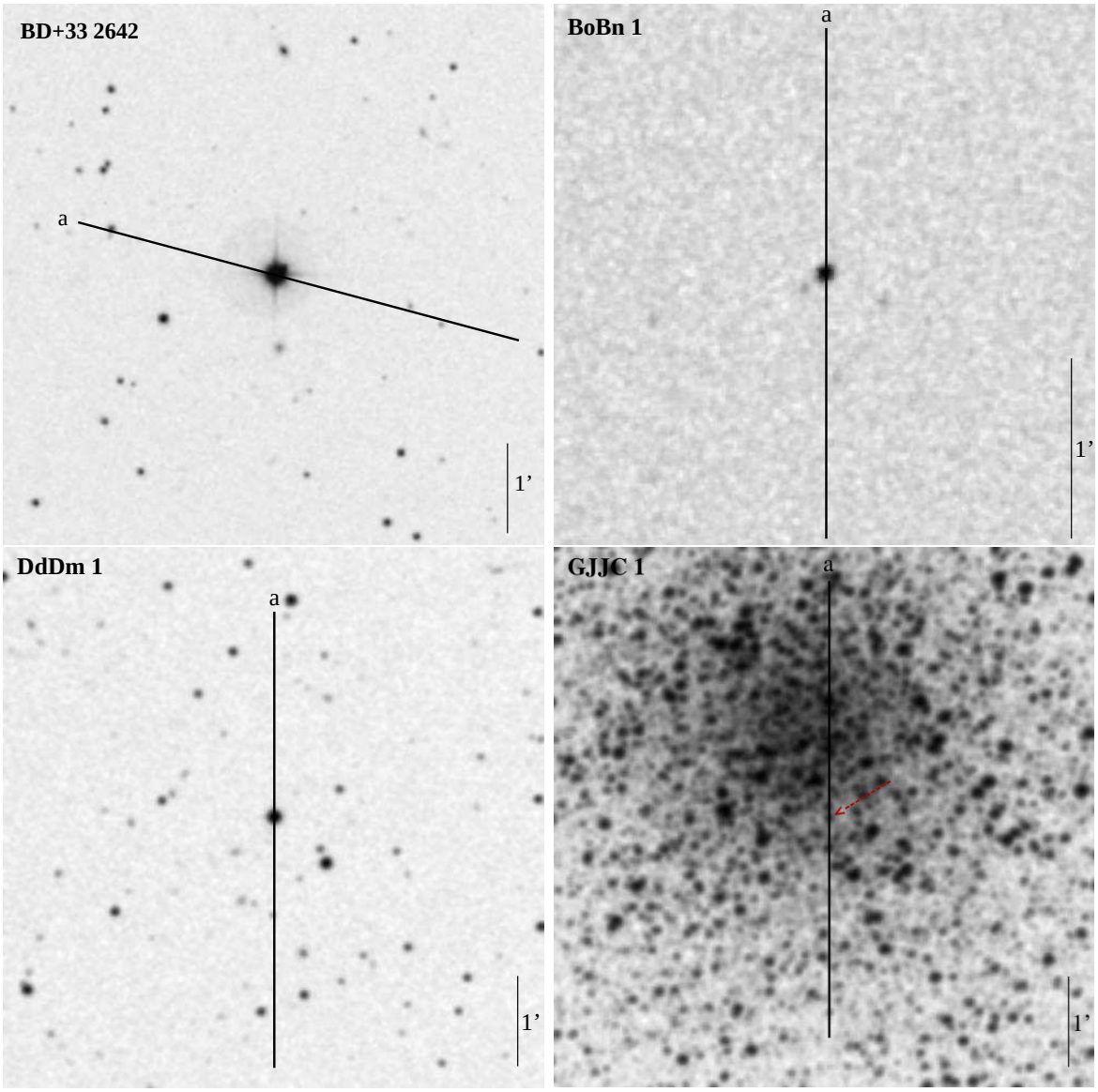

Figure B.1 **Images for the Halo PNe taken from the DSS2R. The slit position is indicated as a solid line.**

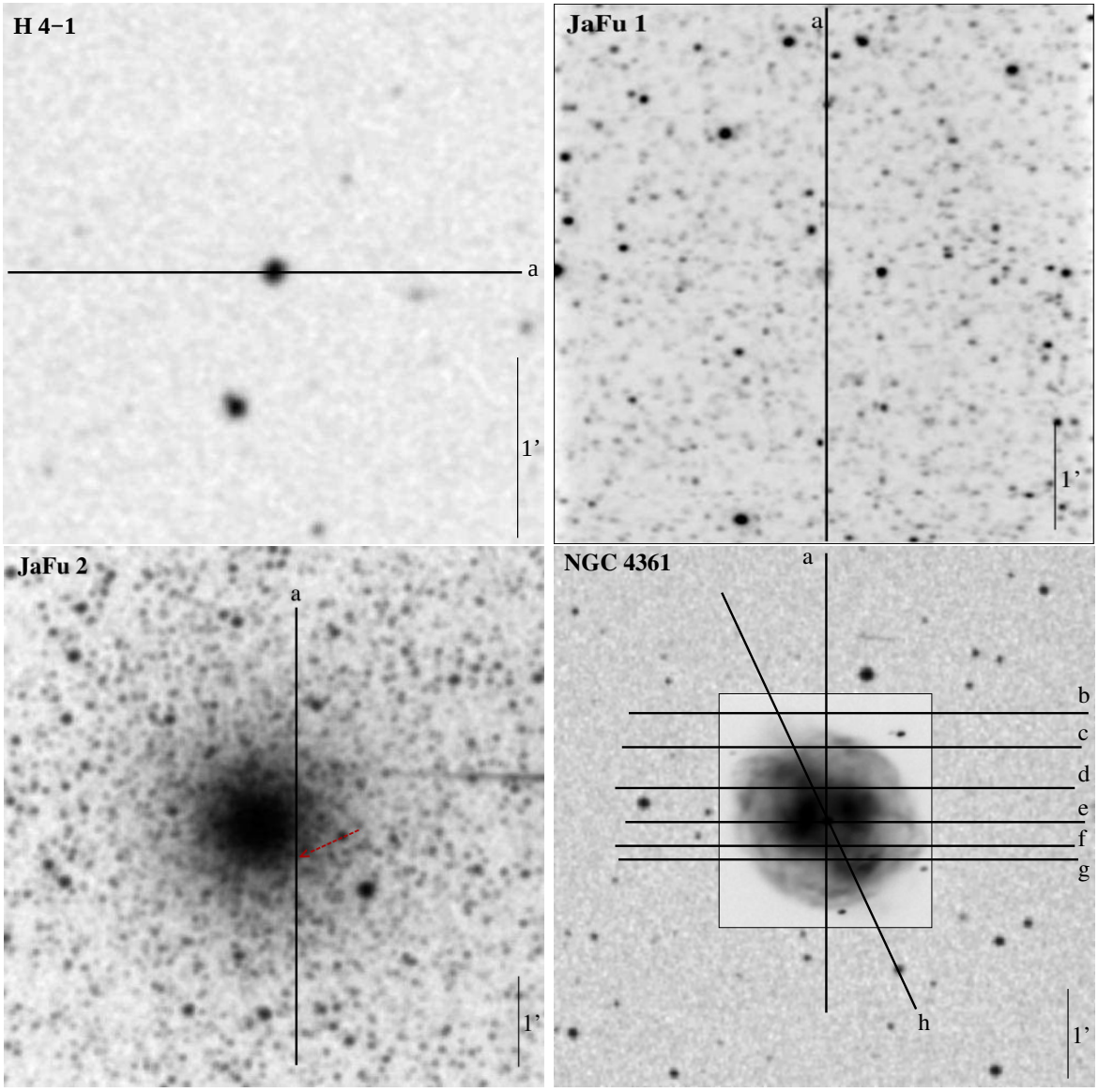

Figure B.2 **Same as Figure B.1.**

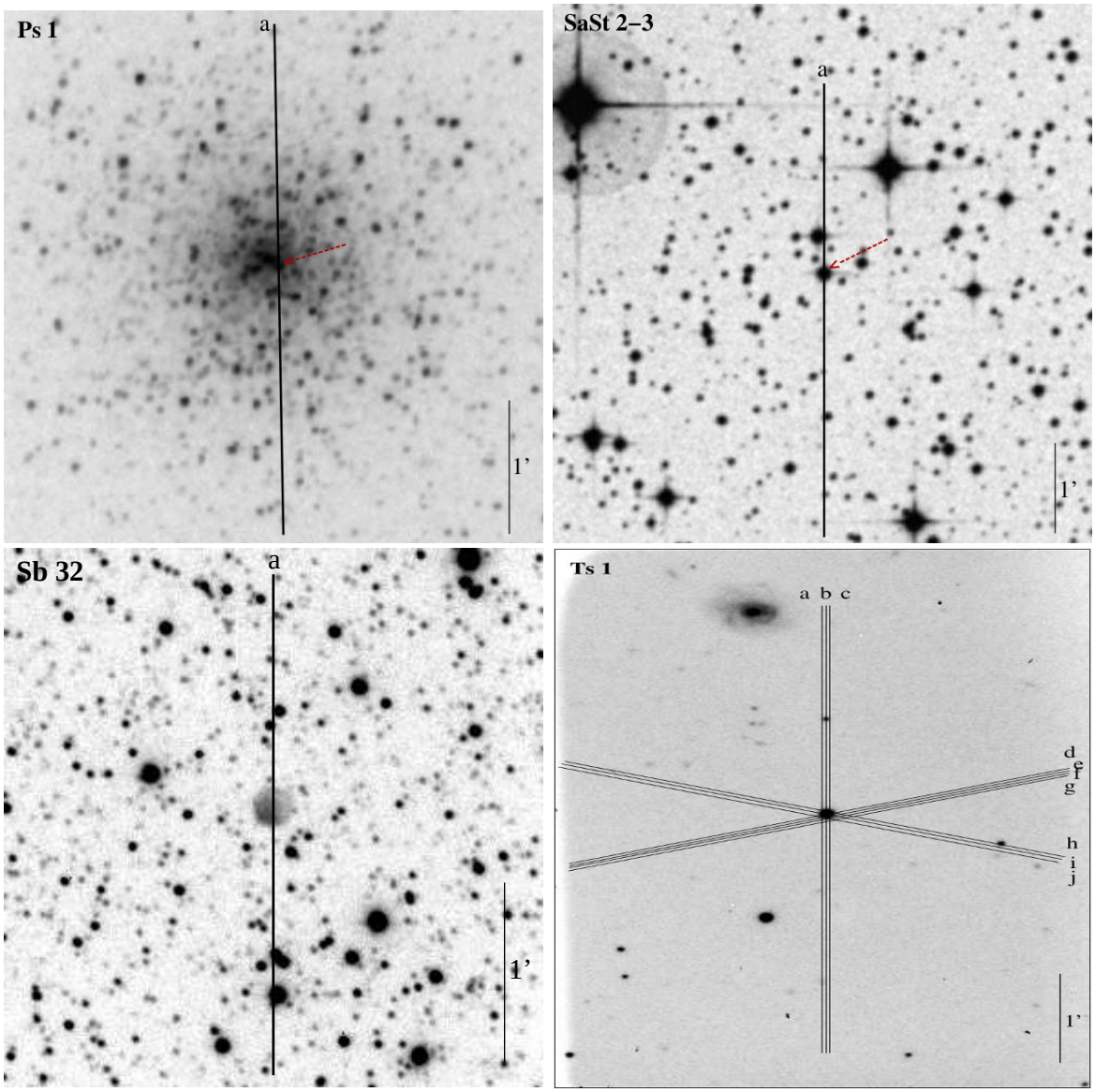

Figure B.3 **Same as Figure B.1.**

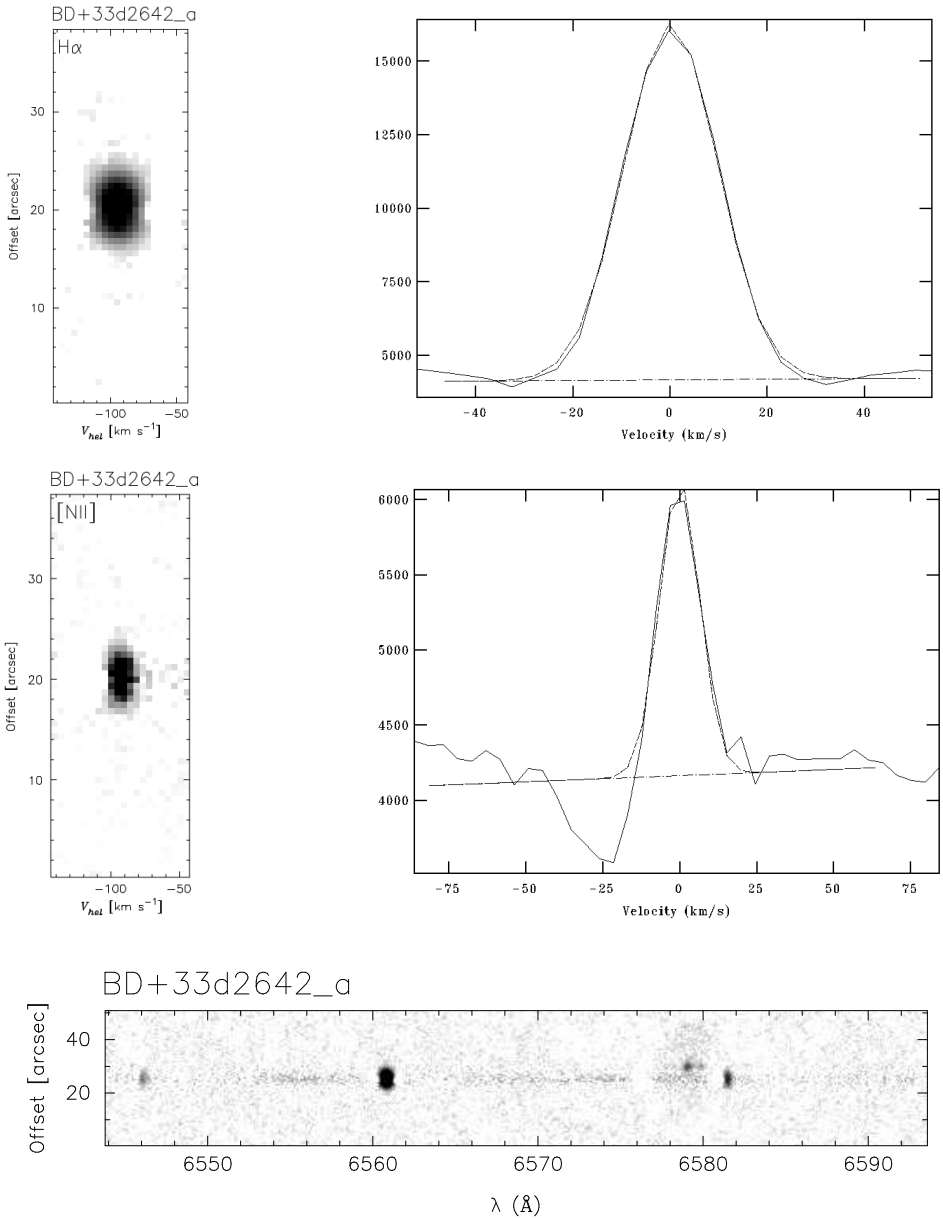

Figure B.4 **Spectra and measurements of the PN BD+33d2642 for slit a. In the left panel we present the two-dimensional array position-velocity (P-V) for the emission line labeled in the upper-left corner, this panel is calibrated in heliocentric velocity (abscissa), and the offset indicates the angular scale along the slit containing the nebular emission from the PNe (ordinate). The right panel shows a plot with the gaussian fit used to velocity measurements for each emission line. In the bottom panel is the full spectral range observed for this PN calibrated in wavelength, and angular scale, where the emission lines detected are [NII] $\lambda\lambda$6548,6584, HeII λ6560, and Hα λ6562.8.**

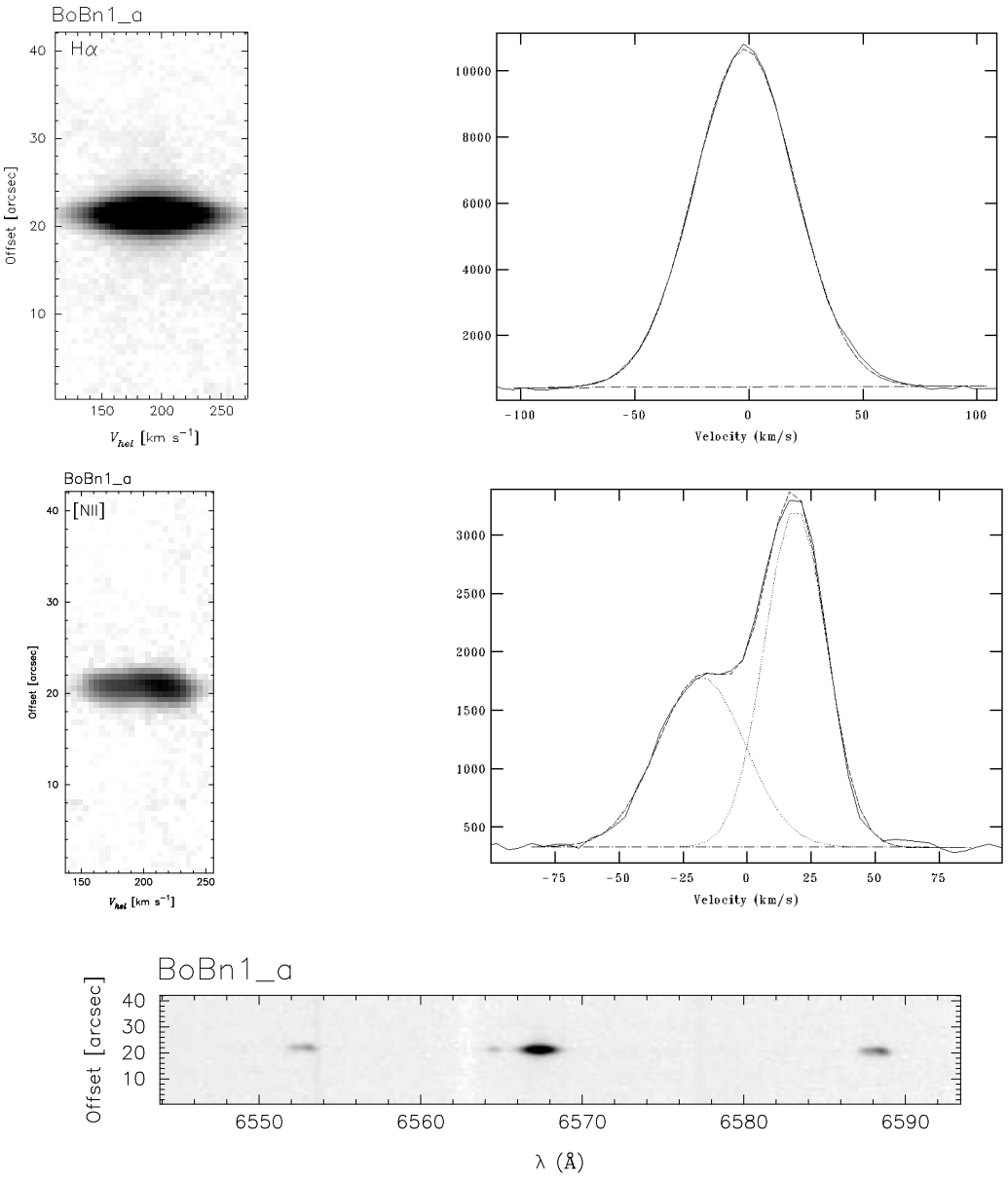

Figure B.5 **Image and data of the PN BoBn1 for slit a. Same as Figure B.4.**

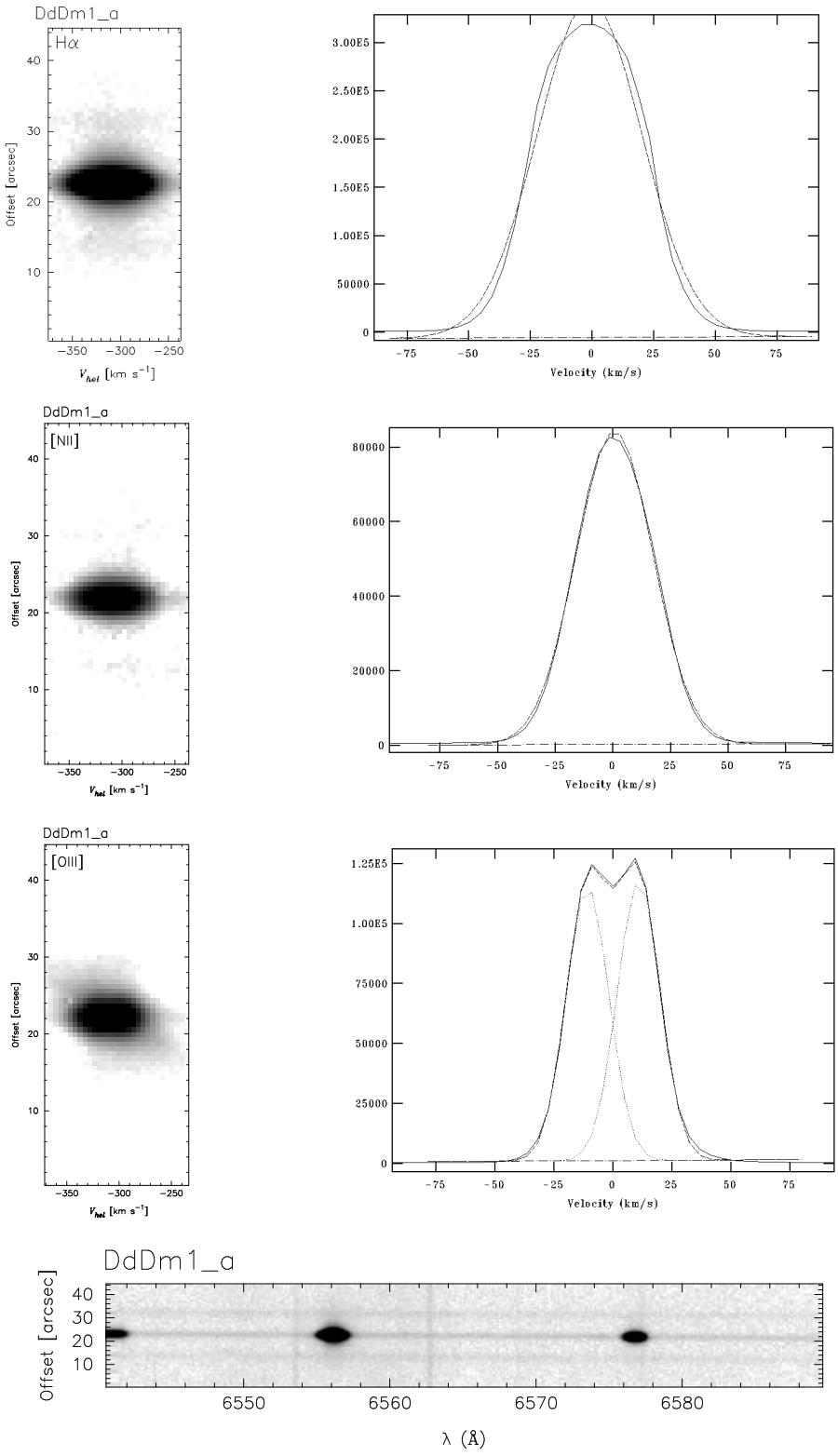

Figure B.6 **Image and data of the PN DdDm1 for slit a. Same as Figure B.4.**

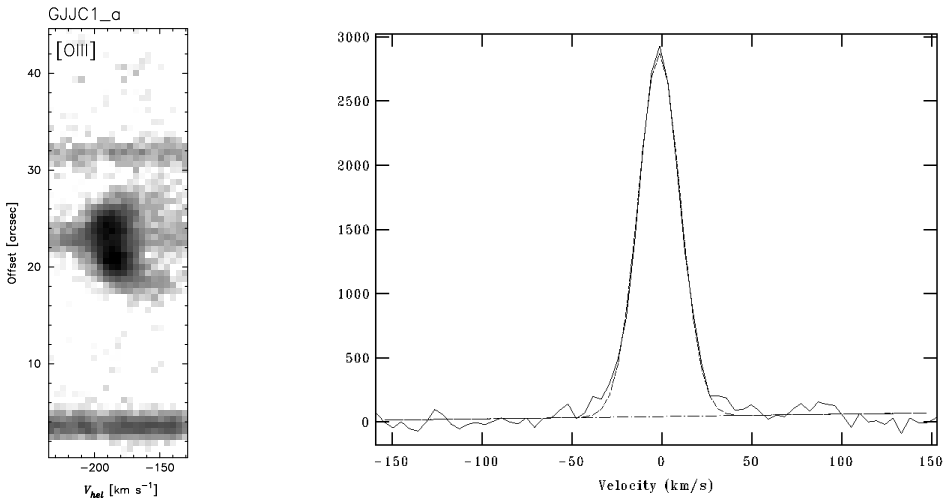

Figure B.7 **Image and data of the PN GJJC1 for slit a. Same as Figure B.4. Full spectral range not available in this case.**

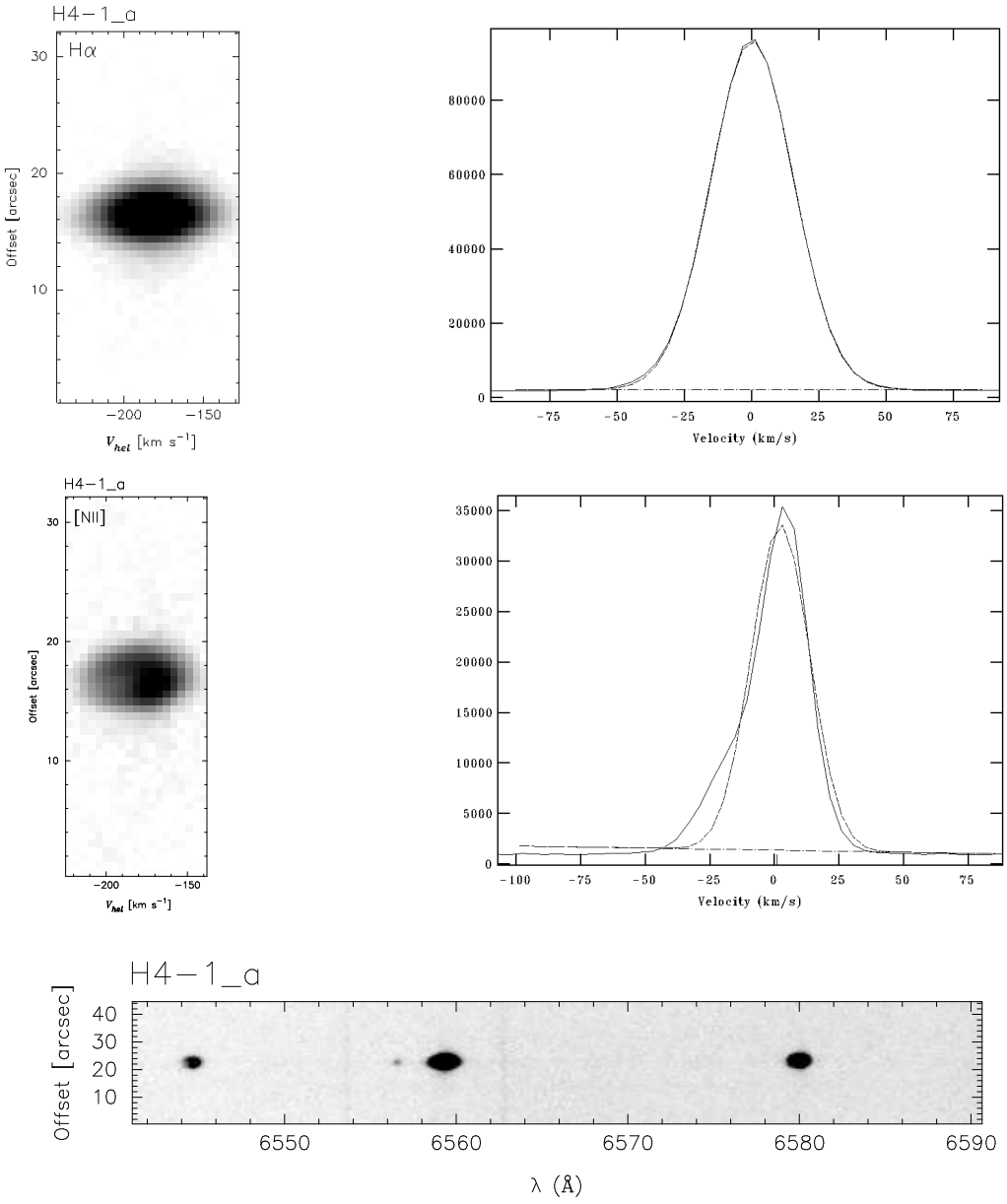

Figure B.8 **Image and data of the PN H4-1 for slit a. Same as Figure B.4.**

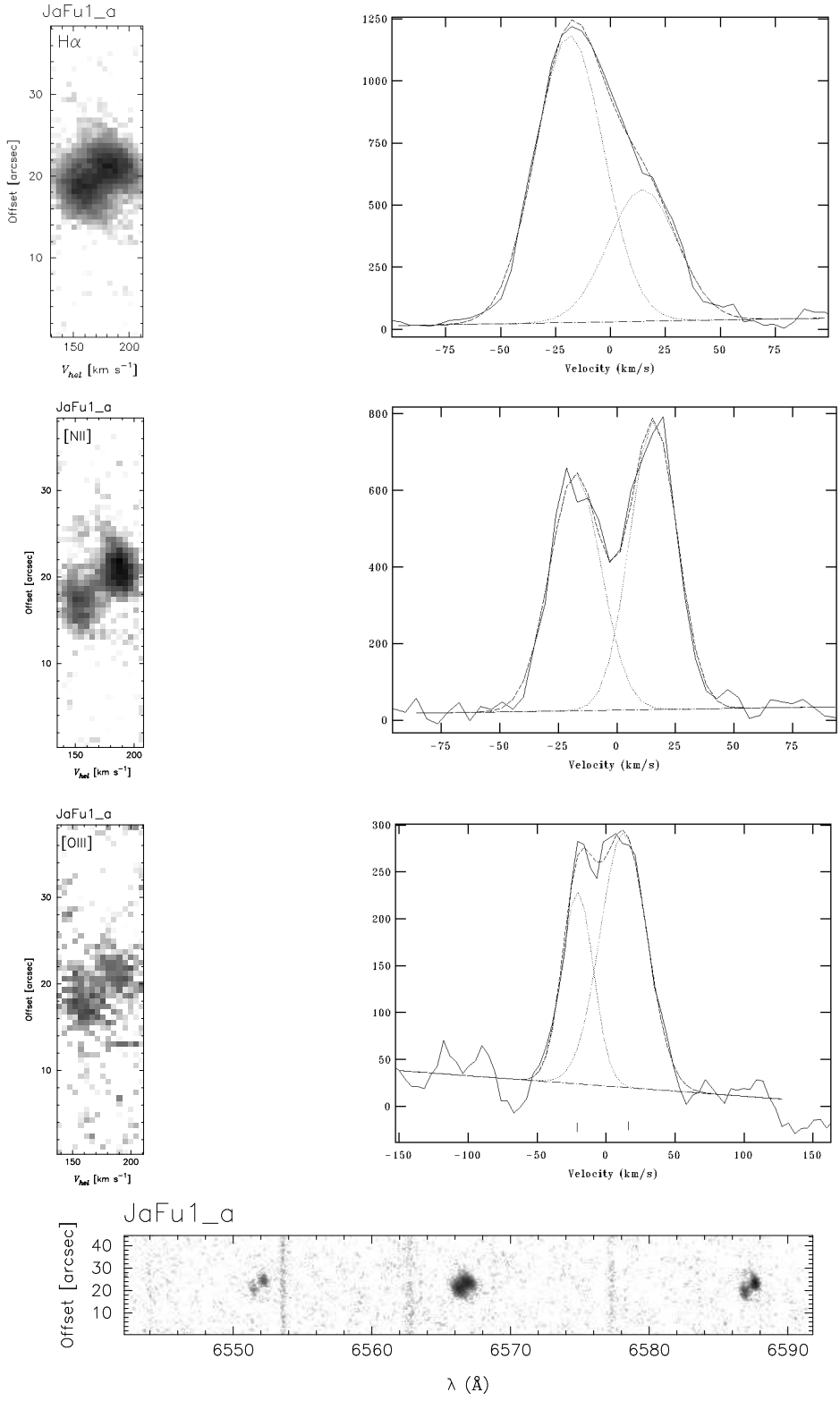

Figure B.9 **Image and data of the PN JaFu1 for slit a. Same as Figure B.4.**

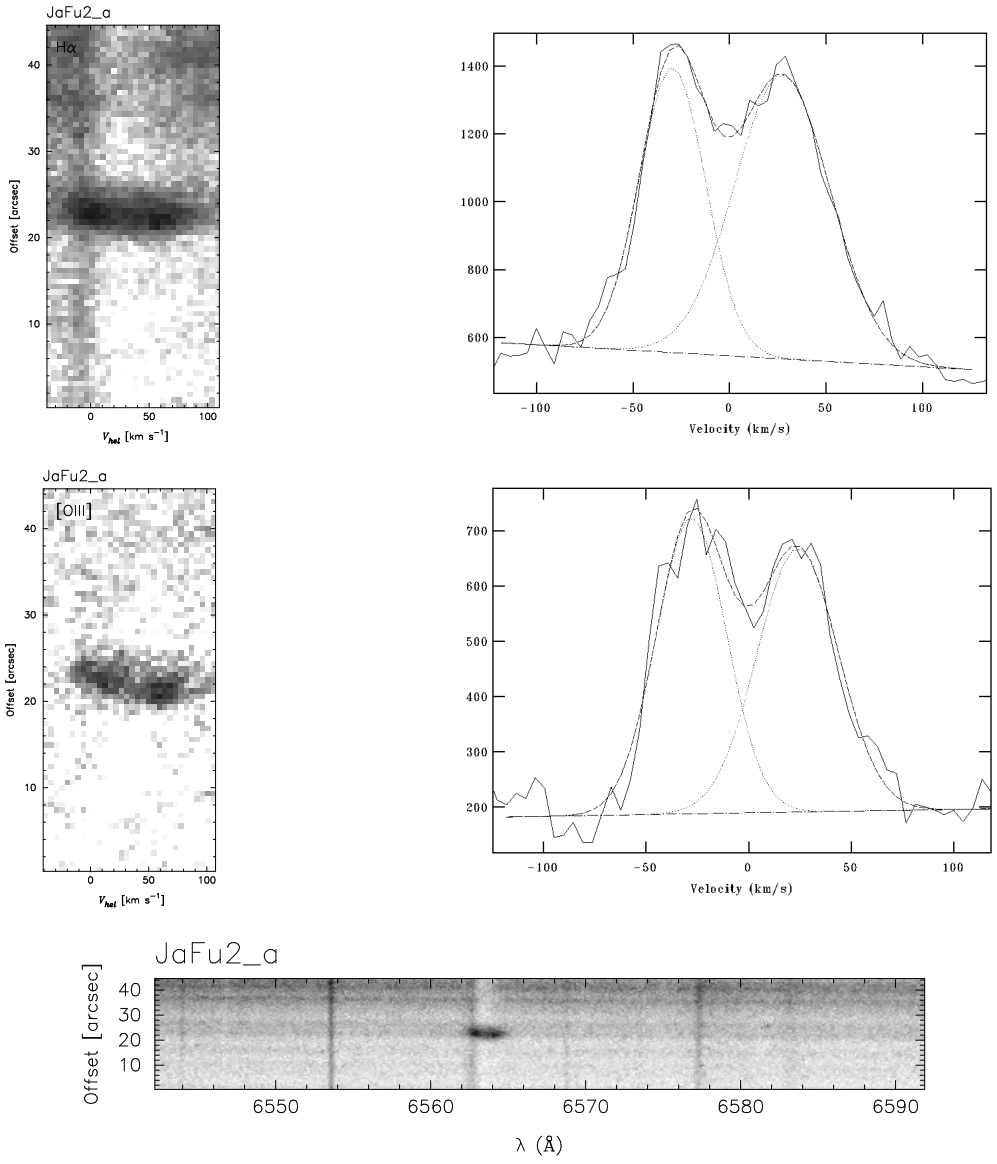

Figure B.10 **Image and data of the PN JaFu2 for slit a. Same as Figure B.4.**

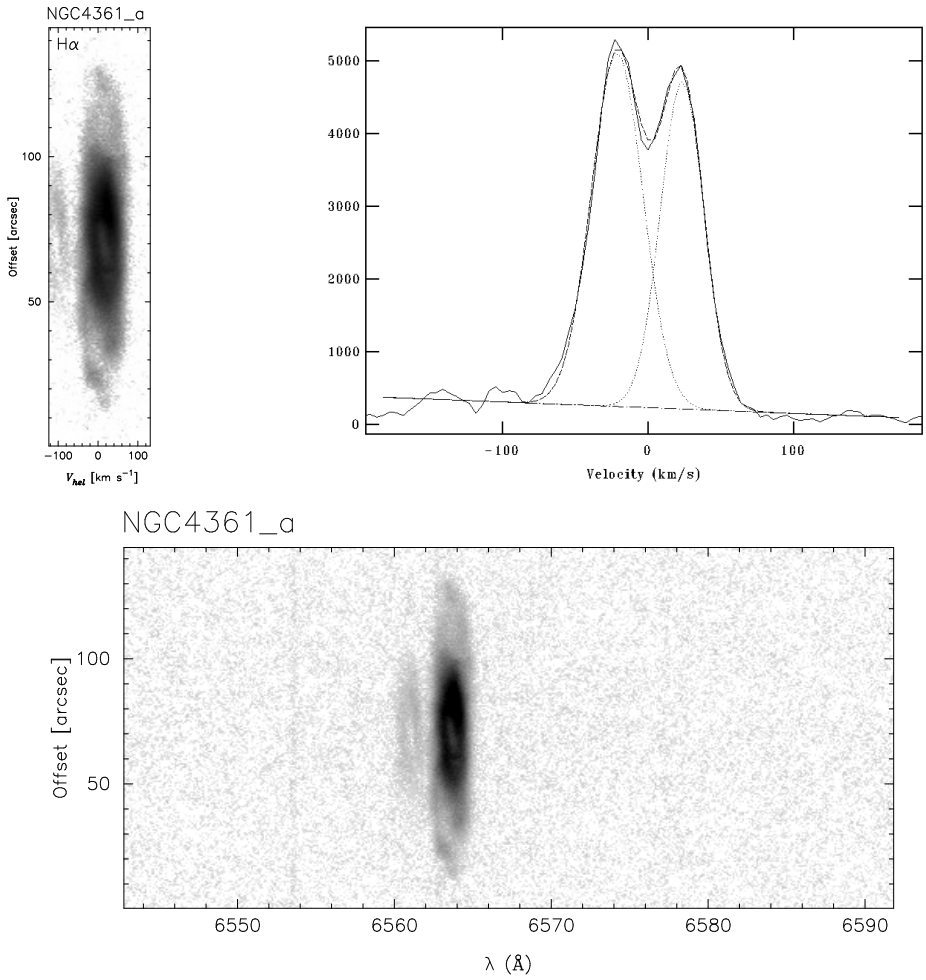

Figure B.11 **Image and data of the PN NGC4361 for slit a. Same as Figure B.4.**

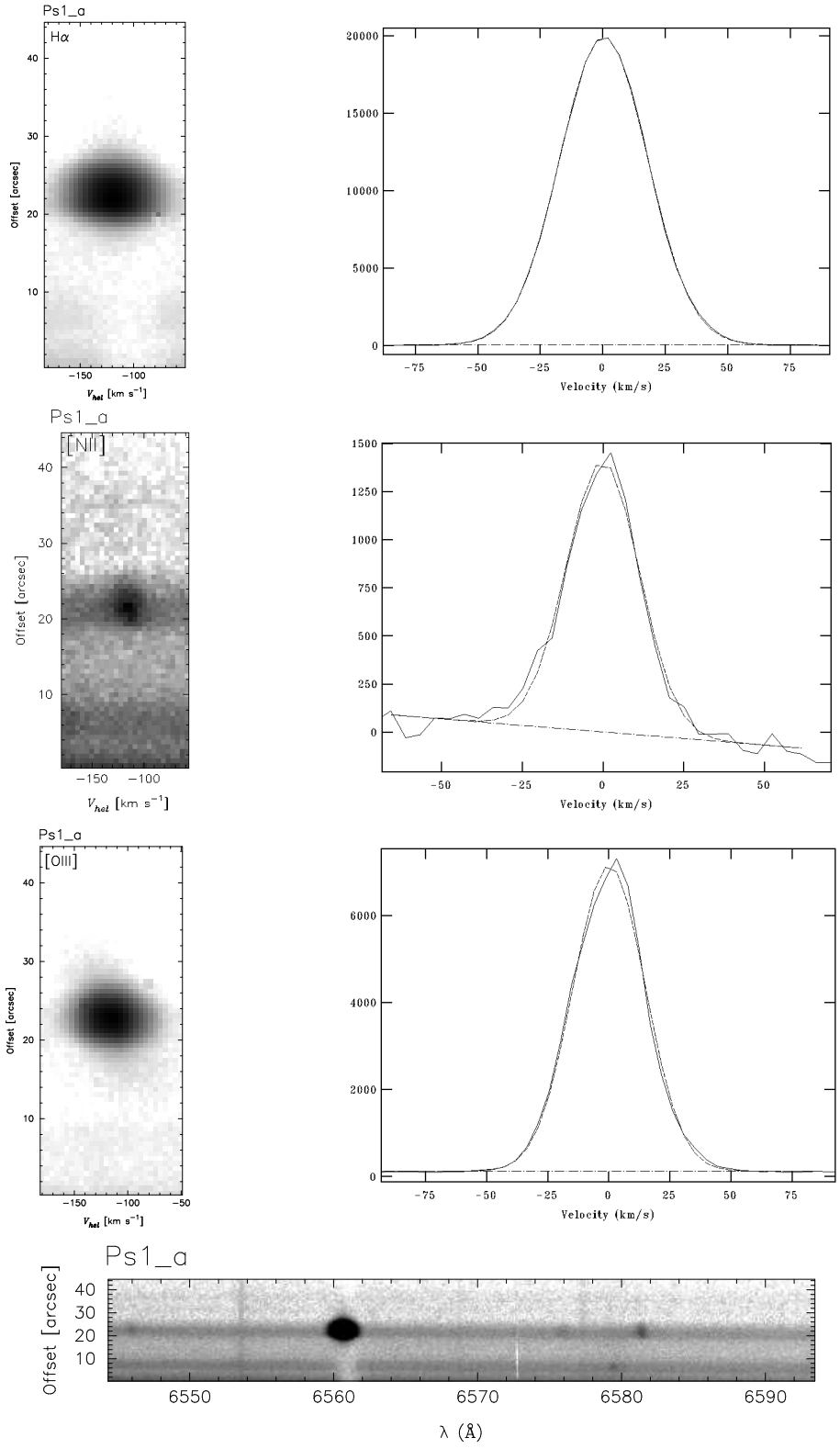

Figure B.12 **Image and data of the PN Ps1 for slit a. Same as Figure B.4.**

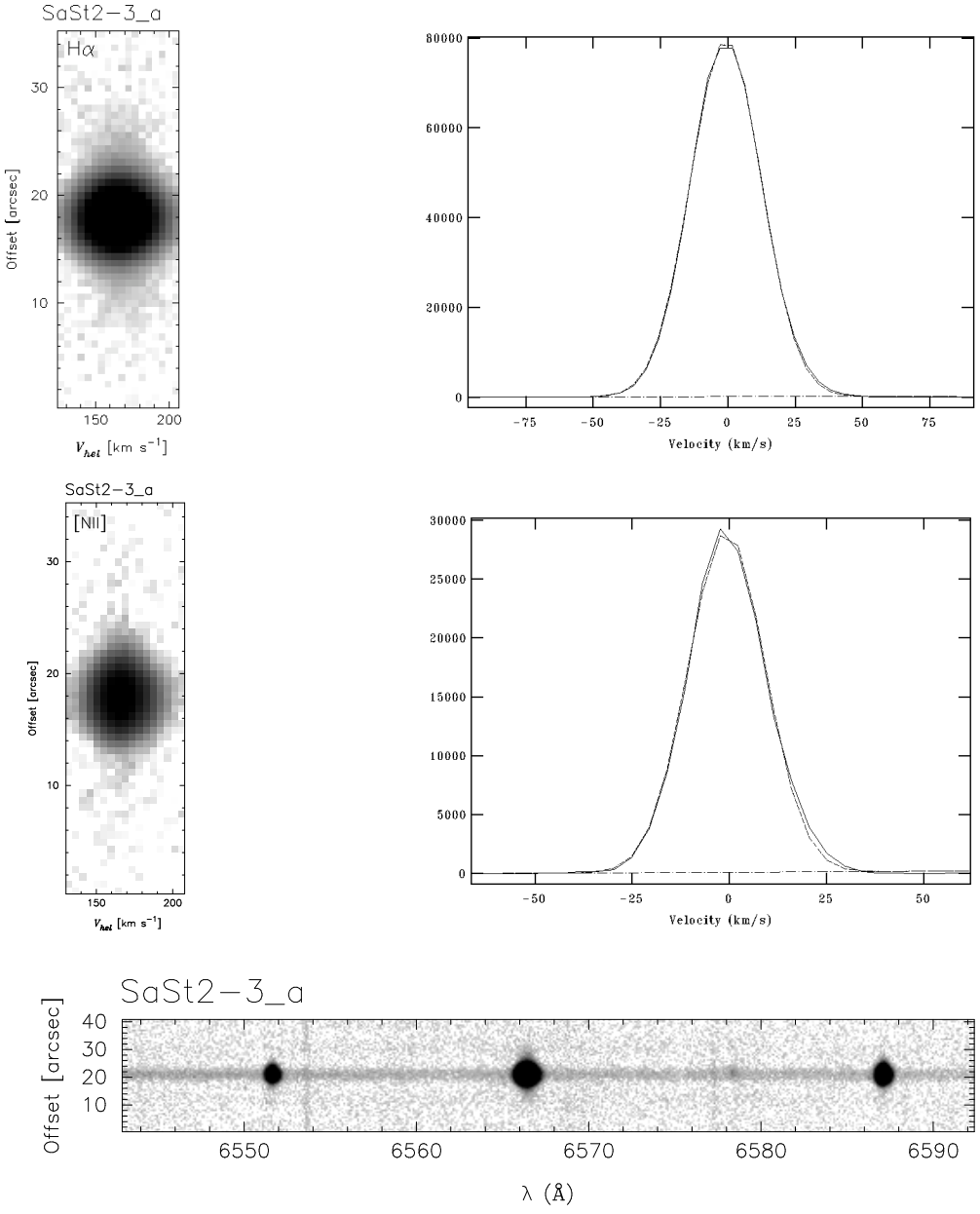

Figure B.13 **Image and data of the PN SaSt2-3 for slit a. Same as Figure B.4.**

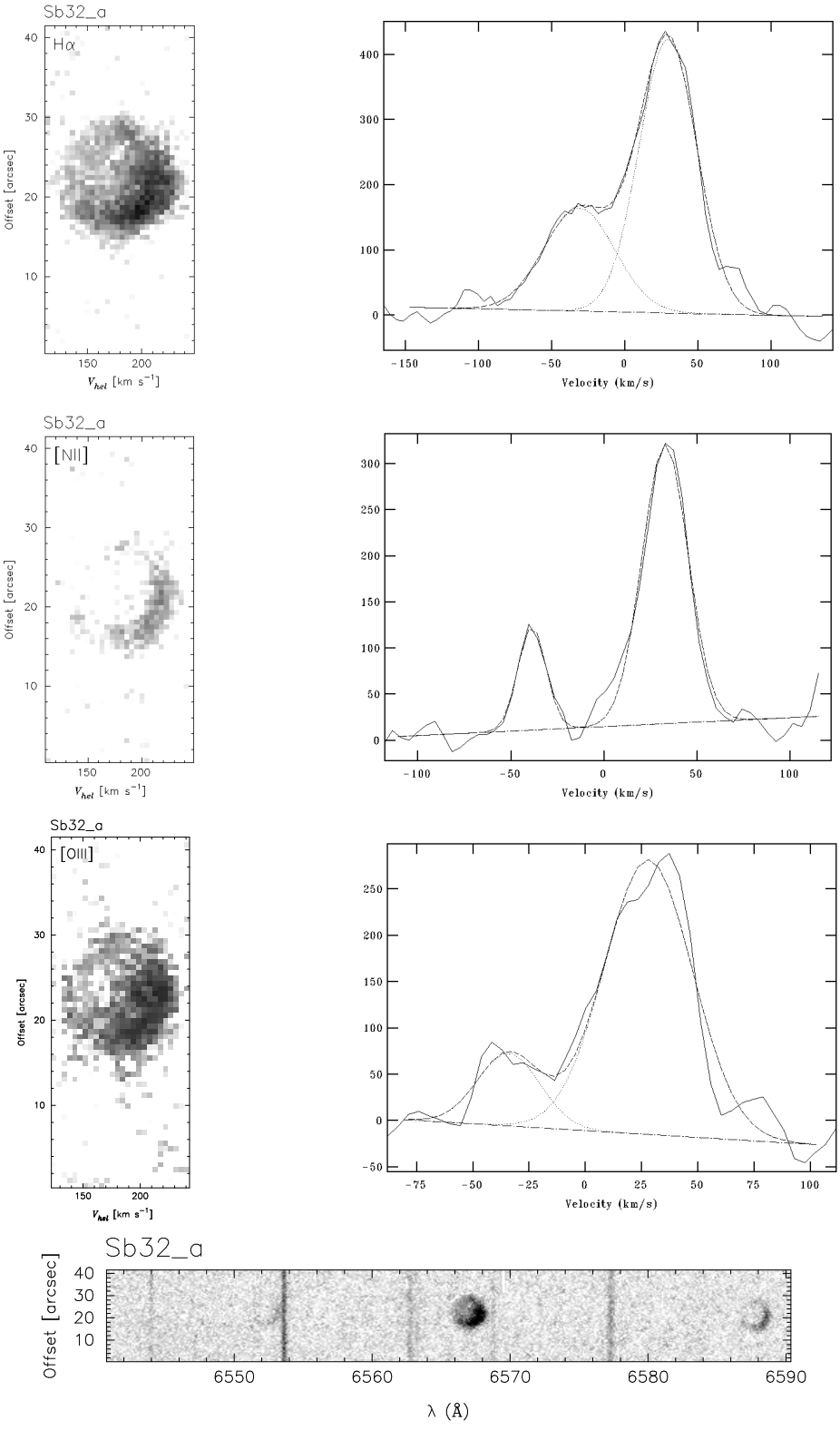

Figure B.14 **Image and data of the PN Sb32 for slit a. Same as Figure B.4.**

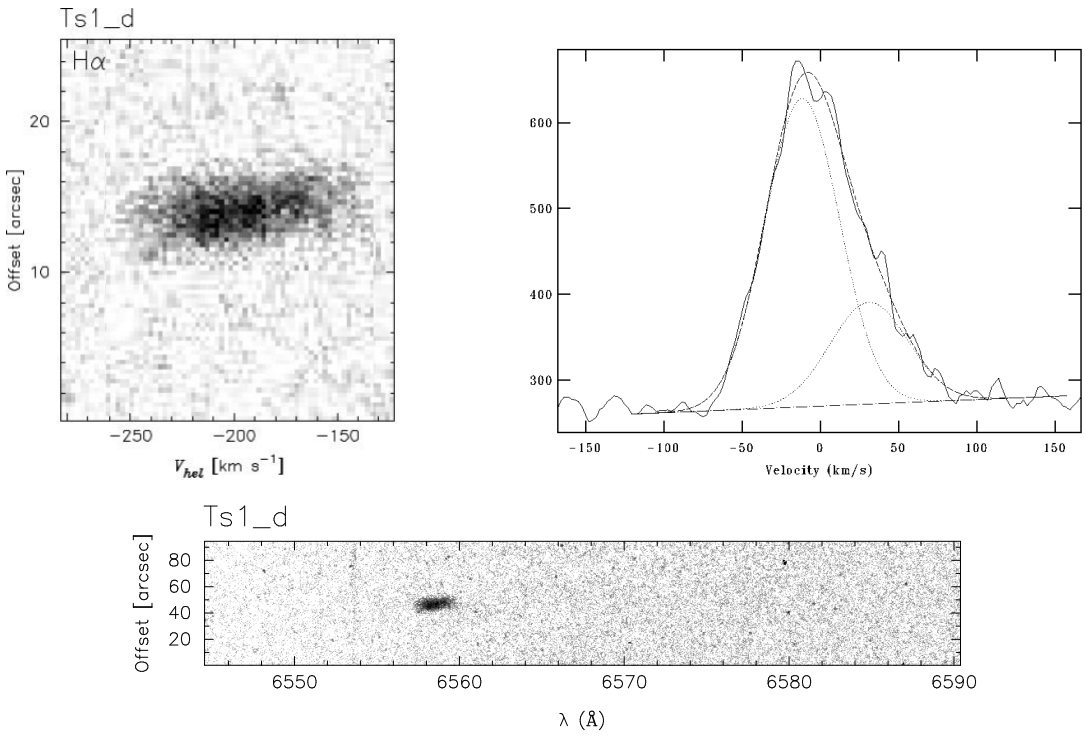

Figure B.15 **Image and data of the PN Ts1 for slit d. Same as Figure B.4.**

Appendix C

Low Metallicity PNe

Images and spectra of the PNe with Low Metal content, used in the analysis presented in section 3, asre shown in this Appendix. In the first five pages the image from the DSS2R for each PNe is presented, with the slit position indicated as a solid line. Their respective spectra can be found in the following pages, every PN in a single page.

The two-dimensional array position-velocity (P-V), calibrated in heliocentric velocity and angular scale, is shown for the emission lines available in each case, as well as the plot of the horizontal cut made on the spectra (using IRAF[1]) considered for velocity measurements. As in the case of the Evolved sample the expansion of the nebular shell of the PN was obtained at the point of maximum splitting of the line profile, averaging 10 lines of the spectral image in most cases. For the faintest objects the average was calculated using the lines enough to obtain a signal to noise to obtained reliable measurements. We take half of the peak to peak distance between the blue- and redshifted components or half of the resulting FWHM as the velocity of the nebular shell depending on each case.

At the bottom panel is the full spectral range used, where the emission lines detected are [NII] $\lambda\lambda$6548,6584, HeII λ6560, and H λ6562.8, for each PN. The spectra in this case is calibrated in wavelength and angular scale.

[1]IRAF is distributed by the National Optical Astronomy Observatories, which are operated by the Association of Universities for Research in Astronomy, Inc., under cooperative agreement with the National Science Foundation.

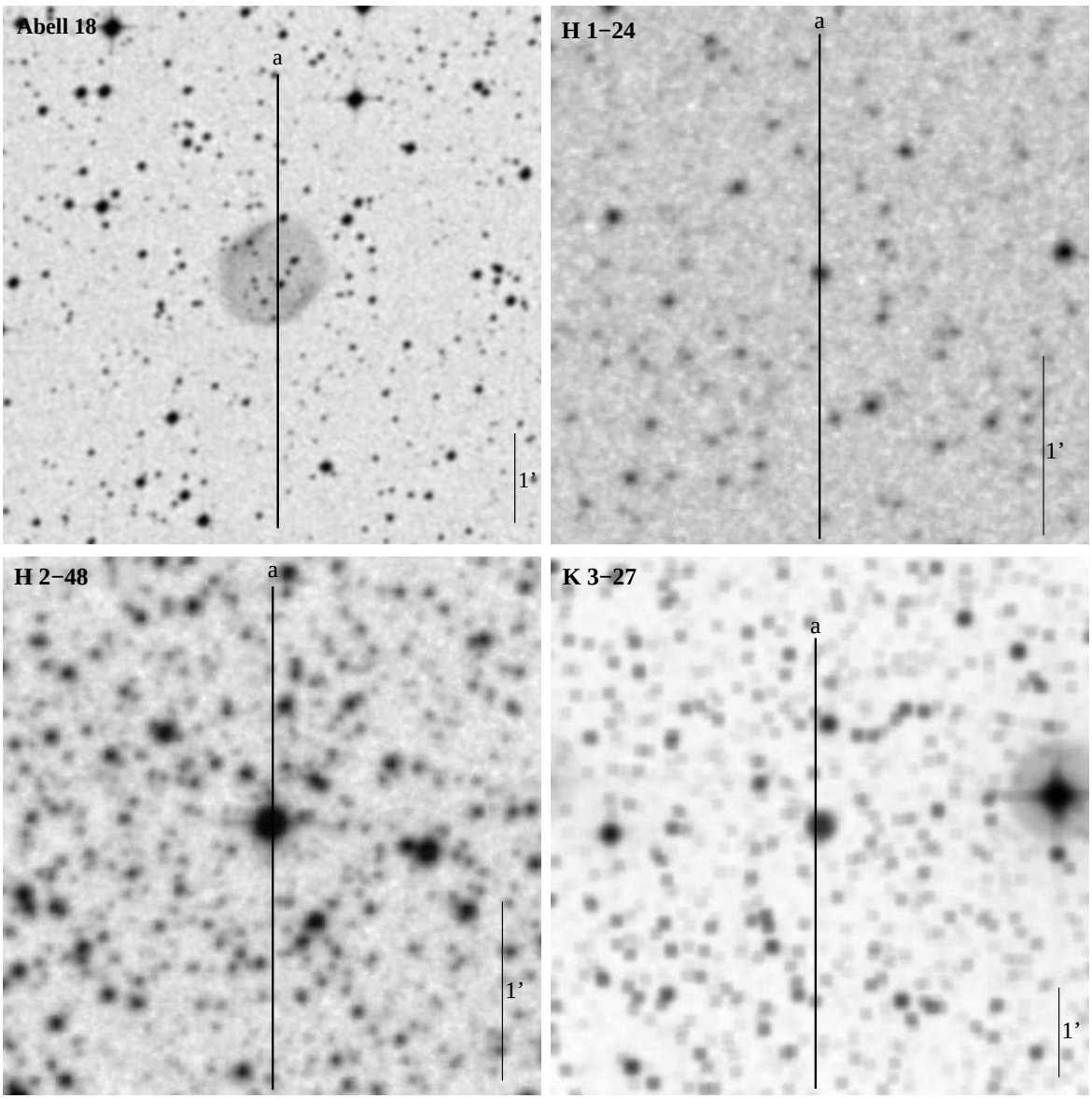

Figure C.1 **Images of the Low Metal PNe taken from the DSS2R. The slit position is indicated as a solid line.**

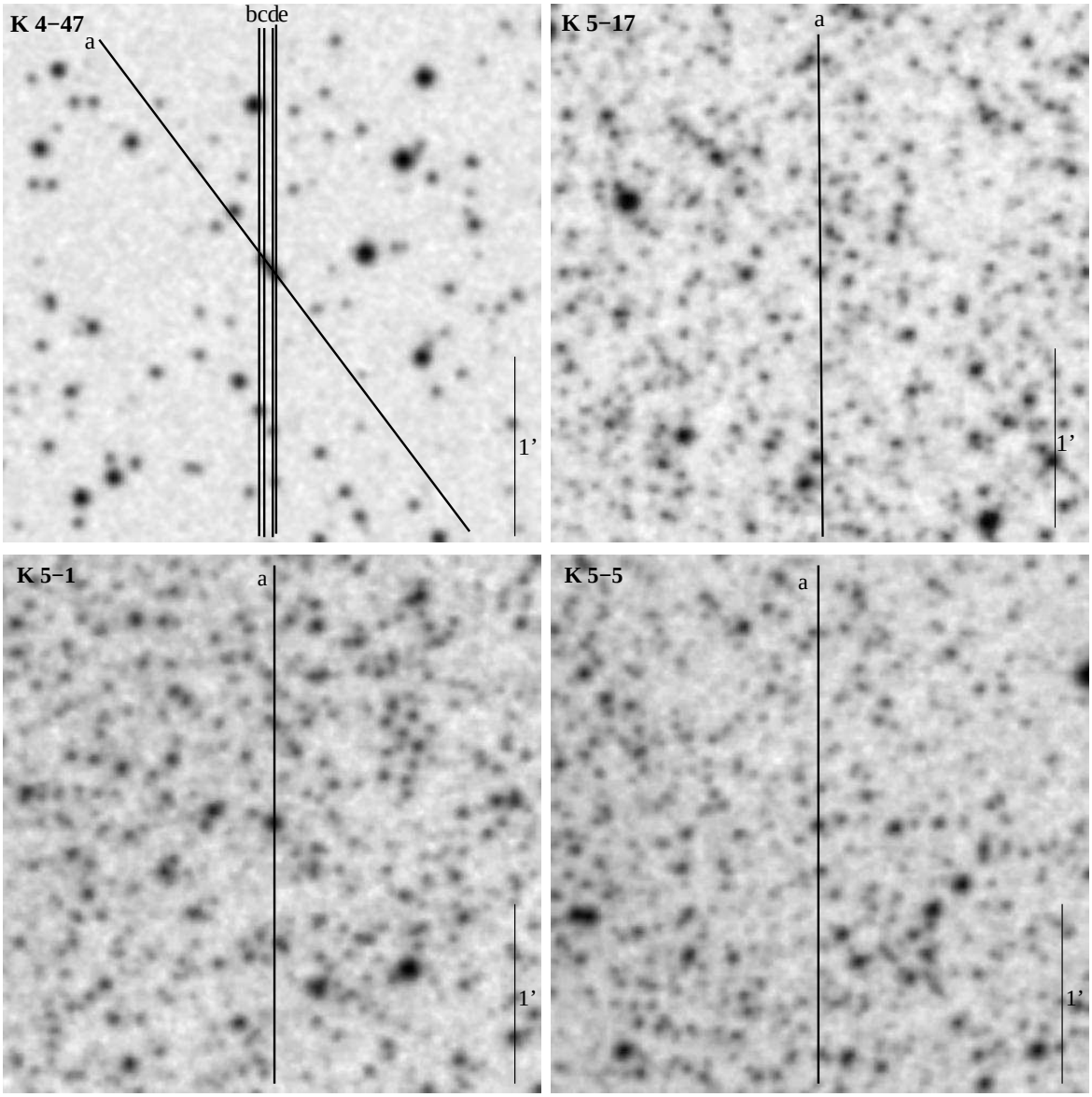

Figure C.2 **Same as Figure C.1.**

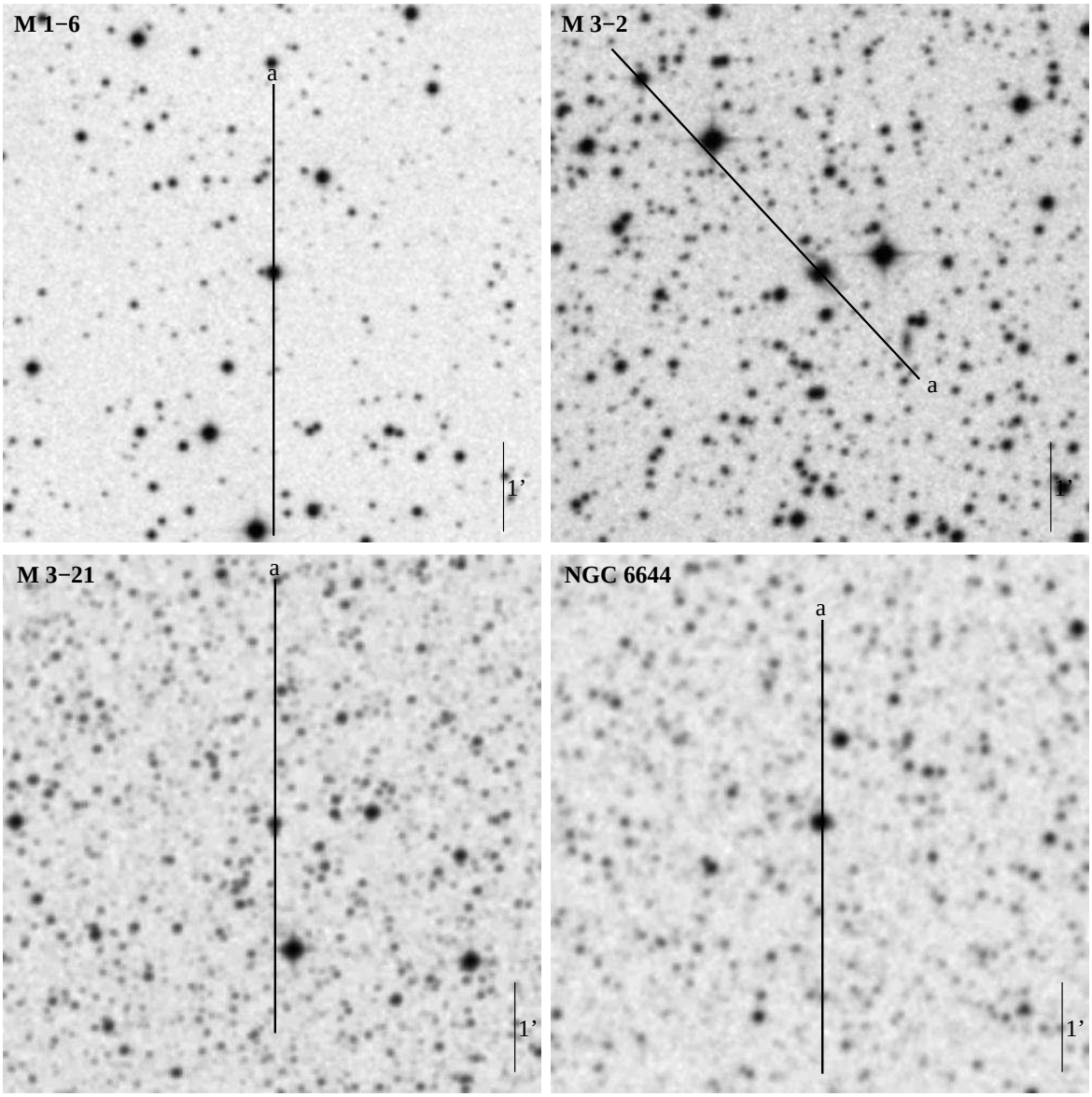

Figure C.3 **Same as Figure C.1**

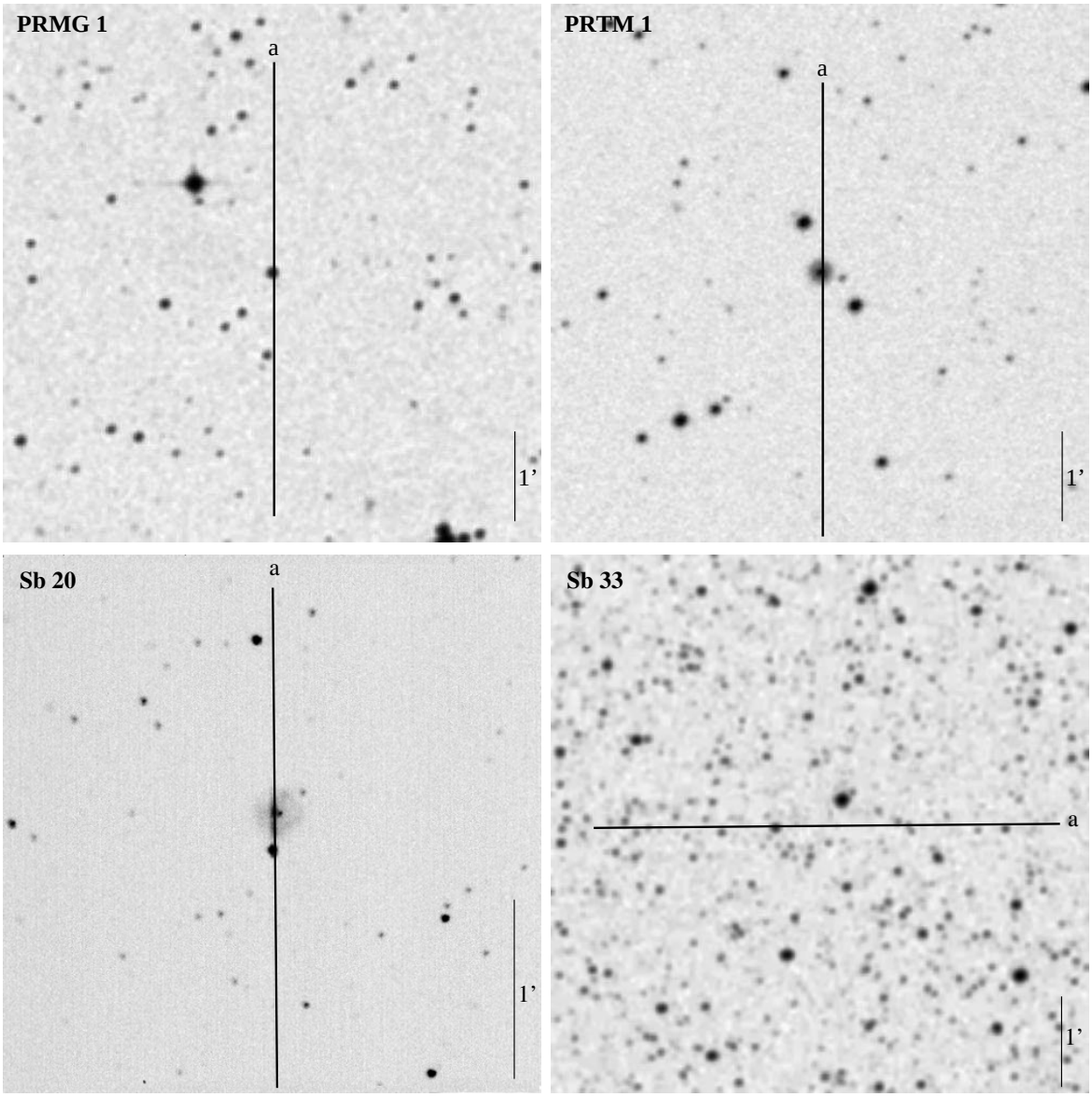

Figure C.4 **Same as Figure C.1**

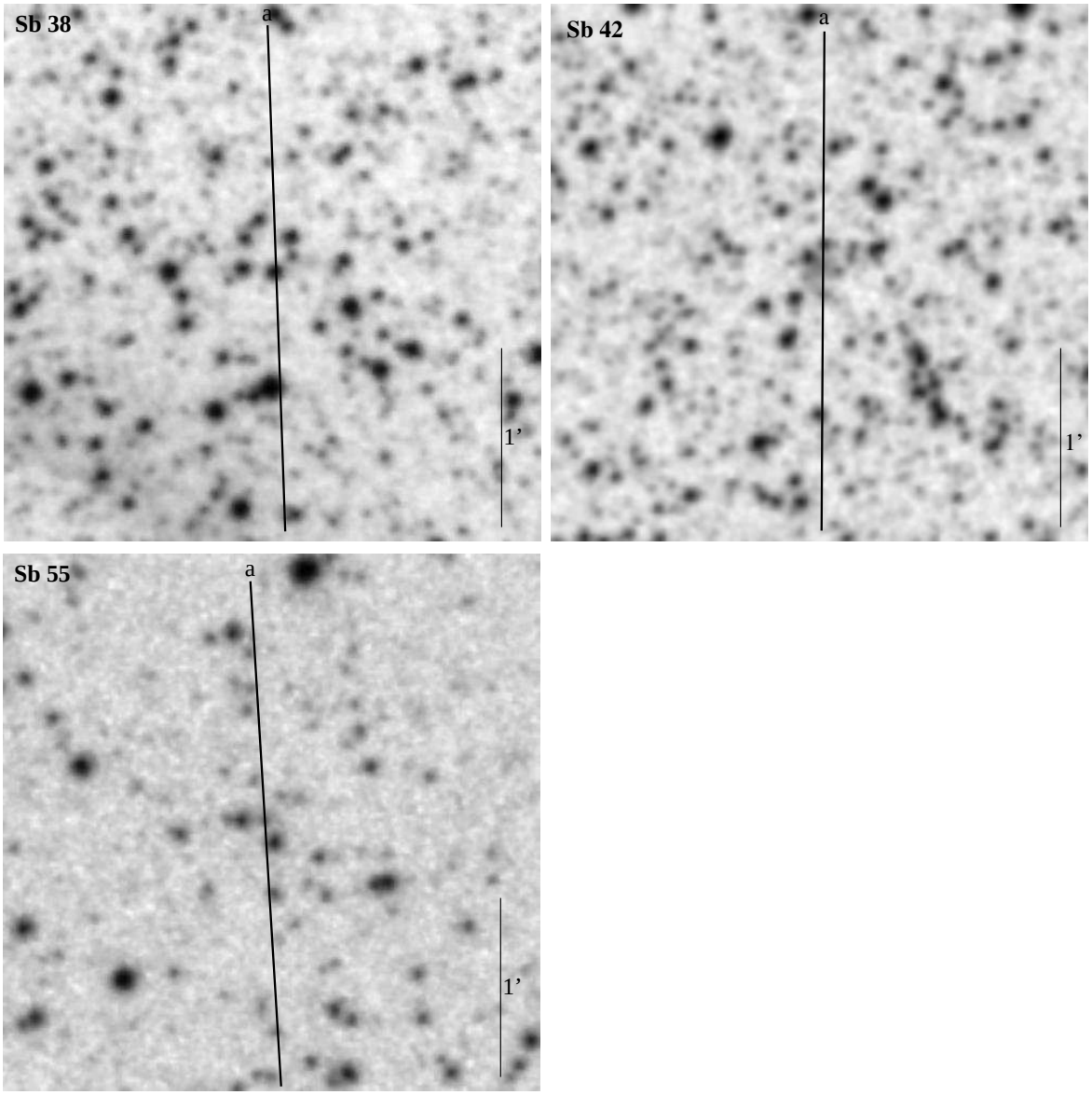

Figure C.5 **Same as Figure C.1**

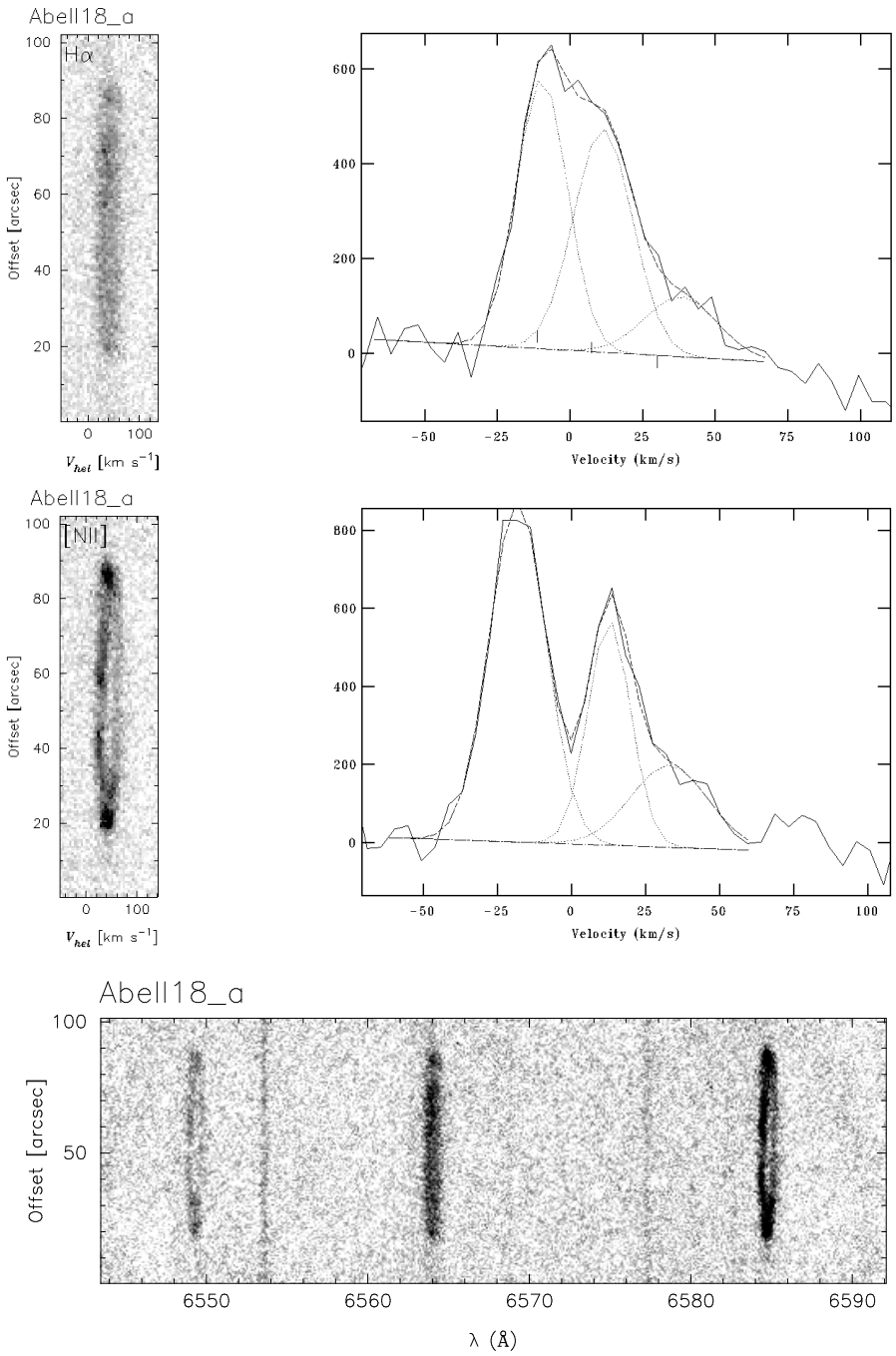

Figure C.6 **Spectra and measurements of the PN A18 for slit a. The left panel present, as in Fig.B.4, the two-dimensional array position-velocity (P-V) for the emission line labeled in the upper-left corner. The right panel shows a plot with the gaussian fit used to velocity measurements for each emission line. At the bottom panel is the full spectral range observed for this PN, calibrated in wavelength and angular scale.**

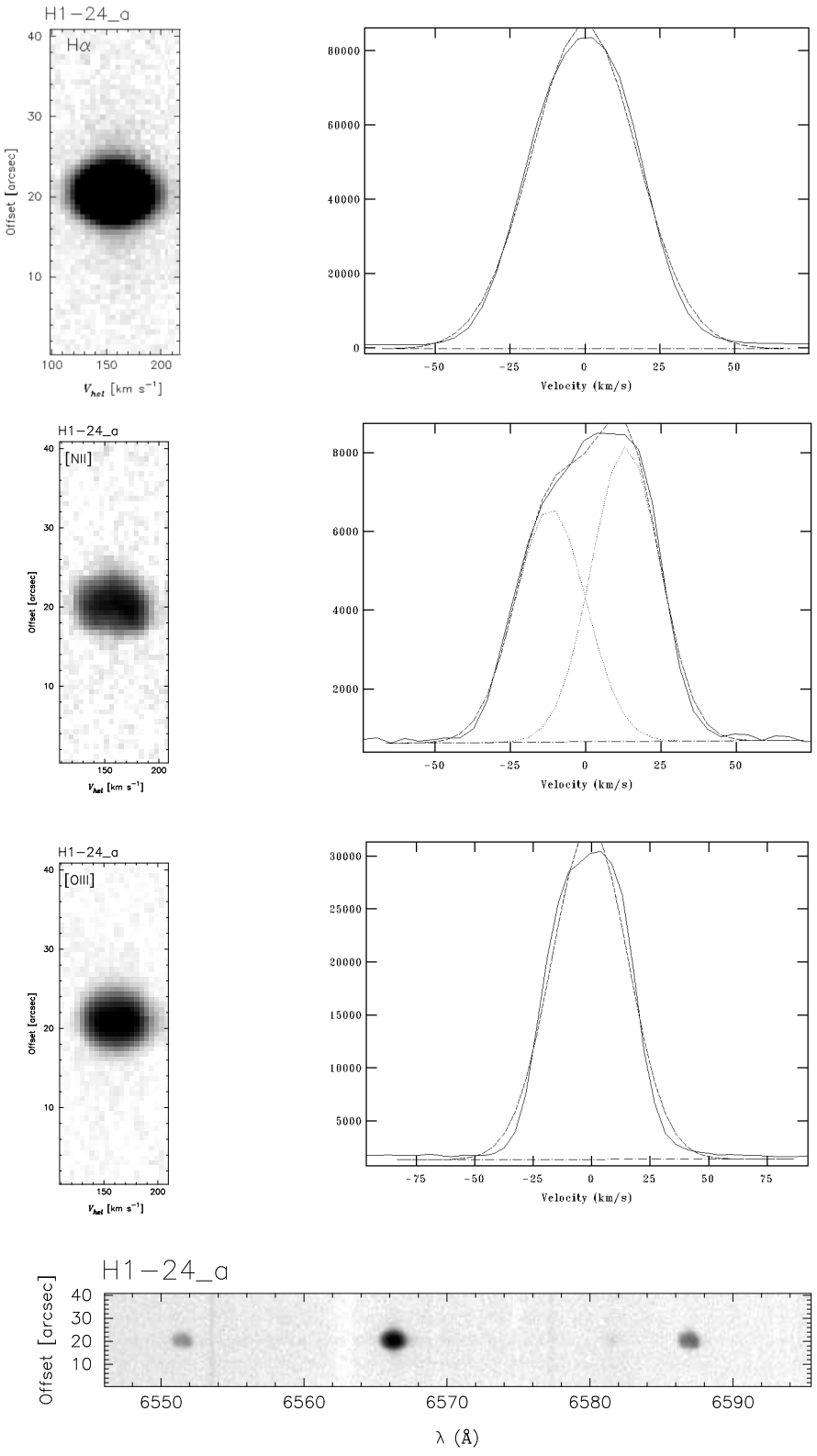

Figure C.7 **Image and data of the PN H1-24 for slit a. Same as Figure C.6.**

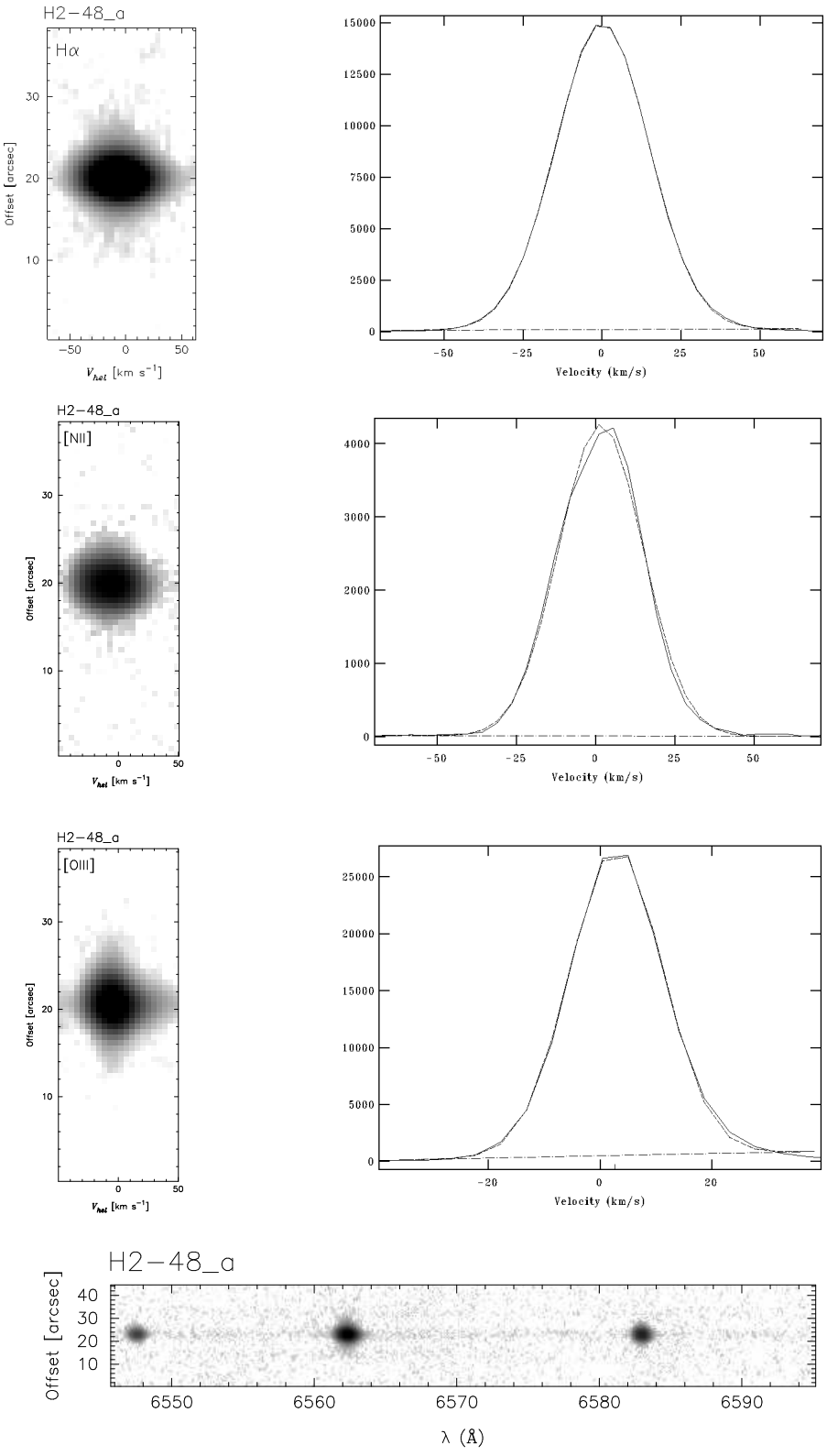

Figure C.8 **Image and data of the PN H2-48 for slit a. Same as Figure C.6.**

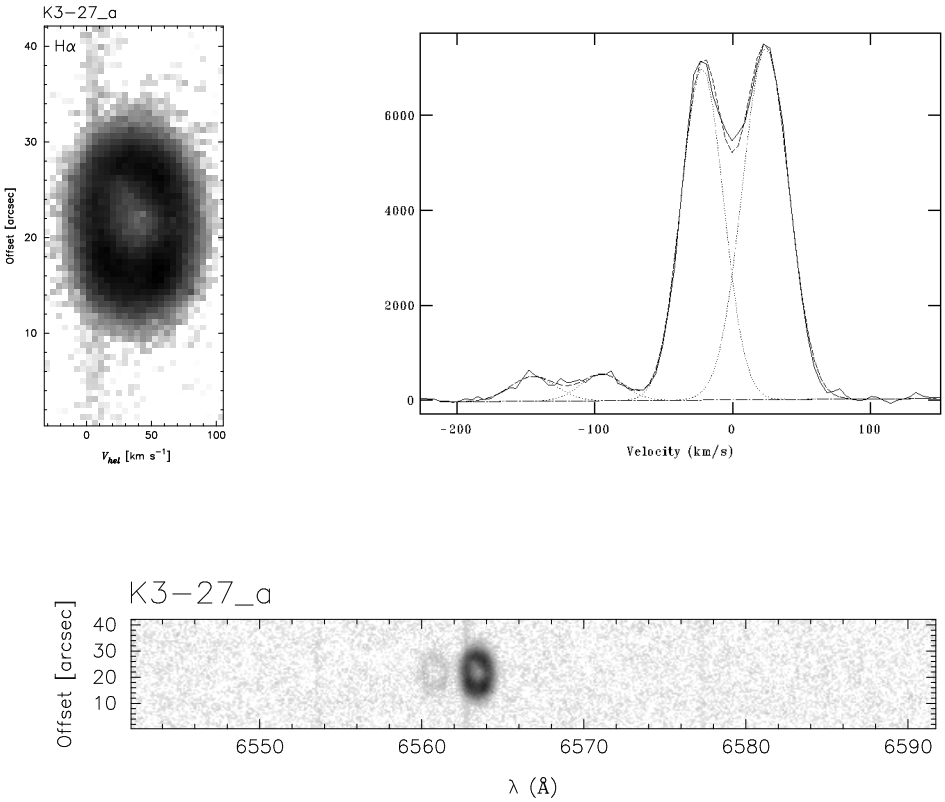

Figure C.9 **Image and data of the PN K3-27 for slit a. Same as Figure C.6.**

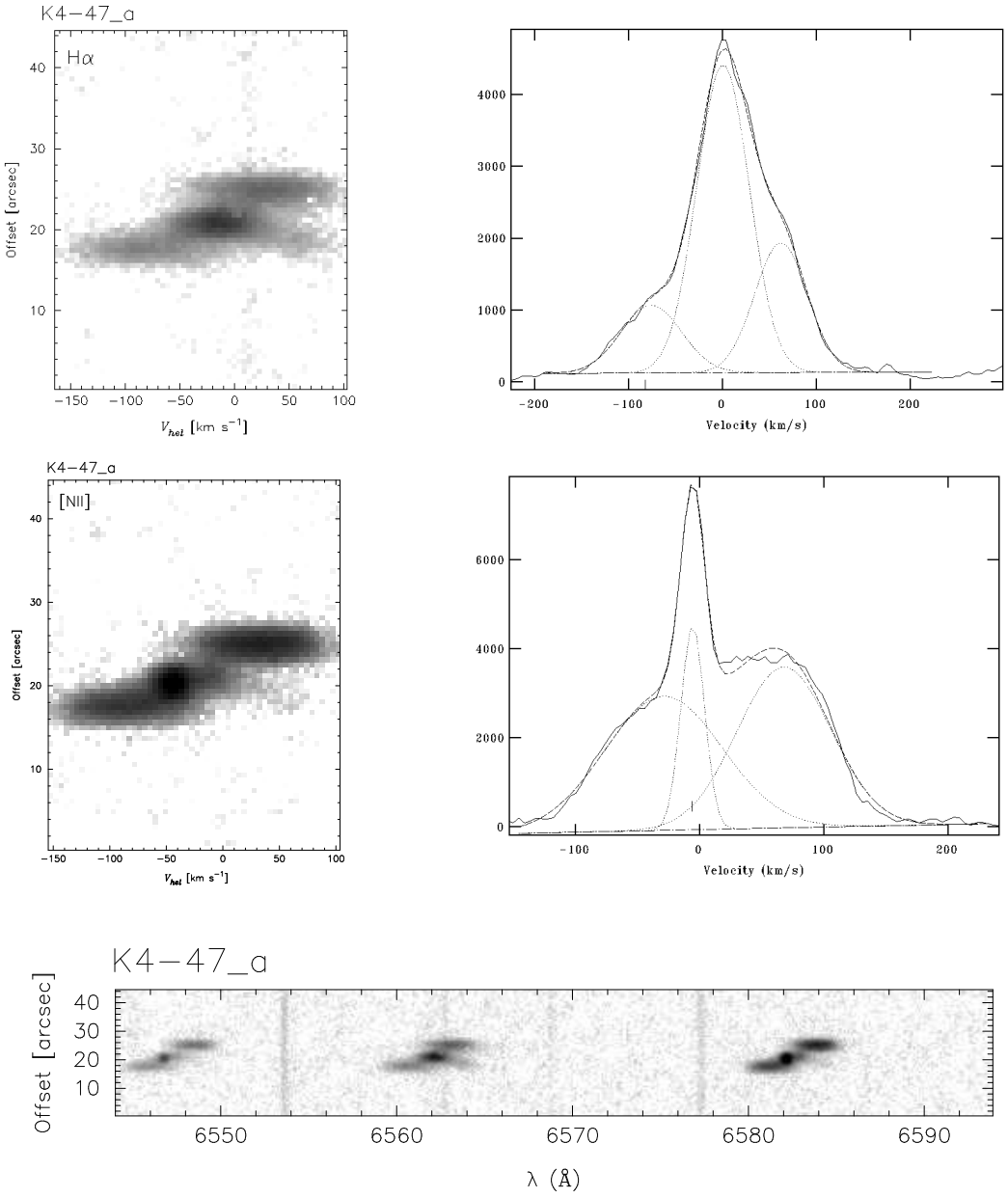

Figure C.10 **Image and data of the PN K4-47 for slit a. Same as Figure C.6.**

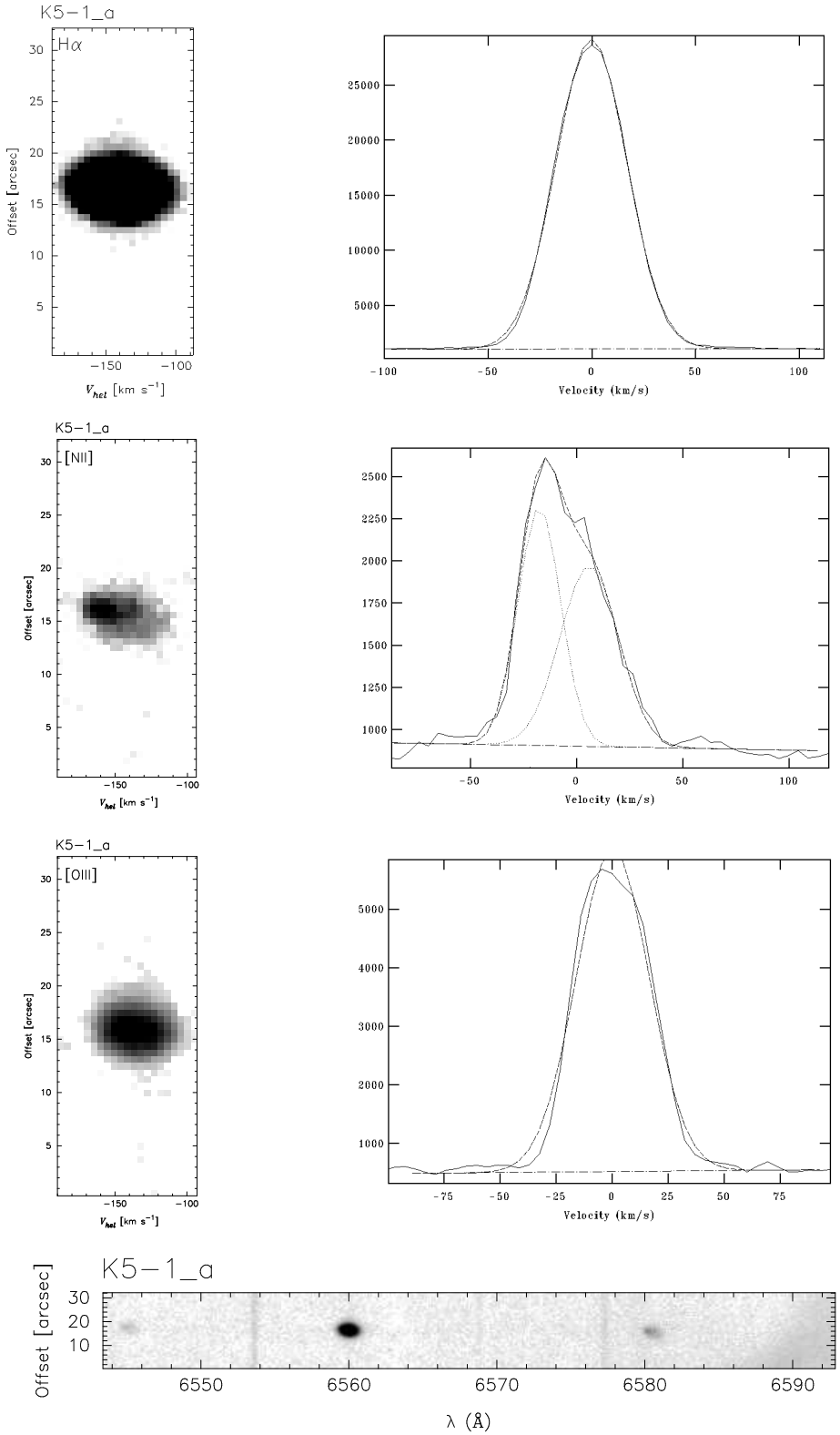

Figure C.11 **Image and data of the PN K5-1 for slit a. Same as Figure C.6.**

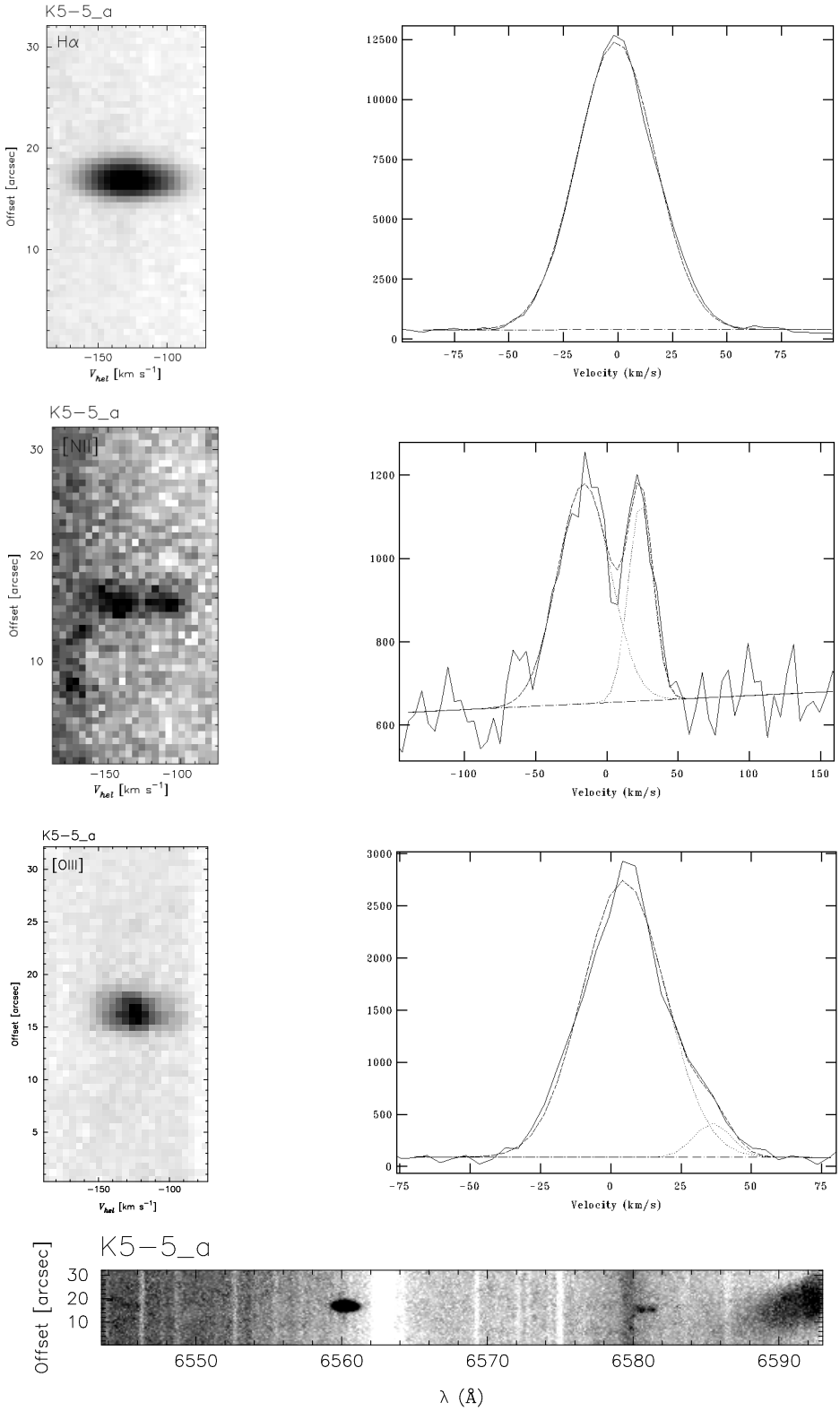

Figure C.12 **Image and data of the PN K5-5 for slit a. Same as Figure C.6.**

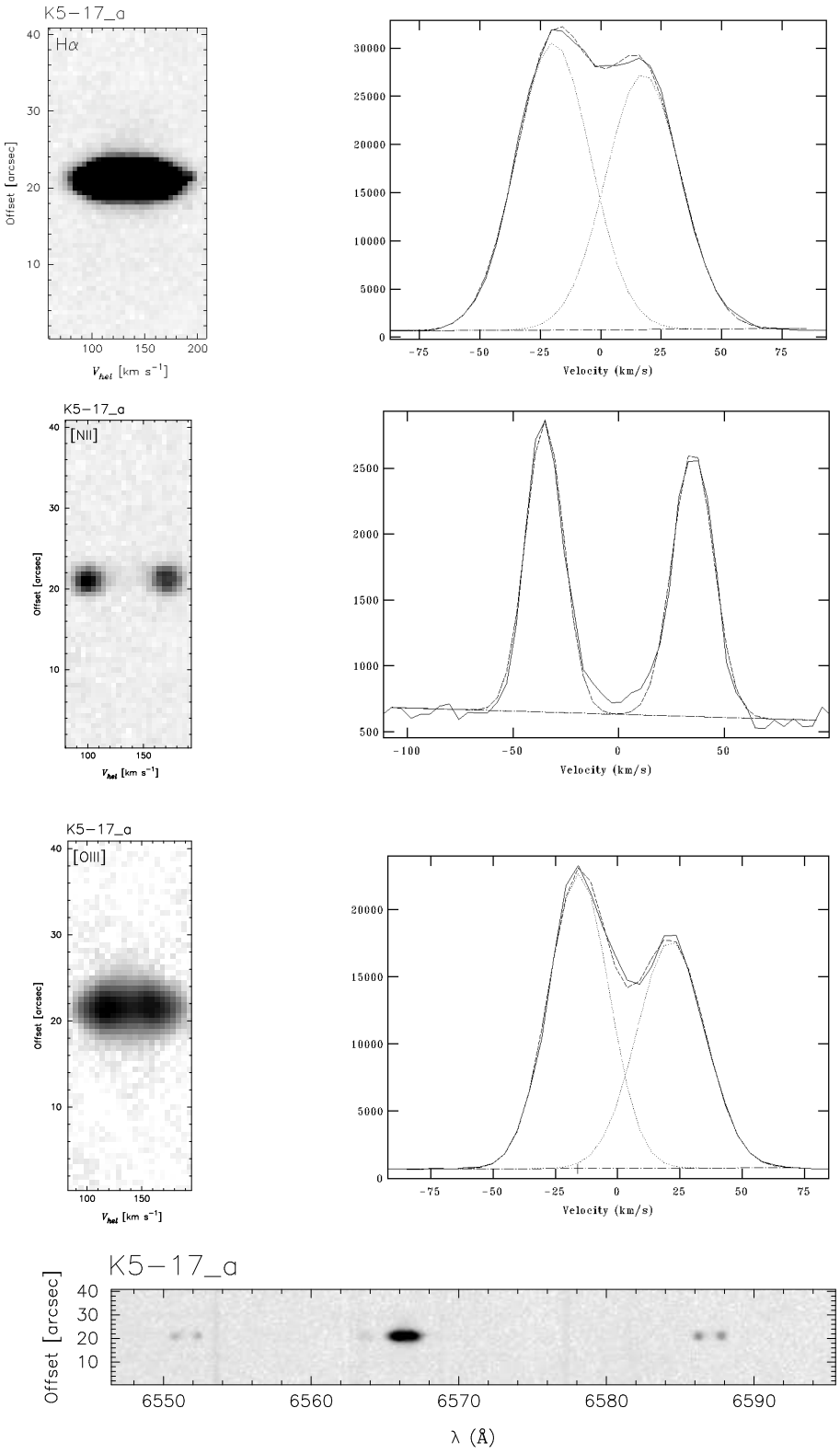

Figure C.13 **Image and data of the PN K5-17 for slit a. Same as Figure C.6.**

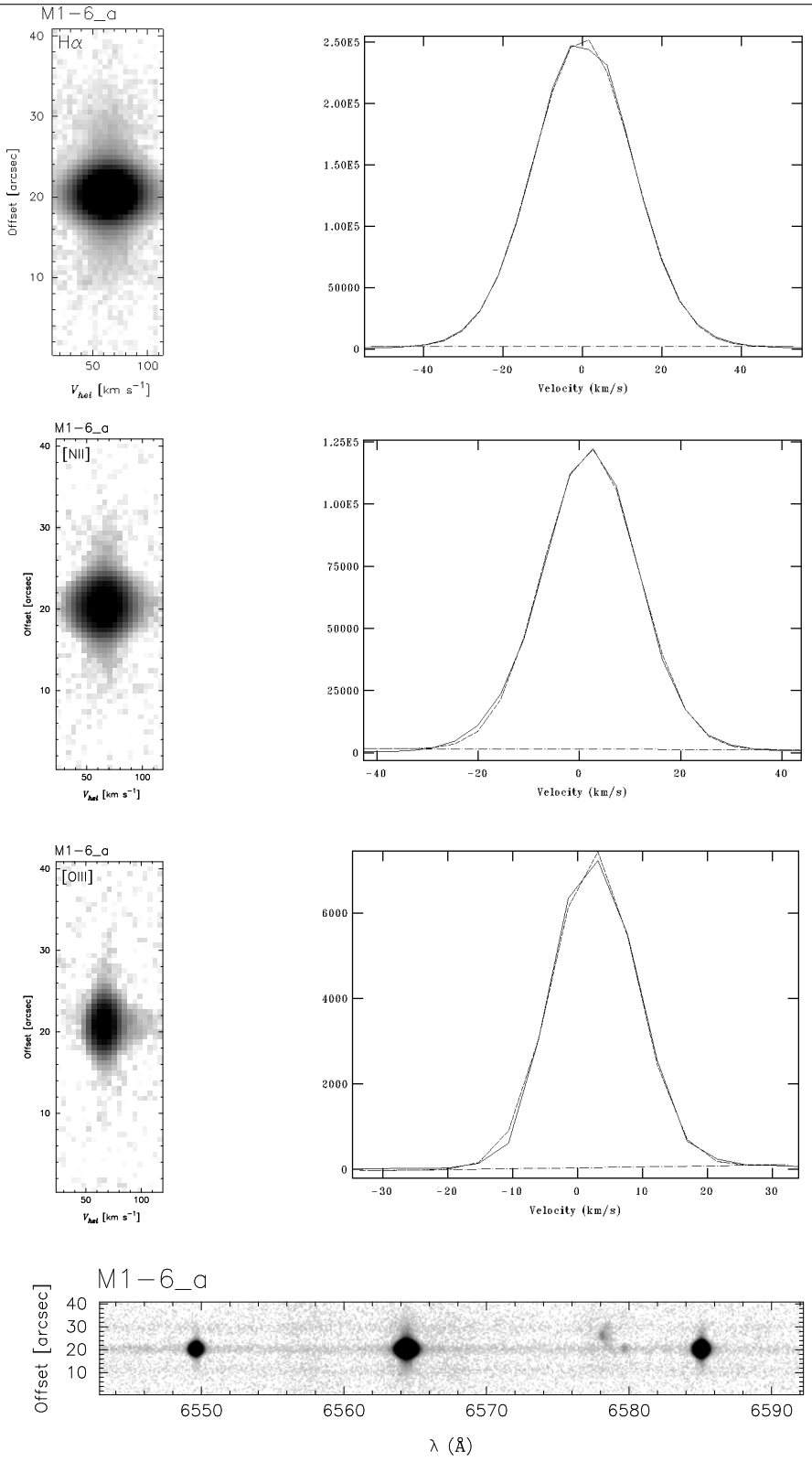

Figure C.14 **Image and data of the PN M1-6 for slit a. Same as Figure C.6.**

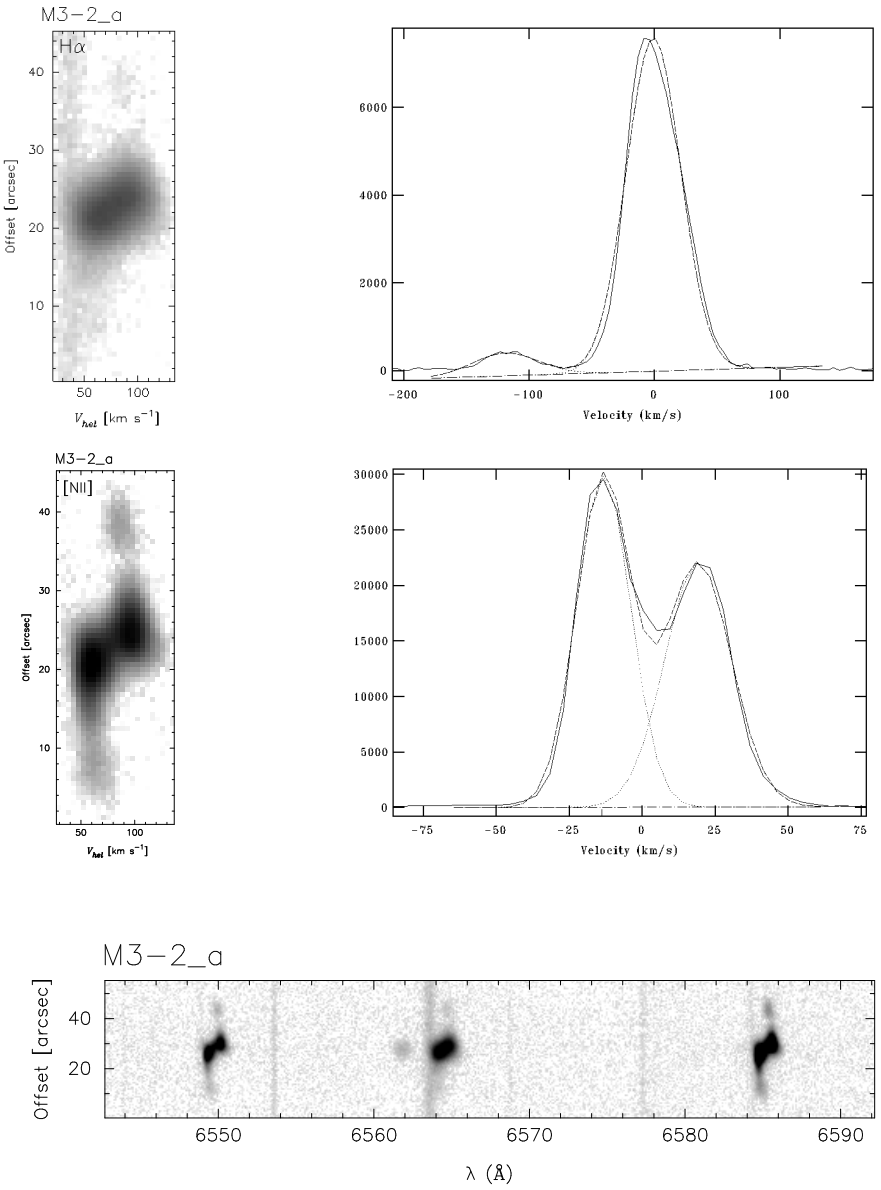

Figure C.15 **Image and data of the PN M3-2 for slit a. Same as Figure C.6.**

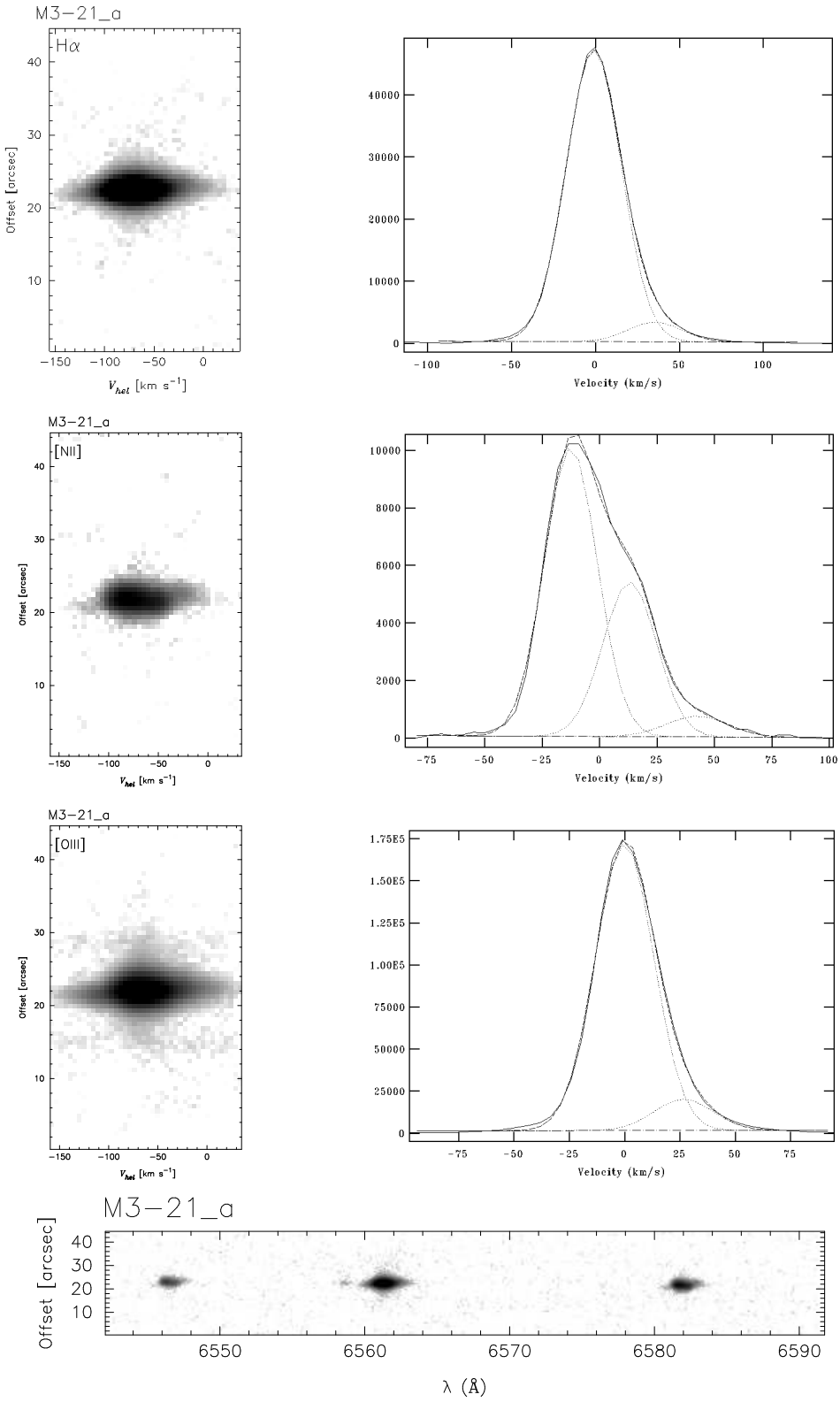

Figure C.16 **Image and data of the PN M3-21 for slit a. Same as Figure C.6.**

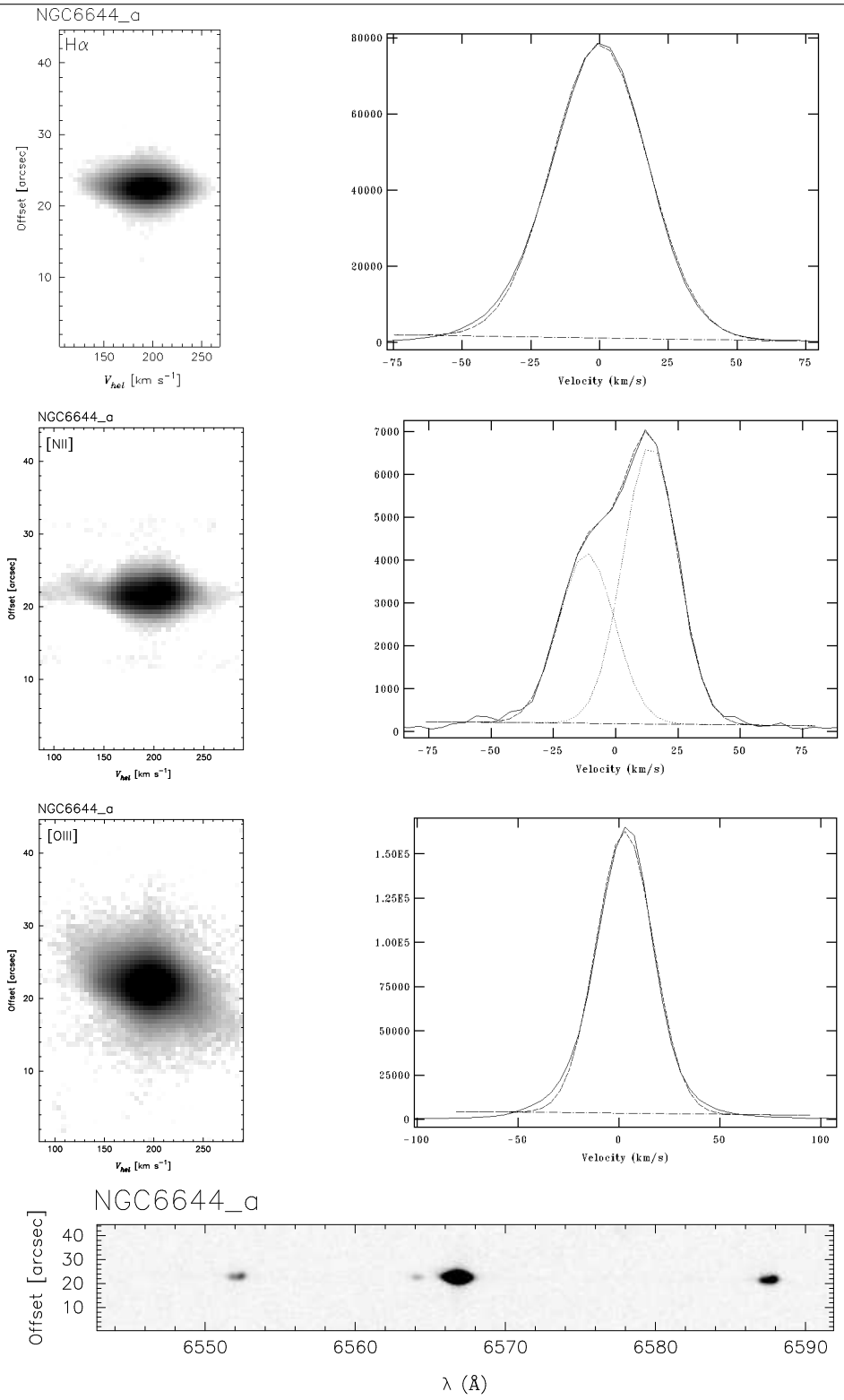

Figure C.17 **Image and data of the PN NGC6644 for slit a. Same as Figure C.6.**

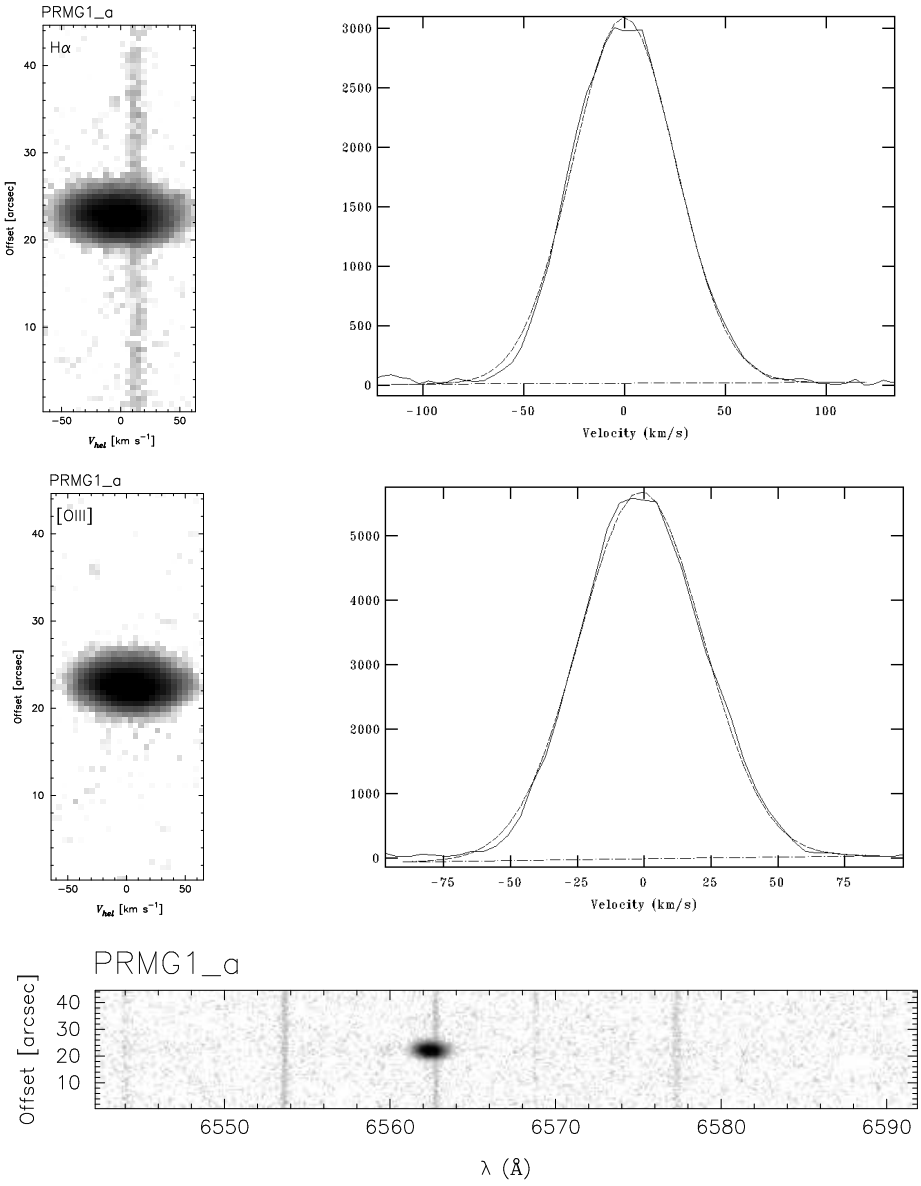

Figure C.18 **Image and data of the PN PRMG1 for slit a. Same as Figure B.4.**

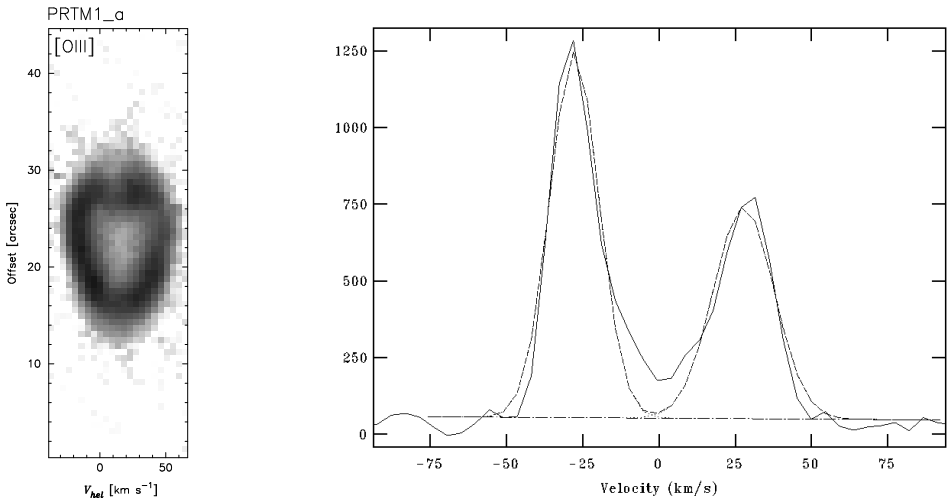

Figure C.19 **Image and data of the PN PRTM1 for slit a. Same as Figure B.4. Full spectral range not available in this case..**

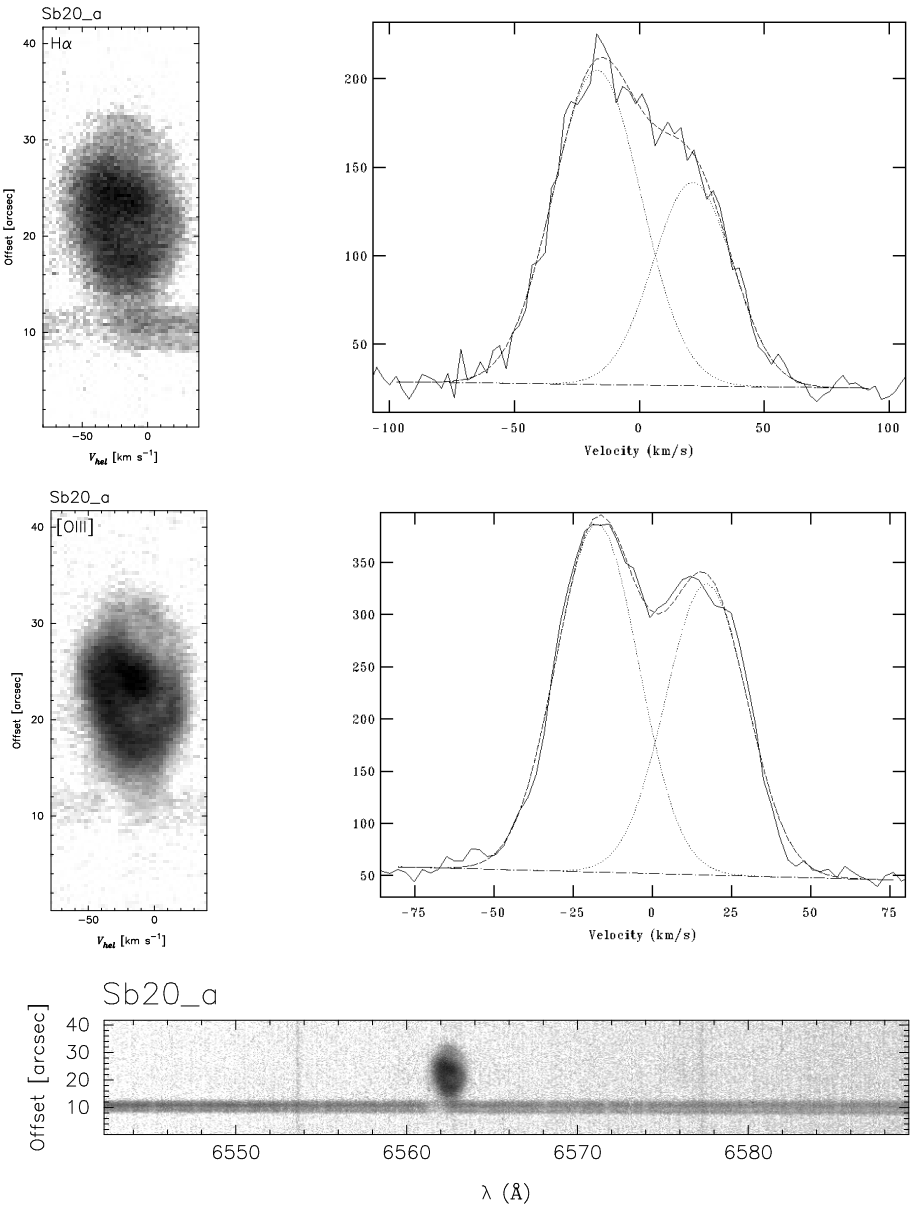

Figure C.20 **Image and data of the PN Sb20 for slit a. Same as Figure C.6.**

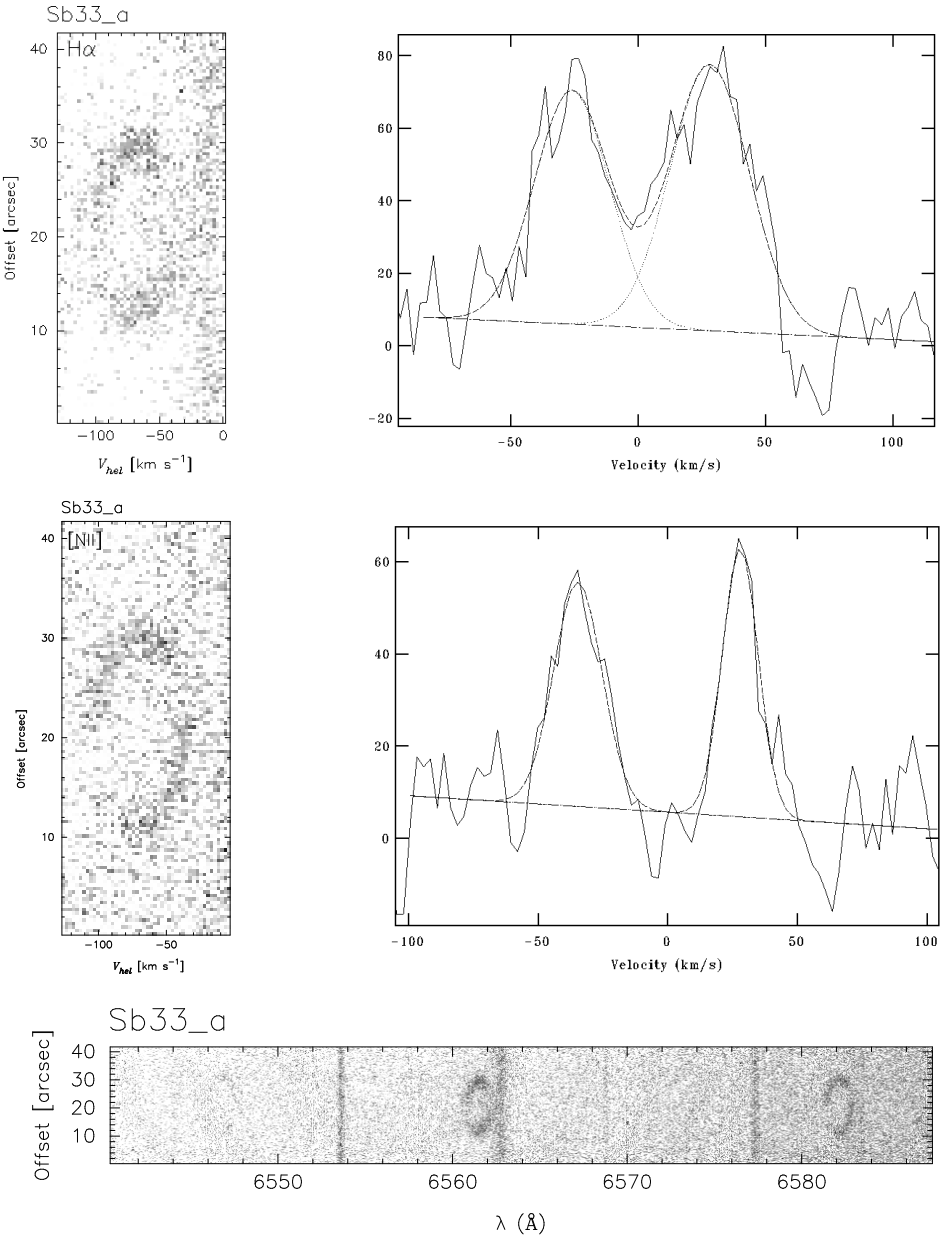

Figure C.21 **Image and data of the PN Sb33 for slit a. Same as Figure C.6.**

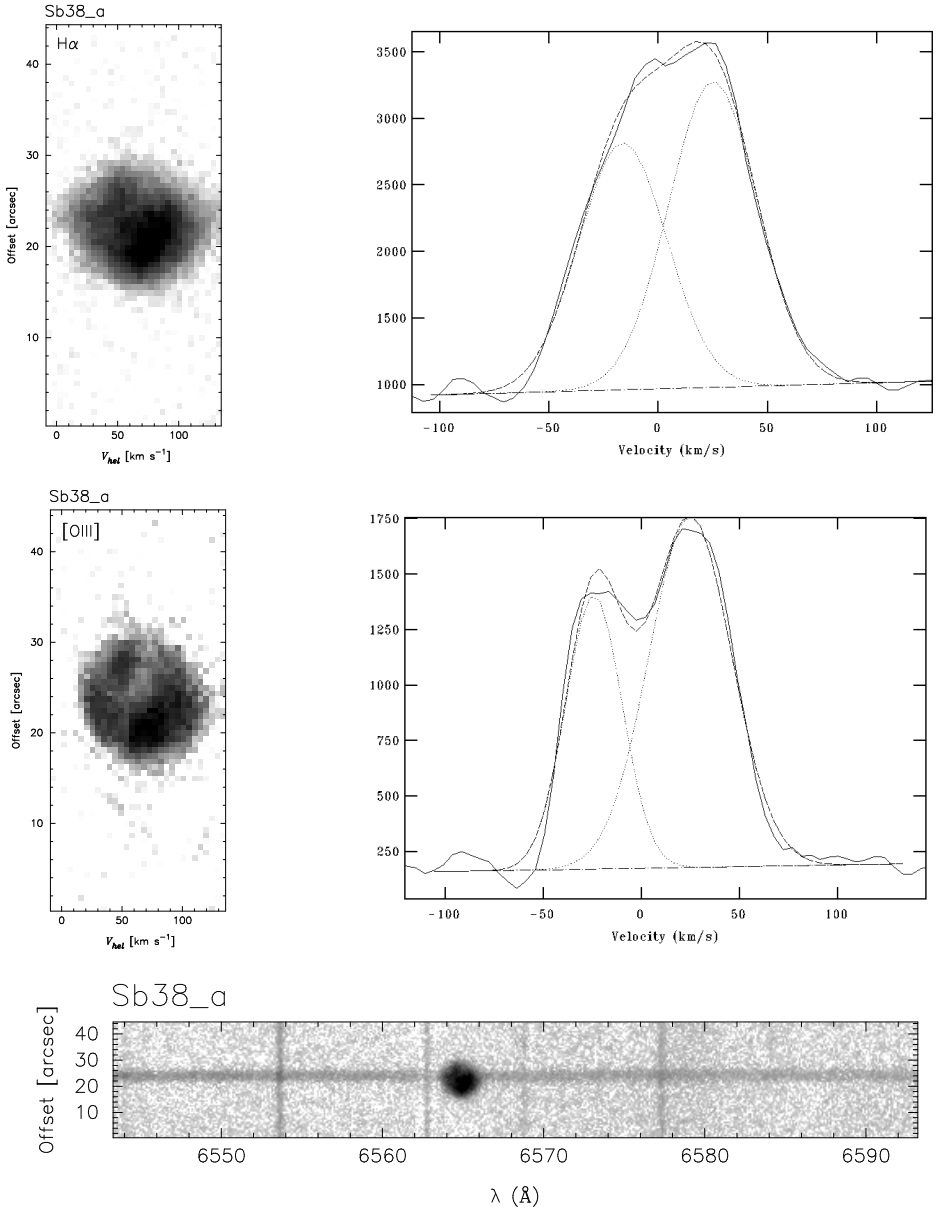

Figure C.22 **Image and data of the PN Sb38 for slit a. Same as Figure C.6.**

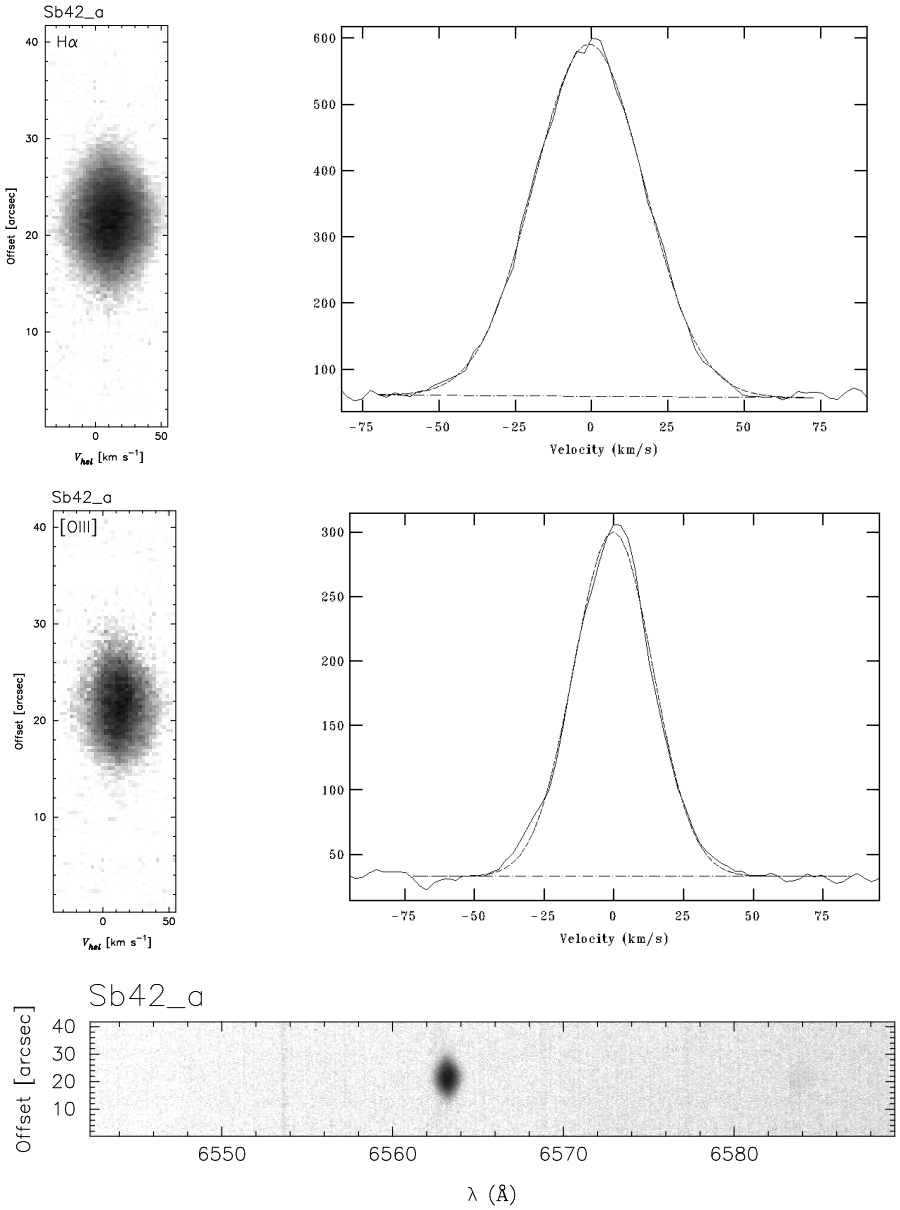

Figure C.23 **Image and data of the PN Sb42 for slit a. Same as Figure C.6.**

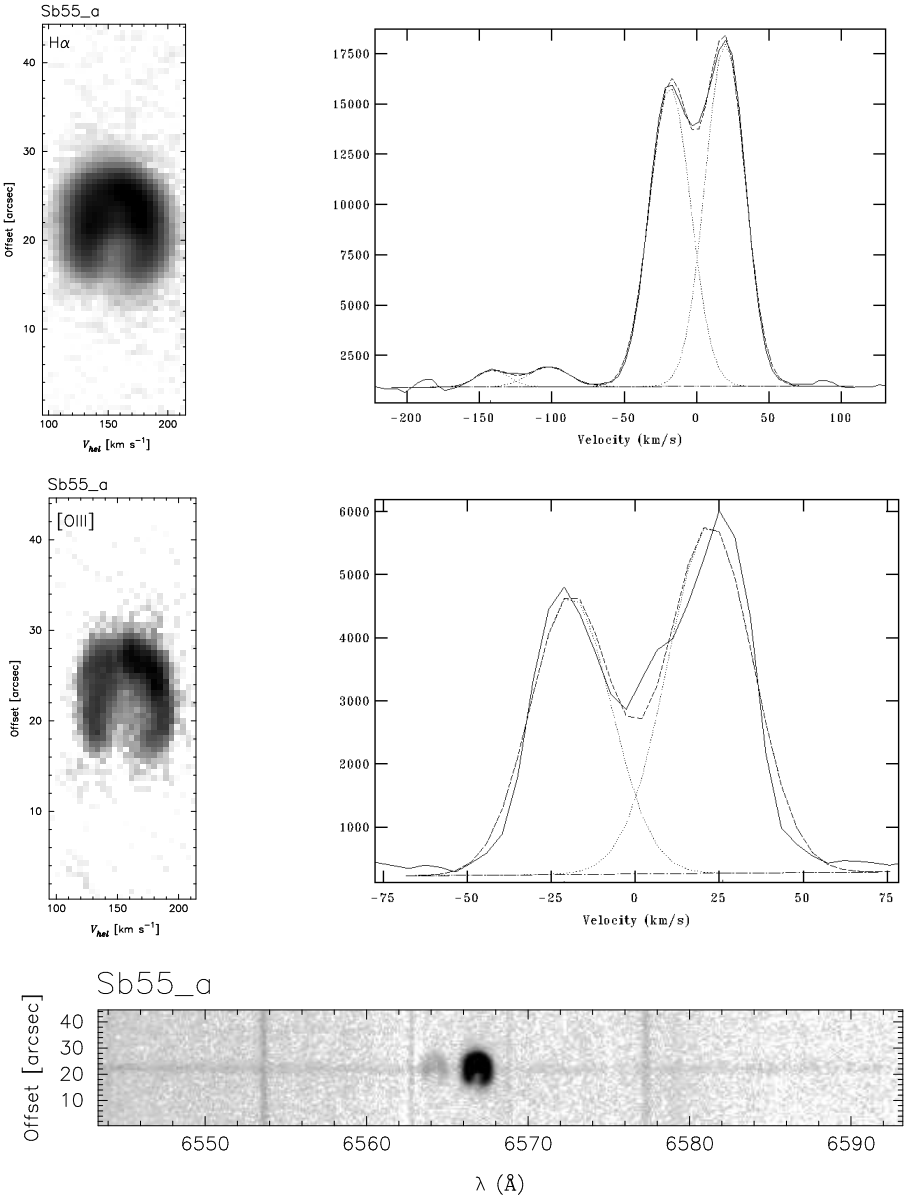

Figure C.24 **Image and data of the PN Sb55 for slit a. Same as Figure C.6.**

Appendix D

Low Metallicity PNe: Objects not considered in statistics

In this Appendix we present the PNe that had to be excluded from the low metallicity sample because, upon detailed inspection, we found that it is likely that they belong to PNe mimics.

Probable symbiotic stars and Post-AGB young nebulae

Using the spectral images drawn from the SPM Catalogue it was possible to realize that some of the PNe in the initial sample, selected from compilations of abundance determinations, show properties similar to those observed in the spectra of D-Type symbiotic stars or Post-AGB young nebulae, mainly very wide wings in the H$\alpha\lambda$6562.8 profile.

D-Type Symbiotic stars are defined as interacting binaries consisting of a hot compact star and a cool giant with a dusty envelope. The giant component loses mass, part of which is ionized by its hot companion, giving rise to nebular emission. The outer neutral hidrogen component scatters Lyβ photons that emerge as wings in the Hα profile (known as Ramman scattering). The process is similar in young Post-AGB nebulae given the amount of neutral hidrogen in the outer envelope of these objects.

Several of the nebulae presented here are confirmed as symbiotic stars by some authors and two cases seem to be young Post-AGB objects. For these reasons we decided to exclude them from the statistical study of the low metallicity sample presented in Chapter 3, to avoid contamination in the final results.

Determining the possible mechanims for the wing broadening seen in H$\alpha\lambda$6562.8 emission (Electron Scattering, Raman Scattering, Rotation Disks or Stellar Winds, see Lee (2000) for further details) is beyond the scope of this thesis, however, we have obtained expansion velocity measurements for these PNe. The results are presented in Table D.1. In the first two columns the common and PNG name for each object is shown. Columns 3 through 8 present our measurements of the expansion velocity for the main shell and the additional components found for each object, obtained from [NII] *lambda*6584, Hα, and [OIII] λ5007 emission lines. Column 8 lists the [O/H] abundance values while column 9 indicates the type of nebula (symbiotic or young nebula). Images, spectra and some remarks for these particular PNe are presented in the following pages.

Table D.1 Expansion velocities for probable Symbiotic and Post-AGB young nebulae.

		Main shell $\pm 2(km\,s^{-1})$		Extended Component $\pm 2(km\,s^{-1})$			
Object	PN G	$V_{H\alpha}$	$V_{[NII]}$	$V_{H\alpha}$	$V_{[NII]}$	log(O/H)+12†	Nebula Type‡
H1-45	002.0-02.0	32*	17			7.52[2]	Symbiotic[b]
H2-43	003.4-04.8	39*	31*	170		6.9[1]	Symbiotic[a]
Hen2-171	346.0+08.5	25	29	156	170	7.79[1]	Symbiotic[a]
M1-37	002.6-03.4	16*	16*	220		7.98[1]	Young
M2-24	356.9-05.8	24*	13	150		7.9[1]	Symbiotic[b]
M2-29	004.0-03.0	13*	9*	290		7.47[1]	Symbiotic[b]
M2-39	008.1-04.7	14	9*	240		7.17[3]	Young

* Velocity measurement obtained from the FWHM of a Gaussian fit.
† References for abundance determinations: 1.-Ratag et al. (1997), 2.-Escudero et al. (2004), 3.-Górny et al. (2004).
‡ Catalogs of symbiotic stars: a.-Belczynski (2000), b.-Miszalski et al. (2013).

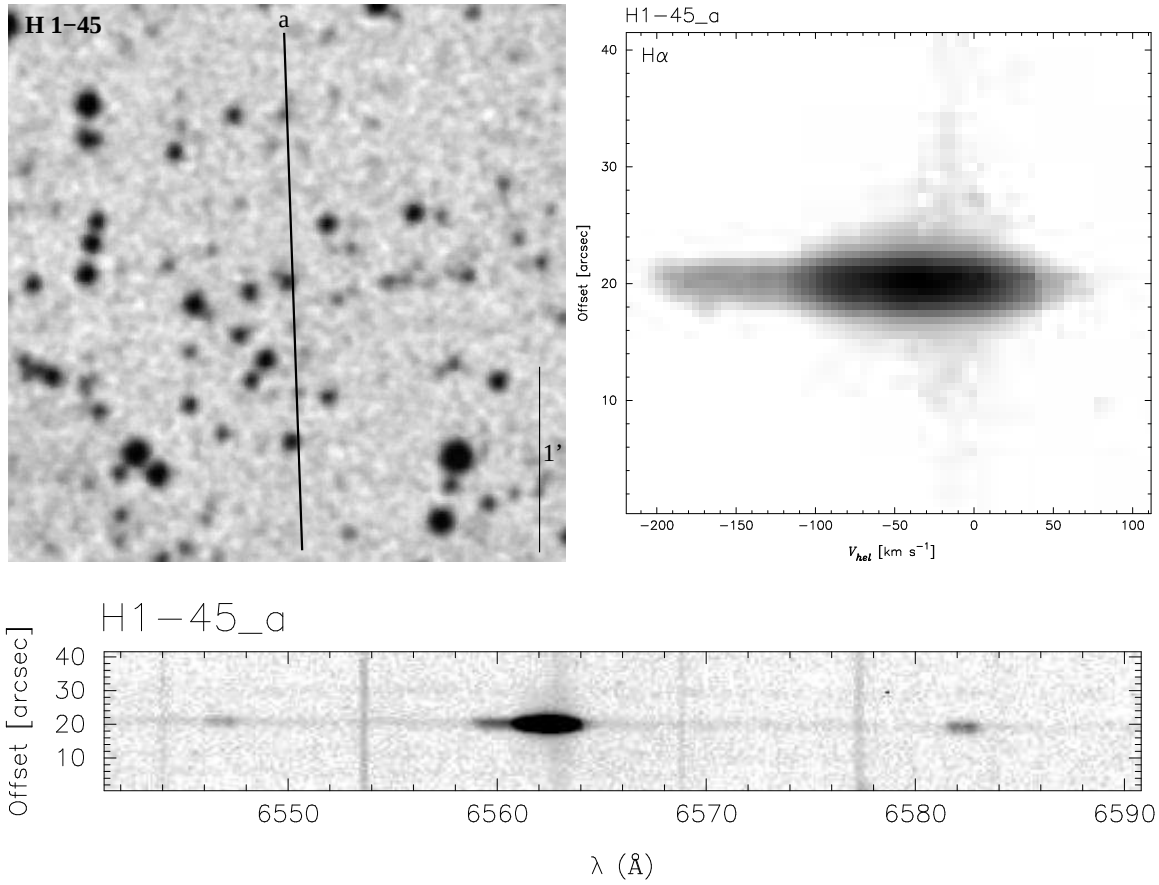

Figure D.1 **Image and data of the PN H1-45 for slit a. In the top-left panel we present the PN image with the slit position indicated as a solid line. The top-right panel shows the two-dimensional array position-velocity (P-V) for the emission line labeled in the upper-left corner, this panel is calibrated in heliocentric velocity (abscissa), and angular scale (ordinate). In the bottom panel is the full spectral range observed for this PN calibrated in wavelength, and angular scale, where the emission lines detected are [NII] $\lambda\lambda$6548,6584, HeII λ6560, and Hα λ6562.8. Although this nebula has been classified as probable symbiotic star by (Miszalski et al., 2013), its [NII] $\lambda\lambda$6548,6584 emission line shows a kinematic structure similar to that of a bipolar PNe seen in the pole-on direction.**

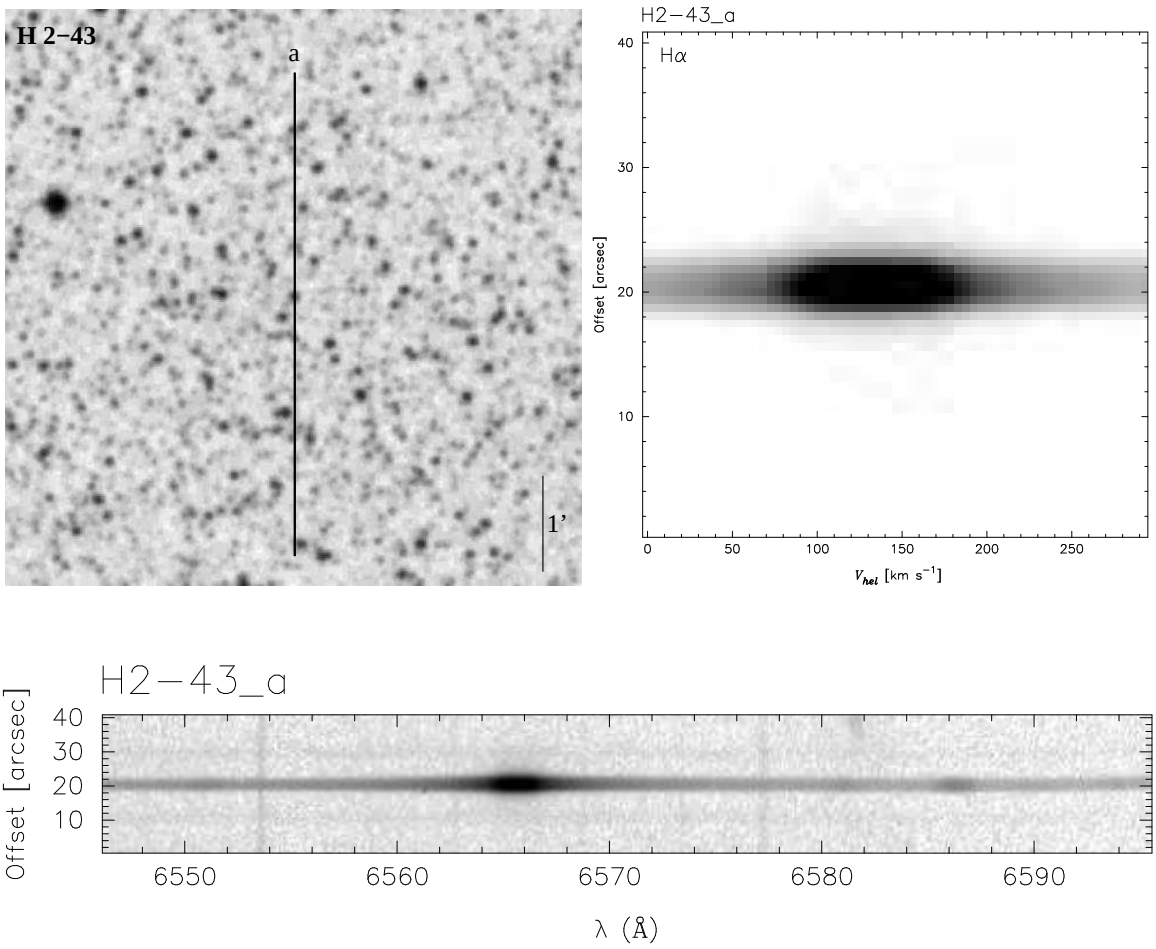

Figure D.2 **Same as Figure D.1, image and data of the PN H2-43 for slit a. Probable symbiotic star (Belczynski, 2000) showing wide wings maybe as a consecuence of Raman scattering. Notice also the strong red continuum indicating the presence of a cool companion.**

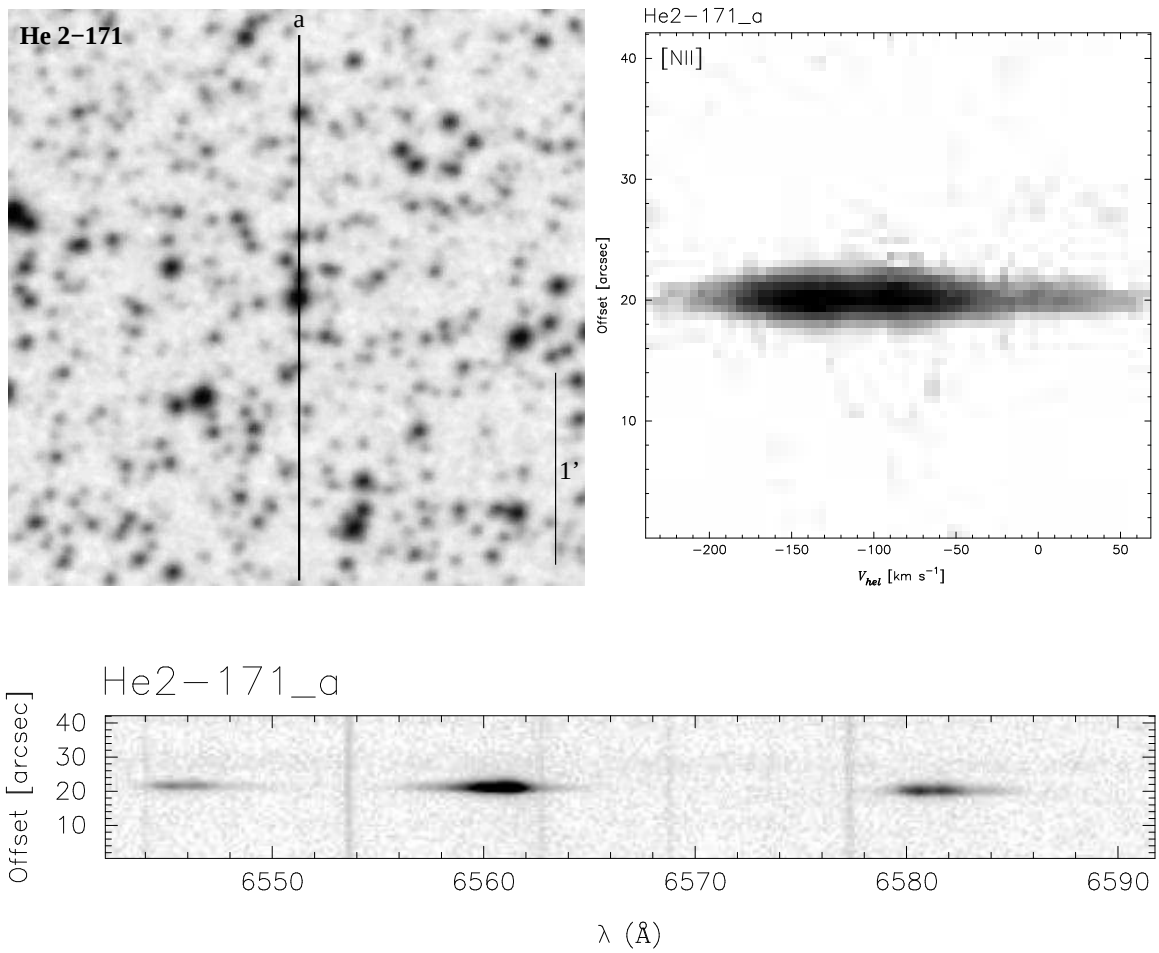

Figure D.3 **Same as Figure D.1, image and data of the PN Hen2-171 for slit a. It was classified as probable symbiotic star (Belczynski, 2000), however it shows high velocity outflows similar to a bipolar PNe seen near the pole-on direction.**

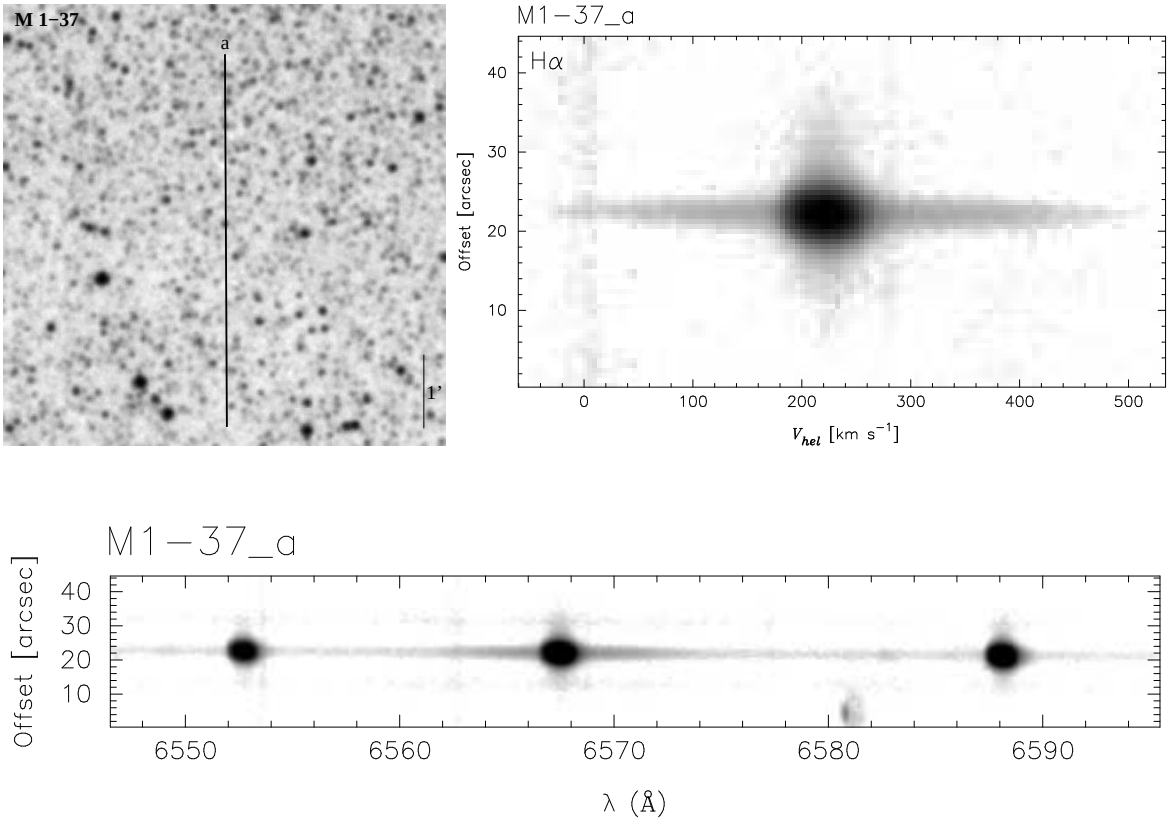

Figure D.4 **Same as Figure D.1, image and data of the PN M1-37 for slit a. Probable Post-AGB young nebula with wide wings likely produced as a consecuence of Raman scattering.**

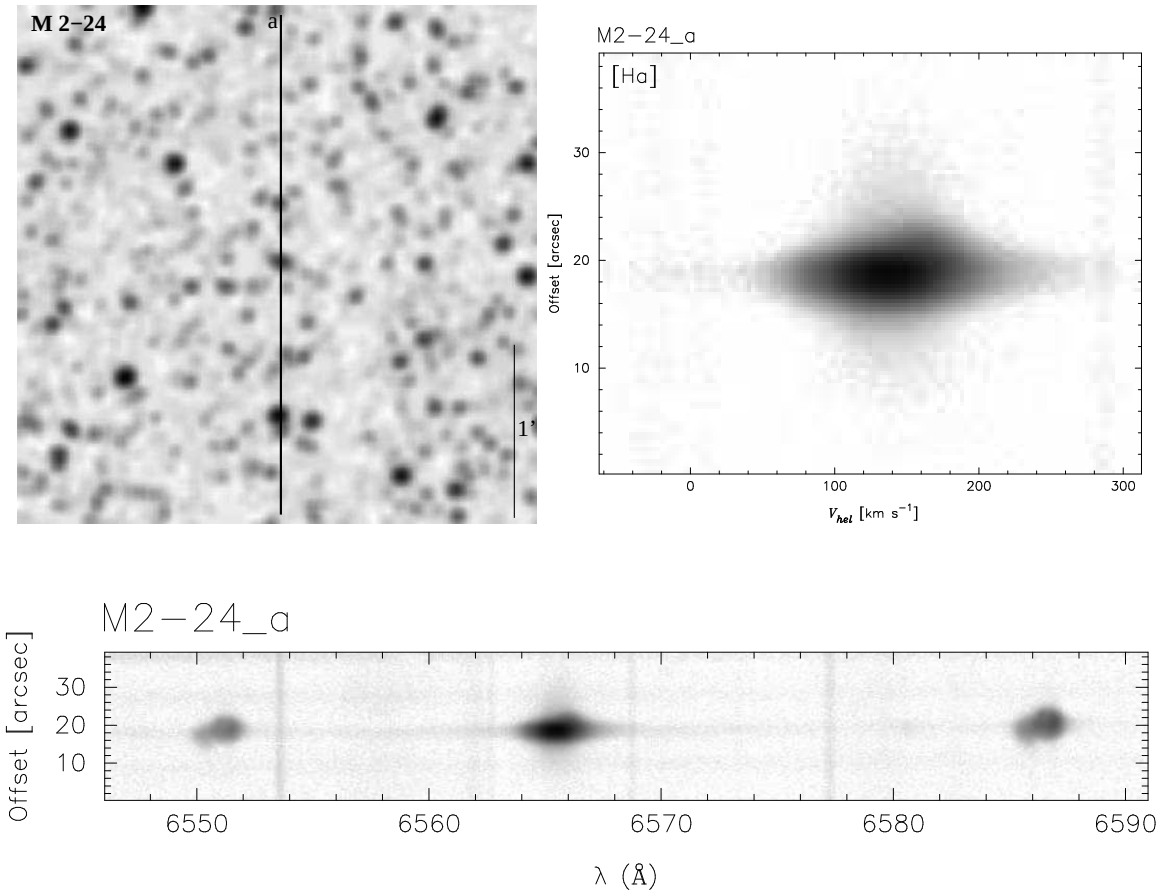

Figure D.5 **Same as Figure D.1, image and data of the PN M2-24 for slit a. Probable symbiotic star (Miszalski et al., 2013).**

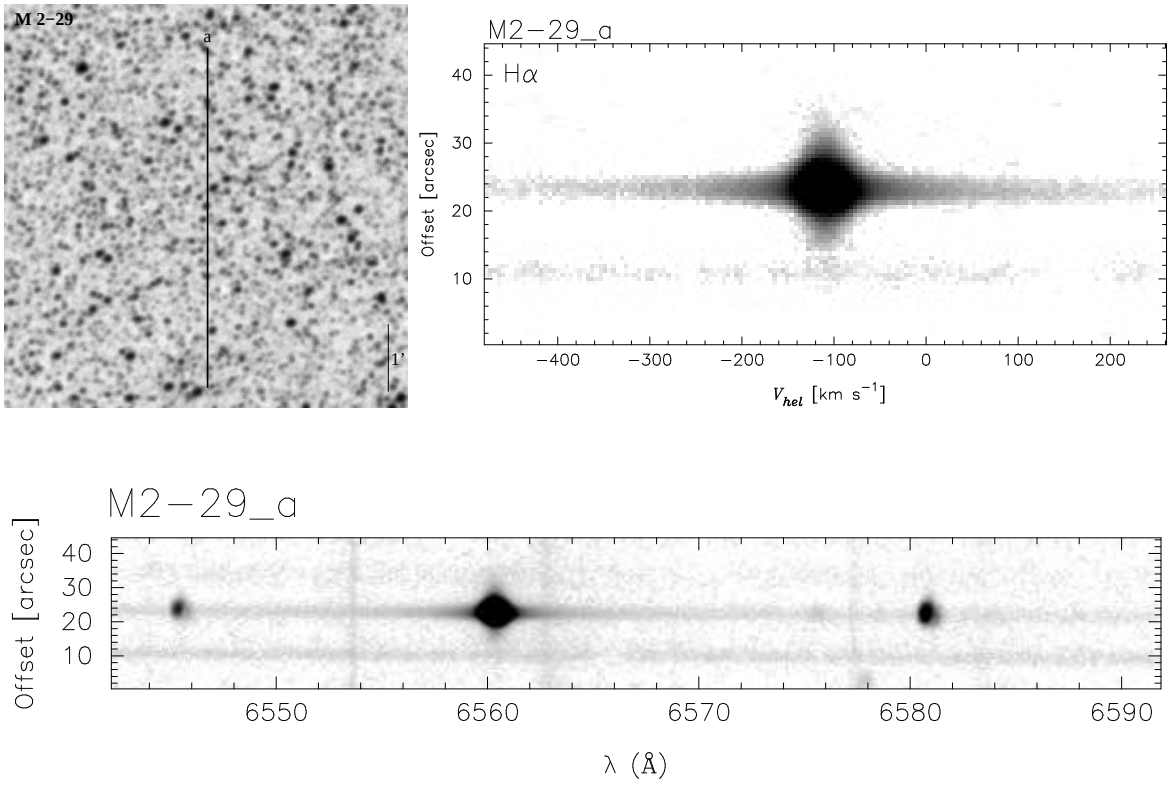

Figure D.6 **Same as Figure D.1, image and data of the PN M2-29 for slit a. Probable symbiotic star (Miszalski et al., 2013) showing wide wings likely produced as a consecuence of Raman scattering.**

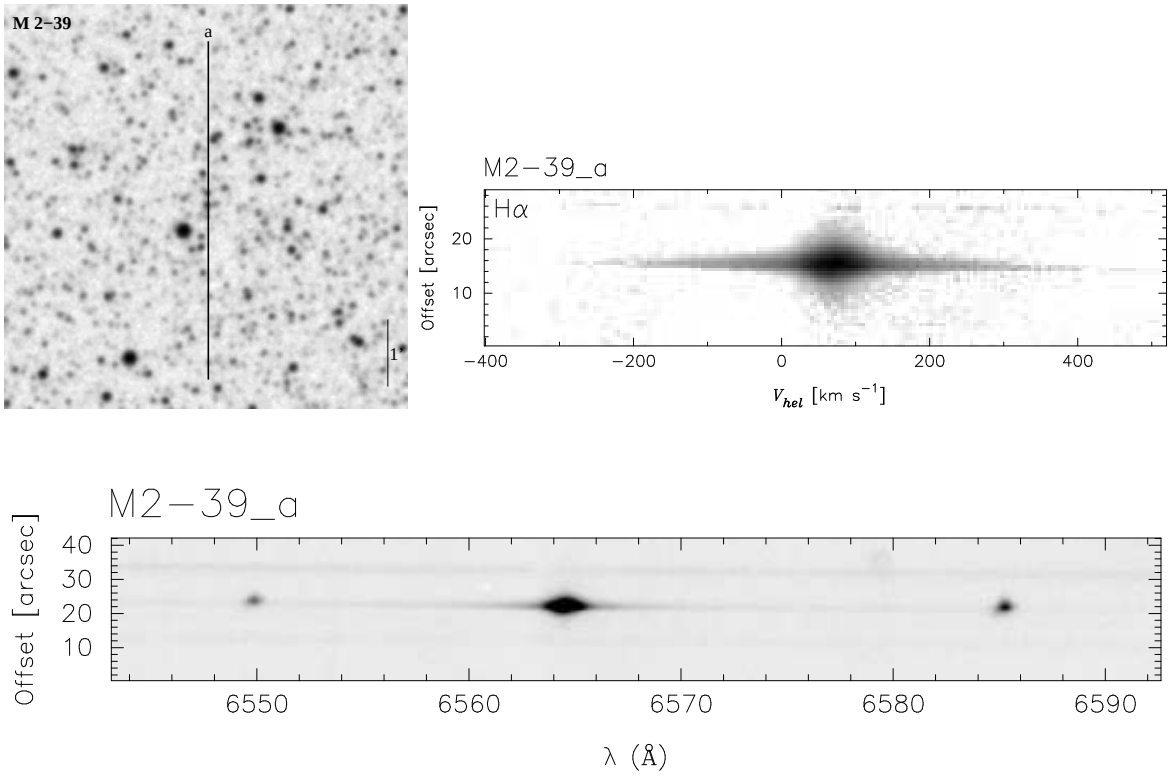

Figure D.7 **Same as Figure D.1, image and data of the PN M2-39 for slit a. Probable Post-AGB young nebula with wide wings, likely produced as a consecuence of Raman scattering.**

Appendix E

Previous work: The Bulge's Sample

As part of the context in which this thesis began to develop, we present in this appendix the published results of our group on recent observational studies about the PNe at the Milky Way Bulge. These studies have shown the acceleration of nebular shells in PNe at early evolutionary stages for this particular galactic population. Since the motivation of my project derives in someway from these results, we considered relevant to include them in this thesis.

In the first paper, the authors separate the Bulge's sample into two groups containing cooler and hotter central stars, defined by the absence or presence, respectively, of the He II λ6560 line in the Hα spectra. This division separates samples of younger and more evolved planetary nebulae. The main conclusion in this study is that the differences between the groups is an evidence for the acceleration of the nebular shells during the early evolution of these planetary nebulae. The acceleration of the nebular shells appears to be the direct result of the evolution of the central stars.

The second paper complements the first, forming a homogeneous sample from a single Galactic population of planetary nebulae, from the earliest evolutionary stages until the cessation of nuclear burning in the central star. They confirm the long-standing predictions of hydrodynamical models of planetary nebulae, where the kinematics of the nebular shell are driven by the evolution of the central star. These works, together with the results presented in this thesis, describe for the first time (observationally) how the kinematic evolution of the shell proceeds troughout the whole PN stage.

The Astrophysical Journal, 689:203–212, 2008 December 10

THE ACCELERATION OF THE NEBULAR SHELLS IN PLANETARY NEBULAE IN THE MILKY WAY BULGE[1]

Michael G. Richer, José Alberto López, Margarita Pereyra, Hortensia Riesgo, and María Teresa García-Díaz
OAN, Instituto de Astronomía, Universidad Nacional Autónoma de México, P.O. Box 439027, San Diego, CA 92143;
richer@astrosen.unam.mx, jal@astrosen.unam.mx, mally@astrosen.unam.mx,
hriesgo@astrosen.unam.mx, tere@astrosen.unam.mx

and

Sol-Haret Báez
Facultad de Física e Inteligencia Artificial, Universidad Veracruzana, Circuito G. Aguirre Beltrán s/n,
Zona Universitaria, Xalapa, Veracruz, México; solharet@hotmail.com
Received 2008 July 2; accepted 2008 August 11

ABSTRACT

We present a systematic study of line widths in the [O III] λ5007 and Hα lines for a sample of 86 planetary nebulae in the Milky Way bulge based on spectroscopy obtained at the Observatorio Astronómico Nacional in the Sierra San Pedro Mártir (OAN-SPM) using the Manchester Echelle Spectrograph. The planetary nebulae were selected with the intention of simulating samples of bright extragalactic planetary nebulae. We separate the planetary nebulae into two samples containing cooler and hotter central stars, defined by the absence or presence, respectively, of the He II λ6560 line in the Hα spectra. This division separates samples of younger and more evolved planetary nebulae. The sample of planetary nebulae with hotter central stars has systematically larger line widths, larger radii, lower electron densities, and lower Hβ luminosities. The distributions of these parameters in the two samples all differ at significance levels exceeding 99%. These differences are all in agreement with the expectations from hydrodynamical models, but for the first time confirmed for a homogeneous and statistically significant sample of Galactic planetary nebulae. We interpret these differences as evidence for the acceleration of the nebular shells during the early evolution of these intrinsically bright planetary nebulae. As is the case for planetary nebulae in the Magellanic Clouds, the acceleration of the nebular shells appears to be the direct result of the evolution of the central stars.

Subject headings: galaxies: abundances — galaxies: individual (M32, NGC 185, NGC 205) — planetary nebulae: general — stars: evolution

1. INTRODUCTION

The interacting stellar winds model of Kwok et al. (1978) provides a general framework for understanding planetary nebulae. Within this framework, a variety of theoretical and numerical studies of the hydrodynamics have been undertaken to explain and predict the kinematic properties of planetary nebulae. Our modern view of the kinematics of planetary nebulae was established in the early 1990s (e.g., Kahn & West 1985; Breitschwerdt & Kahn 1990; Kahn & Breitschwerdt 1990; Mellema 1994). These studies showed that the AGB envelope is accelerated in two phases. The first phase is a result of the shock wave initiated by the ionization front that sweeps through the AGB envelope as the central star's temperature increases. Then, as the central star's wind energy increases, it drives a pressure-driven central bubble that accelerates the AGB envelope through ram pressure. More recent numerical work that attempts to include more realistic AGB evolution confirms these basic results (e.g., Villaver et al. 2002; Perinotto et al. 2004). Eventually, the central star's wind ceases and the inner part of the AGB envelope backfills toward the central star while the outer part maintains its momentum-driven evolution (e.g., García-Segura et al. 2006).

These models have been used extensively to interpret observational studies of the kinematics of many individual planetary nebulae. Unfortunately, to date, systematic, homogeneous studies of planetary nebula populations to compare with these theoretical efforts are scarce. Heap (1993) found a correlation between nebular expansion velocity and the terminal velocity of the central star wind. More recently, Medina et al. (2006) claimed a correlation between expansion velocity and age indicators such as density and central star temperature. However, both of these studies suffer from heterogeneity, at least regarding object selection. Even regarding planetary nebulae with Wolf-Rayet (WR) central stars, the precise role that the winds from the central stars play in the kinematics of the nebular shells is not entirely clear (Gesicki et al. 2006; Medina et al. 2006).

The studies of the kinematics of planetary nebulae in the Magellanic Clouds are perhaps the most systematic (Dopita et al. 1985, 1988). These studies find correlations between expansion velocity, excitation class, and nebular density, suggesting that the properties of the central star dominate the nebular evolution. As they point out, however, their results are not general, since they have been found only for a particular population of (bright) planetary nebulae.

Therefore, there remains a need for a coherent population study in a different galactic environment. Here we present a study of the kinematics for a large sample of planetary nebulae in the bulge of the Milky Way (MW bulge). These objects were selected in a homogeneous way, with the hope of simulating populations of bright extragalactic planetary nebulae in bulgelike systems (bulges of spiral galaxies, dwarf spheroidal galaxies, and elliptical galaxies). The observations were all made with the same instrument and methodology. Likewise, the data reduction and analysis is homogeneous and entirely independent of model parameters. Details are given in § 2. We find that the expansion properties do indeed depend on

[1] The observations reported herein were obtained at the Observatorio Astronómico Nacional in the Sierra San Pedro Mártir (OAN-SPM), B. C., Mexico.

the evolutionary stage of the central star, with planetary nebulae hosting hotter central stars having larger expansion velocities (§ 3). We also find that other parameters that should depend on age, the nebular size, density, and Hβ luminosity, also differ significantly between the two groups (§ 4). We compare these properties with theoretical models and find generally good agreement (§ 5). We present our conclusions in § 6.

2. OBSERVATIONS AND ANALYSIS

2.1. *The Planetary Nebula Sample*

We present the sample of MW bulge planetary nebulae that we observed in Table 1. There are 86 objects in total, drawn from existing spectroscopic surveys (Aller & Keyes 1987; Webster 1988; Cuisinier et al. 1996, 2000; Ratag et al. 1997; Escudero & Costa 2001; Escudero et al. 2004; Exter et al. 2004; Górny et al. 2004).

We selected this sample hoping to simulate a sample of bright extragalactic planetary nebulae in bulgelike systems. Our selection criteria were refined somewhat over the duration of the observations but eventually converged to (1) a position within 10° of the Galactic center, (2) a large observed, reddening-corrected Hβ flux, nominally $\log I(\mathrm{H}\beta) > -12.0$ dex, (3) a large [O III] λ5007/Hβ ratio, usually exceeding a value of 6, and (4) the existence of low-resolution spectroscopy in which the electron temperature may be determined from the [O III] λ4363/λ5007 ratio. Usually, the systemic radial velocity exceeds 30 km s^{-1} in an attempt to exclude disk objects toward the MW bulge. We imposed no explicit limit on the size of the objects. Nor did we impose an upper limit on the flux (Hβ or 6 cm). In practice, however, a flux limit is usually imposed by the surveys from which we selected our objects.

Figure 1 explains the logic of our lower limits on the Hβ flux and the [O III] λ5007/Hβ ratio. Basically, bright extragalactic planetary nebulae in elliptical galaxies, dwarf spheroidal galaxies, and the bulge of M31 fall within these limits (see figure caption). Restricting the sample to objects with large [O III] λ5007/Hβ ratios will exclude planetary nebulae very early in their evolution when their central stars are coolest. Our limit on the Hβ luminosity does not restrict the planetary nebulae to contain central stars that are on the horizontal portion of their evolutionary track, but also includes the initial fading following the extinction of nuclear reactions.

2.2. *Observations and Data Reductions*

We acquired our observations during eight observing runs spanning the period from 2003 June to 2007 August at the Observatorio Astronómico Nacional in the Sierra San Pedro Mártir, Baja California, Mexico (OAN-SPM). More details of the observations will be provided in a forthcoming paper.

High-resolution spectra were obtained with the Manchester echelle spectrometer (MES-SPM; Meaburn et al. 1984, 2003). The MES-SPM is a long-slit, echelle spectrometer that has no cross-dispersion. Instead, narrowband filters were used to isolate orders 87 and 114 containing the Hα and [O III] λ5007 emission lines, respectively. A 150 μm wide slit was used for the observations, resulting in a slit 1.9″ wide on the sky. Coupled with a SITe 1024 × 1024 CCD with 24 μm pixels binned 2 × 2, the resulting spectral resolutions were approximately 0.077 and 0.100 Å pixel^{-1} at [O III] λ5007 and Hα, respectively (equivalent to 11 km s^{-1} for 2.6 pixel FWHM). The spectra were calibrated using exposures of a ThAr lamp taken immediately before or after every object exposure. The internal precision of the arc lamp calibrations is better than $\pm$1.0 km s^{-1}.

Usually, only one deep spectrum was obtained in each of the [O III] λ5007 and Hα filters. The exposure times varied depending on the brightness of the object. At most, the exposure times were of 30 minutes duration. If this was expected to produce saturation, shorter exposure times were used. The exposure time for the Hα spectrum was chosen to achieve a signal level similar to that in the deep [O III] λ5007 spectrum, based on the intensities of these lines observed in the low-resolution spectra, but was also limited to a maximum of 30 minutes duration.

All of the planetary nebulae observed are resolved (see Table 1). In all cases, the slit was centered on the object. Usually, the slit was oriented in the north-south direction.

The spectra were reduced using the `twodspec` and `specred` packages of the Image Reduction and Analysis Facility (IRAF).[2] The procedure for data reduction followed that outlined in Massey et al. (1992, Appendix B) for long-slit spectroscopy. The object spectra were edited of cosmic rays. Then, a nightly mean bias image was subtracted from each object spectrum. Next, the arc lamp spectra were used to map positions of constant wavelength. These maps were then used to rectify the object spectra so that lines of constant wavelength fell exactly along the columns, a process that simultaneously applies a wavelength calibration. Finally, wavelength-calibrated, one-dimensional spectra were extracted for each object. No flux calibration was performed.

2.3. *Kinematic Parameters*

We shall present all of the one-dimensional line profiles in a subsequent publication. For that reason, we do not present the line profiles here. Instead, we turn to an explanation of the analysis of the kinematics.

The one-dimensional spectra were analyzed using a locally implemented software package (INTENS; McCall et al. 1985) to determine the radial velocity, flux, and profile width (FWHM [full width at half-maximum intensity]), as well as the uncertainties in these parameters. This software fits the emission-line profile with a sampled Gaussian function and models the continuum as a straight line. Thus, this analysis assumes that the lines have a Gaussian shape and that they are superposed on a flat continuum. In the case of the Hα line, the He II λ6560 line may also be present. In this case, a fit is made simultaneously to both lines and the continuum.

While the assumption of a Gaussian line shape is reasonable for bright extragalactic planetary nebulae, because they are spatially unresolved, it might seem odd for spatially resolved objects. Nonetheless, for the large majority of the objects, the one-dimensional line profiles are usually not double peaked and the deviations from a Gaussian shape usually represent less than 10% of the total flux (see Fig. 2 for an example; M. G. Richer et al., in preparation).

Table 1 presents the observed line widths (FWHM) and their uncertainties for each object in both Hα and [O III] λ5007. The uncertainties in the line widths are the formal uncertainties (1 σ) from fitting a sampled Gaussian function to the line profile. In order to derive the intrinsic line widths, the observed line widths must be corrected for several effects, all of which are assumed to contribute to the observed line width in quadrature. The effects that broaden the true, intrinsic profile are instrumental (σ_{inst}), thermal (σ_{th}), and fine-structure (σ_{fs}) broadening,

$$\sigma^2_{\mathrm{obs}} = \sigma^2_{\mathrm{true}} + \sigma^2_{\mathrm{inst}} + \sigma^2_{\mathrm{th}} + \sigma^2_{\mathrm{fs}}. \quad (1)$$

[2] IRAF is distributed by the National Optical Astronomical Observatory, which is operated by the Associated Universities for Research in Astronomy, Inc., under contract to the National Science Foundation.

TABLE 1

Bulge Planetary Nebula Sample

Object	PN G	Run	FWHM(Hα)[a] (Å)	$\Delta V_{0.5}$(Hα) (km s^{-1})	FWHM(5007)[a] (Å)	$\Delta V_{0.5}$(5007) (km s^{-1})	Diameter (in Hα)[b] 50% I_{max}	10% I_{max}	N_e[c] (cm^{-3})	log F(Hβ) (erg s^{-1})	6560?	WR?[d]
Bl 3-13	000.9−02.0	2006 Jun	0.9427 ± 0.0028	16.05 ± 0.06	0.6063 ± 0.0079	16.93 ± 0.24	2.4	5.5	1765	34.19	No	Wels
Cn 1-5	002.2−09.4	2004 Jun	1.0384 ± 0.0026	18.87 ± 0.06	1.251 ± 0.041	36.9 ± 1.2	4.4	8.6	...	35.21	No	WR
Cn 2-1	356.2−04.4	2004 Jun	0.9255 ± 0.0039	15.51 ± 0.09	0.6826 ± 0.0074	19.36 ± 0.22	2.7	4.8	6967	34.97	No	No
H 1-1	343.4+11.9	2004 Jun	1.617 ± 0.019	34.04 ± 0.43	1.238 ± 0.043	36.5 ± 1.3	2.5	4.4	...	33.88	Yes	No
H 1-11	002.6+08.2	2006 Jun	0.9219 ± 0.0057	15.40 ± 0.13	0.625 ± 0.011	17.53 ± 0.32	4.4	7.3	10803	34.43	Yes	Wels
H 1-14	001.7+05.7	2005 Jul	1.803 ± 0.036	38.62 ± 0.81	1.313 ± 0.068	38.8 ± 2.0	4.3	7.4	985	34.30	Yes	No
H 1-16	000.1+04.3	2005 May	1.026 ± 0.003	18.51 ± 0.07	0.743 ± 0.012	21.25 ± 0.36	2.8	4.7	7035	35.11	Yes	No
H 1-17	358.3+03.0	2005 Jul	0.9635 ± 0.0035	16.67 ± 0.08	0.6150 ± 0.0072	17.20 ± 0.22	2.1	4.7	16190	35.29	No	No
H 1-18	357.6+02.6	2004 Jun	0.8105 ± 0.0026	11.67 ± 0.06	0.5062 ± 0.0039	13.66 ± 0.12	2.6	4.8	8627	34.94	Yes	No
H 1-20	358.9+03.2	2003 Jun	0.9361 ± 0.0025	15.85 ± 0.06	0.6905 ± 0.0042	19.53 ± 0.13	2.4	4.9	3811	34.85	No	No
H 1-23	357.6+01.7	2005 May	1.0266 ± 0.0080	18.54 ± 0.18	0.754 ± 0.016	21.62 ± 0.49	3.2	5.9	3840	35.05	No	No
H 1-27	005.0+04.4	2003 Jun	1.0238 ± 0.0029	18.48 ± 0.07	0.7004 ± 0.0075	19.94 ± 0.22	1.7	3.8	18385	34.83	No	No
H 1-30	352.0−04.6	2006 Jun	0.9616 ± 0.0044	16.62 ± 0.10	0.6000 ± 0.0052	16.73 ± 0.16	3.2	4.4	6495	34.20	Yes	No
H 1-31	355.1−02.9	2005 May	0.9932 ± 0.0037	17.56 ± 0.08	0.6646 ± 0.0038	18.79 ± 0.11	2.8	5.1	12957	34.84	Yes	No
H 1-32	355.6−02.7	2005 May	0.7685 ± 0.0026	10.08 ± 0.06	0.4385 ± 0.0033	11.37 ± 0.10	3.1	5.2	7897	34.04	No	No
H 1-33	355.7−03.0	2004 Jun	0.7904 ± 0.0018	10.93 ± 0.04	0.5218 ± 0.0022	14.17 ± 0.07	3.9	6.5	3215	34.72	No	No
H 1-40	359.7−02.6	2005 May	1.014 ± 0.014	18.16 ± 0.32	0.643 ± 0.014	18.09 ± 0.42	3.1	7.0	11745	35.42	No	No
H 1-41	356.7−04.8	2006 Jun	1.1607 ± 0.0091	22.30 ± 0.21	0.832 ± 0.014	24.05 ± 0.43	5.7	8.8	2525	34.35	Yes	Wels
H 1-42	357.2−04.5	2006 Jul	0.9351 ± 0.0059	15.81 ± 0.13	0.5362 ± 0.0080	14.65 ± 0.24	3.0	5.2	2270	34.92	No	Wels
H 1-45	002.0−02.0	2005 Jul	1.590 ± 0.011	33.37 ± 0.26	1.016 ± 0.011	29.70 ± 0.34	2.7	4.4	...	35.03	Yes	No
H 1-50	358.7−05.2	2004 Jun	1.0263 ± 0.0018	18.53 ± 0.04	0.7291 ± 0.0038	20.82 ± 0.11	2.2	4.5	6920	34.95	Yes	No
H 1-54	002.1−04.2	2007 Aug	0.9029 ± 0.0045	14.81 ± 0.10	0.5304 ± 0.0028	14.50 ± 0.08	2.8	5.2	11594	34.78	No	No
H 1-56	001.7−04.6	2007 Aug	0.8261 ± 0.0013	12.25 ± 0.03	0.5650 ± 0.0048	15.67 ± 0.14	3.2	6.1	1164	34.52	No	Wels
H 1-59	003.8−04.3	2005 May	1.237 ± 0.015	24.33 ± 0.34	1.115 ± 0.033	32.76 ± 0.99	3.6	6.8	1100	34.26	Yes	No
H 1-60	004.2−04.3	2005 May	0.9560 ± 0.0076	16.45 ± 0.17	0.672 ± 0.013	19.04 ± 0.38	3.2	7.0	...	34.26	No	Wels
H 1-67	009.8−04.6	2005 Jul	1.474 ± 0.030	30.46 ± 0.68	...	...	5.2	9.5	1455	34.36	Yes	WR
H 2-10	358.2+03.5	2004 Jun	1.1028 ± 0.0093	20.70 ± 0.21	0.7907 ± 0.0038	22.75 ± 0.11	1.9	4.1	8140	34.61	No	No
H 2-11	000.7+04.7	2005 Jul	0.7697 ± 0.0058	10.13 ± 0.13	0.4684 ± 0.0055	12.39 ± 0.16	2.6	5.2	15550	35.03	No	Wels
H 2-18	006.3+04.4	2004 Jun	1.473 ± 0.020	30.44 ± 0.47	1.118 ± 0.028	32.84 ± 0.85	2.9	6.6	...	34.14	Yes	No
Hb 8	003.8−17.1	2004 Jun	0.9662 ± 0.0022	16.75 ± 0.05	0.6465 ± 0.0037	18.21 ± 0.11	1.8	4.1	14420	34.05	No	No
He 2-250	000.7+03.2	2003 Jun	1.185 ± 0.021	22.96 ± 0.48	0.797 ± 0.013	22.98 ± 0.40	3.6	7.9	2430	34.62	Yes	No
Hf 2-1	355.4−04.0	2005 May	1.774 ± 0.059	37.9 ± 1.3	1.285 ± 0.069	37.9 ± 2.1	9.1	19.7	...	34.17	Yes	No
K 5-1	000.4+04.4	2006 Jul	0.8709 ± 0.0027	13.76 ± 0.06	0.6191 ± 0.0078	17.34 ± 0.23	3.6	5.7	1400	34.61	No	Wels
K 5-3	002.6+05.5	2006 Jul	1.368 ± 0.041	27.77 ± 0.94	0.538 ± 0.020	14.70 ± 0.59	2.6	9.5	1300	34.01	Yes	WR
K 5-4	351.9−01.9	2006 Jul	0.8187 ± 0.0013	11.97 ± 0.03	0.4946 ± 0.0016	13.28 ± 0.05	2.2	3.4	7600	34.99	No	No
K 5-5	001.5+03.6	2006 Jul	0.9265 ± 0.0047	15.54 ± 0.11	0.612 ± 0.011	17.12 ± 0.31	2.5	4.1	10900	34.85	No	No
K 5-6	003.6+04.9	2006 Jul	1.302 ± 0.018	26.04 ± 0.42	0.866 ± 0.027	25.09 ± 0.82	3.6	8.6	1000	33.85	Yes	No
K 5-7	003.1+04.1	2006 Jul	1.619 ± 0.023	32.49 ± 0.52	1.323 ± 0.035	39.1 ± 1.0	8.9	13.2	300	33.62	Yes	No
K 5-9	355.54−1.4	2006 Jul	1.289 ± 0.035	25.72 ± 0.81	0.964 ± 0.043	28.1 ± 1.3	4.0	7.7	3500	34.60	Yes	No
K 5-11	002.3+02.2	2006 Jul	0.9577 ± 0.0054	16.51 ± 0.12	0.6465 ± 0.0087	18.22 ± 0.26	5.6	10.8	604	34.31	No	No
K 5-12	353.5−03.3	2006 Jul	1.548 ± 0.017	32.33 ± 0.38	1.208 ± 0.031	35.59 ± 0.93	4.1	7.3	4480	34.07	Yes	No
K 5-14	003.9+02.6	2007 Aug	1.0314 ± 0.0087	18.69 ± 0.20	0.5986 ± 0.0052	16.50 ± 0.16	2.0	3.6	8000	34.16	Yes	No
K 5-17	004.3+02.1	2007 Aug	1.435 ± 0.027	29.48 ± 0.62	1.043 ± 0.037	30.5 ± 1.1	2.4	5.1	9960	34.41	Yes	No
K 5-19	005.1+02.0	2007 Aug	1.409 ± 0.016	28.81 ± 0.36	1.191 ± 0.030	35.08 ± 0.91	3.0	5.9	1170	34.15	Yes	No
K 5-20	356.8−03.0	2007 Aug	0.9118 ± 0.0054	15.09 ± 0.12	0.639 ± 0.010	18.02 ± 0.30	3.2	6.1	498	34.00	No	No
M 1-19	351.1+04.8	2005 May	0.8781 ± 0.0022	14.00 ± 0.05	0.5640 ± 0.0056	15.56 ± 0.17	2.6	5.4	6370	34.99	No	Wels

TABLE 1—*Continued*

Object	PN G	Run	FWHM(Hα)[a] (Å)	$\Delta V_{0.5}$(Hα) (km s^{-1})	FWHM(5007)[a] (Å)	$\Delta V_{0.5}$(5007) (km s^{-1})	Diameter (in Hα)[b] 50% I_{max}	10% I_{max}	N_e[c] (cm^{-3})	log F(Hβ) (erg s^{-1})	6560?	WR?[d]
M 1-20	006.1+08.3	2004 Jun	0.7527 ± 0.0037	9.43 ± 0.08	0.2969 ± 0.0031	5.97 ± 0.09	3.0	4.5	7500	35.07	No	Wels
M 1-29	359.1−01.7	2004 Jun	1.0319 ± 0.0033	18.69 ± 0.08	0.7693 ± 0.0060	22.08 ± 0.18	5.3	8.8	3674	35.34	Yes	Wels
M 1-31	006.4+02.0	2005 Jul	0.7954 ± 0.0044	11.11 ± 0.10	0.4899 ± 0.0025	13.11 ± 0.07	2.2	4.3	7830	35.32	No	Wels
M 1-35	003.9−02.3	2007 Aug	1.0215 ± 0.0063	18.40 ± 0.14	0.7336 ± 0.0073	21.03 ± 0.22	4.0	6.7	6040	35.10	No	No
M 1-42	002.7−04.8	2003 Jun	1.0485 ± 0.0038	19.18 ± 0.09	0.6772 ± 0.0055	19.21 ± 0.16	7.9	12.4	1287	34.95	Yes	No
M 1-48	013.4−03.9	2005 Jul	0.8262 ± 0.0024	12.23 ± 0.05	0.5301 ± 0.0046	14.45 ± 0.14	3.8	6.9	1525	34.06	Yes	No
M 2-13	011.1+11.5	2006 Jun	0.7047 ± 0.0025	7.25 ± 0.06	0.4008 ± 0.0020	10.04 ± 0.06	2.8	5.6	4185	34.26	No	No
M 2-15	011.0+06.2	2006 Jun	1.271 ± 0.028	25.23 ± 0.64	0.937 ± 0.035	27.3 ± 1.0	6.6	9.1	2130	34.57	Yes	No
M 2-16	357.4−03.2	2004 Jun	1.1090 ± 0.0057	20.87 ± 0.13	0.7905 ± 0.0077	22.74 ± 0.23	2.5	4.9	4625	35.07	Yes	No
M 2-20	000.4−01.9	2006 Jul	1.2428 ± 0.0041	24.50 ± 0.09	0.8262 ± 0.0027	23.86 ± 0.08	2.1	4.3	2023	35.02	No	WR
M 2-21	000.7−02.7	2005 May	1.280 ± 0.016	25.49 ± 0.37	0.945 ± 0.026	27.52 ± 0.78	2.8	5.3	10	34.65	Yes	Wels
M 2-22	357.4−04.6	2007 Aug	1.234 ± 0.030	24.27 ± 0.67	0.903 ± 0.039	26.3 ± 1.1	3.1	6.9	2300	34.18	Yes	No
M 2-23	002.2−02.7	2004 Jun	0.855 ± 0.0021	13.22 ± 0.05	0.5258 ± 0.0030	14.30 ± 0.09	2.5	4.3	10600	35.00	No	No
M 2-26	003.6−02.3	2006 Jul	1.319 ± 0.024	26.50 ± 0.56	1.011 ± 0.033	29.55 ± 0.99	8.2	11.2	452	34.14	Yes	No
M 2-27	359.9−04.5	2004 Jun	0.9625 ± 0.0034	16.64 ± 0.08	0.6230 ± 0.0044	17.46 ± 0.13	1.9	6.4	7360	35.11	No	Wels
M 2-29	004.0−03.0	2004 Jun	0.7864 ± 0.0026	10.77 ± 0.06	0.4771 ± 0.0036	12.68 ± 0.11	3.6	7.1	2670	34.53	No	No
M 2-30	003.7−04.6	2004 Jun	1.184 ± 0.011	22.91 ± 0.25	0.864 ± 0.016	25.02 ± 0.47	3.2	5.6	2268	34.83	Yes	Wels
M 2-31	006.0−03.6	2004 Jun	1.1907 ± 0.0068	23.10 ± 0.16	0.8266 ± 0.0060	23.87 ± 0.18	2.3	5.6	4710	35.19	No	WR
M 2-33	002.0−06.2	2007 Aug	0.6988 ± 0.0031	6.98 ± 0.07	0.3441 ± 0.0046	7.98 ± 0.14	4.1	6.1	1259	34.94	No	Wels
M 2-39	008.1−04.7	2006 Jul	1.0341 ± 0.0053	18.76 ± 0.12	0.5258 ± 0.0063	14.31 ± 0.19	2.4	3.6	3165	34.62	No	Wels
M 2-4	349.8+04.4	2007 Aug	0.8088 ± 0.0041	11.63 ± 0.09	0.5025 ± 0.0035	13.58 ± 0.10	1.7	4.4	6970	35.39	No	No
M 2-8	352.1+05.1	2006 Jun	0.9742 ± 0.0019	17.00 ± 0.04	0.6275 ± 0.0021	17.61 ± 0.06	2.2	5.3	1670	34.44	Yes	WR
M 3-10	358.2+03.6	2004 Jun	1.0963 ± 0.0085	20.52 ± 0.19	0.7351 ± 0.0069	21.01 ± 0.21	2.5	4.7	11497	34.99	Yes	No
M 3-14	355.4−02.4	2004 Jun	1.1585 ± 0.0075	22.23 ± 0.17	0.8005 ± 0.0087	23.06 ± 0.26	3.5	7.5	3180	35.28	Yes	No
M 3-15	006.8+04.1	2004 Jun	0.9783 ± 0.0033	17.12 ± 0.08	0.6470 ± 0.0062	18.23 ± 0.19	4.0	6.1	9450	35.67	No	WR
M 3-16	359.1−02.3	2005 May	1.0279 ± 0.0074	18.58 ± 0.17	0.6229 ± 0.0085	17.46 ± 0.25	6.0	11.2	1155	35.06	No	No
M 3-20	002.1−02.2	2007 Aug	1.1206 ± 0.0093	21.20 ± 0.21	0.7629 ± 0.0046	21.89 ± 0.14	3.5	4.8	10	34.64	No	Wels
M 3-21	355.1−06.9	2004 Jun	0.8936 ± 0.0062	14.49 ± 0.14	0.5682 ± 0.0056	15.69 ± 0.17	1.8	4.4	3172	35.06	No	No
M 3-26[e]	004.8−05.0	2005 Sep	1.462 ± 0.052	30.2 ± 1.2	1.141	33.5	7.0	10.7	1415	34.13	Yes	No
M 3-32	009.4−09.8	2005 Jul	1.176 ± 0.012	22.70 ± 0.27	0.811 ± 0.013	23.37 ± 0.38	4.0	7.4	1850	34.38	Yes	No
M 3-33	009.6−10.6	2004 Jun	1.098 ± 0.012	20.55 ± 0.28	0.806 ± 0.020	23.24 ± 0.61	5.3	8.8	1140	34.05	Yes	Wels
M 3-38	356.9+04.4	2004 Jun	0.9558 ± 0.0086	16.44 ± 0.20	0.5289 ± 0.0077	14.41 ± 0.23	3.2	4.4	9550	34.31	Yes	No
M 3-42	357.5+03.2	2003 Jun	1.710 ± 0.096	36.4 ± 2.2	0.602 ± 0.046	16.7 ± 1.4	4.1	9.8	1000	33.72	Yes	No
M 3-45	359.7−01.8	2005 Jul	1.1658 ± 0.0068	22.43 ± 0.16	0.8117 ± 0.0095	23.41 ± 0.28	5.1	7.4	7897	34.86	Yes	No
M 3-54	018.6−02.2	2006 Jul	1.340 ± 0.020	27.03 ± 0.46	0.957 ± 0.026	27.89 ± 0.79	4.4	7.4	1385	33.97	Yes	No
M 4-3	357.2+07.4	2005 May	0.8502 ± 0.0022	13.07 ± 0.05	0.5271 ± 0.0025	14.35 ± 0.07	3.6	6.0	...	35.27	No	No
M 4-6	358.6+01.8	2004 Jun	1.1311 ± 0.0067	21.48 ± 0.15	0.772 ± 0.014	22.15 ± 0.40	3.7	6.6	12881	34.26	No	No
M 4-7	358.5−02.5	2006 Jun	1.0558 ± 0.0060	19.38 ± 0.14	0.730 ± 0.012	20.86 ± 0.36	4.8	8.0	1580	34.15	No	No
PC 12	000.1+17.2	2005 May	0.8346 ± 0.0019	12.53 ± 0.04	0.4749 ± 0.0019	12.61 ± 0.06	3.1	6.3	5110	34.27	No	No
Te 1580	002.6+02.1	2007 Aug	1.883 ± 0.065	40.6 ± 1.5	1.367 ± 0.075	40.42 ± 2.23	7.4	9.9	1200	34.48	Yes	No

[a] This is the observed line width, uncorrected for instrumental, thermal, or fine-structure broadening.
[b] These diameters were measured by collapsing the Hα spectra into one-dimensional spatial profiles and measuring the diameters at 50% and 10% of peak intensity.
[c] The electron densities are measured from the [S II] λλ6716, 6731 lines. When no density is given, this information is unavailable.
[d] Classifications of "WR" and "Wels" are taken from an extended version of Table 4 from Górny et al. (2004) kindly provided by S. Górny. A classification of "No" indicates that no information is available or that the central star is classified as non-WR.
[e] The [O III] λ5007 line width was measured using IRAF's `splot`.

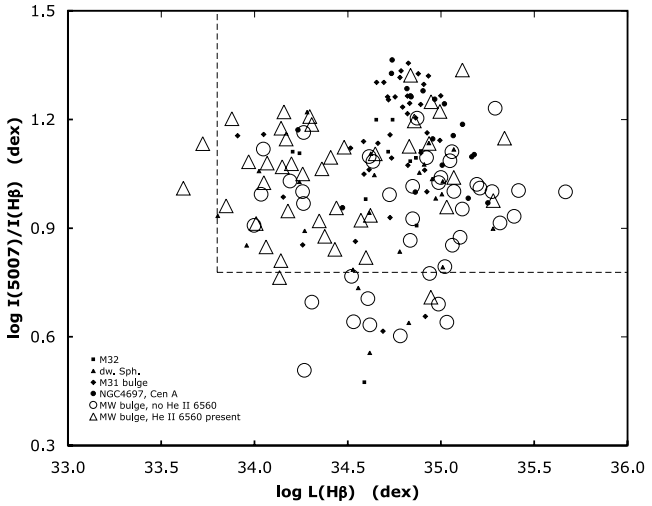

FIG. 1.—Selection criteria for our sample of MW bulge planetary nebulae were designed to yield a sample that mimics the populations of bright extragalactic planetary nebulae in bulgelike systems. The extragalactic planetary nebulae are shown in filled symbols, while the MW bulge planetary nebulae, divided according to the presence or absence of He II λ6560, are shown with open symbols. The dotted lines indicate that the limits that we chose for the Hβ luminosity and [O III] λ5007/Hβ ratio were motivated by the range of these parameters among extragalactic planetary nebulae with spectroscopic observations (Jacoby & Ciardullo 1999; Richer et al. 1999; Walsh et al. 1999; Dudziak et al. 2000; Roth et al. 2004; Méndez et al. 2005; Zijlstraa et al. 2006; Gonçalves et al. 2007; Richer & McCall 2008).

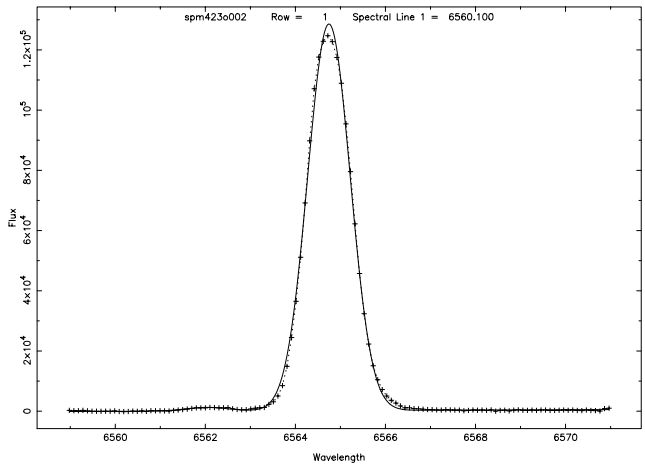

FIG. 2.—Hα line profile for M 2-16 as an example of our spectra. The crosses represent the data, and the solid line is the fit. The faint line on the blue wing of Hα is the He II λ6560 line and has an intensity of 0.9% that of Hα. For the Hα line, the S/N in the flux is 200, which is approximately the median value for our sample.

The first term, $\sigma^2_{\rm true}$, is the true, intrinsic line width resulting from the kinematics of the planetary nebula. The instrumental profile has a measured FWHM of 2.5–2.7 pixels. We adopt a FWHM of 2.6 pixels for all objects, which amounts to about 11 km s^{-1} (FWHM). We compute the thermal broadening from the usual formula (Lang 1980, eq. [2-243]), adopting rest wavelengths of 6562.83 and 5006.85 Å for Hα and [O III] λ5007, respectively, and assuming no turbulent velocity. The thermal broadening (FWHM) amounts to 0.47 Å (21.4 km s^{-1}) and 0.089 Å (5.3 km s^{-1}) for Hα and [O III] λ5007, respectively. The fine-structure broadening was taken to be $\sigma_{\rm fs} = 3.199$ km s^{-1} for Hα and zero for [O III] λ5007 (García-Díaz et al. 2008).

The interpretation of the resulting line width, ΔV,

$$\Delta V = 2.3556\sigma_{\rm true}, \tag{2}$$

is not necessarily simple. In the case of an expanding, spherical shell that is spatially unresolved, the line width corresponds to the expansion velocity. If the velocity field or matter distribution is more complicated or if the object is resolved spatially, then the line width is a luminosity-weighted velocity width for the mass projected within the spectrograph slit.

The velocity width that we measure should typically exceed the luminosity-weighted line width for the entire object. The spectrograph slit was centered on each object, and all of the objects are wider than the slit (Table 1). Therefore, matter near the edges of the objects is excluded and this matter is likely to have the lowest projected velocity along the line of sight. Since the matter at the edges of the objects would contribute low systematic velocities for each object, the line profile that we measure for the matter included within the slit will be slightly larger than the true mass-weighted line width. These arguments are supported by the results presented by Gesicki & Zijlstra (2000) and Rozas et al. (2007). Their simulations of thin, expanding, spherical shells indicate that the line widths that we measure may overestimate the integrated line widths for the entire objects by up to approximately 15% but that the exact amount will depend on the fraction of the object covered by the slit.

Fortunately, the discussion that follows does not depend on any interpretation of the line width. Since it is clear, however, that this line width will be similar to twice the expansion velocity, Table 1 presents half of the line width in velocity units for each object, i.e.,

$$\Delta V_{0.5} = 0.5\Delta V = 1.1778\sigma_{\rm true}. \tag{3}$$

3. NEBULAR KINEMATICS VERSUS THE EVOLUTIONARY STATE OF THE CENTRAL STAR

For about half of the objects in our sample, the He II λ6560 line is present in the Hα spectra. Figure 2 presents M 2-16 as an example. In practice, we can detect He II λ6560 provided its intensity is at least 0.4% that of Hα and a signal-to-noise ratio of at least 50 is achieved for the Hα line. For comparison with theoretical models, this limit is predicted to occur for an effective temperature of about 9×10^4 K according to the hydrodynamical models presented in Schönberner et al. (2007) if we use the atomic data for hydrogen and helium in Osterbrock (1989). Table 1 indicates the objects for which the He II λ6560 line was observed in our Hα spectra.

Obviously, the objects in which the He II λ6560 line appears are those with the hotter central stars. Therefore, we may separate our sample into two samples with cooler and hotter central stars according to whether the He II λ6560 line is observed. Given our selection criteria, this separation into samples with cooler and hotter central stars is equivalent to a separation into samples in different stages of evolution. The planetary nebulae with the hotter central stars are in a more advanced stage of evolution than those with the cooler central stars.

Figure 3 presents histograms of the line width ($\Delta V_{0.5}$) distributions for the two samples of planetary nebulae. Clearly, the distributions appear different. The sample of planetary nebulae with the cooler central stars have predominantly low line widths, while the sample with the hotter central stars have a much broader distribution of line widths that extends to substantially higher values.

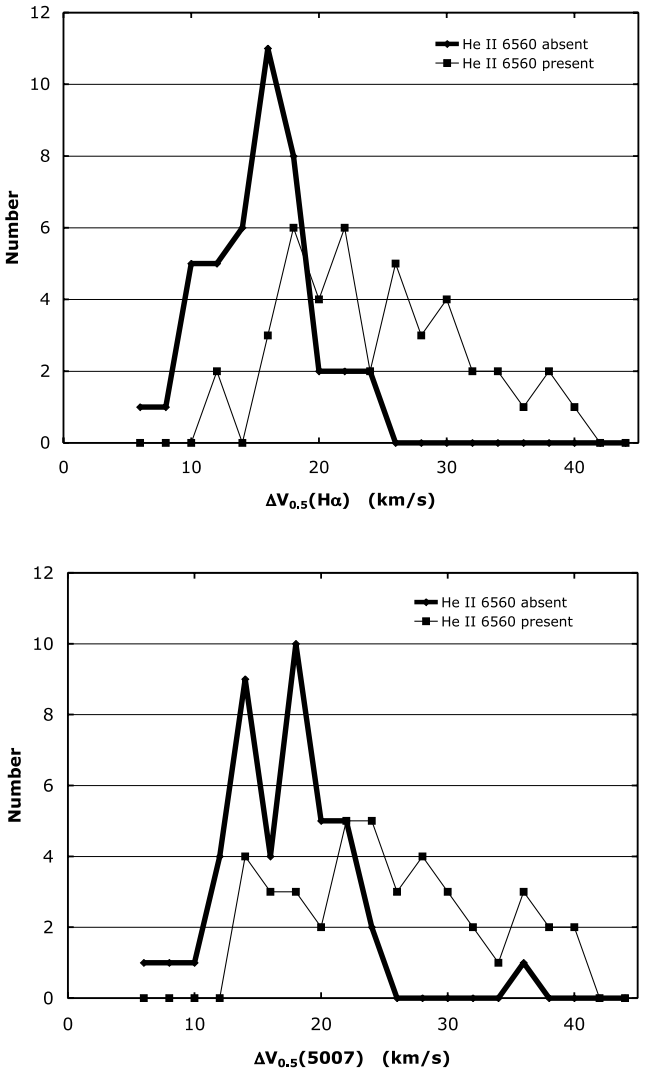

FIG. 3.—We find distributions of line widths that are very different if we divide our objects according to whether the He II λ6560 line is absent or present. *Top,* distribution of Hα line widths; *bottom,* distribution of [O III] λ5007 line widths. The probability of drawing such different distributions (He II λ6560 absent or present) at random from the same parent population is less than 1.3×10^{-7} (Table 2).

A variety of statistical tests may be applied to these distributions to determine whether it is probable that they may result from a single parent distribution. Since we do not know a priori the form of the distribution that the line widths should have, nonparametric statistical tests are most appropriate. Perhaps the best known of these tests is the Kolmogorov-Smirnov two-sample test to the cumulative distribution functions of the line widths. However, a more powerful nonparametric test is the Wilcoxon-Mann-Whitney U-test (e.g., Wall & Jenkins 2003, § 5.4.3). This is a rank test in which the line widths from the two samples are combined into a single sample and ranked. Then, the rankings of the line widths for the two samples are compared with a uniform distribution of rankings.

The U-test indicates that the probability of drawing the two samples of line widths from the same parent distribution is only 1.3×10^{-7}. The nebular shells surrounding hotter central stars are expanding systematically more rapidly than their counterparts surrounding cooler central stars. Since all of these hotter central stars were necessarily cooler in the past, the simplest conclusion is that the nebular shells in bright planetary nebulae are accelerated as the star gets hotter.

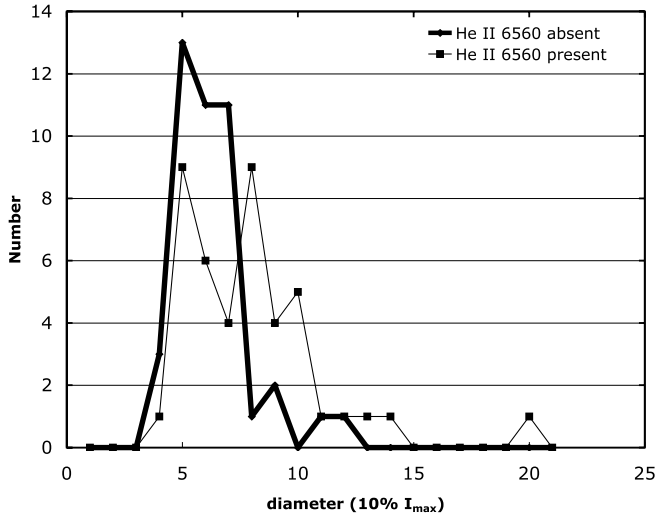

FIG. 4.—The distributions of diameters at 10% of peak intensity (or 50% of peak) are very different for the MW bulge planetary nebulae divided according to whether the He II λ6560 line is absent or present. The probability of drawing such different distributions of diameters at random from the same parent population is 7.0×10^{-4} (Table 2).

4. OTHER PROPERTIES VERSUS THE EVOLUTIONARY STATE OF THE CENTRAL STAR

Considering that the nebular shells of bright planetary nebulae are accelerated as the central star gets hotter, one might expect other properties of the two samples of planetary nebulae to differ. Essentially, characteristics that vary systematically with the age or evolutionary stage of the planetary nebula should differ between the two samples.

The most obvious characteristic to consider is the nebular size. The cooler central stars should be found in younger planetary nebulae that have had less time to expand and should be systematically smaller than those surrounding the hotter central stars. There are no systematic measurements of the diameters of the planetary nebulae in our sample, so we measured nebular diameters from our deep Hα spectra. To determine the diameters, we collapsed the spectra along the wavelength axis to produce one-dimensional spatial profiles. We then measured the nebular sizes at 50% and 10% of the peak intensity. These diameters are found in Table 1.

The distributions of diameters at 10% of the peak flux are shown in Figure 4. Again, it is clear that the sample with the hotter central stars has a distribution of diameters that tends to larger sizes than the sample of planetary nebulae with the cooler central stars. Applying the U-test, we obtain a probability of only 7×10^{-4} that the two samples arise from a single parent population. Hence, the nebulae surrounding the hotter central stars are larger than those surrounding the cooler, less evolved, central stars.

Conceivably, the larger sizes of the nebulae around hotter central stars might artificially bias their line widths to larger values because the fixed spectrograph slit covers a smaller fraction of these larger nebulae. As shown by Gesicki & Zijlstra (2000) and Rozas et al. (2007) this might cause the line widths for larger nebulae to be overestimated. To test whether this is the case, we estimated how much the line widths could be overestimated based on the results presented in Table 1 of Gesicki & Zijlstra (2000). We then divided the line widths of all objects in Table 1 ($\Delta V_{0.5}$)

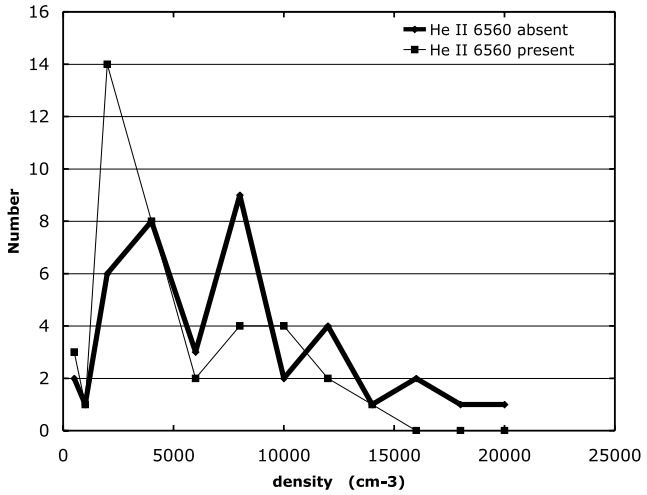

FIG. 5.—The distributions of densities are very different for the MW bulge planetary nebulae hosting cooler and hotter central stars (He II λ6560 absent and present, respectively). The probability of drawing these distributions of densities at random from the same parent population is 8.0×10^{-3} (Table 2).

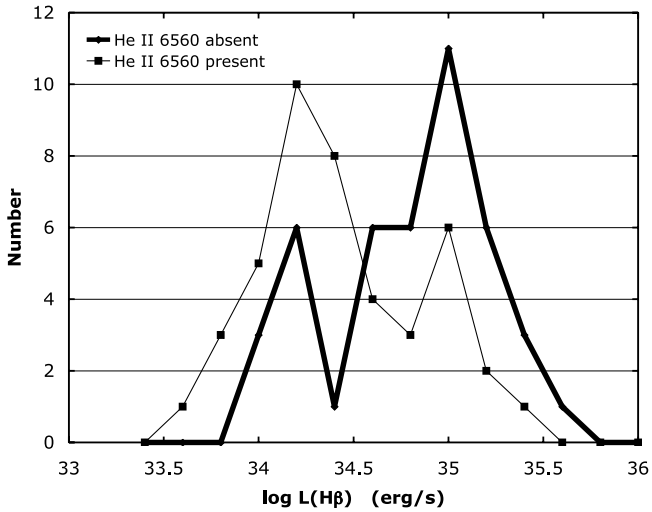

FIG. 6.—As was found for the line widths, diameters, and densities, the distributions of Hβ luminosities are very different for the MW bulge planetary nebulae hosting cooler and hotter central stars (He II λ6560 absent and present, respectively). The probability of drawing these distributions of luminosities at random from the same parent population is 2.2×10^{-4} (Table 2).

by this correction and recalculated the probability that the two samples arise from a single parent population. The probability increases, but to only 2.5×10^{-7} (considering the [O III] λ5007 line widths), so the conclusion that the two distributions are statistically very different is not affected.

The nebular density is also expected to evolve, decreasing as the nebular volume increases. Table 1 lists the electron densities determined from the [S II] $\lambda\lambda$6716, 6731 ratio as measured in low-resolution spectroscopy from the literature. When there was more than one measurement, the measurements were averaged. The distributions of nebular density in the two samples are shown in Figure 5. In this case, the difference is more subtle, but the planetary nebulae with the hotter central stars tend to have lower densities. Applying the U-test, we find a probability of 8×10^{-3} that the two samples arise from the same parent population. Therefore, the planetary nebulae with hotter central stars have systematically lower electron densities.

Finally, we compare the Hβ luminosities of the two samples. We expect all of the planetary nebulae without He II λ6560 emission to contain central stars on the horizontal portion of their evolutionary tracks. It is unlikely that any of these objects contain central stars that are fading toward the white dwarf regime, since virtually all of the central stars should be sufficiently massive to achieve temperatures in excess of 10^5 K before fading, by which time emission from He^{2+} ions should be evident. On the other hand, the sample of planetary nebulae with hotter central stars should contain objects whose central stars are fading toward the white dwarf regime. Therefore, we would expect that the Hβ luminosities of the two samples could differ, with the sample with the cooler central stars having higher luminosities.

The Hβ luminosities for the MW bulge planetary nebulae in Table 1 and Figure 1 are not very accurate for a variety of reasons. First, the observed Hβ fluxes are usually those measured through a spectrograph slit and not from photometry. Likely, the Hβ fluxes are underestimated for many MW bulge planetary nebulae. Second, these fluxes must be corrected for reddening. The reddening may include instrumental or observational effects, such as differential atmospheric refraction, and so may overestimate the true reddening. These reddenings have been used to correct the Hβ fluxes for extinction. Third, the individual distances for the planetary nebulae are unknown. To compute the Hβ luminosities in Table 1, we adopted a common distance of 7.5 kpc. In all likelihood, the mean distance for the sample will be less than this, and it is probably this assumption that leads to larger Hβ luminosities than are observed in extragalactic planetary nebulae.

Figure 6 presents histograms of the Hβ luminosity distributions for the two samples, divided according to the presence or absence of He II λ6560 emission. The Hβ luminosities are taken from Table 1. Clearly, the distribution for the sample with the cooler central stars extends to higher Hβ luminosities. The mean luminosities for the two samples differ by 0.36 dex, or 0.90 mag. The U-test indicates that the probability that two distributions arise from the same parent population is only 2.2×10^{-4}. Therefore, the planetary nebulae with the cooler central stars are brighter, on average, than those with the hotter central stars.

Summarizing our results, we find significant differences between our samples of planetary nebulae with cooler and hotter central stars. The planetary nebulae with cooler central stars have smaller line widths, smaller sizes, higher densities, and higher Hβ luminosities. The differences are all significant at confidence levels exceeding 99% (Table 2).

5. DISCUSSION

At present, the theory of the evolution of planetary nebulae outlined earlier is unable to predict definitive expansion velocities for planetary nebulae or the AGB stars from which they arise. Observations of AGB stars find that their winds usually have an expansion velocity below 15 km s^{-1} and often below 10 km s^{-1} (e.g., Ramstedt et al. 2006; Lewis 1991). Observations of planetary nebulae typically find expansion velocities of 15–30 km s^{-1} (e.g., Gesicki & Zijlstra 2000; Medina et al. 2006). At least qualitatively, theory may explain the difference: The ionization front drives a shock wave through the AGB envelope, raising the expansion velocity by $\sim$5–6 km s^{-1} over that of the AGB envelope (Chevalier 1997; Perinotto et al. 2004). Then, the pressure-driven bubble expands into the AGB envelope, sweeping up a dense, inner rim of matter that may increase the expansion velocity significantly, particularly if this rim is able to overtake the density enhancement produced by the shock wave.

The median line width in [O III] λ5007 (Hα) for our sample of MW bulge planetary nebulae with cooler central stars is 17.2 km s^{-1}

TABLE 2
STATISTICAL TESTS (U-TEST)

Hypothesis	Prob(False)	Comment
$\Delta V_{0.5,5007}$(hotter CS) > $\Delta V_{0.5,5007}$(cooler CS)	1.3×10^{-7}	H 1-67 excluded
$\Delta V_{0.5,\mathrm{H}\alpha}$(hotter CS) > $\Delta V_{0.5,\mathrm{H}\alpha}$(cooler CS)	7.4×10^{-10}	
Diameter(hotter CS) > diameter(cooler CS)	7.0×10^{-4}	Measured at 10% intensity
Density(cooler CS) > density(hotter CS)	8.0×10^{-3}	Based on [S II] $\lambda\lambda$6716, 6731
$L(\mathrm{H}\beta$, cooler CS) > $L(\mathrm{H}\beta$, hotter CS)	2.2×10^{-4}	

(15.4 km s^{-1}), and the standard deviation of the distribution is 5.1 km s^{-1} (4.0 km s^{-1}). Since we expect our line widths to be slightly larger than the expansion velocity, the median line width for the sample with the cooler central stars is approximately that expected if the AGB envelopes had expansion velocities of about 10 km s^{-1}, as observations suggest commonly occurs (Ramstedt et al. 2006). It is therefore natural to associate these planetary nebulae with models during the stage in which the ionization front is driving a shock wave through the AGB envelopes.

The median line width in [O III] λ5007 (Hα) for the sample of MW bulge planetary nebulae with the hotter central stars is substantially higher, 23.7 km s^{-1} (24.3 km s^{-1}), as is the dispersion in velocities, 7.6 km s^{-1} (7.1 km s^{-1}). In the models, by the time that the central star has a temperature of 9×10^4 K, the stellar wind-powered bubble is expanding into the ionized AGB envelope and raising the observed expansion velocities. Thus, our sample of planetary nebulae with hotter central stars is naturally associated with this second stage of envelope acceleration (Villaver et al. 2002; Perinotto et al. 2004).

It is more difficult to compare the differences in size that we find for our two samples with existing theoretical models. In part, this has to do with how we have determined our nebular sizes. The main problem is the mismatch in spatial resolution between our observations and one-dimensional theoretical profiles. Our observations generally include a substantial fraction of the object, while one-dimensional theoretical profiles have infinite spatial resolution. In spite of this difficulty, the available theoretical profiles indicate that the outermost dense/bright regions increase in size as time progresses (Mellema 1994; Villaver et al. 2002; Perinotto et al. 2004), even though the size of the *brightest* structure may not increase monotonically with time (Villaver et al. 2002).

Theoretical models indicate that the entire AGB envelopes should become ionized relatively early for the stellar masses of relevance here ($M_i \lesssim 2\,M_\odot$; e.g., Mellema 1994; Villaver et al. 2002; Perinotto et al. 2004). They are also expected to remain entirely ionized. Once the envelope is entirely ionized, its Hβ luminosity will decrease with time as a result of dilution (e.g., Osterbrock 1989). As a result, that we find lower Hβ luminosities for the sample of objects that is more evolved is entirely compatible with theoretical expectations.

Likewise, theoretical models are compatible with our findings concerning the electron density. Theoretical models indicate that the densities are higher while the expansion velocities are dominated by the ionization front than later on when the pressure-driven bubble dominates. However, this agreement is bittersweet. We use densities derived from [S II] lines. In principle, these lines from the recombination zone should not exist in the objects with the hotter central stars, since these objects are predicted to have completely ionized their AGB envelopes. In practice, this emission no doubt arises in density enhancements that are absent from the models, and so the [S II] densities are likely an upper limit to the typical densities in these objects. Nonetheless, the models predict a general dilution of the entire AGB envelope, and this dilution is probably what gives rise to the decay in [S II] densities that we observe.

It is not unusual that the line width distributions overlap for our samples of planetary nebulae with cooler and hotter central stars. As the theoretical models make very clear, the expansion velocity depends on the AGB envelope expansion velocity and the mass-loss rate at the end of the AGB evolution. Undoubtedly, these properties varied among the stellar progenitors of the planetary nebulae in both samples. Furthermore, even if they did not, the planetary nebulae in both samples are found in a range of evolutionary states, particularly for the sample with the hotter central stars. Consequently, the line widths that we observe will have varying contributions from the accelerations due to the shock front and the pressure-driven bubble. Unless the objects are all spherical (unlikely), the different orientations will also broaden the line width distributions.

It is also not unusual that the distributions of line widths differ more than do those for the nebular diameters, densities, and luminosities. The structure that appears brightest varies with time (Villaver et al. 2002; Perinotto et al. 2004), depending on the development of the density enhancements due to the ionization front or the swept-up inner rim. It is therefore not surprising that there is less difference between the distributions of densities and diameters than there is between the distributions of line widths. Likewise, since the Hβ luminosity will depend on how much mass is swept up by the AGB envelope (Villaver et al. 2002), and this may vary significantly from one object to the next depending on location, the Hβ luminosities may be somewhat scattered.

Our findings confirm those of Heap (1993) and Medina et al. (2006), who found correlations between the nebular kinematics and the evolutionary state of the central star. Our findings, however, are based on a sample of planetary nebulae that is larger and more homogeneous and whose analysis is entirely independent of models. It is perhaps not surprising that our results demonstrate much more clearly the intimate relationship between the central star's evolution and the kinematics of the nebular shell.

Perhaps the most relevant studies for comparison are those of Dopita et al. (1985, 1988) for planetary nebulae in the Magellanic Clouds. They found that the nebular expansion velocity depends on the excitation class and Hβ luminosity of the nebula. Both the excitation class and the Hβ luminosity are functions of the evolutionary stage of both the central star and nebular shell. In other words, the kinematics of planetary nebulae in the Magellanic Clouds require a coordination between the evolutionary states of the central star and the nebular shell. Our results clearly demand the same sort of coordination between the evolution of the central star and the surrounding nebular shell.

The exact relationship between the central star and the nebular kinematics need not be conserved between the Magellanic Clouds and the MW bulge. Indeed, it is difficult to compare the results directly, as many complications may arise. Ideally, the nebular kinematics should be related to the properties of the central star

in both environments (temperature, wind velocity, mass-loss rate). However, for most of the objects in both the MW bulge and the Magellanic Clouds, observations of the central star's wind are unavailable. Excitation classes or line ratios provide indirect temperature diagnostics, but these will usually depend on the chemical composition of the nebula and are also susceptible to systematic biases if there are differences in the distributions of the central star masses or AGB wind properties.

Our findings, like those of Gesicki et al. (2006), do not support the claim that the nebular shells surrounding WR central stars have larger expansion velocities (Medina et al. 2006). We made no special attempt to include planetary nebulae with WR central stars in our sample, so it includes only eight examples (see Table 1). Of these, five of the central stars are cool and three are hot enough to produce He II emission. With such small numbers, the statistics are clearly not conclusive. While the cooler WR central stars are found in nebulae with a higher mean velocity than the rest of the planetary nebulae with cool central stars, the hotter WR central stars are found in nebulae with the same line widths as the rest of the sample of hotter central stars. Perhaps WR central stars are able to initiate the wind-driven phase of nebular acceleration earlier, but they may not necessarily afford greater acceleration in the long run. The planetary nebulae with normal central stars in our sample span a larger range in line width than do the expansion velocities observed in nebulae surrounding WR central stars by Medina et al. (2006). Resolving this issue will require a more careful, dedicated study.

Therefore, our observations of bright planetary nebulae in the Milky Way bulge confirm the kinematics predicted by theoretical models. It is notable not only that observations recover the sequence of nebular acceleration that is predicted, but also that these stages coincide with particular properties of the central stars. The details of the models differ considerably in parameters that are difficult to both observe and model, such as the structures within the AGB envelopes or the transition time between the AGB and planetary nebula stages.

6. CONCLUSIONS

We have obtained kinematic data for a large sample of planetary nebulae in the Milky Way bulge, selected with the goal of simulating samples of bright extragalactic planetary nebulae in bulgelike environments. For most of the sample, our criteria also included a reddening-corrected Hβ flux exceeding $\log F(\mathrm{H}\beta) > -12.0$ dex and [O III] λ5007/H$\beta > 6$, in addition to the usual criterion of projected proximity to the Galactic center. We measure line widths for Hα and [O III] λ5007. Our sample is the largest that has been selected and observed in a homogeneous way. We have also analyzed it in a completely model-independent manner.

For half of the sample, the He II λ6560 line is observed in the Hα spectra. Since this line appears only for hotter central stars, it allows us to divide our sample according to the evolutionary stage of the central star, with the more evolved objects found in the subsample containing the hotter central stars. The kinematics of the two samples are significantly different, with the sample containing the hotter central stars expanding faster. We also compare the diameters, electron densities (from [S II] $\lambda\lambda$6716, 6731), and Hβ luminosities for the two subsamples. In all cases, there are statistically significant differences. The planetary nebulae hosting the hotter central stars are larger, less dense, and less luminous than their counterparts with cooler central stars. All of these differences exceed a statistical significance of 99%. Also, all of these differences are compatible with the results of hydrodynamical models (e.g., Mellema 1994; Villaver et al. 2002; Perinotto et al. 2004).

Our primary conclusion is that we have clearly observed the acceleration of the nebular shells in planetary nebulae in the bulge of the Milky Way and that this occurs during the early evolution of their central stars. Our findings, based on a large, homogeneous sample, constitute the first unequivocal evidence that the nebular kinematics depend on the evolutionary state of the central star for planetary nebulae in the Milky Way and are far clearer and more convincing than any previous results. Hence, there is now very clear evidence that this dependence occurs in at least two environments: the Magellanic Clouds and the bulge of the Milky Way. Given the differences in the stellar populations in these two environments, it is likely that the dependence of the nebular kinematics on the evolutionary state of the central star is more general and that it occurs in all environments.

We thank the technical personnel at the OAN-SPM, and particularly Gabriel García, Gustavo Melgoza, Salvador Monrroy, and Felipe Montalvo, who were the telescope operators during our observing runs. Their excellent support was a great help in obtaining the data presented here. We thank S. Górny for kindly providing a list of classifications for the central stars of planetary nebulae toward the Galactic bulge. We acknowledge financial support throughout this project from CONACyT through grants 37214 and 43121 and from UNAM-DGAPA via grants IN112103, IN108406-2, IN108506-2, and IN116908-3. We thank the anonymous referee for a very constructive report that helped improve this manuscript.

REFERENCES

Aller, L. H., & Keyes, C. D. 1987, ApJS, 65, 405
Breitschwerdt, D., & Kahn, F. D. 1990, MNRAS, 244, 521
Chevalier, R. A. 1997, ApJ, 488, 263
Cuisinier, F., Acker, A., & Köppen, J. 1996, A&A, 307, 215
Cuisinier, F., Maciel, W. J., Köppen, J., Acker, A., & Stenholm, B. 2000, A&A, 353, 543
Dopita, M. A., Ford, H. C., Lawrence, C. J., & Webster, B. L. 1985, ApJ, 296, 390
Dopita, M. A., Meatheringham, S. J., Webster, B. L., & Ford, H. C. 1988, ApJ, 327, 639
Dudziak, G., Péquignot, D., Zijlstraa, A. A., & Walsh, J. R. 2000, A&A, 363, 717
Escudero, A. V., & Costa, R. D. D. 2001, A&A, 380, 300
Escudero, A. V., Costa, R. D. D., & Maciel, W. J. 2004, A&A, 414, 211
Exter, K. M., Barlow, M. J., & Walton, N. A. 2004, MNRAS, 349, 1291
García-Díaz, Ma. T., Henney, W. J., López, J. A., & Doi, T. 2008, Rev. Mex. AA, 44, 181
García-Segura, G., López, J. A., Steffen, W., Meaburn, J., & Manchado, A. 2006, ApJ, 646, 61
Gesicki, K., & Zijlstra, A. A. 2000, A&A, 358, 1058
Gesicki, K., Zijlstra, A. A., Acker, A., Górny, S. K., Godziewski, K., & Walsh, J. R. 2006, A&A, 451, 925
Gonçalves, D. R., Magrini, L., Leisy, P., & Corradi, R. L. M. 2007, MNRAS, 375, 715
Górny, S. K., Stasińska, G., Escudero, A. V., & Costa, R. D. D. 2004, A&A, 427, 231
Heap, S. R. 1993, in IAU Symp. 155, Planetary Nebulae, ed. R. Weinberger & A. Acker (Dordrecht: Reidel), 23
Jacoby, G. H., & Ciardullo, R. 1999, ApJ, 515, 169
Kahn, F. D., & Breitschwerdt, D. 1990, MNRAS, 242, 505
Kahn, F. D., & West, K. A. 1985, MNRAS, 212, 837
Kwok, S., Purton, C. R., & Fitzgerald, P. M. 1978, ApJ, 219, 125
Lang, K. R. 1980, Astrophysical Formulae (Berlin: Springer)
Lewis, B. M. 1991, AJ, 101, 254
Massey, P., Valdes, F., & Barnes, J. 1992, A User's Guide to Reducing Slit Spectra with IRAF, IRAF User Guide, Vol. 2B (Tucson: NOAO)
McCall, M. L., Rybski, P. M., & Shields, G. A. 1985, ApJS, 57, 1
Meaburn, J., Blundell, B., Carling, R., Gregory, D. F., Keir, D., & Wynne, C. G. 1984, MNRAS, 210, 463

Meaburn, J., López, J. A., Gutiérrez, L., Quiroz, F., Murillo, J. M., Valdéz, J., & Pedrayez, M. 2003, Rev. Mex. AA, 39, 185
Medina, S., Peña, M., Morisset, C., & Stasińska, G. 2006, Rev. Mex. AA, 42, 53
Mellema, G. 1994, A&A, 290, 915
Méndez, R. H., Thomas, D., Saglia, R. P., Maraston, C., Kudritski, R. P., & Bender, R. 2005, ApJ, 627, 767
Osterbrock, D. E. 1989, Astrophysics of Gaseous Nebulae and Active Galactic Nuclei (Mill Valley: University Science Books)
Perinotto, M., Schönberner, D., Steffen, M., & Calonaci, C. 2004, A&A, 414, 993
Ramstedt, S., Schöier, F. L., Olofsson, H., & Lundgren, A. A. 2006, A&A, 454, L103
Ratag, M. A., Pottasch, S. R., Dennefeld, M., & Menzies, J. 1997, A&AS, 126, 297
Richer, M. G., & McCall, M. L. 2008, ApJ, 684, 1190
Richer, M. G., Stasińska, G., & McCall, M. L. 1999, A&AS, 135, 203
Roth, M. M., Becker, T., Kelz, A., & Schmoll, J. 2004, ApJ, 603, 531
Rozas, M., Richer, M. G., Steffen, W., García-Segura, G., & López, J. A. 2007, A&A, 467, 603
Schönberner, D., Jacob, R., Steffen, M., & Sandin, C. 2007, A&A, 473, 467
Villaver, E., Manchado, A., & García-Segura, G. 2002, ApJ, 581, 1204
Wall, J. V., & Jenkins, C. R. 2003, Practical Statistics for Astronomers (Cambridge: Cambridge Univ. Press)
Walsh, J. R., Walton, N. A., Jacoby, G. H., & Peletier, R. F. 1999, A&A, 346, 753
Webster, B. L. 1988, MNRAS, 230, 377
Zijlstraa, A. A., Gesicki, K., Walsh, J. R., Péquignot, D., van Hoof, P. A. M., & Minniti, D. 2006, MNRAS, 369, 875

The Astrophysical Journal, 716:857–865, 2010 June 10 doi:10.1088/0004-637X/716/1/857

THE EVOLUTION OF THE KINEMATICS OF NEBULAR SHELLS IN PLANETARY NEBULAE IN THE MILKY WAY BULGE*

Michael G. Richer[1], José Alberto López[1], María Teresa García-Díaz[1], David M. Clark[1], Margarita Pereyra[1], and Enrique Díaz-Méndez[2]

[1] OAN, Instituto de Astronomía, Universidad Nacional Autónoma de México, P.O. Box 439027, San Diego, CA 92143, USA; richer@astrosen.unam.mx, jal@astrosen.unam.mx, tere@astrosen.unam.mx, dmclark@astrosen.unam.mx, mally@astrosen.unam.mx

[2] Department of Physics and Astronomy, Texas Christian University, Fort Worth, Texas 76109, USA; e.d.mendez@tcu.edu

Received 2010 January 30; accepted 2010 April 27; published 2010 May 21

ABSTRACT

We study the line widths in the [O III]λ5007 and Hα lines for two groups of planetary nebulae in the Milky Way bulge based upon spectroscopy obtained at the Observatorio Astronómico Nacional in the Sierra San Pedro Mártir (OAN-SPM) using the Manchester Echelle Spectrograph. The first sample includes objects early in their evolution, having high Hβ luminosities, but [O III]λ5007/Hβ < 3. The second sample comprises objects late in their evolution, with He II λ4686/Hβ > 0.5. These planetary nebulae represent evolutionary phases preceding and following those of the objects studied by Richer et al. in 2008. Our sample of planetary nebulae with weak [O III]λ5007 has a line width distribution similar to that of the expansion velocities of the envelopes of asymptotic giant branch stars and shifted to systematically lower values as compared to the less evolved objects studied by Richer et al. The sample with strong He II λ4686 has a line width distribution indistinguishable from that of the more evolved objects from Richer et al., but a distribution in angular size that is systematically larger and so they are clearly more evolved. These data and those of Richer et al. form a homogeneous sample from a single Galactic population of planetary nebulae, from the earliest evolutionary stages until the cessation of nuclear burning in the central star. They confirm the long-standing predictions of hydrodynamical models of planetary nebulae, where the kinematics of the nebular shell are driven by the evolution of the central star.

Key words: Galaxy: bulge – ISM: kinematics and dynamics – planetary nebulae: general – stars: evolution

Online-only material: color figures

1. INTRODUCTION

Hydrodynamical models of planetary nebulae have long predicted a particular kinematic evolution for the nebular shells, driven primarily by the evolution of the central stars (e.g., Kwok et al. 1978; Kahn & West 1985; Schmidt-Voigt & Köppen 1987a, 1987b; Breitschwerdt & Kahn 1990; Kahn & Breitschwerdt 1990; Marten & Schönberner 1991; Mellema 1994; Villaver et al. 2002; Perinotto et al. 2004; Schönberner et al. 2007). Initially, the central stars are cool and their winds relatively slow. This wind interacts with the wind that the precursor asymptotic giant branch (AGB) star emitted in a momentum-conserving mode (Kwok 1982). However, the central star's temperature and wind velocity increase rapidly, with the consequences that an ionization front is driven through the AGB envelope and the interaction between the two winds switches to an energy driven mode, and a hot bubble is created behind the shocked wind. The ionization front first accelerates the AGB envelope, now seen as the rim of the planetary nebula. In time, once the internal pressure of the hot bubble exceeds that of the nebular shell, it further accelerates the nebular shell. Theoretically, the latest phases of evolution are less clear, though the central star will cease nuclear energy generation, fade rapidly, and emit an ever-weaker wind, in principle, allowing the inner part of the nebular envelope to backfill into the central cavity (e.g., García-Segura et al. 2006).

Although the many extant observations of the kinematics of planetary nebulae all show expansion of the nebular shell, there are few systematic observations of how these shells acquire their motion and how it evolves with time. Dopita et al. (1985, 1988) were the first to provide observational support for the early acceleration of the nebular shell from studies of planetary nebulae in the Magellanic Clouds. Studies of Milky Way planetary nebulae provided much less convincing results (e.g., Chu et al. 1984; Heap 1993; Medina et al. 2006). Recently, Richer et al. (2008) demonstrated the acceleration of nebular shells in bright planetary nebulae in the Milky Way bulge during the early evolution of their central stars and were able to associate the acceleration seen in different evolutionary stages with the phases of acceleration expected from theoretical models.

Here, we undertake a study that complements Richer et al. (2008), selecting objects earlier and later in their evolution than they selected. The addition of these objects allows us to study the evolution of the kinematics of the nebular shell from the earliest stages of the planetary nebula phase until the cessation of nuclear burning in the central stars. In Section 2, we present our new data and their analysis. In Section 3, our results and their implications are outlined, the principal ones being that (1) the line widths in Hα and [O III]λ5007 are similar, (2) our sample of least evolved objects has a line width distribution shifted to the lowest values while the sample of most evolved objects has a size distribution with the largest sizes, and (3) the evolutionary state correlates with the Hβ luminosity. In Section 4, we summarize our conclusions.

2. OBSERVATIONS AND ANALYSIS

2.1. The Planetary Nebula Sample

Table 1 lists our two new samples of Bulge planetary nebulae. There are 24 objects in the sample with low [O III]λ5007/Hβ

* The observations reported herein were acquired at the Observatorio Astronómico Nacional in the Sierra San Pedro Mártir (OAN-SPM), B.C., Mexico.

Table 1
Bulge Planetary Nebula Sample

Object	PN G	Sample	Run	FWHM(Hα)[a] (Å)	$\Delta V_{0.5}$(Hα) (km s^{-1})	FWHM(5007)[a] (Å)	$\Delta V_{0.5}$(5007) (km s^{-1})	Hα Diameter[b] 10% I_{max}	L(Hβ) (erg s^{-1})
H 1–24	004.6+06.0	Weak 5007	2008jun	0.8783 ± 0.0044	11.22 ± 0.10	0.6288 ± 0.0081	17.54 ± 0.24	7.3	34.84
H 1–34	005.5+02.7	Weak 5007	2008jun	0.8168 ± 0.0072	12.31 ± 0.16	0.5422 ± 0.0077	14.88 ± 0.23	5.0	34.60
H 1–39	356.5−03.9	Weak 5007	2008jun	0.7737 ± 0.0019	11.31 ± 0.04	0.3343 ± 0.0030	7.77 ± 0.09	5.9	34.80
H 1–43	357.1−04.7	Weak 5007	2008jun	0.7230 ± 0.0030	10.82 ± 0.07			5.8	34.45
H 1–44	358.9−03.7	Weak 5007	2008jun	0.6198 ± 0.0022	5.37 ± 0.05	0.2950 ± 0.0028	6.19 ± 0.08	6.3	34.10
H 1–55	001.7−04.4	Weak 5007	2008jun	0.6369 ± 0.0014	6.30 ± 0.03	0.2939 ± 0.0047	6.18 ± 0.14	5.7	34.38
H 2–25	004.8+02.0	Weak 5007	2008jun	0.6923 ± 0.0023	2.37 ± 0.05	0.2747 ± 0.0087	4.79 ± 0.26	7.1	34.54
H 2–29	357.6−03.3	Weak 5007	2008jun	0.9433 ± 0.0062	15.28 ± 0.14			12.7	33.49
H 2–48	011.3−09.4	Weak 5007	2008jun	0.7564 ± 0.0012	9.45 ± 0.03	0.3293 ± 0.0015	7.42 ± 0.04	5.9	35.26
He 2–260	008.2+06.8	Weak 5007	2008jun	0.7031 ± 0.0012	6.48 ± 0.03	0.2903 ± 0.0035	5.91 ± 0.10	7.7	34.39
M 1–26	358.9−00.7	Weak 5007	2008jun	0.7352 ± 0.0023	10.13 ± 0.05	0.3477 ± 0.0031	8.23 ± 0.09	7.3	36.07
M 1–27	356.5−02.3	Weak 5007	2008jun	0.7270 ± 0.0018	10.43 ± 0.04			8.9	35.54
M 1–30	355.9−04.2	Weak 5007	2008jun	0.8701 ± 0.0029	14.10 ± 0.07	0.5549 ± 0.0058	15.32 ± 0.17	6.5	34.97
M 1–44	004.9−04.9	Weak 5007	2008jun	0.6746 ± 0.0030	8.13 ± 0.07			7.6	34.75
M 1–45	012.6−02.6	Weak 5007	2008jun	0.7768 ± 0.0028	12.15 ± 0.06			5.6	35.15
M 2–10	354.2+04.3	Weak 5007	2008jun	0.6916 ± 0.0010	9.00 ± 0.02	0.4007 ± 0.0024	10.21 ± 0.07	7.5	34.90
M 2–12	359.8+05.6	Weak 5007	2008jun	0.6136 ± 0.0011	4.81 ± 0.03	0.2955 ± 0.0447	6.13 ± 1.34	7.1	34.56
M 2–14	003.6+03.1	Weak 5007	2008jun	0.7703 ± 0.0038	11.30 ± 0.09	0.4426 ± 0.0048	11.63 ± 0.14	5.3	34.47
M 2–19	000.2−01.9	Weak 5007	2008jun	0.7534 ± 0.0022	10.59 ± 0.05	0.3885 ± 0.0036	9.73 ± 0.11	8.8	34.75
M 2–7	353.7+06.3	Weak 5007	2008jun	0.8499 ± 0.0026	14.13 ± 0.06	0.5337 ± 0.0035	14.61 ± 0.10	9.9	34.15
M 3–13	005.2+04.2	Weak 5007	2008jun	1.2876 ± 0.0282	26.20 ± 0.64	0.9708 ± 0.0556	28.38 ± 1.67	6.2	35.24
M 3–17	359.3−03.1	Weak 5007	2008jun	0.8316 ± 0.0020	13.47 ± 0.05	0.4159 ± 0.0051	10.70 ± 0.15	5.7	34.90
SwSt 1	001.5−06.7	Weak 5007	2008jun	0.9277 ± 0.0027	16.43 ± 0.06	0.5919 ± 0.0033	16.54 ± 0.10	4.6	35.03
Th 3–16	357.5−03.1	Weak 5007	2008jun	0.6639 ± 0.0017	7.10 ± 0.04			6.3	34.05
Al 1	006.8−08.6	Strong 4686	2008sep	1.2782 ± 0.0056	24.04 ± 0.17	0.7609 ± 0.0162	21.73 ± 0.49	13.0	34.12
Al 2-E	359.3+03.6	Strong 4686	2008sep	1.6281 ± 0.0246	33.31 ± 0.74	1.0817 ± 0.0283	31.66 ± 0.85	8.6	33.19
Al 2-H	357.2+01.4	Strong 4686	2008sep	1.0106 ± 0.0065	16.07 ± 0.19	0.7402 ± 0.0180	21.08 ± 0.54	9.3	
Al 2-I	359.5+02.6	Strong 4686	2008sep	1.1852 ± 0.0099	21.41 ± 0.30	0.9063 ± 0.0210	26.25 ± 0.63	6.6	
H 2–44	005.5−04.0	Strong 4686	2008sep	1.4812 ± 0.0266	29.51 ± 0.80	1.1545 ± 0.0395	33.89 ± 1.18	12.4	34.16
KFL 02		Strong 4686	2008sep	1.2658 ± 0.0102	23.70 ± 0.31	0.9265 ± 0.0169	26.89 ± 0.51	8.6	31.49
KFL 09		Strong 4686	2008sep	1.3491 ± 0.0240	25.99 ± 0.72	1.0010 ± 0.0259	29.18 ± 0.78	12.0	33.82
KFL 16	005.6−04.7	Strong 4686	2008sep	1.5910 ± 0.0254	32.36 ± 0.76	1.2402 ± 0.0450	36.51 ± 1.35	13.9	33.38
M 2–38	005.7−05.3	Strong 4686	2008sep	1.3917 ± 0.0185	27.95 ± 0.55	0.9841 ± 0.0315	28.71 ± 0.94	14.4	33.50
M 3–22	000.7−03.7	Strong 4686	2008sep	1.2684 ± 0.0125	23.70 ± 0.37	0.9609 ± 0.0250	27.94 ± 0.75	9.3	34.21
M 3–23	000.9−04.8	Strong 4686	2008sep	1.4720 ± 0.0291	29.27 ± 0.87	1.0804 ± 0.0538	31.62 ± 1.61	14.0	34.69
Pe 1–12	004.0−05.8	Strong 4686	2008sep	1.5601 ± 0.0428	31.84 ± 1.28	1.2239 ± 0.0589	36.03 ± 1.76	11.9	33.38
Pe 1–13	010.7−06.7	Strong 4686	2008sep	1.0811 ± 0.0059	18.42 ± 0.18			9.4	33.69
Pe 2–13	006.4−04.6	Strong 4686	2008sep	1.3648 ± 0.0129	26.42 ± 0.39			9.8	34.08
Sa 2-230	010.7+07.4	Strong 4686	2008sep	1.7239 ± 0.0576	35.74 ± 1.73	1.1654 ± 0.0490	34.23 ± 1.47	15.1	33.63
SB 15	009.3−06.5	Strong 4686	2008sep	1.2971 ± 0.0067	23.40 ± 0.20	0.9568 ± 0.0116	27.76 ± 0.35	8.5	32.76
SB 37	352.6−04.9	Strong 4686	2008sep	1.5842 ± 0.0175	32.18 ± 0.52	1.2002 ± 0.0297	35.29 ± 0.89	10.0	33.92
SB 38	352.7−08.4	Strong 4686	2008sep	1.4677 ± 0.0154	28.59 ± 0.46	1.1736 ± 0.0255	34.43 ± 0.76	14.0	32.18
SB 55	359.4−08.5	Strong 4686	2008sep	1.4107 ± 0.0356	25.56 ± 1.07	1.0770 ± 0.0490	31.41 ± 1.47	14.9	32.88
ShWi 2–1	001.4−03.4	Strong 4686	2008sep	1.0534 ± 0.0250	17.45 ± 0.75			11.8	33.60
Th 3–26	358.8+03.0	Strong 4686	2008sep	1.0768 ± 0.0090	20.97 ± 0.27	0.6937 ± 0.0103	19.78 ± 0.31	9.7	34.05
H 2–13	357.2+02.0	6560 Present	2008jun	0.9376 ± 0.0023	16.72 ± 0.05	0.5785 ± 0.0045	16.12 ± 0.13	6.0	34.47
H 2–43	003.4−04.8	6560 Absent	2008jun	1.9363 ± 0.0185	39.20 ± 0.42	1.7300 ± 0.0658	51.28 ± 1.97	4.6	34.88

Notes.
[a] This is the observed line width, uncorrected for instrumental, thermal, or fine structure broadening.
[b] The diameter was measured by collapsing the Hα spectra into one-dimensional spatial profiles and measuring the diameter at 10% of the maximum intensity.

ratios, all drawn from existing spectroscopic surveys (Aller & Keyes 1987; Webster 1988; Cuisinier et al. 1996, 2000; Ratag et al. 1997; Escudero & Costa 2001; Escudero et al. 2004; Exter et al. 2004; Górny et al. 2004). There are 21 objects in the sample with strong He II 4686, only some of which have extensive spectroscopy (see the previous references). Many of these objects were selected on the basis of the He II 4686 line intensity from Tylenda et al. (1994). Figure 1 explains the logic of the selection criteria for the two samples.

The sample with weak [O III]λ5007 comprises objects entirely excluded from Richer et al. (2008) and its selection criteria were (1) a position within 10° of the galactic center; (2) a large observed, reddening-corrected Hβ flux, nominally $\log I(\mathrm{H}\beta) > -12.0$ dex; and (3) an intensity ratio [O III]λ5007/Hβ < 3. Since even the less evolved objects from Richer et al. (2008) show the effects of acceleration of the nebular shell due to the passage of the ionization front, our last criterion should select objects that are significantly less evolved and thus probe the nebular kinematics at a stage that most closely reflects the kinematics of the undisturbed AGB envelope. The weak [O III]λ5007 sample should include bright, young planetary nebulae whose central stars are still relatively cool. All

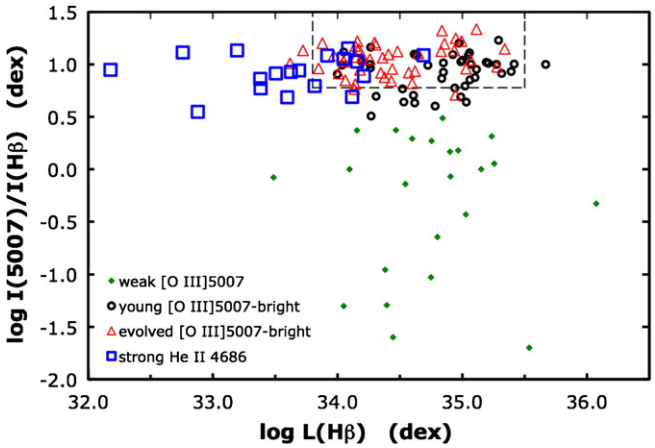

Figure 1. Selection criteria for the two samples of Bulge planetary nebulae presented here were designed to select planetary nebulae that are (1) less evolved and (2) more evolved than the sample studied by Richer et al. (2008). The area within the dotted box is approximately the area occupied by bright extragalactic planetary in stellar systems without ongoing star formation (Jacoby & Ciardullo 1999; Richer et al. 1999; Walsh et al. 1999; Dudziak et al. 2000; Roth et al. 2004; Méndez et al. 2005; Zijlstraa et al. 2006; Gonçalves et al. 2007; Richer & McCall 2008).

(A color version of this figure is available in the online journal.)

of the central stars should be on the horizontal part of their post-AGB evolutionary track.

The selection criteria for the "strong He II λ4686" sample were (1) a position within 10° of the galactic center and (2) an intensity ratio He II λ4686/Hβ > 0.5. There was no restriction on the Hβ flux. The second criterion should select a sample of objects biased to more advanced evolutionary phases than the more evolved objects included in Richer et al. (2008), since their requirement for their more evolved objects was equivalent to a ratio He II λ4686/Hβ > 0.09. This sample should include planetary nebulae whose central stars are at or slightly before their maximum temperature or fading toward the white dwarf cooling track.

2.2. Observations, Data Reduction, and Derived Parameters

We acquired the observations reported here and measured the derived properties in a very similar fashion to our previous observations (Richer et al. 2008). More details of our analysis may be found in Richer et al. (2008, 2009).

We obtained high-resolution spectra with the Manchester echelle spectrometer (MES–SPM; Meaburn et al. 1984, 2003) on 2008 June 1–2 and 10–17 and September 1–11 at the Observatorio Astronómico Nacional in the Sierra San Pedro Mártir, Baja California, Mexico (OAN-SPM). A 150 μm wide slit (1.″9 wide on the sky, 5′ long) yielded a spectral resolution equivalent to 11 km s^{-1} (2.6 pixels FWHM) and a spatial sampling of 0.″6 pixel^{-1} when coupled to an SITe 1024 × 1024 CCD with 24 μm pixels binned 2 × 2. We used a ThAr lamp for the wavelength calibration, which typically yielded an internal precision better than ±1.0 km s^{-1}.

We usually obtained a single deep spectrum in each of the [O III]λ5007 and Hα filters of, at most, 30 minutes duration. When possible, the exposure time for the Hα and [O III]λ5007 spectra was chosen to achieve similar signal levels. The slit was

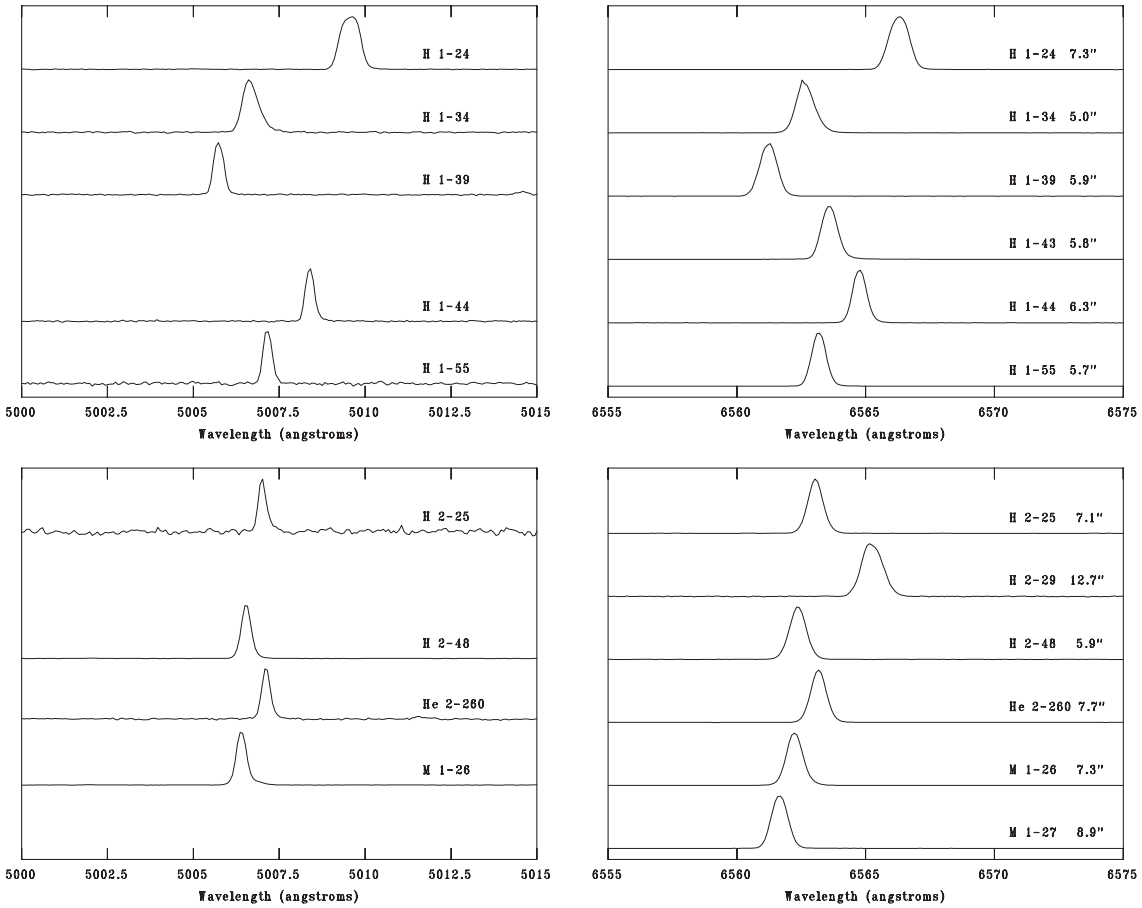

Figure 2. We present the line profiles in [O III]λ5007 and Hα for the sample of planetary nebulae with weak [O III]λ5007 lines. The wavelength interval plotted is always that indicated on the bottom panels. The number beside the name in the Hα panels is the angular diameter of the object at 10% of maximum intensity.

oriented north–south and, except for M 2–38, centered on the object. All of the planetary nebulae we observed are resolved (see Table 1).

The spectra were reduced using the twodspec and specred packages of the Image Reduction and Analysis Facility[3] (IRAF), following Massey et al. (1992, Appendix B). We edited the spectra to remove cosmic rays and subtracted a nightly mean bias image. We rectified the object spectra and calibrated them in wavelength using the ThAr spectra. Finally, wavelength-calibrated, one-dimensional spectra were extracted for each object. No flux calibration was performed. Figures 2–5 present the final, reduced spectra.

The single exception to the foregoing was M 2–38, for which two 30 minute Hα spectra were obtained at different positions. The two spectra were reduced as described above and the final one-dimensional spectra were summed to produce the final Hα spectrum.

We analyzed the one-dimensional spectra using a locally implemented software package (INTENS; McCall et al 1985). INTENS models the emission line with a sampled Gaussian function and models the continuum as a straight line. For the strong He II λ4686 sample, the Hα line was usually accompanied by the He II λ6560 line. In these cases, a fit was made simultaneously to both lines and the continuum, assuming that both lines had the same width.

Table 1 presents the observed line widths (FWHM) for each object in both Hα and [O III]λ5007. The formal uncertainties from fitting a Gaussian function with INTENS (1σ; Table 1) increase as the line width increases, a result of the line shape departing more from the Gaussian form at larger line widths (Richer et al. 2009). To obtain an idea of the real uncertainties, we measured the FWHM of the Hα line profiles directly (using implot/IRAF). For FWHM $<$ 1.2 Å, there is no systematic difference between the line width and the Gaussian fit, though there is a dispersion of approximately $\pm$5% of the line width. For larger line widths, the Gaussian fit systematically underestimates the line width, with the difference reaching 8%–9% of the line width at FWHM $\sim$ 2 Å.

We derive the true, intrinsic profile ($\sigma_{\rm true}$), resulting from the kinematics of the planetary nebula, by correcting the observed profile ($\sigma_{\rm obs}$) for instrumental ($\sigma_{\rm inst}$), thermal ($\sigma_{\rm th}$), and fine structure ($\sigma_{\rm fs}$) broadening:

$$\sigma^2_{\rm obs} = \sigma^2_{\rm true} + \sigma^2_{\rm inst} + \sigma^2_{\rm th} + \sigma^2_{\rm fs}. \quad (1)$$

We adopted an instrumental profile of FWHM of 2.6 pixels (measured: 2.5–2.7 pixels) for all objects. We use the usual formula (Lang 1980, Equation 2–243) to compute the thermal broadening, adopting rest wavelengths of 6562.83 Å and 5006.85 Å for Hα and [O III]λ5007, respectively, assuming no turbulent velocity, and adopting the observed electron temperature, when available (preferably from [O III] lines, but [N II] otherwise). If no electron temperature was available, we used the mean temperature for the other objects in each sample (weak [O III]λ5007 or high He II 4686). For the fine structure broadening (Meaburn 1970), we adopted $\sigma_{\rm fs} = 3.199$ km s^{-1} for Hα and zero for [O III]λ5007 (García-Díaz et al. 2008a).

For real, spatially resolved objects, the resulting line width, ΔV,

$$\Delta V = 2.3556\,\sigma_{\rm true}, \quad (2)$$

will be a luminosity-weighted, projected velocity width for the mass of the zone containing the emitting ion (O^{2+} or H^+) enclosed within the spectrograph slit. We adopt half of this intrinsic line width in velocity units

$$\Delta V_{0.5} = 0.5\Delta V = 1.1778\,\sigma_{\rm true} \quad (3)$$

as our measure of the kinematics for each object.

We obtain angular diameters (see Table 1) by collapsing the spectra along the wavelength axis to produce one-dimensional Hα spatial profiles and then measuring the diameter at 10% of the peak intensity (Richer et al. 2008). The uncertainty in the diameters is less than half a pixel (0.″3) for the sample with weak [O III]λ5007 and no more than a full pixel (0.″6) for the sample with strong He II 4686 (the Hα profiles contained at least 320,000 and 71,000 photons, respectively).

3. RESULTS AND DISCUSSION

We separate the Bulge planetary nebulae studied here and by Richer et al. (2008) into four evolutionary groups based upon the properties of the central star. The sample with weak [O III]λ5007 presented here has central stars whose temperatures are sufficiently low that only low ionization ions exist and so should be the least evolved. Then, we follow the younger [O III]λ5007 bright objects from Richer et al. (2008; He II λ6560 absent), with central stars that are hot enough to ionize O^+, but not O^{2+} or He^+. The central stars in both groups should be on the horizontal portion of their post-AGB evolutionary track in the H-R diagram. The evolved [O III]λ5007 bright objects from Richer et al. (2008; He II λ6560 present) and our sample with strong He II λ4686 have the hottest, most evolved central stars, with He^{2+} present to differing degrees. While we expect some overlap between the two groups, the strong He II λ4686 should be biased to later evolutionary stages (Section 2.1). These hotter central stars, particularly those with strong He II λ4686, may have extinguished nuclear reactions and be fading toward the white dwarf domain.

Had we assigned our planetary nebulae excitation classes instead of defining our four groups (e.g., Aller 1956; Gurzadyan 1988; Dopita & Meatheringham 1990; Reid & Parker 2010), there would be little difference in practice. Our weak [O III]λ5007, young and evolved [O III]λ5007 bright, and strong He II λ4686 groups correspond to very low, low-to-medium, medium-to-high, and high excitation classes, respectively. Thus, our separation into evolutionary groups should be adequate for our purposes.

3.1. Hα and [O III]λ5007 Line Widths

We present the relation between the line widths ($\Delta V_{0.5}$) in [O III]λ5007 and Hα in Figure 6. As has been found previously for bright Bulge planetary nebulae, there is a near equality between these line widths (Richer et al. 2009, 2010). The weak [O III]λ5007 data set extends this relation to smaller line widths while the sample with strong He II λ4686 is well mixed with previous data.

The tendency of finding systematically smaller line widths in [O III]λ5007 at the smallest Hα line widths in Figure 6 may be due to ionization stratification (e.g., Wilson 1950). Hydrodynamical models clearly predict that the innermost parts of the ionized shell expand more slowly than the majority of the matter during the earliest phases of a planetary nebula's evolution (Villaver et al. 2002; Perinotto et al. 2004) since the central star's wind is not fast enough to create a hot bubble.

[3] IRAF is distributed by the National Optical Astronomy Observatory, which is operated by the Association of Universities for Research in Astronomy, Inc., under cooperative agreement with the National Science Foundation.

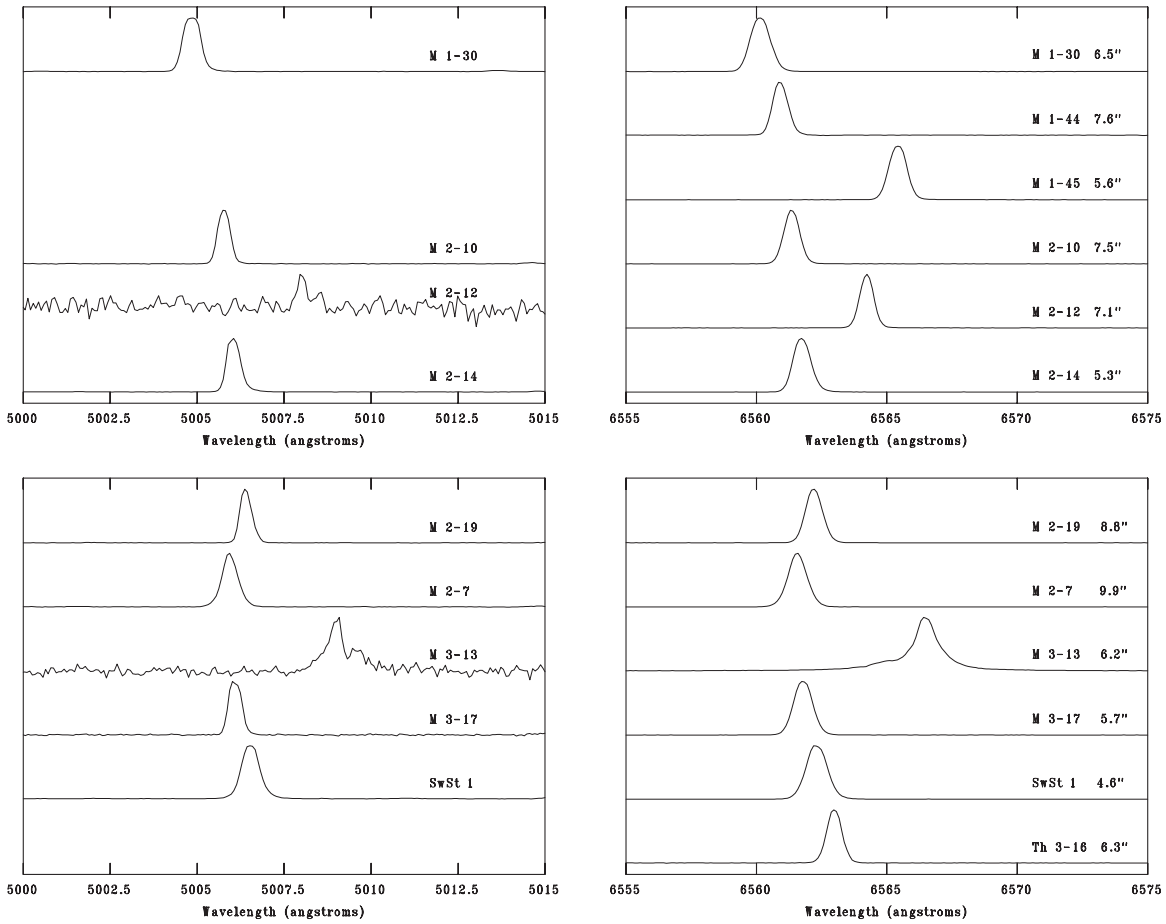

Figure 3. As in Figure 2, we present the line profiles for the sample of planetary nebulae with weak [O III]λ5007 lines. Note the very wide wings on the profiles for M 3–13.

The other feature in Figure 6 is the kink near Hα line widths of about 33 km s^{-1}. The objects that lie at higher velocities than the kink all have hot, evolved central stars. Presumably, the kink results from a drop in the projected outflow velocity in [O III]λ5007, since that would seem energetically more feasible near the time when the central star is running out of nuclear energy. Might the kink be the result of the loss of pressure from the central star's wind after nuclear reactions cease (collapse of the hot bubble, e.g., García-Segura et al. 2006; García-Díaz et al. 2008b)? Alternatively, the kink might also be produced via the passage of an He II ionization front (Figures 3 and 5; Schönberner et al. 2005a). Hydrodynamical models do not clearly predict this behavior (Villaver et al. 2002; Perinotto et al. 2004; Schönberner et al. 2005a, 2007). More observations and detailed modeling of individual objects will be required to understand the origin of the kink.

3.2. Evolution of the Nebular Kinematics

Figure 7 presents the line width distributions for the four groups of Bulge planetary nebulae. The sample with weak [O III]λ5007 clearly differentiates itself from the young [O III]λ5007 bright objects, which is the evolutionary phase following it. On the other hand, there is no noticeable difference between the kinematics of the evolved [O III]λ5007 bright objects and those with strong He II λ4686.

Statistical tests bear out these visual impressions. The nonparametric *U*-test (e.g., Wall & Jenkins 2003, Section 5.4.3) indicates that the probability of obtaining the line width distributions for the objects with weak [O III]λ5007 and the young [O III]λ5007 bright objects from the same parent distribution is only 1.0×10^{-4} when M 3–13 is included (the highest line width in the weak [O III]λ5007 sample) or 1.4×10^{-5} if it is excluded. Thus, the line width distributions for these two samples of objects are clearly different statistically. Not surprisingly, there is no statistical evidence for any difference in the line width distributions for the evolved [O III]λ5007 bright objects and those with strong He II λ4686.

The line width distribution for the sample with weak [O III]λ5007 (Figure 7) is very similar to the distribution of envelope expansion velocities in AGB stars (Lewis 1991; Ramstedt et al. 2006). This is exactly what hydrodynamical models suggest for the earliest stages of evolution of the nebular shell before the central star's wind has created a hot bubble (Villaver et al. 2002; Perinotto et al. 2004; Schönberner et al. 2005a, 2007). Thus, this group of objects contains planetary nebulae whose nebular shells have not yet been significantly accelerated by the passage of the ionization front and stellar winds. Richer et al. (2008) have already argued that the young and evolved samples of [O III]λ5007 bright objects have the line width distributions expected from hydrodynamical models if they correspond, respectively, to the phase when a well-developed ionization front has swept through the nebular shell and the phase when the hot bubble is actively accelerating the nebular shell.

The line width distributions for the two groups of most evolved planetary nebulae are indistinguishable. This implies

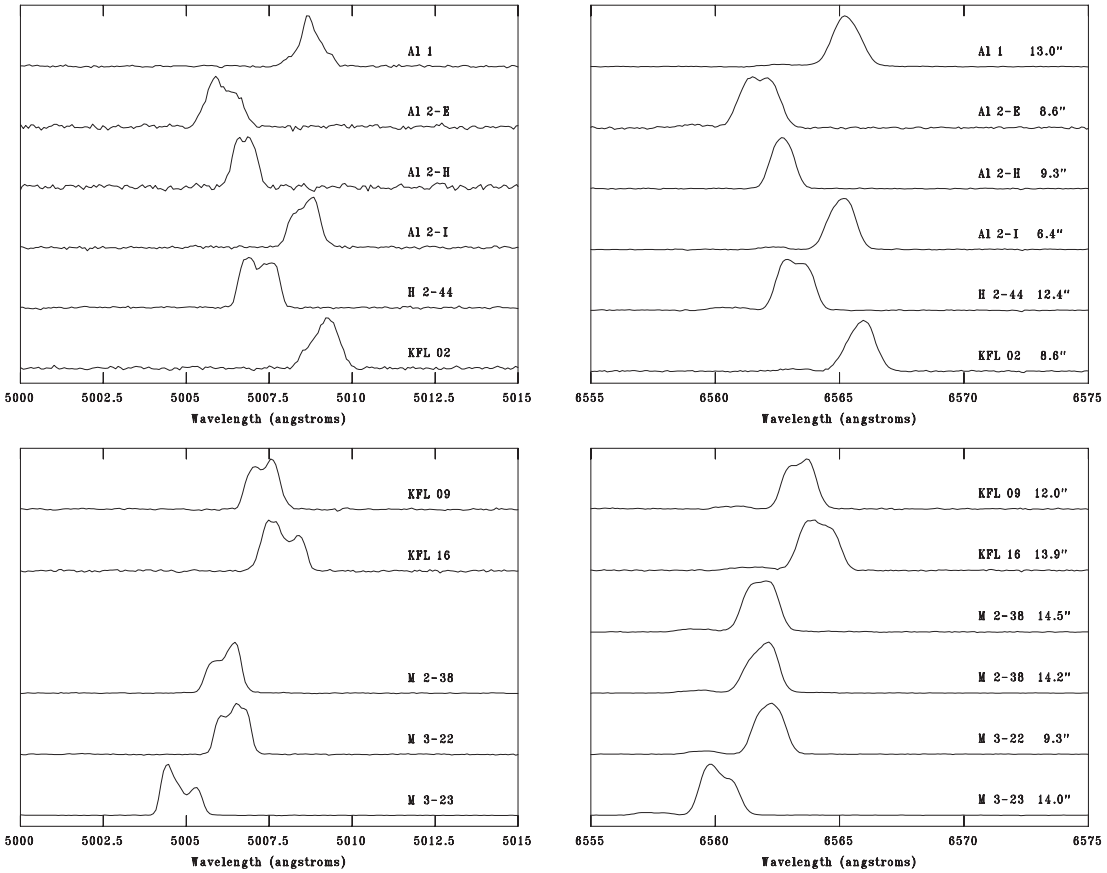

Figure 4. As in Figure 2, we present the line profiles for the sample of planetary nebulae with strong He II 4686 lines.

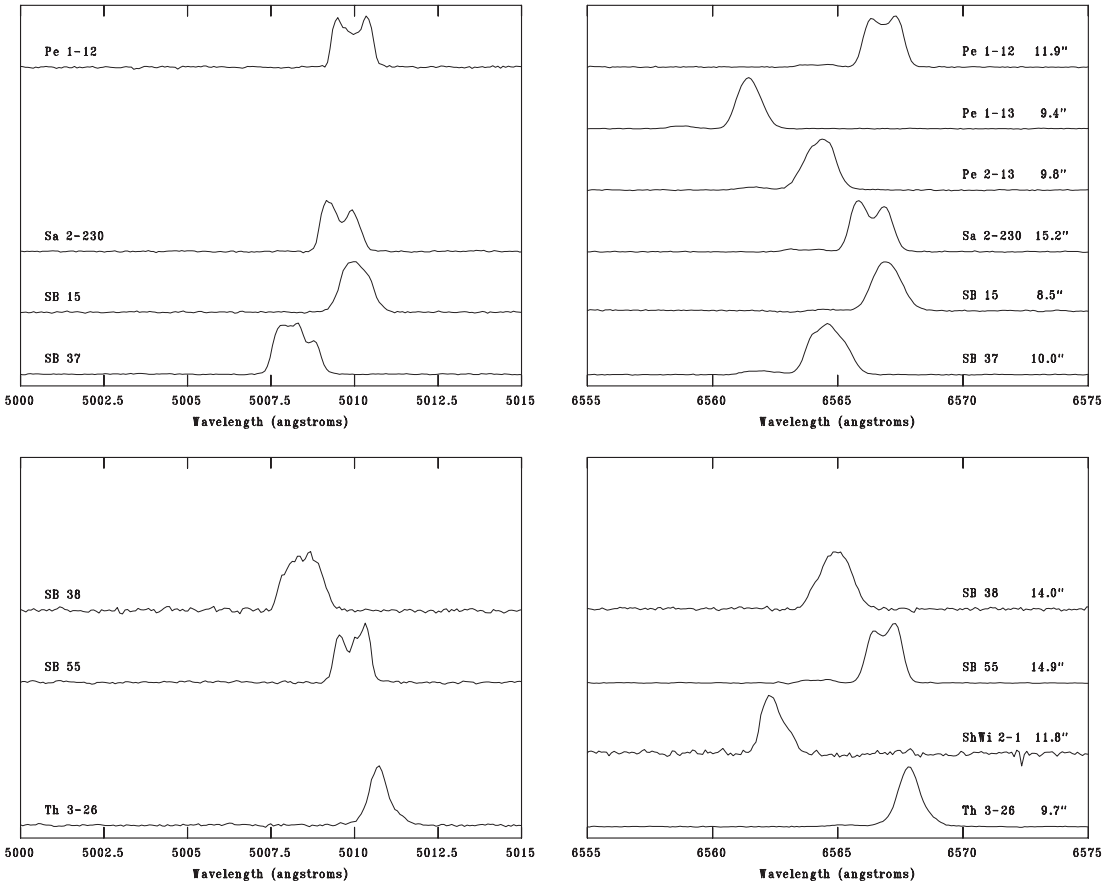

Figure 5. As in Figure 2, we present the line profiles for the sample of planetary nebulae with strong He II 4686 lines.

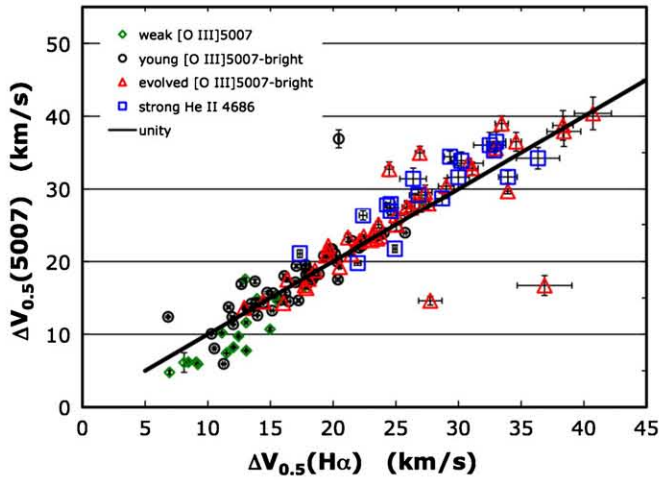

Figure 6. Intrinsic line width in [O III]λ5007 is plotted as a function of the intrinsic line width in Hα for the two samples presented here as well as the data from Richer et al. (2008). The intrinsic line widths are corrected for the instrumental resolution, fine structure broadening, and thermal broadening. The solid line indicates the locus of identical line widths in the two emission lines. The weak [O III]λ5007 sample extends the results of Richer et al. (2008) to lower line widths while the strong He II λ4686 sample is well mixed with their data. The error bars appear to fill many of the symbols for the objects in the samples with weak [O III]λ5007 and He II λ6560 absent.

(A color version of this figure is available in the online journal.)

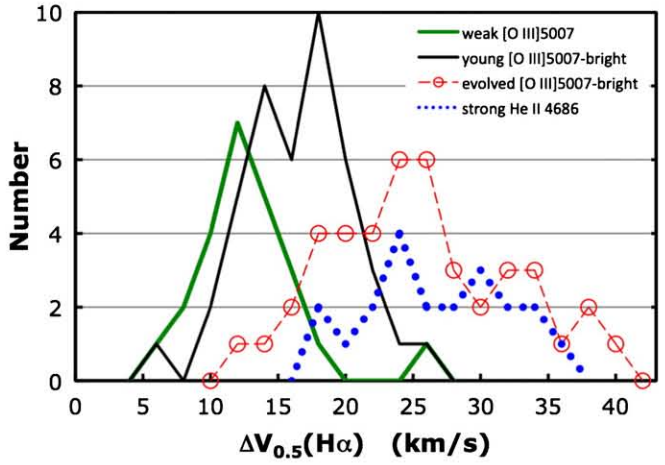

Figure 7. There is a very clear increase in the line width, progressing from planetary nebulae with weak [O III]λ5007 to the young and evolved [O III]λ5007 bright objects, clearly demonstrating that the nebular shells are accelerated throughout these phases. From the perspective of line widths, these three phases are statistically distinct. Planetary nebulae in the most evolved phase, with strong He II 4686 line intensities, have line widths very similar to the evolved [O III]λ5007 bright planetary nebulae. M 3–13 is the "anomalous" object with weak [O III]λ5007 and a line width of 26 km s^{-1} (see Figure 3). We correct the line widths from Richer et al. (2008) for thermal broadening using the observed electron temperature, instead of a constant value of 10^4 K. As a result, our histograms for those data differ.

(A color version of this figure is available in the online journal.)

that most of the nebular mass is not dramatically decelerated as the central star's luminosity decreases near the extinction of nuclear reactions, but continues expanding in a momentum-conserving mode.

3.3. Nebular Diameters

Figure 8 presents the distributions of angular diameters for the weak [O III]λ5007 and strong He II λ4686 samples as well as those studied by Richer et al. (2008). Although the sample

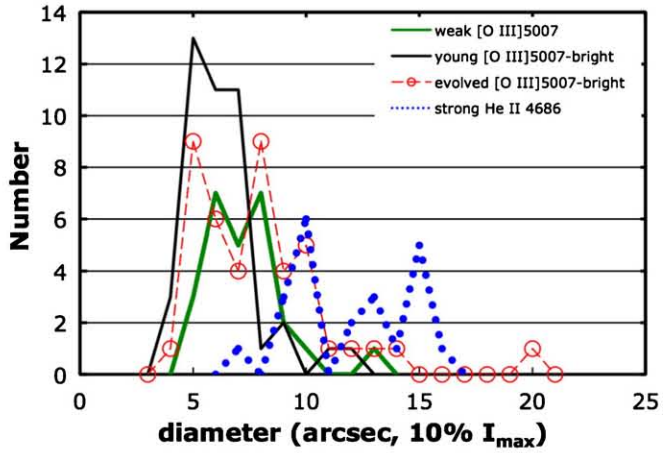

Figure 8. There is a clear increase in the diameters for the planetary nebulae in the young and evolved [O III]λ5007 bright and strong He II 4686 groups. The least evolved planetary nebulae, with weak [O III]λ5007, break this evolutionary sequence.

(A color version of this figure is available in the online journal.)

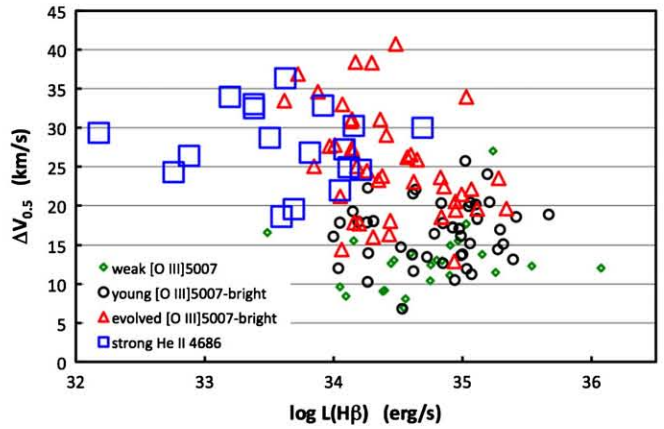

Figure 9. Line widths are plotted as a function of the Hβ luminosity for the four samples of Bulge planetary nebulae. A variety of effects are responsible for mixing the objects from different evolutionary stages.

(A color version of this figure is available in the online journal.)

with weak [O III]λ5007 is the least evolved, it does not have the smallest size distribution. Its distribution of angular diameters is statistically different from that for the young [O III]λ5007 bright objects, with the *U*-test indicating a probability of only 6.1×10^{-4} of drawing the two distributions from the same parent distribution.

On the other hand, the distribution of diameters for the strong He II λ4686 sample is clearly shifted to larger sizes compared to that for the evolved [O III]λ5007 bright objects. The *U*-test indicates that the probability of drawing the two distributions from the same parent population is 1.3×10^{-6}. Assuming that the two groups are at the same distance, the difference in the distributions of angular sizes also argues that the objects with He II λ4686 are the most evolved.

Hydrodynamical models might help explain these results. Models predict maximum Hβ luminosities when the [O III]λ5007 emission is strong (e.g., Schönberner et al. 2007). Our requirement that the weak [O III]λ5007 objects have high luminosity could cause us to preferentially select objects closer than the Bulge, which would make them appear larger. Also, models predict important structural changes during the early evolution, depending upon the relative importance of the

ionization front and hot bubble (e.g., Perinotto et al. 2004) that could affect the sizes we measure. Whatever the reason, a lack of a strong correlation between nebular diameter and evolutionary indicators has been obtained before (Chu et al. 1984; Gurzadyan 1997).

3.4. Hβ Luminosities

In Figure 9, we plot the line width as a function of Hβ luminosity for the four planetary nebula samples. Although the Hβ luminosities are not very accurate (Richer et al. 2008), there is a very clear progression as a function of evolutionary state, from the weak [O III]λ5007 sample, with the smallest line widths and high luminosities, through the young and evolved [O III]λ5007 bright objects to the strong He II λ4686 sample, which has large line widths and the faintest luminosities.

The mixing of objects from the different samples in Figures 1 and 6–9 is undoubtedly due to the different effects that can affect the expansion of the nebular shell. Although the range in masses of the progenitor stars is likely relatively small, given their ages, the range in metallicity is substantially larger (e.g., Sahu et al. 2006; Zoccali et al. 2008). At lower metallicity, the envelope expansion velocities for AGB stars are also lower (e.g., Wood et al. 1992; Marshall et al. 2004; Mattsson et al. 2008; Wachter et al. 2008; Groenewegen et al. 2009). On the other hand, hydrodynamical models find larger accelerations of the nebular shell at lower metallicity due to the higher electron temperature (Schönberner et al. 2005b). The progenitor mass should affect the nebular kinematics primarily via the central star mass and its strong influence upon the wind output and evolutionary time scale (e.g., Villaver et al. 2002; Perinotto et al. 2004). Considering that the nebular shells are not likely to always be spherical, projection effects will further affect the measured line widths. Thus, the dispersion seen in Figures 1 and 6–9 would seem plausible from natural causes.

4. CONCLUSIONS

We have obtained kinematic data for two samples of planetary nebulae in the Milky Way bulge, selected so as to include objects very early and late in their evolution (Section 2.1). We measure line widths for Hα and [O III]λ5007 in most cases. We combine these data sets with that studied by Richer et al. (2008). We define four evolutionary groups, based upon the temperature of the central star, which allow us to study the kinematics of the nebular shell from the earliest phases until the central star ceases nuclear burning.

Generally, we find a near equality of the line widths for the Hα and [O III]λ5007 lines in any given object. Ionization stratification likely accounts for the deviations: the [O III]λ5007 line widths are systematically smaller than the Hα line widths for the smallest and largest Hα line widths, corresponding to the earliest and latest evolutionary phases, respectively.

We see clear evolution of the kinematics of the nebular shell. The least evolved objects, our planetary nebulae with weak [O III]λ5007, have cool central stars and the nebular envelopes have a line width distribution similar to that of the envelope expansion velocities of AGB stars, indicating that the ionization front has not yet been able to substantially accelerate the nebular shell. In subsequent phases (Richer et al. 2008), the nebular shell is first accelerated by the passage of an ionization front and then further accelerated once the central star's wind produces a hot bubble. The line width distributions for the planetary nebulae in these three evolutionary phases are statistically distinct. The most evolved objects, with high He II λ4686 ratios, have a similar line width distribution to evolved [O III]λ5007 bright objects, suggesting that no further acceleration occurs as the central stars reach their highest temperatures, their nuclear reactions cease, and their winds decline.

This kinematic evolution of the nebular shell has long been predicted by hydrodynamical models (e.g., Kahn & West 1985; Marten & Schönberner 1991; Mellema 1994; Villaver et al. 2002; Perinotto et al. 2004). Our results, together with those of Richer et al. (2008), based upon a large sample of Galactic planetary nebulae from a single stellar population, clearly confirm these predictions. At least until the point at which nuclear reactions cease in the central stars, their ionizing fluxes and winds continuously accelerate the nebular envelopes. What happens thereafter is not yet completely clear and would require samples of planetary nebulae chosen specifically to contain hot central stars of low luminosity.

We thank the technical personnel at the OAN-SPM, particularly Gabriel García, Gustavo Melgoza, Salvador Monrroy, and Felipe Montalvo who were the telescope operators during our observing runs. Their excellent support was a great help in obtaining the data presented here. We acknowledge financial support throughout this project from CONACyT through grants 43121, 49447, and 82066 and from UNAM-DGAPA via grants IN108406-2 and IN116908-3. This research has made use of the SIMBAD database, operated at CDS, Strasbourg, France.

REFERENCES

Aller, L. H. 1956, Gaseous Nebulae (New York: Wiley)
Aller, L. H., & Keyes, C. D. 1987, ApJS, 65, 405
Breitschwerdt, D., & Kahn, F. D. 1990, MNRAS, 244, 521
Chu, Y.-H., Kwitter, K. B., Kaler, J. B., & Jacoby, G. H. 1984, PASP, 96, 598
Cuisinier, F., Acker, A., & Köppen, J. 1996, A&A, 307, 215
Cuisinier, F., Maciel, W. J., Köppen, J., Acker, A., & Stenholm, B. 2000, A&A, 353, 543
Dopita, M. A., Ford, H. C., Lawrence, C. J., & Webster, B. L. 1985, ApJ, 296, 390
Dopita, M. A., & Meatheringham, S. J. 1990, ApJ, 357, 140
Dopita, M. A., Meatheringham, S. J., Webster, B. L., & Ford, H. C. 1988, ApJ, 327, 639
Dudziak, G., Péquignot, D., Zijlstraa, A. A., & Walsh, J. R. 2000, A&A, 363, 717
Escudero, A. V., & Costa, R. D. D. 2001, A&A, 380, 300
Escudero, A. V., Costa, R. D. D., & Maciel, W. J. 2004, A&A, 414, 211
Exter, K. M., Barlow, M. J., & Walton, N. A. 2004, MNRAS, 349, 1291
García-Díaz, Ma. T., Henney, W. J., López, J. A., & Doi, T. 2008a, RevMexAA, 44, 181
García-Díaz, Ma. T., López, J. A., García-Segura, G., Richer, M. G., & Steffen, W. 2008b, ApJ, 676, 402
García-Segura, G., López, J. A., Steffen, W., Meaburn, J., & Manchado, A. 2006, ApJ, 646, 61
Gonçalves, D. R., Magrini, L., Leisy, P., & Corradi, R. L. M. 2007, MNRAS, 375, 715
Górny, S. K., Stasińska, G., Escudero, A. V., & Costa, R. D. D. 2004, A&A, 427, 231
Groenewegen, M. A. T., Sloan, G. C., Soszyński, I., & Petersen, E. A. 2009, A&A, 506, 1277
Gurzadyan, G. A. 1988, Ap&SS, 149, 343
Gurzadyan, G. A. 1997, The Physics and Dynamics of Planetary Nebulae (Berlin: Springer)
Heap, S. R. 1993, in IAU Symp. 155, Planetary Nebulae, ed. R. Weinberger & A. Acker (Dordrecht: Reidel), 23
Jacoby, G. H., & Ciardullo, R. 1999, ApJ, 515, 169
Kahn, F. D., & Breitschwerdt, D. 1990, MNRAS, 242, 505
Kahn, F. D., & West, K. A. 1985, MNRAS, 212, 837
Kwok, S. 1982, ApJ, 258, 280
Kwok, S., Purton, C. R., & Fitzgerald, P. M. 1978, ApJ, 219, 125

Lang, K. R. 1980, Astrophysical Formulae (Berlin: Springer)
Lewis, B. M. 1991, AJ, 101, 254
Marshall, J. R., van Loon, J. Th., Matsuura, M., Wood, P. R., Zijlstra, A. A., & Whitelock, P. A. 2004, MNRAS, 355, 1348
Marten, H., & Schönberner, D. 1991, A&A, 248, 590
Massey, P., Valdes, F., & Barnes, J. 1992, IRAF User Guide 2B, A User's Guide to Reducing Slit Spectra with IRAF (Tucson, AZ: National Optical Astronomy Observatory)
Mattsson, L., Wahlin, R., Höfner, S., & Eriksson, K. 2008, A&A, 484, L5
McCall, M. L., Rybski, P. M., & Shields, G. A. 1985, ApJS, 57, 1
Meaburn, J. 1970, Nature, 228, 44
Meaburn, J., Blundell, B., Carling, R., Gregory, D. F., Keir, D., & Wynne, C. G. 1984, MNRAS, 210, 463
Meaburn, J., López, J. A., Gutiérrez, L., Quiroz, F., Murillo, J. M., Valdéz, J., & Pedrayes, M. 2003, RevMexAA, 39, 185
Medina, S., Peña, M., Morisset, C., & Stasińska, G. 2006, RevMexAA, 42, 53
Mellema, G. 1994, A&A, 290, 915
Méndez, R. H., Thomas, D., Saglia, R. P., Maraston, C., Kudritski, R. P., & Bender, R. 2005, ApJ, 627, 767
Perinotto, M., Schönberner, D., Steffen, M., & Calonaci, C. 2004, A&A, 414, 993
Ramstedt, S., Schöier, F. L., Olofsson, H., & Lundgren, A. A. 2006, A&A, 454, L103
Ratag, M. A., Pottasch, S. R., Dennefeld, M., & Menzies, J. 1997, A&AS, 126, 297
Reid, W. A., & Parker, Q. A. 2010, PASA, in press, http://xxx.lanl.gov/abs/0911.3689
Richer, M. G., Báez, S.-H., López, J. A., Riesgo, H., & García-Díaz, Ma. T. 2009, RevMexAA, 45, 239
Richer, M. G., López, J. A., Pereyra, M., Riesgo, H., García-Díaz, M. T., & Báez, S.-H. 2008, ApJ, 689, 203
Richer, M. G., & McCall, M. L. 2008, ApJ, 684, 1190
Richer, M. G., Stasińska, G., & McCall, M. L. 1999, A&AS, 135, 203
Richer, M. G., et al. 2010, RevMexAA, in press
Roth, M. M., Becker, T., Kelz, A., & Schmoll, J. 2004, ApJ, 603, 531
Sahu, K. C., et al. 2006, Nature, 443, 534
Schmidt-Voigt, M., & Köppen, J. 1987a, A&A, 174, 211
Schmidt-Voigt, M., & Köppen, J. 1987b, A&A, 174, 223
Schönberner, D., Jacob, R., & Steffen, M. 2005a, A&A, 441, 573
Schönberner, D., Jacob, R., Steffen, M., & Roth, M. M. 2005b, in AIP Conf. Proc. 804, Planetary Nebulae as Astronomical Tools, ed. R. Szczerba, G. Stasińska, & S. Górny (New York: AIP), 269
Schönberner, D., Jacob, R., Steffen, M., & Sandin, C. 2007, A&A, 473, 467
Tylenda, R., Stasińska, G., Acker, A., & Stenholm, B. 1994, A&AS, 106, 559
Villaver, E., Manchado, A., & García-Segura, G. 2002, ApJ, 581, 1204
Wachter, A., Winters, J. M., Schröder, K.-P., & Sedlmayr, E. 2008, A&A, 486, 497
Wall, J. V., & Jenkins, C. R. 2003, Practical Statistics for Astronomers (Cambridge: Cambridge Univ. Press)
Walsh, J. R., Walton, N. A., Jacoby, G. H., & Peletier, R. F. 1999, A&A, 346, 753
Webster, B. L. 1988, MNRAS, 230, 377
Wilson, O. C. 1950, ApJ, 111, 279
Wood, P. R., Whiteoak, J. B., Hughes, S. M. G., Bessell, M. S., Gardner, F. F., & Hyland, A. R. 1992, ApJ, 397, 552
Zijlstraa, A. A., Gesicki, K., Walsh, J. R., Péquignot, D., van Hoof, P. A. M., & Minniti, D. 2006, MNRAS, 369, 875
Zoccali, M., Hill, V., Lecureur, A., Barbuy, B., Renzini, A., Minniti, D., Gómez, A., & Ortolani, S. 2008, A&A, 486, 177

Bibliography

Abell G.O. & Goldreich, P. 1966, *PASP*, **78**, 232

Ali, A., Sabil, L., Snaid, S. & Basurah, H.M. 2012, *A&A*, **541**, A98

Belczynski, K., Mikolajewska, J., Munari, U., Ivison, R. J. & Friedjung, M. 2000, *A&ASS*, **146**, 407

Bohuski T.J. & Smith, M.G. 1974, *ApJ*, **193**, 197

Borkowski, K.J., Sarazin, C.L., & Soker, N. 1990, *ApJ*, **360**, 173

Blöcker, T. 1995, *A&A*, **299**, 755

Cahn, J. H., Kaler, J. B. & Stanghellini, L. 1992, *A&AS*, **94**, 399

Cavichia, O., Costa, R. D. D., & Maciel, W. J. 2010, *RMxAA*, **46**, 159

Chevalier, R. A. 1997, *ApJ*, **488**, 263

Chu, Y.-H., Kwitter, K. B., Kaler, J. B. & Jacoby, G. H. 1984, *PASP*, **96**, 598

Corradi, R. L. M., Steffen, M., Schnberner, D. & R. Jacob 2007, *A&A*, **474**, 529

Costa R. D. D., Chiappini C., Maciel W.J. & de Freitas Pacheco, J. A. 1996, *A&A*, **116**, 249

Costa R. D. D., Uchida M. M. M., & Maciel W.J. 2004, *A&A*, **423**, 199

Curtis, H. D. 1918, *Publ. Lick Obs.*, Vol. ***XIII***, Part. III, p.57

Dickey, J. M., & Lockman, F. J. 1990, *ARA&A*, **28**, 215

Escudero A. V. & Costa R. D. D. 2001, *A&A*, 380, 300

Escudero A. V., Costa R. D. D. & Maciel W. J. 2004, *A&A*, 414, 211

Frew, D.J. 2008, *PhD Thesis, Macquarie University*

García-Díaz, M. T., López, J. A., Richer, M. G. & Steffen, W. 2006, *ApJ*, 676, 402

García-Segura, G., López, J. A., Steffen, W., Meaburn, J. & Manchado, A. 2006, *ApJ*, **646**, L61

Gesicki, K. & Zijlstra, A.A. 2000, *A&A*, 358, 1058

Górny S.K., Stasińska G., Escudero A. V. & Costa R. D. D. 2004, *A&A*, 427, 231

Henry R. B. C., Kwitter, K. B. & Balick B. 2004, *AJ*, 127, 2284

Henry R. B. C., Kwitter, K. B., Jaskot A. E., Balick B., Morrison M. A. & Millingo J. B. 2010, *ApJ*, 724, 748

Herwig, Falk 2005, *Annu. Rev. A&A*, **43**, 435

Hippelein, H. & Weinberger, R. 1990, *A&A*, **232**, 129

Henry J.W., Henry R. B. C. & McCartney S. 1997, *MNRAS*, 284, 465

Iben,I. 1984, *ApJ*, **277**, 333

Jacob, R., Schönberner, D., Lehmann, H., Zwanzing, A., Sandin, C. & Steffen, M. 2011, *IAU Sym.*, **283**, 400

Jacob, R., Schönberner, D. & Steffen, M. 2013, *A&A*, **558**, 78

Kahn, F. D. 1983, *IAU Sym.*, **103**, 305

Kaler, J.B., Shaw, R. A. & Kwitter, K.B. 1990, *ApJ*, **359**, 392

Kwok, S. 1982, *ApJ*, **258**, 280

Kwok, S. 2000, *¨The origin and evolution of Planetary Nebulae"* Cambridge AstroPhysics, Series **31**

Lee, Hee-Won 2000 *ApJ*, **541**, L25

López, J. A., Richer, M. G., García-Díaz, Ma. T., Clark, D. M. , Meaburn, J. , Riesgo, H., Steffen, W. & Lloyd, M. 2012, *Rev. Mexicana AyA* **48**, 3

Meaburn, J., Boumis, P., López, J. A., Harman, D. J., Bryce, M., Redman, M. P. & Mavromatakis, F. 2005, *MNRAS*, **360**, 963

Meaburn, J., Blundell, B., Carling, R., Gregory, D. F., Keir, D., & Wynne, C. G. 1984, *MNRAS*, **210**, 463

Meaburn, J., López, J. A., Gutiérrez, L., Quiróz, F., Murillo, J. M., Valdéz, J., & Pedrayez, M. 2003, *RevMexAA*, **39**, 185

Medina, S. & Peña, M. 2003, *IAU Sym.*, **209**, 545

Medina, S., Peña, M., Morisset, C. & Stasińska, G. 2006, *Rev. Mexicana AyA*, **42**, 53

Meléndez J. & Asplund M. 2008, *A&A*, **490**, 817

Mellema, G. 1994, *A&A*, **209**, 915

Miszalski, B., Mikolajewska, J. & Udalski, A. 2013, *MNRAS*, **432**, 3186

Montez, R., Jr., De Marco, O., Kastner, J. H., & Chu, Y.-H. 2010 *ApJ*, **721**, 1820

Oey, M. S. & García-Segura, G. 2004, *ApJ*, **613**, 302

Paczyński, B. 1971, *Acta Astr.*, **21**, 417

Patriarchi, P. & Perinotto, M. 1991, *A&AS*, 91, 325

Peimbert, M. 1971, *BOTT*, **6**, 101

Peimbert, M. 1990, *Reports on Progress in Physics*, **53**, 1559

Peña, M., Torres-Peimbert, S. & Ruiz, M. T. 1992, *A&A*, **265**, 757

Peña, M., Medina, S. & Stasinńska, G. 2003, *RevMexAA(SC)*, **15**, 38

Peña, M., Stasinńska, G. & Richer M. G. 2007, *A&A*, **476**, 745

Pereira C. B. & Miranda L. F. 2007, *A&A*, **467**, 1249

Pereyra M., Richer, M.G., & López, J.A. 2013, *ApJ*, **771**, 114

Perinotto, M., Schönberner, D., Steffen, M. & Calonaci, C. 2004, *A&A*, **414**, 993

Phillips, J. P. 2002, *A&A*, **393**, 1027

Ratag M.A., Pottasch S. R., Dennefeld M. & Menzies J. 1997, *A&A*, **126**, 297

Richer, M., McCall, M. L., & Stasińska, G. 1998, *A&A*, **340**, 67

Richer, M. G., López, J. A., Pereyra, M., Riesgo, H. & García-Díaz, Ma. T. 2008, *ApJ*, **689**, 203

Richer, M. G., López, J. A., García-Díaz, Ma. T., Clark, D. M. , Pereyra, M. & Díaz-Méndez E. 2010, *ApJ*, **716**, 857

Richer, M. G.,López, J. A., Díaz-Méndez, E., et al. 2010, *RMxAA*, **46**, 191

Schönberner, D. 1979, *A&A*, **79**, 108

Schönberner, D. 1981, *A&A*, **103**, 119

Schönberner D. & Blöcker T. 1996, *Ap&SS*, **245**, 201

Schönberner, D., Jacob, R., Steffen, M., Perinotto, M., Corradi, R. L. M., & Acker, A. 2005, *A&A*, **431**, 963

Schönberner, D., Jacob, R. & Steffen, M. 2005, *A&A*, **441**, 573

Schönberner, D., Jacob, R., Sandin, C. & Steffen, M. 2010, *A&A*, **523**, A86

Shklovsky, I. 1956, *Astr. Zh.*, **33**, 315

Stanghellini L. & Renzini L. 2000, *ApJ*, **542**, 308

Stanghellini L., Villaver E., Manchado A. & Guerrero M.A. 2002, *ApJ*, **576**, 285

Stanghellini L. & Haywood M. 2010, *ApJ*, **714**, 1096

Stasińska G., Morisset C., Tovmassian G., Rauch T., Richer M. G., Pea M., Szczerba R., Decressin T., Charbonnel C., Yungelson L., Napiwotzki R., Simn-Daz S., and Jamet L. 2010 *A&A*, 511, A44

Steffen M. & Schönberner D. 2006, *IAU Sym.*, **234**, 285

Tovmassian G., Yungelson L., Rauch T., Suleimanov V., Napiwotzki R., Stasińska G., Tomsick J., Wilms J., Morisset C., Pea M. and Richer M. G. 2010, *ApJ*, **714**, 178

Tylenda, R., Stasińka, G., Acker, A. & Stenholm, B. 1994, *A&AS*, **106**, 559

Tweedy, R. W., & Kwitter, K. B. 1994, *AJ*, **108**, 188

Vassiliadis, E. & Wood, P.R. 1994, *ApJS*, **92**, 125

Villaver, E., García-Segura, G., Manchado, A. 2002a, *ApJ*, **571**, 880

Villaver, E., Manchado, A. & Garía-Segura G. 2002, *ApJ*, **581**, 1204

Villaver, E., Garía-Segura G. & Manchado, A. 2003, *ApJ*, **585**, L49

Wall, J. V., & Jenkins, C. R. 2003, *Practical Statistics for Astronomers* (Cambridge University Press: Cambridge, UK)

Wareing, C.J., Zijlstra, A. A. & O'Brien, T. J. 2007, *MNRAS*, **382**, 1233

Wood, P.R. & Faulkner, D. J. 1986, *ApJ*, **307**, 659